



HAL
open science

Coherent dating of deep polar ice cores and implications for understanding climate mechanisms

Marie Bouchet

► **To cite this version:**

Marie Bouchet. Coherent dating of deep polar ice cores and implications for understanding climate mechanisms. *Climatology*. Université Paris-Saclay, 2024. English. NNT : 2024UPASJ020 . tel-04767332

HAL Id: tel-04767332

<https://theses.hal.science/tel-04767332v1>

Submitted on 5 Nov 2024

HAL is a multi-disciplinary open access archive for the deposit and dissemination of scientific research documents, whether they are published or not. The documents may come from teaching and research institutions in France or abroad, or from public or private research centers.

L'archive ouverte pluridisciplinaire **HAL**, est destinée au dépôt et à la diffusion de documents scientifiques de niveau recherche, publiés ou non, émanant des établissements d'enseignement et de recherche français ou étrangers, des laboratoires publics ou privés.

Coherent dating of deep polar ice cores and implications for understanding climate mechanisms

*Datation fédérative des forages polaires profonds et implications sur la
compréhension des mécanismes climatiques*

Thèse de doctorat de l'université Paris-Saclay

École doctorale n° 129 : Sciences de l'environnement d'Île-de-France (SEIF)

Spécialité de doctorat : Géosciences

Graduate school : Géosciences, climat, environnement et planètes

Réfèrent : Université de Versailles-Saint-Quentin-en-Yvelines

Thèse préparée dans les unités de recherche :

LSCE (Université Paris-Saclay, CNRS, CEA, UVSQ) et **IGE** (Université Grenoble-Alpes,
CNRS, CEA, INRAE, IRD)

Sous la direction d'**Amaëlle Landais**, directrice de recherche, et la co-direction de
Frédéric Parrenin, directeur de recherche

Thèse soutenue à Paris-Saclay, le 4 Octobre 2024, par

Marie BOUCHET

Composition du Jury

Membres du jury avec voix délibérative

Sébastien NOMADE

Directeur de recherche, LSCE (CEA)

Président

Barbara DELMONTE

Professeure, Université de Milan

Rapporteur & Examinatrice

François FRIPIAT

Professeur, Université Libre de
Bruxelles

Rapporteur & Examinateur

Claire WAELBROECK

Directrice de recherche, LOCEAN
(CNRS)

Examinatrice

Titre : Datation fédérative des forages polaires profonds et implications sur la compréhension des mécanismes climatiques

Mots clés : paléoclimat, forages glaciaires, chronologie, traceurs climatiques, déglaciations

Résumé : Les données paléoclimatiques fournissent des estimations empiriques des changements climatiques pré-anthropiques à des échelles de temps variées. Elles ont documenté des réchauffements globaux de la Terre (+5 à 10°C) se déroulant sur des milliers d'années tous les ~100 000 ans au cours du dernier million d'années, les déglaciations. Ces transitions sont particulièrement intéressantes pour les projections climatiques, car elles permettent d'estimer le taux de fonte des calottes glaciaires. Les données paléoclimatiques témoignent aussi d'événements plus rapides (quelques décennies), les "points de bascule", qui indiquent que le système climatique peut être déstabilisé significativement. Les forages polaires sont uniques car ils fournissent une mesure directe de la composition atmosphérique passée et permettent la reconstruction du climat local. Mon doctorat s'est concentré sur le forage EPICA Dome C (EDC) en Antarctique de l'Est, qui fournit le plus long enregistrement continu à ce jour. Il documente les changements climatiques qui se sont produits à l'échelle de quelques décennies à plusieurs milliers d'années au cours des derniers 800 000 ans.

Alors que les isotopes de l'eau mesurés dans les archives glaciaires sont classiquement utilisés pour déduire les variations passées de la température et de précipitation locales, nous montrons que le $\delta^{15}\text{N}$ de N_2 mesuré dans les bulles d'air piégées dans la glace peut être utilisé de façon complémentaire. En effet, le $\delta^{15}\text{N}$ de N_2 reflète la profondeur de piégeage des bulles dans la glace, elle-même déterminée par la température et le taux d'accumulation de neige à la surface. Un nouvel enregistrement de $\delta^{15}\text{N}$ de N_2 est présenté. Il permet d'identifier précisément le phasage entre le CO_2 atmosphérique et le climat de l'Antarctique au cours des huit dernières déglaciations.

Deuxièmement, j'ai développé une chronologie cohérente pour quatre forages situés en Antarctique et un forage au Groënland, couvrant les 800 000 dernières années. Cette chronologie a été construite à l'aide du modèle probabiliste Paleochrono-1.1 et est contrainte par de nouvelles mesures faites sur le forage EDC et par des données issues de modélisation glaciologique. L'incertitude de l'échelle d'âge d'EDC est réduite de 1700 à 900 ans en moyenne. La chronologie révisée est en meilleur accord avec des chronologies absolues obtenues de manière indépendante pour d'autres paléo-archives. Enfin, une méthodologie est proposée pour construire des chronologies cohérentes, relatives et absolues pour les archives marines et glaciaires au cours des sept dernières déglaciations. Elle permet d'identifier de manière plus précise l'ordre dans lequel se produisent les changements relatifs de l'insolation, de concentration atmosphérique en gaz à effet de serre, du niveau de la mer et des températures régionales lors des déglaciations. Dans une étude préliminaire, nous avons identifié une avance de quelques milliers d'années du CO_2 sur le niveau marin lors des déglaciations. Des perspectives de recherche sont proposées pour atteindre une meilleure compréhension des relations de cause à effet entre le forçage externe et la réponse interne du climat. Mon travail de thèse a combiné la modélisation glaciologique et statistique, l'analyse expérimentale de l'air piégé dans la carotte de glace EDC ainsi que l'analyse de données paléoclimatiques issues d'archives polaires, de carottes sédimentaires marines et de spéléothèmes. Mes recherches contribuent à l'amélioration (i) des reconstructions climatiques à partir des forages polaires et (ii) des chronologies des forages polaires et marins. Ces avancées sont essentielles pour mieux comprendre la réponse du climat à un forçage externe lors des changements climatiques de grande amplitude, ce qui est essentiel pour prévoir les changements climatiques à venir.

Title: Coherent dating of deep polar ice cores and implications for understanding climate mechanisms

Keywords: paleoclimate, ice cores, chronology, climatic tracers, deglaciations

Abstract: It is possible to gain insights from past climate natural variability in order to constrain the response of the climate system to change in the external forcing and future projections. Paleoclimate data provide empirical estimates of pre-anthropogenic large-scale climate change across a range of timescales, including the long timescales (several thousand years) associated with the glacial-interglacial transitions of great amplitude that affected Earth's climate every ~100 thousand years over the past million years. This is of particular interest for climatic projections, as it may allow for the estimation of the rate of ice cap melting. Furthermore, paleoclimate data can be employed to investigate "tipping point" events, which show the potential for rapid (over a few decades) and significant instabilities in the climate system. Among the paleo archives, deep polar ice cores are distinctive in that they offer direct records of ancient global atmospheric composition in greenhouse gases and documented past local changes in snowfall and temperature. My PhD focused on the EPICA Dome C (EDC) drilling site in East Antarctica which provides the oldest continuous ice core record so far. It documents climate change that occurred over a wide range of timescales (from a few decades to several thousands of years) over the past 800,000 years.

While water isotopes are classically used to infer past temperature and accumulation rate when measured in ice cores, we show that $\delta^{15}\text{N}$ of N_2 measured in air bubbles trapped in ice core can be a complementary tool. $\delta^{15}\text{N}$ of N_2 indeed reflects the depth of bubble enclosure in the ice sheet, itself driven by surface temperature and snow accumulation rate at surface. A new record of $\delta^{15}\text{N}$ of N_2 over the last 800 kyr is presented and provides an accurate identification of the lead-lag relationship between atmospheric CO_2 and Antarctic climate over deglaciations.

Secondly, I developed a precise, coherent timescale for five deep polar ice cores, spanning the past 800,000 years, known as the Antarctic Ice Core Chronology (AICC) 2023. This timescale is built using the probabilistic dating model PaleoChrono-1.1 and constrained by new EDC measurements and glaciological modeling outputs. This permitted to reduce the average uncertainty of the EDC age scale from 1,700 to 900 years. The revised chronology aligns better with independent and absolute chronologies of other paleo archives.

Furthermore, we proposed a methodology for constructing coherent, relative, and absolute chronologies for marine and glacial archives over past glacial-interglacial cycles. Evaluating the sensitivity of the coherent chronology to dating methodologies produced robust error bars, aiding in the precise identification of climatic event sequences (e.g. relative timing of changes in insolation, atmospheric greenhouse gases, global sea level, and regional temperatures) during glacial-interglacial transitions. In a preliminary study, we identify a few-year lead of atmospheric CO_2 with respect to sea level in six of the seven latest deglaciations. Further research is needed to study the implications of such chronologies to understand the causal relationships between external forcing and the climate's internal response.

My approach combined glaciological and statistical modeling with an experimental analysis of air trapped in EDC ice core and a data analysis of various paleo records from polar ice cores, marine sedimentary cores and speleothems. My research contributes significantly to improving climate reconstructions from ice cores, reducing dating uncertainties, and developing coherent chronological frameworks. These advancements enhance our understanding of the climate's response to an external forcing and of the interactions between different Earth System components during glacial-interglacial transitions.

TABLE OF CONTENTS

RÉSUMÉ	2
ABSTRACT	3
TABLE OF CONTENTS.....	4
REMERCIEMENTS.....	8
TABLE OF ABBREVIATIONS.....	12
FOREWORD.....	13
1 CHAPTER 1.....	16
INTRODUCTION TO PAST CLIMATE DYNAMICS AND ARCHIVES – CONTEXT AND OBJECTIVES OF THE PHD	16
1.1 MODERN CLIMATE OF THE EARTH.....	17
1.1.1 Spatial and seasonal variability	17
1.1.1.1 Solar energy	17
1.1.1.2 Atmosphere.....	18
1.1.1.3 The spherical shape of the Earth and inclination of its rotation axis.....	19
1.1.1.4 Internal distribution of energy.....	20
1.1.2 The energy budget at the Earth’s surface.....	23
1.1.2.1 External forcing	24
1.1.2.2 Internal processes and feedback parameters.....	26
1.1.3 Climate system modeling.....	26
1.2 THE PAST HISTORY OF EARTH’S CLIMATE.....	28
1.2.1 Over the past 70 million years: global cooling trend and emergence of large ice caps	28
1.2.2 Focus on the past 2.6 million years: the glacial-interglacial dynamics of the Quaternary period 30	
1.2.2.1 Paleorecords archives of the Quaternary period.....	31
1.2.2.2 Pacing of the Quaternary glacial-interglacial variability.....	37
1.2.2.2.1 Orbital forcing: the theory of Milankovitch.....	37
1.2.2.2.2 The role of internal processes and feedback parameters in the warming of the Southern Hemisphere	39
1.2.2.2.3 Factors favoring the glacial inception and glacial Termination	42
1.2.2.3 Millennial-scale climate variability.....	42
1.2.2.3.1 Climatic records.....	43
1.2.2.3.2 Glacial millennial variability mechanisms	45
1.2.2.3.3 Implications of understanding mechanisms involved in DO-Heinrich events to refine understanding of mechanisms involved in the deglaciations	50
1.3 CONTEXT, OBJECTIVES AND METHODS OF THE PHD.....	53
1.3.1 Context	53
1.3.2 Objectives.....	53
1.3.3 Methods and research directions	54
2 CHAPTER 2.....	55
RECONSTRUCTING CLIMATE HISTORY USING DEEP POLAR ICE CORES: ANALYSIS AND DATING METHODS.....	55
2.1 ON THE RECONSTRUCTION OF PAST CHANGES IN LOCAL TEMPERATURE AND PRECIPITATION USING ICE CORE RECORDS	57
2.1.1 Stable isotopes definition.....	57
2.1.2 Isotope fractionation processes	57

2.1.3	Climatic reconstruction based on water stable isotopes	59
2.1.3.1	δD and $\delta^{18}O$ in the hydrosphere	59
2.1.3.2	Isotopic composition of water molecules from evaporation to deposition in Antarctica.....	60
2.1.3.3	The global and local meteoric water lines	62
2.1.3.4	The isotopic thermometer	62
2.1.3.5	Other factors affecting water isotopic records in ice cores	65
2.1.3.6	Local snow accumulation rate inferred from local temperature.....	67
2.2	FROM THE TRAPPING OF ATMOSPHERIC AIR IN ICE TO ITS EXTRACTION AND ANALYSIS IN THE LABORATORY.....	69
2.2.1	Snow accumulation, densification and transformation to ice	69
2.2.1.1	The firn.....	69
2.2.2	Isotopic fractionation occurring in the firn	70
2.2.2.1	Gravitational fractionation	71
2.2.2.2	Thermal fractionation	71
2.2.3	Firn densification modeling.....	72
2.2.3.1	Model description.....	72
2.2.3.2	The relationship between the densification speed and local climate via the overburden pressure.....	73
2.2.3.3	The GOUJON configuration of the IGE model	74
2.2.3.4	The BREANT configuration of the IGE model	75
2.2.3.5	Snow metamorphism in the top two meters	77
2.2.4	Interesting elemental and isotopic ratios.....	77
2.2.4.1	$\delta^{15}N$ of N_2	78
2.2.4.2	$\delta^{18}O$ of O_2	80
2.2.4.3	The $\delta O_2/N_2$	80
2.2.4.4	The radioisotope ^{81}Kr	81
2.2.5	Analytical methods.....	82
2.2.5.1	$\delta^{15}N$ measurements.....	82
2.2.5.2	^{81}Kr measurements.....	86
2.3	DATING ICE CORES.....	89
2.3.1	Dating techniques using measurements in the ice phase.....	89
2.3.2	Dating techniques using measurements in the gas phase	92
2.3.3	Synchronization to other archives	93
2.3.4	Orbital dating.....	94
2.3.5	Sedimentation modeling	96
2.3.6	The inverse method: a federative approach.....	97
2.3.7	Conclusion	98
3	CHAPTER 3	100
	DOCUMENTING PAST CHANGES IN TEMPERATURE AND SNOWFALL USING ^{15}N MEASUREMENTS IN AIR TRAPPED IN EAST ANTARCTIC ICE CORES.....	100
3.1	MOTIVATION.....	102
3.2	DOCUMENTING PAST CHANGES IN TEMPERATURE AND SNOWFALL USING ^{15}N MEASUREMENTS IN AIR BUBBLES TRAPPED IN THE EPICA DOME C ICE CORE (MANUSCRIPT).....	104
3.3	ANTARCTIC CLIMATE-ATMOSPHERIC CO_2 PHASING OVER THE FIVE MOST RECENT GLACIAL TERMINATIONS.....	134
3.4	PERSPECTIVES.....	134
3.4.1	The influence of obliquity on the relationship between atmospheric CO_2 concentration and Antarctic climate.....	134
3.4.2	Paleotemperature inferred from the combination of $\delta^{15}N$ and water isotopic data of EDC	

over the last deglaciation.....	135
3.4.3 On the need for additional $\delta^{15}\text{N}$ measurements over past glacial periods.....	137
4 CHAPTER 4.....	139
BUILDING THE ANTARCTIC ICE CORE CHRONOLOGY (AICC) 2023: A PRECISE, COHERENT AND FEDERATIVE TIMESCALE FOR DEEP POLAR ICE CORES OVER THE PAST 800 KYR.....	139
4.1 PUBLICATION: THE AICC2023 CHRONOLOGICAL FRAMEWORK AND ASSOCIATED TIMESCALE FOR THE EPICA DOME C ICE CORE.....	142
4.2 LIMITATIONS AND PERSPECTIVES.....	198
4.2.1 On the next coherent Antarctic ice core chronology.....	198
4.2.1.1 Corrections of AICC2023.....	198
4.2.1.2 Suggestions for the next coherent Antarctic ice core chronology.....	201
4.2.2 On the development of the Paleochrono-tuning tool.....	202
4.3 IMPLICATIONS.....	202
4.3.1 On the use of the AICC2023 chronology as a tool.....	202
4.3.2 On the use of the AICC2023 chronology for determining the temporal sequence of events over glacial Terminations.....	205
5 CHAPTER 5.....	215
BUILDING COHERENT CHRONOLOGICAL FRAMEWORK FOR MARINE AND GLACIAL ARCHIVES OVER THE PAST GLACIAL-INTERGLACIAL TRANSITIONS.....	215
5.1 INTRODUCTION AND CONTEXT.....	218
5.2 DATING METHODOLOGY.....	219
5.2.1 Bayesian approach: Paleochrono-1.1.....	219
5.2.2 Experiment construction.....	220
5.2.3 Background chronological information related to the archives newly integrated in the dating experiment.....	222
5.2.3.1 Dated horizons.....	222
5.2.3.2 Stratigraphic links.....	222
5.3 ASSESS THE SENSITIVITY OF THE COHERENT AGE MODEL TO THE DATING METHODOLOGY.....	226
5.3.1 Speleocomposite – U1308.....	226
5.3.2 Speleocomposite – EDC.....	230
5.3.3 Confidence intervals evaluated from the sensitivity tests.....	233
5.4 SEQUENCES OF CLIMATIC EVENTS OVER GLACIAL TERMINATIONS.....	234
5.4.1 Methods.....	235
5.4.2 Preliminary discussion of limitations.....	236
5.4.3 Temporal phasing estimates.....	237
5.4.4 Results.....	238
5.5 CONCLUSIONS.....	240
5.6 PERSPECTIVES.....	241
5.6.1 Refine the implications of the speleocomposite – EDC sensitivity tests.....	241
5.6.2 Integrate additional archives to the coherent chronology.....	241
5.6.3 Test various fitting functions for detecting the Termination onset and end.....	245
5.6.4 Refine the interpretation of the climatic processes at play during glacial Terminations 190.....	245
5.6.5 On the use of the coherent chronological framework for developing a modeling protocol over TV-MIS 11c.....	246
6 CHAPTER 6.....	247
CONCLUSION AND PERSPECTIVES.....	247

6.1	RESEARCH STRATEGY	247
6.2	MAIN RESULTS	248
6.2.1	Ameliorating paleoclimatic reconstruction.....	248
6.2.2	Ameliorating the precision of deep polar ice core chronology over the past 800 kyr	249
6.2.3	Developing a coherent, relative and absolute chronology for glacial and marine archives over the past 640 kyr	249
6.3	PERSPECTIVES.....	250
6.3.1	Orbital dating and climatic interpretation	250
6.3.2	On further use of the multi-approach strategy.....	253
6.4	OPENING.....	255
	REFERENCES	256
7	APPENDIXES	291
	APPENDIX 7.1	292
	APPENDIX 7.2	294
	APPENDIX 7.3	297
	APPENDIX 7.4	331
	APPENDIX 7.5	362
	APPENDIX 7.6	390
	RÉSUMÉ EN FRANCAIS.....	442

REMERCIEMENTS

Je m'excuse d'avance pour le manque probable de clarté, d'effort de synthèse et d'exhaustivité de ces remerciements (alors que le reste du manuscrit est parfaitement clair, synthétique et exhaustif cela va de soi).

Tout d'abord, je tenais à remercier Amaëlle et Frédéric pour leur immense confiance tout au long de ce doctorat...

Amaëlle, j'ai été - et je suis toujours - très inspirée par ta passion contagieuse pour la recherche en groupe. Je te remercie pour ta bienveillance et ta disponibilité (7j/7 - 24h/24) pour répondre à mes questions, et ce même lorsque je pose quinze fois les mêmes. Merci d'avoir fait tout ton possible pour que je puisse m'épanouir professionnellement et humainement en m'ayant encouragée à donner des cours, à m'essayer à la médiation scientifique, à participer à toutes sortes de conférences et discussions,... Merci aussi de me faire confiance pour l'Antarctique et de croire en la poursuite de mon parcours dans la recherche. J'ai hâte de continuer à discuter hypothèses plus ou moins farfelues avec toi.

Frédéric, j'ai énormément apprécié commencer la thèse à tes côtés à Grenoble. Cela m'a permis de m'immiscer doucement dans le monde du paléoclimat par la porte des mathématiques. Un immense merci pour ton aide tout au long de la thèse et d'avoir toujours pris le temps de m'expliquer le fonctionnement de Paleochrono malgré notre éloignement. Petit à petit, je commence à mieux comprendre le modèle (même si j'ai le sentiment de ne pas être au bout de mes surprises !). Ta vision mathématique de la recherche en paléoclimat est très inspirante (que ce soit pour les modèles conceptuels ou les modèles probabilistes, ceux auxquels j'ai particulièrement été confrontée pendant la thèse), donc j'ai hâte de continuer à travailler à tes côtés dans le futur !

Je remercie les membres de mon jury : Barbara, Claire, François et Sébastien, de vous être armés d'une patience inouïe afin de lire ce manuscrit. Ce fut un plaisir d'échanger à la suite de la soutenance. Merci pour tous vos commentaires qui m'ont permis d'étayer et solidifier mes travaux de recherche.

Pour introduire doucement le thème de la thèse, je vais tenter de procéder au reste des remerciements de manière chronologique.

Les 25 années avant la thèse (the last 25 a BP ; i.e. years before PhD)

Tout d'abord, je remercie mes parents pour toute la curiosité pour les sciences que vous m'avez transmise. Merci aussi pour votre soutien infaillible depuis le début... Merci Elliot d'avoir éveillé mon intérêt pour les technologies excentriques et absurdes en m'offrant quelques cadeaux incroyables (je n'oublie pas la lampe... euh de chevet ?). Merci Laëtitia d'éclairer nos vies avec Elena, Louis et Mia depuis quelques années maintenant déjà. Merci à tous les membres de ma famille d'avoir été des petits rayons de soleil finalement.

Merci à mes copains de prépa avec qui j'ai pu construire mes premières vraies hypothèses farfelues : Aurélie, Carla, Julien, Kémo, Théo. Merci pour les weekend entre parenthèses à

démasquer les loups garous en jetant de l'eau bénite.

Mille mercis en vrac aux copains d'école : à Consti pour toutes les aprem' chez toi, à Pati pour ta tendresse, à Elsa pour toutes nos folies, à Hippo pour tes blagues si bien placées (je suis jalouse), à Mouchez pour nos discussions de campagnards, à Rodrigue pour tous tes objets saugrenus du BonCoin, à Armand pour tous nos convoit' inoubliables, à Lisa pour tous les karaokés et concerts, à Jo' pour toutes nos bêtises d'ados, à Coco & Alex pour l'accueil supra chaleureux sur Grenoble, à Mariz pour toutes nos aventures intenses et discussions toutes aussi intenses sur la Vie, à mon soleil pour nos soirées Philippe Lacheau, nos rando en duo, nos cours séchés, nos mots fléchés, et toutes nos bêtises finalement, et enfin à Juliette pour toutes nos (més)aventures. Merci d'avoir lu mes articles même si c'est très éloigné de ton taff (sur les... ordinateurs ?). En bref, merci d'être venue t'asseoir à côté de moi sur un banc de ce parvis Néel il y a maintenant six ans.

Merci aussi Guillaume pour tout ce que l'on a traversé ensemble, pour tous les fous-rires et toutes les aventures. Merci pour m'avoir accompagnée et encouragée si longtemps.

Je tenais aussi à remercier les petits aiguillages humains qui m'ont orienté vers la thèse sans le savoir : merci à Mr. Gouygou, Mr. Fiat, Mr. Volpi ; et Mme Cordier.

La thèse (0 a BP)

Merci à l'équipe ICE³ de l'IGE. Merci en particulier à Greg et Patricia pour toute votre aide. Merci Ari d'avoir partagé ce premier bureau de thèse. Merci Emilie, pour tous tes conseils et nos échanges tout au long de la thèse. Merci à Axel et Marine d'avoir égayé mon début de thèse avec vos chamailleries. Merci Ailsa d'avoir partagé toutes ces aventures pre-Antarctique, je suis tellement heureuse de partir en mission avec toi cet hiver. Merci Sara de m'avoir fait découvrir ton terrain de jeu : le Lautaret ! Merci Benoît de nous avoir emmené.es plus d'une fois à l'aventure !! (RIP mes cheveux abandonnés dans cette grotte au fin fond du vercors.) Merci à Etienne et Alexis d'avoir été mes deux gourous d'initiation à la communauté des carottes de glace. Votre enthousiasme m'a contaminée tout de suite et a rendu ce début de thèse exceptionnel. Merci pour vos conseils sur les plans personnel et professionnel (quoique la frontière est floue) que je continue de suivre. J'espère que nous grandirons et vieillirons « professionnellement » ensemble en respectant la promesse qu'Etienne et moi nous sommes faites à Rome l'été dernier !

Merci ensuite à Jérôme et Nathalie, de m'avoir accueillie chaleureusement lors de mes premiers pas sur le plateau de Saclay. Merci à ma famille crapulante de Gif-sur-Yvette : Adèle, Alex, Aurélie, Cécile, Céline, Elsa, Juliette H., Juliette B., Lucas, Matteo, Quentin, Rebecca, Romane, Thibault, grâce à qui je me suis sentie chez moi à Paris. Merci pour les diners presque parfaits, les gâteaux, les accents du sud et du nord, les brunch dans le jardin, les cinés en plein air de l'été, les soirées aquarelles, les soirées confessions intimes sur le rebord de la baignoire, les soirées dans les péniches,... Le soleil dans cette maison m'a fait oublier l'éloignement des montagnes.

Merci à l'équipe GLACCIOS du LSCE de m'avoir accueillie chaleureusement en plein milieu de l'hiver. Merci à Bénédicte, Cécile A., Elise, Elodie, Frédéric, Jean, Jeanne, Mathieu, Olivier J. et

Valérie pour toute votre aide. Merci aussi à Aurélien Q., Christophe D., et Sébastien pour le temps consacré à nos échanges scientifiques ! Merci Ji-Woong de m'avoir accueillie dans ton bureau (jusqu'à ce que je traverse le plancher et fasse de la speleo au sous-sol, comme quoi on peut aussi vivre des aventures fortes sur le plateau).

Merci à Antoine de m'avoir recueillie dans ton bureau suite à cet incident. Merci pour toutes nos discussions, pour ton aura d'ours apaisante (ça fait du bien pendant une thèse), pour tes blagues nulles, mais surtout pour avoir ri à toutes mes blagues nulles. A bientôt j'espère.

Merci à ceux qui sont venus me rejoindre dans ce bureau (que je me suis un peu appropriée) ensuite : Baptiste, Gabriel et Igor (sans oublier Philippe Lacheau - merci Clems).

Merci à celles et ceux qui sont devenu.es des ami.es :

Merci Clems pour le timing exact des pauses cafés, pour les paillettes dans nos vies, pour ta bonne humeur (et toutes tes humeurs de manière générale, qui nous font tellement de bien au labo), pour les conseils, pour ton oreille patiente, pour nos longues discussions, pour tes petites têtes de castor. Je suis immensément fière de la prof' inspirante que tu es, je n'ai qu'une hâte : penser avec toi notre futur projet incroyable et qui sait ? Peut-être se retrouver un jour dans le sud...

Cécile, merci à la coloc' et incroyable amie que tu es devenue. Merci pour tous tes cœurs à taille humaine sur mes photos de montagne, merci pour ton immense générosité et pour la passion dont tu débordes : le sport, le dessin, la musique, la vie, que tu partages avec moi. J'ai énormément aimé vivre la thèse, et tous les changements qui vont avec, quasi en même temps que toi. Je suis si contente pour les futurs possibles à Bruxelles et j'ai hâte de t'y rendre visite !

Merci Thomas pour le seul et l'unique cours de guitare (pour l'instant !) et pour bien d'autres choses avant ça ! J'ai hâte de te retrouver en Antarctique et de partager un tout petit bout de cette aventure avec toi.

Merci Roxanne pour ta bonne humeur rayonnante au labo.

Thanks Romilly for all the ideas that we exchanged during the PhD!

Merci Marie K. pour ta bienveillance et ton enthousiasme à monter des activités de médiation en tout genre. J'ai énormément aimé t'aider à préparer certaines d'entre elles. Tu peux compter sur moi si tu as besoin d'aide pour une prochaine idée.

Niels, je suis tellement contente que l'on ait partagé ce petit bureau si longtemps, je ne veux juste pas que ça s'arrête. Merci pour tous les moments au labo et hors labo. Merci de nous avoir initié.es à tes passions (montagne, musique, vulgarisation,...), merci de m'avoir incluse dans ta vie parisienne... Même si je déménage et qu'une page se tourne, je sais que nous continuerons de partager des projets incroyables, j'ai juste hâte de voir comment le futur va nous ré-amener à nous croiser.

Merci Titouan pour avoir apporté au labo un humour et un style vestimentaire encore plus douteux que les miens !

Merci Nico pour toutes nos discussions d'été en musique sur les tables dehors, tu es un puits

d'inspiration de 2 m (et je pèse mes mots).

Merci Anna & Adrien pour la poésie et la douceur dans cette équipe de fous.

Christophe, comme tu me l'as si bien écrit, je ne m'attendais pas à partager autant avec le vieux mec du bureau d'en face. Tu es franchement dérangé mais dans le bon sens du terme. J'ai été ravie de partager le bureau avec toi, tes vidéos youtube, tes appels, tes gosses, ta chasse au trésor, tes projets, ta nonchalance et un peu de tes conseils quand même (vraie anecdote : ma mère - qui m'observe - vient de me dire « c'est marrant tu souris quand tu rédiges », si c'est pas une belle preuve d'amour ça quand même). J'ai hâte de suivre l'évolution de la coquille, je passerai vous faire coucou à ta famille, tes pommiers, ton figuier et toi un jour promis.

Merci Ellyn d'avoir passé des HEURES avec moi à calculer des lead-lag. Alors qu'en plus nous de base on voulait quantifier les incertitudes, pas les lead-lag, bref ! Je te remercie pour avoir été une alliée de travail infatigable et exceptionnelle, je suis immensément contente que tu continues et j'ai hâte de bosser avec toi encore.

Merci Louis pour ta folie (qui ressemble un peu à ma folie j'avoue), pour ton amour des gens et pour tous nos bavardages au fond de nos sièges quand tu squattais mon bureau.

Merci Hassiba pour tous les fous rires explicables (et inexplicables (et inextricables ?)).

Merci aussi à ceux qui même à distance ont su m'apporter des conseils, je pense en particulier à P.H. et Thomas E. Merci à Mélanie et Sophie, les deux rayons de soleil de mon comité, pour nos nombreux échanges ! Anders, I warmly thank you for having been a wise and solar guide during all my PhD.

Merci enfin aux récents copains d'ODG, Antoine, Arthur, Baptiste, Charlotte, Elliot, Lorentz, Matthis, Pauline, avec qui j'ai appris plein de trucs utiles (comme le nombre d'arbres sur Terre), mais surtout avec qui j'ai partagé l'amour de la vulgarisation !

My final thanks go to my most recent friends from the paleo & ice core communities': Agnese, Anika, Antoine H., Ariane, Charlotte, Flo-kus, Henrique, Inès, Lisa, Lison, Thale, with who I hope to keep crossing paths at labs, conferences and/or on the field in the future!

Merci bonus à celles et ceux qui sont venu.es assister à la soutenance, j'étais heureuse de vous voir si nombreux.ses.

TABLE OF ABBREVIATIONS

AABW: Antarctic Bottom Water	LGM: Last glacial maximum
AAMV: Abrupt Asian monsoon variability	LIA: Little Ice Age
AICC2012: Antarctic ice core chronology 2012	LID: Lock-in-depth
AICC2023 : Antarctic ice core chronology 2023	LIG: Last interglacial
AIM: Antarctic isotopic maxima	LR04 : The benthic stack of Lisiecki and Raymo (2004)
AMOC: Atlantic meridional overturning circulation	LSCE: Laboratoire des Sciences du Climat et de l'Environnement
BCE: Before common era (equivalent to BC)	Ma BP: Millions of years before present (1950 CE)
BE-OI: Beyond EPICA – Oldest Ice	MB: Matuyama-Brunhes
BHT: Borehole thermometry	MBE: Mid-Brunhes event
CDJ: Carbon dioxide jump	MIS: Marine isotope stage
CE : common era (equivalent to AD)	MPT: Mid-Pleistocene transition
CFA: Continuous flow analysis	Myr: Millions of years
COD: Close-off depth	NADW: Northern Atlantic deep waters
DC: Dome C	NAO: North Atlantic oscillation
DCH: Diffusive column height	NEEM: North Greenland Eemian ice drilling
DF: Dome Fuji	NGRIP: North Greenland Ice Core Project
D-O: Dansgaard-Oeschger	PD: Present-day
EDC: EPICA Dome C	PETM: Paleocene-Eocene thermal maximum
EDML: EPICA Dronning Maud Land	SST: Sea surface temperature
EGRIP: East Greenland Ice core Project	T: Termination
EPICA: European Project for Ice Coring in Antarctica	TAC: Total air content
ESM: Earth system model	TALDICE: Talos Dome ice core
GCM: General circulation model	TBS : Thermal bipolar seesaw
GHGs: Greenhouse gases	U/Th: Uranium/Thorium
GICC05: Greenland ice core chronology 2005	V-SMOW: Vienna Standard Mean Ocean Water
GISP2: Greenland Ice Sheet Project 2	WAIS: West Antarctic ice sheet
GRIP: Greenland Ice core Project	WD: WAIS Divide
HE: Heinrich event	WMI: Weak monsoon interval
IGE: Institut des Géosciences de l'Environnement	
IODP: Integrated ocean drilling program	
IPCC: Intergovernmental Panel on Climate Change	
IRD: Ice-rafted debris	
ISI: Integrated summer insolation	
ITCZ: Intertropical convergence zone	
ka BP: thousands of years before present (1950 CE)	
kyr: thousands of years	

FOREWORD

“Human activities, principally through emissions of greenhouse gases, have unequivocally caused global warming, with global surface temperature reaching 1.1°C above the pre-industrial level (1850–1900) in 2011–2020”

(Intergovernmental Panel on Climate Change (IPCC), 2023)

The Intergovernmental Panel on Climate Change (IPCC) reports on current global warming. The purpose of this group is to regularly review our knowledge of the climate, observations of climate change, as well as to study the possible evolutions through the use of climate models.

Climate is the result of multiple and complex interactions between the atmosphere, continents, oceans, biosphere, and cryosphere through a variety of chemical and physical processes on time scales ranging from a few hours to several thousand years.

It is possible to draw insights from past climate natural variability to constrain the response of the climate system and future projections. Paleoclimate data provide empirical estimates of pre-anthropogenic large climate change across a range of timescales, including the long timescales (several thousands of years) associated with deglaciation. This is of particular interest for climatic projections, as it allows for the estimation of the rate of ice cap melting. Additionally, paleo data can be used to examine "tipping point" events, such as Heinrich or D-O events, which reveal the potential for rapid (over a few decades) and significant instability in the climate system.

The slow response of some components is recorded in paleo data (e.g. carbon cycle, continental ice). This inertia disrupts the balance of incoming and outgoing energy in the Earth-atmosphere system and induces what is called a radiative forcing. For instance, since at least the 1970s, less energy is flowing out than is flowing in because of the ongoing accumulation of greenhouse gases (GHGs) in the atmosphere, inducing a radiative forcing (Fig. 0.1). Paleo data permit to quantify the change in global temperature in response to a radiative forcing change. This quantity is called the climate sensitivity.

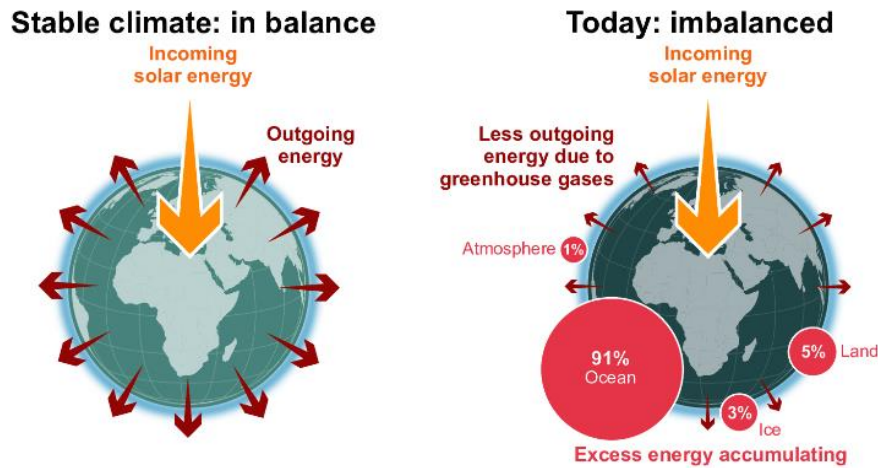


Figure 0.1 The Earth's energy budget and climate change. The Earth's energy budget compares the flows of incoming and outgoing energy that are relevant for the climate system. Since at least the 1970s, less energy is flowing out than is flowing in, which leads to excess energy being absorbed by the ocean, land, ice and atmosphere, with the ocean absorbing 91% (IPCC, 2023).

The chapter 7 of IPCC's last report (IPCC, 2023) mentions for the first time the use paleoclimate data as a complementary source of information to assess the sensitivity of the Earth system at equilibrium to a given external forcing, internal process or feedback mechanism. However, they highlight that despite advances in modeling and data analysis, uncertainties remain about (i) complex interactions between the internal components of the Earth system in response to external perturbation and about (ii) sensitivity of the climate to radiative forcing and its potential variability through time. A better understanding of past climate response to radiative forcing is imperative for accurately characterizing the future climate and undertaking the adaptation of our societies to the ongoing and future climate change.

Deep polar drilling in Antarctica and Greenland allows for the reconstruction of key climate parameters over the past 800 thousand years. These include temperature and precipitation data over the polar ice sheets, as well as atmospheric concentrations in GHGs such as CO₂ and CH₄. Precise ice core chronologies are key to identify the temporal sequence and lengths of significant warmings that occurred over relatively short timescales (such as the "tipping point" events) and over longer timescales (such as the deglaciations). This enables an investigation of the causal relationships between the external forcing (changes in the Earth's orbit) and the climatic response (variations in sea level, in atmospheric GHGs and in temperature).

The last federative dating effort provided the coherent Antarctic Ice Core Chronology over the past 800 thousand years (AICC2012, Bazin et al., 2013; Veres et al., 2013). In this context, the term "federative" designates the fact that this chronology was accepted as a reference chronology by the ice core community. However, it has become obsolete as new dating approaches have been developed and new chronological information have been collected.

My PhD started in this context with the aim of refining the chronological information for the Antarctic EPICA Dome C (EDC) ice core using data measured by A. Grisart, F. Prié and A. Landais at LSCE and by V. Lipenkov, D. Raynaud and E. Capron at IGE as well as the snow-ice

densification model developed by J.-M. Barnola at IGE and more recently adapted by Bréant et al. (2017). The following expected step was to integrate these various sources of chronological information available on different ice cores using the probabilistic Paleochrono-1.1 model developed by F. Parrenin at IGE to yield a new federative coherent chronology of reference for deep polar ice cores. I spent the first five months of the PhD at IGE (Oct. 2021 -Fev. 2022) before coming to the LSCE for the rest of the PhD.

The manuscript is organized in six chapters:

Chapter 1 constitutes a comprehensive introduction to past climate dynamics and paleoclimate archives and presents the PhD context and objectives.

Chapter 2 focuses on the analysis and dating approaches employed for reconstructing climate history using deep polar ice cores.

Chapter 3 explores the potential of $\delta^{15}\text{N}$ of N_2 measurements in air trapped in East Antarctic ice cores to document past changes in temperature and snowfall. This Chapter is composed of a first-authored article in prep. and the other co-authored (Legrain et al.).

Chapter 4 describes the building the Antarctic Ice Core Chronology AICC2023: a precise, coherent and federative timescale for deep polar ice cores over the past 800 kyr. This chapter is composed of a first-authored article published in *Climate of the Past* (Bouchet, Landais, Grisart, et al., 2023).

Chapter 5 presents preliminary work on the development of a coherent chronological framework for marine and glacial archives over the past glacial-interglacial transitions. This work was undertaken in the framework of E. Auriol's Master Thesis project which I co-supervised with A. Landais. We hope it can serve as a foundation for a co-authored publication.

Chapter 6 concludes the PhD thesis and suggests possible future research directions to explore.

In complement to the thesis, Appendixes are given at the end in Section 0. They gather two first-authored short articles published in the *Past Global Changes Magazine*: (7.1) Bouchet et al. (2024) and (7.2) Bouchet et al. (2023a) as well as co-authored papers related to the PhD project: (7.3) Parrenin et al. (2024), (7.4) Legrain et al. (in preparation), (7.5) Legrain et al. (submitted to *Nature Geosciences*) and (7.6) Paul et al. (in preparation).

1 CHAPTER 1

INTRODUCTION TO PAST CLIMATE DYNAMICS AND ARCHIVES – CONTEXT AND OBJECTIVES OF THE PHD

“I ever desired to discern physical phenomena in their widest mutual connection, and to comprehend Nature as a whole, animated and moved by inward forces”

(Humboldt, 1884)

Foreword

This first chapter constitutes a comprehensive introduction to facilitate a broader understanding of the work done in the framework of my PhD among the paleoclimate and climate communities. It may serve as a toolkit with key notions and orders of magnitude characterizing Earth’s climate to which we will refer in the remaining of the manuscript.

First, the role of external forcing and internal components of the Earth system in determining the climate of the late Quaternary period is introduced. We focus over the past 800,000 years, which is the time interval of interest of this PhD project. Second, various natural archives that documented the past variations in the Earth’s climate are listed. Complementary information is given for the archives providing records that were studied within the framework of the PhD. Third, the context, objectives and research directions of the PhD project are described.

1.1 MODERN CLIMATE OF THE EARTH

1.1.1 Spatial and seasonal variability

Climate at a specific point at the surface of the Earth is defined by various features including air temperature and precipitation amount. These climatic parameters vary across the globe from low latitudes to high latitudes and across the year through seasons depending on the spatial and seasonal distribution of the total energy received at the Earth's surface (Fig. 1.1). The energy amount received at one point of the Earth's surface is determined by various parameters detailed below.

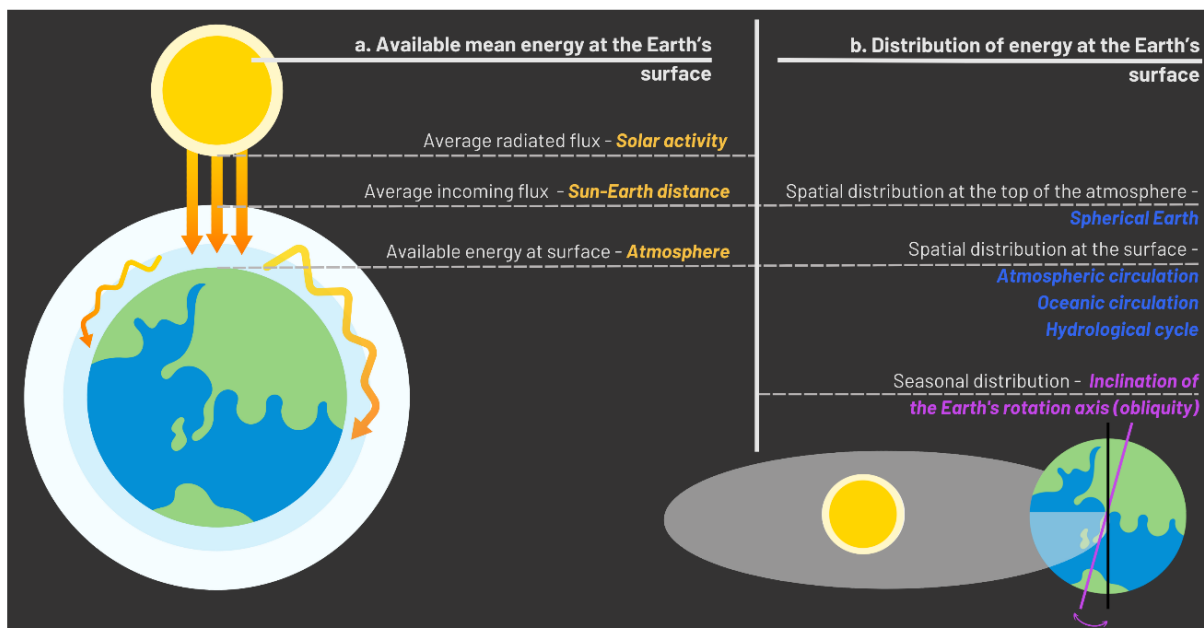


Figure 1.1 Successive steps in the distribution of energy available at the Earth's surface. a) The energy available at the global Earth's surface is determined by the factors in yellow (solar activity, sun-earth distance and atmosphere composition). b) The amount of solar energy available at surface varies across latitudes depending on the factors in blue (the shape of the Earth, the oceanic and atmospheric circulations, the hydrological cycle) and varies across seasons depending on the inclination of the Earth's rotation axis.

1.1.1.1 Solar energy

The flux is the amount of energy delivered per m^2 and can be calculated by dividing the energy by the surface. The flux is also referred to as insolation and is expressed in W m^{-2} . The mean solar flux arriving at the top of the atmosphere on a surface that faces the Sun (πr^2) is equal to 1367 W m^{-2} . Its value is determined by the solar activity and by the Sun-Earth distance. When averaging the solar influx on the global top of atmosphere surface ($4\pi r^2$), its value is decreased by four and equals 342 W m^{-2} . The solar source of energy results in a mean temperature of -18°C at the top of the atmosphere and is dominant when compared to the other energy sources:

- Geothermal influx accounts for 0.05 W m^{-2} under the oceans and for 0.01 W m^{-2} under the continents, where it is mainly concentrated under the volcanoes. It equals $\sim 10^{-4}$ of the solar energy input.
- The energy received from the rest of the Universe is equivalent to $\sim 10^{-6}$ of the solar energy input.

1.1.1.2 Atmosphere

Then intervenes the atmosphere entered by the solar influx as well as by the telluric radiation, an infrared thermal radiation that is emitted by continent's and ocean's surface when they are warmed and whose intensity is determined by the Earth's surface temperature.

The resulting incoming energy flux at the Earth's surface is of 492 W m^{-2} and is distributed through different types of heat:

- Radiative heat: through solar and telluric fluxes (390 W m^{-2} , corresponding to the mean surface temperature of $+15^\circ\text{C}$).
- Latent heat: through water exchanges in different states between oceans, continents and atmosphere (78 W m^{-2}).
- Sensitive heat: through cooling/warming of air masses in contact with ocean/continent surface (24 W m^{-2}).

The global atmospheric composition modifies the solar influx reaching the Earth's surface. For example, greenhouse gases (GHGs) absorb the infrared radiation from the Sun in the form of heat that then circulates within the atmosphere. Among the gases that contribute most to the modern-day greenhouse effect we find water vapor (H_2O), carbon dioxide (CO_2), nitrous oxide (N_2O), methane (CH_4) and ozone (O_3). Since the Industrial Revolution (in the 1850s), human activities including fossil fuel combustion, land use and cement manufacture have significantly elevated the concentrations of GHGs in the atmosphere. These additional GHGs are referred to as anthropogenic.

The major components of the atmosphere are shown in Fig. 1.2.

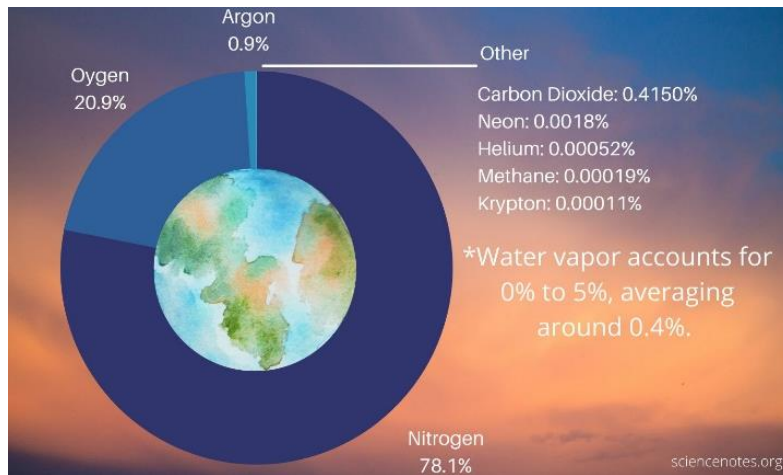


Figure 1.2 Major gas components of the contemporary atmosphere of the Earth.

1.1.1.3 The spherical shape of the Earth and inclination of its rotation axis

The spherical shape of the Earth is responsible for the uneven distribution of the energy across latitudes. The surface onto which is delivered energy is larger at higher latitudes, therefore the insolation is smaller at high latitudes than in the equator region (Fig. 1.3). This results in lower temperatures in the poles than in the tropical region. The resulting surplus of heat in the equator region with respect to the poles is represented in Fig. 1.4.

The axial tilt of the Earth (i.e. the angle between its rotational axis and the perpendicular to the elliptic plan, Fig. 1.1) is responsible for variations in the amount of solar energy received at one point of the Earth surface over the year, giving rise to seasons.

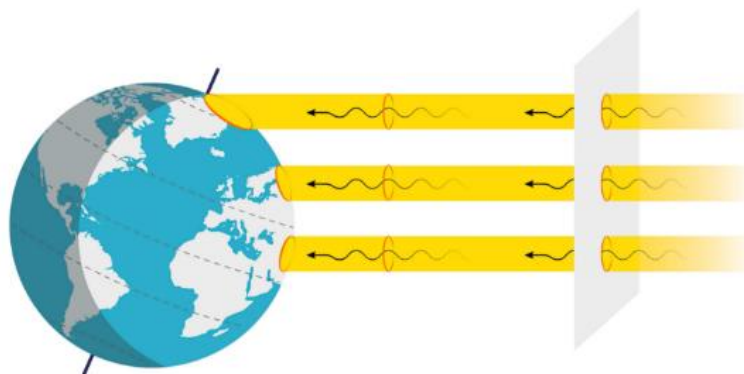


Figure 1.3 Latitudinal distribution of solar incoming flux (insolation) at the top of the Earth's atmosphere. The larger the surface is, the smaller the insolation is (i.e. in high latitudes) (Forçage Externe Du Climat: Variation Des Paramètres Orbitaux de La Terre - Jean-Baptiste Madeleine | Canal U).

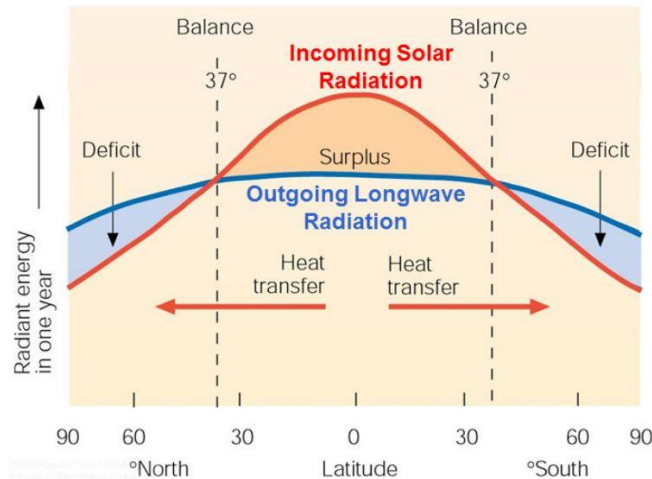


Figure 1.4 The energy imbalance from equator to each pole which motivates heat transfer through oceanic and atmospheric circulations combined to the hydrological cycle (Geuskens, 2020).

1.1.1.4 Internal distribution of energy

✂ *The key notions presented in this section are used in Chapters 3 and 4.*

The spread of heat from equator to the poles is ensured by the oceanic and atmospheric circulations combined to the hydrological cycle. The atmospheric circulation, as well as the hydrological cycle, also determines the distribution of water precipitation. The oceanic and atmospheric circulations are animated by vertical (density-driven re-organization) and horizontal movements (second principle of thermodynamics, i.e. heat goes from warm to cold regions) that develop at the 10^6 m-scale. At such scale, the Coriolis force induced by the rotation of the Earth's around its axis shapes the atmospheric circulation and superficial oceanic circulation.

Atmospheric cells and winds

From the equator to both poles, there are three distinct zones of wind circulation (Fig. 1.5):

- (i) The first zone is composed of Hadley cells and is located between the equator and 30° North (N) and South (S). In the northern hemisphere, regular winds blow from the northeast, while in the southern hemisphere, they blow from the southeast. For centuries, sailors have travelled this zone of consistent winds to traverse the globe's oceans.
- (ii) The second zone is situated between 30° and 60° (N and S) and is composed of mid-latitude (or Ferrel) cells. The circulation near the Earth surface is dominated by transient depression systems (associated with bad weather conditions, i.e. clouds, precipitations and strong winds) below a prevailing westerly upper-level circulation.

- (iii) The third zone, composed of the polar cells, is situated above 60° N and S and generally exhibits an easterly surface circulation.

Between these three zones, between 6 and 15 km of altitude, fast and confined air currents circulate around the globe between the troposphere (where temperature decreases with altitude) and the stratosphere (where temperature increases with altitude). These currents, called jet streams, permit the development or intensification of cyclonic circulation in the atmosphere, which ultimately results in the formation of a depression system.

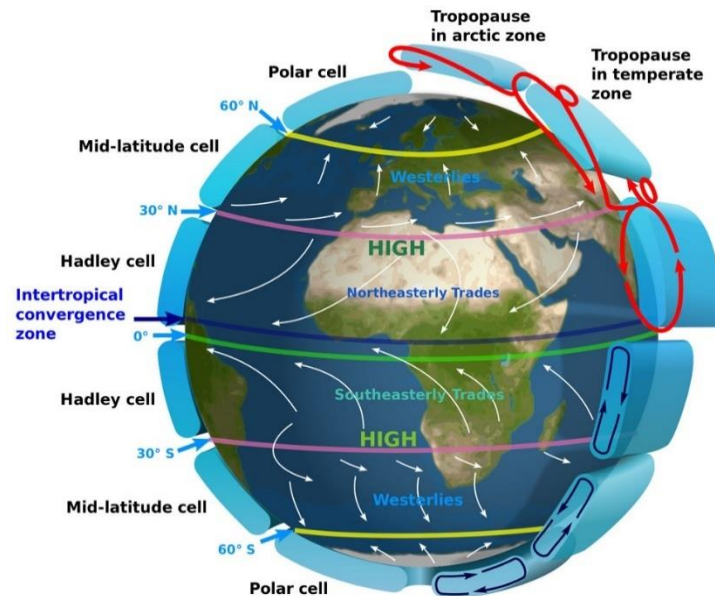


Figure 1.5 The atmospheric circulation can be decomposed in three cells and wind belts (NASA, Wikimedia Commons).

The Intertropical Convergence Zone & monsoon

The ITCZ, or Intertropical Convergence Zone, is a meteorological phenomenon. The ITCZ is situated at the equator, where the maximum solar radiation is received. The atmosphere naturally seeks to distribute this heat through the process of thermal convection. Consequently, atmospheric movements are initiated to distribute the surplus heat from the equatorial zone towards the poles, thereby giving rise to convection cells. The ITCZ is the source of the most significant atmospheric convection on Earth. In this ITCZ, horizontal winds are nearly absent, while vertical movements are active, resulting in a high humidity that gives rise to the presence of large quantities of clouds and rain. Furthermore, the significant temperature differential between the oceans and continents serves to fuel the monsoon. At the seasonal scale, the ITCZ migrates in accordance with the largest solar radiation. July is associated with the ITCZ and rainy seasons in India, China, Central America, and Brazil, while the January is associated with Indonesian monsoon (Fig. 1.6).

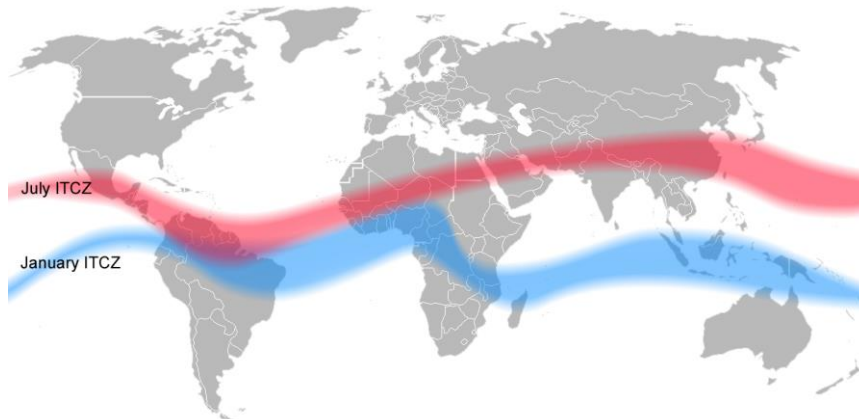


Figure 1.6 Intertropical Convergence Zone (ITCZ) position in July and January for present-day climate conditions (Mats Halldin, GFDL, CC-BY, PD).

The oceanic circulation: NADW/AABW and AMOC

The primary determinant of oceanic currents is the contrasting densities of water masses, with winds and tides also exerting a significant influence. Ocean circulation can be conceptualized as comprising two primary components: a fast surface circulation driven by winds (illustrated in red in Fig. 1.6). Once surface waters have migrated to high latitudes and lost all their excess heat to the atmosphere, they become colder and denser, and subsequently plunge deeper into high latitudes. This results in the formation of a broad, slower deep circulation (blue in Fig. 1.7), which is primarily influenced by water density. Density, in turn, is contingent upon temperature and salinity.

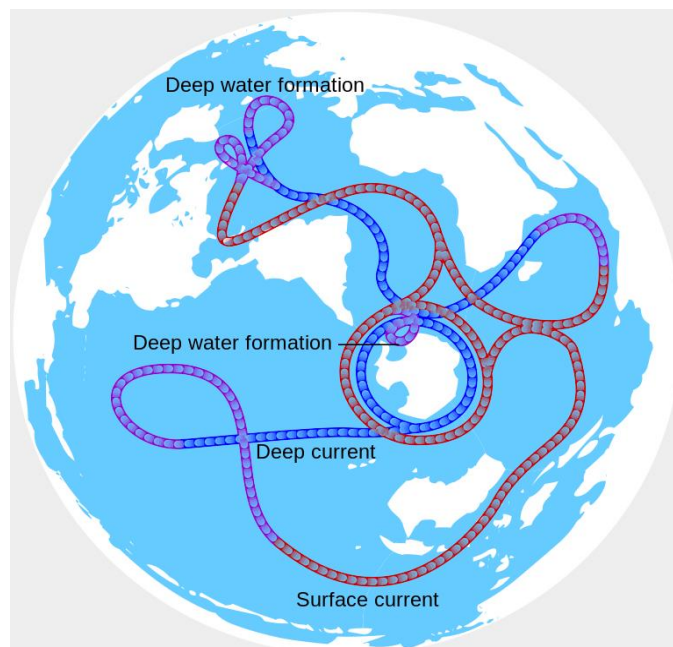


Figure 1.7 The thermohaline oceanic circulation (C.N.G. Lee, Wikipedia Commons). Surface waters are in contact with atmosphere and rich in dissolved carbon and oxygen. In the North Atlantic region, the formation of sea ice rejects salt, increasing the density of surface waters, which plunge in deep water formation zones represented in Figs. 1.7 and 1.8. They join the water mass that circulates in the deep section of the northern Atlantic Ocean called the North Atlantic Deep Water (NADW, Fig. 1.8) and participate to the ventilation of the deep oceanic circulation by bringing

carbon and oxygen-rich water. In the Antarctic sector, cold temperatures and sea ice formation enhanced by strong winds result in the continuous formation of deep water that feed the Antarctic Bottom Water (AABW). The AABW sometimes move 4,000 m below the sea level and constitutes the densest water masses of the globe. Their intensity and spatial extent varied over past climate states (Section 1.2.2.2).

The AMOC (Atlantic Meridional Overturning Circulation) represents one of the Earth's principal oceanic circulation systems. This current functions as a giant conveyor belt, transporting warm, salty water from the equator in a northerly direction. Subsequently, the water cools and becomes denser. Once it has reached a sufficient depth, it sinks to the deeper ocean layers and returns progressively to the south. The intensity of this current has varied over time (Section 1.2.2.2).

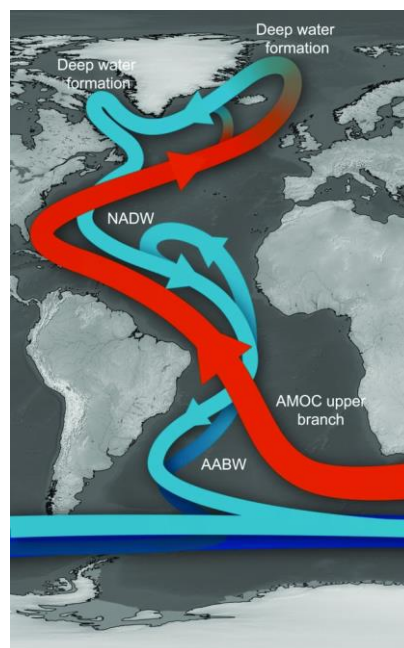


Figure 1.8 The AMOC conveyor belt (Crivellari, 2018). It currently exhibits an average velocity of approximately $2 \times 10^7 \text{ m}^3 \text{ s}^{-1}$, which is about one hundred the flow rate of the Amazon River.

1.1.2 The energy budget at the Earth's surface

Some factors affecting the energy budget of the Earth are classified in two categories detailed below: the external forcing and the internal causes. These factors evolve more or less slowly so that their influence is exerted at different timescales (Fig. 1.9).

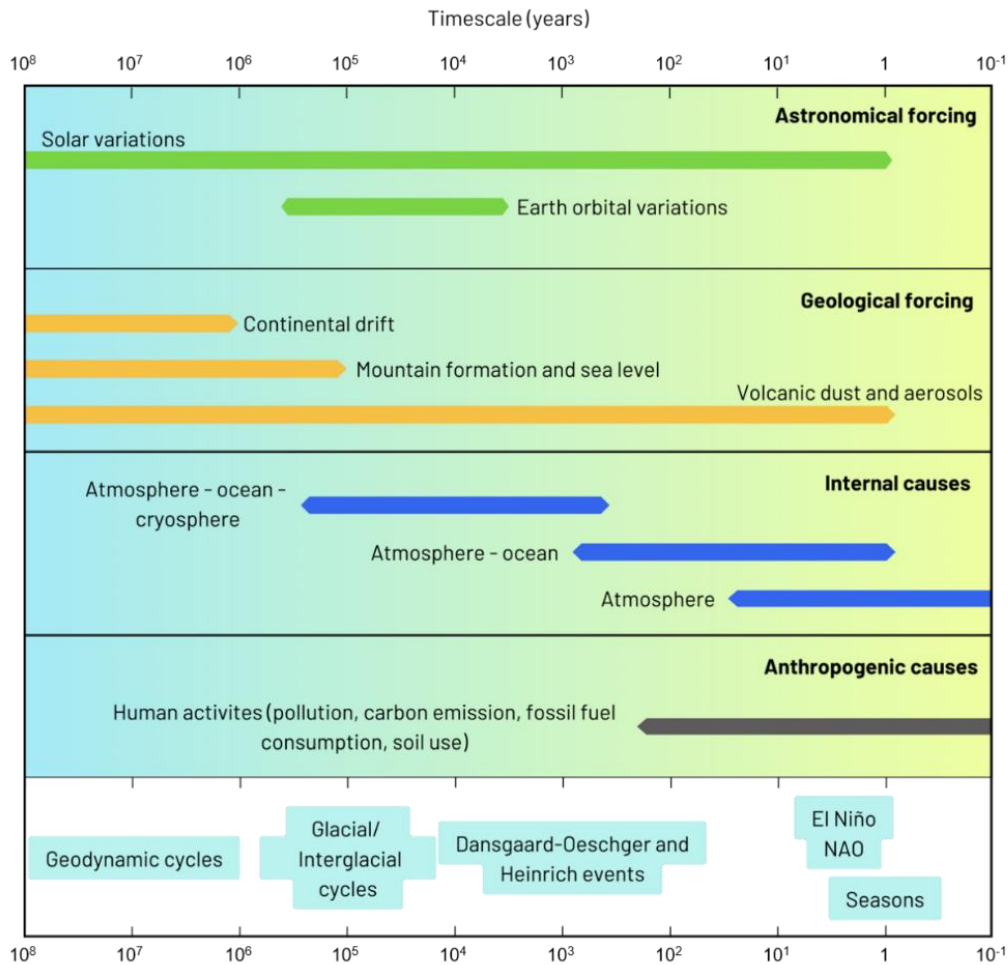


Figure 1.9 Logarithmic unit scheme presenting the main causes for climate change as well as some characteristic examples of climate fluctuation. Green and orange: external forces acting upon the climatic system; blue: internal rearrangements of the system; gray: human-made effects (modified from Kutzbach, 1974).

1.1.2.1 External forcing

The factors external to the Earth system that alter the energy budget by inducing radiative forcing to the system, hence disrupting the balance, are referred to as external forcings. Among the external forcings, we count:

- The alterations of the atmospheric composition caused by external forcing. An example is the increase in GHGs and aerosols due to human activity (at the timescale of 1 to 10^2 years).
- The changes in Earth's albedo, mainly induced by changes in the atmospheric concentration of sulfate aerosols (due to volcanic or human industrial activity, at the timescale of 1 to 10^8 years).
- The variations in the solar forcing (at different timescales from 1 to 10^8 years).

- Decadal variations induce a radiative forcing resulting in at most 0.2°C-amplitude variations of surface temperature.
- Centennial scale fluctuations of the solar intensity are thought to be responsible for the particularly large extent of glaciers during the Little Ice Age that occurred during the medieval epoch (refs).
- The variations in the Earth orbit affect the distribution of insolation inducing local and zonal changes (at the timescale of 10^4 to 10^6 years; Fig. 1.10). The three orbital parameters are:
 - Obliquity with a main periodicity of 41,000 years
 - Precession with main periodicities of 19,000 and 23,000 years
 - The eccentricity parameter e characterizes the shape of the Earth's orbit and varies from a circle to a very plane ellipse with a periodicity of 10^6 years.

Though we should note that the mean solar energy arriving annually at the global surface of the Earth is not significantly changed by these orbital parameters.

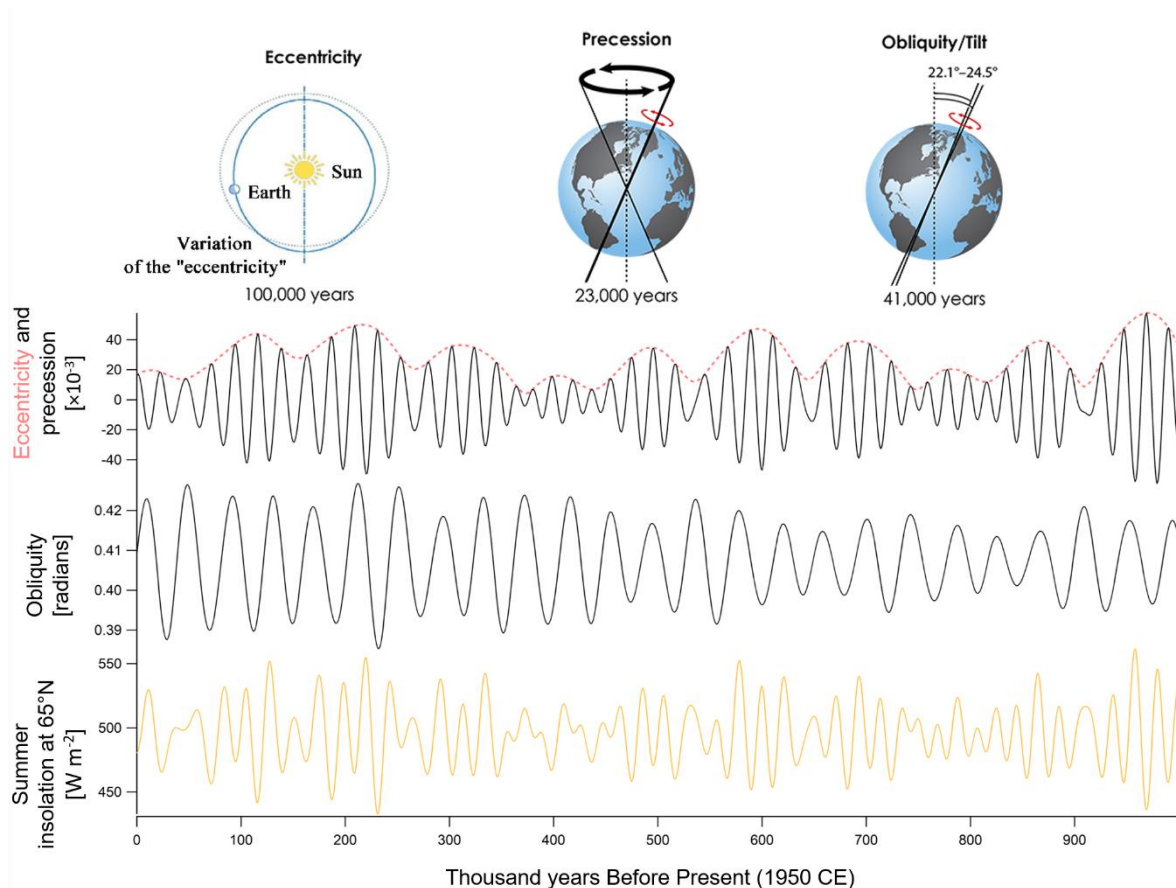


Figure 1.10 The variations in the orbital parameters over the past million years (Laskar et al., 2004). Schematic representations (credit: K. Cantner, AGI ; Latsis foundation, 2001) of the eccentricity (red dashed curve), precession (black curve) and obliquity (back curve) are also shown along with their main periodicity: respectively 100, 23 and 41 thousand years. The resulting insolation received in summer at 65°North is represented (yellow curve).

1.1.2.2 Internal processes and feedback parameters

The external forcings sometimes induce modifications in the functioning of internal components of the Earth's system, inducing consequences referred to as feedbacks. The feedbacks either amplify (positive) or attenuate (negative) the external forcing and affect the response of the Earth's system at different timescales. The rapid feedbacks are caused by variations of the hydrological cycle and are related to the change of physical state of water. They involve:

- The dynamical interactions between oceans and the atmosphere (at the timescale of 1 to 10^2 years) which determine the water vapor content and the presence of clouds in the atmosphere.
- The changes in atmospheric composition due to variations in biogeochemical cycles (at the timescale of 1 to 10^3 years). For example, the variations of the carbon cycle in the pre-anthropogenic system influence the atmospheric CO_2 concentration.
- The changes in oceanic circulation (at the timescale of 10^3 years).
- The changes affecting the cryosphere (i.e. ice sheets and sea ice) at the timescale of 10^3 to 10^5 years and associated with changes in (i) albedo of the Earth as well as in (ii) the lapse rate effect, referring to the temperature vertical profile in the atmosphere and related latent heat transfer. It can be modified by changes in elevation of ice sheets at the poles for example.
- The spatial distribution and/or biophysical properties of vegetation, influencing the reflection of the solar radiation as well as the cycles of water and carbon, and atmospheric content in CO_2 .
- The variations in the continents, such as mountain formation, sea level fluctuation and continental drift (at the geological timescale, i.e. 10^5 to 10^8 years).

1.1.3 Climate system modeling

Different approaches to model climate system have been developed. Global climate models (GCMs) are complex mathematical representation of the major components of the climate system, including the atmosphere, land surface, ocean, and sea ice, as well as the physical interactions between these components. Climate models are constructed with a three-dimensional grid of cells, each representing a specific geographic location and elevation. The temporal evolution of each component is determined by equations calculated on the global grid for a set of climate variables (e.g. temperature). The different components also exchange fluxes of heat, water, and momentum, thus interacting as a coupled system.

Earth system models (ESMs) attempt to simulate all relevant aspects of the Earth system. They include physical, chemical and biological processes, going beyond the GCMs, which represented only the physical atmospheric and oceanic processes.

Intermediate-complexity models describe the Earth system (or only one component) in less detail than conventional climate models, with a coarser spatial resolution. They are fast, so they can treat slow climate variations and include components of the climate system that are associated with long-term feedbacks like ice sheets, vegetation, and biogeochemical cycles. They use more sophisticated equations than box or conceptual models.

Climate models are essential tools for understanding the behavior of the climatic system and predicting the future evolution of climate in response to natural and anthropogenic forcing.

1.2 THE PAST HISTORY OF EARTH'S CLIMATE

The first subsection (1.2.1) is a brief introduction on the past history of climate of the Earth over the past 70 million years to introduce the Quaternary period that started 2.6 Ma ago, which is the paleoclimatic context of interest for my PhD. Therefore, the methods used to reconstruct the past climate variations over the past 70 Ma are not described here.

The second subsection (1.2.2) focuses on the Quaternary period and describes the classical methods used for reconstructing past climate evolution and the current state of understanding of the climatic mechanisms at play during the Quaternary period.

1.2.1 Over the past 70 million years: global cooling trend and emergence of large ice caps

Past history of Earth climate has been recorded in geological archives (some of them are described in Section 1.2.2.1). This geological library documented the intermittent development and shrinkage of large continental ice caps since 2.3 billion of years before present. The discontinuous presence of these large ice sheets characterizes periods referred to as the glaciations. After the period of Cretaceous (145-65 Ma BP, i.e. millions of years before present) associated with warmer temperatures than today by +10°C, the Early Eocene (~50 Ma BP) marked the beginning of a global cooling that led to the glaciation of the Eocene-Oligocene transition at around ~35 Ma BP (Fig. 1.11). The main hypotheses invoked to explain this cooling are the decline of atmospheric CO₂ and induced greenhouse effect diminution as well as the continental drift and topography modification. The cooling trend led to the emergence of an ice sheet over the Antarctic continent which was centered at the South Pole since tens of millions of years and slowly isolated from other lands because of continental drift.

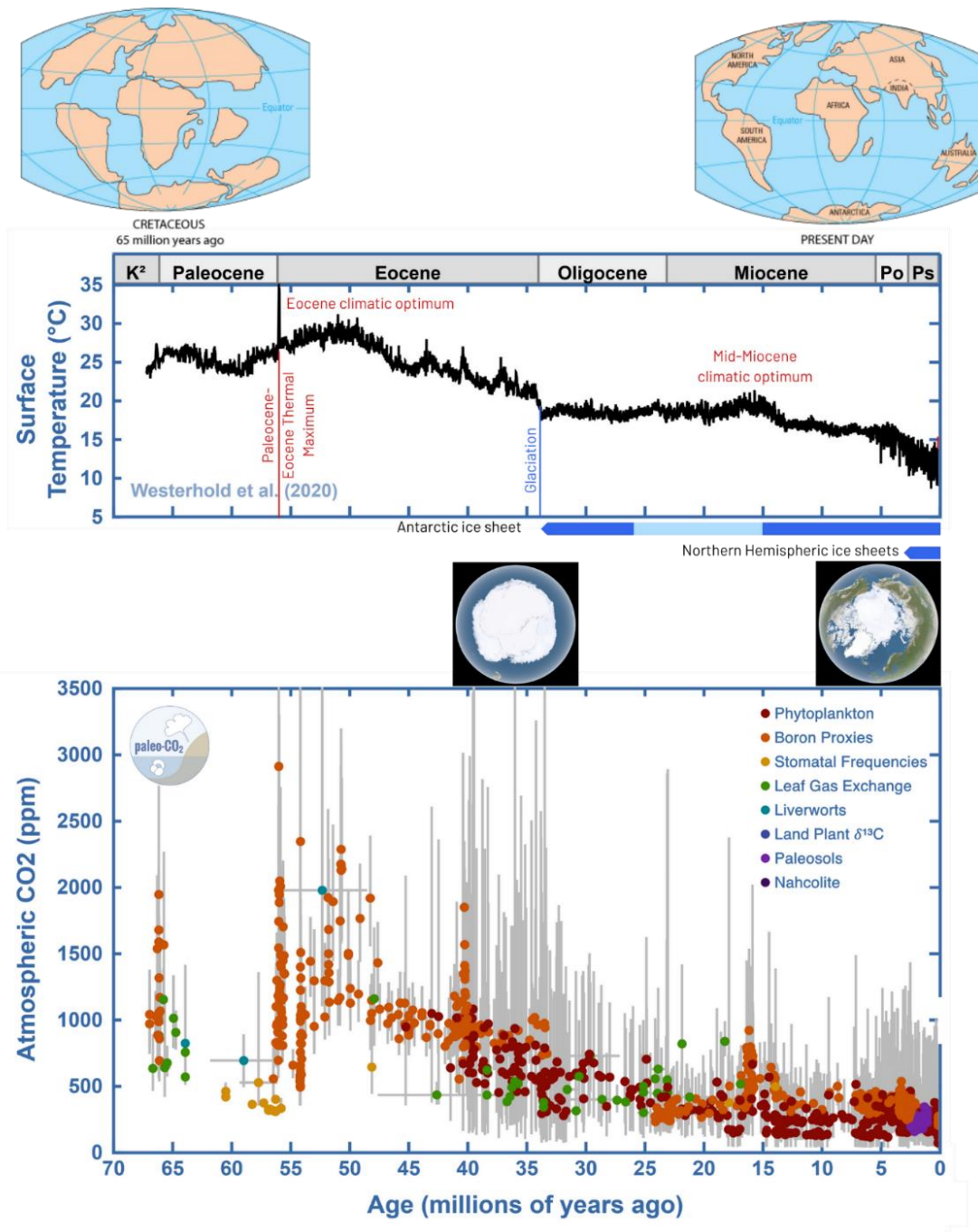


Figure 1.11 Evolution of the surface temperature and atmospheric CO₂ concentration from paleorecords between 70 Ma BP and present. The distribution of the continents at 65 Ma BP and today are schematically represented (Kious & Tilling, 1996). The proxy-based global surface temperature is shown (Westerhold et al., 2020). The development and thawing of the Antarctic and Northern Hemispheric ice sheets are shown by horizontal arrows (respectively in blue and light blue) and represented by satellite data view of June 2023 (<https://svs.gsfc.nasa.gov/5099/>). The atmospheric CO₂ concentration is reconstructed by the CenCO₂PIP Consortium using different proxies (Hönisch et al., 2023; <https://www.paleo-co2.org/>).

At ~2.6 Ma BP, the further progressive cooling led to the glaciation extent to the high latitudes of the Northern Hemisphere with the emergence of several ice sheets covering Greenland (Greenland ice sheet), the north of America (Laurentide ice sheet) and the north of Eurasia (Fennoscandian ice sheet). Despite warm seasons, the low temperature allows ice sheets to gain mass year after year and persist over thousands of years. By opposition with the permanent Antarctic ice sheet, the northern ice sheets are strongly sensitive to particularly high summer solstice insolation due to their remoteness of the north pole. The northern ice sheets volume thus varies depending on variations in the summer insolation at 65°N, itself determined by the relative position of the Earth with respect to the sun, i.e. the orbital parameters defined in Section 1.1.2.1.

1.2.2 Focus on the past 2.6 million years: the glacial-interglacial dynamics of the Quaternary period

This transition at around 2.6 Ma ago marks the passage to the Quaternary-world that is featured by an alternation between cold intervals characterized by low sea level and large ice sheets, named glacial periods, and warm period intervals characterized by reduced northern hemispheric ice sheets and high sea level, named interglacial periods (Fig. 1.12). The glacial-interglacial cycles show a periodicity between 40,000 and 120,000 years.

In a first section (1.2.2.1), we describe the paleoclimatic records of the glacial-interglacial climatic variability. In a second section (1.2.2.2) we provide clues for understanding the climate mechanisms at the origin of the glacial-interglacial variability.

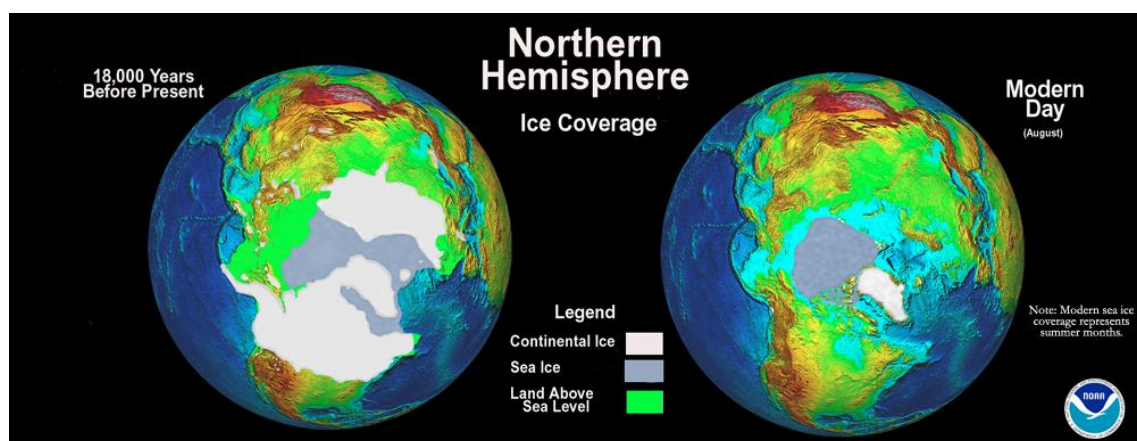


Figure 1.12 Ice coverage in the Northern Hemisphere during the last glacial period (18 ka ago, left) and today during the current interglacial, i.e. the Holocene (right) (Mark McCaffrey, National Oceanic and Atmosphere Administration, Wikipedia Commons).

1.2.2.1 Paleorecords archives of the Quaternary period

First, we provide examples of paleoclimatic archives of the Quaternary along with the type of climatic parameters they document and the time interval they cover. Then we focus on the major paleorecords measured in marine, continental and glacial archives that permitted to identify the alternation between glacial and interglacial periods.

Natural archives documented chronological sequence of past climatic events through their shape, size, colors, physical properties or geochemical composition. This is typically the case of marine and glacial archives that are drilled through sediments or ice that accumulated year after year on the ocean floor or at the top of the ice sheet. This is also the case of tree-rings, speleothems or corals which grow and gain new layers year after year. These stratigraphically continuous archives allow for reconstructing past temporal histories of Earth climate variables (atmospheric concentration in GHGs, temperature, vegetation, ice volume, sea level) during past climate variations of great amplitude.

The analysis of these paleoclimate archives provides continuous reconstructions of past climate across different timescales (Fig. 1.13).

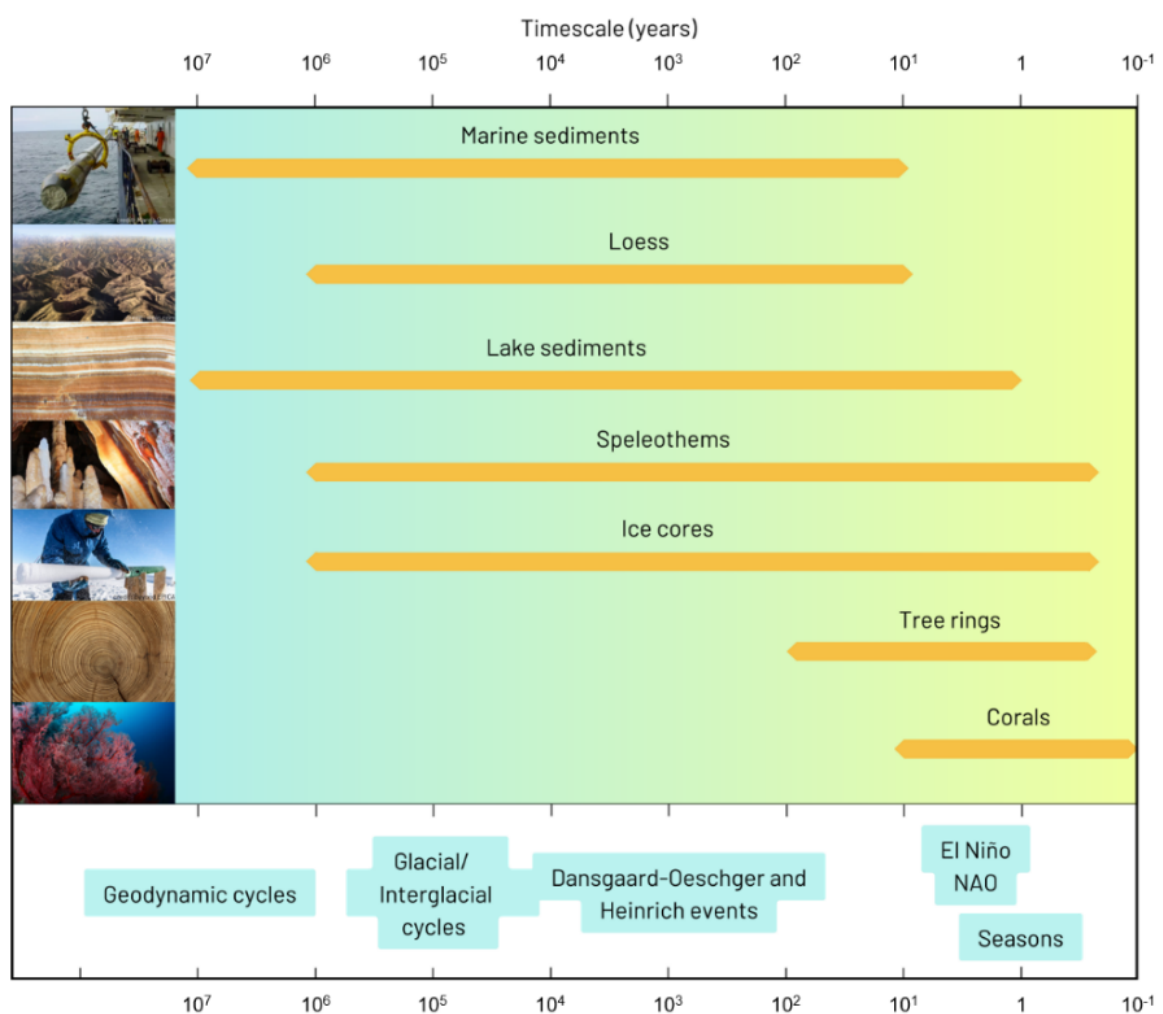


Figure 1.13 Logarithmic unit scheme presenting the main paleoclimatic archives and associated timescales as well as some characteristic examples of climate fluctuation (adapted from Yan, 2020).

Marine sediments

Marine sequences provide the longest continuous paleorecord so far, reaching back to ~six million years. In marine sediments are found fossils of foraminifera, which are single-celled organisms. The majority of these organisms live on or near the ocean floor, i.e. benthic foraminifera. A smaller number of these organisms float in the water column at various depths, i.e. planktonic foraminifera. The oxygen isotopic composition (noted $\delta^{18}\text{O}$ and defined in Chapter 2) of their carbonate shells is influenced by the temperature of water. Benthic $\delta^{18}\text{O}$ records thus reflect deep water temperature while planktonic $\delta^{18}\text{O}$ records reflect surface water temperature. Both benthic and planktonic $\delta^{18}\text{O}$ records are also dependent on the isotopic composition of seawater, which is linked to the volume of continental ice.

The first marine sequences retrieved showed a carbonate $\delta^{18}\text{O}$ isotopic signal that alternates between high and low values (Emiliani, 1955). The cycles in the isotope ratio were found to correspond to terrestrial evidence of glacial and interglacial periods. The cyclicity can be explained by the fact that during glacial periods, large amounts of water depleted in ^{18}O are trapped in continental ice sheets, which enriches the seawater in ^{18}O . Conversely, during interglacial periods, the melting of continental ice reduces the proportion of ^{18}O in seawater.

Emiliani (1955) thus proposed to divide the marine sequence into isotope stages on the basis of what he called variations in *paleotemperatures* (even though they are in reality a function of paleo ice volume and paleotemperatures). His division methodology was adopted by other studies (Shackleton, 1969; Shackleton et al., 2003) and constitutes the reference basis of the temporal sequence of glacial-interglacial cycles.

Lisiecki & Raymo (2005) built a stack of 57 globally distributed benthic $\delta^{18}\text{O}$ records extending over 5.3 million years. Prior to the radiocarbon dating limit, around 50 ka BP, the marine sediment chronologies are based on the orbital dating approach, which results in imprecise chronologies with average uncertainties of the order of 6 to 10 thousand years over the last million years. In the manuscript we use the scheme of lettered marine isotope stages and substages proposed by Railsback et al. (2015) for the LR04 $\delta^{18}\text{O}$ benthic stack over the past 1.0 million year. $\delta^{18}\text{O}$ values smaller than 3.5 ‰ correspond to interglacial stages and substages MIS 1, 5e, 7a, 7c, 7e, 9e, 11c, 13a, 15a, 15e, 17c and 19c (see Fig. 1.15).

Among Quaternary climatic proxies retrieved in marine sediments, large round-shaped debris were found in deep-sea sediments drilled off Antarctic Peninsula and South-Eastern Greenland (Heinrich, 1988a; Labeyrie et al., 1986). The analysis of the elemental composition of these debris permits to identify their exact source and revealed that they were originally formed below the ice sheets during their flow on the continental floor. When the polar ice sheets collapse at the continental edge, icebergs are detached and carry these debris away from the continents, until they melt and debris are deposited on the ocean's floor. The latitudes at which these Ice-Rafted-Debris (IRD) are found give information on the size of the debacle. The finding of the IRD at high latitudes in both hemispheres indicates that significant advance or retreat of polar ice sheets affected both hemispheres (figure 1.14).

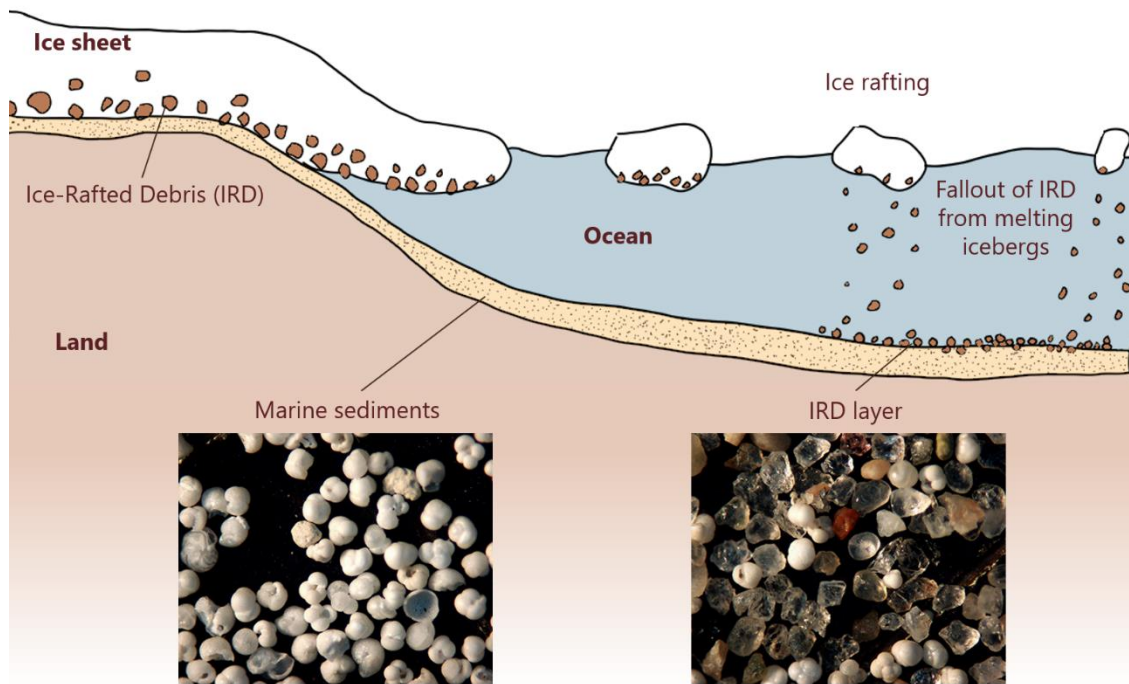


Figure 1.14 Schematic representation of ice rafting and melting leading to the deposition of Ice-Rafted Debris into marine sediments. On the left-hand side is a picture of sediment dominated by planktonic foraminifera. On the right-hand side is a picture of sediment dominated by terrigenous material that represents an ice rafting event. Both pictures are from the 300–355 μm size fraction (Pictures from Metcalfe, 2013).

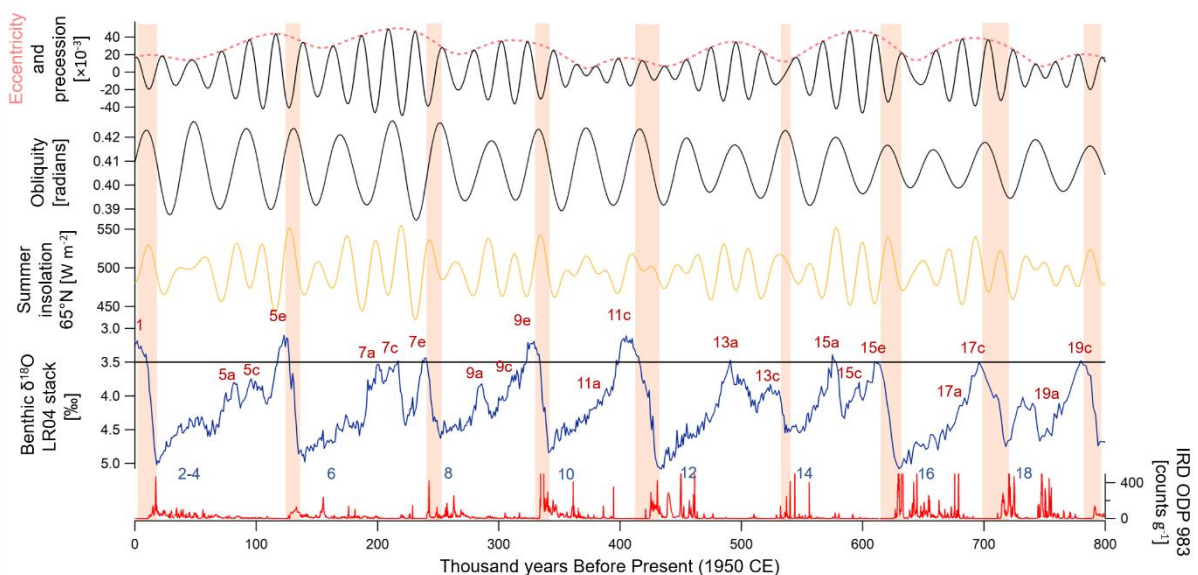


Figure 1.15 The evolution of the LR04 benthic $\delta^{18}\text{O}$ stack (blue curve) as a sea level proxy as well as of the Earth's orbital parameters and the summer insolation at 65°N over the past 800 kyr. Ice-Rafted debris (number of particles $>150\ \mu\text{m}$) from site ODP 983 in the Northern Atlantic sector are also shown (red curve; Barker et al., 2021). Red frames indicate sea level rises associated with glacial-interglacial transitions. Interglacial/glacial stages and substages are numbered in red/blue as per Railsback et al. (2015).

Continental records

The continental archives are mainly controlled by regional climatic conditions. Lacustrine sediments and peatlands show large amplitude changes in past vegetation during glacial-interglacial transitions via fossilized pollens.

Calcareous deposits including speleothems provide information on the past intensity of rainfall events as their growth requires rain input, thus indicating intensity of pluvial events associated with glacial-interglacial dynamics. In particular, the oxygen isotopic composition of calcite of speleothems depends on the isotopic composition of the drip water and on the temperature at which calcite formed. Consequently, the $\delta^{18}\text{O}$ of calcite from Chinese speleothems reflect both changes in the strength of the Asian monsoon as well as changes in the precipitation source regions.

Studies based on Asian cave records have demonstrated that the Asian monsoon exhibits cyclical variations over ~ 100 kyr (Cheng et al., 2012). In a recent study, Cheng et al. (2016) have provided a composite speleothem record from Chinese cave samples that extends earlier records to 640,000 years ago, which is close to the maximum age that can be achieved with U/Th dating.

Stratigraphic sequences also testify of the glacial-interglacial cycles, for example on the Asian continental Plateau via the alternation between loess deposits (eolian sediments essentially deposited during glacial periods) and organic-rich paleosols accumulated during warmer interglacial periods.

Ice core records

The deep ice cores drilled in Antarctica and Greenland (Figure 1.15) provide direct records of ancient global atmospheric composition (e.g. GHGs, dust, ...). They also enable the paleo-reconstruction of various climatic parameters at the local scale as well as over a wide range of latitudes. Temperature and snowfall conditions at the site of precipitation are traced by water stable isotopes (δD and $\delta^{18}\text{O}$ of H_2O). Temperature and moisture at the source of the evaporation are documented in the deuterium excess record. Further description of water isotopic records is provided in Chapter 2.

Ice core records also document:

- continental wetland temperature and moisture in tropics and northern hemisphere via methane concentration,
- sea ice surface area in the Southern Ocean via sea salt sodium
- terrestrial and marine carbon sinks via carbon dioxide
- dust production in the Southern Hemisphere mid-latitudes continents and transport efficiency towards Antarctica via dust or non-sea-salt calcium

Depending on where the glacial archives are drilled, they provided climatic information across

different timescales. Deep polar drillings in Greenland document climatic variability of the most recent glacial-interglacial cycle at the annual resolution. This high resolution is permitted by the high amount of snowfall per year. For example, the Northern Greenland ice coring project (NGRIP) drilling site reaches a depth 3084 m and dates back to 125 ka BP (thousand years Before Present, i.e. 1950 CE) (Andersen et al., 2006). Its average annual snow accumulation rate is of 14 cm i.e. (ice equivalent) per year (Bouchet, Landais, Grisart, et al., 2023).

The regions of western and coastal Antarctica are also characterized by high snow accumulation rates. The EPICA (European project for ice coring in Antarctica) Dronning Maud Land drilling site shows an average snow accumulation rate of 6 cm i.e. per year (Bouchet, Landais, Grisart, et al., 2023; Wilhelms et al., 2014). It reaches a depth of 2465 m and an age of 200 ka BP at the bottom of the core. Another example is the peripheral (with respect to the East Antarctic plateau) TALDICE drilling site (Frezzotti et al., 2007). It is associated with an annual snow accumulation rate of 8.5 cm i.e. and reaches back to 1597 m, documenting the past 500 thousand years (kyr) of climatic history.

The central and eastern Antarctica are rather featured by very low snow accumulation rates (inferior to 3 cm i.e. per year). Consequently, drilling sites such as Vostok (Petit, Jouzel, Raynaud, Barkov, Barnola, Basile, Bender, Chappellaz, Davis, Delaygue, Delmotte, Kotlyakov, et al., 1999), Dome Fuji (Kawamura et al., 2007) and EPICA Dome C (Augustin et al., 2004) provide climatic records over several glacial-interglacial cycles with an optimal resolution of 10 years because of stratigraphic noise. The specific EDC drilling site constitutes the longest continuous ice core record collected so far. It retrieves 800 kyr of past climate history. The younger 100-kyr amount of climate data is stored within the top 1000 meters while the oldest 100-kyr amount of climate data is zipped in the bottom 100 meters.

Some deep drilling sites in East and Central Antarctica are shown in Fig. 1.16 along with their respective age and depth. Over the past 800 kyr, deep polar ice cores retrieved significant covariations of atmospheric concentration in GHGs and of polar temperature over the glacial-interglacial transitions (Augustin et al., 2004) (red frames in Fig. 1.17).

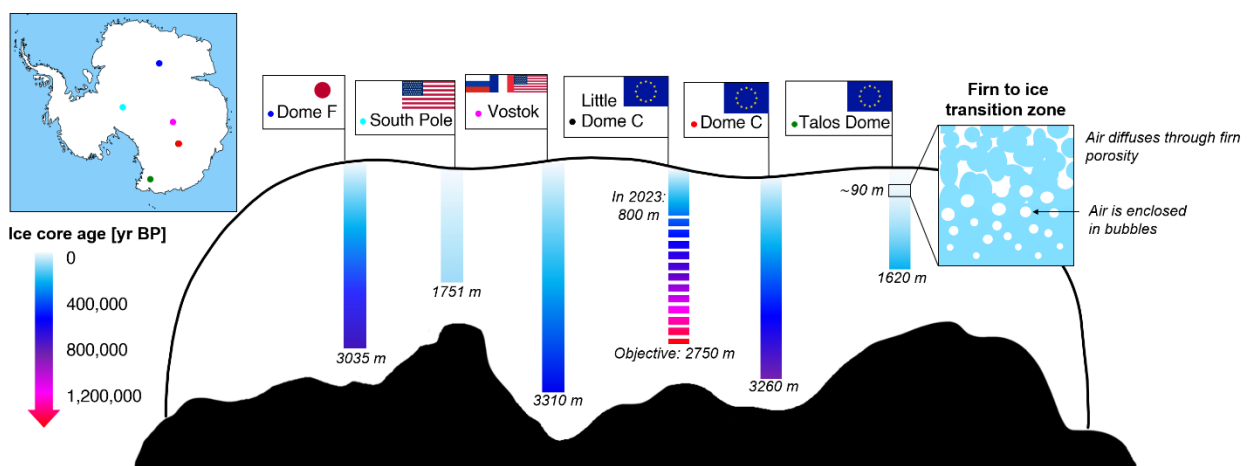


Figure 1.16 Deep East Antarctic ice cores and age scale: Dome Fuji ice core (720 ka BP), South Pole ice core (54 ka BP), Vostok ice core (420 ka BP), EPICA Dome C ice core (800 ka BP) and Talos Dome ice core (340 ka BP). The Little Dome C drilling aims at reaching 2750 m and 1.5 Ma BP (million years before present).

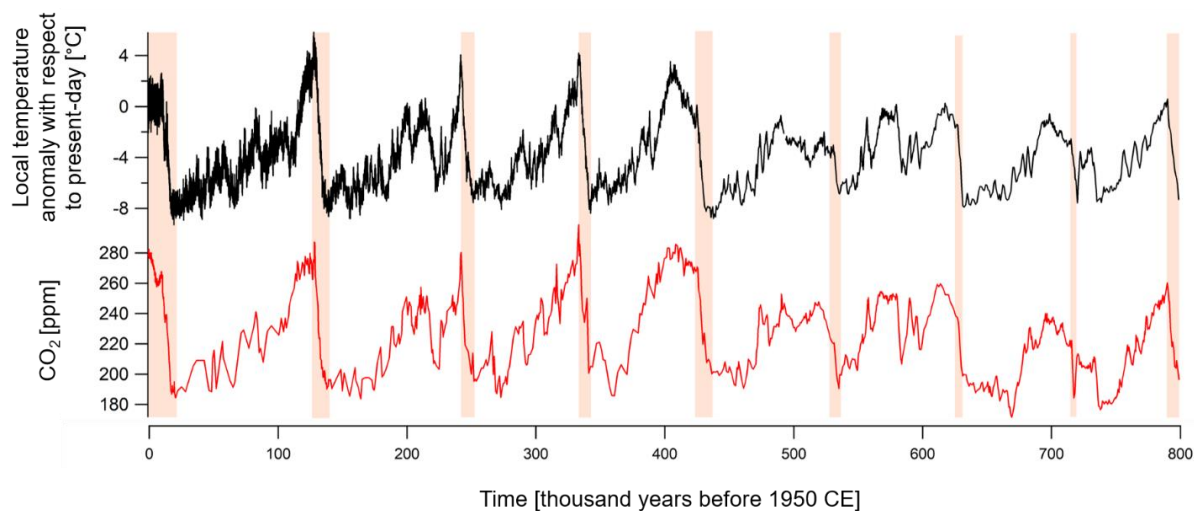


Figure 1.17 Evolution of temperature at Dome C with respect to the atmospheric CO₂ concentration measured in EDC ice core over the past 800 kyr. The temperature is inferred from δD measurements in EDC ice core (black curve; Landais & Stenni, 2021) and represented on the Antarctic Ice Core Chronology (AICC) 2023 ice age scale (Chapter 4). The CO₂ atmospheric content (red curve; Bereiter et al., 2015) is represented on AICC2023 gas age scale. Red frames indicate Antarctic warming and rise in atmospheric CO₂ associated with glacial-interglacial transitions.

Paleoreconstruction of typical glacial conditions

The various paleorecords mentioned in the preceding sections show that the typical climatic conditions featuring the past glacial periods are the following:

- The global sea level was lower by -50 to -120 m than today.
- The annual mean global temperature was lower by -5°C than today, with lower temperatures above continents (-10°C in France against -2°C for the surface of the tropical ocean) and decreasing temperatures with increasing latitudes (-20°C in Greenland, -10°C in Central Antarctica and -10°C for Northern Atlantic surface waters).
- The concentrations in atmospheric greenhouse gases were lower than during past interglacials, with CO₂ decreasing from ~300 to 200 ppm and CH₄ from ~0.7 to 0.35 ppm.

The glacial continental landscape was very different with the northern Hemisphere characterized by the presence of large ice caps (3 km-thick), covering northern America as well as Eurasia, and almost reaching current locations of Berlin and London (Fig. 1.18). Large alpine glaciers also developed, with modern cities as Grenoble or Geneva buried beneath 1 km of ice. The development of these large ice caps contributed significantly to the decrease in sea level. In the southern Hemisphere, low continental shelves emerged, prolonging Southern America, and, swept by strong winds, became an important source of dust production. The Antarctic ice sheet did not expand very much because of being surrounded by ocean, it thickened a bit, slightly contributing to decrease the sea level.

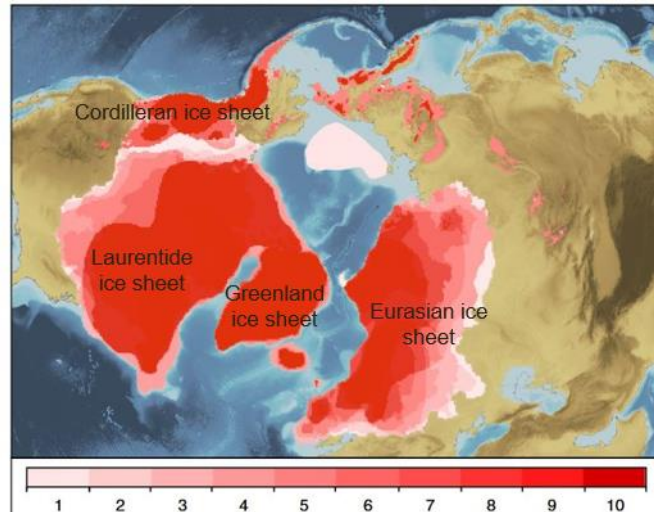


Figure 1.18 Intensity map of the number of times that each region of the Northern Hemisphere was covered by ice sheets, produced by overlaying the best-estimate ice-sheet reconstructions from MISs 2, 3, 4, 5, 6, 8, 10, 12, 16 and 20–24. Regions shaded dark red were subject to glaciation 8–10 times through the last 1 Myr, adapted from Batchelor et al. (2019).

1.2.2.2 Pacing of the Quaternary glacial-interglacial variability

In this section, we provide clues on understanding how orbital parameters and CO₂ forcing paced the glacial-interglacial variability which is maintained, amplified or hampered by many internal processes and feedbacks.

In the Early Quaternary, between 2.6 and 1.2 Ma BP, the alternations between glacial and interglacial periods are associated with sea level fluctuations of 50 m and occur every ~40,000 years in phase with the obliquity parameter. This era is classically referred to as the 40ka-world. Between 1.2 and 0.8 Ma BP, a transition marks the passage from the 40ka-world to an era where glacial-interglacial transitions occur every 80,000 to 120,000 years and are accompanied by sea level variations of up to 120 m (classically referred to as the 100ka-world). The sea level oscillations are documented by the $\delta^{18}\text{O}$ record of benthic foraminifers found in marine sediments which can be decomposed into major frequencies ~ 19, 23, 41 and 100 kyr (Hays et al., 1976). These frequencies also characterize the orbital parameters of the Earth (precession: 19 and 23 kyr, obliquity: 41 kyr and eccentricity: 100 and 400 kyr).

1.2.2.2.1 Orbital forcing: the theory of Milankovitch

Milankovitch (1941) suggested that the alternation between glacial and interglacial periods is due to variations in the Earth's orbital parameters that affect the Earth-Sun distance as well as the inclination of the Earth with respect to the Sun. Since then, the hypothesis of Milankovitch has been refined and some studies assert that the onset of glacial periods is triggered by a minimum of insolation at 65°N in summer, which allows snow to persist all year round, building up the Northern Hemispheric ice sheets. For example, at the last glacial onset, around 116 ka ago, summer solstice insolation at 65°N was around 40 W m⁻² (10%) lower than today. It is now

well established that the orbital forcing controls the summer insolation at 65°N, a key parameter in the development or shrinkage of the northern hemispheric ice sheets, and thus paces the glacial-interglacial cycles (Berger, 1980). However, the relative importance of obliquity and precession in driving glacial-interglacial variability remains a matter of discussion (Barker et al., 2022; Huybers, 2011; Huybers & Wunsch, 2005).

The strength and duration of interglacial periods depend on the orbital context. On average, the past interglacial periods are initiated by deglaciations – or glacial terminations – during which the climate warms by +5 to 10°C in 5 to 10 kyr. The interglacial conditions then typically last half a precessional cycle (10 kyr) until climate progressively cools again so that the Earth slowly slides into full glacial conditions. This slow glacial onset is sometimes interrupted by relatively warm intervals named interstadials during which the sea level is higher than the glacial level. Examples are the interstadials of MISs 5c and 5a that followed the last Interglacial (LIG or MIS 5e; Fig. 1.15).

As explained in Section 1.1.2.1, the precession determines whether the summer solstice in the northern hemisphere occurs at the perihelia or at the aphelia. Within a time interval of 11 ka, the summer intensity (in terms of insolation) in the northern hemisphere shifts from strong values (at the perihelia) to weak values (at the aphelia). The amplitude of this shift is modulated by the eccentricity of the Earth's orbit. If the eccentricity is low, the orbit is nearly circular and the summer intensity is not much amplified over the precession period, as perihelia and aphelia positions are equivalent. This effect is therefore modulated by the precession and eccentricity values determining the Earth-Sun distance on the 21st of June as well as by the obliquity parameter which determines the seasonality. The succession of several strong/weak summer periods induces retreat/extent of Northern Hemispheric ice sheets.

Nevertheless, only 25% of insolation maxima are associated with deglaciation and some deglaciations occur when the insolation maximum is of low amplitude. Invoking the variability in 65°N summer solstice insolation as the only driver of the glacial-interglacial dynamics is insufficient. Calder (1974) solely used an insolation threshold to simulate whether ice volume would linearly grow/shrink with decreasing/increasing insolation (Fig. 1.19). Although his model managed to predict all major glacial terminations retrieved in marine sediments in the last million years, it is too sensitive to the precession pacing and expects glacial termination to occur every 23 kyr (Paillard, 2001).

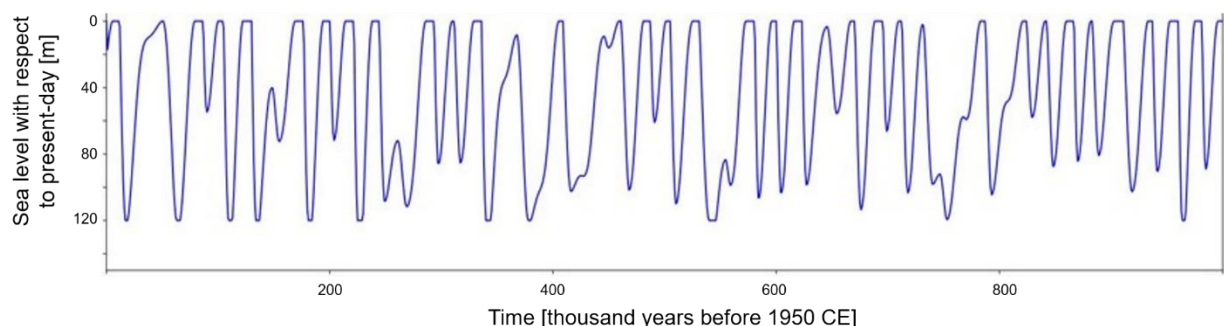


Figure 1.19 The sea level variations over the past million years as predicted by the model of Calder (1974).

The detailed sequence of events that lead to glacial-interglacial transitions remains

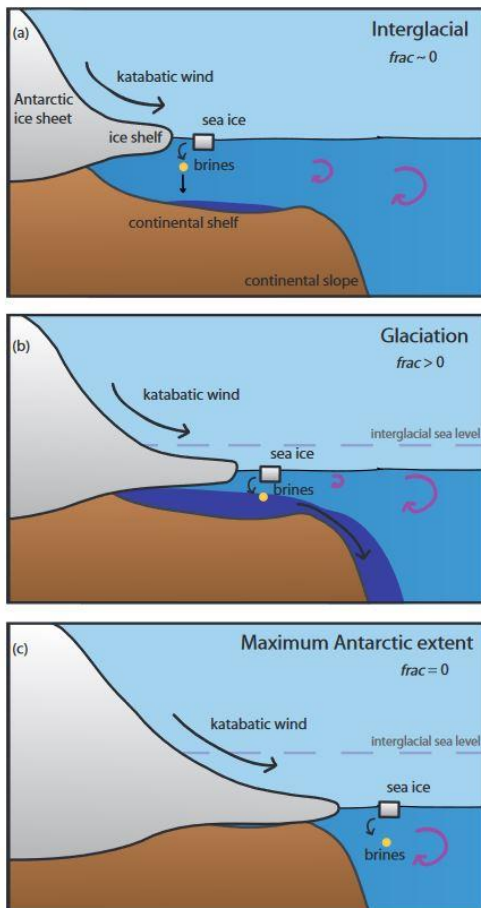
controversial. We list below the possible role of internal processes and feedback parameters in triggering and/or amplifying glacial inception and terminations.

1.2.2.2.2 The role of internal processes and feedback parameters in the warming of the Southern Hemisphere

Several mechanisms can be invoked to justify the observed concomitant Antarctic warming and atmospheric CO₂ increase over deglaciations (Fig. 1.17). Indeed, in the majority of deglaciations, the progressive warmings in Antarctica over several millennia are accompanied by the most significant increases in atmospheric CO₂ content of the Pleistocene (J. M. Barnola et al., 1987a; Lüthi et al., 2008; Siegenthaler et al., 2005).

(i) The role of greenhouse gases via the formation of carbon-rich bottom waters on the Antarctic margins

Since the model of Calder (1974) was not sufficient to explain all deglaciations, another model was developed by Paillard and Parrenin (2004) based on the observation that deglaciations occur when the ice caps have reached a maximum size. To develop this model, mechanisms were explored to link deglaciations to solar radiation and ice cap size, using CO₂ as a factor in triggering deglaciations. A first mechanism posits the **formation of brine (dense salt water) on the Antarctic margins**. The maximum expansion of the Antarctic ice sheet could potentially halt brine formation, resulting in CO₂ outgassing and concomitant Antarctic warming due to the enhanced greenhouse effect (Bouttes et al., 2012; Paillard, 2015).



The formation of sea ice in Antarctica is accompanied by the release of salt. This results in the formation of columns of cold, dense salt water (brines) that plunge deep over the Antarctic continental margins.

The dissolution of CO₂ in these cold waters is accelerated before they sink, and the resulting brines carry the dissolved gas to the bottom ocean. In cases a and b, the gas remains trapped in deep waters (dark blue zone in fig. 1.20).

In case c, the ice shelf is more extensive and goes beyond the continental shelf. Consequently, the oceanic column is too deep, and no further brines are formed. A smaller quantity of CO₂ is retained and a greater quantity is thus released into the atmosphere.

Figure 1.20 Diagram by (Bouttes et al., 2012) illustrating the mechanism proposed by Paillard and Parrenin (2004) that the extent of the Antarctic ice shelf affects the formation of carbon-rich deep salty waters (dark blue) during (a) the interglacial, (b) glacial, and (c) deglacial periods. The primary drivers of the fraction of salt sinking to the deep ocean (*frac*) are the Antarctic ice sheet extent on the continental shelf and sea level, which regulate the volume of water above the continental shelf. The greater the volume of water, the greater the mixing of brines, and the less they can sink into the deep ocean. When sea ice formation is shifted to the open ocean, brines are mixed and the sinking process ceases.

As the Earth's climate cools, the ice shelves expand around Antarctica. This region also experiences a reduction in precipitation, accompanied by an increase in surface salinity and an increase in the Antarctic Bottom Water (AABW) flux. This results in the transport of CO₂ into the deep ocean, thereby reducing the concentration of CO₂ in the atmosphere. The greenhouse effect is reduced, resulting in a decline in global temperature and enhanced growth of ice shelves. This is a positive feedback as temperature cooling amplifies the extension of the Antarctic ice sheet.

However, as the Earth's climate further cools, the ice shelves keep expanding around Antarctica and encroach upon the continental margins, preventing the formation of brines and the storage of CO₂ in bottom waters. CO₂ is released into the atmosphere, resulting in an increase in the greenhouse effect and a rise in temperature. This is a negative feedback as a decrease in temperature attenuates the extension of the Antarctic ice sheet.

The conceptual model developed by Paillard and Parrenin (2004) successfully predicts the past

four glacial-interglacial cycles by inducing a dependence of ice volume to insolation and CO₂ forcings as well as to the size of the ice sheet itself. A more recent modeling study of Yin and Berger (2012) revealed that greenhouse gas forcing could have a dominant role on the variations of the annual mean temperature of both the globe and the Southern Hemisphere high latitudes, while insolation forcing would control the variations of tree fraction, precipitation and of the Northern Hemisphere high latitude temperature and sea ice.

(ii) Possible feedback parameters amplifying/attenuating the glacial-interglacial variability

As defined in Section 1.1.2.2, feedback mechanisms either amplify (positive feedback) or attenuate (negative feedback) the initial global temperature forcing.

Sea ice extent

Global cooling induces the widening of the sea ice area around ice sheets, which prevents evaporation of water. There is no subsequent precipitation over the ice sheet, hampering its further growth (negative feedback).

Dust, albedo and CO₂

The cooling of the atmosphere reduces the atmospheric moisture amount and induces a drier climate. The dust production is enhanced via continental erosion and the dust transport to polar ice sheets is facilitated by reduced precipitation across their travel. As a result, more dust is deposited over ice caps, which reduces the albedo and increases the temperature. This is a negative feedback. In parallel, as the continental erosion increases, more iron is dissolved in the Southern Ocean. The introduction of nutrients to the marine environment enhances the productivity of micro-algae and of the biosphere, thus augmenting oxygen production and carbon dioxide consumption through photosynthesis (Lamy et al., 2014; Martin, 1990). Although, the Southern Ocean is one of the least nutrient-rich oceans, and is relatively less productive than others, this is a positive feedback as reducing the atmospheric CO₂ content dampers greenhouse effect, thus reducing temperature.

Ice sheets expansion

Ice sheets expansion leads to an increase in albedo. This decreases the temperature and the ice sheet further extends. Ice sheet expansion also induces an increase in ice sheet elevation. The temperature at the surface of the ice sheet is lower, thus the ice sheet further enlarges (Abe-Ouchi et al., 2013). Both mechanisms are positive retroactions.

Yet, increasing the surface of oceans and lakes covered by ice sheets increases the iceberg calving, resulting in shrinkage of the ice cap. In addition, increasing the interface between ice sheets and land increases the geothermal heating beneath the ice sheet, enhancing destabilization and melting beneath the ice sheets. These are negative feedbacks.

(Berends et al., 2021) developed a model considering these feedbacks and divided the sensitivity of the ice sheets to changes in insolation into three distinct regimes: small, medium, and large. These regimes correspond to the size of the ice sheet. In the small regime, the ice

cap is insufficiently large to survive the summer solstice insolation, and its response to insolation forcing is approximated linearly. Beyond the first threshold, the ice sheet shifts in the medium regime, where positive feedbacks (such as albedo and the effect of elevation on temperature) result in a positive feedback loop, whereby the larger the ice sheet, the greater its size. The ice sheet becomes self-sustaining, and it is possible for it to survive maximum summer solstice insolation. This results in a lower sensitivity to insolation. Beyond a second threshold, other mechanisms induce negative feedbacks. The ice cap becomes increasingly susceptible to disruption and instability. A maximum summer solstice insolation could result in a retreat of the ice sheet, which would then be subject to rapid disintegration.

The model of Berends et al. (2021) successfully reproduces the passage from a 41-ka pacing to a 100-ka pacing of the glacial-interglacial cycles at around 1 Ma ago using the insolation forcing combined with a gradual temperature decline. This idea agrees with the study of (Legrain et al., 2023) who found that a gradual change (in temperature for example) is more likely to have caused such a transition in cyclicity.

1.2.2.3 Factors favoring the glacial inception and glacial Termination

(Khodri et al., 2001) assert that the influence of orbital forcing alone on insolation and atmospheric transport is not sufficient to sustain large ice sheet during last glacial inception. Their data-modeling approach revealed the need for considering ocean feedbacks inducing cooling of high latitudes and enhanced atmospheric northward transport of moisture via the influence of the obliquity parameter that could have permitted the building of a perennial ice sheet.

To explain the timing of deglaciation, Tzedakis et al. (2017) proposed that ice sheet grows until reaching critical size and propensity for complete deglaciation increases with time elapsed since last termination. The exact sequence of events during a deglaciation remains controversial and many questions still are unanswered. Examples are the following:

- ✳ What is the sequence of climatic events triggering and sustaining the past deglaciations?
Are the mechanisms involved in each deglaciation the same? (Chapters 4 and 5).
- ✳ More specifically, does the Antarctic warming lead the atmospheric CO₂ increase over glacial Terminations? (Chapter 3)

The questions of interest mentioned in Chapter 1 and marked by ✳ are discussed over the course of the manuscript.

1.2.2.3 Millennial-scale climate variability

After having focused on the orbital-scale (10 to 100 kyr) variability of the climate over glacial-interglacial cycles, we now examine the climate variability at the sub-orbital scale (<10 kyr). In

this section, we first describe the records of millennial-scale variability over past glacial periods (Section 1.2.2.3.1). The climate mechanisms involved in the millennial-scale variability are detailed in section 1.2.2.3.2. Some studies assert that understanding the processes involved in the millennial-scale climatic variability provide insights on the mechanisms at the origin of the deglaciations. Arguments to defend this idea are presented in section 1.2.2.3.3.

1.2.2.3.1 Climatic records

The last glacial period (116-20 ka BP) in the Northern Hemisphere high latitudes

Heinrich (1988) highlighted the trace of icebergs debacle in Northern Atlantic sediments that occurred seven times over the past 60 kyr, leaving IRD in marine sediments (Hemming, 2004). The IRD can be found down to 45°N. They indicate the retreat or advance of past northern ice caps. When the IRD originate from the debacle of the Laurentide ice sheet, the events are referred to as Heinrich events. Four strict Heinrich events (H1, H2, H4, H5) have been documented over the past 60 kyr (Bond & Lotti, 1995; Vidal et al., 1999). They coincide with cold freshwater input in the Northern Atlantic surface waters, as documented in the planktonic foraminifers retrieved in this region. The other iceberg debacle events (namely H3 and H6) originate from the debacle of the Fennoscandian ice sheet.

Dansgaard-Oeschger events (D-O) were identified in 1980 in water isotopic content of Greenland ice cores which retrieved the past glacial-interglacial cycle with high temporal resolution (Grootes et al., 1993; Johnsen et al., 1992). They are characterized by the succession of a cold phase (Greenland Stadal, GS), an abrupt warming of 5-16°C occurring in a few years or decades (Landais et al., 2004) followed by a warm period (Greenland Interstadial, GI) marked by a gradual cooling into the next GS. The D-O abrupt warming is associated with a significant increase in atmospheric methane (+50 ppb; (Rhodes et al., 2015), rapid fluctuations of the vegetation cover in Europe, as well as inflexions in the ice core record of $\delta^{18}\text{O}$ of O_2 (Landais et al., 2007). Fossilized pollens found in Mediterranean and Atlantic cores indicate that warm and humid GIs were characterized by the expansion of an open forest in Europe with pines, green oaks, olive and pistachio trees while cold and drier GSs were associated with steppes and tundra vegetation. The GSs that coincide with Heinrich events recorded in North Atlantic sediments are named Heinrich stadials.

Marine sediments from the Northern Atlantic sector also traced millennial-scale changes in local sea surface temperature (SST), bearing distinct similarities to D-O variability, with the most extreme changes observed during Heinrich Stadials, leading to ~4 °C decreases in SST at Mediterranean latitudes in the Iberian margin (Martrat et al., 2007; Vautravers & Shackleton, 2006)

The last glacial period in the Southern Hemisphere high latitudes

Traces of the D-O events are also visible in Antarctic water isotopic records, revealing that both hemispheres are connected, but appear to be in phase opposition (Blunier & Brook, 2001). During stadial periods, when Greenland experiences cold temperatures, Antarctica gradually warms until that the Antarctic isotopic record reaches a maximum (Antarctic Isotopic

Maximum, AIM). Conversely, during interstadial periods, when Greenland is experiencing warmer temperatures, Antarctica gradually cools. This pattern has been designated the thermal “bipolar seesaw”, or TBS (Stocker and Johnsen, 2003; Fig. 1.21). The Greenlandic isotopic record is strongly anti-correlated with the time derivative of Antarctic isotopic record which seems to react with an inertia (Roe & Steig, 2004; Schmittner et al., 2003). However, this inertia is not always present in the response of the Antarctic climate. This is the case for the coastal site EDML located in the Atlantic sector of Antarctica which almost instantaneously warms/cools approximately in phase with cooling/warming of Greenlandic sites respectively (Fig. 1.21) (Landais et al., 2015)

South Atlantic marine sediments also trace abrupt changes in local temperature that occur in parallel with abrupt temperature variations observed in the Northern Hemisphere and that show no inertia (see fig. 1.21) (Barker et al., 2009).

Markle et al. (2017) used water isotopic content of the WD ice core to trace changes in evaporation source in the southern hemisphere. They found that abrupt meridional shifts of the evaporation source occur in phase with abrupt warming/cooling in the Northern Hemisphere.

Recently, (Buizert, 2023) pointed out that a decadal-scale warming in Antarctic ice core records is superimposed onto the AIM millennial-scale variability and occurs synchronously with rapid D-O warming in the Northern Hemisphere.

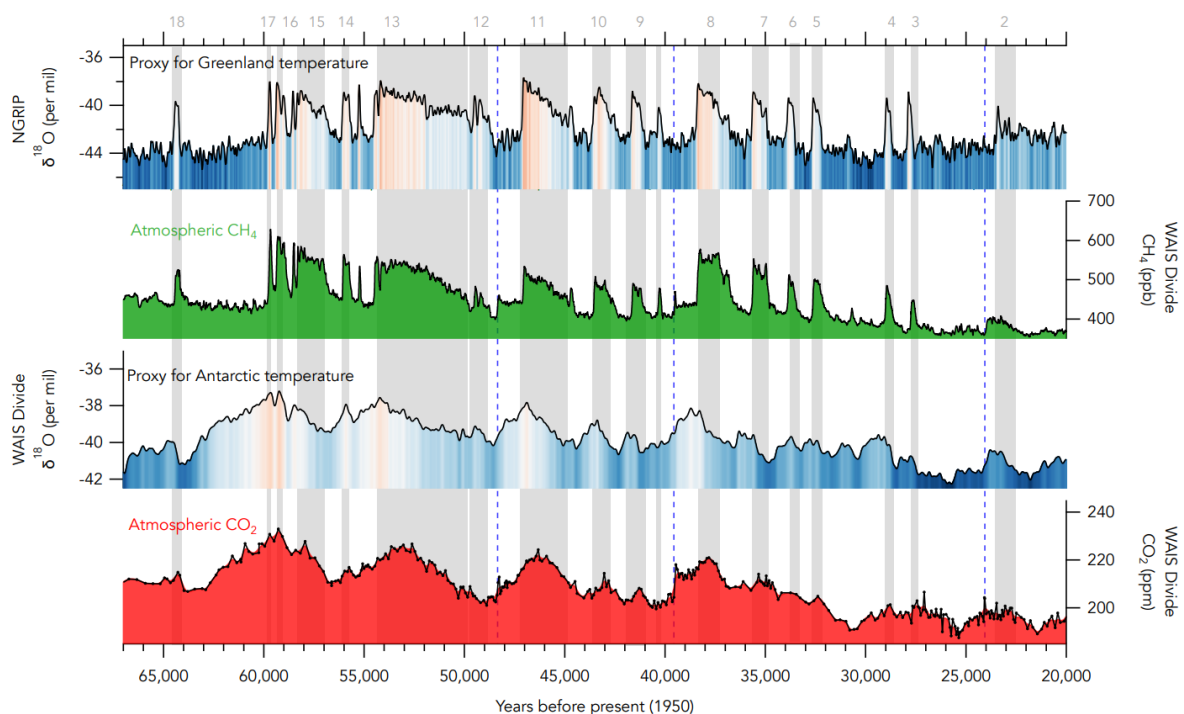


Figure 1.21 A synthesis of climate and carbon cycle variability over the 67-20 ka BP time interval of the Last Glacial Period. From top to bottom: (1) a proxy for Greenland temperature based on NGRIP oxygen isotopes (Andersen et al., 2004) a red (warm)-to-blue (cold) color ramp as fill; (2) the CH₄ record from WAIS Divide (Rhodes et al., 2015) with a green fill; (3) a proxy for Antarctic temperature from the WAIS Divide oxygen isotopes (Buizert, Adrian, et al., 2015) with a similar red-to-blue fill; and (4) the WAIS Divide record of atmospheric CO₂ (Bauska et al., 2021) with a red fill. Grey bars show interstadial periods; blue bars show some of the major Heinrich Events.

The last glacial period in the low latitudes

Over the course of the last glacial period, the $\delta^{18}\text{O}$ measured in speleothems reflects regional rainfall episodes on a millennial scale. Many studies observed an anti-correlation between pluvial events in East Asian, Indian, Northern African regions versus Southern America and Africa. While East Asian (Y. J. Wang et al., 2001), Indian (Deplazes et al., 2014) and Northern African (Mulitza et al., 2008) monsoon activity is increased during Glacials, the monsoon activity in Brazil (X. Wang et al., 2004) and Southern Africa (Simon et al., 2015) is intensified during GSs.

The global atmospheric composition during the last glacial period

Over the succession of D-O cycles, the atmospheric methane concentration appears well correlated with Greenland temperature (Fig. 1.21). Exceptions are abrupt release of methane that occur over Heinrich stadials (Rhodes et al., 2015) and deglaciations.

The atmospheric CO_2 concentration seems to increase in parallel with the Antarctic temperature with the exception of some AIM which do not find their analogues in the CO_2 (Fig. 1.21). Superimposed onto this sawtooth-shaped millennial-scale variation of CO_2 , recent studies highlight abrupt centennial-scale releases of CO_2 in the atmosphere (+5 to +14 ppm within a few decades) that appear unrelated to changes in Antarctic temperature (Ahn et al., 2012; Wendt et al., 2024).

Glacial intervals before the last glacial period

During the last glacial period, changes in the strength of the oceanic circulation led to changes in the interhemispheric heat transport resulting in cooling/warming in the Northern Hemisphere and opposite warming/cooling in Antarctica. Some studies demonstrated that this bipolar seesaw feature was also characteristic of the penultimate glacial period (Fohlmeister et al., 2023; Margari et al., 2010) and beyond. Martrat et al. (2007) used proxies of sea surface temperature and water mass distribution measured in marine sediments from the Iberian margin to show that the interhemispheric bipolar seesaw pattern was pervasive over glacial periods of the last 420 kyr. Birner et al. (2016) also found traces of this millennial variability prior to 1.2 Myr ago in proxies of sea surface temperature and oceanic circulation in marine sediments from the Iberian margin. Their study led them to assert that the bipolar see-saw was active during most major stadials in the early Pleistocene, prior to the Mid-Pleistocene Transition.

1.2.2.3.2 Glacial millennial variability mechanisms

The exact sequence of events triggering the D-O cycle remains a subject of discussion but studies demonstrated the potential role of several mechanisms involving the ocean, the atmosphere and sea ice in causing and/or amplifying the abrupt variability characteristics of past glacial periods. The main mechanisms are listed and explained in the following section.

Most studies based on marine sediment proxy data and climate modeling agree that the anti-

correlation observed between Greenland and Antarctica during D-O events over the last glacial period, i.e. the TBS, implies that interhemispheric heat exchange is modulated via changes in oceanic circulation which conveys heat from South to the North (Buizert, Adrian, et al., 2015).

During GSs, regions in the Atlantic sector of Antarctica seem to warm faster than sites located in the Indian and Pacific sectors (Landais et al., 2015), thus suggesting that the AMOC could be the underlying mechanism of the bipolar seesaw (Boyle, 2000; Lynch-Stieglitz, 2017). It is known that ocean circulation, particularly in the North Atlantic, is susceptible to sudden changes in its mode of operation.

Recent studies suggest that these oceanic processes are combined with a second contribution: interhemispheric heat transfer via atmospheric processes (Buizert et al., 2018; Markle et al., 2017). These studies advocate for decomposing the interhemispheric heat transport characterizing the TBS in two contributions: the oceanic processes resulting in Southern Hemisphere and Northern Hemisphere anti-phasing and atmospheric processes resulting in Southern Hemisphere and Northern Hemisphere phasing.

(i) Oceanic processes

AMOC disruption and Greenland Stadials

It is likely that the extent of sea ice cover in the North Atlantic plays a significant role in the variability of the D-O system.

First, because it is linked to the thermohaline circulation (THC) and AMOC. Broecker (1997) proposed a conceptual model in which the THC was able to switch between modes of operation and could generate the climate oscillations featuring the D-O cycles (Broecker et al., 1999; Broecker & Denton, 1989). This mechanism lies on the link between sea ice formation and water salinity in the regions where NADW are usually formed, hence activating/disrupting the THC and AMOC. Several studies assert that these changes in the global THC are either the consequence or the precipitating factor of observed ice sheet instabilities (Heinrich events). The collapses of ice sheet induce freshwater input to the Atlantic Ocean, impeding the formation of NADW. This results in further disruption of AMOC and amplification of the cooling in Greenland associated with Heinrich Stadials (Elliot et al., 2002; Ganopolski & Rahmstorf, 2001; Stocker & Wright, 1991).

Second, the sea ice extent acts as a positive feedback to instabilities in the AMOC (Gildor et al., 2003). Based on the findings of (Pedro et al., 2022), it can be inferred that sea ice likely extended southward to around 45°N during stadial periods. Extensive sea ice cover results in strong atmospheric cooling, particularly during winter months when the ice insulates the atmosphere from the relative warmth of the ocean (Denton et al., 2005). Rather than being the result of external forcing, the switches in AMOC state are likely an internal oscillation of the coupled ocean-sea ice-atmosphere system (Li & Born, 2019; Peltier & Vettoretti, 2014; Vettoretti et al., 2022).

Along with iceberg discharges in the North Atlantic, the polar front is displaced northward as sea ice extent retreats to high latitudes. This results in meridional shifts of the rain belts and

associated intensification of pluvial episodes in the region where NADW usually forms. This phenomenon disrupts the AMOC. Margari et al. (2010) showed that intensification of pluvial events in the Northern Atlantic region caused protracted stadials than when AMOC is solely disrupted by iceberg discharges.

One might expect that AMOC disruption would produce a simple inverse pattern of Antarctic and Greenland temperatures. Indeed, Barker et al. (2009) observed a symmetric anti-correlation between Greenland temperature and Southern Atlantic temperatures.

However, we rather observe an asymmetric anti-correlation between abrupt variations in Greenland temperature (as well as in methane) versus slow, saw-tooth-shaped, variations in atmospheric CO₂ and in Antarctic temperature proxies. Exceptions are temperature reconstructions at Dome Fuji and EDML located in the Atlantic sector which warm relatively rapidly at the onset of GS, which may reflect their proximity to upwelling of northern-sourced water masses, or regional effects. This asymmetric anti-correlation could be caused by the large thermal inertia of both global ocean and of the Southern Ocean that provides a heat reservoir in the south, accumulating the heat flow from the north (Buizert, 2023).

During GSs, global atmospheric CO₂ increases in parallel with warming of the Southern Ocean. The increase in atmospheric CO₂ is coherent with a disrupted AMOC which prevents formation of carbon-rich AABW and the carbon-rich AABW formation could be further dampened due to increased precipitation during Antarctic warming (see section 1.2.2.2.2).

AMOC resumption and Greenland Interstadial

At the end of prolonged GSs, the THC is activated because of salt rejection at the extremity of very large northern ice caps (reaching low latitudes) which increases the salinity of surface waters, inducing spontaneous plunging of North Atlantic waters. This mechanism combined with no freshwater input in the zone of NADW formation permits the resumption of AMOC and the interhemispheric heat transport from the South to the North. As a result, the Southern Hemisphere cools and Northern Hemisphere warms. During D-O warming at the inception of GIs, the atmospheric CO₂ decreases via carbon uptake and storage in deep ocean through enhanced formation of carbon-rich AABW.

(ii) Atmospheric processes

ITCZ meridional displacement

The changes in sea ice affect the position of the polar front and westerly winds, itself impacting the migration of the rain belts. During GIs, the regress of the polar front to higher latitudes induces a northward displacement of the ITCZ and westerly winds. The monsoon activity is enhanced in Asia, India and Northern Africa. The variability of the atmospheric CH₄ content can be attributed to melting of permafrost during D-O warmings combined with latitudinal shifts of the ITCZ and associated tropical rain belts, leading to subsequent release of CH₄ to atmosphere from Northern Hemisphere tropical wetlands (Deplazes et al., 2013; Rhodes et al., 2015; X. Wang et al., 2006). During GSs, the sea ice and ice caps reach lower latitudes in the Northern Hemisphere which result in a southward shift of the ITCZ position. Regions such as

Brazil and South Africa are in turn affected by intense rainfall events. During protracted GSs, a prolonged southward position of the tropical rain belts induces excessive flooding of southern hemispheric wetlands and could explain additional release of methane to the atmosphere (Rhodes et al., 2015).

Latitudinal moisture and heat transport

Markle et al. (2017) used the deuterium-excess record from West Antarctica to demonstrate that the moisture source for Antarctic precipitation was latitudinally displaced in phase with abrupt changes in Northern Hemisphere climate, and significantly in advance with respect to changes in Antarctic temperature (AIM). Their study evidenced that Southern Hemisphere mid-latitude moisture pathways were displaced in parallel (within decades) with abrupt climate variability in the North Atlantic and associated meridional migrations of the intertropical convergence zone.

Recent studies summarized in the review of (Buizert, 2023) indicate that at the time of the D-O warming transitions, the average Antarctic temperature maximum occurs in synchrony with the Greenland temperature maximum. This rapid warming is superimposed on the millennial bipolar seesaw warming in Antarctica, and strongly suggests that the abrupt change observed in Greenland is associated with a direct atmospheric circulation change at a global scale. The aforementioned pattern is not observed at the EDML ice-coring site, which is located in the Atlantic sector of Antarctica.

Global sea level

The marine data synthesis of Siddall et al. (2008) showed that ice volume fluctuated in accordance with an Antarctic rhythm during the last glacial period, i.e. gradually decreasing/increasing sea level during GIs/GSs respectively. Their finding is coherent with the modeling work of Clark et al. (2007) which suggests that the mass balance of the major northern hemisphere ice sheets may be dominated by an Antarctic-like temperature signal.

Summary on the bipolar seesaw

As summarized in the review of Buizert (2023), pleistocene glacial periods exhibit D-O oscillations, in which the North Atlantic climate underwent abrupt and repeated transitions between millennial-scale warm GIs and cold GSs phases. In a pattern known as the thermal bipolar seesaw, interstadials are associated with a robust AMOC and gradual cooling of Antarctica, which is mediated by cooling of the global ocean interior. In contrast, stadials are associated with a weak circulation and gradual warming of Antarctica, which is mediated by warming of the global ocean interior. Variations in sea ice in both hemispheres serve to amplify the oceanic changes. Superimposed on the bipolar seesaw, Antarctic climate exhibits an abrupt, spatially heterogeneous mode of climate change that is synchronous with Greenland D-O events and linked to meridional shifts in the position of the southern hemisphere westerly winds.

Therefore, the D-O cycle is an internal oscillation of the coupled ocean-sea ice-atmosphere system, rather than a series of individually forced events (Kuniyoshi et al., 2022; Obase & Abe-Ouchi, 2019; Peltier & Vettoretti, 2014). The climatic behavior in the two hemispheres over the last glacial period is ideally summarized in Fig. 1.22.

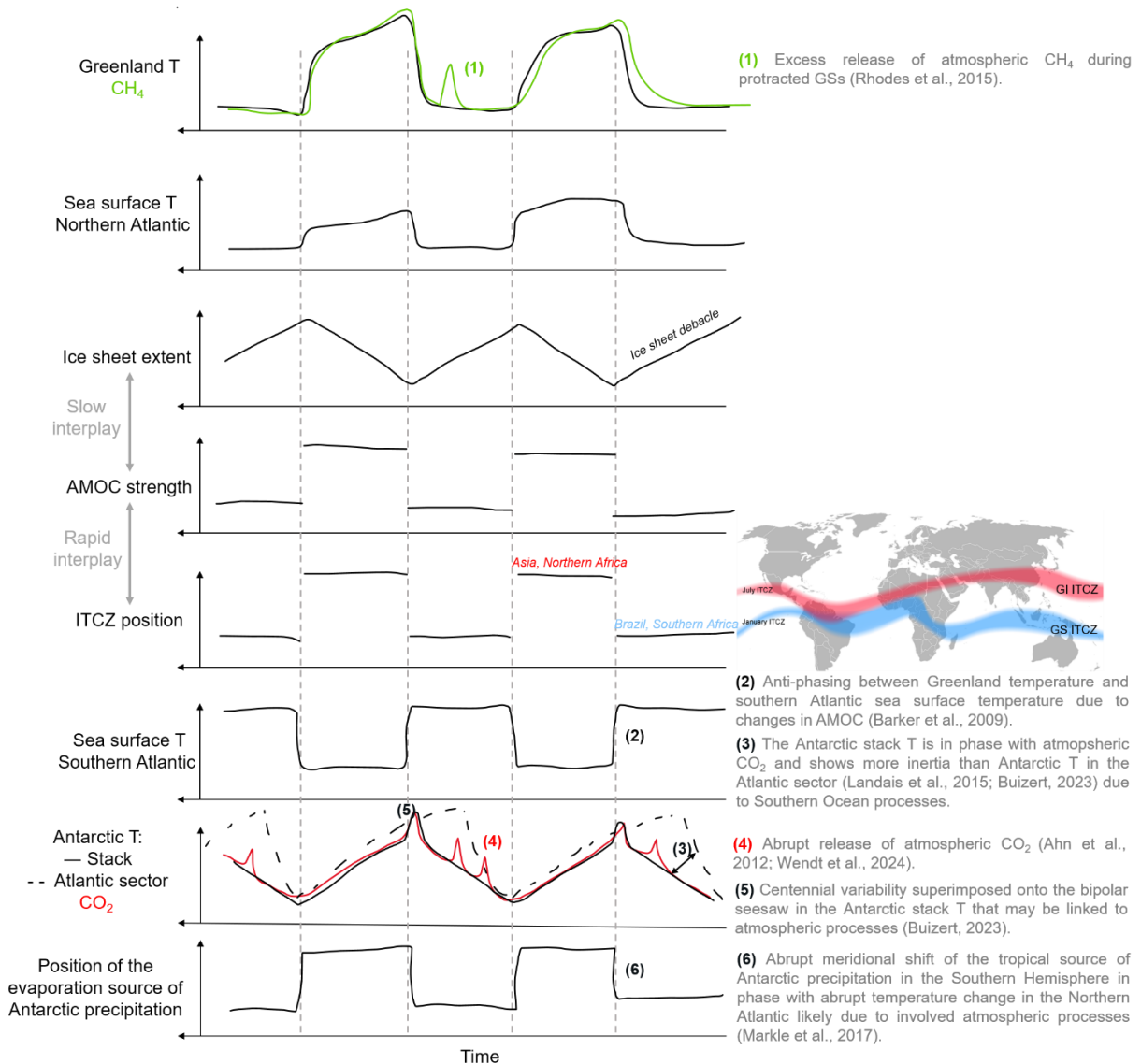


Figure 1.22 A synthetic schematic representation of the millennial climatic variability over the last glacial period. From top to bottom: Idealized temporal evolution of Greenland temperature, atmospheric CH_4 , sea surface temperature in the Northern Atlantic, global ice sheet extent, AMOC strength, the latitudinal position of ITCZ, sea surface temperature in the Southern Atlantic, Antarctic stack temperature as well as the Antarctic temperature in the Atlantic sector (e.g. EDML site), atmospheric CO_2 and the position of the evaporation source of Antarctic precipitation. The mechanisms evoked in the preceding sections to explain the climatic variability of the last glacial period are indicated on the graph and numbered from 1 to 6.

1.2.2.3.3 Implications of understanding mechanisms involved in DO-Heinrich events to refine understanding of mechanisms involved in the deglaciations

Having understood the mechanisms involved in the millennial-scale climatic variability of past glacial periods (D-O and Heinrich events) may help us to refine potential mechanisms at play during the deglaciations. In particular, we describe here the potential roles of changes in AMOC and in the atmospheric circulation that may have led to and/or amplified the glacial Terminations.

The role of the AMOC disruption in the deglaciation

A proposed mechanism involves AMOC changes leading to a TBS (Landais et al., 2013). In this view, the cooling of the North Atlantic is associated with the warming of the Southern Ocean (and Antarctic) and the outgassing of CO₂.

The collapse of northern ice sheets can be caused by several factors including the critical size of the ice sheet and the warming of subsurface water in the northern Atlantic seas induced by large summer insolation (Marcott et al., 2011). Such collapses induce massive inflows of freshwater linked with glacial ice sheet collapses (traced by IRD in marine sediments) affect deep-water formation in the north or the south inducing AMOC changes and Greenland cooling. Climate modeling confirmed this hypothesis as simulated freshwater discharge applied in the North Atlantic induces AMOC weakening and South Atlantic systematically warming (Landais et al., 2015). Although Heinrich events in the North Atlantic system might not be the trigger of AMOC weakening but rather an amplifier.

An analogy can thus be proposed between the Southern Atlantic warming occurring during Heinrich stadials and the Southern Ocean warming occurring during glacial Terminations. The analogous mechanisms that could be involved are schematically represented in Fig. 1.22.

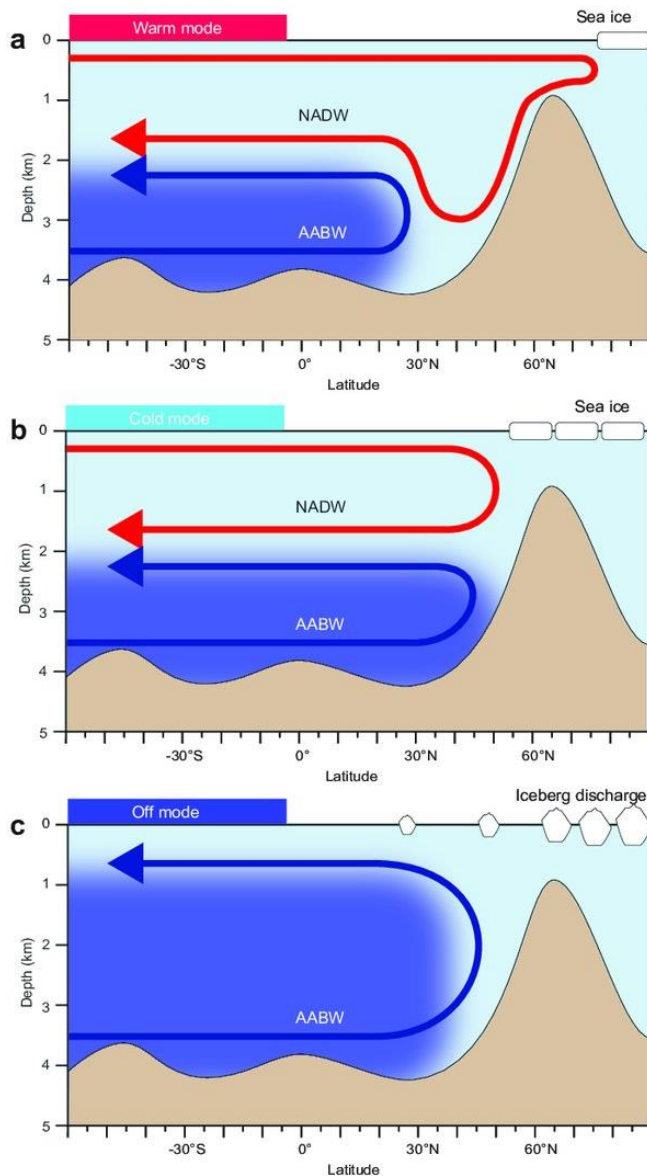


Figure 1.23 Schematic representation of the Atlantic Meridional Overturning Circulation (AMOC) under different climatic states (adapted from Bohm et al., 2014; Crivellari, 2018). a) A warm mode, analogue to the Holocene, describes a vigorous overturning with strong production of NADW at northern high latitudes. The northern penetration of the AABW is reduced. b) A cold mode, analogue to the LGM, presents a reduced production of NADW, extensive sea-ice and a further penetration of southern sourced AABW. c) The overturning circulation is greatly or completely reduced. This state is analogue to Heinrich Stadials which are characterized by the absence of NADW formation, release of iceberg and important northern penetration of AABW.

The role of the atmospheric circulation

Another proposition for explaining glacial Termination invokes atmospheric teleconnections, which result in increased winter northern hemisphere sea ice and concomitant southward shifts of the ITCZ and southern westerly winds. This leads to both an outgassing of CO₂ in the Southern Ocean and Antarctic warming (Clement et al., 2015). In any case, ITCZ shifts can in turn magnify AMOC variations by affecting input of freshwater in the oceanic system and thus modify the water movements driven by density (salinity) gradients.

Conclusion

However, these hypotheses relying an analogy between the terminations of Heinrich stadials and of glacial periods remain exploratory and inconclusive. Indeed, past glacial periods and glacial terminations remain poorly constrained (in terms of paleoclimatic reconstructions of atmospheric and oceanic circulations), complicating the analogy with relatively well-documented Heinrich stadials and their end.

The climate changes observed at millennial- and orbital-scale during glacial-interglacial cycles involve the same interactions and feedbacks between the different components of the Earth system (ice sheets, ocean, atmosphere). Tzedakis et al. (2004) argued that although the broad timing of interglacials is consistent with orbital theory, their specific duration may be dictated by millennial variability. More recently, Buizert (2023) asserted that "there exists an interdependency between the D-O cycle and the glacial-interglacial cycle that we are only just beginning to understand." These statements guide us towards the following list of pending questions concerning the diversity in length and intensity of past interglacials:

- ✳ Why do some interglacials such as the MIS 11c or the MIS 7e not align with the astronomical theory of ice ages? (Chapters 3 and 4)
- ✳ Why is there a long-term change in interglacial intensity observed over the past 800 kyr? And how to choose a relevant metrics of interglacial intensity? (Chapter 3 ; Appendix 7.1)

The questions of interest mentioned in Chapter 1 and marked by ✳ are discussed over the course of the manuscript.

1.3 CONTEXT, OBJECTIVES AND METHODS OF THE PHD

1.3.1 Context

From orbital to decadal timescales, complex interactions exist between:

- External forcing (insolation)
- Climatic response (surface temperature, atmospheric concentration in GHGs, sea level)
- Climate system dynamics and retroactions:
 - o Oceanic and atmospheric circulations
 - o geochemical cycles
 - o Ice sheet dynamics

These interactions can change and evolve depending on global climate mean state and thus must be questioned to understand how the climate machine works.

Among the paleoclimatic archives that documented Quaternary climate, we focus on deep polar ice cores which are unique as they provide direct records of ancient global atmospheric composition in GHGs and documented past local changes in snowfall and temperature.

Among deep polar ice cores, we focused on the EDC ice core which recorded eight glacial-interglacial cycles that affected Earth's climate every ~100 kyr over the past 800 kyr. EDC constitutes the first continuous ice core record that goes that far back in time. The temporal resolution of the EDC ice core permits to document climate change at the millennial (1 kyr) to orbital (10-100 kyr) timescales.

Hence, the EDC ice core is perfectly suited to understand the climatic variability of the Quaternary, in particular the links between external forcing and the climate dynamics and response over a wide range of latitudes and timescales.

1.3.2 Objectives

This PhD aims at:

- ✓ Assessing the reliability of proxy-based paleoreconstructions of local climate (temperature and precipitation) in East Antarctica
- ✓ Providing a precise, coherent and federative timescale for deep polar ice cores
- ✓ Studying its implications for the comprehension of climatic mechanisms

1.3.3 Methods and research directions

To tackle the three abovementioned objectives, we explored three research directions described in Chapters 3, 4 and 5:

- 🔍 Providing an additional tool for documenting past changes in temperature and snowfall using $\delta^{15}\text{N}$ measurements in air trapped in EDC ice core (Chapter 3).
- 🔍 Building the Antarctic Ice Core Chronology (AICC) 2023: a precise, coherent and federative timescale for deep polar ice cores over the past 800 kyr (Chapter 4).
- 🔍 Building coherent chronological framework for marine and glacial archives over the past glacial-interglacial transitions (Chapter 5).

Our general methodology combines modeling experiments with experimental analysis of EDC ice core records and data analysis of paleo records from glacial and marine archives as well as from speleothems.

2 CHAPTER 2

RECONSTRUCTING CLIMATE HISTORY USING DEEP POLAR ICE CORES: ANALYSIS AND DATING METHODS

“Do you hear the snow against the window-panes, Kitty? How nice and soft it sounds! Just as if some one was kissing the window all over outside. I wonder if the snow loves the trees and fields, that it kisses them so gently? And then it covers them up snug, you know, with a white quilt; and perhaps it says, go to sleep, darlings, till the summer comes again.”

(Carroll & Tenniel, 1871)

Foreword

In this chapter, we first describe how changes in local temperature and precipitation are documented in ice core records and how to reconstruct their past variations using ice core data. Secondly, the process of trapping of ancient atmosphere in air bubbles trapped within the ice matrix is detailed. The analytical methods performed at LSCE which permit the air extraction from ice for ^{81}Kr analysis and the measurement of the $\delta^{15}\text{N}$ isotopic composition of the gas molecules enclosed in ice cores are presented. Third, the methodology for dating ice cores is introduced. A 2-page paper reviews the approaches existing for dating deep polar ice cores (Bouchet, Landais, & Parrenin, 2023) was published in *Past Global Changes Magazine* and is attached in Appendix 7.2.

Objectives

The objectives of this chapter are to provide a state-of-the-art of different methodologies used by the ice core community for:

- ✓ Reconstructing past variations of local climatic parameters such as temperature and precipitation using ice core records
- ✓ Understanding how atmospheric air is trapped in ice using snow densification models
- ✓ Measuring past atmospheric composition in air bubbles trapped in ice cores
- ✓ Providing age models for deep polar ice cores using measurements as well as glaciological and statistical models

Highlights

My PhD aimed at tackling the challenges linked with the abovementioned methodologies presented in this Chapter. To do so, I contributed to:

- Perform new measurements on the EDC ice core for dating purposes and for estimating Δ age (Chapter 2).
- Circumvent the limitations of classical local climate reconstruction inferred from water isotopic records (Chapter 3)
- Reduce the uncertainty on Δ age (Chapter 4)
- Ameliorate the precision of deep polar ice core chronologies (Chapter 4) and connect ice core age scales with other archives (Chapter 5).

The questions of interest mentioned in Chapter 2 and marked by ✳ are tackled over the course of the manuscript.

2.1 ON THE RECONSTRUCTION OF PAST CHANGES IN LOCAL TEMPERATURE AND PRECIPITATION USING ICE CORE RECORDS

2.1.1 Stable isotopes definition

Isotopes are atoms in which the nuclei exhibit the same number of protons but a different number of neutrons, thus occupying the same position on the periodic table. The official notation for isotopes is written: A_zE where A is the mass number (i.e., the sum of the number of protons and neutrons in the nucleus), z denotes the atomic number and E is the element symbol. It is possible that each element may have a different number of isotopes, with each isotope possessing a unique abundance in nature. These isotopes may be either stable or radioactive.

Radioactive isotopes decay over time such as the ${}^{14}_6C$ which undergoes beta decay. This process involves the decay of ${}^{14}_6C$ into an atom of ${}^{14}_7N$ through the conversion of one of the neutrons in the carbon atom into a proton, thereby transforming the element into a nitrogen atom (an electron and an antineutrino particle are also generated). If ${}^{14}_6C$ is always decaying, why do we still find it in our atmosphere? Cosmic rays are high-energy particles that originate in outer space. Upon colliding with matter in the atmosphere, cosmic rays can shatter a nucleus into smaller pieces, a process known as spallation that results in the production of neutrons. Subsequently, neutrons decelerate through collisions with atmospheric matter. Once it has sufficiently slowed, it can be absorbed by a ${}^{14}_7N$ nucleus, giving ${}^{14}_6C$ and an ejected proton.

The radioactive isotopes are opposed to stable isotopes that do not undergo decay into another element. The stability of nuclides is governed by two main rules (Hoefs, 2015):

- The symmetry rule, which states that in a stable nuclide, the neutron-to-proton ratio (N/Z) is approximately equal to 1 and may reach 1.5 at most for isotopes with more than 20 protons or neutrons.
- The Oddo-Harkins rule states that nuclides of even atomic numbers are more abundant than those with odd numbers.

2.1.2 Isotope fractionation processes

Variations in the atomic mass of an element result in differences in its chemical and physical properties. This phenomenon is known as isotope fractionation and occurs when isotopes are unevenly distributed between two compounds or two phases of the same compound. The mass differences that characterize isotopic compounds (i.e. chemical compounds consisting of molecules containing various isotopes of the same element) give rise to different behaviors of isotopic molecules. In particular, heavier isotopic molecules are distinguished by a lower mobility in comparison to the lighter ones. This results in slower diffusion and a reduced frequency of collisions with other molecules. Moreover, heavier molecules exhibit higher binding energies, necessitating a greater energy input to break chemical bonds in comparison to the lighter ones. Elements that show significant isotopic fractionation are the most

extensively studied and share several common characteristics including:

- relatively low atomic mass,
- large mass difference between the rare (heavy) and abundant (light) isotope,
- chemical bonds that have a high degree of covalent character (linked to the size and charge of bonding ions),
- relatively high abundance of the rare isotope, which can be detected by instrumentation, such as a mass spectrometer (Sharp, 2017).

Equilibrium fractionation

Equilibrium fractionation designates a change in the isotope partition among different chemical substances, different individual molecules, or different phases without a net reaction. Equilibrium fractionation can be written as:



where A and B are the chemical species containing either light (1) or heavy (2) isotopes. The equilibrium constant K is expressed as follows:

$$K = \frac{\left(\frac{A_2}{A_1}\right)^a}{\left(\frac{B_2}{B_1}\right)^b} \quad (2.2)$$

where the terms in parentheses are the molar ratios of the different isotopic species. The magnitude of this equilibrium isotopic effect is related to the bonding environment of the phases involved. Furthermore, the fractionation between two phases is only a function of temperature, and tends to be zero at very high temperatures (Hoefs, 2015).

Kinetic fractionation

Kinetic fractionation is very frequent in nature. The phenomenon is irreversible and usually associated with unidirectional and fast or incomplete processes such as diffusion and evaporation. It can be explained by the disparate velocities of the different isotopic forms of molecules as they move across a phase boundary or through a phase. For example, during diffusion, light isotopic forms of molecules will preferentially move out of the initial source, leaving it enriched in heavy isotopic forms. During evaporation, lighter isotopic forms of molecules will break through the liquid-vapor interface and diffuse across a boundary layer thanks to their larger average migration velocity relative to isotopically heavier molecules. This creates isotopic fractionation between vapor and liquid (Sharp, 2017).

In the case of kinetic fractionation, the equilibrium constant K is expressed by the fractionation factor α :

$$\alpha = \frac{\left(\frac{A_2}{A_1}\right)}{\left(\frac{B_2}{B_1}\right)} \quad (2.3)$$

where the terms in parentheses are the ratio of the numbers of isotopes in the substances/phases A and B.

The delta notation

Isotopic composition is expressed in delta units (δ). The delta notation was introduced by McKinney et al. (1950) and is written as:

$$\delta = \left(\frac{R_x}{R_{std}} - 1\right) \times 1000 \quad (2.4)$$

expressed in per mil (‰) with R_x the ratio of the abundance of the heavy isotope to the light isotope in the sample and R_{std} the standard ratio. The δ values can be positive or negative, respectively indicating enrichment or depletion of the sample in heavier isotopes with respect to the standard.

2.1.3 Climatic reconstruction based on water stable isotopes

2.1.3.1 δD and $\delta^{18}O$ in the hydrosphere

Hydrogen and oxygen composing the water molecules can exist as various stable isotopes, each with a specific natural abundance. Hydrogen has two stable isotopes, 1H and 2H (deuterium also denoted D), with relative abundances of 99.9885 and 0.0115 %, respectively. Oxygen has three stable isotopes, ^{16}O , ^{17}O , and ^{18}O with relative abundances of 99.757, 0.03, and 0.205 %, respectively (Hoefs, 2015).

Thus, water molecules can exist as nine possible isotopic combinations of H and O, with mass numbers ranging from 18 ($H_2^{16}O$) to 22 ($D_2^{18}O$). The abundance of these possible combinations is indicated in (Sharp, 2017).

Consequently, the major changes in $\delta^{18}O$ and δD values in the hydrosphere occur during phase changes such as evaporation and condensation. Measurements of O and H isotopic composition are made against the international standard Vienna Standard Mean Ocean Water (V-SMOW) for which both $\delta^{18}O$ and δD equal 0 ‰.

2.1.3.2 Isotopic composition of water molecules from evaporation to deposition in Antarctica

Evaporation of oceanic water

The first step-change in isotopic composition of water molecules occurs during evaporation from the oceanic source. The δD and $\delta^{18}O$ composition of evaporated water molecules is affected by two effects (Craig et al., 1965; Horita et al., 2008). The first is the equilibrium isotope fractionation at the vapor-liquid interface which results in negative δD and $\delta^{18}O$ of evaporated water molecules as they are depleted in heavier isotopes. Indeed, isotopically lighter molecules have a higher vapor pressure than the isotopically heavier molecules. In other words, the attractive interactions bonding the water molecules in the liquid are weaker for the isotopically lighter molecules. The latter are thus more easily transferred from the liquid to the gas phase than the heavier isotopomers. An additional effect is the diffusion-controlled kinetic fractionation which arises during the transport of evaporated water molecules from the liquid-vapor interface to the free atmosphere. As they diffuse through the laminar and turbulent sections, they are progressively depleted in heavier isotopes.

Transport of water vapor from low to high latitudes and Rayleigh distillation

After leaving the ocean surface, the vapor cools as it ascends and forms clouds. When condensation occurs in the air mass and a rainfall event subsequently occurs, the isotopic composition of the air mass undergoes a change. The "closed" Rayleigh distillation model describes the distribution of isotopes between two reservoirs of meteoric water as one reservoir decreases in size. Such a model can be applied with the assumption that rainout is the sole factor regulating the atmospheric-moisture budget (Dansgaard, 1964). The equations of the Rayleigh distillation model describe an isotope fractionation process where the condensate material (droplets) is continuously and irreversibly removed (rainfall) from the system (cloud). In a cloud, isotopically heavy water molecules are preferentially lost as precipitation, since they easily pass from the vapor to the liquid state due to their relatively lower vapor pressure. Consequently, the δ value of the remaining vapor becomes progressively more negative (depleted). As an air mass originating at sub-tropical latitudes (between 20° and 40°S) moves down to the south pole, it undergoes several rainfall events. Its isotopic composition will repeatedly decrease from an initial value of $\delta^{18}O$ of -10‰, -15‰, to -50‰ upon reaching Antarctica (Figure 2.1). As moisture travels poleward, the isotopic composition of the precipitation and vapor is continuously depleted as a function of remaining water vapor fraction because of cooling and precipitation (Figure 2.1).

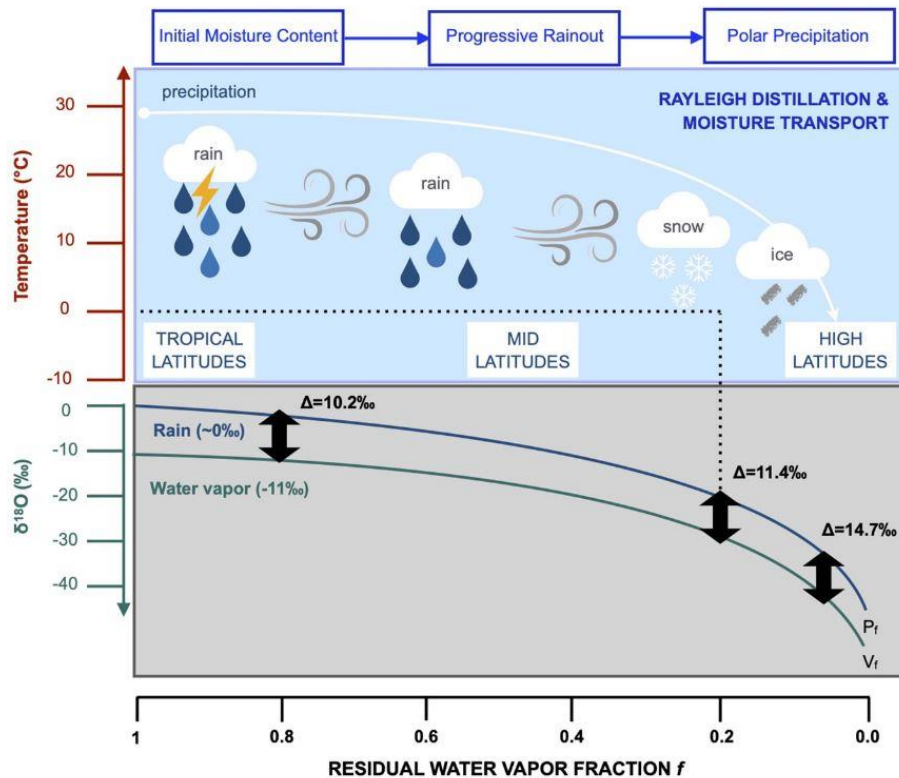


Figure 2.1 Isotopic fractionation during rainout and Rayleigh distillation (from (Dee et al., 2023)). The figure shows a simple approximation for moisture transport from the equatorial latitudes (left-hand side) towards the poles (right-hand side). As the moisture travels poleward, decreases are observed in the residual water vapor fraction in the cloud as well as in the temperature and in respective $\delta^{18}\text{O}$ of precipitation and water vapor. The difference between $\delta^{18}\text{O}$ content of precipitation and water vapor (noted Δ) increases from 10 to 14.7 ‰ as moisture travels northward.

The simplicity of the Rayleigh distillation model, however, fails to account for the complex dynamic processes underlying precipitation formation. To achieve a more accurate representation of the processes, models should incorporate cloud microphysics and its interactions with the various fractionation mechanisms that occur during the phase transitions of water in the atmosphere (Bergeron, 1935; Ciais & Jouzel, 1994; Jouzel & Merlivat, 1984). Recent studies have focused on ameliorating cloud isotopic models with the implementation of the contribution of other phenomena affecting the fractionation process, including:

- the presence of sea ice (Faber et al., 2017)
- the contribution from multiple moisture sources (Sodemann et al., 2008)
- cloud condensation and changes in precipitation (Pausata & Löffverström, 2015)
- re-evaporation of droplets (Hoffmann et al., 2000)

These different contributions have been implemented in atmospheric general circulation models now fully equipped with isotopic modules (LMDZ-iso in Risi et al., 2010; ECHAM5 in Werner et al. 2011). These models simulate the fractionation and migration effects on the water isotopic content during the hydrological cycle (from seawater evaporation, through continental evapotranspiration, atmospheric transport and mixing, precipitation from clouds, and until

return of water to the Earth's surface; Galewsky et al., 2016).

2.1.3.3 The global and local meteoric water lines

The oxygen and hydrogen isotopic distributions of meteoric waters exhibit a correlation that follows the relationship defined by Craig (1961), known as the Global Meteoric Water Line (GMWL):

$$d - excess = \delta D - 8 \delta^{18}O \quad (2.5)$$

In polar snow, d-excess is affected by non-equilibrium processes occurring during sea water evaporation and snow formation. The ice core d-excess record thus depends on the temperature at the site where snow is formed (T_{site}) and on the source temperature where the moisture first evaporated (T_{source}). Through an inversion procedure, T_{site} and T_{source} can be retrieved from the d-excess (Masson-Delmotte et al., 2004; Stenni et al., 2010). This method allows for reconstructions of the latitudinal temperature gradient between T_{site} and T_{source} which drives distillation in the hydrological cycle. Since it is likely that the moisture sources spatially varied, the d-excess is not used to yield the evolution of T_{source} but as an integrated tracer of past changes in the hydrological cycle and thus to inform on past changes in moisture transport and in air mass trajectories.

2.1.3.4 The isotopic thermometer

When the air mass reaches high latitudes after traveling north/south, the remaining vapor is depleted of heavy isotopes and the fractionation becomes larger due to the low temperature. Temperature is one of the controlling parameters of the isotopic composition of meteoric water, as it limits the amount of water lost by the air mass along its path. Dansgaard (1964) was the first to observe the existence of a relationship between $\delta^{18}O$ in precipitation and mean annual temperature at the sampling site, T_{site} . Global correlations between $\delta^{18}O$, δD and mean annual surface temperature are described by the following equations:

$$\delta^{18}O = 0.69 T_{site} - 13.6 \text{ ‰} \quad (2.6)$$

$$\delta D = 5.6 T_{site} - 100 \text{ ‰} \quad (2.7)$$

where T is the mean annual temperature at precipitation site and 0.69 and 5.6 are the spatial slope coefficients respectively for $\delta^{18}O$ and δD .

Dansgaard's pioneering work was followed by the work of Lorius & Merlivat (1975) who estimated the relationship between the isotopic composition of East Antarctic snow and site temperature along a traverse from Dumont D'Urville to Dome C, and calculated the following relationship:

$$\delta D = 6.04 T_{site} - 51 \text{ ‰} \quad (2.7)$$

Since the 1980s it is possible to confront this empirical spatial relationship between site temperature and the snow isotopic content to the equivalent relationship yielded by isotope-enabled GCMs. However, the temperature reconstructions provided by the GCMs over the past glacial-interglacial cycles are less robust than ice core records. Recent studies couple model and multi-core records to better understand surface processes in polar regions and to identify drivers of the water stable isotopic composition (Ollivier et al., 2024; Ooms et al., 2024).

The existing spatial relationship between water stable isotopic composition analyzed in ice cores and site temperature can also be utilized as a surrogate for the temporal relationship to evaluate past temperature changes. Past local surface temperatures (T) are estimated using a "paleothermometer" gradient a :

$$a = \frac{\Delta\delta}{\Delta T} \quad (2.8)$$

The isotopic variation in the ice record, corrected for past changes in $\delta^{18}\text{O}$ seawater due to global ice volume (Bintanja et al., 2005a), is represented by $\Delta\delta$. The variation of temperature over time is represented by ΔT . The $\Delta\delta/\Delta T$ slope can be estimated for past glacial and interglacial conditions using GCMs equipped with water stable isotopic modules. Recent studies estimated the present-day spatial $\Delta\delta/\Delta T$ relationship for Central Antarctica and asserted that it can be reasonably used for evaluating the Last Glacial Maximum to present-day temperature change, namely $\Delta T_{\text{LGM-PD}}$ (Jouzel et al., 2003; Werner et al., 2018).

✂ *It has been postulated that $\Delta T_{\text{LGM-PD}}$ is of $\sim 9^\circ\text{C}$ for East Antarctica, which is close to the $\sim 10^\circ\text{C}$ difference estimated independently for West Antarctica (Jouzel et al., 2003, 2007; Masson-Delmotte et al., 2010) (these estimates are used for comparison in Section 3.4).*

Conversely, $\delta^{18}\text{O}$ appears to be less sensitive to temperature variations (slope of $0.34\text{‰ }^\circ\text{C}^{-1}$) for relatively warm past interglacials and future warming scenarios (Sime et al., 2008, 2009). The d-excess record can be used in combination with $\delta^{18}\text{O}$ and δD to reconstruct past temperature variations at the precipitation deposition site (T_{site}) and at the moisture source (T_{source}) for EDC, EDML, and Dome Fuji ice cores (Landais et al., 2021; Stenni et al., 2010; Uemura et al., 2012).

Additional methodologies may be employed to reconstruct past temperature changes from ice cores including:

(i) Borehole thermometry (BHT):

This approach involves the insertion of a temperature probe into the borehole. The red curve in Fig. 2.2 represents the hypothetical scenario in which T_{site} is assumed to be constant, while the blue curve represents the actual measurement. Using a model inverting the heat diffusion equation driven by the geothermal heat flux, the ice flow pattern and the BHT vertical temperature profile, it is possible to yield the past scenario of temperature at the surface of the ice sheet.

The scenario is also adjusted by the model so that it complies with the temperature reconstructions using water isotopic records. This approach permitted to estimate the temperature difference between the LGM and present-day at NGRIP, i.e. $\Delta T_{\text{LGM-PD}} = 23^{\circ}\text{C}$ (Dahl-Jensen et al., 1998).

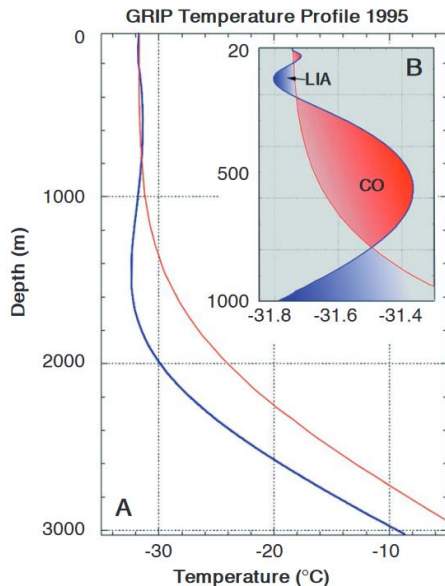


Figure 2.2 The GRIP temperature profiles in depth (from Dahl-Jensen et al. 1998). A) The red curve represents the hypothetical scenario in which T_{site} is assumed to be constant, while the blue curve represents the actual temperature measured with borehole thermometry. B) The top 1000 m of the GRIP temperature profiles are enlarged so the Climatic Optimum (CO, 8 to 5 ka), the Little Ice Age (LIA, 1550 to 1850 CE), and the warmth around 1930 CE are indicated.

(ii) Fluctuations in isotopic composition of atmospheric gases ($\delta^{15}\text{N}$, $\delta^{40}\text{Ar}$) trapped in air bubbles in ice cores:

It has been demonstrated that the gas isotopic composition of air bubbles in ice cores is influenced by rapid temperature fluctuations occurring at the ice sheet surface which induce thermal diffusion and associated fractionation of gas molecules in the firn (further details are provided in Section 2.2.2; Kindler et al., 2014; Severinghaus & Brook, 1999).

The aforementioned techniques are typically not employed in Antarctica due to the low accumulation rates observed at plateau sites. Similarly, the application of isotopic anomalies in air bubbles is limited, as central Antarctica did not experience abrupt temperature changes that could induce significant thermal fractionation of $\delta^{15}\text{N}$ and $\delta^{40}\text{Ar}$ (Jouzel et al., 2003).

However, Buizert et al. (2021) recently estimated LGM temperature in East Antarctica through BHT and firn density reconstruction using ice core records of $\delta^{15}\text{N}$ records combined with modeling. Indeed, the $\delta^{15}\text{N}$ is affected by two processes occurring in the firn: the thermal fractionation and the gravitational fractionation, and therefore both integrates temperature changes occurring at the scale of the decadal scale via thermal fractionation and at orbital timescales via variations of the firn thickness which affect the $\delta^{15}\text{N}$ via gravitational fractionation. This approach is described in Section 2.2.2 and employed in the Chapter 3.

✂ Using this approach, Buizert et al. (2021) estimate that $\Delta T_{\text{LGM-PD}}$ for East Antarctica is of ~ 4 to 7°C (this estimate is used for comparison in Section 3.4).

The temperature reconstruction based on water isotopic records sometimes disagrees with the

alternative methods (Buizert et al., 2021). These discrepancies can be explained by additional factors that affect the water isotopic records in ice cores.

2.1.3.5 Other factors affecting water isotopic records in ice cores

Although the temperature at the deposition site is the primary determinant of the stable water isotopic composition in snow and subsequently in glacier ice, other factors may also contribute to the final signal. This section provides a concise overview of the most common factors and their impact on the isotopic composition.

Source effect

Temperature changes in the evaporative region where the precipitation originates from and displacement of this region affect the isotopic composition of snow precipitation in polar regions (Stenni et al., 2010)

Continental effect

As the air mass travels poleward over a considerable distance from the moisture source and towards the interior of the polar continent, the concentration of heavy isotopes in precipitations become increasingly negative. The continental effect is associated with the progressive depletion of heavier isotopes and the lack of moisture recharge on the way to the interior of the continent. In Antarctica, the continental effect is also associated with a progressive decrease in temperature from the coast to the interior (from -15°C to -60°C). The combination of these two mechanisms results in decreasing the isotopic composition of snow precipitation.

Elevation effect

Topography exerts a significant influence on the isotopic composition of snow precipitation. The isotopic composition of air masses undergoes a shift towards lighter isotopes with increasing altitude. When vapor is deviated upward by a mountain, it decompresses, cools adiabatically, and more precipitation occurs. The percentage of vapor remaining in the air mass will decrease significantly with increasing elevation. A highly negative correlation between altitude and snow isotopic composition is evident along the two NS transects. In this specific case, elevation gradients are in the order of -1.3‰ to $-1.5\text{‰}/100\text{ m}$ (for $\delta^{18}\text{O}$; Becagli et al., 2004). However, distinct areas in Antarctica are subjected to different altitude effects, as the relationship depends on other factors, such as the provenance of the air masses. In addition, it is complex to disentangle the elevation effect and the effect associated with the vertical profile of temperature in atmosphere (lapse-rate).

In general, the isotopic record in snow and subsequently in ice in Antarctica is primarily influenced by temperature at the precipitation site, as well as both latitudinal and continental effects, contingent on the ice core drilling site. The isotopic composition of plateau ice cores is, on average, more negative than that of coastal sites. This is due to the colder temperatures, higher elevation, and greater distance from moisture sources (Masson-Delmotte et al., 2011).

Seasonal effect

(Werner et al., 2000) allotted the disagreement between temperature reconstructions inferred from BHT and water isotopic records to the seasonality of precipitations. Indeed, their study shows that paleotemperatures derived from water isotopes measured in ice cores are biased by a substantially increased precipitation intermittency over Greenland during the LGM, meaning that boreal summers are associated with much higher snowfall amount than boreal winters during the LGM whereas the distribution of precipitation is less contrasted between seasons during the Holocene. The annual temperature inferred from water isotopic composition during LGM is thus skewed towards summer values (Fig. 2.3).

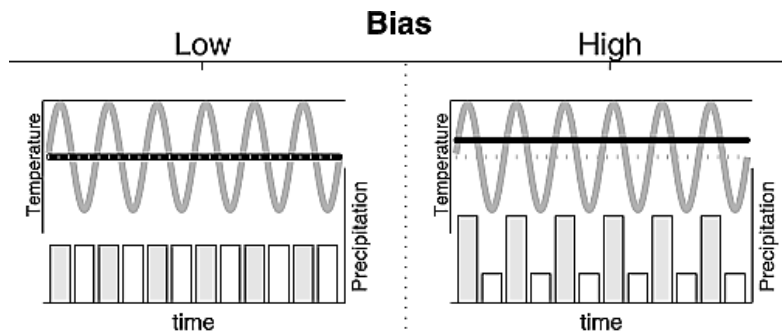


Figure 2.3 A seasonal temperature variation (gray solid lines) is sampled using different seasonal distribution of precipitation (histograms). Depending on the seasonality of the precipitation, the resulting precipitation-weighted temperature (black lines) is biased (from Persson et al., 2011).

This bias induced by the precipitation intermittency is pervasive over past glacial-interglacial cycles and is also observed in Antarctica (Laepfle et al., 2011). Therefore, the annual temperature can be weighted by the respective quantities of precipitation occurring in each season:

$$T_w = \frac{T_{DJF}PP_{DJF} + T_{MAM}PP_{MAM} + T_{JJA}PP_{JJA} + T_{SON}PP_{SON}}{PP_{DJF} + PP_{MAM} + PP_{JJA} + PP_{SON}} \quad (2.9)$$

with PP_{JJA} the amount of precipitation over the months of June, July and August.

✂ *The precipitation-weighted temperature defined in Eq. 2.9 will be used in Chapter 3.*

Post-deposition effect

The isotopic composition of snowfall on the ice sheet is subject to modification following deposition due to a number of processes acting on the snow during the climate signal archival process. Studies have recently evidenced that the isotopic composition of snow during summer in both Greenland and Antarctica is significantly affected by molecular exchanges between snow and water vapor (Casado et al., 2018; Ritter et al., 2016; Steen-Larsen et al., 2014). Additionally, snow metamorphism may also influence changes in the isotopic composition of deposited snow, in particular during the precipitation-free summer months (Harris Stuart, Faber, et al., 2023). These changes in isotopic composition do not affect only the surface snow but can also be rapidly transferred to the subsurface.

(Ollivier et al., 2024) observed that the mean effect of post-depositional processes over the 2017-2021 period enriches the snow surface in $\delta^{18}\text{O}$ by 3.3 ‰ to 6.6 ‰ and diminishes the snow surface d-excess by 3.5 ‰ to 7.6 ‰ with respect to the isotopic signal of the incoming precipitation.

Diffusion in the firn

Due to heat diffusion, the temperature gradient within the firn is smaller than the true surface temperature change. Therefore, water isotopic signals are attenuated during snow densification because of molecular diffusion in the firn column. The magnitude of the diffusion depends on the vertical temperature gradient and is different for δD and $\delta^{18}\text{O}$ (Johnsen et al., 2000). Combining δD and $\delta^{18}\text{O}$ measurements thus allows to identify the differential diffusion signal and also enables to reconstruct temperature (Holme et al., 2018).

Summary

The reconstruction of temperature changes at seasonal scales at certain sites, such as Dome C, is a complex endeavor because of various challenges. All factors mentioned above which have a profound influence on the isotopic composition of snow/ice, thereby undermining the correlation between isotopic composition in the snow and the temperature at site deposition. Isotopic composition depends on condensation T which may differ from T_{site} . The condensation temperature may not always be strongly related to the surface air temperature due to variations of both the transport level and the strength of the near-surface temperature inversion during winter (Persson et al., 2011). Finally, paleotemperature reconstruction based on water isotopes measured in ice core rely on the strong assumption that modern-day spatial relationship between T and isotopic composition can be used as a temporal surrogate. This assumption will be questioned in Chapter 3.

2.1.3.6 Local snow accumulation rate inferred from local temperature

Reconstructing past snow accumulation rates in East Antarctica is difficult since the very low accumulation rates make annual layer counting impossible and no other direct proxy for snow accumulation exists in ice cores. The current accumulation rate at Dome C is 2.7 cm of ice equivalent per year (cm i.e./yr; Genthon et al., 2016) and is even lower during the last glacial maximum (1.5 cm i.e./yr; Bouchet et al., 2023) because cold air contains less moisture. In East Antarctica, the classical approach to reconstruct past snow accumulation rates is based on temperature estimated from water isotopic data. Lorius et al. (1985) and Ritz (1992) predict change in past snow accumulation rate from change in saturation vapor pressure over ice itself linked to surface air temperature through the Clausius Clapeyron equation. If the saturation vapor pressure augments from P_1 to P_2 , then the surface air temperature increases from T_1 to T_2 as per:

$$\ln\left(\frac{P_1}{P_2}\right) = \frac{\Delta H_{vap}}{R} \left(\frac{1}{T_2} - \frac{1}{T_1}\right) \quad (2.10)$$

with ΔH_{vap} the enthalpy of evaporation of water. Their approach ignores possible variations in circulation intensity over the precipitation region and requires approximation of the condensation temperature using measurements from weather stations or firn (Connolley, 1996; Ekaykin, 2003).

For East Antarctic sites as EDC, it is thus possible to link snow accumulation to temperature through an exponential relationship: $A = A_0 \times \exp(\beta \times \Delta\delta D)$ where A_0 is present-day accumulation rate and β a parameter which is adjusted during the chronology construction to comply with age constraints and ice flow modeling (Bouchet, Landais, Grisart, et al., 2023; Parrenin, Barnola, et al., 2007). Yet, there is no guarantee that the relationship between snow accumulation rate and temperature remains constant over time in polar regions, and uncertainties up to 40% are proposed for past snow accumulation rates in East Antarctica (as per the study presented in Chapter 4).

- 🔍 In the Chapter 3 of my manuscript, I present a study which aims at providing an additional tool for documenting past changes in temperature and snowfall using $\delta^{15}\text{N}$ measurements in air trapped in EDC ice core.

2.2 FROM THE TRAPPING OF ATMOSPHERIC AIR IN ICE TO ITS EXTRACTION AND ANALYSIS IN THE LABORATORY

Ice cores are unique archives since they are the only paleoclimatic archive to provide direct record of past atmospheric concentration in greenhouse gases (CO_2 , CH_4 , ...). Beyond greenhouse gases, analyzing the exact composition of other gases (O_2 , N_2 , Kr) present in air bubbles provides additional information. The isotopic and elemental content of the gas species are influenced by changes in global and/or local climatic conditions which can induce fractionation between heavy and light isotopes before being fixed when air bubbles are trapped within the ice matrix. As a result, the isotopic and elemental ratios of gas molecules measured in ice cores vary in depth and age.

During the PhD, I focused on the following quantities:

- The isotopic ratio $\delta^{15}\text{N}$, measuring $^{15}\text{N}/^{14}\text{N}$ of N_2 (description in section 2.2.4.1 and analytical method detailed in Section 2.2.6.1)
- The isotopic ratio $\delta^{18}\text{O}$, measuring $^{18}\text{O}/^{16}\text{O}$ of O_2 (description in Section 2.2.4.2)
- The elemental ratio $\delta\text{O}_2/\text{N}_2$, characterizing the relative proportion of O_2 vs N_2 molecules (description in Section 2.2.4.3)
- The isotopic abundance in ^{81}Kr (description in Section 2.3.2.3 and analytical method detailed in Section 2.2.6.2)

2.2.1 Snow accumulation, densification and transformation to ice

Thin layers of snowflakes accumulate at the East Antarctic ice sheet surface throughout the years. Under the weight of newly accumulated layers, older snow layers are progressively buried up. As the snow is buried, its density augments from a density of $\sim 350 \text{ kg m}^{-3}$ at surface, while snowflakes are progressively transformed to snow grains which coalesce and are sintered, and finally turn to ice (at the density of about 920 kg m^{-3}). We can divide the vertical column piercing the ice sheet in distinct sections:

2.2.1.1 The firn

A coat of unpacked snow (50–120 m), the firn, literally covers and isolates the ice sheet from the atmosphere. The atmospheric air circulates freely within the firn through open pores. The firn is itself divided in three subsections: the convective, diffusive and non-diffusive zones.

The convective zone

This zone situated beneath the surface is affected by wind, temperature, and pressure gradients. These effects induce convection, resulting in mixing with the atmospheric air and leading to the firn air having the same isotopic composition (Colbeck, 1989). The thickness of

the convective zone varies depending on surface conditions. For sites with high accumulation rates, such as Greenland, the convective layer is typically negligible in thickness. The North GRIP ice core has a thickness of approximately 2 meters, while the NEEM ice core has a thickness of around 3 meters (Landais, Masson-Delmotte, et al., 2006). In Antarctica, a ~20 m deep convective zone has been evidenced in the megadunes site (Severinghaus & Battle, 2006). Though, previous work based on dating constraints over the last glacial period (MIS 3) have revealed that the possibility of significant convective zones at Dome C is improbable (Bazin et al., 2013; Parrenin et al., 2012; Veres et al., 2013).

The diffusive zone

This zone situated beneath the convective zone constitutes the major part of the firn. This zone is no longer sensitive to surface perturbations and within this zone, the atmospheric air is transported through molecular vertical diffusion. During this slow process of molecular diffusion, gravitational and thermal fractionation affects the gas molecules. Isotopes of the gas molecules are spread out along the vertical gradients of temperature and strength of the gravity force present in the firn column depending on their masses. Vertical diffusion ceases when the size of the channels within the ice matrix becomes smaller than that of the gas molecules, i.e. at the lock-in-depth (LID).

The non-diffusive zone

This zone is situated below the LID. The complete pore close-off is expected to occur a few meters below, at the bottom of the non-diffusive zone, specifically the close-off depth (COD), is where complete physical separation between air and the atmosphere occurs. In contrast, the LID is the deepest point where air can diffuse. Molecular diffusion is impossible in this zone where the air is trapped in the ice and is physically isolated from the ambient atmosphere. As a consequence, the air isotopic composition remains unchanged beyond the LID.

The convective and non-diffusive zones usually do not surpass 10 meters, making the diffusive zone the principal element of the firn.

For dating applications, we call Δ_{age} the age difference between ice and gas phases at the same depth and Δ_{depth} the depth difference between ice and gas of the same age. These values are linked with LID variations. Therefore, to precisely date the gas phase in ice cores, knowledge of the values of these three variables is necessary. Using firn densification models, we yield past evolutions of these three parameters.

2.2.2 Isotopic fractionation occurring in the firn

Atmospheric gases (N_2 , O_2 , Ar, Kr) are affected by isotopic fractionation occurring in the firn.

2.2.2.1 Gravitational fractionation

This process occurs from the ice sheet surface to the LID. The heavier gas molecules tend to concentrate at the bottom of the diffusive zone as they undergo a larger gravitational force than lighter molecules. The gravitational fractionation term designates the proportion of rare isotopes (Y neutrons) vs. abundant isotopes (Z neutrons). When gas is locked in air bubbles below the LID, the gravitational fractionation term ($\delta_{g,atm}$) is expressed as a function of the mass difference between the two isotopes $|Y - Z|$ in atomic mass units, the mean temperature in the firn (T , in K) and the diffusive column height (DCH, in m) which depends on surface climatic parameters (air temperature and snow accumulation rate). $\delta_{g,bubbles}$ follows the barometric equation and can be approximated by its first order development (Craig et al., 1988; Schwander, 1989; Sowers et al., 1989, 1992):

$$\delta_{g,bubbles}(\text{‰}) = 1000 \left(\exp\left(\frac{|Y - Z|gDCH}{RT}\right) - 1 \right) \approx 1000 \left(\frac{|Y - Z|gDCH}{RT} \right) \quad (2.11)$$

with g the Earth's gravitational constant (9.8 m s^{-2}) and R the perfect gas constant ($8.314 \text{ J mol}^{-1} \text{ K}^{-1}$). Thus, the gravitational fractionation affecting the isotopic ratios of gas molecules trapped in ice cores are linked by the following relationship: $\delta^{15}\text{N} = \delta^{18}\text{O}/2 = \delta^{40}\text{Ar}/4 = \delta^{86}\text{Kr}/4$.

2.2.2.2 Thermal fractionation

This process occurs in the diffusive zone. It is modulated by changes in air temperature at the surface of the ice sheet which can induce a transient thermal gradient in the diffusive column. The temperature likely affects the interactions between the gas molecules and heavier molecules tend to accumulate in the colder extremity of the thermal gradient. When there is a flux equilibrium between diffusion and temperature gradient, an isotope concentration gradient is formed and the relationship traducing this equilibrium is the following:

$$\delta_{th,bubbles}(\text{‰}) = 1000 \left(\frac{R}{R_0} - 1 \right) \approx 1000 \alpha_T \left(\frac{\Delta T}{T_0} - 1 \right) \quad (2.12)$$

with R and R_0 the isotopic ratios associated with temperatures T and T_0 , α_T the thermal diffusion coefficient (in ‰ K^{-1}) and ΔT the temperature difference between the surface and the bottom of the thermal gradient which may differs from the bottom of the diffusive column (Severinghaus et al., 2001).

Thermal fractionation caused by changes in surface air temperature can originate from different sources. Temperature gradients of a few degrees do arise on sub-annual timescales within the upper 20 m of the firn in the East Antarctic plateau in response to the seasonal surface temperature cycle (J. D. Morgan et al., 2022). The corresponding gas isotope thermal fractionation signals only penetrate to a depth of approximately 10–15 m (Severinghaus et al., 2001; Weiler et al., 2009). These seasonal effects are referred to as the rectifier effects. It is typically assumed that these signals cancel out each year, such that the deep firn (and thus the ice core gas archive) reflects the annual mean. Morgan et al. (2022) measured the difference

between $\delta^{15}\text{N}$ and $\delta^{40}\text{Ar}/4$, termed $\delta^{15}\text{N}_{\text{excess}}$, which reflects thermal fractionation in the firn column at South Pole over the past 30 kyr. Their study evidenced that the rectifier effects may not cancel out each year. In particular, they found that enhanced downward advection of the thermal signal in winter at South Pole may induced deeper penetration of the thermal gradient in the firn in winter.

The rapid D-O warmings recorded in Greenland over the last glacial period induced a thermal gradient in the entire firn column in Greenland (Capron et al., 2010; Guillevic et al., 2013; Landais et al., 2004). The air at the bottom of the diffusive column was affected by thermal fractionation, which was traduced by a positive anomaly in its isotopic content. Thus, the isotopic composition of the air at the base of the firn in Greenland is influenced by both gravitational and thermal fractionation during D-O events.

2.2.3 Firn densification modeling

Firn densification models have been developed to simulate the process of snow densification occurring in the firn. These models predict the LID so that it is possible to estimate the Δage between ice and gas at the same depth. The Δage estimate is essential for providing both ice and gas timescales in ice cores and thus identifying the sequences of climatic events that can be recorded in either the ice matrix (δD -based temperature) or the air bubbles (GHGs).

2.2.3.1 Model description

The firn densification model is forced with past temporal evolution of snow accumulation rate and air temperature at the ice sheet surface. The thermomechanical model comprises four modules (Table 2.1). The ice sheet flow module is a simple module that calculates the vertical speed in a one-dimensional firn and ice column. This vertical speed is used in the thermal module to calculate heat advection. The thermal module solves the heat transfer equation, which combines heat advection and heat diffusion across the entire ice sheet thickness. Using the resulting temperature profile in the firn, the mechanical module evaluates the densification rates resulting from three successive mechanisms, which are detailed below. Finally, a gas–age module is employed to monitor the sinking of snow layers in a Lagrangian mode. This module employs a gas trapping criterion to evaluate the gas trapping depth (LID) and the ice age–gas age difference (Δage).

Table 2.1 The four modules of the firn densification model.

Ice sheet flow module	Thermal module	Mechanical module	Gas-age module
Yielding the vertical speed in the snow-ice column	Yielding the temperature profile in the snow-ice column	Yielding the densification rate profile as per different mechanisms	Using a criterion to estimate Δage and Δdepth

2.2.3.2 The relationship between the densification speed and local climate via the overburden pressure

Under the weight of newly accumulated snow, older snow is progressively buried up and its relative density augments ($\sim 350 \text{ kg m}^{-3}$ at surface). Snowflakes turn to snow grains which coalesce and are sintered, before transforming to ice at the critical relative density of $\sim 920 \text{ kg m}^{-3}$.

The speed of the snow densification process determines the firn thickness. The climatic parameters at the surface of the ice sheet, i.e. the snow accumulation rate and the air temperature, control the firn densification mechanism involved and its speed. A simple explanation is that an increased accumulation rate increases the firn sinking speed, thus thickening the firn while an increased surface air temperature accelerates the firn densification process, thus thinning the firn. During a deglaciation, however, both temperature and accumulation increase, resulting in opposing effects on the LID but the accumulation rate effect is expected to be dominant in East Antarctica (Capron et al., 2013). Furthermore, it has been proposed that the concentration of impurities (measured by Ca^{2+} concentration) can accelerate the densification process in the firn (Hörhold et al., 2012). Given that the concentration of impurities declines during deglaciation (Röthlisberger et al., 2008), this effect should also contribute to firn thickening.

To mimic this behavior, firn densification models have been progressively refined over the years through various studies (Alley, 1987; Arthern et al., 2010; Freitag et al., 2013; Herron & Langway, 1980; Kuipers Munneke et al., 2015; Ligtenberg et al., 2011; Oraschewski & Grinsted, 2022). The models typically employ macroscopic mechanical laws that correlate the densification speed (dD_{rel}/dt , in terms of relative density $D_{\text{rel}} = \rho/\rho_{\text{ice}}$) to the main driving force: the overburden pressure of overlying snow.

In the Herron and Langway (1980) model, the snow accumulation rate exerts an influence on the densification speed via different power laws that are tuned to fit density profiles measured in the firn. The approach of Herron and Langway (1980) is empirical.

In the IGE model (Arnaud et al., 2000; Goujon et al., 2003), the influence of accumulation rate is parameterized differently, using mechanics theoretical laws. The effect of snow accumulation rate on the densification speed is solely expressed through the overburden pressure P :

$$P(h) = g \int_0^h \rho dz \quad (2.13)$$

with g the gravity constant and ρ the density in kg m^{-3} . In porous materials, the overburden pressure P is transmitted through contact areas between grains rather than the entire surface of the material. This phenomenon can be expressed by replacing P with an effective pressure (P_{eff}) in mechanical stress–strain laws, depending on the material geometry (Goujon et al., 2003). Higher temperatures (T) facilitate the deformation of materials, and this effect is commonly traduced by an Arrhenius law: $\exp(Q/RT)$, where R is the gas constant and Q is an activation energy. The value of the activation energy depends on the underlying physical mechanism of ice and snow deformation. The relationship between densification speed and

overburden pressure take the following general form:

$$\frac{dD_{rel}}{dt} = A_0 \times \exp\left(-\frac{Q}{RT}\right) \times (P_{eff})^n \quad (2.14)$$

with $A_0 = 7.89 \times 10^{-15} \text{ Pa}^{-3} \text{ s}^{-1}$ (Goujon et al., 2003) and n the stress exponent. The term $A_0 \times \exp\left(-\frac{Q}{RT}\right)$ is referred to as the creep parameter A . In the following section, the relationships between $\frac{dD_{rel}}{dt}$, P_{eff} and T are given for the IGE models in two configurations: (i) GOUJON (described in Section 2.2.3.3) and (ii) BREANT (described in Section 2.2.3.4). For detailed equations see Goujon et al. (2003) and (Bréant et al., 2017).

2.2.3.3 The GOUJON configuration of the IGE model

In the configuration (i) GOUJON (Arnaud et al., 2000; J. -M Barnola et al., 1991; Goujon et al., 2003; Pimienta & Duval, 1987) the firm column is organized in three zones depending on the densification mechanism at play (Ebinuma & Maeno, 1985).

In the first zone, named **snow densification** (Goujon et al., 2003), the snow grains are reorganized and packed through isothermal grain boundary sliding (Alley et al., 1987). The densification rate at a given depth increases proportionally with the pressure induced by the weight of the overlying snow column:

$$\frac{dD_{rel}}{dt} = \gamma \left(\frac{P}{D_{rel}^2} \right) \left(1 - \frac{5}{3} \times D_{rel} \right) \quad (2.15)$$

The density increases until it approaches the maximum compaction which is observed at the critical density of about 550 kg m^{-3} for snow (relative density of 0.6; Anderson & Benson, 1963).

In the second zone, the **snow grains are sintered** via isostatic viscoplastic deformation (Arzt, 1982) and the deformation speed is determined by the following equation:

$$\frac{dD_{rel}}{dt} = A_0 \times \exp\left(-\frac{Q}{RT}\right) \times (P_{eff})^n \quad (2.16)$$

A strong hypothesis is the constant activation energy chosen ($Q = 60 \text{ kJ mol}^{-1}$). This choice assumes that densification is driven by a unique mechanism, dislocation creep and associated lattice diffusion or self-diffusion (Ebinuma & Maeno, 1985). At the grain scale, lattice diffusion processes associated with dislocations can be described as diffusion within the grain volume of a water molecule from a dislocation site in the ice lattice to the grain neck to reduce the energy associated with grain boundaries (Blackford, 2007). Typically, an activation energy of 60 to 75 kJ mol^{-1} is associated with this mechanism (referred to as mechanism 2 in Fig. 2.5) (Arthern et al., 2010; Barnes et al., 1971; Pimienta & Duval, 1987; Ramseier, 1967).

In Goujon et al. (2003), **the third and final densification zone** commences at the close-off density, which is derived from air content measurements in mature ice. This density is

calculated using the temperature-dependent close-off pore volume, as defined by Martinerie et al. (1994). In the third stage, the densification of the bubbly ice is permitted by changes in porosity (Martinerie et al., 1992) and driven by a pressure difference between the air bubbles and the surrounding ice matrix (Maeno & Ebinuma, 1983; Pimienta & Duval, 1987). The rate of densification is significantly reduced with depth, as the opposing pressures tend to balance each other out (Goujon et al., 2003). This stage is not a necessary component of this study, as $\delta^{15}\text{N}$ entrapped in air bubbles has ceased to evolve.

The close-off depth yielded by the IGE model in the GOUJON configuration depending on snow accumulation rate and air temperature at surface is shown in Fig. 2.4.

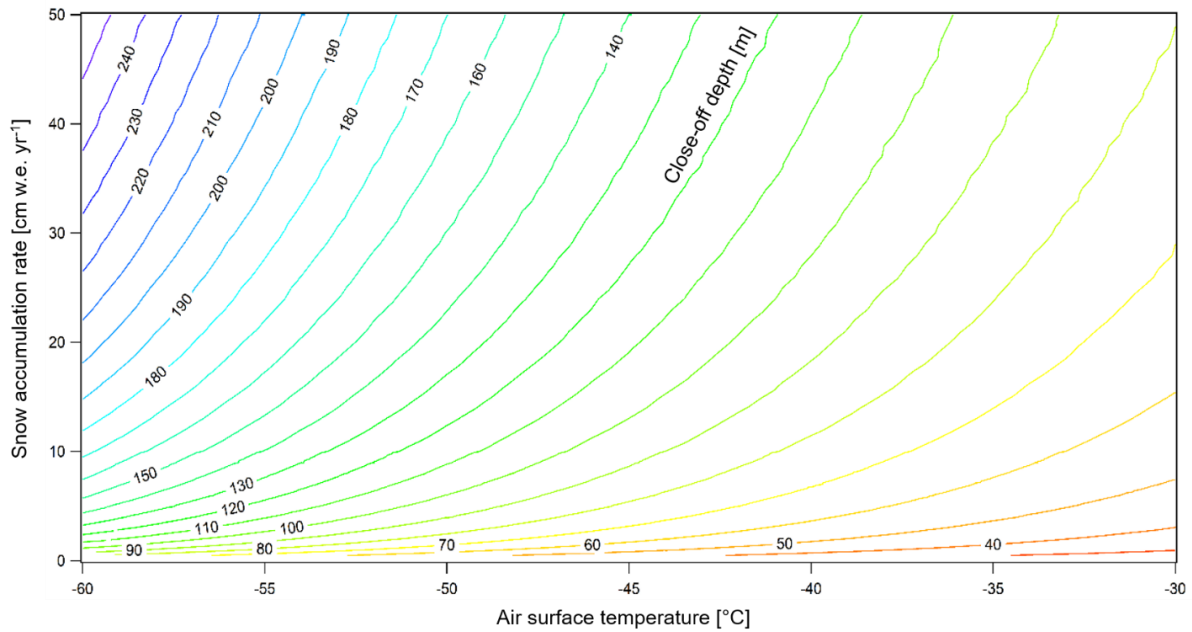


Figure 2.4 Evolution of the close-off depth (m) yielded by the IGE model (Arnaud et al., 2000; Goujon et al., 2003) depending on snow accumulation rate in cm water equivalent (w.e.) per year and air temperature at surface (courtesy of A. Landais).

2.2.3.4 The BREANT configuration of the IGE model

Recently, researchers have advanced the firn model presented in Bréant et al. (2017) from the IGE model to which I will refer to as BREANT. They conserved the three zones of the GOUJON model but modified the equations used:

In the first zone, the classical formulation of the densification rate is modified with a temperature dependence following Arrhenius law, where an activation energy Q_0 as per $\exp(-Q_0/RT)$ with R being the ideal gas constant and T being the firn temperature. Hence, the reorganization of the grains is likely activated if the temperature T is high enough so that RT is larger than the activation energy Q_0 evaluated at 49.5 kJ mol^{-1} , which is coherent with the values found by Alley (1987). In practice, γ in Eq. 2.15 is replaced by $\gamma' \times \exp\left(-\frac{Q_0}{RT}\right)$:

$$\frac{dD_{rel}}{dt} \propto \gamma' \times \exp\left(-\frac{Q_0}{RT}\right) \times \left(\frac{P}{D_{rel}^2}\right) \left(1 - \frac{5}{3} \times D_{rel}\right) \quad (2.17)$$

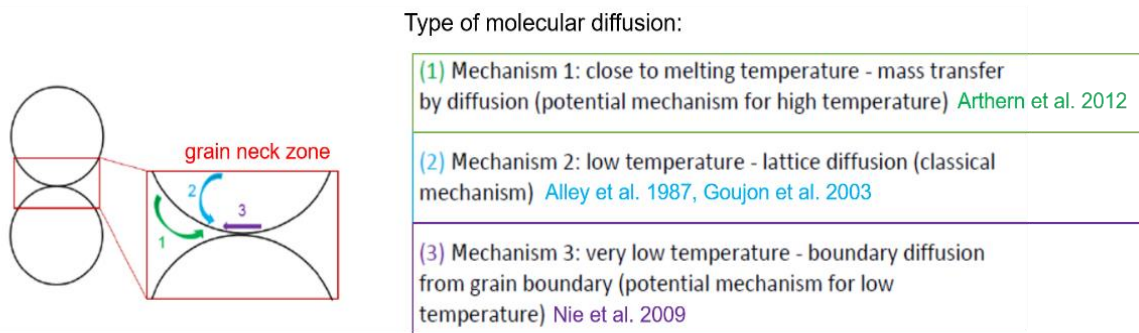
In the second zone, instead of employing a constant activation energy thus assuming that only one mechanism is involved (Goujon et al., 2003), Bréant et al. (2017) followed the idea that six or more mechanisms can operate together for firn or ceramic sintering (Ashby, 1974; Blackford, 2007; Maeno & Ebinuma, 1983; Wilkinson & Ashby, 1975). These possible mechanisms include:

- lattice diffusion from dislocations, grain surfaces, or grain boundaries (classical mechanism used in GOUJON),
- vapor transport,
- and surface and grain boundary diffusion.

However, only two of these mechanisms allow densification (lattice diffusion and grain boundary diffusion).

It has been observed that at warm temperatures, an activation energy significantly higher than 60 kJ mol^{-1} (up to 177 kJ mol^{-1} between -1 and $-5 \text{ }^\circ\text{C}$; Jacka & Jun, 1994) can be favored to best fit density profiles with firn densification models (Arthern et al., 2010; Barnes et al., 1971; Jacka & Li, 1994; V. I. Morgan, 1991). This suggests that a mechanism other than lattice diffusion dominates grain densification at high temperatures (i.e., above $-10 \text{ }^\circ\text{C}$). At low temperature ($-50 \text{ }^\circ\text{C}$), by analogy with ceramic sintering, lattice diffusion from the grain surface and/or boundary diffusion from grain boundaries should be favored (Ashby, 1974). The activation energy for surface diffusion is estimated to be in the range of $14\text{-}38 \text{ kJ mol}^{-1}$ (Jung et al., 2004; Nie et al., 2009). The temperature dependency reveals the predominance of one physical mechanism over others for material compaction at a specific temperature. To properly account for these different mechanisms, Bréant et al. (2017) introduced three distinct activation energies (corresponding to the three dominant mechanisms involved in snow densification, Fig. 2.5) into the firn densification model.

Through various sensitivity tests, Bréant et al. (2017) first determined the three temperature ranges corresponding to the three mechanisms. They estimate the three associated activation energies (Q_1 , Q_2 and Q_3) and finally adjusted the values of the three pre-exponential coefficients (a_1 , a_2 and a_3) to best replicate the firn thickness reconstructed from gas measurements during the last deglaciation at East Antarctic sites (Section 2.2.4.1).



Activation energy (J mol^{-1})	Coefficient
$Q_1 = 110\ 000$	$a_1 = 1.05 \times 10^9$
$Q_2 = 75\ 000$	$a_2 = 1400$
$Q_3 = 1500$	$a_3 = 6.0 \times 10^{-15}$

Figure 2.5 Different sintering mechanisms of snow for different temperatures proposed by analogy with the hot ceramic sintering (inspired by Ashby, 1974 and adapted from Bréant et al., 2017). More sintering mechanisms can be found in the literature: in their initial figure, Ashby (1974) mentioned six different mechanisms. The values for the three activation energies and associated coefficients set by Bréant et al. (2017) are reported in the table.

In the BREANT configuration, Eq. 2.16 is replaced by:

$$\frac{dD_{rel}}{dt} = A_0 \times \left(a_1 \times \exp\left(-\frac{Q_1}{RT}\right) + a_2 \times \exp\left(-\frac{Q_2}{RT}\right) + a_3 \times \exp\left(-\frac{Q_3}{RT}\right) \right) \times (P_{eff})^n \quad (2.18)$$

Additionally, the firn model acknowledges that the densification of firn is aided by the presence and the amount of dissolved impurities within the snow (Freitag et al., 2013). If the concentration of calcium ions in snow exceeds a certain threshold, it affects the densification rate dependence on impurities. This is determined by a relationship between the new activation energy Q' and the concentration of calcium ions $[Ca^{2+}]$:

$$Q' = f_1 \times \left(1 - \beta \ln\left(\frac{[Ca^{2+}]}{[Ca^{2+}]_{threshold}}\right) \right) \times Q \quad (2.19)$$

as described by Freitag et al. (2013). Bréant et al. (2017) assumed that the impurity effect is uniform across all physical mechanisms. They then fine-tuned β and f_1 constants to minimize the mismatch between modeled- $\delta^{15}N$ data and actual $\delta^{15}N$ data from cold East Antarctic sites during the last glacial termination.

The firn densification mechanism **in the third zone** is the same as in the GOUJON configuration.

2.2.3.5 Snow metamorphism in the top two meters

Significant temperature gradients, wind and post-deposition effects induce complex mechanisms affecting snow metamorphism in the 1-3 top meters beneath the surface (Colbeck, 1983; Kojima, 1967; Mellor, 1964). But these processes do not have a strong influence on the firn thickness yielded by the model, therefore they are not considered in neither of the two model configurations (GOUJON and BREANT) I used during my PhD (Chapters 3 and 4). The proposed solutions for these top two meters are either:

- Imposing a constant density (GOUJON configuration),
- Or imposing a constant pressure of 0.1 mbar (as observed for the top two meters) to the model parameterized with Alley et al. (1987) snow densification (BREANT configuration).

2.2.4 Interesting elemental and isotopic ratios

Fractionation may result from different processes and is subject to various factors depending on the chemical species under consideration.

2.2.4.1 $\delta^{15}\text{N}$ of N_2

According to Mariotti (1983), the atmospheric isotopic composition of N_2 is constant over orbital timescales (i.e. 10 to 100 kyr). Therefore, any deviation between isotopic composition of N_2 measured in atmosphere and in air bubbles trapped in ice cores can be attributed to physical processes occurring in the ice sheet, before snow transformation to ice and associated bubble close-off. The studies conducted on modern firn confirm that the $\delta^{15}\text{N}$ in the firn is enriched with depth owing to gravitational settling as per the barometric equation (Eq. 2.11). Further studies have shown that $\delta^{15}\text{N}$ measured in air bubbles enclosed beneath the LID is directly proportional to the DCH as per Eq. 2.7 (Kawamura et al., 2006; Landais, Barnola, et al., 2006; Sowers et al., 1992). The DCH is determined by subtracting the depth of the convective zone, at the top of the firn, from the LID, at its base.

For the specific site of Dome C, previous work based on dating constraints have revealed that during glacial periods, the possibility of significant convective zones is improbable so that $\text{LID} \sim \text{DCH}$ (Bazin et al., 2013; Parrenin et al., 2012; Veres et al., 2013). At Dome C, the thermal effect (Eq. 2.8) is of second-order.

The sum of the gravitational and thermal contributions respectively given by Eq. 2.11 and 2.12 should be equal to the $\delta^{15}\text{N}$ measured in air bubbles:

$$\delta^{15}\text{N} = \delta^{15}\text{N}_g + \delta^{15}\text{N}_{th} \quad (2.20)$$

$$\delta^{15}\text{N} \sim g \times \frac{\text{LID}}{RT} + \Omega\Delta T \quad (2.21)$$

An overview of snow densification mechanism involved in the distinct zones of the firn along with their influence on the $\delta^{15}\text{N}$ profile is given in Fig. 2.6.

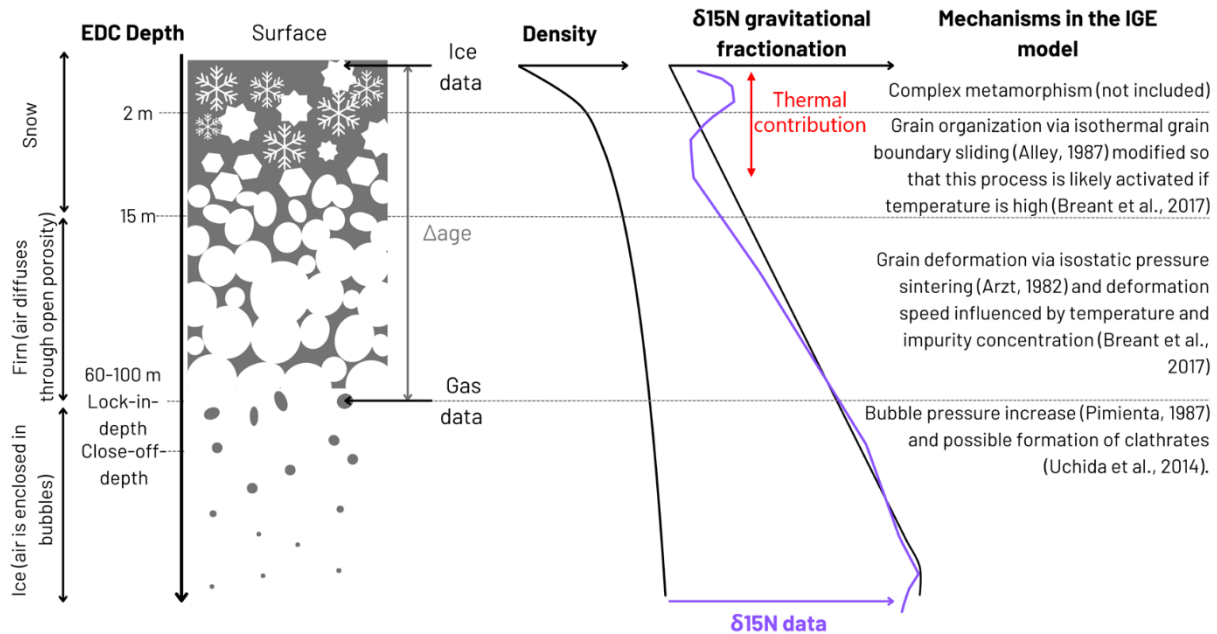


Fig. 2.6 Overview of snow densification and influence on the $\delta^{15}\text{N}$ profile (adapted from Bréant et al., 2017). The $\delta^{15}\text{N}$ profile is portrayed in the absence of any significant convective zone as observed in most present-day $\delta^{15}\text{N}$ profiles (Landais, Barnola, et al., 2006; Witrant et al., 2012). The barometric line determining gravitational fractionation is represented.

The firm densification model calculates the scenarios of LID and thermal gradient (ΔT) in the firm and then infers the respective contribution to the $\delta^{15}\text{N}$ signal: $\delta^{15}\text{N}_g$ and $\delta^{15}\text{N}_{th}$. The BREANT configuration of the model permitted to reconcile modeled $\delta^{15}\text{N}$ with the data over glacial-interglacial cycles at Dome C. This region used to be a challenge for empirical firm models as it is characterized by very cold temperatures and low snow accumulation rates which lack comparable present-day climatic conditions that are classically used to calibrate the model (Dreyfus et al., 2010). Though, (Bréant et al., 2017) call for further work on firm modeling to tackle remaining challenges listed below:

- (i) Laboratory or field studies of firm densification are needed to verify the dominance of one mechanism over another at very low temperatures (-60°C) and slow deformation rates.
 - (ii) The parameterization of impurity on firm softening could be revised, especially for very high impurity content in the firm in Greenland.
 - (iii) Additional constraints on firm modeling can also be obtained by using cross-dating with high-resolution signals on new ice cores, as already used by Parrenin et al. (2012).
- 🔍 During my PhD, we explored the perspective (iii) in Chapter 4 using new chronological constraints inferred from gas measurements on the EDC ice core over the past 800 kyr and confronting them to LID scenarios yielded by firm modeling using a probabilistic approach.
- (iv) The separate effects of impurities, snow accumulation rate and temperature on firm compaction and hence $\delta^{15}\text{N}$ evolution should be tested in periods other than the last deglaciation. Sequences of events associated with non-synchronous changes in surface

temperature, accumulation rate, and impurity content would be particularly valuable for this purpose.

- (v) Finally, discrepancies remain between the modeled $\delta^{15}\text{N}$ and the data for the EDC record. We believe these discrepancies may be attributed to imprecise estimations of glacial temperature and accumulation rates at the surface that are used to drive the firn densification model (Buizert et al. 2021). Indeed, past variations of local climate at Dome C are classically retrieved using water isotopic records although we know such reconstructions are associated with several limitations.

- Q We explored the perspectives (iv) and (v) in the Chapter 3. We provide a new compilation of $\delta^{15}\text{N}$ measurements on the EDC ice core covering the 100-800 kyr time period to explore the perspective (iv). The new measurements were mainly collected by A. Grisart, A. Klussendorf, A. Landais and F. Prié at LSCE (with extra help from E. Legrain and me). I combined these new measurements to the already published datasets to build a final compilation. The compilation is confronted to firn modeling scenarios to disentangle the contribution of snow accumulation rate and temperature on the $\delta^{15}\text{N}$ and to elucidate the model-data mismatch.

2.2.4.2 $\delta^{18}\text{O}$ of O_2

This is different for $\delta^{18}\text{O}$ of O_2 , which is affected by both fractionation in the firn and fractionation in the atmosphere. In the atmosphere, $\delta^{18}\text{O}$ of O_2 (noted $\delta^{18}\text{O}_{\text{atm}}$) is modulated by variations in the hydrological cycle at low latitudes and/or as variations of the relative proportion of the oceanic vs terrestrial biosphere productivity (M. Bender et al., 1994; Blunier et al., 2002; Landais et al., 2010, 2013; Luz et al., 1999; Luz & Barkan, 2011; Malaizé et al., 1999; Severinghaus et al., 2009). It is possible to get rid of the gravitational effect that affected $\delta^{18}\text{O}$ measured in air trapped in ice cores (using $\delta^{15}\text{N}$) to retrieve the past atmospheric $\delta^{18}\text{O}_{\text{atm}}$ signal. Ice core $\delta^{18}\text{O}_{\text{atm}}$ values fluctuated over the glacial-interglacial cycles of the Late Quaternary. Over the past 800 ka, strong similarities are observed between $\delta^{18}\text{O}_{\text{atm}}$, and Chinese speleothem calcite $\delta^{18}\text{O}$ (thereafter $\delta^{18}\text{O}_{\text{calcite}}$) tracking the East Asian monsoon change at millennial and orbital scale (Extier et al., 2018a; Y. Wang et al., 2008). This correlation suggests that the low-to-mid latitude hydrological cycle of the Northern hemisphere could be the dominant driver of $\delta^{18}\text{O}_{\text{atm}}$ variations at these timescales (Landais et al., 2010).

- Q During my PhD, I made use of new high-resolution data of $\delta^{18}\text{O}_{\text{atm}}$ from the EDC ice core collected at LSCE by A. Grisart during his PhD over the Terminations TVI-II for dating deep polar ice cores (Chapter 4) as well as for building coherent chronologies for marine and glacial archives over past glacial-interglacial cycles (Chapter 5).

2.2.4.3 $\delta\text{O}_2/\text{N}_2$

Variations in ice core records of $\delta\text{O}_2/\text{N}_2$ are influenced by atmospheric changes such as the decline in global O_2 concentration (Landais et al., 2012; Stolper et al., 2016; Y. Yan et al., 2021)

as well as by fractionation occurring at bubble close-off. Indeed, studies demonstrated that the trapping process is associated with a relative loss of O₂ with respect to N₂ (Fig. 2.7; Battle et al., 1996; Huber et al., 2006; Severinghaus & Battle, 2006). The fractionation of $\delta O_2/N_2$ during close-off is driven by snow surface characteristics determined by insolation and local climatic parameters (snow accumulation rate and temperature) (Harris Stuart, Landais, et al., 2023). Records of $\delta O_2/N_2$ are also employed for dating deep East Antarctic ice cores (M. L. Bender, 2002; Kawamura et al., 2007; Landais et al., 2012). A description on the use of the $\delta O_2/N_2$ signal for ice core dating applications is provided in the Section 2.3.4.

- Q During my PhD, I made use of new high-resolution data of $\delta O_2/N_2$ from the EDC ice core collected at LSCE by A. Grisart during his PhD over the Terminations TVI-II for dating deep polar ice cores over the past 800 kyr in Chapter 4.

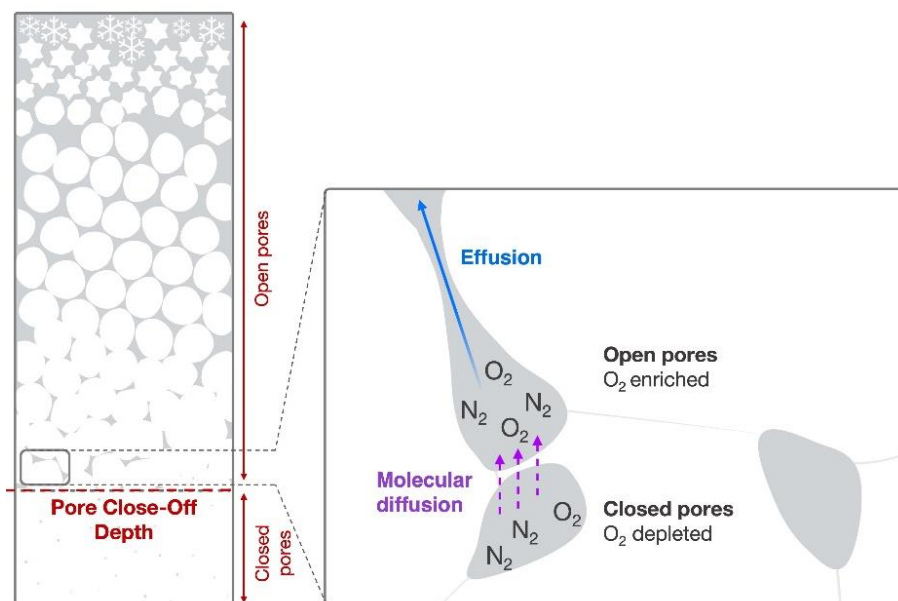


Figure 2.7 The firn column and fractionation of $\delta O_2/N_2$ during close-off (from (Harris Stuart, Landais, et al., 2023)). The box illustrates the two proposed mechanisms of gas loss during pore closure using a diagram modified from Severinghaus and Battle (2006).

2.2.4.4 The radioisotope ⁸¹Kr

The ⁸¹Kr content measured in air bubbles trapped in ice cores depends on the radioactive decay of ⁸¹Kr which is naturally produced in the upper atmosphere by cosmic-ray induced spallation (Loosli et al., 1970; Lu et al., 2014). Thus, the ⁸¹Kr can be used as an absolute dating tool for ice core chronologies following an approach briefly described in Section 2.3.2.3.

- Q During my PhD, I participated to the air extraction from samples from the Skytrain Ice Rise ice core at the LSCE, the analytical method is described in section 2.2.6.2. In Chapter 4, I propose a new chronology for deep polar ice cores over the past 800 kyr that relies on ⁸¹Kr-age constraints on the EDC ice core.

2.2.5 Analytical methods

The two following sections present the various operations required for measuring the isotopic composition in $\delta^{15}\text{N}$ and ^{81}Kr of air bubbles trapped in ice.

2.2.5.1 $\delta^{15}\text{N}$ measurements

I contributed to the collection of 43 $\delta^{15}\text{N}$ of N_2 measurements on the EDC ice core over MIS 7 (between Aug. 2023 and Sept. 2023).

Sample preparation

The ice samples were stored and cut in a cold room at LSCE at $\sim 25^\circ\text{C}$. Approximately 20 g of ice are required for isotope analysis of the inert gases such as N_2 . However, due to the potential for gas losses to affect the isotopic composition of the air bubbles, 3-5 mm must be trimmed from all sides of the sample prior to analysis. Therefore, a sample of ~ 30 g is required. If the ice sample available at one depth level was big enough, we cut the ice sample into two or three replicas for the measurement. Once the cutting stage has been completed, the air must be extracted during the day to avoid further contamination of the sample.

Gas extraction

I used the semi-automatic gas extraction line initially developed by E. Capron and A. Landais at the LSCE (Capron, 2010) and further ameliorated throughout the years (Bazin et al., 2016; Bréant et al., 2017; Extier et al., 2018a; Grisart, 2023). The extraction line is composed of stainless-steel tubes and valves (manual and automatic, Fig. 2.8) and allows the analysis of eight air samples per day.

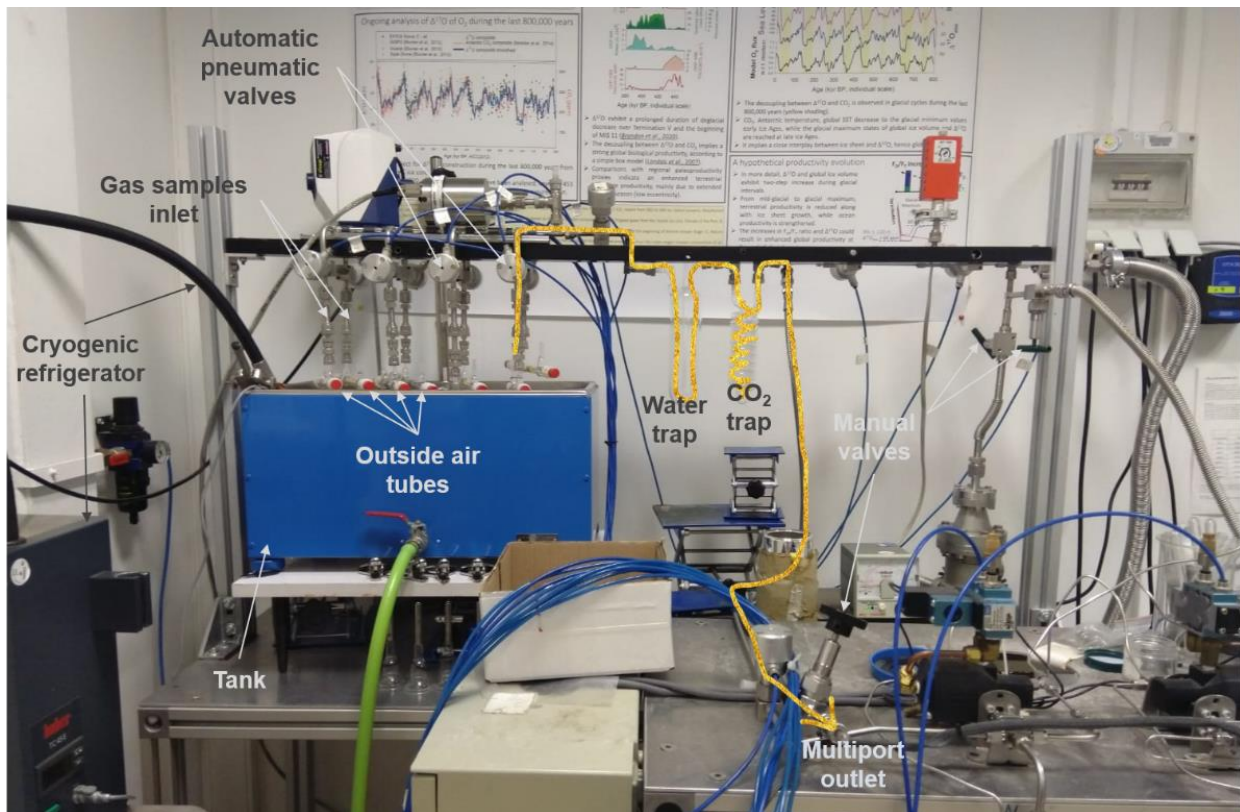


Figure 2.8 Semi-automated wet extraction line at LSCE. The trajectory of one gas sample is outlined by the golden arrow.

The extraction procedure is conducted as follows:

1. The day before the extraction, the eight glass bottles are subjected to a 2-hour drying process in an oven and placed in a freezer overnight.
2. The day of the extraction, six ice samples of ~30 g are cut in the cold room. To fit into the glass bottles that will be connected to the extraction line, the samples are cut into small cubes of around 1 cm³. They are placed into six glass bottles. The two remaining glass bottles are filled outside the laboratory with atmospheric air. These two samples are necessary for calibration and to verify that the line is functioning properly.
3. The eight bottles are sealed using a rubber gasket and clamps to prevent contamination with atmospheric air and connected to the extraction line. At the same time, they are immersed in an ethanol bath maintained at a temperature of -20°C using a cryogenic refrigerator.

4. The multiport stainless-steel sample holder composed of eight tubes (sometimes referred to as "rosette") is connected to the other extremity of the line by a flexible tube and a manual valve.
5. Prior to the air extraction procedure (i.e. before opening the glass bottles), the external air is progressively removed from the line and the rosette using a primary pump. Once the pressure of 10^{-1} mbar is reached, we switch on the turbopump for 45 additional minutes of pumping.
6. When the line is pumped, the valves connected to the glass bottles are closed. The ethanol bath is replaced by a water bath at room temperature (20°C). The ice samples are left to melt for approximately two hours to ensure the release of any air that may be trapped within the ice bubbles into the bottles.
7. Once the ice has completely melted, the warm water bath is replaced by an ethanol bath maintained at a temperature of -20°C using a cryogenic refrigerator. The aim is to refreeze the water samples with no air trapped within ice. In parallel, the cold traps for the removal of water vapor and CO_2 from the air samples are prepared. The water trap is submerged in a Dewar containing cold ethanol at a temperature of -95°C , while the CO_2 trap is immersed in a Dewar filled with liquid nitrogen at a temperature of -196°C . The nitrogen Dewar is replenished every ~ 30 min throughout the gas extraction process. The other extremity of the rosette's tubes is plunged into a liquid helium bath. Such a low temperature (-269°C) permits to trap the air extracted from the samples within the metal tubes.
8. Once the water is frozen in each glass bottle, the air sample contained in each bottle is transferred independently into one of the rosette's stainless-steel tube using an automated program. The complete transfer of all samples takes 45 minutes.
9. Once the extraction procedure is complete, the rosette is removed from the liquid helium tank and placed at room temperature for 40 minutes.
10. Subsequently, the water bath for the glass bottles is emptied and the latter are removed from the line, which is evacuated with the turbo pump overnight.

Mass spectrometer

After defrost, the multiport is connected to a dual inlet Delta V plus (Thermo Electron Corporation) mass spectrometer which is composed of three elements. The first is a source where atoms are ionized into charged particles by a tungsten filament that emits electrons. The particles are then accelerated by an electric current. The second element is a magnetic field, which curves the direction of the ions within a radius which depends on their mass/charge ratio. The third and final element is comprised of ten collectors for simultaneous measurement of the isotopic compositions of nitrogen (masses 28, 29 and 30), oxygen (masses 32, 33 and 34), argon (masses 36, 38 and 40) and CO₂ (mass 44, not used for my analyses). The measurement of the eight samples trapped in the multiport automatically follows a predefined sequence using the ISODAT control software to manage valve closing/opening and pumping. The sequence is performed overnight after the day of gas extraction.

We use CO₂-free dry air as a laboratory standard. It is calibrated daily against atmospheric air. An aliquot of laboratory standard (1 cm³) and the sample are introduced simultaneously by expansion into the bellows of the spectrometer. The simultaneous introduction of the sample and standard allows for the comparison of any isotopic fractionation that may occur during the transfer phase. This ensures that any potential bias is consistent for both the sample and the standard.

Subsequently, the gases are introduced into the source. The volumes are automatically adjusted for both the standard and the sample, ensuring that the voltage is identical on both sides at the onset of each measurement sequence. This pressure adjustment will ensure that the voltage for the sample and standard remains consistent at the outset of each measurement sequence. The data acquisition process takes approximately 45 minutes and comprises two blocks of 16 measurements. In each block, the channels alternate between a sample measurement and a standard measurement, concluding with a standard measurement. A background measurement and a pressure adjustment precede each block. As a result, each sample and the standard are compared 32 times against each other.

Correction

Corrections are applied to the raw mass spectrometer data in order to limit the biases induced by the experimental procedure on the one hand, and by the spectrometer measurement on the other. These corrections enhance analytical precision by reducing the standard deviation of measurements between raw and processed data. The initial definition of these corrections to isotopic analyses was provided by Sowers et al., (1989) with subsequent modifications proposed by Caillon et al. (2001), Landais et al. (2003), Severinghaus et al. (2003) and Severinghaus & Brook (1999).

The initial correction is attributed to a pressure discrepancy. As the volume of the sample differs from that of the standard when introduced into the mass spectrometer, this results in a pressure difference between the two variable volumes. Although the volumes are initially set to have the same voltage at the outset of each sequence of 16 measurements, the voltages will evolve differently for the standard and sample over the course of the 16 measurements. This correction is not significant (~0.007‰) for the $\delta^{15}\text{N}$ measured at LSCE (Bréant, 2017).

The second correction is related to the presence of interfering masses. The proportions of certain elements exert a non-negligible influence on the measurement of the isotopes of interest. For instance, the value of $\delta^{15}\text{N}$ is contingent upon the O_2/N_2 elemental ratio. The calculation is as follows: $\delta^{15}\text{N}_{\text{final correction}} = \delta^{15}\text{N}_{\text{pressure correction}} - \alpha \times \delta\text{O}_2/\text{N}_2_{\text{measured}}$ where $\delta^{15}\text{N}_{\text{pressure correction}}$ corresponds to the $\delta^{15}\text{N}$ measurement already corrected for pressure difference. α is the chemical slope and depends on the source parameters of the mass spectrometer.

There is also a correction with respect to outside air, which is our standard and introduces a systematic offset with respect to measurements taken with our standard laboratory gas. The two atmospheric air samples analyzed each day enable to monitor the stability of the instrument and the standard.

Q I measured 43 duplicate samples at the depths of 1869.6 and 1873.3 and on the interval of 2027.3 – 2189.6 m in the EDC ice core. The average temporal resolution of the measurements is of 780 years. These $\delta^{15}\text{N}$ measurements are expressed as an anomaly to atmospheric air and complement the unpublished datasets of A. Grisart, E. Legrain, S. Shin and A. Klüssendorf. I provide the compilation of these unpublished datasets with the already published ones in Chapter 3.

2.2.5.2 ^{81}Kr measurements

During three days in June 2022, I contributed to the air extraction of four ice samples from the Skytrain Ice Rise ice core (Mulvaney et al., 2021) supplied by E. Wolff (BAS, Univ. of Cambridge, UK). Once extracted, the gas samples were sent to W. Jiang (LLTAPM, Univ. of Science and Technology of China) for purification and ^{81}Kr and ^{85}Kr analysis using atom counting.

Sample preparation

Four ice samples of ~3 kg are taken. A slight shaving (1 mm) of the external layer is performed before processing to avoid modern air pollution. Then samples are re-examined to remove cracks and melted layers. As a final step, the ice sample is cut into smaller sticks and placed in a 40 L stainless-steel chamber. The air extraction is performed through a manual extraction line following the protocol described in Crotti (2022) and Tian et al. (2019).

The air extraction system for ^{81}Kr ice samples is a manual extraction system set up at LSCE (Fig. 2.9).

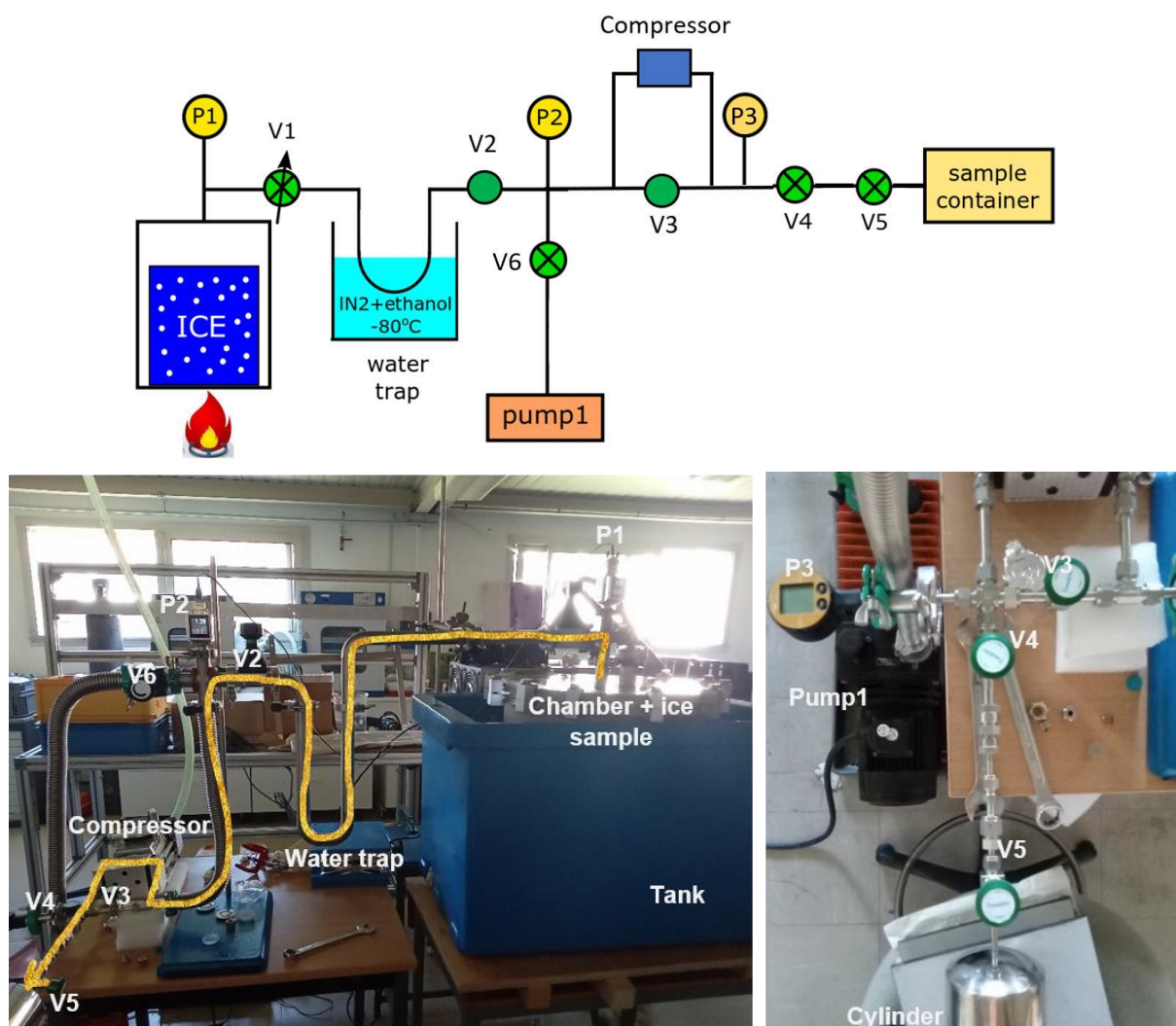


Figure 2.9 Schematic of the setup for extracting air from ice samples (Tian et al., 2019). The ice sample is placed in the stainless-steel chamber. P1-P3 are pressure gauges. V1-V6 are valves in the pump line. Pump1 is a primary oil vacuum pump for evacuating the system, and the compressor is used to compress the gas released from the ice in the sample container. Below are pictures of the corresponding elements of the line at LSCE. The trajectory of the gas sample is outlined by a golden arrow.

The air extraction system consists of a large stainless-steel tank in which the ice sample is placed. The atmospheric air is pumped while the chamber is kept at $-20\text{ }^{\circ}\text{C}$. The ice is then melted after vacuum conditions have been created. The air released from the ice sample is first retained in the chamber and then slowly extracted by pumping. It passes through a water trap for vapor removal. Then it is compressed in a stainless-steel cylinder, which is sealed after the air extraction is complete. The air sample is ready to be sent to the LLTAPM (Univ. of Science and Technology of China, USTC) for purification and krypton analysis. In contrast to the $\delta^{15}\text{N}$ extraction line, which allows us to perform air transfer of six samples in parallel, with this method, each sample is treated separately due to the large size. Once the four samples were

extracted, we fill an additional cylinder with outside atmospheric air so that five cylinders are sent.

To ensure the quality and reproducibility of the measurements, air extraction is performed according to the following protocol:

1. After decontaminating the ice samples in the cold room at -20°C and cutting them into smaller sticks, all the ice belonging to one sample is placed in the stainless-steel chamber, also located in the cold room. The chamber is closed with a heavy O-ring sealed lid to prevent contamination from outside air. The chamber is transferred to the laboratory at ambient temperature and placed in the large blue tank (Fig. 2.9).
2. The atmospheric air in the chamber is removed by pumping (using Pump1) for 30 minutes. The gases pass through a water trap which is plunged in ethanol cooled to -80°C with liquid N_2 to protect the pumps from the water vapor produced by the sublimated ice.
3. After the chamber has been evacuated of atmospheric air, the chamber is isolated from the rest of the line by closing the manual valve V1 (see Fig. 2.9). The ice is melted by adding warm water to the tank in which the chamber is placed. During the melting process, the rest of the of the line is continuously pumped to flush out any water vapor still in the line.
4. When the ice is completely melted and all the air trapped in the bubbles is released, the V1 valve is opened and the gas sample is pumped through the line. The air passes through the water trap and then transferred to a stainless-steel sample cylinder. After approximately ten minutes of compression, the rate of pressure increase in the cylinder slows down. After another five minutes the sample cylinder is closed with the manual valve V5. Since the cylinder volume is known, the air content of the sample is determined by reading the final pressure on the pressure gauge P3.

The extracted krypton is analyzed by the Atom Trap Trace Analysis (ATTA) instrument set up at the Laser Laboratory for Trace Analysis and Precision Measurement (LLTAPM, USTC, Hefei, China) (Jiang et al., 2020). This technique is based on the counting of individual ^{81}Kr atoms in the sample using a magneto-optic trap. The counting is then compared to the atmospheric reference and the ^{81}Kr abundance in the sample is determined. The anthropogenic ^{85}Kr is measured simultaneously with ^{81}Kr to control any present-day air contamination. From the ^{81}Kr abundance, it is possible to estimate ^{81}Kr radioactive decay and to calculate the age of the ice sample as per a methodology described in Section 2.3.2.3 and reminded in Section 4.1.

2.3 DATING ICE CORES

How to date your favorite ice core in six steps?

In order to derive the greatest benefit from the information provided by glacial archives, it is essential to precisely date these different records. In order to date glacial archives, which may contain signals recorded in ice or air bubbles, two distinct chronologies - one for the ice phase and one for the gas phase - are required.

Ice cannot be dated with radioactive methods such as carbon-14 or uranium-thorium. Carbon-14 dating can only be employed in exceptional circumstances (e.g. when plant debris is discovered or when sufficient quantities of carbon dioxide are available). Despite the decrease in the quantities of ice required for carbon-14 dating since the advent of particle accelerator mass spectrometry, the dates obtained are only average values over a few meters of ice. Moreover, this method is inapplicable beyond a few tens of kyr due to the radioactive decay of carbon-14, which has a half-life of 5,730 years (meaning that its concentration is halved every 5,730 years).

The dating methods developed by glaciologists are based on a combination of complementary methods. These include analyses of the ice, analyses of trapped air, comparison with other dated records or with variations in orbital parameters, as well as modeling the process of glacial sedimentation (modeling of snow accumulation, air trapping and ice flow). Hereafter is provided an overview of the various dating methods employed in this field.

2.3.1 Dating techniques using measurements in the ice phase

Step 1: Break the ice

Annual layer counting

The properties of snow differ significantly depending on whether it accumulates in the summer or winter on polar ice caps and glaciers. For instance, during the summer season, the accumulation of dust particles in snow is more prevalent due to the prevailing winds, which facilitate the transport of dust particles towards the polar regions. It is therefore possible to identify annual layers either visually, through chemical analysis, or by isotopic analysis. Thus, counting annual layers represents a straightforward method of dating, provided that snow accumulation is sufficient and the stratigraphy is not destroyed by wind action, which mixes the layers near the surface. For this reason, it is not possible to perform layer counting in the central regions of the Antarctic plateau, where the Vostok, Dome C, and Dome Fuji deep boreholes are located but it is perfectly adapted to Greenland and Antarctic coastal regions. The Greenland Ice Core Chronology 2005 (GICC05) is a significant project that systematically counts annual layers. It was conducted by the Danish team at the Niels Bohr Institute in Copenhagen and is based on the analysis of cores from DYE-3, GRIP, and NGRIP. It now spans

the last 60 kyr (Svensson et al., 2008). Similar work has been conducted on cores with sufficiently high accumulation rates in Antarctica (WAIS Divide and South Pole; Buizert et al., 2015; Winski et al., 2019) and Greenland (EGRIP and NEEM; Rasmussen et al., 2023)

Glaciologists employ a variety of seasonal records to identify annual layers, as sulfate, nitrate or sea salt. It should be noted that none of these indicators is perfect; however, when used in combination, they allow for annual dating as long as the thickness of the layers, which become thinner as they sink into the ice sheet, remains sufficient. For GICC05, the counting conducted independently by different individuals on distinct cores were compared to minimize errors. Even though the counting error increases with age (as a mistake done at the beginning propagates), each layer with an uncertain age has been listed in order to obtain a confidence interval on the final chronology. The errors are minimal, with less than 2% observed up to the last deglaciation (from -18 to -11 ka BP) and approximately 5% prior to this period.

Volcanic ashes layers

Volcanic ashes have been identified in boreholes in both Antarctica and Greenland (Fig. 2.10). In some instances, the intensity of the event or the proximity of the drilling site to the event result in the deposition of visible volcanic dust, i.e. tephra layer. The majority of these deposits consist of only small aerosols. Such deposits can then be identified by chemical analysis of the ice. Sulfate, in particular, exhibits numerous peaks corresponding to volcanic inputs that are readily discernible, as they far exceed the usual concentrations. Furthermore, the volcanic deposits modify the acidity of the ice, which can be identified by measuring its conductivity.



Figure 2.10 Tephra layer in ice core (credit: Oregon state university).

Over the past few millennia, numerous volcanic events have been dated by various methods (Sigl et al., 2014). These include counting layers for sites with sufficiently high accumulation, historical writings, and dating on volcanic material close to the volcano in question, particularly by the carbon-14 method applied to biological debris (e.g., trees caught in lava). Based on approximate glaciological dating, these events can be identified in ice core samples by their intensity. Furthermore, two ice cores can be stratigraphically linked by matching identical sulfate signature over the past glacial-interglacial cycle (Svensson et al., 2020).

Prior to the Holocene (the last 11 kyr), only a few tephra layers can be precisely dated. Their chemical analysis unambiguously identifies the original volcanic eruption. This signature can be related to that of volcanic material in the vicinity of a volcano on occasion. The conventional

radio-chronological methods can be employed to date the volcanic material.

Variations in the magnetic field and solar activity

Beryllium-10 (^{10}Be), Chlorine-36 (^{36}Cl) and carbon-14 (^{14}C) are produced in the upper atmosphere by the flow of cosmic particles. The flux is modulated by two factors: the magnetic field of the solar wind, which deflects the charged particles, and the Earth's magnetic field. In contrast to ^{10}Be and ^{36}Cl , whose deposition flux at the Earth's surface is largely determined by production in the upper atmosphere, the ^{14}C composition of the atmosphere is also influenced by exchanges between the various terrestrial carbon reservoirs. However, the most significant fluctuations in these indicators (^{14}C , ^{10}Be and ^{36}Cl) occur concurrently. ^{10}Be and ^{36}Cl can be accurately quantified in ice cores, both in Antarctica (Raisbeck et al., 2007) and Greenland (Elmore et al., 1987).

In contrast, ^{14}C is measured in the rings of trees, which have been dated over the last 12,550 years thanks to dendrochronology (Reimer et al., 2013). The ^{14}C production rate can be reconstructed for the entire Holocene using an "inverse method" that corrects the tree-ring ^{14}C record to take into account effects related to the carbon cycle (Marchal, 2005; Usoskin & Kromer, 2000). This ^{14}C production rate can be directly compared with the ^{10}Be flux record obtained from inland Antarctica over the Holocene epoch. Horiuchi et al. (2008) thus developed a ^{10}Be – ^{14}C correlation age model for the Dome Fuji ice core over the last millennium.

Finally, recurring significant anomalies affected the Earth's magnetic field throughout history. They can be attributed to a disturbance in the stability of the Earth's core. The geomagnetic field experiences a period of instability, lasting between 1 and 10 kyr, during which the magnetic poles rapidly move around the globe, or disappear, depending on the theory. During this transition, the geomagnetic field is significantly weakened, and the planet's surface is exposed to solar wind and cosmic rays. Such events, as the Laschamp anomaly (~41 ka ago) or the Matuyama-Brunhes reversal (~769 ka ago), correspond to increases in the production of ^{10}Be that can be observed in the EDC record (Fig. 2.11). They also are identified in other types of archive, such as volcanic lavas, which can be dated using Ar/Ar or Kr/Ar methods. The Laschamp anomaly has been dated with great accuracy (Guillou et al., 2004). The older Brunhes-Matuyama transition has been the subject of recent studies with the objective of providing the most accurate dating possible (Haneda et al., 2020; Macrì et al., 2018; Sagnotti et al., 2016).

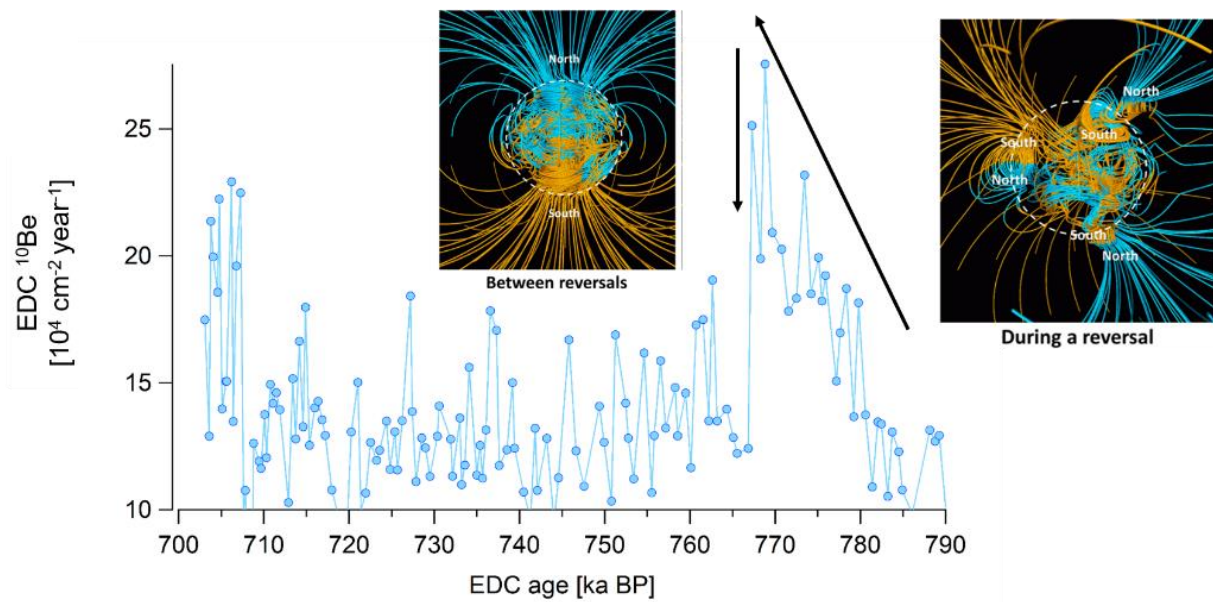


Figure 2.11 EDC ^{10}Be record between 790 and 700 ka BP. The gradual increase corresponds to a geomagnetic field reversal period. The abrupt decline followed by a relatively low level corresponds to a return to stability in the geomagnetic field. The illustrations of the geomagnetic field are from NASA (https://science.nasa.gov/science-news/science-at-nasa/2003/29dec_magneticfield/).

2.3.2 Dating techniques using measurements in the gas phase

Step 2: Listen to your ice core's deepest secrets

Δ age problem

As explained in Section 2.2.1.1, at any depth of an ice core, the gas contained in a trapped air bubble is always younger than the surrounding ice. The age difference between ice and air bubbles is noted Δ age. Expressed another way, the difference in depth between ice and gas samples of same age is noted Δ depth.

Synchronization of Greenland and Antarctic ice cores via atmospheric CH_4 and $\delta^{18}\text{O}_{\text{atm}}$

The knowledge of Δ age allows for the transfer of chronological data from air to ice. For instance, distinctive fluctuations in global atmospheric records of CH_4 and $\delta^{18}\text{O}_{\text{atm}}$ can be employed to synchronize disparate ice cores drilled in various polar regions (Landais et al., 2003). Significant atmospheric CH_4 and $\delta^{18}\text{O}_{\text{atm}}$ variations are measured in air bubbles trapped in both Greenland and Antarctic ice cores over the last glacial period (EPICA Community Members, 2006). Consequently, both records provide effective dating constraints over glacial-interglacial transitions as well as over the past glacial period.

⁴⁰Ar and ⁸¹Kr

The radioactive decay of potassium-40 (⁴⁰K) from the Earth's mantle results in an increase in the concentration of argon-40 (⁴⁰Ar) in the atmosphere. By measuring the isotopic ratio ⁴⁰Ar/³⁶Ar (expressed as $\delta^{40}\text{Ar}$), it is possible to estimate the age of the air trapped in the bubbles. From the measurement of $\delta^{40}\text{Ar}$ in air bubbles from the EDC ice core dated otherwise, a rate of increase of $\sim 0.066 \text{ ‰ Myr}^{-1}$ was estimated (M. L. Bender et al., 2008). This is still very low in comparison to the $\delta^{40}\text{Ar}$ measurement accuracy of $\sim 0.020 \text{ ‰}$, which is also affected by thermal and gravitational fractionations in the diffusive zone of the firn (Section 2.2.2). The uncertainty related with $\delta^{40}\text{Ar}$ -age determination remains significant, with an estimated range of 100 to 200 kyr (Higgins et al., 2015). The method is also limited for oldest ice near bedrock where $\delta^{40}\text{Ar}$ is typically increased (indicating a younger age) by the release of ⁴⁰Ar from bedrock.

The half-life of krypton-81 (⁸¹Kr) is 229 kyr. The measurement of its atmospheric concentration renders it a particularly useful tool for dating ice cores up to 2 Ma BP. However, the ⁸¹Kr concentration is challenging to measure due to its low abundance in the atmosphere. The initial measurements necessitated the utilization of several tens of kilograms of ice. Hence, they were conducted on the Taylor Dome horizontal core, where ice older than 100 ka is exposed at the surface (Buizert et al., 2014). In recent years, the quantity of ice required for measurements has been significantly reduced to 3 kg (Section 2.2.6.2) to achieve an uncertainty of 10% in the absolute age.

2.3.3 Synchronization to other archives

Step 3: Make sure that your ice core is on the same wavelength as your friends

Example of speleothems

The climatic variations of the D-O events are evident in speleothems across Europe, Asia, South America, and the Indian Ocean (Section 1.2.2.3.1). The uranium/thorium (U/Th) method allows for the precise dating of speleothems, with an accuracy of a few hundred years to 2 kyr over past glacial-interglacial cycles. Consequently, they provide a precise age for the transitions marking D-O events and can be used as a chronological reference if the hypothesis is made of a synchronism between the variations recorded in the $\delta^{18}\text{O}$ of the calcite of low-latitude speleothems (mainly South-East Asia for the best dated) and the variations in methane, mainly emitted by low-latitude wetlands during glacial periods. This method has been employed to date the WAIS core beyond the layer count during the last glacial period (Buizert, Cuffey, et al., 2015; Sinnl et al., 2022).

Recently, isotope-enabled climate modeling studies suggested that atmospheric variations in the $\delta^{18}\text{O}$ of O₂ measured in air bubbles in ice cores ($\delta^{18}\text{O}_{\text{atm}}$), could be aligned with $\delta^{18}\text{O}_{\text{calcite}}$ variations in low-latitude speleothems (Fig. 2.12), thereby reducing dating error bars (Reutenauer et al., 2015). This approach of aligning the $\delta^{18}\text{O}_{\text{atm}}$ with the $\delta^{18}\text{O}_{\text{calcite}}$ of the speleothems is based on the sensitivity of both records to millennial- and orbital-scale changes

in the hydrological cycle. Extier et al. (2018) explored the potential of this method and synchronized EDC record with the speleothem composite record of Cheng et al. (2016) back to 640 ka BP. Their study emphasized the potential of using $\delta^{18}\text{O}_{\text{atm}}$ as a reliable tool for further reducing the uncertainty of ice core chronologies as well as for building age scales that are coherent for polar glacial archives and mid-latitudes speleothem archives.

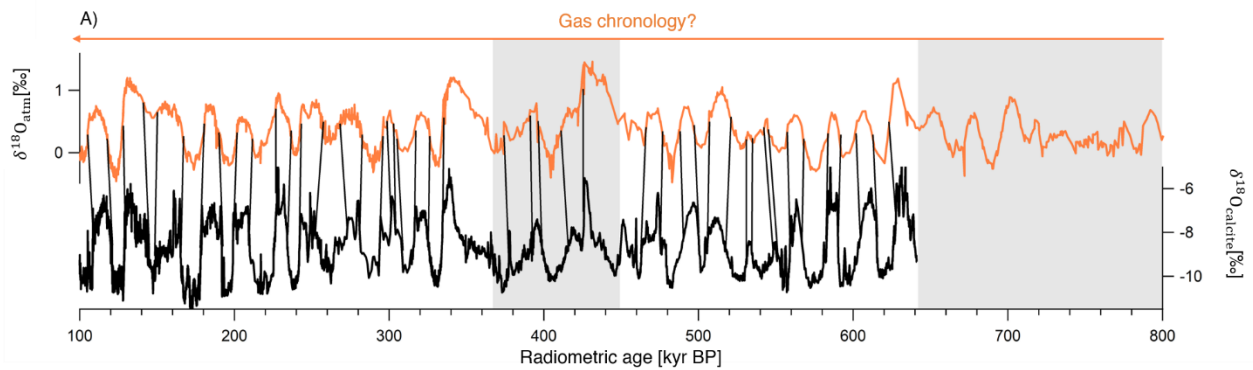


Figure 2.12 Alignment of EDC record of $\delta^{18}\text{O}_{\text{atm}}$ to $\delta^{18}\text{O}_{\text{calcite}}$ from East Asian speleothems (Bouchet, Grisart, Landais, et al., 2023a; Cheng et al., 2016). Gray areas indicate time intervals of large dating uncertainty.

2.3.4 Orbital dating

Step 4: Keep the flame alive by coming up with original dating ideas

The temporal evolution of the Earth's orbital parameters over the last few million years is modeled by mechanistic equations with great precision (Laskar et al., 2004), and these variations have a signature in most climate records, including ice core records (Section 1.2.2.1). To date polar ice cores, it is possible to align the ice core records sensitive to insolation to temporal variations in insolation determined by the Earth's orbital parameters (Laskar et al., 2004). The uncertainty of this dating method is due to two factors: firstly, the assumption of a constant phase shift between orbital and climatic variations, and secondly, the determination of this phase shift. The advantage of this type of dating is that it has an approximately constant uncertainty of a few thousand years throughout the drilling process, particularly in the deeper sections. This is due to the fact that the uncertainty is dependent on the number of orbital cycles that can be counted.

Some stable isotopic ratios measured in ice core demonstrate fluctuations in orbital frequencies. For instance, the δD of the ice, an indicator of local temperature, and the $\delta^{18}\text{O}_{\text{atm}}$, were used for the orbital setting of the ice cores. For aligning δD with orbital parameters, the approach is based on the Milankovitch theory and assumes that local temperature varies in phase with local insolation, itself determined by orbital parameters.

The $\delta^{18}\text{O}_{\text{atm}}$ is dependent on the $\delta^{18}\text{O}$ of ocean water (determined by total ice volume) as well as on the biosphere productivity and on the water cycle of low-latitude regions (where

productivity is the largest). The transfer from the ocean $\delta^{18}\text{O}$ to the air occurs through the biosphere, with an offset of 23.5 ‰ (referred to as the Dole effect; Bender et al., 1994). There is a clear correlation between $\delta^{18}\text{O}_{\text{atm}}$ and summer insolation received at 65°N (or precession) at the orbital timescale. It is relatively straightforward to use this method to identify precession cycles, at least during periods when they are clearly evident in orbital variations (Dreyfus et al., 2007; Landais et al., 2010; Petit, Jouzel, Raynaud, Barkov, Barnola, Basile, Bender, Chappellaz, Davis, Delaygue, Delmotte, Kotiyakov, et al., 1999). However, the phase shift between $\delta^{18}\text{O}_{\text{atm}}$ and insolation is considerable (~5kyr) and likely to vary over time due to the interaction between millennial variability and orbital variability, which limits the accuracy of the chronological constraint obtained with this tool. Both records $\delta^{18}\text{O}_{\text{atm}}$ and $\delta^{18}\text{O}_{\text{calcite}}$ in low-latitude regions are susceptible to fluctuations in ocean water $\delta^{18}\text{O}$ and the low-latitude water cycle and show important similarities (Extier et al., 2018). Consequently, it has been proposed to align $\delta^{18}\text{O}_{\text{atm}}$ with the U/Th-dated $\delta^{18}\text{O}_{\text{calcite}}$ record observed in East Asian speleothems (Fig. 2.12; Extier et al., 2018).

In addition, more direct indicators of local insolation have been proposed to complete the range of orbital dating tools. In particular, local summer insolation modifies the surface snow structure, and this signature remains present until the closure. This modification of physical parameters in the snow has an impact on the air content at the trapping depth and also on the molecular fractionation processes between O_2 and N_2 when the pores close. During pore closure, O_2 is expelled more readily than N_2 , due to its smaller size. Bender (2002) was the first to propose that the O_2/N_2 ratio of the air bubbles he analyzed in the Vostok core was dependent on local insolation at the summer solstice. This link was subsequently validated in the initial core sample extracted from Dome Fuji (Kawamura et al., 2007). It is thus possible to align the ice core record of $\delta\text{O}_2/\text{N}_2$ to the local summer solstice insolation (Fig. 2.13) (Landais et al., 2012).

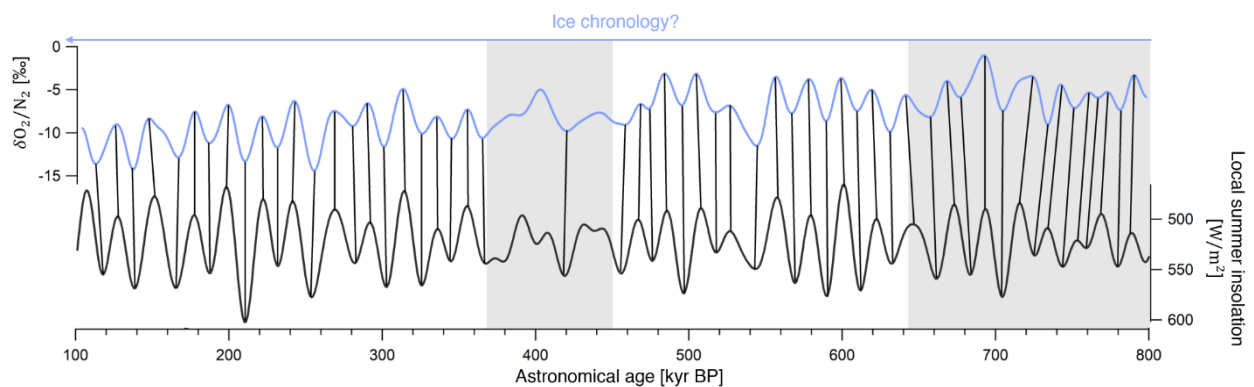


Figure 2.13 Alignment of the EDC record of $\delta\text{O}_2/\text{N}_2$ (Bouchet, Grisart, Landais, et al., 2023b) to local (75°S) summer solstice (21st Dec) insolation. $\delta\text{O}_2/\text{N}_2$ is filtered in the insolation frequency band. Gray areas indicate time intervals of large dating uncertainty.

At the same time, (Raynaud et al., 2007) demonstrated that the air content of the EDC borehole was influenced by local insolation, with the effect being greatest during a period centered on the summer solstice (Raynaud et al., 2024). However, in order to ascertain the second indicator, it is also necessary to consider altitude variations at the bubble-formation site, which has an impact on atmospheric pressure and the air content of these bubbles.

2.3.5 Sedimentation modeling

Step 5: Settle down with your ice core

Dating ice can be achieved using physical models that describe the process of glacial sedimentation. The age of ice and gas at a given depth in the ice core can be calculated on the basis of yielding past scenarios of:

- The initial snow accumulation rate at surface, noted A ;
- the ratio between the thickness of a layer in the borehole and its initial thickness at surface. This ratio is known as the thinning function and is noted τ ;
- and the modeling of the air trapping process, yielding the LID .

Evaluating the past initial snow accumulation rate

Past accumulation rates are classically retrieved using stable water isotopic ratios recorded in ice cores (δD or $\delta^{18}O$) as per the equation given in Section 2.1.3.6. An alternative approach for reconstructing paleo accumulation rates is based on the concentration of trace substances in the ice. The net flux (atmosphere to ice) of any impurity is the product of the accumulation rate and the concentration in the ice. Consequently, past accumulation rates can be calculated by measuring concentrations and estimating past fluxes. This approach has enabled the assessment of accumulation rates for Central Greenland using the cosmogenic radionuclides ^{10}Be and ^{36}Cl (Cauquoin et al., 2015).

Ice flow modeling

Ice is a solid with viscoplastic behavior. The relationship between stress and strain can be determined experimentally and theoretically. Deformation can be simulated by modeling the trajectory followed over time of an ice particle within a glacier. This allows the production of a chronology. Modeling the behavior of ice within an ice sheet requires not only knowledge of the viscoplastic properties of the material, but also the boundary conditions of the ice sheet. These boundary conditions are surface temperature and accumulation rate over time, as well as basal conditions such as geothermal flux or the rate of friction on the bedrock. Such mechanical models employ two possible expressions for yielding trajectories of ice particles: either with a basal shear layer (Johnsen & Dansgaard, 1992) or with a polynomial approximation derived from the Shallow Ice Approximation (also referred to as the Liboutry type velocity profile; Liboutry, 1979). These local models are used for dating in the vicinity of drilling sites (Obase et al., 2023; Parrenin, Dreyfus, et al., 2007), and the lateral conditions are generally derived from global simulations of the polar ice sheet over time (Ritz et al., 2001; Salamatin & Ritz, 1996). The result is the thinning function.

LID

Past LID scenarios are either evaluated using firn densification models (Section 2.2.3) or $\delta^{15}\text{N}$ data in East Antarctic sites (see section 2.2.4.1).

Limitations of modeling

Ice core dating based on modeling becomes increasingly imprecise as one approaches the bottom of the ice sheet for multiple reasons. Firstly, the mechanical properties of ice remain poorly understood. The mechanical properties of ice are not solely contingent upon pressure and temperature conditions; rather, they are also influenced by the size and orientation of the crystals composing the ice. Secondly, the conditions at the base of the bedrock cannot be directly measured in situ. Finally, the spatial conditions inferred from large-scale modeling may also be subject to significant error, particularly in the past. However, these lateral conditions determine the position of domes and thus the trajectories of ice particles.

2.3.6 The inverse method: a federative approach

Step 6: Is it a match?

The preceding sections have described a number of different dating methods, each of which has its own set of advantages and disadvantages. As the various sources of chronological information are mutually reinforcing, it is evident that the optimal dating of glacial archives necessitates the integration of these sources. For this reason, an optimization method has been developed (e.g. the Paleochrono-1.1 model of Parrenin et al., 2024). This method reverses the three variables of the sedimentation model (accumulation rate, lock-in-depth, and thinning function) and is applied to multiple ice cores simultaneously, considering stratigraphic links between the glacial archives as well as dated horizons, dated intervals, and Δdepth observations for each core (Fig. 2.14). This method was applied to obtain the reference Antarctic Ice Core Chronology (AICC) 2012, for four Antarctic cores (EDC, EDML, Vostok, TALDICE) in accordance with the GICC05 chronology of the NGRIP ice core in Greenland (Bazin et al., 2013; Veres et al., 2013). Over the course of my PhD project, the dating tool Paleochrono-1.1 was finalized (Parrenin et al., 2024; Appendix 7.3). It can be applied to multiple archives such as ice cores (referred to as *ice-core archives* in the model, and associated with two distinct chronologies for the ice and gas phases) as well as to other archives (referred to as *simple archives* in the model) such as speleothems and marine cores. Stratigraphic links connecting the different archives can be considered in the model (Fig. 2.14).

- Q I made use of this model to build (i) the coherent AICC2023 spanning the last 800 kyr presented in Chapter 4 as well as (ii) a coherent chronological framework between ice cores, speleothems and marine sediments over the past 640 kyr presented in Chapter 5.

- Parrenin et al. (2024) perform a new ice-core–speleothem dating experiment with Paleochrono-1.1, combining the AICC2023 dating experiment with data from two Chinese speleothems from Hulu Cave (China). I contributed to this study as a co-author by providing input files relative to AICC2023 dating experiment. It is attached in Appendix 7.3 and further described in Chapter 5.

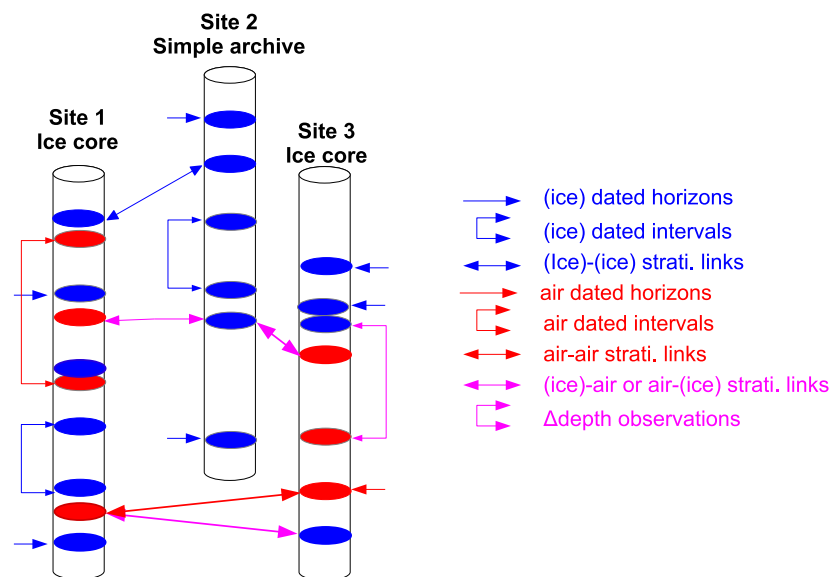


Fig. 2.14 Scheme illustrating the different kinds of observations used to constrain the chronologies of the paleoclimatic sites in the Paleochrono-1.1 probabilistic dating model (from Parrenin et al., 2024). Different types of archives can be integrated into the dating experiment: ice-core (with two distinct age scales for the ice and gas phases, e.g. sites 1 and 3) or simple archives (e.g. site 2).

2.3.7 Conclusion

Dating glacial archives is therefore a complex problem which, in the absence of precise radioactive methods, relies on several complementary techniques. For dating the Holocene climate documented in Greenland ice cores, annual layer counting provided the GICC05 timescale which is accurate within about 1%. This dating has been confirmed by comparison with dendrochronology through ^{10}Be or ^{14}C -dated volcanic horizons. In Antarctica, the last thousand years can be dated to within a few years by recognizing volcanic eruptions. For the rest of the Holocene, synchronization with Greenland dating or the dendrochronological scale using ^{10}Be yields an error of a few decades.

For the last glacial period age, the accuracy of the annual layer counting in Greenland ice cores decreases to approximately 5% up to 60 ka ago. This dating method provides ages for D-O events that are corroborated by U-Th dating of speleothems in Europe and Asia. Additionally, it is consistent with some volcanic horizons that have been dated by ^{14}C or Ar/Ar methods. The principal dating techniques employed to date the past 60 kyr now appear to agree within a few hundred years. The annual layer counting chronology has been transferred onto Antarctic

ice cores using synchronization of CH₄ records. However, this methodology necessitates an assessment of the Δ_{age} , which remains particularly uncertain over glacial periods in Central Antarctica.

Beyond the last glacial period, the counting of layers becomes increasingly challenging. The existence of speleothems or well-dated horizons becomes exceedingly rare, and the dating is mainly based on the orbital approach. The latter is limited by an accuracy of ~5 kyr with classical methods relying on climatic records. Local insolation proxies ($\delta\text{O}_2/\text{N}_2$, air content) have the potential to achieve a precision of 1 to 2 kyr, although this requires confirmation through independent methods. Furthermore, new speleothems records have emerged spanning older periods, providing new age constraints through the $\delta^{18}\text{O}_{\text{atm}}$ records of air bubbles. In this instance, it will be necessary to employ U/Pb dating for speleothems (Woodhead & Petrus, 2019).

I reviewed some of the possible methods for building optimized and coherent timescales of deep polar ice cores in a 2-page paper published in the *Past Global Changes Magazine* (Bouchet, Landais, & Parrenin, 2023; Appendix 7.2). This review paper focuses on drilling sites characterized by a low temporal resolution due to minimal accumulation of snow at the ice-sheet surface.

3 CHAPTER 3

DOCUMENTING PAST CHANGES IN TEMPERATURE AND SNOWFALL USING ^{15}N MEASUREMENTS IN AIR TRAPPED IN EAST ANTARCTIC ICE CORES

Foreword

In this chapter, we first explain why the interpretation of climatic records extracted from ice cores is impeded by limitations associated with existing water isotope-based paleoreconstructions of temperature and snow accumulation. These limitations motivated the study in preparation that is presented in the second section of the chapter. It focuses on the use of an additional gas-phase proxy, the $\delta^{15}\text{N}$ isotopic ratio of N_2 measured in EDC ice core, in complementation to water isotopic records to trace local climate change. Implications and perspectives of this study are respectively stated in the third and fourth sections of this chapter.

Objectives

The objectives of this chapter are:

- ✓ To combine $\delta^{15}\text{N}$ measured in the gas phase of EDC ice core with firn densification model outputs to bring additional constraints for reconstruction of the past local temperature and accumulation rate
- ✓ To identify temporal sequence of relative changes in atmospheric concentration in GHGs versus Antarctic climate over the glacial-interglacial transitions

Methods

To achieve the stated objectives, I participated to the different efforts listed below:

- 🔍 I performed 43 $\delta^{15}\text{N}$ measurements on the EDC ice core (between Aug. 2023 and Sept. 2023). They complement the unpublished measurements of A. Grisart, E. Legrain, S. Shin and A. Klüssendorf. I worked on the compilation of the unpublished datasets with the already published ones.

- 🔍 I compared the data compilation with simulated $\delta^{15}\text{N}$ signal yielded by a firn densification model forced by various climatic scenarios.
- 🔍 I wrote a draft of a study that we are planning to submit conjointly with Legrain et al. (in prep.) to PNAS (Proceedings of the National Academy of Sciences).
- 🔍 I contributed as a co-author to the study of Legrain et al. (in prep.) on the evolution of the Antarctic climate-atmospheric CO_2 phasing over the past five glacial Terminations. My contribution constituted in the reviewing of the article as well as in the questioning the interpretation of the overall research outputs.

Highlights

- Changes in obliquity affect the annual mean and seasonality of snowfall and temperature in East Antarctica. The resulting effects on δD and $\delta^{15}\text{N}$ are different, causing $\delta^{15}\text{N}$ and δD to diverge over obliquity maxima during glacial periods.
- During a deglaciation, the large amplitude warming and the associated precipitation increase outweigh other drivers and augment both δD and $\delta^{15}\text{N}$. This supports the use of the $\delta^{15}\text{N}$ record to document deglacial warmings in East Antarctica, thus allowing to circumvent uncertainties linked with Δage reconstructions when studying the lead-lag relationship between temperature and CO_2 changes (Legrain et al., in prep).
- Beyond the deglaciation context, it is essential to combine various local climate proxies such as water stable isotopes and $\delta^{15}\text{N}$ to better understand the complex physical processes at play linking snow accumulation, temperature and isotopic ratios.

Data and code availability

The compiled record of $\delta^{15}\text{N}$ from EDC that covers the past 800 kyr will be published along with the paper. The firn densification model of Bréant et al. (2017) adapted from Arnaud et al. (2000) and Goujon et al. (2003) still is under development and thus cannot be shared without the permission of P. Martinerie (patricia.martinerie@univ-grenobles-alpes.fr).

3.1 MOTIVATION

Ice cores provide information on past changes in polar air temperature and snow accumulation rate (through measurements of δD of H_2O ; black curves in Fig. 3.1) and in global atmospheric composition (through measurements in the air bubbles; red curve in Fig. 3.1).

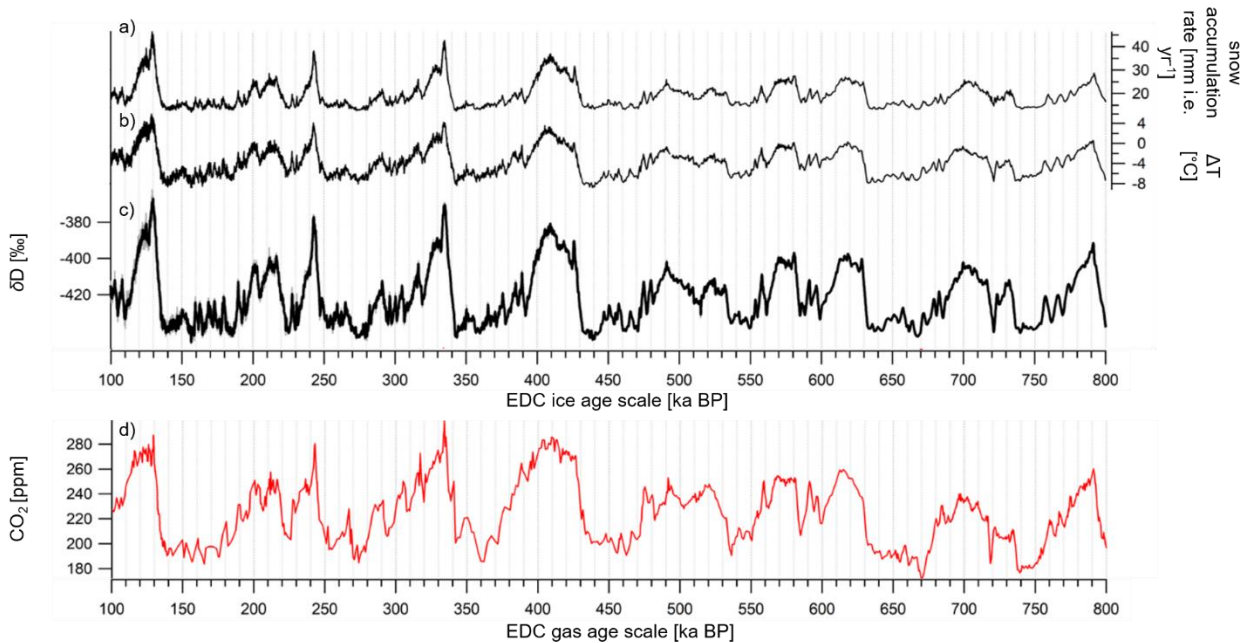


Figure 3.1 Evolution of local climate traced by EDC δD record with respect to the atmospheric CO_2 concentration between 800 and 100 ka BP. a) Snow accumulation rate and b) temperature inferred from c) δD measurements in EDC ice core (black curves; Landais & Stenni, 2021) on AICC2023 ice age scale (Chapter 4). d) CO_2 atmospheric content (red curve; Bereiter et al., 2015) on AICC2023 gas age scale. The difference between the ice and gas age scales is constrained by $\delta^{15}N$ measurements and tuned by the probabilistic model Paleochrono-1.1 (Parrenin et al., 2024) to respect gas and ice age dated horizons (Chapter 4).

However, limitations remain for providing clear sequences of relative changes in these local climatic parameters vs. CO_2 over glacial-interglacial cycles. Past variations in precipitation and temperature in East Antarctica are classically retrieved from ice core δD measurements assuming that the present-day relationship observed between polar temperature, snow accumulation and δD has always been true in the past. However, the water isotope-based climate reconstructions are associated with three challenges outlined in the Section 2.1:

- i. First, the δD records are sensitive to multiple effects such as precipitation intermittency and potential variations in the origin and routes of air masses. Therefore, there is no guarantee that the relationship observed today between δD and temperature is valid for different past climate states.

- ii. Then, no other direct proxy for snow accumulation exists in ice cores and the East Antarctic reconstructions based on δD are associated with large uncertainties due to the limits cited above (up to 40% as per the study presented in Chapter 4).
- iii. Finally, the air is trapped at the bottom of the firn, where snow transforms into ice. Therefore, at a given depth, the air is always younger than the surrounding ice. To establish how local climate inferred from δD evolved with respect to the greenhouse gas concentrations, it is desirable to accurately determine the thickness of the firn, and thus the age difference between the ice and gas phases, Δ_{age} . But modeled Δ_{age} estimates are associated with uncertainties of up to 1000 years in East Antarctica for glacial periods.

Thus, limitations remain for providing clear sequences of relative changes in local climatic parameters inferred from δD and global atmospheric concentration over glacial-interglacial cycles.

3.2 DOCUMENTING PAST CHANGES IN TEMPERATURE AND SNOWFALL USING ^{15}N MEASUREMENTS IN AIR BUBBLES TRAPPED IN THE EPICA DOME C ICE CORE (MANUSCRIPT)

Documenting past changes in temperature and snowfall using $\delta^{15}\text{N}$ measurements in air trapped in the EPICA Dome C ice core

Marie Bouchet¹, Amaëlle Landais¹, Anna-Maria Klüssendorf¹, Etienne Legrain², Emilie Capron², Frédéric Parrenin², Laurie Menviel³, Antoine Grisart¹, Frédéric Prié¹, Thomas Extier⁴, Roxanne Jacob¹, Elise Fourré¹.

¹Laboratoire des Sciences du Climat et de l'Environnement, LSCE-IPSL, CEA-CNRS-UVSQ, Univ. Paris-Saclay, 91190 Gif-sur-Yvette, France.

²Univ. Grenoble Alpes, CNRS, INRAE, IRD, Grenoble INP, IGE, 38000 Grenoble, France.

³Climate Change Research Centre and ARC Centre of Excellence for Climate System Science, University of New South Wales, NSW 2052, Sydney, Australia.

⁴Univ. Bordeaux, CNRS, Bordeaux INP, EPOC, UMR 5805, 33600 Pessac, France.

Correspondance to: Marie Bouchet (marie.bouchet@lsce.ipsl.fr)

Abstract

East Antarctic ice cores registered local surface temperature variations and atmospheric composition over the past 800,000 years. These records evidence a climatic cyclicity between glacial and interglacial periods, marked by correlated changes in Antarctic climate and atmospheric greenhouse gas concentrations. However, precisely identifying the sequence of relative changes in Antarctic temperature inferred from analyses on the ice and the greenhouse gas composition measured on the trapped air is challenging because (i) the classical approach to reconstruct past temperature using ice composition (δD) is based on the present-day relation between δD and temperature whereas this relation can evolve in time as the Earth's climate state changes; (ii) there is an age difference existing between ice and gas measurements measured at same depth in an ice core. To tackle these challenges, an alternative approach uses the isotopic composition of nitrogen ($\delta^{15}\text{N}$) as a tracer for past temperature and snow accumulation rate changes that is directly measured in air. Up to now, we still miss a complete understanding of the governing processes of the $\delta^{15}\text{N}$. We present here a new $\delta^{15}\text{N}$ record spanning the 800-100 ka interval with the aim of understanding the $\delta^{15}\text{N}$ variability at the glacial/interglacial scale. By comparing this record to a modeled $\delta^{15}\text{N}$ signal from a firn densification model driven by δD -inferred local climate history, we notice strong divergences between the two during glacial intervals occurring under periods of maximum obliquity. Additional Earth System Model simulations and firn densification modeling indicate that large obliquity changes probably modulate local temperature as well as moisture source, atmospheric transport and snow precipitation in East Antarctica. Consequently, the variations of δD vs $\delta^{15}\text{N}$ differ during these periods of peak obliquity. Therefore, we recommend to combine δD and $\delta^{15}\text{N}$ to understand past East Antarctic climatic conditions over these periods. During glacial

terminations however, changes in obliquity are not the dominant governing processes of $\delta^{15}\text{N}$ variability at the glacial-interglacial scale and thus not alter the relationship between δD , $\delta^{15}\text{N}$ and local climate. Hence, we conclude that $\delta^{15}\text{N}$ is a reliable complementary proxy for studying relative changes in local temperature and global atmospheric CO_2 composition during glacial terminations.

Significance

East Antarctic ice cores allow for reconstructions of past changes in local temperature and atmospheric greenhouse gas concentrations, providing valuable insights into Earth's climate history over the past 800,000 years. However, precisely identifying the sequence of relative changes in Antarctic temperature and greenhouse gas composition is challenging because of two reasons. First, the classical temperature reconstruction is based on present-day relation between ice composition and air temperature but there is no guarantee that this relation is true for very different Earth's climatic conditions. Second, the age difference existing between ice and gas measurements measured at same depth in one ice core prevents from accurately studying their relative temporal evolution. To address this, we assess the reliability of the isotopic composition of nitrogen ($\delta^{15}\text{N}$) as a complementary tracer for East Antarctic climate that can be directly measured in air bubbles trapped in ice cores (as greenhouse gas composition). This approach helps refining our understanding of Antarctic climate dynamics, especially during glacial periods, by considering factors such as obliquity variations and their impact on local temperature and snow precipitation patterns.

Introduction

East Antarctic ice cores are unique archives capturing variations of past temperature (through the ice isotopic composition, e.g. δD) and past atmosphere composition over the past 800 kyr (thousand years). Their analysis revealed that glacial-interglacial transitions (hereafter, also referred to as glacial terminations), pacing the Earth's climate over the past 800 kyr, are associated with significant variations in temperature and in the atmospheric concentration of CO_2 and CH_4 (EPICA members, 2004; Barnola et al., 1987; Loulergue et al., 2008; Petit et al., 1999). Numerous high-resolution Antarctic temperature and CO_2 records have been measured over the recent years (Bereiter et al., 2015; Landais et al., 2021; Nehrbass-Ahles et al., 2020a) in parallel to progress in quantitative interpretation. Nevertheless, several limitations remain for providing clear sequences of relative changes in local climatic parameters (temperature and snow accumulation rate) and global atmospheric composition over the succession of glacial-interglacial periods.

Firstly, the validity of existing paleoreconstructions of temperature and snow accumulation rates based on ice core records may be limited by several factors. The classical way to reconstruct past temperature

in polar ice cores assumes that the observed present-day water isotopic records (e.g. δD) – temperature spatial slope in polar regions can be used as a surrogate of the temporal slope (Jouzel et al., 2003). However, this δD -based temperature reconstruction in East Antarctic ice cores is challenged due to the sensitivity of δD records to the seasonality of precipitations (Laepple et al., 2011), to temperature changes in the evaporative region where the precipitation originates from (or to the displacement of this region; Stenni et al., 2010), to the condensation temperature which differs from air temperature at the ice sheet surface (Buizert et al., 2021), or to post-deposition processes (Casado et al., 2018).

Reconstructing past snow accumulation rates in East Antarctica is also difficult. The very low accumulation rates (e.g. the current accumulation rate at Dome C is 2.7 cm of ice equivalent per year, cm i.e. yr^{-1} ; Genthon et al., 2016) make annual layer counting impossible and no other direct proxy for snow accumulation exists in ice cores. Hence, the classical indirect approach is based on temperature estimated from water isotopic data. Lorius et al. (1985) and Ritz (1992) compute change in past snow accumulation rate from change in saturation vapor pressure over ice, itself linked to surface air temperature through the Clausius Clapeyron equation. For East Antarctic sites as EPICA Dome C (EDC), it is thus possible to link snow accumulation to temperature through an exponential relationship: $A = A_0 \times \exp(\beta \times \Delta\delta D)$ where A_0 is present-day accumulation rate and β a parameter which is adjusted during the chronology construction to comply with age constraints and ice flow modeling (Bouchet, Landais, Grisart, et al., 2023; Parrenin, Barnola, et al., 2007). Yet, there is no guarantee that the relationship between snow accumulation rate and temperature in polar regions is valid in the past. Therefore, the use of the present-day calibrated relationship induces uncertainties of more than 30% for past snow accumulation rates in East Antarctica (Cauquoin et al., 2015).

Another limitation to the identification of clear sequence of relative changes in local climate vs atmospheric greenhouse gas concentrations lies in the fact that air is trapped at a depth of 50-100 m, at the bottom of the firn, where snow transforms into ice, i.e. the lock-in-depth (LID). Therefore, at a given depth, the air is always younger than the surrounding ice. To establish how past temperature evolved with respect to the greenhouse gas concentrations, it is crucial to determine accurately the LID and thus the age difference between the ice and gas phases, Δage , calculated from LID and accumulation rate. LID and Δage are classically inferred from firn densification models (e.g. Goujon et al., 2003; Herron & Langway, 1980; Ligtenberg et al., 2011; Oraschewski & Grinsted, 2022). The modeled Δage estimates are associated with uncertainties of up to 1000 years in East Antarctica (Bouchet, Landais, Grisart, et al., 2023) hence limiting the study of phasing between local climate reconstructions from ice measurements and global atmospheric concentration measured in the gas phase.

These limitations call for pas-phase proxy of local climatic parameters in Antarctic ice cores. In this study, we explore the potential of the isotopic composition of N_2 ($\delta^{15}N$) as a proxy measured in air bubbles for local temperature and snow accumulation. The use of such a gas-phase proxy would

circumvent the need to estimate past variations of LID or Δ age to connect the sequences of events involving local climate and greenhouse gas concentration.

$\delta^{15}\text{N}$ of N_2 is driven by changes in surface air temperature and snow accumulation rate (classically measured on the ice phase) through thermal and gravitational molecular fractionation occurring in the firn before the bubble close-off (Severinghaus et al., 1996). Thermal fractionation leads to $\delta^{15}\text{N}$ enrichment/decrease in the bubbles formed at LID when there is a positive/negative temperature gradient from the top to the bottom of the firn (Grachev & Severinghaus, 2005). Gravitational fractionation induces a proportional increase in $\delta^{15}\text{N}$ with the LID augmentation, itself linked to accumulation and temperature by the firnification process (Craig et al., 1988; Sowers et al., 1989, 1992). As past variations of temperature and snow accumulation rate are classically retrieved from water isotopic content of East Antarctic ice cores, we expect $\delta^{15}\text{N}$ variations to correlate with δD records.

The observation of a robust correlation between ice core records of $\delta^{15}\text{N}$ and δD (Dreyfus et al., 2010) confirms the strong influence of local climate on the $\delta^{15}\text{N}$. As a consequence, $\delta^{15}\text{N}$ measurements in air bubbles have been used to determine lead or lag between increases in Antarctic temperature and CO_2 over glacial terminations directly on the gas age scale hence without the need to estimate Δ age (Landais et al., 2013; Legrain et al., in revision). However, the details of the underlying mechanisms linking past snow accumulation and temperature changes to $\delta^{15}\text{N}$ are not fully understood (Caillon et al., 2003; Dreyfus et al., 2010). Thus, even though this method appears straightforward, it should be applied with caution given the lack of complete understanding of the links between water isotopes, temperature and snow accumulation.

In this study, we combine new $\delta^{15}\text{N}$ series from the EPICA Dome C ice core, firn densification modeling estimates and output from a climate model of intermediate complexity to investigate whether the $\delta^{15}\text{N}$ can be reliably used as a tracer for local temperature and snow accumulation rate in air trapped in East Antarctic ice cores. We present a comprehensive framework to reconcile the information provided by δD and $\delta^{15}\text{N}$ regarding the past evolution of temperature and snow accumulation rate in the deep ice cores of the East Antarctic plateau.

$\delta^{15}\text{N}$ data vs. model evolution over glacial-interglacial cycles

Figure 1 shows the time-varying evolution of $\delta^{15}\text{N}$ measured in EDC ice core between 800 and 100 ka BP with new measurements presented in this study indicated by dark blue squares. They include high-resolution data between 800 and 600 ka BP, over the glacial terminations VI-II as well as over MISs 7 and 6 (see Methods). The absolute values of older datasets were readjusted so that they fit with the most recent measurements (600-800 ka BP) in which we have greater confidence (Supplementary Section 1). All measurements were compiled to build the final record spanning the 100-800 ka BP interval. A general trend reveals more enriched $\delta^{15}\text{N}$ values during interglacial periods and lighter values during

glacial periods. In particular, the range of $\delta^{15}\text{N}$ values varies between 0.535 ‰, as observed at 420 ka BP during the interglacial period of Marine Isotope Stage (MIS) 11c, and 0.315 ‰, as observed at 167 ka BP during the glacial period associated with MIS 6.

At Dome C, $\delta^{15}\text{N}$ gravitational enrichment dominates and correlates with the firn diffusive column thickness, i.e. the LID, as there is no evidence for a convective zone (Parrenin et al., 2012). LID deepens with increasing snow accumulation rate and gets shallower with a rise in temperature (accelerating the snow densification process). During a deglaciation, both temperature and accumulation increase, resulting in opposing effects on the LID. However, the accumulation rate effect is expected to be dominant in East Antarctica (Capron et al., 2013). Furthermore, it has been proposed that the concentration of impurities (inferred from measurements of Ca^{2+} concentration) can accelerate the densification process in the firn (Hörhold et al., 2012). Given that the concentration of impurities declines during past deglaciations (Röthlisberger et al., 2008), this effect should also contribute to $\delta^{15}\text{N}$ increase.

These mechanisms can be considered in the firn densification models which compute $\delta^{15}\text{N}$ using past histories of surface temperature, snow accumulation rate and impurity concentration (Bréant et al., 2017; Freitag et al., 2013; Lundin et al., 2017). However, most firn models fail to replicate the increase in $\delta^{15}\text{N}$ data systematically observed over the deglaciations in low temperature and accumulation regions such as Dome C (Capron et al., 2013; Landais, Barnola, et al., 2006). This $\delta^{15}\text{N}$ model-data discrepancy may be attributed to imprecise estimations of temperature and accumulation rate histories used to drive the firn model at the surface (Buizert, 2021) or to the difficulty of calibrating empirical firn models in the low temperature and accumulation regions (Bréant et al., 2017). Indeed, extreme climatic conditions that characterize East Antarctic sites during glacial periods lack present-day equivalent (Dreyfus et al., 2010). Still, Bréant et al. (2017) adapted the activation energy of the snow densification mechanism to cold temperature sites and to the presence of impurities and thus managed to properly reproduce the increase in $\delta^{15}\text{N}$ of N_2 over the last deglaciation in EDC which is mostly due to gravitational signal complemented by a significant contribution of thermal fractionation.

In this study, we compare the modeled $\delta^{15}\text{N}$ to the observed $\delta^{15}\text{N}$. The direct comparison between δD and $\delta^{15}\text{N}$ measurements is not detailed in the main text but is described in the Supplementary Section 2. Using the firn densification model adapted to Dome C by Bréant et al. (2017) with temperature and snow accumulation forcing deduced from δD , we find that, as expected, the modeled $\delta^{15}\text{N}$ captures most climatic features of the EDC $\delta^{15}\text{N}$ record (Supplementary Section 3). Especially, the modeled $\delta^{15}\text{N}$ reproduces well the glacial-interglacial transitions, the precursor of termination III between 252 and 247 ka BP (Bréant et al., 2019) and the strong peak occurring during the relatively cold period of MIS 7d between 230 and 226 ka BP. The apparent positive correlation between the model and the data over the whole 800-100 ka BP period is confirmed by a linear regression (correlation coefficient $r^2 = 0.57$). The $\delta^{15}\text{N}$ model-data difference tends to be positive over glacial maxima and negative during glacial onset (panel c in Fig. 1).

The orbital-scale (10 to 100 kyr) temporal evolutions of modeled $\delta^{15}\text{N}$ and $\delta^{15}\text{N}$ data sometimes are weakly correlated ($-0.5 < \text{linear correlation coefficient } r < 0.5$), resulting in an absolute difference exceeding one standard deviation of the $\delta^{15}\text{N}$ dataset (model-data mismatch $> 1 \sigma = 0.038 \text{ ‰}$). These periods include the glacial maxima preceding the glacial terminations TII, III, IV, V, VI and VII where the $\delta^{15}\text{N}$ data admit significant V-shape negative excursions with respect to the modeled $\delta^{15}\text{N}$ as well as short intervals occurring within MISs 7a-c, 11c-d, 13a, and 15e (see red shaded areas in Fig. 1). The deglaciations are associated with a high correlation coefficient between modeled $\delta^{15}\text{N}$ and data ($r > 0.75$; see green shaded areas in Fig. 1).

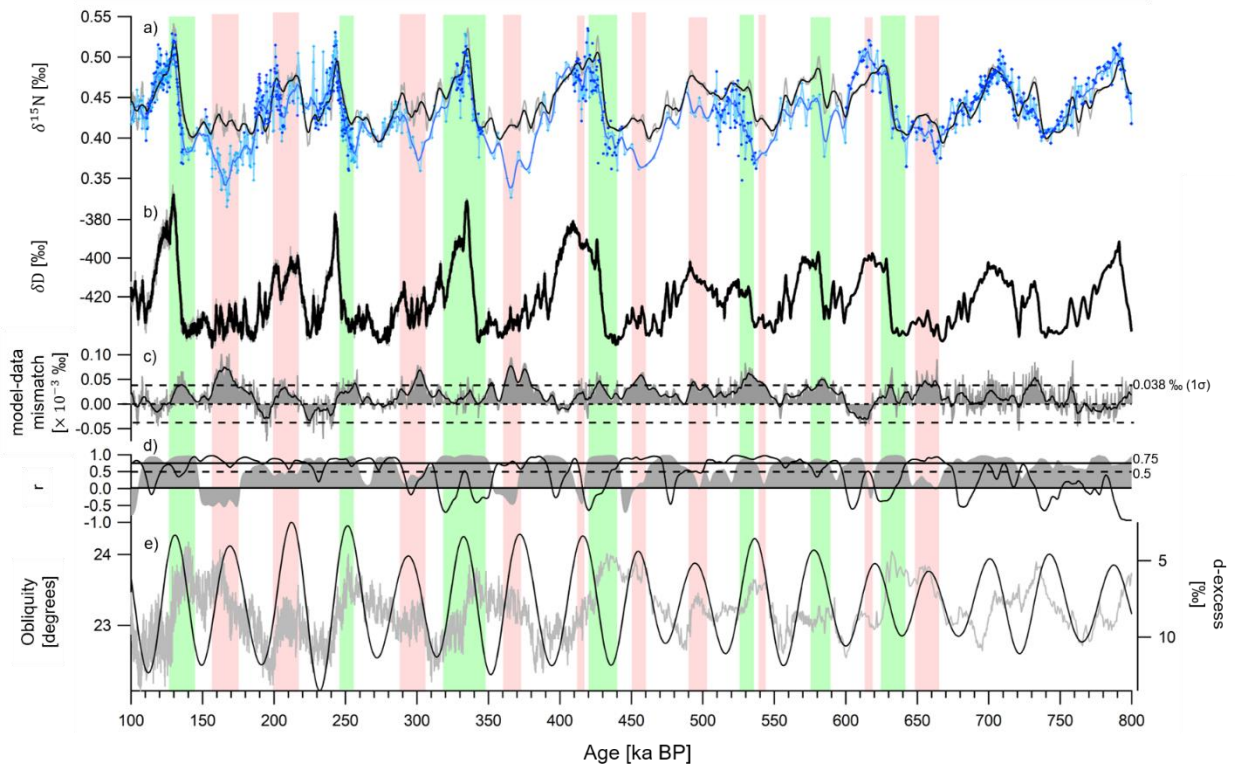


Figure 1. EDC $\delta^{15}\text{N}$ data-model comparison over the 800-100 ka BP time period. a) $\delta^{15}\text{N}$ measured in EDC ice core (already published data indicated by light blue diamonds; new dataset indicated by dark blue lozenges); $\delta^{15}\text{N}$ smoothed (5,000-year-averaged, dark blue line); $\delta^{15}\text{N}$ modeled using the Bréant et al. (2017) firn densification model forced by δD -inferred temperature and snow accumulation rate (gray line) and smoothed (5,000-year-averaged, black line). b) 55-cm resolution raw δD data (gray) and 400-year smoothed δD (black) from EDC ice core (Landais & Stenni, 2021). c) $\delta^{15}\text{N}$ model-data difference (gray shading) smoothed over 5-kyr interval (black line). d) The linear correlation coefficients r of the regression between modeled $\delta^{15}\text{N}$ and data (gray shading) and between the model-data difference and obliquity (black line). The coefficients are calculated over a sliding interval of 25 kyr. The 0.5 threshold is indicated by the horizontal dashed line and the 0.75 threshold by the horizontal plain line. e) Obliquity parameter in black (Laskar et al., 2004) and EDC deuterium-excess record in gray (Landais & Stenni, 2021). Red shaded areas indicate time intervals wider than 5,000 years where $-0.5 < r < 0.5$ and during which the model-data mismatch exceeds 0.038 ‰ (1σ of the $\delta^{15}\text{N}$ data). Green shaded areas frame deglaciations where $r > 0.75$.

Many tests were performed to reduce the model-data mismatch (Supplementary Section 3). We either vary the physics involved in the model (parameterizations of Arnaud et al., 2000; Bréant et al., 2017) or the climatic scenarios driving the model (choosing among existing paleoreconstructions of temperature, e.g. Buizert et al., 2021 or Landais et al., 2021; and of snow accumulation rates, e.g. Bazin et al., 2013 or Bouchet et al., 2023). The model-test mismatch is not reduced in any of the tests (Supplementary Section 3).

The best explanation for the large divergences observed between model and data over the past glacial intervals is that reconstructions of past snow accumulation rate and air temperature derived from the δD record are inaccurate. Indeed, these paleoreconstructions can be limited by the δD sensitivity to numerous parameters, i.e. precipitation intermittency, possible changes in evaporation source, atmospheric circulation pattern, condensation temperature and post deposition effects (Casado et al., 2020; Stenni et al., 2010; Ollivier et al., 2024).

We note that the largest $\delta^{15}N$ model-data differences occur during glacial periods and correspond to maximum values of obliquity which is the Earth's axial tilt (see red shaded areas in Fig. 1). For instance, over the glacial period of MIS 6, obliquity increases to a local maximum at around 170 ka BP while the $\delta^{15}N$ decreases and hits its lowest value throughout the past 800 kyr (0.314 ‰) at ~170 ka BP. In parallel, the modeled $\delta^{15}N$ follows the δD evolution and exhibits 1 kyr-scale oscillations around a relatively high value of 0.42 ‰ without displaying any singular minimum. Over the 170-150 ka BP time interval, obliquity decreases and $\delta^{15}N$ data rise until being reconciled with the modeled scenario. This behavior seems generalized over the 800-100 ka BP interval. The linear regression between the $\delta^{15}N$ model-data difference and the obliquity gives a correlation coefficient above 0.5 (panel d in Fig. 1) during most of the periods associated with the largest $\delta^{15}N$ model-data differences (red shaded areas in Fig. 1).

Discussion

Influence of obliquity on the $\delta^{15}N$ model-data mismatch

The obliquity varies up by $\sim 2.5^\circ$ at the frequency of 41,000 years, affecting the latitudinal distribution of insolation. Large obliquity values reduce the southern hemispheric latitudinal annual insolation gradient by up to 4% (between $20^\circ S$ and $60^\circ S$), which could modulate snowfall over ice sheets due to subdued atmospheric latent heat transport and internal climate processes (e.g., ENSO-like oscillation) (Kukla & Gavin, 2004). Large obliquity indeed decreases the moisture evaporation in lower latitudes and its transportation to Antarctica, as indicated by significant decrease in deuterium excess measured in ice cores (Landais et al., 2021; Vimeux et al., 1999). δD is affected by the change in origin of moisture, and local temperature reconstruction from δD and deuterium excess at least partly corrects for this effect (Landais et al., 2021; Stenni et al., 2010). However, its influence on accumulation is not taken into

account yet. We hypothesize here that obliquity modulates the evolution of the relationship between snow accumulation, air temperature and δD and hence explain the $\delta^{15}N$ model-data mismatch observed at high obliquity during glacial periods.

During high obliquity periods, the annual insolation is increased in East Antarctica (Laskar et al., 2004), which would augment the mean annual temperature. We thus expect an increased δD and decreased $\delta^{15}N$ if both are sensitive to annual temperature. The change in obliquity should also influence the snow accumulation rate. At high obliquity, the increase in annual insolation at high latitudes reduces the annual equator-to-pole insolation and temperature gradients. We thus expect the atmospheric meridional circulation to be less intense and a reduced moisture transport from the low latitudes to the high latitudes. Thus, high obliquity could result in decreased mean annual snow precipitation in East Antarctica, leading to a $\delta^{15}N$ decrease magnifying the decrease already expected because of the obliquity-driven rise in temperature. Changes in obliquity may drive opposite variations of temperature and snow accumulation rate at the orbital timescale (with a cyclicity of ~ 40 kyr). Therefore, we question the validity of a constant exponential relationship between snow accumulation rate and δD -inferred air temperature in East Antarctica. This would result in varying relationships between $\delta^{15}N$ and δD .

In addition, at the seasonal scale, high obliquity increases the contrast of seasonal insolation at high latitudes in both hemispheres, i.e. maximum obliquity induces maximum difference between summer insolation and winter insolation. We expect these changes in seasonal polar insolation to affect the relative seasonal contribution to the annual snowfall amount and, in turn, to influence the temperature weighted by seasonal precipitation and the ice core δD content.

Earth System Model simulations to assess the obliquity influence on local climate in East Antarctica

To assess the obliquity influence on annual mean and seasonality of precipitation and temperature in East Antarctica, and how this would differentially affect $\delta^{15}N$ and δD , we use two experiments to simulate the atmospheric circulation under high and low obliquity boundary conditions with the Earth System Model LOVECLIM (Goosse et al., 2010). We decide to focus on a period starting at 49 ka BP because it is a good analogue to the orbital and climatic contexts associated with strong $\delta^{15}N$ model-data mismatch (i.e. maximum obliquity during a glacial period). We thus make use of two existing simulations over this period (Legrain et al., in revision). The first simulation is run under 49 ka boundary conditions, i.e., with realistic orbital parameters, including an obliquity of 24.3° . The second simulation is run under the same boundary conditions except for an obliquity value of 22.1° (i.e. the lowest value of the last 800 kyr). At high obliquity, the annual insolation is increased in East Antarctica. This leads

to an increase of the simulated mean annual temperature by +2°C (Table S3 in Supplementary Section 6). Such obliquity-induced rise in temperature could explain a change of +12 ‰ in the deuterium record using the δD versus temperature relationship inferred for East Antarctica (Jouzel et al., 2003) as well as a fall in the $\delta^{15}N$ by -0.035 ‰ as per the firn densification models (Supplementary Section 7).

In the East Antarctic coastal region (65°S-77°S), LOVECLIM simulations indicate that high obliquity during glacial context decreases the annual snow accumulation rate by -5% due to the significant reduction of its major contributor, i.e. austral summer precipitation (Table S3). Indeed, the transient simulation performed over the past 140 kyr shows that the relative contribution of summer precipitation to the annual amount admits a local maximum at 49 ka (Fig. S4 in Supplementary Section 6) and the experiment at 49 ka points out a reduction of -18 % in the summer snowfall amount with little changes in fall, winter and spring (Table S3). We estimate that the high-obliquity-driven decrease of -18 % in summer snowfall induces a -0.8°C reduction (at most) in the temperature weighted by seasonal precipitation with respect to low obliquity (Table S3). This could explain a decrease of δD by -5 ‰, counterbalancing the +12 ‰ increase induced by the obliquity-driven rise in temperature. In parallel, the -5 % decrease in annual snowfall induces a reduction of the firn thickness and hence diminishes $\delta^{15}N$ values by approximately -0.01 ‰ as per the firn densification model, hence amplifying the -0.035 ‰ decrease induced by the obliquity-driven rise in temperature (Supplementary Section 7). The orbital control on insolation, Dome C climate, induced firn response and on the δD and $\delta^{15}N$ records during the generic contexts of deglaciation and of glacial period is schematically represented along with some orders of magnitude in respective panels a and b of Fig. 2.

Temperature-driven mechanisms are written in orange on the left-hand side of Fig. 2 and snow accumulation-depending processes are written in purple on the right-hand side. Deglacial changes in temperature ($\Delta T_{\text{deglaciation}}$) and snow accumulation rate ($\Delta A_{\text{deglaciation}}$) are derived from δD data over the Termination II and reported in panel a of Fig. 2 (Bouchet, Landais, Grisart, et al., 2023; Jouzel et al., 2003). They are given to indicate the order of magnitude of the typical changes affecting local climate during deglaciations of the past 400 kyr. The changes observed in $\delta^{15}N$ and δD records over TII are noted $\Delta \delta^{15}N_{\text{deglaciation}}$ and $\Delta \delta D_{\text{deglaciation}}$ and equal 12 and 75 ‰ respectively (second line of the summary box of panel a in Fig. 2).

For comparison, the changes in temperature and snow accumulation rate over an obliquity increase during a glacial period yielded by LOVECLIM simulations are reported in panel b of Fig. 2 as relative proportions of $\Delta T_{\text{deglaciation}}$ and $\Delta A_{\text{deglaciation}}$. In the first line of summary box of the two panels of Fig. 2 are indicated qualitative estimates of the deglacial (panel a) and obliquity-driven (panel b) variations of $\delta^{15}N$ and δD . They are estimated using firn densification modeling (Supplementary Section 7) and the linear relationship between temperature and δD (Jouzel et al., 2003). They are expressed as relative proportions of $\Delta \delta^{15}N_{\text{deglaciation}}$ and $\Delta \delta D_{\text{deglaciation}}$.

The qualitative estimates suggest that an obliquity rise-driven change in local climate could explain a

decrease in $\delta^{15}\text{N}$ equivalent to $\sim 40\%$ of the change observed in $\delta^{15}\text{N}$ during deglaciations due to the influence of obliquity on both temperature and accumulation. By contrast, the differentiated influence of obliquity on temperature and on precipitation intermittency counteract each other so that we expect the response of the δD to be attenuated ($\sim 15\%$ of the change observed during deglaciations).

The variations actually measured in $\delta^{15}\text{N}$ and δD records over the obliquity increase of the penultimate glacial period (from 190 to 170 ka BP) are given for comparison (second line of the summary box of panel b in Fig. 2). The observed change in $\delta^{15}\text{N}$ is approximately equivalent to what is observed over the Termination II, thus approximately 2 times superior to what we expected. As expected, the δD does not show any significant change but rather oscillates with a maximum amplitude of 25% of the change in δD observed over the Termination II.

As LOVECLIM lacks sufficient resolution (horizontal resolution of 5.6°) and has not been developed for Antarctic climate, the numerical estimates given in Fig. 2 should only be interpreted as qualitative. These qualitative model results confirm the contrasting influence of obliquity on δD and $\delta^{15}\text{N}$ evolutions. This can explain why the modeled $\delta^{15}\text{N}$ diverges from the measurements which show a V-shape negative excursion over glacial periods at high obliquity (for example during the penultimate glacial period between 190 and 150 ka BP).

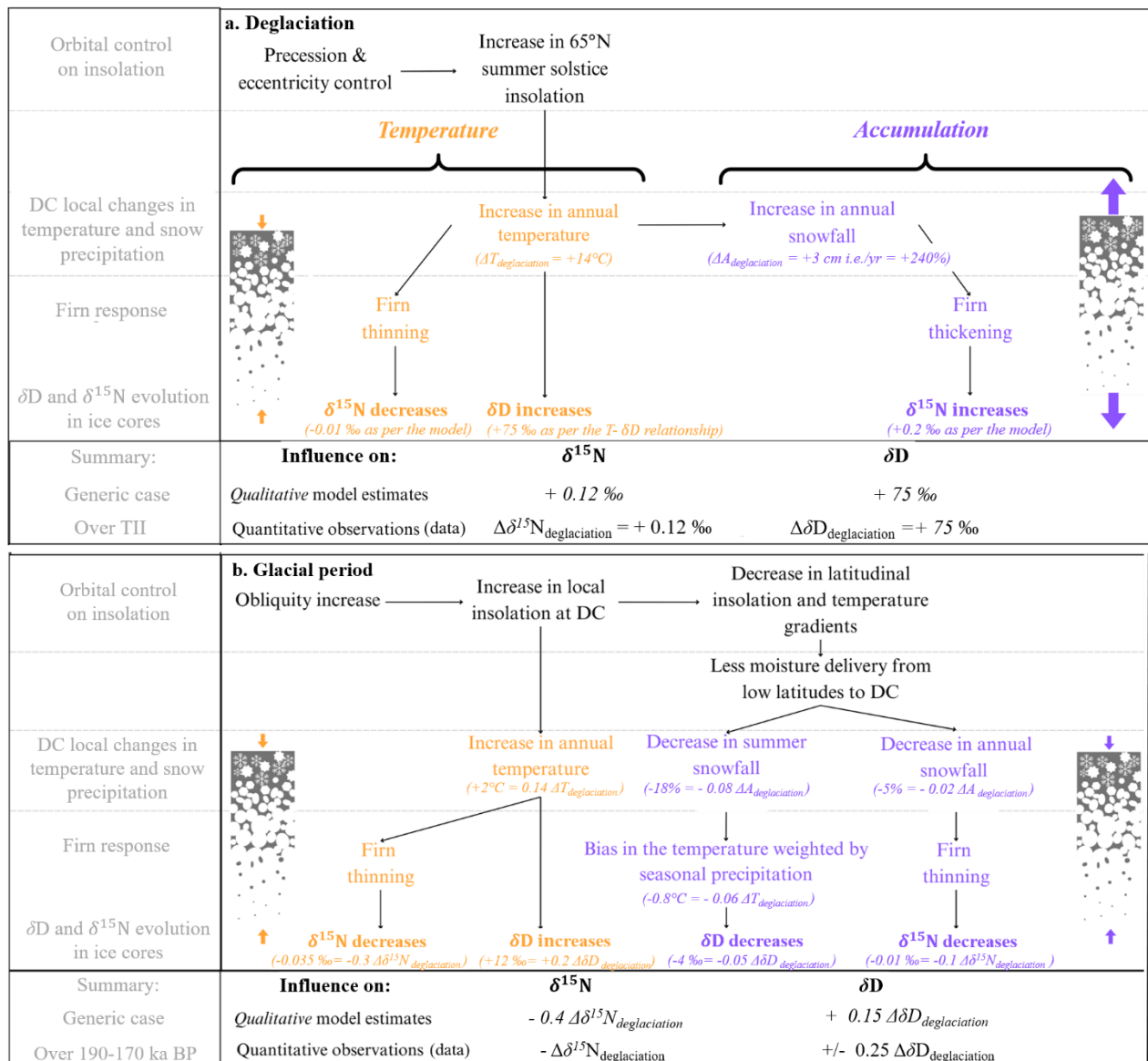


Figure 2. Schematic representation of orbital controls on insolation, Dome C temperature and snow accumulation, induced firn response and δD and $\delta^{15}\text{N}$ ice core variations during a) a deglaciation and b) a glacial period. Temperature-driven mechanisms are written in orange on the left-hand side and snow accumulation-dependent processes are written in purple on the right-hand side. a) Deglacial changes in temperature ($\Delta T_{\text{deglaciation}}$) and snow accumulation rate ($\Delta A_{\text{deglaciation}}$) are derived from δD data over TII (Jouzel et al., 2003; Bouchet et al., 2023). They are given to indicate the order of magnitude of the typical changes affecting local climate during deglaciations of the past 400 kyr. The changes observed in $\delta^{15}\text{N}$ and δD records over TII are noted $\Delta\delta^{15}\text{N}_{\text{deglaciation}}$ and $\Delta\delta\text{D}_{\text{deglaciation}}$ and equal 12 and 75 ‰ respectively. b) Changes in temperature and snow accumulation rate over an obliquity increase during a glacial period are yielded by LOVECLIM simulations and expressed as relative proportions of $\Delta T_{\text{deglaciation}}$ and $\Delta A_{\text{deglaciation}}$ (Supplementary Section 6). The qualitative estimates of the (a) deglacial and (b) obliquity-driven variations of $\delta^{15}\text{N}$ and δD are given in the first line of the summary box of each panel. They are estimated using firn densification modeling (Supplementary Section 7) and the linear relationship between temperature and δD (Jouzel et al., 2003). They are expressed as relative proportions of $\Delta\delta^{15}\text{N}_{\text{deglaciation}}$ and $\Delta\delta\text{D}_{\text{deglaciation}}$. The changes actually measured in $\delta^{15}\text{N}$ and δD records over the

penultimate deglaciation (TII) (panel a) and over the obliquity increase of the penultimate glacial period (from 190 to 170 ka BP; panel b) are given for comparison in the second line of the summary box of each panel.

$\delta^{15}\text{N}$ yielded by the firn densification model

Modeled $\delta^{15}\text{N}$ and data can be reconciled using scenarios of temperature and snow accumulation rate at the firn surface based on both δD and obliquity variations. We first modify the temperature anomaly scenario inferred from EDC water isotopic records (ΔT ; Landais et al., 2021), using an index i modulated by obliquity changes ($i = \frac{\text{obliquity value} - 23.3}{24.5 - 23.3}$ if obliquity is superior to its mid-value of 23.3° and $i = 0$ if obliquity is inferior to 23.3°). The new temperature anomaly ($\Delta T + i \times 4^\circ\text{C}$) is not modified when obliquity is inferior to its mean value (23.3°) but it is increased by up to 4 degrees when obliquity is maximum (24.5°) (red line in panel b in Fig. 3). We then modulate the snow accumulation rate according to changes in obliquity, as suggested by the LOVECLIM model. The original scenario based on EDC water isotopic records (A; Bouchet et al., 2023) is modified using the index i modulated by obliquity changes. The new accumulation scenario ($A - i \times 0.35 \text{ cm i.e. yr}^{-1}$) is not modified when obliquity is inferior to its mean value (23.3°) but it is reduced by up to $0.35 \text{ cm i.e. yr}^{-1}$ (i.e., its 800-kyr mean 1σ -uncertainty; Bouchet et al., 2023) when obliquity is maximum (24.5°) (purple line in panel c in Fig. 3). The construction of the new forcing scenarios of temperature and accumulation is further described in the Methods. The proposed scenarios for temperature and accumulation rate do not significantly differ from the δD -derived scenarios (Fig. 3), thus we believe that suggesting these new scenarios is coherent.

The simultaneous application of obliquity modulation to both snow accumulation rate and temperature results in a reduction in the modeled $\delta^{15}\text{N}$ by up to -0.05‰ , which reproduces well the V-shape excursions observed in the $\delta^{15}\text{N}$ data at high obliquity during glacial periods (dark blue line in panel a in Fig. 3).

Although the 4°C -increased temperature should increase δD by $\sim 20 \text{ ‰}$ (Jouzel et al., 2003) at the maximum of obliquity at around 170 ka, δD does not exhibit a monotonous rise and rather oscillates with an amplitude of 20 ‰ . Such behavior can be explained by the intermittency of precipitations assuming a seasonal signal of an amplitude of 24 ‰ of δD in the surface snow at Dome C (likely underestimated due to wind-caused redistribution of snow at the surface; Ollivier et al., 2024). A 4°C -increase in mean annual temperature can be conciliated with no change in δD data by assuming a shift from a regularly distributed snowfall over the year (50% summer/50% winter) to winter-dominated precipitations (100% of the snowfall occurring during the coolest 25% of the year; Supplementary Section 7). This is consistent with the high obliquity-induced significant reduction in austral snowfall predicted by LOVECLIM (by $\sim 18\%$, Fig. 2 and Table S3).

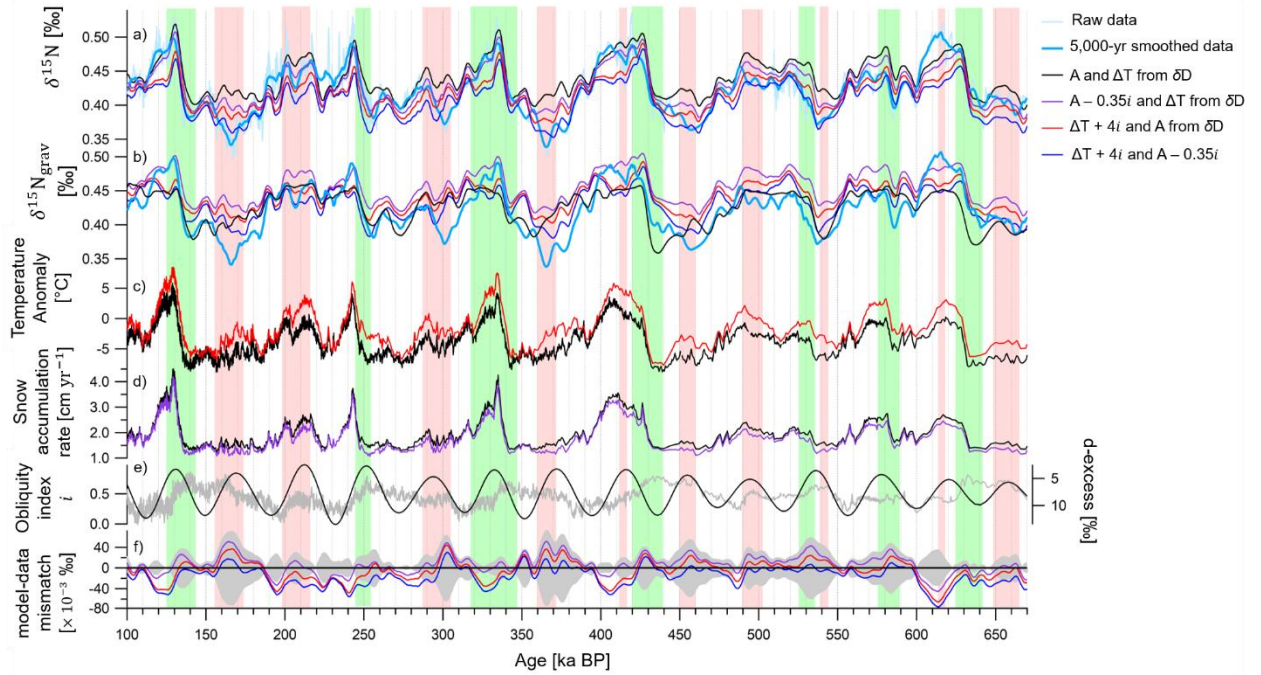


Figure 3 Reconciling modeled $\delta^{15}\text{N}$ with data between 800 and 100 ka using an obliquity index to modulate past reconstructions of snow accumulation rate and temperature. a) $\delta^{15}\text{N}$ raw data (light blue) and smoothed over 5,000 years (cyan). The modeled $\delta^{15}\text{N}$ is obtained using (i) temperature of Landais et al. (2021) and snow accumulation rate of Bouchet et al. (2023) (black); (ii) temperature of Landais et al. (2021) and snow accumulation rate modulated by obliquity (purple); (iii) temperature modulated by obliquity and snow accumulation rate of Bouchet et al. (2023) (red); and (iv) temperature and snow accumulation modulated by obliquity (dark blue). b) Temperature anomaly of Landais et al. (2021) (ΔT ; black) and modulated by obliquity as per ($\Delta T + 4i$; red). c) Snow accumulation rate of Bouchet et al. (2023) (A ; black) and modulated by obliquity ($A - 0.35i$; purple). d) d -excess on reversed y-axis (gray line; right-hand side); obliquity index i varying between 0 (obliquity lower than its mid-value of 23.3°) and 1 (obliquity maxima) (red dashed line; left-hand side); and obliquity (black line; right-hand side). e) $\delta^{15}\text{N}$ model-data mismatch for configurations (i) (gray envelop); (ii) (purple); (iii) (red) and (iv) (dark blue).

Our study, demonstrating the influence of obliquity on local temperature and accumulation rate, is consistent with the work of Erb et al. (2018) and Lee & Poulsen (2008), who highlighted the sensitivity of snow precipitation variability in high latitudes regions to the obliquity forcing and the associated potential bias of ice core-based temperature reconstructions.

Implications on the use of $\delta^{15}\text{N}$ as a climate proxy in the air trapped in bubbles

We modulated the climatic scenarios based on δD data at Dome C according to obliquity changes: when obliquity increases, we increase the air temperature and decrease the snow accumulation rate. Modifying the snow accumulation rate and the temperature according to obliquity changes has less effect on the evolution of the $\delta^{15}\text{N}$ yielded by the firn densification model over glacial Terminations than over glacial

maxima. Over the 800-100 kyr period indeed, reducing the snow accumulation rate and increasing the local temperature at high obliquity induces an average reduction in the model-data mismatch of 50% for the glacial periods of MISs 6, 8, 10, 12 and 14 against 40% for the deglaciations TII to TVIII (panel e in Fig. 3 and Supplementary Section 8). This indicates that the obliquity-control on snow precipitation and temperature in East Antarctica, and thus on $\delta^{15}\text{N}$ and δD , is of second order over glacial Terminations.

During a deglaciation, concomitant significant increases in both temperature and snow accumulation drive the augmentation of δD and $\delta^{15}\text{N}$ respectively. Outside the deglacial context, there is no such significant covariation of the accumulation and temperature drivers and – in the same way that obliquity fluctuations control the moisture delivery to the polar regions and the deuterium-excess (Vimeux et al., 1999) – obliquity could become one of the main factors driving the annual mean and seasonality of precipitation and temperature in East Antarctica, causing diverging behaviors of δD and $\delta^{15}\text{N}$.

Based on qualitative estimates yielded by the firn densification model, we assert that $\delta^{15}\text{N}$ can be faithfully used for tracing past changes in temperature and snow accumulation rate in air trapped in ice cores. Concomitant changes in snow accumulation and temperature exert opposite influences on the gravitational component of $\delta^{15}\text{N}$ over glacial Terminations. However, the significant increase in temperature contributes to increase the thermal fractionation component of $\delta^{15}\text{N}$, accentuating the effect of accumulation on the gravitational $\delta^{15}\text{N}$. This results in a significant increase in $\delta^{15}\text{N}$ over glacial Terminations due to increases in both thermal and gravitational $\delta^{15}\text{N}$ components. We also showed that significant changes in obliquity cause δD and $\delta^{15}\text{N}$ to diverge over glacial maxima. This work thus upholds the use of the $\delta^{15}\text{N}$ in combination with δD to trace past climate change in East Antarctica. This approach helps to circumvent uncertainties linked with Δage reconstructions when studying the lead-lag relationship between temperature and CO_2 changes (Caillon et al., 2003; Landais et al., 2013; Legrain et al., in prep. in Appendix 7.4).

Perspectives

This study emphasizes the need for improving firn densification modeling in the East Antarctic Plateau, in particular for more quantitative estimate of the respective thermal and gravitational contributions to the $\delta^{15}\text{N}$ signal. This would enable more precise climatic reconstruction using $\delta^{15}\text{N}$ data.

Materials and Methods

$\delta^{15}\text{N}$ measurements

Measurements of $\delta^{15}\text{N}$ of N_2 have been performed over MIS 7 and between 800 and 600 ka BP on the EDC ice core at LSCE using a semi-automated wet extraction line. The air is extracted using a melt extraction technique and is then analyzed on a dual inlet Delta V plus (Thermo Electron Corporation) mass spectrometer (see Capron et al., 2010 for the detailed analytical procedure). Results are expressed as an anomaly to atmospheric air. The results have been corrected from chemical interferences of $\delta\text{O}_2/\text{N}_2$ (Landais et al., 2003).

EDC $\delta^{15}\text{N}$ record

EDC $\delta^{15}\text{N}$ measurements were previously published by:

- Landais et al. (2006) over the age intervals 0-217; 342.89-424.91 and 428.09-800 ka BP
- Dreyfus et al. (2010) over the age intervals 0-228.06; 333.82-342.89 and 424.91-438.09 ka BP.
- Bréant et al. (2017) over the age interval 186-217 ka BP
- Bréant et al. (2019) over the age interval 218-338 ka BP

The new measurements presented in this study have been measured by:

- A. Grisart and E. Legrain (in 2022) and cover the age intervals corresponding to TII-TV I
- F. Prié and A. Landais (in August-September 2022) and cover the age intervals of TIV, TV and MIS 7
- M. Bouchet (August-September 2023) and cover the age interval 186.60-206.65 ka BP
- A. Klüssendorf (October 2023-March 2024) and cover the age interval 600-800 ka BP. The mass spectrometer used for measuring this dataset is new and different from the instrument used for the collection of the other datasets.

Remark: *In the framework of her PhD, A. Klüssendorf is currently working on the treatment of the most recently collected $\delta^{15}\text{N}$ measurements. Therefore, the sections in the Methods and in the Supplementary Material that describe the development of the final compilation of the $\delta^{15}\text{N}$ series that will be published along with this study might change between this version of the manuscript and the submission of the paper.*

All dataset except the one of A. Klüssendorf were compiled. We notice an average offset of 0.04 ‰ between the compilation and new measurements collected by A. M. Klüssendorf with the new mass spectrometer between 800 and 600 ka BP. We have great confidence in the most recently measured

dataset therefore we decide to raise the compilation by 0.04 ‰ (see Supplementary Fig. S1).

For the purpose of this study, we compiled all the datasets raised by 0.04 ‰ with the one of A. Klüssendorf. We get rid of 43 $\delta^{15}\text{N}$ measurements (25 shown in Bouchet et al. 2023 and 18 identified in this study) out of 1359 as they show a deviation greater than 0.038 ‰ (1σ) with respect to the smoothed $\delta^{15}\text{N}$ compiled record (25 points with a Savitzky-Golay algorithm).

Firn modeling and isotopic composition of N_2

$\delta^{15}\text{N}$ is related to the thickness of the firn section where diffusive mixing is dominant (i.e. diffusive column height, DCH) through gravitational fractionation, given by $\delta^{15}\text{N}_{\text{grav}} = g \times \text{DCH} / RT$ at first order approximation, where g is the gravity acceleration constant, R is the gas constant, and T is the mean temperature (Kawamura et al., 2006; Landais, Barnola, et al., 2006; Sowers et al., 1992). Note that in Antarctica, a second-order thermal effect can occur when temperature gradients arise in the firn. This thermal effect follows the equation $\delta^{15}\text{N}_{\text{th}} = \Omega \times \Delta T$, where Ω is the thermal fractionation coefficient for stable isotopes of nitrogen (Grachev & Severinghaus, 2003), and ΔT is the temperature gradient throughout the firn column. DCH is determined by subtracting the depth of the convective zone, at the top of the firn, from the LID, at its base. Previous work based on dating constraints have revealed that during glacial periods, the possibility of significant convective zones at Dome C is improbable so that $\text{LID} \sim \text{DCH}$ (Bazin et al., 2013; Parrenin et al., 2012; Veres et al., 2013). Therefore, we have:

$$\delta^{15}\text{N} = \delta^{15}\text{N}_{\text{grav}} + \delta^{15}\text{N}_{\text{th}} \quad (1)$$

$$\delta^{15}\text{N} \sim g \times \frac{\text{LID}}{RT} + \Omega \Delta T \quad (2)$$

We input scenarios of surface temperature, accumulation rate, and calcium ion concentration to the firn densification model developed by Bréant et al. (2017). The model calculates both the LID and the thermal gradient (ΔT) in the firn and then infers the $\delta^{15}\text{N}_{\text{grav}}$ and $\delta^{15}\text{N}_{\text{therm}}$. The sum of the two contributions equals $\delta^{15}\text{N}$.

Obliquity index to modulate temperature and snow accumulation rate scenarios driving the firn densification model

We calculate a positive index i reflecting obliquity variations over the last 800 kyr: $i = \frac{\text{obliquity value} - 23.3}{24.5 - 23.3}$ if *obliquity value* > 23.3° and $i = 0$ if *obliquity value* < 23.3°. The index ranges between 1, when the obliquity reaches its Pleistocene maximum level (24.5°), and 0 when obliquity is lower than its Pleistocene mid-value (23.3°).

1. Accumulation

We note A the snow accumulation rate scenario derived from δD data and tuned to AICC2023 age constraints (Bouchet, Landais, Grisart, et al., 2023). Its 800-kyr mean uncertainty (1σ) is of $0.35 \text{ cm i.e. yr}^{-1}$.

At high obliquity during glacial period, LOVECLIM predicts a reduction of the mean annual snow accumulation rate by up to $0.02 \Delta A_{\text{deglacial}} = 0.06 \text{ cm i.e. yr}^{-1}$. As LOVECLIM lacks sufficient resolution and was not developed for Antarctic region, we suppose that this prediction might be underestimated.

Using the positive index, we express the contribution to the accumulation rate imputable to large obliquity changes as the following: $A_{\text{obl}} = i \times 0.35 \text{ cm i.e. yr}^{-1} (\sim 6 \times i \times 0.02 \Delta A_{\text{deglacial}})$.

We use the snow accumulation rate history given by $A - A_{\text{obl}}$ to force the firn densification model.

2. Temperature

We note ΔT the temperature anomaly reconstructed using δD data by Landais et al. (2021). The temperature difference among various reconstructions (using water isotopes, Landais et al., 2021; Δ_{age} , Buizert et al., 2021; or ice sheet model simulations) reaches at most 4 degrees during glacial periods.

At high obliquity during glacial period, LOVECLIM predicts an augmentation of the mean annual temperature by up to $0.14 \Delta T_{\text{deglacial}} = 2^\circ\text{C}$. As LOVECLIM lacks sufficient resolution and was not developed for Antarctic region, we suppose that this prediction might be underestimated.

Using the index, we express the contribution to the local temperature imputable to large obliquity changes as the following: $\Delta T_{\text{obl}} = i \times 4^\circ\text{C} (\sim 2 \times i \times 0.14 \Delta T_{\text{deglacial}})$.

We input the temperature anomaly scenario given by $\Delta T + \Delta T_{\text{obl}}$ to the firn densification model.

As a result, when obliquity exceeds its mean value (23.3°), the proposed temperature/accumulation scenario is progressively reduced/increased with respect to the δD -based scenario (proportionally to the obliquity value) until obliquity reaches its maximum value. The new temperature/accumulation is progressively reconciled with the initial δD -based scenario until obliquity returns to its mean value. When obliquity is inferior to its mean value, the scenario is unchanged.

Supplementary Material

Supplementary Section 1: Compilation of the old and new $\delta^{15}\text{N}$ datasets for EDC

The new data collected between October 2023 and March 2024 at the LSCE by A. M. Klüssendorf with the new mass spectrometer are shown by the blue circles in Fig. S1. The old dataset (red dashed line in Fig. S1) shows a constant offset of -0.04‰ with respect to the new data. Therefore, we upraise the old dataset over this time interval so that they fit with the new data. We get rid of one outlier as it deviates from the compiled dataset (old + new data) of more than one standard deviation calculated over the whole series. The compilation is smoothed over 5,000-year intervals (purple line in Fig. S1).

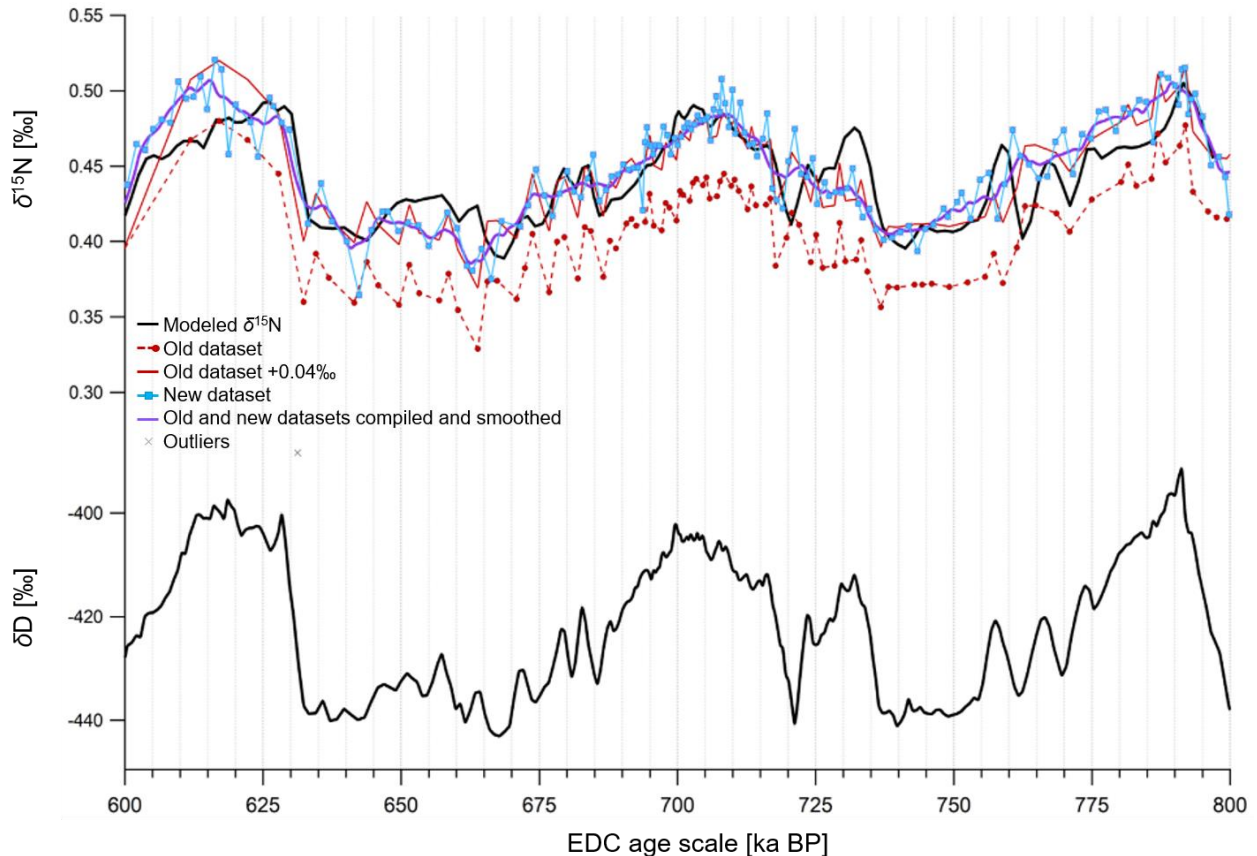


Figure S1 Compilation of the old and new $\delta^{15}\text{N}$ datasets for EDC between 800 and 600 ka BP. The old dataset (red dashes and circles) is raised up by 0.04‰ (red line) to be aligned with the new dataset absolute value (blue). The augmented old dataset is compiled to the new dataset and the compiled record is smoothed over 5,000-year interval (purple). The modeled $\delta^{15}\text{N}$ obtained by forcing the model with δD -based climate scenario is also represented (black). The δD of Landais & Stenni (2021) is shown for comparison.

Supplementary Section 2: Comparison $\delta^{15}\text{N}$ versus δD measurements

The δD series of Landais & Stenni (2021) is interpolated at the remaining ages where $\delta^{15}\text{N}$ was measured. Small imprecisions in the Δage estimates (several hundreds of years, Bouchet et al. 2023)

hence introduce minor inaccuracies into the inferred $\delta^{15}\text{N}$ - δD relationship. The apparent positive correlation between the $\delta^{15}\text{N}$ and δD signals is confirmed by a linear regression which is able to predict 67% of the $\delta^{15}\text{N}$ variability using the following relationship: $\delta^{15}\text{N} = 0.00180 + 1.18 \pm 0.02 \times \delta\text{D} \pm 0.00004$ (correlation coefficient $r^2 = 0.67$).

Following the strategy of Dreyfus et al. (2010), the regression is repeated with a 400-year smoothed (running mean) δD record. There is only a marginal improvement to the fit which accounts 68% of the $\delta^{15}\text{N}$ variability using the same linear relationship within the uncertainty range (Table S1). Therefore, the centennial scale variations in the δD signal do not help explaining the unpredicted $\delta^{15}\text{N}$ variance and the origins of the discrepancies between the two climate proxies remain unclear. Table S1 displays the regression parameters of $\delta^{15}\text{N}$ against the δD ice content.

Table S1. Linear regression between $\delta^{15}\text{N}$ versus δD and atmospheric CO_2 . The linear fit is performed using a least square algorithm. The deuterium content is either directly interpolated onto $\delta^{15}\text{N}$ ages or smoothed using a 400-year moving average to get rid of the centennial scale variability beforehand.

$\delta^{15}\text{N}$ versus	Linear relationship	Correlation coefficient r^2
δD interpolated on $\delta^{15}\text{N}$ ages	$\delta^{15}\text{N} = 1.18 \pm 0.02 + 0.00180 \pm 0.00004 \times \delta\text{D}$	0.67
δD 400-year smoothed then interpolated on $\delta^{15}\text{N}$ ages	$\delta^{15}\text{N} = 1.20 \pm 0.02 + 0.00182 \pm 0.00004 \times \delta\text{D}$	0.68
Atmospheric CO_2 (CO_2 , [ppm])	$\delta^{15}\text{N} = 0.150 \pm 0.006 + 0.00122 \pm 0.00002 \times \text{CO}_2$	0.70
δD versus		
Atmospheric CO_2 (CO_2 , [ppm])	$\delta\text{D} = -545.2 \pm 0.9 + 0.554 \pm 0.004 \times \text{CO}_2$	0.76

Supplementary Section 3: Linear regression of modeled $\delta^{15}\text{N}$ versus data

The firn densification model is tuned to fit the old $\delta^{15}\text{N}$ dataset over the last deglaciation (Bréant et al., 2017). However, the old dataset was augmented by 0.04 ‰ over the 800-600 ka BP interval to fit high-confidence recent measurements. Similarly, on the last glacial Termination, the absolute value of the old dataset used to tune the firn model may be too low. This could explain the slight offset observed between the modeled $\delta^{15}\text{N}$ and the data by up to 0.04 ‰ for the past 600 kyr.

Possible explanations for larger mismatches observed during glacial maxima at high obliquity could be:

- (i) The existence of a convective zone in the upper part of the firn, where atmospheric air is mixed and no molecular diffusion occurs. The diffusive zone thickness is therefore different from the

LID and as the $\delta^{15}\text{N}$ only reflects the diffusive zone thickness, the $\delta^{15}\text{N}$ is not proportional to the firn thickness (i.e., LID) anymore.

- (ii) Inadequate physical parameterization of the firn model and/or inaccurate climatic scenarios forcing the firn model (snow accumulation rate, temperature anomaly at the ice sheet surface, dust content in the firn).

(i) ***Convective zone***

Some studies suggested that wind activity could be responsible for the existence of a convective zone in the upper part of the firn during glacial periods, thus challenging the linearity of the relationship between $\delta^{15}\text{N}$ data and firn thickness, and preventing the firn model from forecasting $\delta^{15}\text{N}$ values. Previous work based on dating constraints over the last glacial period (MIS 3) have revealed that the possibility of significant convective zones at Dome C is improbable (Parrenin et al., 2012; Bazin et al., 2013; Veres et al., 2013). Dust flux reconstructions in EDC ice core (Lambert et al., 2012) indicate, similarly to MIS 3, no significant wind activity during MIS 6. Indeed, if wind induces sublimation of the near-surface snow, we could detect wind activity by a significant increase ($\times 2-3$) in the absolute dust flux reconstructions (Pers. Comm. B. Delmonte), which is not the case in the record of Lambert et al. (2012) during MIS 6. We thus believe that no convective zone existed at Dome C during the penultimate glacial period of MIS 6.

(ii) ***Varying the model configuration***

We varied the configurations of the firn densification model to yield different $\delta^{15}\text{N}$ scenarios (Table S2). The various configurations are described in the following sections. The modeled scenarios are then interpolated every 100 years and smoothed using a box algorithm over a 5,000-year interval to get rid of the millennial variability (panel a in Fig. S2). Two alternative smoothing are tested for comparison: without smoothing (configuration B) and smoothed over a 2,500-year interval (configuration B-2500). The linear correlation coefficient r between the modeled scenarios and the measurements is calculated over a sliding 25-kyr interval (panel b in Fig. S2). A sliding interval of 10 kyr is also used for comparison for the configuration B.

Table S2. Parameters for the different configurations of the firn densification model. The different parameters include the physics involved in the model, the forcing scenarios and the type of smoothing used prior to linear regression. For the configuration B, the sliding correlation coefficient is calculated over intervals of 10 kyr and 25 kyr. The $\delta^{15}\text{N}$ scenario is either raw (B), smoothed over an interval of 2,500 years (B-2500) or 5000 years (B-

5000). For the rest of the configurations, the interval of 25 kyr is kept and the smoothing over a 5,000-year interval is kept.

Configuration	Physics	Temperature anomaly	Snow accumulation rate	Dust [Ca ²⁺]	Smoothing of the modeled $\delta^{15}\text{N}$
B	Bréant et al. 2017	inferred from δD and corrected from source effects (Landais et al., 2021)	inferred from δD and tuned to respect AICC2023 age constraints (Bouchet et al., 2023).	Lambert et al. (2012)	No smoothing
B-2500	//	//	//	//	Over a 2500-year interval
B-5000	//	//	//	//	Over a 5000-year interval
A-T1 (varying model physics wrt B)	Arnaud et al. (2000)	//	//	//	//
A-T2 (varying temperature forcing wrt A-T1)	Arnaud et al. (2000)	$\Delta\text{TPD-LGM}$ divided by 2 as per Buizert et al. (2021)	//	//	//
B-dust0 (varying dust parameter wrt B)	Bréant et al. 2017	inferred from δD and corrected from source effects (Landais et al., 2021)	//	No dust	//
B-dust2008 (varying dust parameter wrt B)	//	//	//	Röthlisberger et al. (2008) (used in Bréant et al. 2017; 2019)	//
B-A1 (varying accumulation forcing wrt B)	//	//	inferred from δD and tuned to respect AICC2012 constraints (Bazin et al. 2013)	//	//
B-A2 (varying accumulation forcing wrt B)	//	//	Inferred from the GRISLI ice sheet model (Quiquet, Dumas)	//	//

Varying the physics in the model

We first varied the physics involved in the model either using the configuration described in Bréant et al. (2017) or in Arnaud et al. (2000). We will refer to these configurations respectively as B and A. The configuration of Arnaud et al. (2000) is close to the one of Herron & Langway (1980), which is used in many studies focusing on the use of firn thickness as a proxy for climatic paleoreconstructions (Buizert, 2021; Buizert et al., 2021).

Remark: The parameterizations of the firn model are described in Section 2.3.3.

Varying the forcing scenarios

We force the firn densification model with different histories of 1) temperature, 2) accumulation and 3) dust flux and compare the modeled $\delta^{15}\text{N}$ timeseries to the measurements to evaluate the likeliness of the different scenarios.

1. Air temperature anomaly with respect to present-day at the ice sheet surface

The A parameterization of the model is tested with two temperature scenarios. The configuration A-T1 is forced by a temperature history based on δD and corrected for source effects using d-excess (Landais et al., 2021) (see orange line in Fig. S2). The configuration A-T2 is forced by the same temperature history whose magnitude has been reduced so that the temperature difference between pre-industrial period and the LGM ($\Delta T_{\text{PI-LGM}}$) is divided by two (as suggested by Buizert et al., 2021).

2. Snow accumulation rate history

The parameterization B of the model is tested with three accumulation scenarios derived from δD record. In the B-5000 configuration, the snow accumulation rate scenario is inferred from δD and statistically adjusted to comply with AICC2023 age constraints (Bouchet et al., 2023). In the B-A1 configuration, the accumulation rate is inferred from δD measurements and adjusted to respect AICC2012 chronology (Bazin et al., 2013). In the B-A2 configuration, the history of the local snow accumulation rate is yielded by the GRISLI ice sheet model (Quiquet et al., 2018). It is therefore constrained by past histories of local air temperature inferred from ice core δD data and of sea surface temperature derived from marine $\delta^{18}\text{O}$ data.

3. Dust content in the firn

The parameterization B of the model is tested with no dust (B-dust0) as well as with two different records of dust content: the calcium ions record of Lambert et al. (2012) for configuration B-5000 and the calcium ions record of Röthlisberger et al. (2008).

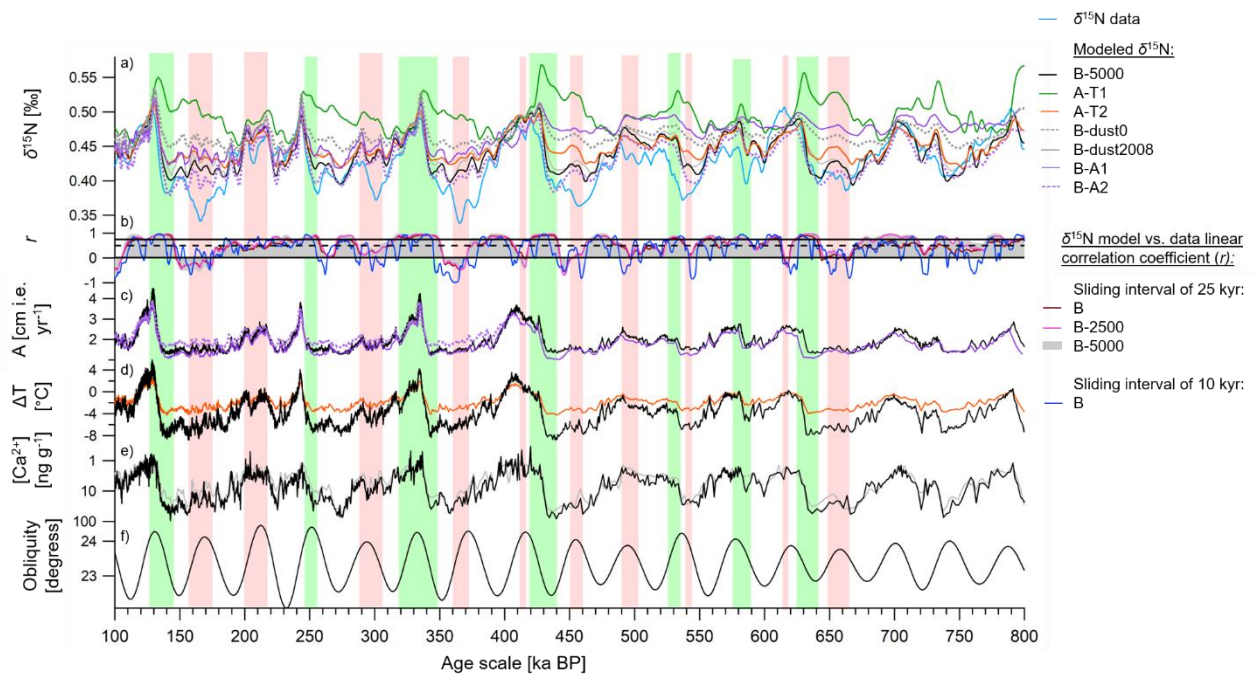


Figure S2 Evolution of the $\delta^{15}\text{N}$ model-data mismatch depending on the model configuration. a) Modeled $\delta^{15}\text{N}$ as per various configurations of the firn model (Table S2). b) Correlation coefficient of the linear regression $\delta^{15}\text{N}$ data versus the modeled $\delta^{15}\text{N}$ using different time intervals for smoothing or for linear regression. The different histories of c) snow accumulation rate (A), d) site temperature anomaly with respect to present-day (ΔT) and e) dust content [Ca^{2+}]. f) Obliquity parameter.

The comparison of the various modeled $\delta^{15}\text{N}$ scenarios in panel a of Figure S2 shows that no significant reduction of the $\delta^{15}\text{N}$ model-data mismatch can be achieved by complexifying the physics involved in the firn densification model (Arnaud et al., 2000.; Bréant et al., 2017) nor using various δD -inferred forcing scenarios of snow accumulation rate (Bazin et al., 2013; Bouchet et al., 2023; Quiquet et al., 2018), temperature (Buizert et al., 2021; Landais et al., 2021) and impurity concentration in the firn (Rothlisberger et al., 2008; Lambert et al., 2012).

We also show in Fig. S2 the model-data correlation coefficients calculated with different type of smoothing for the modeled $\delta^{15}\text{N}$ (no smoothing, 2,500 year-interval or 5,000-year interval) and with different length of sliding intervals (10 or 25 kyr). The correlation coefficients all agree and indicate a poor model-data correlation during glacial periods at maximum obliquity (red frames in Fig. S2).

Supplementary section 5: Linear regression of $\delta^{15}\text{N}$ model-data mismatch versus obliquity

We calculate the correlation coefficient of the linear regression between the model-data mismatch and the obliquity over a sliding interval of 25 kyr. The mismatch is smoothed over a 5-kyr box interval

beforehand. The average value of the linear correlation coefficient over the past 800 kyr is of 0.45. The coefficient indicates a good linear correlation between the mismatch and the obliquity ($r > 0.5$) over the majority of the intervals where the modeled $\delta^{15}\text{N}$ diverges from the data.

Supplementary section 6: LOVECLIM simulations

Model functioning

To understand the processes that could lead to a different atmospheric circulation pattern as a function of obliquity, numerical experiments are performed with the Earth system model LOVECLIM. LOVECLIM includes a free surface primitive equation ocean model with a horizontal resolution of $3^\circ \times 3^\circ$ and 20 unevenly spaced vertical levels, a dynamic/thermodynamic sea-ice model, a quasi-geostrophic T21 atmospheric model, a dynamic global vegetation model (DGVM) and a marine carbon cycle model. The DGVM used, VECODE (Vegetation Continuous Description model), simulates the vegetation structure, and associated terrestrial carbon reservoirs (Goosse et al., 2010). The initial 49 ka state was derived from a transient experiment that started at 140 ka. The penultimate deglaciation (140-120 ka) followed the PMIP4 protocol (Menviel et al., 2019), with the model being forced by changes in orbital parameters (Berger, 1978), atmospheric greenhouse gases (Köhler et al., 2017) and changes in continental ice-sheets. That simulation was continued between 120 and 49 ka forced with estimates of changes in continental ice-sheets from an offline simulation (Abe-Ouchi et al., 2013). The Bering strait was gradually closed at 70 ka, and kept closed until the early Holocene. From that initial state at 49 ka, the model was run for 4000 years with prognostic atmospheric CO_2 concentration and under constant 49 ka boundary conditions. The last 1000 years of this experiment serve as control run for the 49 ka experiments. From the initial transient state, another experiment was run under 49 ka boundary conditions but with an obliquity of 22.1° . The experiment at 49 ka has the advantage of being associated with well constrained northern hemispheric ice-sheet extent, topography and associated albedo.

High vs low obliquity at 49 ka

Annual and seasonal temperatures and precipitations at high (true) and low obliquity in the 65°S - 77°S grid cell are reported in Table S3.

The temperature weighted by the amount of seasonal precipitation is calculated as per: $T_w = (T_{\text{DJF}}PP_{\text{DJF}} + T_{\text{MAM}}PP_{\text{MAM}} + T_{\text{JJA}}PP_{\text{JJA}} + T_{\text{SON}}PP_{\text{SON}}) / (PP_{\text{DJF}} + PP_{\text{MAM}} + PP_{\text{JJA}} + PP_{\text{SON}})$ for low and high obliquity contexts. T_{DJF} and PP_{DJF} designate the austral summer temperature and precipitation, averaged over the months of December, January and February.

The difference in the temperatures obtained at low and high obliquity are given in the line called ΔT (**high-low**) in the Table S3. This value for the annual temperature (**+2°C**) provides an estimate for the

effect of an obliquity change on the mean annual temperature at Dome C during a glacial period. We report this estimate in the panel b of Fig. 2 of the main text. The ΔT (high-low) value for the weighted temperature (**-0.4°C**) provides an estimate of the obliquity-driven effect of precipitation intermittency on the δD -inferred temperature.

We also calculate a biased temperature T_b which is obtained by weighting seasonal temperatures at high obliquity by seasonal precipitation at low obliquity: $T_b =$

$$(T_{DJF_high}PP_{DJF_low}+T_{MAM_high}PP_{MAM_low}+T_{JJA_high}PP_{JJA_low}+T_{SON_high}PP_{SON_low})/(PP_{DJF_low}+PP_{MAM_low}+PP_{JJA_low}+PP_{SON_low}).$$

We subtract the biased temperature to the weighted temperature at high obliquity context, giving $T_w - T_b$ in Table S3. This comparison yields a second estimate (**-0.8°C**) of the effect of obliquity-induced accumulation changes on δD -inferred temperature. These two estimates provide a range from **-0.4 to -0.8°C** for the changes in δD -inferred temperature that can be attributed to obliquity-driven changes in seasonality of precipitation during a glacial period. We report the largest estimate (**-0.8°C**) in the panel b of the Fig. 2 of the main text.

The difference in the precipitation amount obtained at low and high obliquity, ΔA (**high-low**), during the year and during austral summer are highlighted in bold in Table S3. This value for the annual precipitation (**-5%**) provides an estimate for the effect of a change in obliquity on the annual mean accumulation rate at Dome C during a glacial period. We report this estimate in the panel b of Fig. 2 of the main text. This value for the austral summer is of **-18%**. It provides an estimate for the reduction in austral summer snowfall at Dome C due to a rise in obliquity during a glacial period. This value is reported in the panel b of Fig. 2 of the main text.

Table S3. Annual and seasonal temperature (in °C) and precipitation amount (water + snow; in w.e. cm) estimated by LOVECLIM model under 49 ka boundary conditions at high (true) and low obliquity in the 65-77°S grid cell. The difference in temperature and precipitation amounts suggested by the LOVECLIM model over an obliquity increase are respectively given in the lines named ΔT (high – low) and ΔA (high – low). The weighted temperature is defined for low and high obliquity as per $T_w = (T_{DJF}PP_{DJF}+T_{MAM}PP_{MAM}+T_{JJA}PP_{JJA}+T_{SON}PP_{SON})/(PP_{DJF}+PP_{MAM}+PP_{JJA}+PP_{SON})$. The biased temperature is only defined for high obliquity as per $T_b = (T_{DJF_high}PP_{DJF_low}+T_{MAM_high}PP_{MAM_low}+T_{JJA_high}PP_{JJA_low}+T_{SON_high}PP_{SON_low})/(PP_{DJF_low}+PP_{MAM_low}+PP_{JJA_low}+PP_{SON_low})$ with T_{DJF_high} the austral summer temperature at high obliquity and PP_{DJF_low} the austral summer snowfall at low obliquity. The difference between T_w and T_b is indicated.

	Temperature							
	Annual	DJF	MAM	JJA	SON	Weighted T_w	Biased T_b	$T_w - T_b$
High obliquity (24.3°)	-32.2	-21.35	-33.95	-39.02	-34.56	-31.06	-30.29	-0.8°C
Low obliquity (22.1°)	-34.2	-26.1	-35.4	-39.5	-35.8	-32.75		
ΔT (high-low)	+2°C							-0.4°C
Precipitation								

High obliquity (24.3°)	26.07	32.8	30.1	19.5	21.9
Low obliquity (22.1°)	27.2	39.9	28	17.8	23.2
ΔA (high-low)	-5%	-18%			

We emphasize the fact that LOVECLIM simulations provide qualitative estimates of obliquity-driven effect on accumulation and temperature for the orbital context that correspond to the last glacial period (49 ka BP). This period is an analogue to the intervals of interest in our study, i.e. the largest disagreements between the modeled $\delta^{15}\text{N}$ and the data that occur during glacial periods at maximum obliquity. Further work would be needed to extend this study beyond the last glacial period by performing LOVECLIM simulations at high and low obliquity contexts over older glacial periods. However, this is beyond the scope of this study.

Transient simulation over the past 140 kyr

The transient simulation performed over the past 140 kyr shows that the relative contribution of summer precipitation to the annual amount ($PP_{\text{DJF}}/PP_{\text{ann}}$) admits a local maximum at 49 ka in the 70-77°S; 100-140°E cell where Dome C is located (blue curve in Fig. S4). This indicates that the contribution of austral summer precipitation to the annual amount at Dome C is relatively important over the maximum of obliquity reached at 49 ka BP during the last glacial period with respect to the rest of the glacial-interglacial cycle.

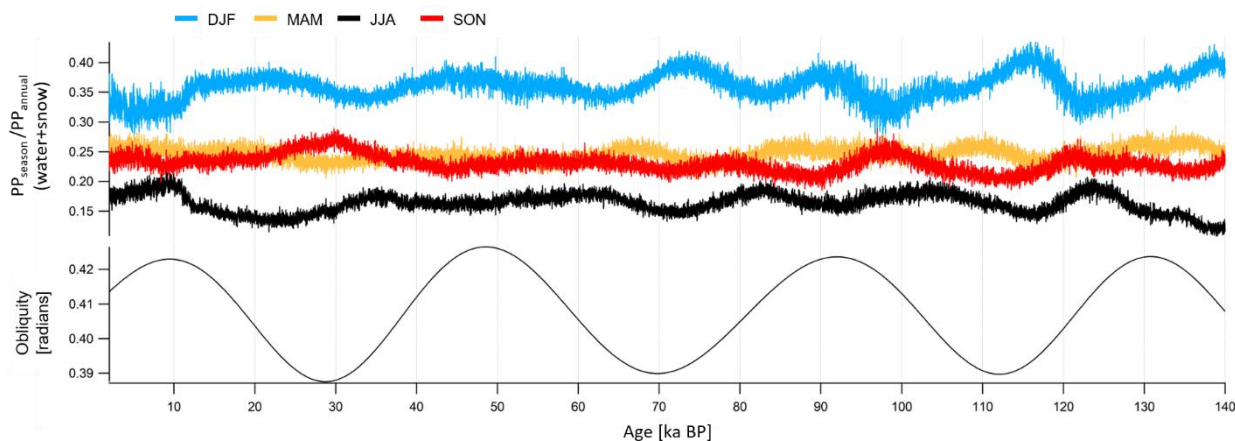


Figure S4 Relative contribution of seasonal precipitation to the annual amount at Dome C over the past 140 kyr. $PP_{\text{DJF}}/PP_{\text{ann}}$ (blue), $PP_{\text{MAM}}/PP_{\text{ann}}$ (orange), $PP_{\text{JJA}}/PP_{\text{ann}}$ (black), $PP_{\text{SON}}/PP_{\text{ann}}$ (red) are yielded by the LOVECLIM transient simulation. Their evolution is shown with respect to the obliquity parameter.

Supplementary section 7: Obliquity influence on local climate and tracers

Obliquity influence on $\delta^{15}\text{N}$ via changes in temperature and snow accumulation rate

(i) **Temperature**

We run the firn densification model parameterized as per Bréant et al. (2017) using two different forcing scenarios of temperature: (1) water isotopes-based temperature by Landais et al. (2021) and (2) this same scenario increased by $+2^{\circ}\text{C}$. We use the same scenario of snow accumulation rate and impurities to constrain the models for the two simulations. We believe that the decrease of -0.03‰ observed from one modeled $\delta^{15}\text{N}$ scenario to the other provides an order of magnitude of the $\delta^{15}\text{N}$ change that could be caused by a high-obliquity-driven 2°C -rise in mean annual temperature. The rise in temperature of $+2^{\circ}\text{C}$ (from -60°C to -58°C) induces a decrease by -0.04‰ in $\delta^{15}\text{N}$ as per the model of Arnaud et al. (2000) for a snow accumulation rate of $1.4 \pm 0.2\text{ cm w.e. yr}^{-1}$ at Dome C at 49 ka BP (Bouchet, Landais, Grisart, et al., 2023) (orange frame in Fig. S5).

Thus, regardless of the physics involved in the model, a $+2^{\circ}\text{C}$ increase in temperature at Dome C could be responsible for a decrease in $\delta^{15}\text{N}$ of -0.03 to -0.04‰ . We report the -0.035‰ estimate in the panel b of Fig. 2 in the main text.

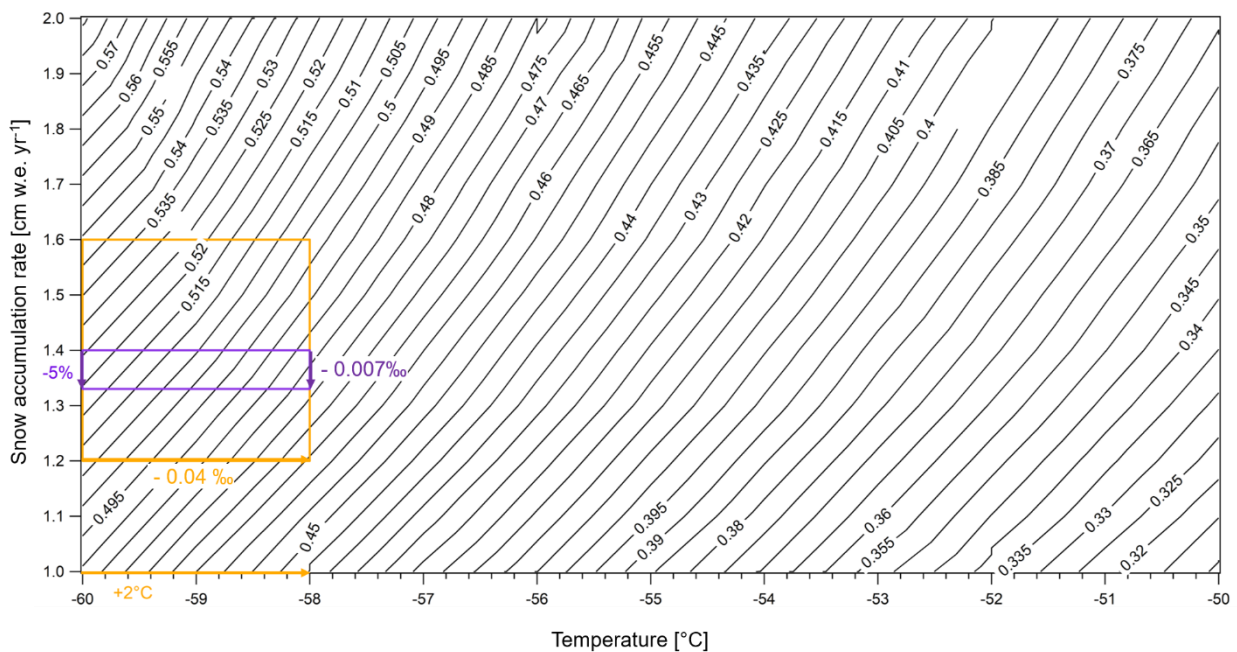


Figure S5 Predicted $\delta^{15}\text{N}$ value as per the Arnaud et al. (2000) model in function of site temperature and snow accumulation rate. The orange arrow depicts a 2°C -increase in temperature from -60°C to -58°C (on x-axis) and the orange rectangle frames the corresponding decrease in the $\delta^{15}\text{N}$ for a snow accumulation rate value comprised between 1.6 and 1.2 cm w.e. per year. The purple arrow depicts the 5%- decrease in snow accumulation rate from 1.4 to 1.33 cm w.e. yr^{-1} and associated decrease in $\delta^{15}\text{N}$ for a site temperature comprised between -58 and -60°C .

(ii) **Snow accumulation rate**

To quantify the influence of the high-obliquity-induced decrease in annual snowfall by -5% evaluated by LOVECLIM on the $\delta^{15}\text{N}$, we run the firn densification model of Bréant et al. (2017) using two different forcing scenarios of snow accumulation rate: (1) the scenario of Bouchet et al. (2023) and (2) the former scenario decreased by 5%. We force the two simulations with the same scenario of temperature and impurities. The decrease observed between modeled $\delta^{15}\text{N}$ yielded by the two experiments is of about -0.01‰. We believe this provides an order of magnitude of the $\delta^{15}\text{N}$ change induced by the high-obliquity-driven 5%-decrease in mean annual snowfall. As per the Arnaud et al. (2000) model (see Fig. S5), a reduction of -5% in the snow accumulation rate of 1.4 cm w.e. yr⁻¹ causes a reduction of -0.007 ‰ in the $\delta^{15}\text{N}$ for a site temperature comprised between -60 and -58°C.

Therefore, the two models indicate that a **-5% decrease in annual snowfall** at Dome C could induce a reduction of the firn thickness and hence diminish $\delta^{15}\text{N}$ values by **-0.01‰**. This estimate is reported in the panel b of Fig. 2 in the main text.

Obliquity influence on δD via changes in temperature and precipitation intermittency

To conciliate the modeled $\delta^{15}\text{N}$ with the data, we propose to increase the temperature by up to 4°C when obliquity is maximum. This increase in mean annual temperature should increase the δD value by ~21 ‰ but the δD record does not show a monotonous rise over the obliquity increase from 180 to 170 ka BP and rather oscillates with an amplitude of 20 ‰.

To conciliate a 4°C-increase in mean annual temperature with the δD observed behavior, we invoke a shift in precipitation intermittency induced by the obliquity increase.

The red curve in Fig. S6 shows seasonal fluctuations of a hypothetical δD signal around an average level (red dashed line) with an amplitude of ± 24 ‰ (Ollivier et al., 2024). This average level is augmented by 21‰ with respect to the measured δD (black dashed line). It corresponds to an increase of 4°C in the annual mean temperature. The blue box, which is centered on the δD measured value and which frames the maximum of our hypothetical δD signal, only overlaps the 6‰-lowest values of the hypothetical δD (blue segments). We believe that if the totality of the precipitations occurs when the δD values are comprised within this blue envelope, then a 4°C-rise in temperature can be reconciled with no shift in the measured δD . Approximating the δD oscillations by a sinus function, we calculate that the δD values comprised within the blue box correspond to 22% of the coldest time.

We conclude that the absence of obliquity-induced response in the δD could be explained by the fact that the totality of the precipitations occurs in the lowest 6‰- δD values. The time intervals corresponding to these lowest δD values account for 22% of the year. A 4°C-increase in mean annual temperature can thus be conciliated with no change in δD data by assuming a shift from a regularly distributed snowfall over the year (50% summer/50% winter) to winter-dominated precipitations (100%

of the snowfall occurring during the coolest 22% of the year).

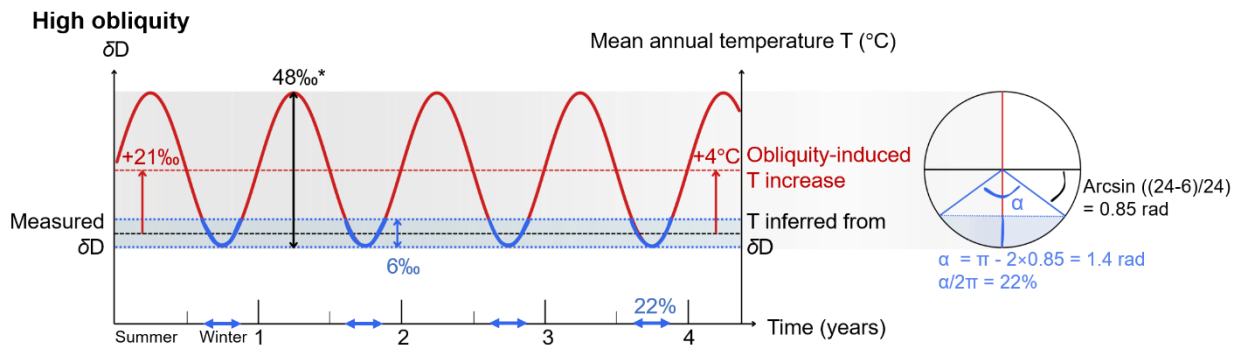


Figure S6 Change in precipitation intermittency to conciliate the 4°C-increase in mean annual temperature at Dome C and the absence of increase in the EDC δD data. Hypothetical δD signal (red curve) oscillating around a level augmented by 21‰ (red dashed line) with respect to the measured δD (black dashed line), corresponding to a 4°C-increase in annual temperature. The blue box centered on the δD measured value and overlapping the maximum of our hypothetical δD signal frames the 6‰-lowest values of the hypothetical δD (blue segments). Making the extreme (but plausible) assumption that all precipitations occur when the δD covers these values, then we can conciliate a 4°C-rise in temperature with no shift in the measured δD . Approximating the δD oscillations by a sinus function, we calculate that the δD values comprised within the blue box correspond to 22% of the time. *The ± 24 ‰-amplitude seasonal variations might be underestimated due to wind-effects, which mixes surface snow, smoothing the seasonal fluctuations (Ollivier et al., 2024).

Supplementary section 8: Reduction of the $\delta^{15}N$ model-data mismatch using the obliquity-modulated climatic scenarios

Using the graph in Fig. 3 of the main text, we fetch the order of magnitude of the reduction in the $\delta^{15}N$ model-data mismatch that is permitted by modification of the climatic forcing scenarios at maximum obliquity. The relative reduction obtained over deglaciations TII to TVIII as well as over the glacial periods of MISs 6, 8, 10, 12 and 14 are displayed in Table S4. The mismatch is reduced by -40% on average for the past glacial terminations and by -50% on average for the past glacial periods.

Table S4. Relative reduction in the $\delta^{15}N$ data-model mismatch values for terminations (TII-TVIII) and glacial periods (MISs 6, 8, 10, 12 and 14) at obliquity maxima.

	TII	TIII	TIV	TV	TVI	TVII	TVIII	Average
Maximum relative reduction in the model-data mismatch	-50%	-70%	-95%	-0%	-60%	-30%	-0%	-40%
	MIS 6	MIS 8	MIS 10	MIS 12	MIS 14			Average
	-50%	-60%	-50%	-50%	-50%			-50%

3.3 ANTARCTIC CLIMATE-ATMOSPHERIC CO₂ PHASING OVER THE FIVE MOST RECENT GLACIAL TERMINATIONS

The temporal relationship between Antarctic climate and atmospheric concentration in CO₂ has been quantified across the glacial Terminations of the Quaternary in order to elucidate the processes responsible for carbon cycle alterations during global warming transitions. Previous studies have yielded disparate results across the past three glacial terminations (Chowdhry Beeman et al., 2019; Parrenin et al., 2013a; Pedro et al., 2012). However, these studies rely on a number of different sources of data, including: (i) paleoclimate reconstructions of multi-decadal to thousand-year temporal resolutions; (ii) Antarctic ice cores drilled at different locations; (iii) climate proxies measured either on the ice or the gas phase; and (iv) heterogeneous statistical methods used to quantify the phasing. These methodological differences preclude unambiguous climatic interpretations.

Following the statement that $\delta^{15}\text{N}$ can be used as a gas-phase proxy of Antarctic surface climate during glacial terminations (Bouchet et al., in prep.). Legrain et al. (submitted; attached in Appendix 7.4) quantify the phasing evolution between Antarctic climate and atmospheric CO₂ across the past five glacial terminations using new and existing high-resolution records of atmospheric CO₂ and the $\delta^{15}\text{N}$ measured on the EDC ice core.

By comparing three statistical methods, this study reveals that the phasing at the termination onsets depends on the considered methodology and Termination. Conversely, the peak atmospheric CO₂ concentration lags Antarctic climate change by approximately 500 years at the end of Terminations I, II, III and V, regardless of the methodology employed. When combined with a multi-proxy analysis, these results demonstrate similarities between the end of Terminations and the last glacial millennial-scale variability (described in Section 1.2.2.3). This finding suggests that glacial Terminations are ultimately terminated by a millennial-scale event occurring under favorable orbital conditions.

The draft of the paper of Legrain et al. (submitted) is attached in Appendix 7.4. My contribution as a co-author to this study consisted in the reviewing of the article as well as in the questioning the interpretation of the overall research outputs.

3.4 PERSPECTIVES

3.4.1 The influence of obliquity on the relationship between atmospheric CO₂ concentration and Antarctic climate

The EDC record of $\delta^{15}\text{N}$, reflecting East Antarctic climate, agrees well with CO₂ variations over the Termination II (Landais et al., 2013). This agreement is also discernible over glacial inceptions. For example, over the transitions from MIS 7e to MIS 7d and from 5e to 5d, the relatively slow declines in CO₂ and $\delta^{15}\text{N}$ both lag behind the abrupt δD decreases respectively observed at ~245 and 130 ka BP (Fig. 3.2).

The atmospheric CO₂ concentration thus seems to lag the Antarctic climate reconstructed using δD over these two glacial inceptions. Ai et al. (2020) argued that the obliquity influence on

upwelling in the glacial polar domain of Southern Ocean could cause this relative inertia observed in CO₂ behind regional climate change.

However, we argue that further study combining the examination of CO₂ and various Antarctic climate proxies (e.g. δD and $\delta^{15}N$) outside the deglaciation context would help identifying precisely the lead-lag relationship between atmospheric CO₂ concentration and Antarctic climate and whether it could be influenced by the orbital context such as the obliquity value (Timmermann et al., 2014; Uemura et al., 2018).

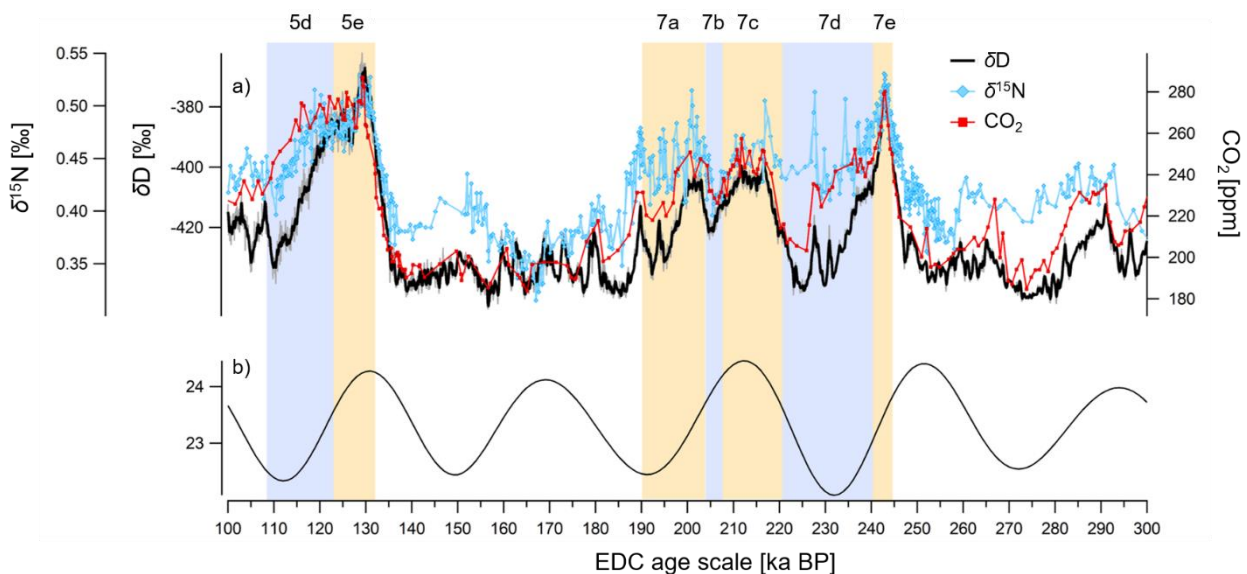


Figure 3.2 Evolution of local climate traced by EDC δD and $\delta^{15}N$ records with respect to the atmospheric CO₂ concentration and obliquity between 300 and 100 ka BP. EDC records of a) δD (black curve; Landais & Stenni, 2021), $\delta^{15}N$ (blue diamonds, this study) and CO₂ (red squares; Bereiter et al., 2015). b) Obliquity parameter (Laskar et al., 2004). Blue/orange rectangles frame cold/warm substages of MISs 7 and 5.

3.4.2 Paleotemperature inferred from the combination of $\delta^{15}N$ and water isotopic data of EDC over the last deglaciation

Jouzel et al. (2003, 2007), Masson-Delmotte et al. (2010) and Landais et al. (2021) use ice core records of water isotopes and suggest that East Antarctica was $\sim 9^\circ C$ cooler during the LGM than today ($\Delta T_{LGM-PD} = 9^\circ C$, see definition in Section 2.1.3.4). The paleotemperature of Dome C reconstructed by Landais et al. (2021) is shown by the black curve in Fig. 3.3. In Section 3.1, we suggest to modify the water isotope-based paleotemperature at Dome C (Landais et al., 2021) by adding a contribution varying in phase with obliquity. This new paleotemperature (blue line in Fig. 3.3) is used to drive the firn densification model, providing a modeled $\delta^{15}N$ scenario that better complies with the $\delta^{15}N$ data of EDC. Over the 18-0 ka BP time period, we suggest to increase the East Antarctic paleotemperature over the obliquity increase (between 18 and 9.5 ka BP) and to decrease it over the obliquity decrease (9.5 to 0 ka BP). Our approach thus does not modify significantly the temperature difference between 20 and 0 ka BP (ΔT_{LGM-PD}) with respect to the study of Landais et al. (2021). Buizert et al. (2021) employed borehole thermometry, Δ age estimates derived from firn modeling (Herron & Langway, 1980) and data, and climate modeling and rather propose a ΔT_{LGM-PD} of $\sim 4^\circ$ to $7^\circ C$ for this region. Their

temperature reconstruction is also shown in Fig. 3.3 for comparison (purple curve).

We now suggest speculative interpretations that would require future investigation. Although caution should be employed when comparing East Antarctic temperature to global temperature because of polar amplification (Casado et al., 2023; Manabe & Stouffer, 1980), it is possible to examine their respective evolution. Marine and terrestrial proxy records have been used for reconstructing the global paleotemperature over the last glacial Termination and the Holocene (Marcott et al., 2013; Shakun et al., 2012a). The global paleotemperature of Marcott et al. (2013) (dark blue curve in Fig. 3.3) shows a period of warmth during the Early Holocene (10-5 ka BP, orange frame in Fig. 3.3) followed by a global cooling into the Late Holocene (5-0 ka BP, blue frame in Fig. 3.3). The global cooling traced by proxies over the last 5 kyr could be consistent with the cooling of East Antarctica that is suggested by our temperature reconstruction while neither the classical water isotope-based temperature nor the approach of Buizert et al. (2021) indicate a similar gradual cooling.

However, this proxy-based global temperature reconstruction disagrees with annual mean temperature yielded by climate modeling (yellow curve in Fig. 3.3; Liu et al., 2014). The climate models better reproduce the proxy-based temperature by simulating the seasonally-weighted temperature (red curve in Fig. 3.3). Liu et al. (2014) argue that this result may indicate a seasonal bias in the proxy-based temperature, that is why they advocate for the reexamination of both proxy data and models to elucidate the reasons of this model-data inconsistency.

We also advocate for further examination of the $\delta^{15}\text{N}$ model-data inconsistency using an approach combining climate modeling, water isotopic data as well as firn modeling and nitrogen isotopic data. Such work would help to refine Antarctic paleotemperature reconstruction.

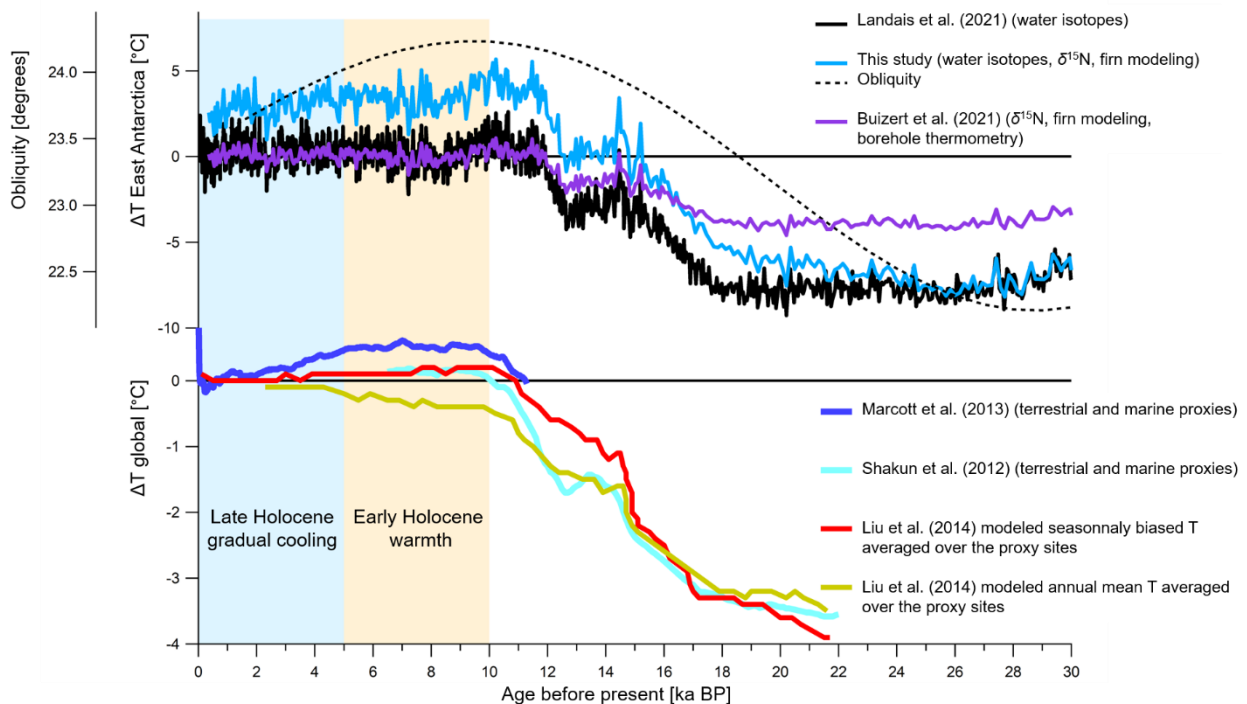


Figure 3.3 East Antarctic and global paleotemperature anomalies with respect to present-day over the last glacial Termination and the Holocene. Top panel: proxy-based East Antarctic temperature anomalies with respect to present-day (Buizert et al., 2021; Landais et al., 2021; this study) and

obliquity parameter (dashed curve; Laskar et al., 2004). Bottom panel: proxy-based global temperature anomalies with respect to present-day (Marcott et al., 2013; Shakun et al., 2012a) as well as modeled temperature anomalies averaged over the proxy sites (Liu et al., 2014). The modeled temperatures are seasonally biased (red curve) or annual mean (yellow curve).

3.4.3 On the need for additional $\delta^{15}\text{N}$ measurements over past glacial periods

New high-resolution measurements of $\delta^{15}\text{N}$ in EDC and upcoming BE-OIC ice cores could help investigating whether the same decoupling is observed between $\delta^{15}\text{N}$ data and modeled $\delta^{15}\text{N}$ during older glacial intervals marked by high-amplitude obliquity changes.

New measurements would be of particular interest over the two most recent glacial periods. Firstly, no EDC data are currently available over the whole last glacial period because of poor ice quality. More specifically, $\delta^{15}\text{N}$ data over the 60-40 ka BP time interval would permit to test our hypothesis over the obliquity maximum at 49 ka BP for which LOVECLIM simulations at high and low obliquity exist. The penultimate glacial period (MIS 6) is also of interest. MIS 6 ice sheet reconstructions are strongly constrained by empirical data and hint that the MIS 6 (along with MISs 12 and 16) glacial period was characterized by the largest ice sheet extent among other glacial periods of the past ~1 million years (Batchelor et al., 2019; Colleoni et al., 2010). Mitsui et al. (2022) argue that the magnitude of MIS 6 is partly attributable to the legacy left by the preceding weak and short interglacial MIS 7e. In the context of low insolation during MIS 6, the residual ice that remained at the end of the relatively cold MIS 7e reduced the albedo and served as a nucleus for ice formation.

Around 430 ka BP, a change in interglacial strength, known as the Mid-Brunhes Event (MBE), was observed in atmospheric CO_2 levels, and in proxy records of Antarctic and global surface temperatures, marking a transition to stronger interglacials (Bouchet et al., 2024; Appendix 7.1). Therefore, the MIS7-6 pair is unusual among post-MBE interglacial-glacial cycles, traditionally characterized by strong interglacials and moderate glacials.

Hence the need for further work on establishing reliable East Antarctic climatic reconstructions during MIS 6 that combine water isotopic records along with $\delta^{15}\text{N}$ measurements. Such reliable climatic reconstructions would help understanding climate processes at play during the MISs 7-6 periods and thus answering one of the questions raised in Chapter 1:

- ✱ Why do some interglacials, such as MIS 11c or MIS 7e, seem to deviate from the astronomical theory of ice ages?

More generally, the understanding of glacial climate in Antarctica is relatively less studied than interglacials and Terminations. However, it is crucial to study various climate states as the internal response of Antarctic climate to the same external forcing can vary depending on the global state of the climate, e.g. from glacial to interglacial conditions.

In addition, precise local climate reconstructions from various sites in the Antarctic and Southern Ocean are of great interest as different rates of climate change are observed within this region. For example, Jomelli et al. (2018) and Rudolph et al. (2024) dated glacial features in different sub-Antarctic islands and evidenced local glacial maxima reached at ~41 and ~56 ka BP and followed by local warming into the Holocene. These dates lead the LGM observed

in the East Antarctic temperature reconstructions by up to 36 kyr. They argue that variability in deglaciation chronologies at the regional scales (specifically in Antarctica and sub-Antarctic islands) are important to consider when disentangling climate drivers across the Southern Ocean. We agree with their suggestion and believe that further $\delta^{15}\text{N}$ measurements could help refine East Antarctic climate reconstruction during glacial periods for a better comprehension of local climatic variability.

Finally, additional $\delta^{15}\text{N}$ measurements would improve the precision of the Δage estimate, essential for building accurate ice core chronologies. In the study that is presented in the following Chapter, we make use of high-resolution $\delta^{15}\text{N}$ data collected by A. Grisart (2023) over five glacial Terminations (TII-TVII) to refine the ice and gas chronologies of the EDC ice core.

4 CHAPTER 4

BUILDING THE ANTARCTIC ICE CORE CHRONOLOGY (AICC) 2023: A PRECISE, COHERENT AND FEDERATIVE TIMESCALE FOR DEEP POLAR ICE CORES OVER THE PAST 800 KYR

“Time is nature's way of keeping everything from happening at once.”

Wheeler (1990) with the note “discovered among the graffiti in the men's room of the Pecan Street Cafe, Austin, Texas”.

Foreword

It is essential to construct a precise timescale of the sequence of climatic events that featured the glacial-interglacial climatic variability over the past 800 kyr. This enables to identify cause-effect relationships between changes in external climate forcing (e.g. changes in the Earth's orbit) and response of climatic variables documented in ice cores (e.g. changes in atmospheric concentration in GHGs and climate in East Antarctica). In this chapter, we first present a paper describing the construction of AICC2023, i.e. the new reference chronology for the EDC ice core over the past 800 kyr. Perspectives to tackle the limitations of this study are proposed in the second section. The implications of the new AICC2023 chronology for climatic interpretation are outlined in the third section.

Objectives

The objectives of this chapter are:

- ✓ To propose a new reference chronology for the EDC ice core which goes back to 800 ka BP with a reduced uncertainty with respect to the former reference age scale.
- ✓ To study the implications of the new chronology on the comprehension of climatic mechanisms over the past 800 kyr

Methods

To achieve the stated objectives, we employed the following strategies:

- Q We have compiled chronological and glaciological information including novel orbital age markers from new data on EDC ice core as well as accurate firn modeling estimates in a Bayesian dating tool
- Q We evaluated the coherency between the new AICC2023 timescale and independent chronologies of other paleoclimatic archives (Italian Lacustrine succession from Sulmona Basin, Dome Fuji ice core and northern Alpine speleothems)
- Q We have summarized our main findings in a study published in *Climate of the Past* in November 2023 (Bouchet, Landais, Grisart, et al., 2023)

Highlights

- A new reference chronology AICC2023 is provided for the past 800 kyr (Fig. 4.1). It is the official timescale for the EPICA ice cores (EDC and EDML).
- The average chronological uncertainty is reduced from 1.7 kyr in the former chronology to 900 years on average in AICC2023. 90 % of the new AICC2023 timescale is associated with an uncertainty lower than 2 kyr, against only 60 % in the former chronology.
- The majorities of the age disparities observed between AICC2023 and former EDC chronology are smaller than 500 years, hence minor considering the average uncertainty of former EDC age scale. Exceptions are significant age shifts reaching 3.4, 3.8 and 5 kyr towards older ages respectively suggested over MIS 15, MIS 17 and MIS 19.
- Most of these age discrepancies lead to an improved coherency between the new EDC timescale and independent absolute chronologies derived for other climate archives especially over the following periods: MIS 5, MIS 11 and MIS 19.

Code and data availability

The input and output files of the AICC2023 Paleochrono run are available on GitHub. They contain age markers used to construct AICC2023 (including both updated and old ones) (<https://github.com/MarieBouchet/Paleochrono/tree/main>).

A folder is available for each site in the PANGAEA data repository. It includes new gas and ice age scales and their uncertainties, new gas data along with background and analyzed scenarios

for accumulation rate, thinning function and LID. A correspondence between AICC2023 and WD2014 age models is also given (<https://doi.pangaea.de/10.1594/PANGAEA.961017>).

The new $\delta^{18}\text{O}_{\text{atm}}$ and $\delta\text{O}_2/\text{N}_2$ datasets for EDC are also available in the PANGAEA data repository (<https://doi.pangaea.de/10.1594/PANGAEA.961023>).

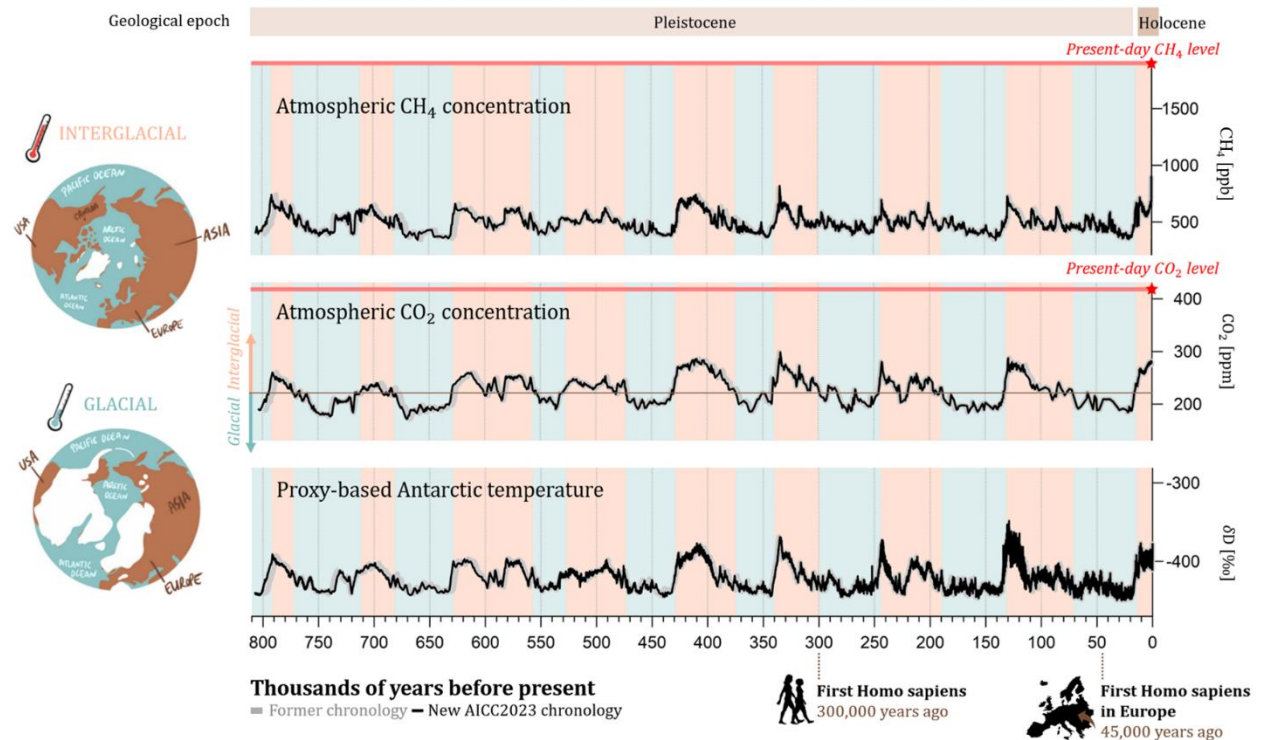


Figure 4.1 EDC records of CH_4 , CO_2 and δD reflecting local surface temperature over the past 800 kyr on the former AICC2012 (gray) and the new AICC2023 (black) age models (Bazin et al., 2013; Bereiter et al., 2015; Bouchet, Landais, Grisart, et al., 2023; Landais et al., 2021; Loulergue et al., 2008; Veres et al., 2013). Red stars indicate the present-day levels for greenhouse gases concentration. Orange/blue frames show interglacial/glacial periods. Interglacials correspond to an atmospheric CO_2 concentration superior to 220 ppm (grey line). The illustration of the glacial and interglacial Earth are from @CireniaSketches.

4.1 PUBLICATION: THE AICC2023 CHRONOLOGICAL FRAMEWORK AND ASSOCIATED TIMESCALE FOR THE EPICA DOME C ICE CORE



The Antarctic Ice Core Chronology 2023 (AICC2023) chronological framework and associated timescale for the European Project for Ice Coring in Antarctica (EPICA) Dome C ice core

Marie Bouchet¹, Amaëlle Landais¹, Antoine Grisart¹, Frédéric Parrenin², Frédéric Prié¹, Roxanne Jacob¹,
Elise Fourné¹, Emilie Capron², Dominique Raynaud², Vladimir Ya Lipenkov³, Marie-France Loutre^{4,5},
Thomas Extier⁶, Anders Svensson⁷, Etienne Legrain², Patricia Martinerie², Markus Leuenberger⁸, Wei Jiang⁹,
Florian Ritterbusch⁹, Zheng-Tian Lu⁹, and Guo-Min Yang⁹

¹Laboratory for Sciences of Climate and Environment, LSCE-IPSL, CEA-CNRS-UVSQ,
University of Paris-Saclay, 91190 Gif-sur-Yvette, France

²Institute of Environmental Geosciences, CNRS, INRAE, IRD, Grenoble INP,
University of Grenoble Alpes, 38000 Grenoble, France

³Arctic and Antarctic Research Institute, 199397 St. Petersburg, Russia

⁴PAGES International Project Office, University of Bern, 3012 Bern, Switzerland

⁵Georges Lemaître Centre for Earth and Climate Research (TECLIM), Earth and Life Institute,
Catholic University of Louvain (UCL), 1348 Louvain-la-Neuve, Belgium

⁶EPOC, UMR 5805, CNRS, University of Bordeaux, 33600 Pessac, France

⁷Physics of Ice, Climate, and Earth, Niels Bohr Institute, University of Copenhagen, 2100 Copenhagen, Denmark

⁸Climate and Environmental Physics, Physics Institute, and Oeschger Centre for Climate Change Research,
University of Bern, 3012 Bern, Switzerland

⁹Department of Engineering and Applied Physics, Hefei National Laboratory,
University of Science and Technology of China, Hefei, 230026, China

Correspondence: Marie Bouchet (marie.bouchet@lsce.ipsl.fr)

Received: 22 May 2023 – Discussion started: 26 May 2023

Revised: 21 September 2023 – Accepted: 25 September 2023 – Published: 10 November 2023

Abstract. The EPICA (European Project for Ice Coring in Antarctica) Dome C (EDC) ice core drilling in East Antarctica reaches a depth of 3260 m. The reference EDC chronology, the AICC2012 (Antarctic Ice Core Chronology 2012), provides an age vs. depth relationship covering the last 800 kyr (thousands of years), with an absolute uncertainty rising up to 8000 years at the bottom of the ice core. The origins of this relatively large uncertainty are twofold: (1) the $\delta^{18}\text{O}_{\text{atm}}$, $\delta\text{O}_2/\text{N}_2$ and total air content (TAC) records are poorly resolved and show large gaps over the last 800 kyr, and (2) large uncertainties are associated with their orbital targets. Here, we present new highly resolved $\delta^{18}\text{O}_{\text{atm}}$, $\delta\text{O}_2/\text{N}_2$ and $\delta^{15}\text{N}$ measurements for the EDC ice core covering the last five glacial–interglacial transitions; a new low-

resolution TAC record over the period 440–800 ka BP (ka: 1000 years before 1950); and novel absolute ^{81}Kr ages. We have compiled chronological and glaciological information including novel orbital age markers from new data on the EDC ice core as well as accurate firn modeling estimates in a Bayesian dating tool to construct the new AICC2023 chronology. For the first time, three orbital tools are used simultaneously. Hence, it is possible to observe that they are consistent with each other and with the other age markers over most of the last 800 kyr (70 %). This, in turn, gives us confidence in the new AICC2023 chronology. The average uncertainty in the ice chronology is reduced from 1700 to 900 years in AICC2023 over the last 800 kyr (1σ). The new timescale diverges from AICC2012 and suggests age shifts

reaching 3800 years towards older ages over marine isotope stages (MISs) 5, 11 and 19. But the coherency between the new AICC2023 timescale and independent chronologies of other archives (Italian Lacustrine succession from Sulmona Basin, Dome Fuji ice core and northern Alpine speleothems) is improved by 1000 to 2000 years over these time intervals.

1 Introduction

1.1 Building age scales for deep polar ice cores

1.1.1 Motivation

Deep polar ice cores are unique archives of past climate, and their investigation is valuable to study mechanisms governing the Earth's climate variations. Precise chronologies are key to identifying the successions and lengths of climatic events, along with exploring phase relationships between the external forcing (changes in the Earth's orbit) and the diverse climatic responses (variations in temperature and atmospheric greenhouse gas concentrations). To date ice cores, we need to construct two separate chronologies: one for the ice and one for the younger air trapped in bubbles. Due to the thinning of horizontal ice layers as depth increases, a wide time span of paleoclimatic information is stored within the deepest part of the ice sheet. Therefore, many of the ice core community's ongoing efforts focus on improving deep-ice-core timescales for ice and gas phases, as well as extending them further back in time (Crotti et al., 2021; Oyabu et al., 2022). Ice cores drilled at sites characterized by a high accumulation rate of snow at the surface (10 to 30 cm a⁻¹) can be dated by counting ice layers deposited year after year (Svensson et al., 2008; Sigl et al., 2016). In contrast, East Antarctica sites are associated with very low accumulation rates (1 to 5 cm a⁻¹), which prevent annual layers from being identified and counted. As a consequence, chronologies of ice cores at low-accumulation sites are commonly established using ice flow and accumulation models (Nye, 1959; Schwander et al., 2001), then tied up with chronological and glaciological constraints (Veres et al., 2013; Bazin et al., 2013; Parrenin et al., 2017).

1.1.2 Glaciological modeling

Glaciological modeling has been historically used to date Greenlandic and Antarctic ice cores. A unidimensional ice flow model was first applied to the Camp Century ice core (Dansgaard and Johnsen, 1969) and later to other ice cores such as the ones drilled at EPICA (European Project for Ice Coring in Antarctica) Dome C (EDC) and Dome Fuji (EPICA Community Members, 2004; Parrenin et al., 2007a). First, water isotope (δD or $\delta^{18}O$) measurements provide estimates of past evolution of the accumulation rate of snow and temperature at the surface. Then, an ice flow model (Par-

renin et al., 2004) takes as inputs past accumulation together with a vertical velocity–depth profile through the ice sheet to determine the thinning of annual snow/ice layers in time and therefore the ice timescale. This approach is very sensitive to some poorly known parameters including boundary conditions such as bedrock topography, geothermal properties or subglacial sliding. For this reason, the glaciological modeling approach is complemented with chronological constraints (gas or ice age known at certain depth levels).

1.1.3 Chronological constraints derived from measurements

Chronological constraints obtained either by measurement of radionuclides or by synchronization to a curve of reference are established for both ice and gas timescales. For building long chronologies, some time constraints can be obtained from the ¹⁰Be series measured in ice. The ¹⁰Be cosmogenic nuclide is produced at different rates depending on the solar activity, and its arrival on Earth is modulated by the strength of the Earth's magnetic field (Yiou et al., 1997; Raisbeck et al., 2007; Heaton et al., 2021). Some links hence exist between ¹⁰Be flux and precisely dated magnetic events such as the Laschamp excursion, an abrupt decline in the geomagnetic field magnitude occurring at about 41 ka BP and visible as a positive excursion in the ¹⁰Be flux records in ice cores (Lascu et al., 2016; Raisbeck et al., 2017). ⁴⁰Ar measurements in the gas phase of Antarctic ice cores also provide dating constraints for old ice, especially for non-continuous stratigraphic sequences (Yan et al., 2019). ⁴⁰Ar is produced in solid earth by the radioactive decay of ⁴⁰K, leading to an increasing concentration of ⁴⁰Ar in the atmosphere at a rate of 0.066 ± 0.006 ‰ Myr⁻¹ (Bender et al., 2008). Recently, the possibility of measuring ⁸¹Kr in ice samples of a few kilograms gave a new absolute dating tool for ice cores (Jiang et al., 2020). ⁸¹Kr is a radioactive isotope that is suitable for dating ice cores in the range from 0.03 to 1.3 Ma BP (Ma: million years before 1950), making it perfectly adapted for Antarctic ice core dating (Buizert et al., 2014; Crotti et al., 2021).

To further constrain the oldest ice core chronologies, the so-called “orbital dating” tools are also used. These tools consist of aligning some tracers measured in ice cores to the Earth orbital series, called targets, whose fluctuations in time are accurately calculated from the known variations in orbital parameters (Berger, 1978; Laskar et al., 2011). The synchronization of the orbital tracer with its target provides ice or gas age constraints. So far, three orbital dating tools have been developed: $\delta^{18}O$ of O₂ ($\delta^{18}O_{atm}$), $\delta O_2/N_2$ and total air content (TAC). The $\delta^{18}O_{atm}$ was typically aligned with the precession parameter (or with the 21 June insolation at 65° N) delayed by 5000 years because such a lag between $\delta^{18}O_{atm}$ and its orbital target was observed during the last deglaciation (Shackleton, 2000; Dreyfus et al., 2007). However, variations in the phasing between $\delta^{18}O_{atm}$ and preces-

sion have been suspected (Jouzel et al., 2002) and identified since (Bazin et al., 2016). In particular, millennial-scale events (as Heinrich-like events) occurring during deglaciations have been shown to delay the response of $\delta^{18}\text{O}_{\text{atm}}$ to orbital forcing (Extier et al., 2018a). Because there was a significant unpredictability in the lag between $\delta^{18}\text{O}_{\text{atm}}$ and its orbital target, a large uncertainty in the $\delta^{18}\text{O}_{\text{atm}}$ -based tie points (up to 6000 years) was assigned in the construction of the AICC2012 (Antarctic Ice Core Chronology 2012; Bazin et al., 2013). To improve the accuracy of the gas timescale, Extier et al. (2018a) rather aligned the variations in $\delta^{18}\text{O}_{\text{atm}}$ to the $\delta^{18}\text{O}_{\text{calcite}}$ recorded in absolute-dated East Asian speleothems between 640 and 100 ka BP. Indeed, the two records show similar orbital (related to the 21 July insolation at 65° N) and millennial variabilities, which may correspond to southward shifts in the Intertropical Convergence Zone (ITCZ) position, themselves linked to Heinrich-like events as supported by the modeling study of Reutenauer et al. (2015).

In parallel, Bender (2002) observed that the elemental ratio $\delta\text{O}_2/\text{N}_2$ of air trapped in the Vostok ice core appears to vary in phase with the 21 December insolation at 78° S (Vostok latitude) between 400 and 160 ka BP. Subsequent observations led Bender (2002) to assert that local summer solstice insolation affects near-surface snow metamorphism and that this imprint is preserved as snow densifies in the firn and, later on, affects the ratio $\delta\text{O}_2/\text{N}_2$ measured in air bubbles formed at the lock-in zone. Wiggle matching between $\delta\text{O}_2/\text{N}_2$ and local summer solstice insolation has been used to construct orbital timescales for the Dome Fuji, Vostok and EDC ice cores reaching back 360, 400 and 800 ka BP, respectively, with a chronological uncertainty for each $\delta\text{O}_2/\text{N}_2$ tie point estimated between 250 and 4000 years (Kawamura et al., 2007; Suwa and Bender, 2008; Bazin et al., 2013; Oyabu et al., 2022). Finally, Raynaud et al. (2007) found very similar spectral properties between the TAC record of EDC and the integrated summer insolation (ISI) at 75° S obtained by a summation over a year of all daily local insolation above a certain threshold over the last 440 kyr. As for $\delta\text{O}_2/\text{N}_2$, these similarities may be explained by the insolation imprint in near-surface snow well preserved down to the lock-in zone, where it could affect the air content in deep ice, although the physical mechanisms involved during the snow and firn densification for $\delta\text{O}_2/\text{N}_2$ and TAC are likely different (Lipenkov et al., 2011). Lately, Bazin et al. (2013) made use of TAC to constrain Vostok and EDC ice core chronologies back to 430 ka BP with an uncertainty for each TAC tie point varying between 3000 and 7000 years. Although these three orbital tools complement each other (TAC and $\delta\text{O}_2/\text{N}_2$ inferred ages agree within less than 1000 years between 390 and 160 ka BP for the Vostok ice core; Lipenkov et al., 2011), they hardly ever have been employed together. Plus, they are often associated with large uncertainties (reaching 7000 years), which lie in the choice of the appropriate orbital target, in its alignment with ice core records that can be ambiguous during pe-

riods of low eccentricity in the Earth's orbit (leading to low-amplitude insolation variations) and in the poor quality of the signals measured in the deepest section of the cores.

To connect ice and gas timescales, the estimation of the lock-in depth (LID), indicating the lowest depth where the air is trapped in enclosed bubbles, and diffusivity becomes effectively zero (Buizert et al., 2013), is used to calculate the ice–gas age difference. Measurements of $\delta^{15}\text{N}$ from N_2 yield a first estimate of this depth, and the LID can also be calculated with firn densification modeling (Goujon et al., 2003; Bréant et al., 2017).

For many years, each polar ice core was characterized by its singular timescale, which was not naturally consistent with other ice core timescales. To address this issue, other measurements provide relative dating constraints (stratigraphic links), improving the coherency between timescales of ice cores from both hemispheres. The synchronization of globally well-mixed atmospheric methane ice core records gives tie points with an accuracy of a few decades to several centuries (60–1500 years) (Lemieux-Dudon et al., 2010; Epifanio et al., 2020). Climate-independent events, such as large volcanic eruptions, can be observed in ice cores from Greenland and Antarctica via singular patterns of the distribution of sulfate. Identification of these deposits permits the precise synchronization of several ice cores (within 5 to 150 years) (Svensson et al., 2020).

1.1.4 Bayesian dating tools

In order to integrate stratigraphic matching, independent synchronization and absolute dating constraints as well as glaciological modeling to produce coherent ice core chronologies, researchers developed Bayesian dating tools such as Datiche (Lemieux-Dudon et al., 2010), IceChrono1 (Parrenin et al., 2015) and Paleochrono (Parrenin et al., 2021). These tools use an inverse method combining all chronological information to provide a coherent age scale for several ice cores. These probabilistic tools adjust prior estimates of ice and gas chronologies built with a glaciological model (background scenario) so that they respect chronological constraints.

Here we focus on the chronology of the EDC deep ice core. The EPICA project provided two cores in East Antarctica, including one at Dome C (EDC). The second (and final) drilling attempt at Dome C gave the 3260 m long EDC99 core, whose drilling was willingly stopped at 15 m above bedrock due to the expected presence of meltwater. EDC furnishes the oldest continuous ice core record so far, covering the last 800 kyr (EPICA Community Members, 2004; Jouzel et al., 2007).

1.2 The AICC2012 chronology

Bazin et al. (2013) and Veres et al. (2013) used the probabilistic dating tool Datiche to establish the coherent

AICC2012 chronology back to 800 ka BP for five ice cores, including EDC, Vostok, EPICA Dronning Maud Land ice core (EDML), North GRenland Ice core Project (NGRIP) and Talos Dome Ice core (TALDICE). To determine the EDC age scale, they used various orbital dating constraints including 39 tie points attached to a 6000-year uncertainty derived from $\delta^{18}\text{O}_{\text{atm}}$ tuning to a 5000-year delayed precession between 800 and 300 ka BP, 20 tie points associated with a 4000-year uncertainty from $\delta\text{O}_2/\text{N}_2$ alignment to local summer solstice insolation between 800 and 300 ka BP, and 14 tie points linked to an uncertainty between 3000 and 7000 years using TAC synchronized to integrated summer insolation between 430 and 0 ka BP. However, due to the lack of data for the orbital dating approach, the AICC2012 1σ uncertainty is of 1700 years on average, reaching 8000 years at the bottom of the core. The origins of AICC2012 uncertainty can be divided in the following points: (i) some inherent dissimilarities between $\delta^{18}\text{O}_{\text{atm}}$, $\delta\text{O}_2/\text{N}_2$ and TAC series and their curve-shaped orbital target; (ii) discontinuity and poor quality of the $\delta\text{O}_2/\text{N}_2$ and TAC records; (iii) uncertainty in the phasing between $\delta^{18}\text{O}_{\text{atm}}$ and precession; (iv) poor constraint on the LID scenario due to a disagreement between $\delta^{15}\text{N}$ data and firn modeling estimates (Bréant et al., 2017).

1.3 The new AICC2023 chronology

It is now possible to address each source of uncertainty thanks to recent advances. (i) Since AICC2012, the $\delta^{18}\text{O}_{\text{atm}}$ and TAC records have been extended, now covering the last 800 kyr (Extier et al., 2018b). In addition, new highly resolved $\delta^{18}\text{O}_{\text{atm}}$ and $\delta\text{O}_2/\text{N}_2$ measurements are available over several glacial terminations (TII, III, IV, V and VI) (Grisart, 2023). (ii) Extier et al. (2018a) recently suggested a $\delta^{18}\text{O}_{\text{atm}}$ -based timescale using $\delta^{18}\text{O}_{\text{calcite}}$ of East Asian speleothems as an alternative tuning target to precession. This choice reduces the chronological uncertainty between 640 and 100 ka BP. (iii) Finally, new highly resolved $\delta^{15}\text{N}$ data covering the terminations II to VI are available (Grisart, 2023). In parallel, firn densification models have been progressively improved, and the model described in Bréant et al. (2017) can be employed to estimate LID evolution in the past when $\delta^{15}\text{N}$ data are still missing.

In this work, we implement new absolute age constraints spanning the last 800 kyr derived from ^{81}Kr measured in air trapped in the EDC ice core as well as new orbital age constraints obtained by synchronizing up-to-date EDC records with their orbital target. We combine these data with recent volcanic matching and methane record synchronization, which provide additional stratigraphic links, relating EDC to other ice cores over the past 122 kyr (Baumgartner et al., 2014; Svensson et al., 2020). Finally, we propose the new chronology AICC2023 with reduced chronological uncertainties. AICC2023 is recommended as the new official age scale for the EPICA ice cores by the EPICA Scientific Steering Committee (Wolff, 2023).

2 Methods

2.1 Dating strategy

The Paleochrono Python software is a probabilistic dating tool similar to Datice and IceChrono1 with improved mathematical, numerical and programming capacities (Parrenin et al., 2021). The dating strategy of Paleochrono relies on the Bayesian inference of three glaciological functions forming the input background scenario: accumulation rate (A), thinning of annual ice layers (τ) and lock-in depth (LID). The three variables evolve along the ice core depth z and are used to estimate the ice (ψ) and gas (χ) age profiles as follows:

$$\psi(z) = \int_0^z \frac{D(z')}{\tau(z')A(z')} dz' \quad (1)$$

$$\chi(z) = \psi(z - \Delta\text{depth}(z)) \quad (2)$$

$$\int_{z-\Delta\text{depth}(z)}^z \frac{D(z')}{\tau(z')} dz' = \text{LID}(z) \times \left. \frac{D}{\tau} \right|_{\text{firn}}^0, \quad (3)$$

where D is the relative density of the snow/ice and $\left. \frac{D}{\tau} \right|_{\text{firn}}^0$ the average value of $\frac{D}{\tau}$ in the firn when the air particle was at the lock-in depth (this parameter is usually ~ 0.7 ; Parrenin et al., 2012). The age scales are further constrained to respect chronological constraints identified from observations. To specify the credibility of the background scenario for the age scales and the chronological constraints, the glaciological functions (accumulation, thinning and LID) and the chronological information can be mathematically expressed as probability densities, which are presumed to be Gaussian and independent (i.e., decorrelated between them). Thus, the inference is based on the least square optimization method (implying all probability densities are Gaussian). It is numerically solved using the trust region algorithm (assuming that the model is roughly linear around the solution), and the Jacobian of the model is evaluated analytically for an improved computation time. As a result, the best adjustment between the background scenario and chronological observations is found, providing the most probable scenario as a posterior evaluation of the three glaciological functions and hence chronologies for ice and air. For each ice core, the input files for Paleochrono are the following: (i) the background values of the three glaciological functions with depth; (ii) gas and ice stratigraphic links; (iii) gas- and ice-dated horizons, which are tie points derived for one core from absolute and synchronization dating methods; (iv) gas and ice intervals of known durations; and (v) depth difference estimates between the same event recorded in the gas and ice matrix (Δdepth). Specific relative or absolute uncertainties are attached to each of these parameters in each input file.

In this study, we added numerous gas- and ice-dated horizons for EDC as well as an updated background scenario for the LID. Then, to construct a new chronology for the EDC

ice core that is consistent with the timescales of the Vostok, TALDICE, EDML and NGRIP ice cores, we followed the same strategy as for the construction of AICC2012. Glaciological background parameters and dating constraints for the Vostok, TALDICE, EDML, NGRIP and EDC drillings are compiled in one run of Paleochrono to obtain AICC2023. The Vostok, TALDICE, EDML and NGRIP background parameters and dating constraints are extracted from Bazin et al. (2013), except for (i) new Vostok gas age constraints determined from the alignment of $\delta^{18}\text{O}_{\text{atm}}$ and East Asian $\delta^{18}\text{O}_{\text{calcite}}$ records as for EDC (see Fig. S10), (ii) new TALDICE background parameters and age constraints from Crotti et al. (2021), and (iii) corrected LID background scenarios for the Vostok and EDML sites (see Fig. S11). In order to prevent any confusion with reference ice core timescales, the new AICC2023 chronology for NGRIP is compelled to respect exactly the layer-counted GICC05 timescale through absolute tie points placed at 1 m intervals over the last 60 kyr (Andersen et al., 2006). For this reason, we did not use the methodology described by Lemieux-Dudon et al. (2015), who implemented layer counting as a constraint on the duration of events in the dating tool, inducing a slight shift (maximum 410 years) in the AICC2012 timescale. The resulting Paleochrono experiment provides the new official chronology AICC2023 for the EDC ice core. The contingent timescales obtained for the four other sites are not the subject of this study but are also provided (see “Data availability” section). We acknowledge the exclusion of the WAIS (West Antarctic Ice Sheet) Divide ice core (WDC) from the construction of the AICC2023 age scale as for the AICC2012 age scale. Over the last 60 kyr, though, we recommend the use of timescales tied to the WAIS Divide 2014 age model (WD2014; Buizert et al., 2015; Sigl et al., 2016). A correspondence between AICC2012, AICC2023 and WD2014 age models based on the volcanic synchronization of WDC and EDC using sulfate data (Buizert et al., 2018) is provided over the 0–58 ka BP period (that is to say for the section above the depth of 915 m for the EDC ice core; see “Data availability” section).

2.2 Analytical method

2.2.1 $\delta^{18}\text{O}_{\text{atm}}$, $\delta\text{O}_2/\text{N}_2$ and $\delta^{15}\text{N}$

The measurements of the isotopic and elemental compositions of O_2 and N_2 were performed by Grisart (2023) at the Laboratory for Sciences of Climate and Environment (LSCE) following the method described by Bréant et al. (2019) and Extier et al. (2018a). The air trapped in the EDC ice core is extracted using the semi-automatic line, which eliminates CO_2 and H_2O . Samples of 30 to 40 g are prepared in a cold environment (-20°C), their exterior layer (3–5 mm) is removed so that there is no exchange with atmospheric air, and each sample is cut in two replicates. Each day, three ice samples (and replicates) are placed in six flasks, and the at-

mospheric air is evacuated from the flasks. Samples are then melted and left at ambient temperature for approximately 1 h 30 min in order to extract the air trapped in ice samples. The extracted air is then cryogenically trapped within a dedicated manifold immersed in liquid helium (Bazin et al., 2016). Along the way to the cryogenic trap, the air goes through cold traps to remove CO_2 and H_2O . Two additional samples containing exterior modern air are processed through the same line every day for calibration and for monitoring the analytical set-up. Lastly, the $\delta^{15}\text{N}$, $\delta^{18}\text{O}$ of O_2 and $\delta\text{O}_2/\text{N}_2$ of each sample are measured by a dual-inlet Delta V plus (Thermo Electron Corporation) mass spectrometer.

Classical corrections are applied on the measurements (pressure imbalance, chemical slopes, as per Landais et al., 2003). In addition, $\delta^{15}\text{N}$ data are used to get the values of atmospheric $\delta^{18}\text{O}$ of O_2 and $\delta\text{O}_2/\text{N}_2$ after gravitational fractionation occurred in the firm so that $\delta^{18}\text{O}_{\text{atm}} = \delta^{18}\text{O}$ of $\text{O}_2 - 2 \times \delta^{15}\text{N}$ and $\delta\text{O}_2/\text{N}_2(\text{corr}) = \delta\text{O}_2/\text{N}_2(\text{raw}) - 4 \times \delta^{15}\text{N}$ (Landais et al., 2003; Bazin et al., 2016; Extier et al., 2018a). Note that our samples were stored at -50°C after drilling to minimize the gas loss effect. As a consequence, no correction for gas loss was applied (see Sect. S1 in the Supplement), and if gas loss may explain a slight scattering in the data, the peak positions are not affected.

Existing and new EDC data are compiled in Table 1. The dataset’s resulting pooled standard deviations for the new measurements are of 0.006 ‰, 0.03 ‰ and 0.4 ‰ for $\delta^{15}\text{N}$, $\delta^{18}\text{O}_{\text{atm}}$ and $\delta\text{O}_2/\text{N}_2$, respectively.

2.2.2 Total air content

The TAC record was measured in the entire EDC ice core at the IGE (Institute of Environmental Geosciences) following the barometric method first described by Lipenkov et al. (1995). The TAC record measured in the younger part of the core (400–0 ka BP) has been published in Raynaud et al. (2007) (Table 2). TAC estimates need to be corrected for the cut-bubble effect. After correction, the uncertainty in TAC values is of about 1 %, and the analysis replicability is better than 1 %.

2.2.3 ^{81}Kr extraction and analysis

The analytical method is the same as described by Crotti et al. (2021). Three 6 kg ice samples are taken from the bottom part of EDC, and a slight shaving (1 mm) of the external layer is performed before processing. The air extraction is performed through a manual extraction line following the protocol described in Tian et al. (2019). The ice sample is placed in a 40 L stainless-steel chamber. The atmospheric air is pumped while the chamber is kept at -20°C . The air is then slowly extracted, passing through a water trap, and compressed in a stainless-steel cylinder. The three cylinders are sent to the University of Science and Technology of China (USTC, Hefei, China) for krypton extraction and analysis.

Table 1. Information on isotopic and elemental compositions measured in air trapped in the EDC ice core. * Details on storage and measurement conditions of $\delta\text{O}_2/\text{N}_2$ are available in Sect. S1 in the Supplement.

	$\delta^{18}\text{O}_{\text{atm}}$			$\delta\text{O}_2/\text{N}_2^*$			$\delta^{15}\text{N}$		
	Depth (m)	AICC2012 gas age (ka BP)	Resolution (kyr)	Depth (m)	AICC2012 ice age (ka BP)	Resolution (kyr)	Depth (m)	AICC2012 gas age (ka BP)	Resolution (kyr)
AICC2012	2479–3260	300–800	1–1.5	2480–3260	300–800	2.5	346–578	11–27	0.35–0.38
Dreyfus et al. (2007, 2008, 2010), Landais et al. (2012), Bazin et al. (2013)							1090–1169	75–83	1.4
							1389–3260	100–800	2.4
Bazin et al. (2016)	1300–1903 2657–3260	90–160 370–800	1.1	1300–1903 2595–3260	93–163 340–800	2.37 2.08			
Extier et al. (2018b, c)	1872–2665	153–374	0.16–0.7	1904–2562	164–332	2–2.5			
Bréant et al. (2019)							1904–2580	160.2–334.5	1.013
This work (Giriat, 2023)	1489.95–1832.6 1995.95–2350.15 2555.85–2633.4 2744.5–2797.85 2873.75–2910.6	108.0–136.3 180.6–255.8 328.3–346.8 408.7–445.9 508.1–535.6	0.333 0.437 0.356 0.744 1.375	1489.95–1832.6 1995.95–2350.15 2555.85–2633.4 2744.5–2797.85 2873.75–2910.6	111.4–148.9 183.9–259.6 330.5–360.6 410.7–449.6 511.3–539.3	0.441 0.437 0.579 0.779 1.401	1489.95–1832.6 1995.95–2350.15 2555.85–2633.4 2744.5–2797.85 2873.75–2910.6	108.0–136.3 180.6–255.8 328.3–346.8 408.7–445.9 508.1–535.6	0.333 0.437 0.356 0.744 1.375

Table 2. Information on TAC measurements in the EDC ice core.

	TAC		
	Depth (m)	AICC2012 ice age (ka BP)	Resolution (kyr)
AICC2012 (Raynaud et al., 2007)	115–2800	0–440	2.000
Unpublished	2800–3260	440–800	2.000

Krypton extraction is performed after the methodology of Dong et al. (2019), who set up an automated system for dual separation of argon and krypton, composed of a titanium getter module followed by a gas-chromatography separator module. The extracted krypton is analyzed by the Atom Trap Trace Analysis (ATTA) instrument set up at the Laser Laboratory for Trace Analysis and Precision Measurement (LL-TAPM, USTC, Hefei, China), giving the ^{81}Kr abundance R_{81} in the sample. R_{81} is determined by the number of counted ^{81}Kr atoms in the sample as compared to the atmospheric reference. The anthropogenic ^{85}Kr is measured simultaneously with ^{81}Kr to control any present-day air contamination. Here, the ^{85}Kr abundance measured in ice samples is inferior to the detection limit, so contamination has occurred.

From the ^{81}Kr abundance, it is possible to estimate ^{81}Kr radioactive decay and to calculate the ice sample's age. As a noble gas isotope, ^{81}Kr is globally mixed in the atmosphere, and its decay cannot be affected by complex chemical reactions (Lu et al., 2014). The ^{81}Kr half-life ($t_{1/2}$) is estimated to be $\approx 229 \pm 11$ kyr (Baglin, 2008). ^{81}Kr age can be calculated as per the following equation:

$$\text{age} = -\frac{t_{1/2}}{\ln(2)} \times \ln(R_{81}). \quad (4)$$

The atmospheric abundance of ^{81}Kr is not constant in the past, and its value is corrected using reconstruction of the geomagnetic field intensity (Zappala et al., 2020). The error in ^{81}Kr age estimates is estimated from the statistical error in atom counting, from the uncertainty in ^{81}Kr half-life (inducing a systematic age error) and from the size of the sample (larger sample resulting in a smaller uncertainty).

2.3 Firm model

Firm densification models have been progressively improved over the years (Herron and Langway, 1980; Alley, 1987; Arthern et al., 2010; Ligtenberg et al., 2011; Kuipers Munneke et al., 2015; Oraschewski and Grinsted, 2022). While these models generally explain the evolution of $\delta^{15}\text{N}$ in time well through changes in the LID, they fail to reproduce values of $\delta^{15}\text{N}$ in some regions, including coastal areas and cold and low-accumulation sites such as EDC (Capron et al., 2013). This disagreement can be explained

by an inaccurate estimate of glacial temperature and accumulation rate at the surface (Buizert, 2021) and/or by the impossibility of tuning empirical firm models to sites with no present-day equivalent in terms of temperature and accumulation rate (Dreyfus et al., 2010; Capron et al., 2013). Recently, the firm model described in Bréant et al. (2017) was developed from the IGE model (Pimienta and Duval, 1987; Barnola et al., 1991; Arnaud et al., 2000; Goujon et al., 2003) by implementing a dependency of the firm densification rate on temperature and impurities. The temperature dependence is added to the classical formulation of the densification rate following an Arrhenius law with an activation energy Q as per $\exp(-Q/RT)$, with R the perfect gas constant and T the firm temperature. Rather than using a constant activation energy (Goujon et al., 2003), Bréant et al. (2017) stated that the value of the activation energy should be contingent on the firm temperature value as observed in material science, where the temperature dependency exhibits the predominance of one physical mechanism among others for a material compaction at a specific temperature. Through several sensitivity tests, Bréant et al. (2017) adjusted three values for activation energy in three different temperature ranges to reproduce best the $\delta^{15}\text{N}$ evolution over the last deglaciation at East Antarctic sites. The firm model also considers that firm densification is facilitated by the dissolution of impurities within the snow (Freitag et al., 2013). If the impurity content in snow (i.e., concentration of calcium ions) is greater than a certain threshold, the densification rate dependence on impurities is traduced by a relationship between the new activation energy Q' and the concentration of calcium ions $[\text{Ca}^{2+}]$: $Q' = f_1 \times \left(1 - \beta \ln\left(\frac{[\text{Ca}^{2+}]}{[\text{Ca}^{2+}]_{\text{threshold}}}\right)\right) \times Q$ (Freitag et al., 2013). Bréant et al. (2017) assumed the impurity effect equal for all physical mechanisms and tuned β and f_1 constants so that the modeled- $\delta^{15}\text{N}$ data mismatch is minimized over the last glacial termination at cold East Antarctic sites.

As a consequence, and in addition to our new extensive $\delta^{15}\text{N}$ dataset, we have chosen to use here the firm model approach of Bréant et al. (2017). In order to make a correct calculation of uncertainties linked to firm modeling at EDC, we ran two tests of the model with and without including the impurity concentration parameter (see Sect. S3.1).

The firm densification model takes as input scenarios of temperature and accumulation rate at the surface. It computes both the LID and the thermal gradient in the firm (ΔT) and then deduces the $\delta^{15}\text{N}_{\text{therm}} = \Omega \cdot \Delta T$ with Ω the thermal-fractionation coefficient (Grachev and Severinghaus, 2003). The final $\delta^{15}\text{N}$ is calculated as $\delta^{15}\text{N} = \delta^{15}\text{N}_{\text{therm}} + \delta^{15}\text{N}_{\text{grav}}$ and $\delta^{15}\text{N}_{\text{grav}} \approx \text{LID} \cdot \frac{g}{RT}$ (first-order approximation), with g the gravitational acceleration (9.8 m s^{-2}), R the gas constant ($8.314 \text{ J mol}^{-1} \text{ K}^{-1}$) and T the mean firm temperature (K).

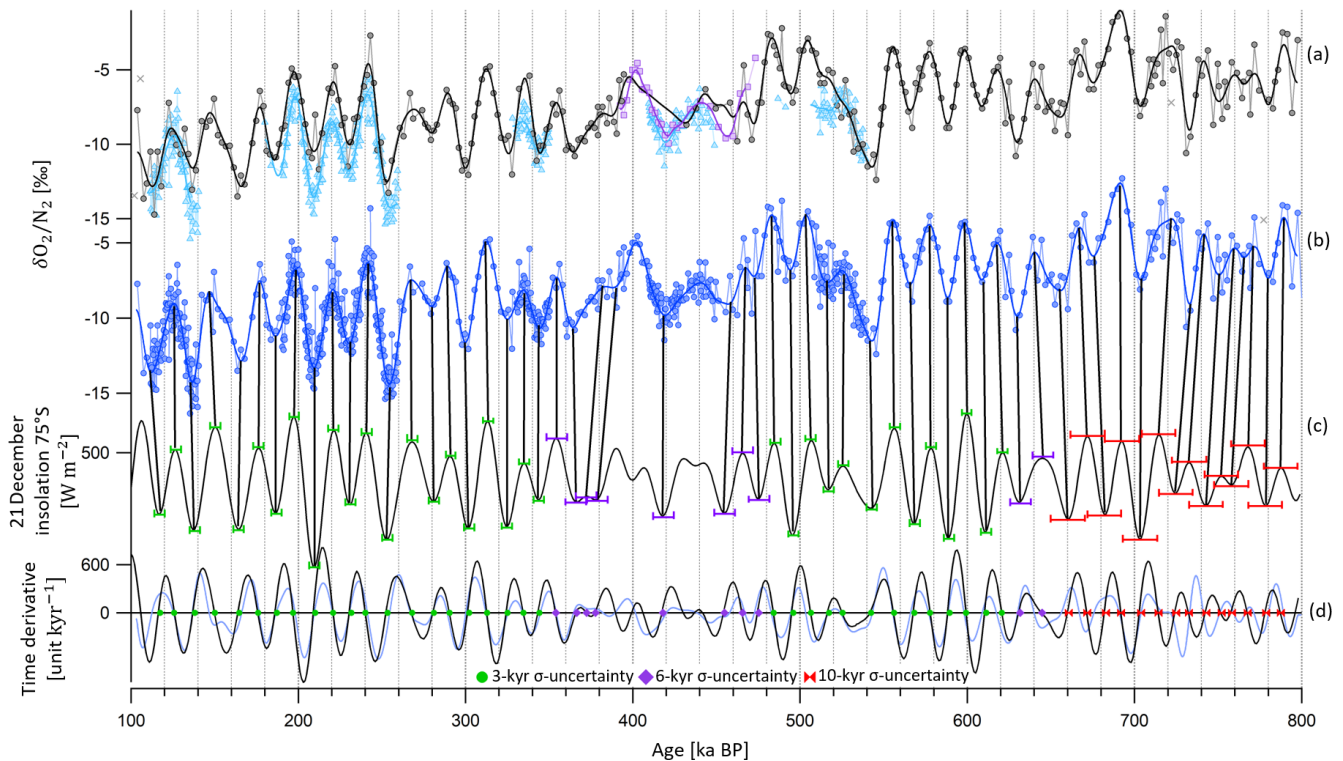


Figure 1. Alignment of $\delta\text{O}_2/\text{N}_2$ and insolation between 800 and 100 ka BP. **(a)** Old raw EDC $\delta\text{O}_2/\text{N}_2$ data between 800 and 100 ka BP (black circles for data of Extier et al., 2018c, and purple squares for data of Landais et al., 2012), outliers (gray crosses) and filtered signal (black and purple lines). New raw EDC $\delta\text{O}_2/\text{N}_2$ data (blue triangles, this study) and filtered signals (blue line). The $\delta\text{O}_2/\text{N}_2$ data are plotted on the AICC2012 ice timescale. Zooms between 270 and 100 ka BP and between 570 and 300 ka BP are shown in Fig. S2. **(b)** Extrema in the compiled filtered $\delta\text{O}_2/\text{N}_2$ dataset (plain blue line) are identified and matched to extrema in the **(c)** 21 December insolation at 75°S plotted on a reversed y axis and on the age scale given by Laskar et al. (2004) (black line). The peaks are matched by vertical black bars. **(d)** The zero value in the time derivative of insolation (black line) and of the filtered $\delta\text{O}_2/\text{N}_2$ dataset (blue line) corresponds to extreme values in the signals. The determined tie points between $\delta\text{O}_2/\text{N}_2$ and insolation are depicted by markers on the horizontal line. Green circles are attached to a 3 kyr 1σ uncertainty (horizontal green error bars show 2σ in panel c), purple squares are associated with a 6 kyr 1σ uncertainty (horizontal purple error bars show 2σ in panel c), and red markers are associated with a 10 kyr 1σ uncertainty (horizontal red error bars show 2σ in panel c). Between 390 and 475 ka BP, all extrema are not tuned to the target due to the poor resemblance between the signal and insolation.

3 Age constraints and background scenarios

3.1 ^{81}Kr age constraints

Three ice samples from the bottom part of EDC have been analyzed and provide three age estimates displayed in Table 3: 629, 788 and 887 ka BP, with statistical age uncertainties between 30 and 50 kyr and a 4.8 % systematic error due to the uncertainty in the half-life of ^{81}Kr . The deepest sample suggests the presence of ice older than 800 ka BP below the 3200 m depth level, and further studies would be valuable in exploring whether the stratigraphy of the lowermost EDC section is continuous (Tison et al., 2015), although this is beyond the scope of this work.

3.2 Determination of orbital age constraints using new data

3.2.1 $\delta\text{O}_2/\text{N}_2$

In this work, new highly resolved $\delta\text{O}_2/\text{N}_2$ data on the EDC ice core are presented over terminations II, III, IV, V and VI (Fig. 1). As these novel $\delta\text{O}_2/\text{N}_2$ measurements have been performed on ice samples stored at -50°C , there is little storage effect, and they can directly be merged with the 800 kyr long record of Extier et al. (2018c) (Table 1). The new dataset improves the resolution of the long EDC record, reaching sub-millennial-scale accuracy over marine isotope stages (MISs) 5, 7 and 9 and in particular over MIS 11 and MIS 13, periods of sparsity in the ancient record (Extier et al., 2018c). Although the two datasets agree well over recent periods (last 350 kyr), they show some discrepancies during older periods (between 550 and 375 ka BP; see

Table 3. Ice sample details and radio krypton dating results. Reported errors are 1σ errors. Upper limits have a 90 % confidence level. The average ^{85}Kr activity in the Northern Hemisphere is about 75 dpm cm^{-3} (decays per minute per cubic centimeter) in 2017. The measured ^{85}Kr concentrations are inferior to the detection limit, verifying that no relevant contamination with modern air has occurred. In addition to the statistical error in the ^{81}Kr age from atom counting, a systematic error due to the uncertainty in the half-life of ^{81}Kr is considered. This error would shift the calculated ^{81}Kr ages up or down for all ice samples. ^a dpm cm^{-3} : decays per minute per cubic centimeter standard temperature and pressure (STP) of krypton (conversion: 100 dpm cm^{-3} corresponds to $^{85}\text{Kr}/\text{Kr} = 3.03 \times 10^{11}$). ^b pMKr: percent modern krypton.

Depth (m)	Air extracted/ ice weight (mL kg^{-1})	Sample Used ($\mu\text{L STP}$, Kr)	Analysis date	^{85}Kr (dpm cm^{-3}) ^a	^{81}Kr (pMKr) ^b	^{81}Kr – age (ka BP) $\text{age}_{-stat-sys}^{+stat+sys}$
3013–3024	440/6.0	~ 0.46	18 Dec 2019	< 0.77	$15.1^{+1.4}_{-1.4}$	629^{+34+31}_{-29-31}
3144–3161	600/8.4	~ 0.67	30 Dec 2019	< 0.67	$9.6^{+1.0}_{-1.0}$	788^{+36+38}_{-33-38}
3216–3225	415/6.4	~ 0.43	16 Jan 2020	< 1.17	$7.1^{+1.0}_{-1.0}$	887^{+51+43}_{-44-43}

Fig. 1). Such dissimilarities are observed over MIS 11 (between 424 and 374 ka BP), where the sampling resolution of the previous dataset is particularly low (2500 years). In addition, MIS 11 is a period characterized by a low eccentricity in the Earth orbit, inducing subdued variations in insolation, causing $\delta\text{O}_2/\text{N}_2$ changes of smaller magnitude and leading to a lower signal-to-noise ratio. Data by Landais et al. (2012) (shown by purple squares in Figs. 1 and S2) are consistent with the highly resolved data presented here, supporting the relevance of the new dataset over this period. Over termination VI (from 550 to 510 ka BP), the old dataset continuously increases, while the novel dataset shows a brief maximum at around 525 ka BP followed by a minimum at around 520 ka BP. These newly revealed variations seem in phase with insolation variations, suggesting that the new dataset shows improved agreement with insolation. Still, highly resolved measurements are needed in the lowermost part of the ice core, where noise is significantly altering the temporal signal.

Following a data processing treatment consistent with the method described in Kawamura et al. (2007), the compiled dataset is linearly interpolated every 100 years and then smoothed using a finite-duration impulse response (FIR) filter with a KaiserBessel20 window (cut-off from 16.7 to 10.0 kyr period, 559 coefficients for the 800 kyr long record) designed with the software Igor Pro in order to reject periods inferior to 10 000 years and erase the noise present in the data. Note that using a low-pass (rejecting periods below 15 kyr) or a band-pass filter (keeping periods between 100 and 15 kyr periods, used by Bazin et al., 2013) does not alter the peak positions in the $\delta\text{O}_2/\text{N}_2$ curve (see Fig. S2). The noise is particularly significant for highly resolved $\delta\text{O}_2/\text{N}_2$ data, and without preliminary filtering, it becomes ambiguous to identify the exact peak position (which needs to be subjectively placed on a 1000- to 2000-year interval; see Sect. S2.1).

The filter is then applied to the local summer solstice insolation curve to check that it does not induce the shift in extrema positions by more than 100 years. This condition is verified over the last 800 kyr, except for the peaks located at the endpoints of the record (respectively around 107 and 788 ka BP), which are then not used for tie point determination. Outliers in the raw $\delta\text{O}_2/\text{N}_2$ dataset are discarded if they show an anomaly greater than 3.2 % when compared to the low-pass-filtered signal. Five outliers are rejected out of 294 points. The $\delta\text{O}_2/\text{N}_2$ is interpolated and filtered again after removal of the outliers.

The orbital target chosen is the 21 December insolation at 75°S , which is calculated every 100 years over the last 800 kyr (Laskar et al., 2004). The peak positions in the compiled filtered $\delta\text{O}_2/\text{N}_2$ signal and in the summer solstice insolation are detected via an automated method using the zero values of the time derivatives of the $\delta\text{O}_2/\text{N}_2$ and its orbital target. Each $\delta\text{O}_2/\text{N}_2$ maximum is matched to an insolation minimum and each $\delta\text{O}_2/\text{N}_2$ minimum to an insolation maximum. The data treatment and tie point identification method used here are consistent with the approach recently conducted by Oyabu et al. (2022) on a novel 207 kyr long $\delta\text{O}_2/\text{N}_2$ record of the Dome Fuji (DF) ice core.

Some periods, such as between 450 and 350 ka BP (encompassing MIS 11) and older ages (before 600 ka BP), are characterized by a poor resemblance between the signal and the target. For instance, two or three peaks in the insolation curve only correspond, respectively, to one or two peaks in the $\delta\text{O}_2/\text{N}_2$ data. This could be explained by a low eccentricity-induced subdued variability in the insolation target and hence in $\delta\text{O}_2/\text{N}_2$ signal over MIS 11 and by the poor resolution of the $\delta\text{O}_2/\text{N}_2$ measurements before 600 ka BP. In such cases, the uncertainty (1σ) associated with each tie point ranges from 6 to 10 kyr (precession half period), and some extrema in the target are not used to tune the $\delta\text{O}_2/\text{N}_2$ record (5 extrema over MIS 11 out of 63 over the last 800 kyr). Otherwise, $\delta\text{O}_2/\text{N}_2$ seems to evolve

in phase with the inverse summer solstice insolation variations, and the tie point uncertainty (1σ) is set at 3 kyr. A 3–4 kyr uncertainty was evaluated by Bazin et al. (2016) on the following arguments. They examined three $\delta\text{O}_2/\text{N}_2$ records from the Vostok, DF and EDC ice cores over MIS 5 and detected some site-specific $\delta\text{O}_2/\text{N}_2$ high-frequency variability that could not be explained by a timescale issue. This observation, along with the presence of a 100 kyr periodicity in the EDC $\delta\text{O}_2/\text{N}_2$ record and the difficulty of identifying $\delta\text{O}_2/\text{N}_2$ mid-slopes and maxima because of a scattering of the $\delta\text{O}_2/\text{N}_2$ signal at the millennial scale, led them to recommend the use of a 3–4 kyr uncertainty. Because our higher-resolution $\delta\text{O}_2/\text{N}_2$ data give the possibility of filtering the signal with more confidence and hence reduces the uncertainty in the identification of $\delta\text{O}_2/\text{N}_2$ tie points, we propose taking a 3 kyr uncertainty. The orbital tuning results in 58 new tie points over the last 800 kyr (displayed in Fig. 1 and compiled in Table S5), replacing the 20 tie points used to constrain AICC2012 between 800 and 300 ka BP that were derived from synchronizing mid-slopes of band-pass-filtered $\delta\text{O}_2/\text{N}_2$ with the insolation (Bazin et al., 2013).

The uncertainty arising from the filter used and from the tie point identification method can be estimated by a comparison of the $\delta\text{O}_2/\text{N}_2$ peak positions identified before and after filtering of the signal with two different methods (see Sect. S2.1). The resulting uncertainty is of 700 years on average (with a standard deviation of 250 years), reaching 2100 years around 230 ka BP.

The new highly resolved data presented here enable a better description of the signal variability and a reduction in the uncertainty associated with orbital tie points.

3.2.2 Total air content

The TAC record is extended over the last 800 kyr with a mean sampling resolution of 2000 years (Fig. 2). The raw data between 800 and 440 ka BP are not shown here and will be published in a separate study. The TAC series shows a good resemblance with the integrated summer insolation (ISI, obtained by a summation over a year of all daily insolation at 75° S above a chosen threshold). After comparing the EDC TAC record, within its frequency domain, with ISI curves obtained using different thresholds, the ISI curve calculated for a threshold of 375 W m⁻² (ISI375) exhibits the finest spectral agreement with the EDC TAC record over the past 800 kyr. The coherency between the TAC record and ISI is deficient over MIS 11 (between 430 and 370 ka BP) and in the deepest part of the core (prior to 700 ka BP), where the signal-to-noise ratio is low.

Following a data processing treatment consistent with the method described by Lipenkov et al. (2011), the 800 kyr long TAC dataset is interpolated every 100 years and then filtered with a band-pass filter rejecting periods below 15 000 and above 46 000 years (Igor Pro FIR filter with a KaiserBessel20 window, cut-off from 15 to 14 kyr and from 46 to 47 kyr,

559 coefficients). Outliers in the raw TAC dataset are discarded if they show an anomaly greater than 1.0 mL kg⁻¹ (standard deviation of TAC record) when compared to the band-pass-filtered signal. A total of 45 outliers are rejected out of 399 data points (among which 16 outliers are identified between 100 and 0 ka BP). The TAC is interpolated and filtered again after removal of the outliers.

Tie points are mostly determined by matching variation extrema of TAC and integrated summer insolation at 75° S (Fig. 2). Indeed, in the case of a non-linear relationship between TAC and insolation, extrema are better indicators of TAC response to insolation forcing. Moreover, filtering the dataset induces a bias in the mid-slope position. The method employed to determine extrema position is the same as for $\delta\text{O}_2/\text{N}_2$ insolation tie points. Only one of the tie points is identified by matching mid-slopes (i.e., derivative extremum) at 362 ka BP rather than minima at 375 ka BP due to the flatness of the insolation minimum, which precludes identification of an accurate tie point. Not all extrema are tuned to the target due to the poor resemblance between the signal and insolation, and 42 unambiguous tie points were kept out of 64 detected by the automated method. The tie point uncertainty finds its origin in the age errors associated with the filtering (~ 700 years), tie point identification and outlier rejection (~ 900 years). The 1σ uncertainty is evaluated to be 3 kyr when there is good agreement: (i) between the signal and its target, meaning that one peak in ISI375 is reflected by a singular peak in the TAC record, and (ii) between the tie points identified by the automated method and manually (age shift < 1300 years, average value) (see green circles, Fig. 2). A 6 kyr uncertainty (1σ) is attached to the tie points if the latter condition is not respected (age shift > 1300 years) (see purple squares, Fig. 2), and a 10 kyr uncertainty (1σ) (precession half period) is ascribed to the tie points if the ISI375 variations are not reflected by the TAC record, meaning that one peak in ISI375 could be associated with two peaks in the TAC record, or if the signal-to-noise ratio of the TAC record is too large (see red markers, Fig. 2). The choices of filter and orbital target have no significant impact on the chronological uncertainty; a further detailed study is thus beyond the scope of this work.

The orbital tuning results in 42 new tie points over the last 800 kyr (displayed in Fig. 2 and compiled in Table S5). They replace the 14 tie points used to constrain the EDC ice timescale in AICC2012 between 425 and 0 ka BP that were derived by directly matching mid-slope variations in unfiltered TAC and ISI target and attached to an uncertainty varying between 2.9 and 7.2 kyr.

3.2.3 $\delta^{18}\text{O}_{\text{atm}}$

In this work, new highly resolved $\delta^{18}\text{O}_{\text{atm}}$ data on the EDC ice core are presented over terminations II, III, IV, V and VI (Fig. 3). The available $\delta^{18}\text{O}_{\text{atm}}$ data can be sorted out in two groups: new $\delta^{18}\text{O}_{\text{atm}}$ data (Grisart, 2023) at high temporal

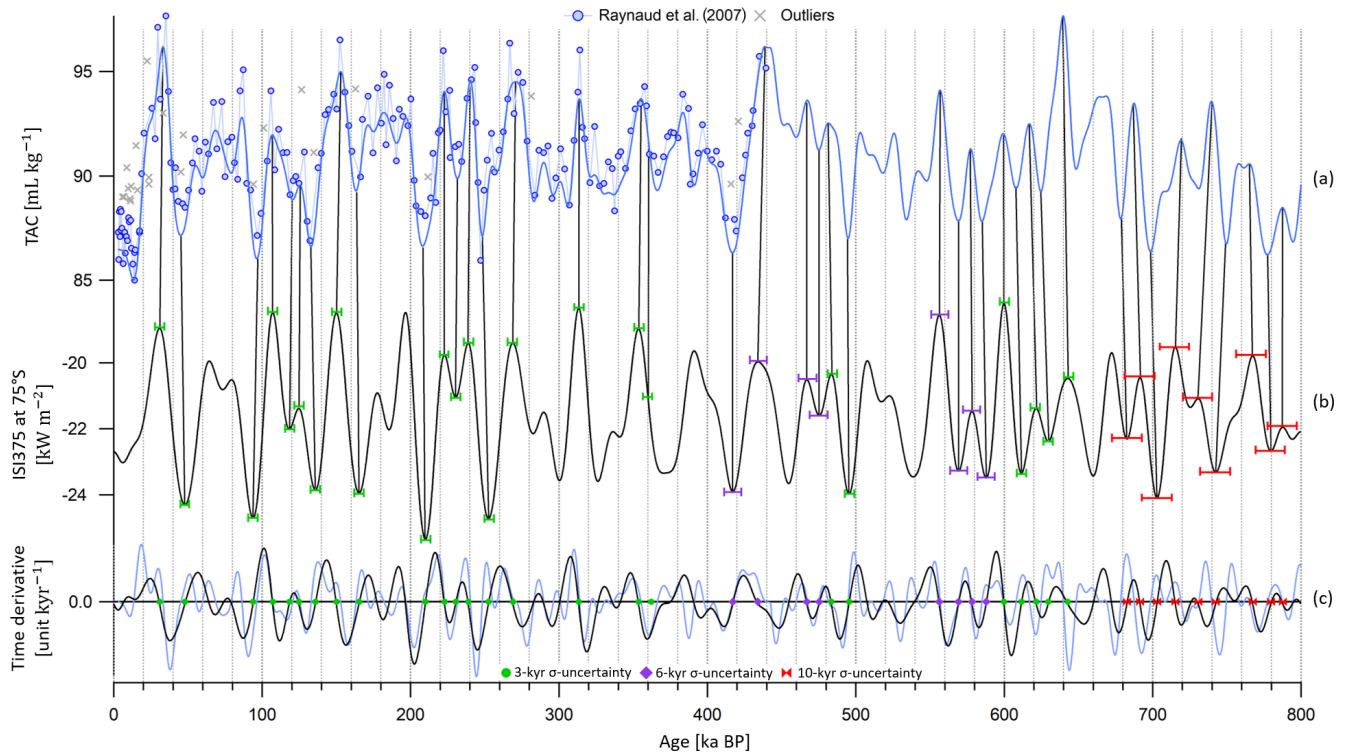


Figure 2. Alignment of TAC and insolation between 800 and 0 ka BP. **(a)** Raw EDC TAC data (blue circles; Raynaud et al., 2007), outliers (gray crosses) and filtered signal (blue line) on the AICC2012 ice timescale. The raw data between 800 and 440 ka BP are not shown here and will be published in a separate study. **(b)** ISI375 at 75° S on a reversed axis. The peaks and mid-slopes are matched by vertical bars. **(c)** Temporal derivative of insolation (black line) and TAC (blue line). Its zero value corresponds to extreme values in insolation and TAC. The determined tie points between TAC and insolation are depicted by markers on the horizontal line. Green circles are attached to a 3 kyr 1σ uncertainty (horizontal green error bars show 2σ in panel c), purple squares are associated with a 6 kyr 1σ uncertainty (horizontal purple error bars show 2σ in panel c), and red markers are associated with a 10 kyr 1σ uncertainty (horizontal red error bars show 2σ in panel c).

resolution (between 333 and 1375 years; see Table 1) and old measurements compiled by Extier et al. (2018b), characterized by a lower sampling resolution (between 1000 and 1500 years; see Table 1), except between 374 and 153 ka BP (resolution between 160 and 700 years; see Table 1). The new dataset improves the resolution of the long EDC record over MISs 5, 7 and 9 and in particular over MISs 11 and 13, periods of sparsity in the ancient record (Extier et al., 2018b). Although the two datasets agree well globally over the last 800 kyr, the new highly resolved dataset refines the signal between 255.5 and 243 ka BP where a lot of noise is present in the record of Extier et al. (2018b) (see inset in Fig. 3). This noise may be explained by the fact that highly resolved (mean sampling resolution of 381 years) measurements were performed on ice samples stored at -20°C in the compilation by Extier et al. (2018b), while the new measurements are performed on ice stored at -50°C . Therefore, we chose to remove the noisy dataset of Extier et al. (2018b) between 255.5 and 243 ka BP before combining the novel dataset with the remaining 800 kyr long record of Extier et al. (2018b).

Following the dating approach proposed by Extier et al. (2018a), $\delta^{18}\text{O}_{\text{atm}}$ and $\delta^{18}\text{O}_{\text{calcite}}$ are aligned using mid-

slopes of their variations over the last 640 kyr. To do so, the compiled EDC $\delta^{18}\text{O}_{\text{atm}}$ record and the Chinese $\delta^{18}\text{O}_{\text{calcite}}$ signal are linearly interpolated every 100 years and smoothed (25-point Savitzky–Golay) and extrema in their temporal derivative are aligned. It should be specified that synchronizing $\delta^{18}\text{O}_{\text{atm}}$ and East Asian $\delta^{18}\text{O}_{\text{calcite}}$ is not always obvious due to the long residence time of oxygen in the atmosphere (1–2 kyr), which may not be compatible with abrupt $\delta^{18}\text{O}_{\text{calcite}}$ variations over glacial inception and terminations. In particular, the slow increase in the $\delta^{18}\text{O}_{\text{atm}}$ record from 370 to 340 ka BP does not resemble the evolution of $\delta^{18}\text{O}_{\text{calcite}}$, which is first moderate then abrupt over the same period (Fig. 4, red area). For this reason, we chose not to use the two tie points identified by Extier et al. (2018a) at 351 and 370.6 ka BP. The new highly resolved data enable the identification of five new tie points and shifting of five tie points that have been determined beforehand by Extier et al. (2018a) (Fig. 4). Between 248 and 244 ka BP, the new $\delta^{18}\text{O}_{\text{atm}}$ measurements do not coincide with the $\delta^{18}\text{O}_{\text{calcite}}$ variations, and we decided to remove the tie point identified by Extier et al. (2018a) at 245.4 ka BP (Fig. 4, red area). Between 480 and 447 ka BP, the $\delta^{18}\text{O}_{\text{atm}}$ variations are

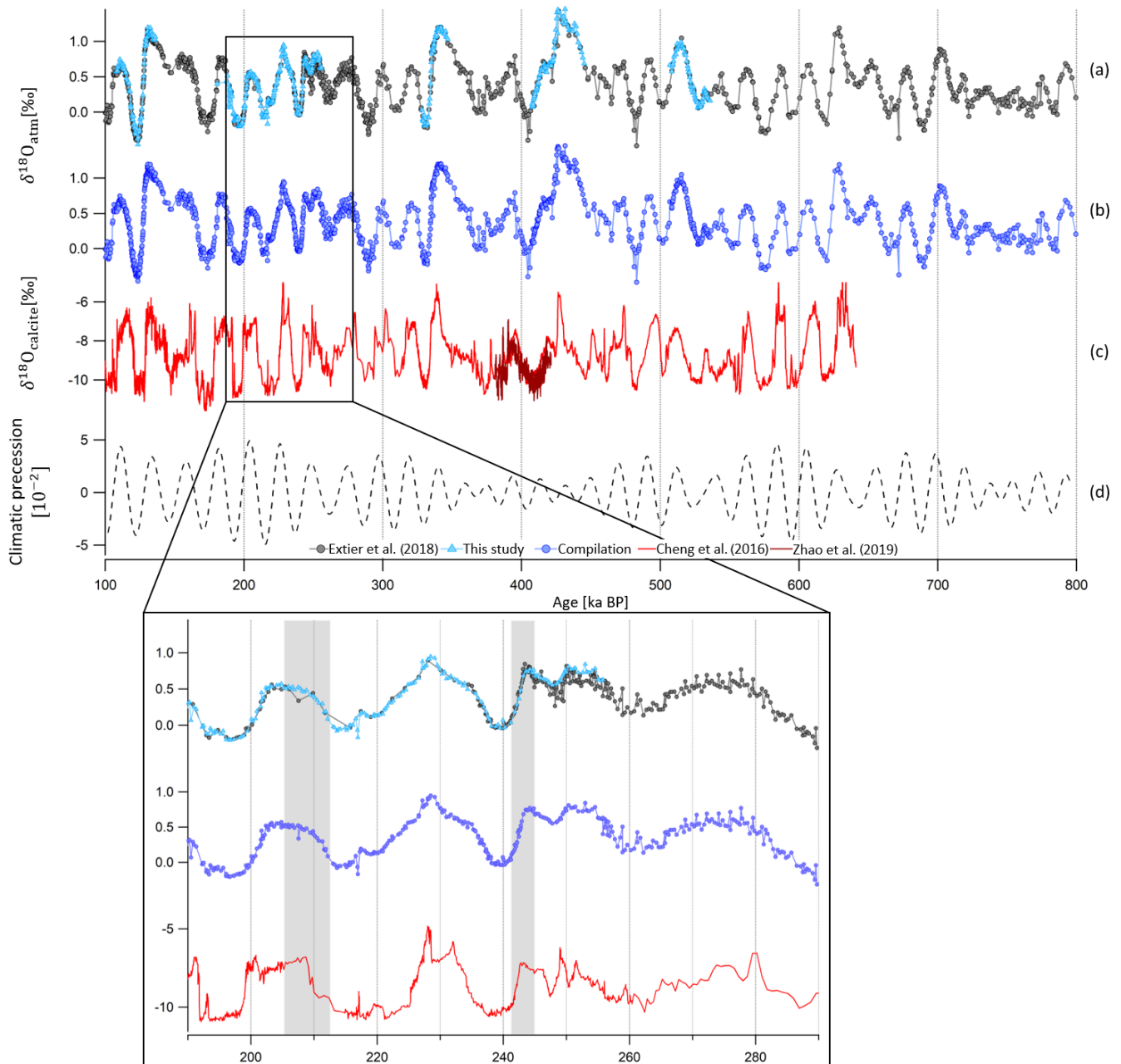


Figure 3. Evolution of EDC $\delta^{18}\text{O}_{\text{atm}}$ record between 800 and 100 ka BP. **(a)** Old raw EDC $\delta^{18}\text{O}_{\text{atm}}$ data (black circles; Extier et al., 2018b) and new raw EDC $\delta^{18}\text{O}_{\text{atm}}$ data (blue triangles; Grisart, 2023) on the AICC2012 gas timescale. **(b)** Compilation of the two datasets after removal of old measurements between 255.5 and 243 ka BP. **(c)** $\delta^{18}\text{O}_{\text{atm}}$ composite record from speleothems from Sambao, Dongge, Hulu (red line) and Yongxing (brown line) caves (Cheng et al., 2016; Zhao et al., 2019) on U–Th age scales. **(d)** Climatic precession from Laskar et al. (2004) delayed by 5000 years. Inset is a zoom between 290 and 190 ka BP. Vertical gray rectangles highlight the improved agreement between new data of Grisart (2023) (blue triangles) and $\delta^{18}\text{O}_{\text{atm}}$ (red line) compared to old data (gray circles) and $\delta^{18}\text{O}_{\text{atm}}$.

characterized by a low resolution (1.1 kyr) and a weak amplitude, which prevents unambiguous matching of $\delta^{18}\text{O}_{\text{atm}}$ and $\delta^{18}\text{O}_{\text{calcite}}$. The four tie points identified by Extier et al. (2018a) at 447.3, 449.9, 455.9 and 462.8 ka BP are thus rejected (Fig. 4, red area). The remaining 39 tie points defined by Extier et al. (2018a) are preserved and used here

to constrain the EDC gas age. Their uncertainty (1σ) varies between 1.1 and 7.4 kyr.

Between 810 and 590 ka BP, the $\delta^{18}\text{O}_{\text{atm}}-\delta^{18}\text{O}_{\text{calcite}}$ dating uncertainty becomes larger than 6 kyr, and no East Asian speleothem $\delta^{18}\text{O}_{\text{calcite}}$ records are available before 640 ka BP. Over this time interval, we updated the following approach of

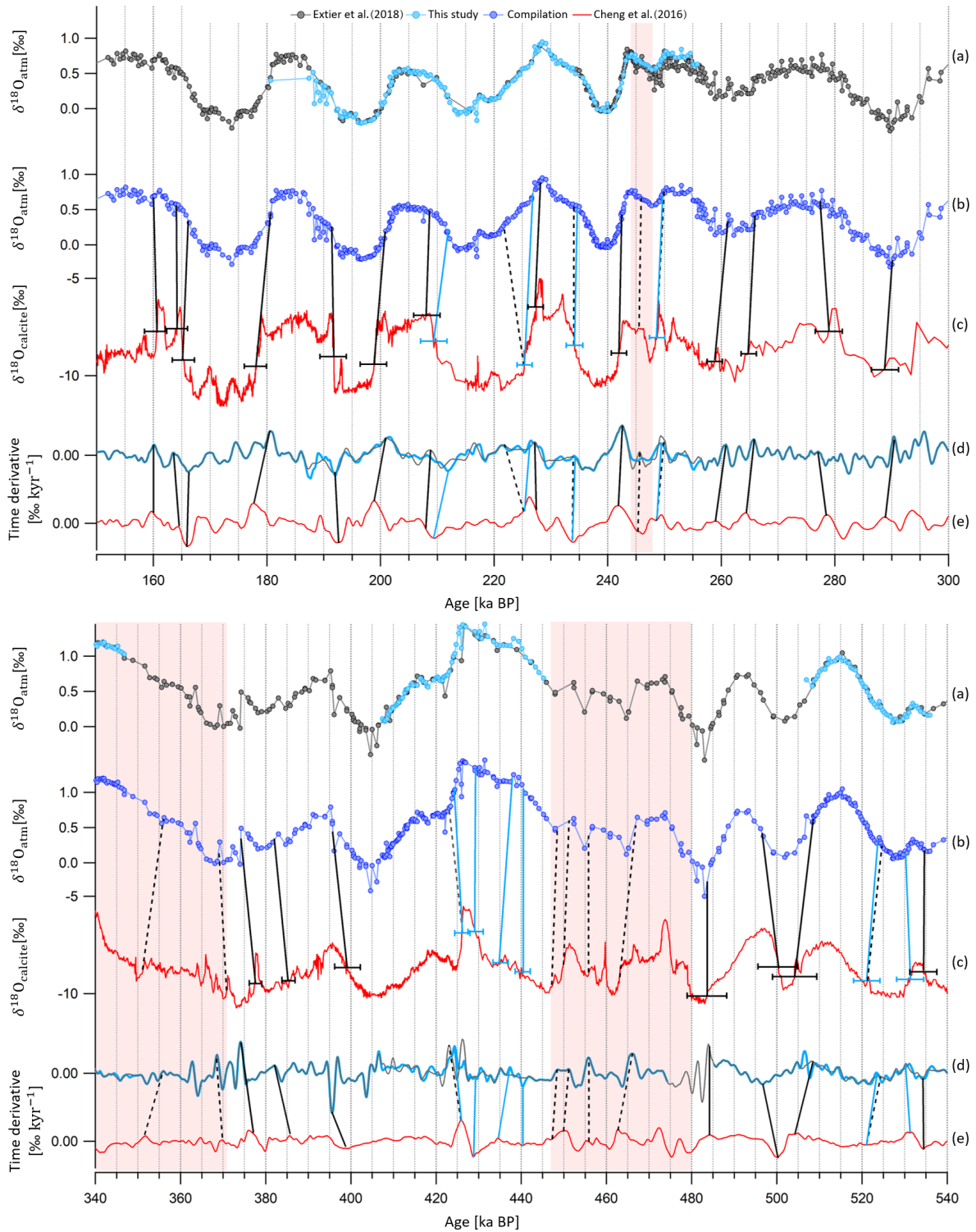


Figure 4. Alignment of EDC $\delta^{18}\text{O}_{\text{atm}}$ and Chinese $\delta^{18}\text{O}_{\text{calcite}}$ records over time periods where new tie points are defined. **(a)** New and old EDC $\delta^{18}\text{O}_{\text{atm}}$ datasets on the AICC2012 gas age scale. **(b)** Compiled EDC $\delta^{18}\text{O}_{\text{atm}}$. **(c)** Chinese $\delta^{18}\text{O}_{\text{calcite}}$ on U–Th age scale (Cheng et al., 2016). **(d)** Temporal derivatives of compiled EDC $\delta^{18}\text{O}_{\text{atm}}$ (blue curve) and of the old $\delta^{18}\text{O}_{\text{atm}}$ dataset (black curve). **(e)** Temporal derivative of Chinese $\delta^{18}\text{O}_{\text{calcite}}$ (red curve). Extrema in temporal derivatives are matched. Tie points represented by vertical black bars are determined by Extier et al. (2018a), and those by vertical blue bars are determined by this study. Both are used in the AICC2023 chronology. Dashed vertical bars show tie points identified by Extier et al. (2018a) that are not used in AICC2023; 2σ uncertainties attached to the tie points are shown by the horizontal error bars in panel c). Vertical red areas frame periods of lacking resemblance between $\delta^{18}\text{O}_{\text{atm}}$ and $\delta^{18}\text{O}_{\text{calcite}}$ variations.

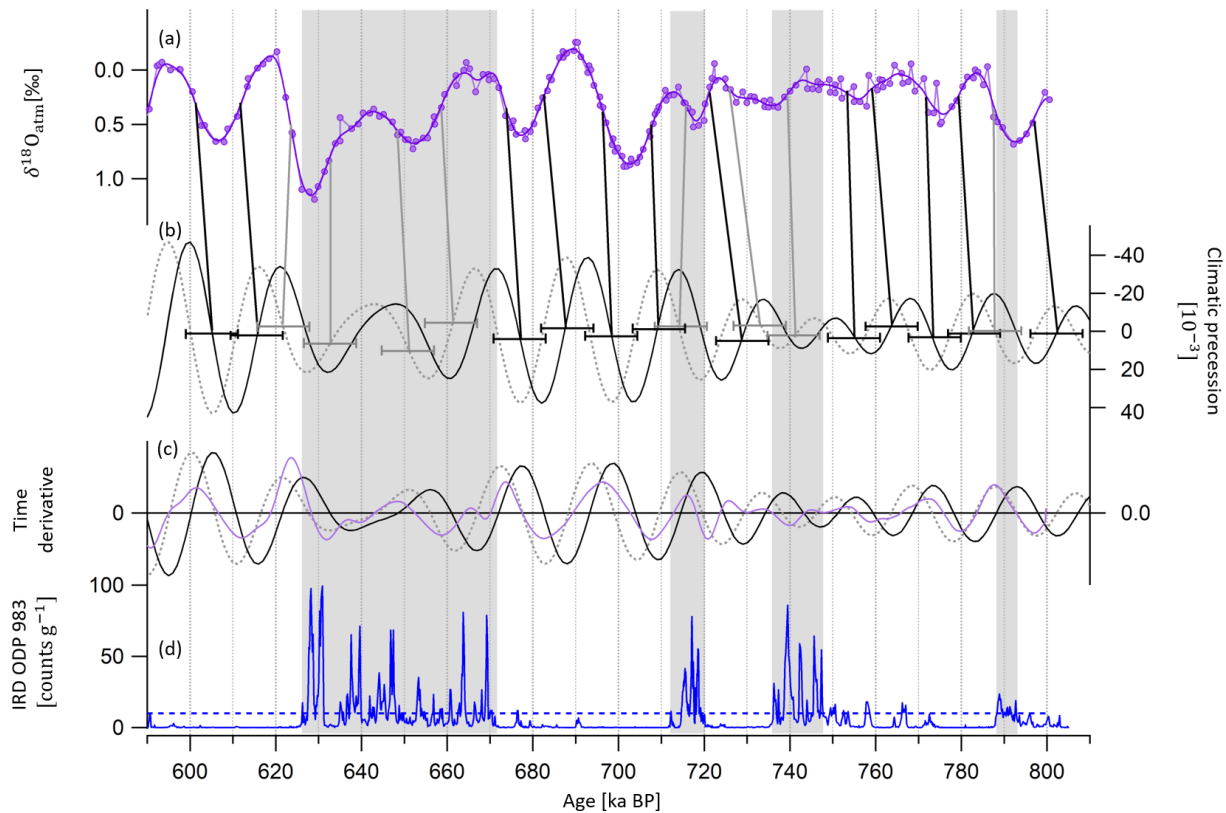


Figure 5. Alignment of EDC $\delta^{18}\text{O}_{\text{atm}}$ and climatic precession between 810 and 590 ka BP. **(a)** Compiled EDC $\delta^{18}\text{O}_{\text{atm}}$ on the AICC2012 gas timescale. **(b)** Precession delayed by 5000 years (dashed gray line) and not delayed (black line) (Laskar et al., 2004). **(c)** Temporal derivative of precession (black line), delayed precession (dotted gray line) and the compiled $\delta^{18}\text{O}_{\text{atm}}$ record (plain purple line). **(d)** Ice-rafted debris at ODP983 site (North Atlantic Ocean, southwest of Iceland) by Barker et al. (2019, 2021). The gray rectangles indicate periods where IRD counts are greater than the 10 counts per gram threshold shown by the dotted horizontal blue line. The gray vertical bars illustrate new tie points between EDC $\delta^{18}\text{O}_{\text{atm}}$ and delayed precession mid-slopes (i.e., derivative extrema) when IRD counts are greater than the threshold. Vertical black bars illustrate new tie points between EDC $\delta^{18}\text{O}_{\text{atm}}$ and precession mid-slopes (i.e., derivative extrema) when no Heinrich-like events are shown by the IRD record. The 12 kyr 2σ uncertainty attached to the tie points is shown by the horizontal error bars in panel **(b)**.

Bazin et al. (2013): EDC $\delta^{18}\text{O}_{\text{atm}}$ and 5 kyr delayed climatic precession are synchronized using mid-slopes of their variations. However, from the findings of Extier et al. (2018a), $\delta^{18}\text{O}_{\text{atm}}$ should rather be aligned to precession without delay when no Heinrich-like events occur. Indeed, $\delta^{18}\text{O}_{\text{atm}}$ is sensitive to both orbital- and millennial-scale variations in the low-latitude water cycle (Landais et al., 2010; Capron et al., 2012), and Heinrich-like events occurring during deglaciations delay the response of $\delta^{18}\text{O}_{\text{atm}}$ to orbital forcing through southward ITCZ shifts (Extier et al., 2018a). We thus chose to align $\delta^{18}\text{O}_{\text{atm}}$ to precession when no ice-rafted debris (IRD) peak is visible in the studied period in the ODP983 record (Barker et al., 2019, 2021) and keep a 5 kyr delay when IRD peaks are identified. This results in shifting 12 tie points of Bazin et al. (2013) by 5000 years towards older ages (Fig. 6). The eight remaining tie points of Bazin et al. (2013) that coincide with peaks in the IRD record are kept (Fig. 6). To confirm the validity of our approach, we tested three methodologies to align $\delta^{18}\text{O}_{\text{atm}}$ and precession over well-

dated periods when $\delta^{18}\text{O}_{\text{atm}}-\delta^{18}\text{O}_{\text{calcite}}$ matching was done (see Sect. S2.2.2). These tests support our approach, but in order to account for potential errors associated with this tuning method (Oyabu et al., 2022), a 6 kyr uncertainty (1σ) is attributed to the $\delta^{18}\text{O}_{\text{atm}}$ -derived tie points over the period between 810 and 590 ka BP.

A total of 69 new $\delta^{18}\text{O}_{\text{atm}}$ tie points are determined over the last 810 kyr (displayed in Figs. 4 and 5 and compiled in Table S5). They replace the 39 tie points used to constrain the EDC gas timescale in AICC2012 between 800 and 363 ka BP (Bazin et al., 2013). The age constraints are attached to an uncertainty varying between 1.1 and 7.4 kyr, which is the sum of the uncertainties in the speleothem ^{230}Th dating, the $\delta^{18}\text{O}_{\text{atm}}$ response to orbital forcing (1 kyr) and the $\delta^{18}\text{O}_{\text{atm}}-\delta^{18}\text{O}_{\text{calcite}}$ matching (0.5 kyr). The same alignment method is applied between Vostok $\delta^{18}\text{O}_{\text{atm}}$ (Petit et al., 1999) and Chinese $\delta^{18}\text{O}_{\text{calcite}}$, and 36 new tie points are determined (see Sect. S4.1.2), replacing the 35 tie points used to constrain the Vostok gas timescale in AICC2012.

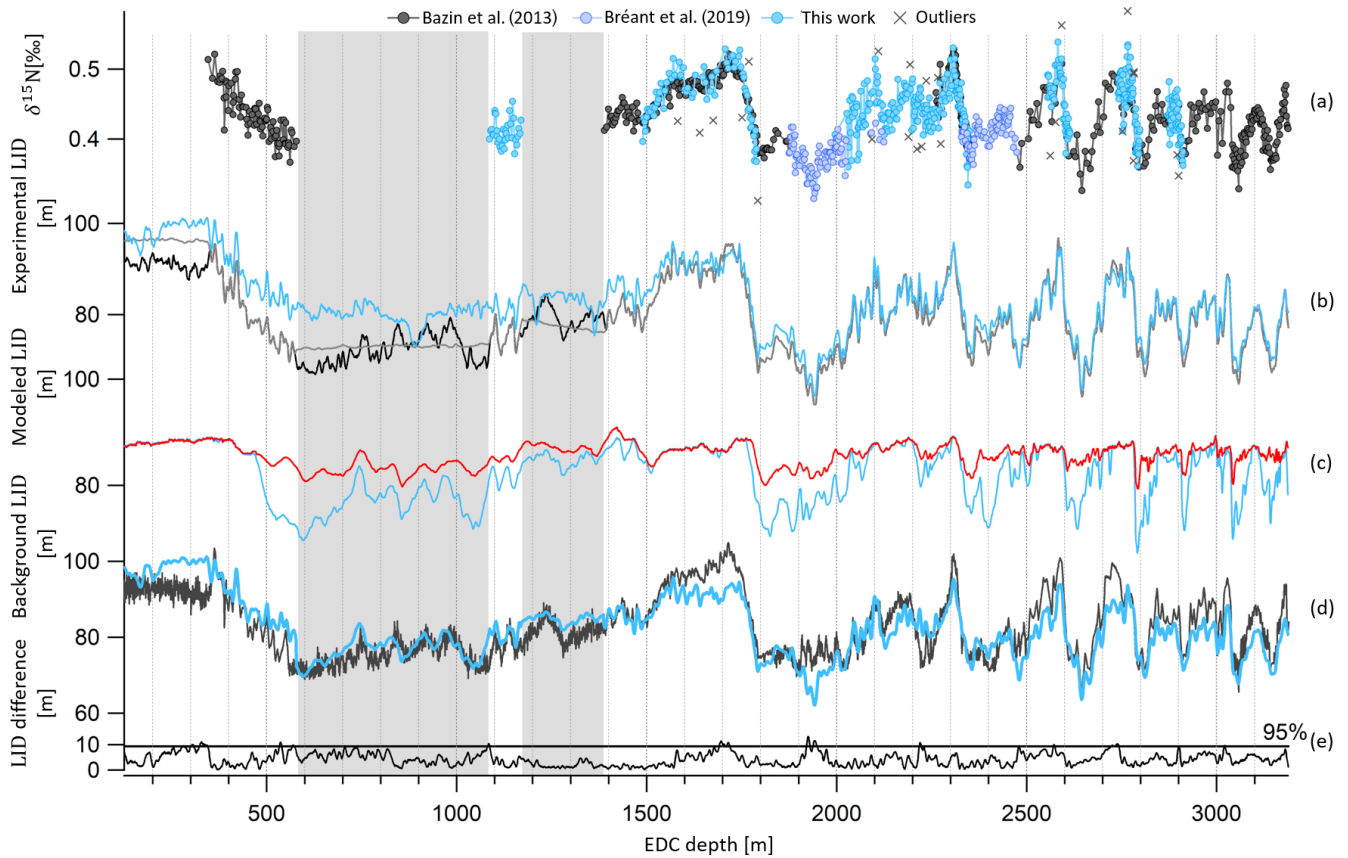


Figure 6. EDC $\delta^{15}\text{N}$ record and past LID evolution as a function of EDC depth. **(a)** New and highly resolved $\delta^{15}\text{N}$ dataset (blue circles), dataset of Bréant et al. (2019) (purple circles), old dataset (black circles) and outliers (rejection criterion of 1σ) (gray crosses). **(b)** LID calculated as per $\text{LID} \simeq \delta^{15}\text{N}_{\text{grav}} \cdot \frac{RT}{g}$ for three cases: (1) $\delta^{15}\text{N}_{\text{grav}} = \delta^{15}\text{N}$ with the $\delta^{15}\text{N}$ record constructed by interpolation between data when no data are available (gray), (2) $\delta^{15}\text{N}_{\text{grav}} = \delta^{15}\text{N}$ with the $\delta^{15}\text{N}$ record constructed by normalization of the δD record when no data are available (black), (3) $\delta^{15}\text{N}_{\text{grav}} = \delta^{15}\text{N} - \delta^{15}\text{N}_{\text{therm}}$ with $\delta^{15}\text{N}_{\text{therm}}$ estimated by the firm model (Bréant et al., 2017) and the $\delta^{15}\text{N}$ record constructed by interpolation between data when no data are available (blue). **(c)** Modeled LID with impurity concentration (blue) and without impurity concentration (red). **(d)** Background scenarios of LID used to construct AICC2012 (black) and inputs in PaleoChrono to obtain AICC2023 (blue). **(e)** Absolute difference between prior LID of AICC2012 and AICC2023. The gray line separates the top 5% values from the rest. The gray rectangles cover areas when no $\delta^{15}\text{N}$ data are available.

Finally, there was a redundancy in the dating of the bottom part of the EDC ice core in AICC2012, where both $\delta^{18}\text{O}_{\text{atm}}$ orbital tie points and ^{10}Be peaks corresponding to the Matuyama–Brunhes geomagnetic reversal event were used. Indeed, the two ^{10}Be dating constraints at 780.3 and 798.3 ka BP were directly derived from the $\delta^{18}\text{O}_{\text{atm}}$ orbital dating and not obtained independently (Dreyfus et al., 2008). We thus decided to remove the ^{10}Be age constraints.

3.3 Background scenario of LID

In this work, new highly resolved $\delta^{15}\text{N}$ data in the EDC ice core are presented over terminations II, III, IV, V and VI (Fig. 6a). The available $\delta^{15}\text{N}$ data can be sorted out in two groups: $\delta^{15}\text{N}$ measured by Grisart (2023) and Bréant et al. (2019) at high temporal resolution (between 333 and 1375 years; see Table 1) and the older measurements (Bazin

et al., 2013) used to estimate LID in AICC2012, characterized by a lower sampling resolution (between 1400 and 2400 years; see Table 1). The measurements of Bazin et al. (2013) and Bréant et al. (2019) have been shifted down by 0.04‰ to account for calibration errors. The new dataset permits the extension of the record by around 1100 m and between 1700 and 2500 m and improvement in the resolution over terminations II to VI.

Outliers are discarded if they show an anomaly greater than 0.045‰ when compared to the smoothed record (Savitzky–Golay algorithm with 25 points). This results in the rejection of 25 data points out of 475 measurements for the new dataset (Fig. 6). The two $\delta^{15}\text{N}$ datasets are merged, and the compiled record is interpolated every 100 years. Then, assuming that the firm is solely a diffusive zone (i.e., no convection layer at the top) at EDC during the last 800 kyr, in

agreement with current observations (Landais et al., 2006), past LID is calculated as per the first-order estimate of the barometric equation:

$$\text{LID} \simeq \delta^{15}\text{N}_{\text{grav}} \frac{RT}{g}, \quad (5)$$

with T the temperature at EDC estimated from combined measurements of ice $\delta^{18}\text{O}$ and δD after correction of the influence of the seawater $\delta^{18}\text{O}$ (Landais et al., 2021).

In the absence of a large thermal gradient within the firn (mostly present in Greenlandic ice cores during Dansgaard–Oeschger events), $\delta^{15}\text{N}$ is mainly modulated by gravitational fractionation of N_2 molecules occurring from the surface down to the lock-in zone, and $\delta^{15}\text{N}$ measured in bubbles hence approximately reflects the LID (Severinghaus et al., 1996; Landais et al., 2006) and $\delta^{15}\text{N}_{\text{grav}} \simeq \delta^{15}\text{N}$ in Eq. (5) (gray and black lines in Fig. 6b). To account for a small temperature gradient in the firn in the Antarctic ice core, the thermal-fractionation term $\delta^{15}\text{N}_{\text{therm}}$ can be estimated by the firn model (Bréant et al., 2017). Past LID is then calculated as per Eq. (5) with $\delta^{15}\text{N}_{\text{grav}} = \delta^{15}\text{N} - \delta^{15}\text{N}_{\text{therm}}$ (blue curve in Fig. 6b). Thermal fractionation represents a maximum correction of 4.2 m to the LID at EDC.

When $\delta^{15}\text{N}$ measurements are not available, Bazin et al. (2013) used a synthetic $\delta^{15}\text{N}$ signal based on the correlation between $\delta^{15}\text{N}$ and δD to estimate the LID background scenario at Dome C (black curve in Fig. 6b). Indeed, for different low-accumulation Antarctic sites, it has been observed that $\delta^{15}\text{N}$ and δD are well correlated over the last termination on a coherent timescale (Dreyfus et al., 2010; Capron et al., 2013). Since then, Bréant et al. (2019) presented new high-resolution EDC measurements of $\delta^{15}\text{N}$ extending the signal over termination III (around 2300 m, 250 ka BP). Their study unveiled the anatomy of this atypical deglaciation: the interplay between Heinrich-like events and the bipolar seesaw mechanism induced a strong warming of Antarctic temperature, resulting in divergent $\delta^{15}\text{N}$ and δD records. Therefore, using δD to construct a synthetic $\delta^{15}\text{N}$ scenario should be done carefully. For this reason, the firn densification model described in Bréant et al. (2017) is employed to estimate EDC LID evolution in the past when $\delta^{15}\text{N}$ data are missing, rather than using the $\delta^{15}\text{N}$ – δD relationship, as was done for AICC2012. After different sensitivity tests, we chose to keep the parameterization preferred by Bréant et al. (2017) (i.e., firn densification activation energy depending on the temperature and the impurity concentration) as it is believed to give the most probable evolution of LID over the last 800 kyr (see Sect. S3.1).

The final background LID scenario is calculated as a function of EDC depth (Table 4, Fig. 6d). It has been smoothed using a Savitzky–Golay algorithm (25 points) and then provided as an input file to Paleochrono.

The other necessary input files for Paleochrono, accumulation (A) and thinning (τ) background scenarios, are the same as in Bazin et al. (2013). A is estimated from water isotopes

(Parrenin et al., 2007b) and τ from unidimensional ice flow modeling (Parrenin et al., 2007a).

3.4 New stratigraphic links between the EDC and other ice cores

EDC can be linked to other ice cores via ice and gas stratigraphic links identified during abrupt climate changes recorded in Greenlandic and Antarctic ice cores. To establish AICC2012, Bazin et al. (2013) used 255 gas stratigraphic tie points coming from the matching of CH_4 (or $\delta^{15}\text{N}$ when CH_4 is not available at NGRIP) or $\delta^{18}\text{O}_{\text{atm}}$ variations between EDC, EDML, Vostok, NGRIP and TALDICE. Here we revise some of these tie points using the synchronization of CH_4 series of EDC, Vostok and TALDICE to up-to-date, highly resolved records from EDML and NGRIP ice cores over the last interglacial offset and the last glacial period (Baumgartner et al., 2014). From 122 to 10 ka BP, Baumgartner et al. (2014) identified 39 stratigraphic links between EDML and NGRIP by matching mid-points of the CH_4 abrupt changes with a precision of 300 to 700 years. When they also detected such rapid variations in lower-resolution CH_4 records of the TALDICE, Vostok and EDC ice cores, they extended the stratigraphic links to the five ice cores but assigned them a larger uncertainty (up to 1500 years). AICC2012 was further constrained by 534 ice stratigraphic links identified from volcanic matching and synchronization of cosmogenic isotopes between the five ice cores. Here we replace some of the stratigraphic links between NGRIP, EDML and EDC by highly resolved volcanic matching points (Svensson et al., 2020). The application of volcanic proxies and annual layer counting helped them identify large volcanic eruptions that left a specific signature in both Greenland and Antarctica. Such a signature is defined by sulfate patterns (indicating singular volcanic events separated by the same time interval in ice cores from both poles). Their study spotted 82 large bipolar volcanic eruptions over the second half of the last glacial period (from 60 to 12 ka BP), providing as many ice stratigraphic links synchronizing EDC with EDML and EDML with NGRIP within a small relative uncertainty (i.e., ranging from 1 to 50 years, 12 years on average). Between 43 and 40 ka BP, five cosmogenic tie points associated with the Laschamp geomagnetic excursion (Raisbeck et al., 2017) replace the volcanic matching over this period (Svensson et al., 2013), shifting the tie points by ~ 30 years.

4 Discussion

4.1 New AICC2023 chronology

4.1.1 Impact of absolute age constraints

A large uncertainty is linked with ^{81}Kr dating; therefore ^{81}Kr age estimates do not significantly change the chronology

Table 4. Method of determination of the background LID scenario according to the EDC depth range.

Depth range (m)	0–345	345–578	578–1086	1086–1169	1169–1386	1386–bottom
$\delta^{15}\text{N}$ data availability	No	Yes	No	Yes	No	Yes
Method of determination of the LID	From constant $\delta^{15}\text{N}$ (measured at 345 m) and corrected for thermal fractionation	From $\delta^{15}\text{N}$ data, corrected for thermal fractionation and smoothed	From firm modeling	From $\delta^{15}\text{N}$ data, corrected for thermal fractionation and smoothed	From firm modeling	From $\delta^{15}\text{N}$ data, corrected for thermal fractionation and smoothed

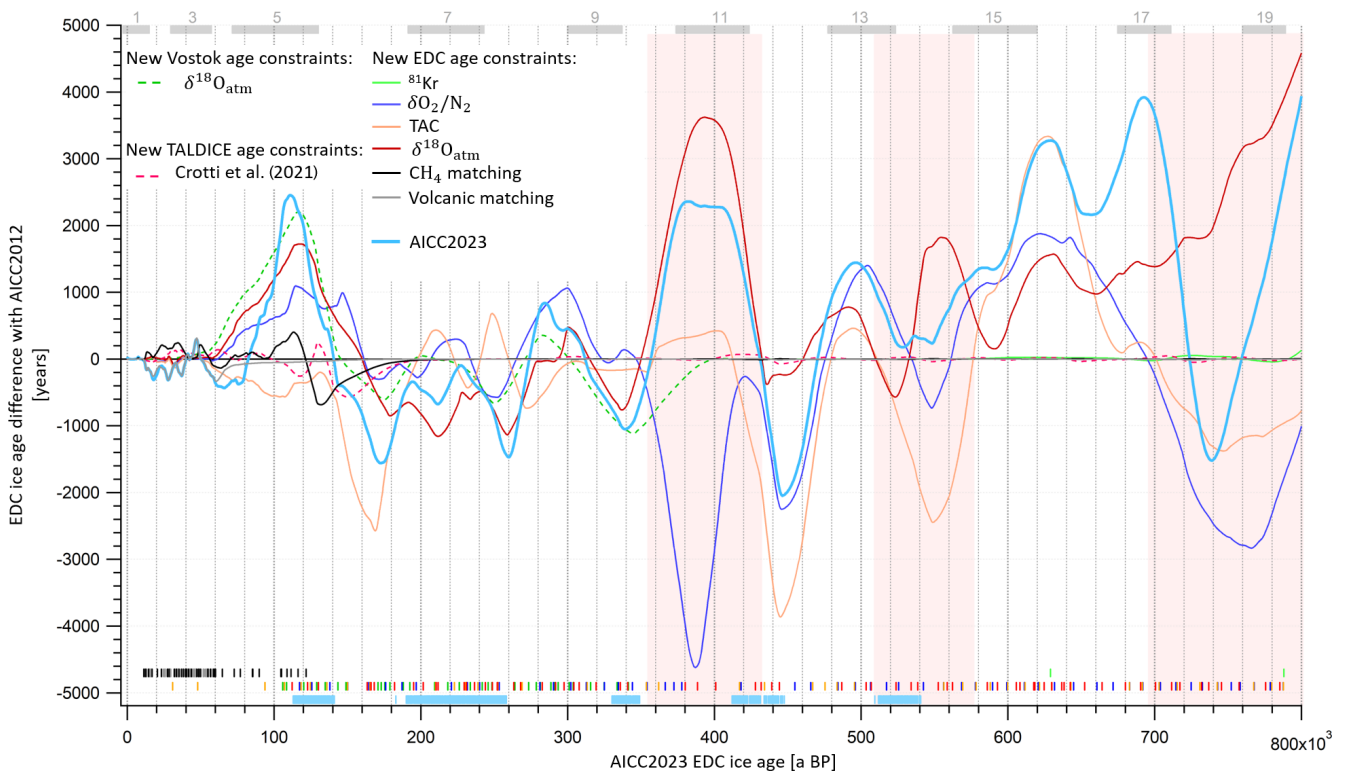


Figure 7. EDC ice age difference between AICC2012 and different test chronologies obtained with PaleoChrono over the last 800 kyr. The ice age difference is calculated as per test chronology – AICC2012. Two test chronologies are obtained by addition of either new Vostok $\delta^{18}\text{O}_{\text{atm}}-\delta^{18}\text{O}_{\text{calcite}}$ age constraints (dotted green line) or stratigraphic and absolute TALDICE constraints between 470 and 129 ka BP from Crotti et al. (2021) (dotted red line). The other “test chronologies” are constructed by replacing AICC2012 constraints by either (1) ^{81}Kr (green); (2) $\delta\text{O}_2/\text{N}_2$ (purple); (3) TAC (orange); (4) $\delta^{18}\text{O}_{\text{atm}}$ (red); (5) CH_4 tie points with NGRIP, EDML, TALDICE and Vostok (black); or (6) volcanic matching points with EDML and NGRIP (gray). Vertical bars represent the corresponding age horizons. AICC2023 is obtained by implementing the new constraints all together (light-blue line). Vertical light-blue bars show new data collected by Grisart (2023) and presented in this work. The three largest inconsistencies between $\delta\text{O}_2/\text{N}_2$, TAC and $\delta^{18}\text{O}_{\text{atm}}$ chronologies are shown by red areas. Gray rectangles indicate interglacials from MIS 19 to MIS 1.

(maximum 200 years) (Fig. 7). ^{81}Kr age estimates are systematically older than the new timescale (by 25 to 36 kyr; see Fig. 8). This observation could also indicate an undervaluation of ^{81}Kr half-life.

4.1.2 Consistency between orbital age constraints

To evaluate the consistency between the orbital age constraints, several “test chronologies” are produced. Each test chronology of the EDC ice core is obtained by running one

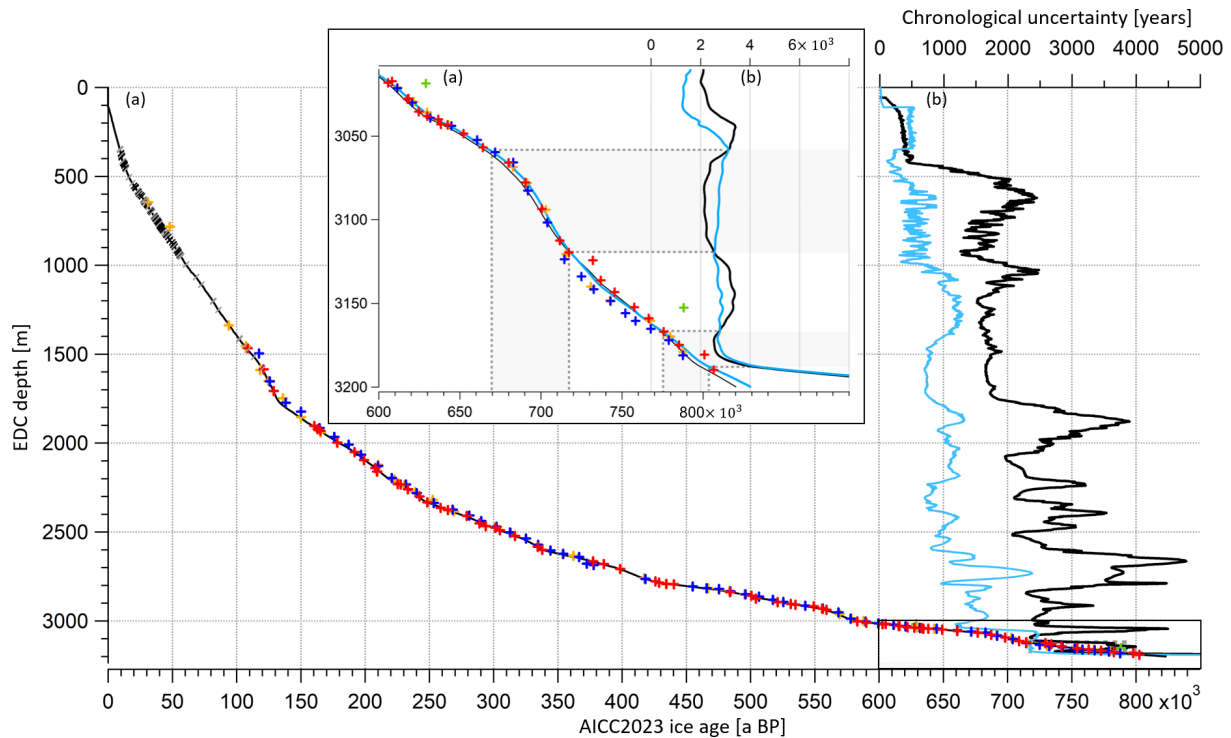


Figure 8. EDC ice age and uncertainty as a function of the depth. (a) EDC ice age (AICC2012 in black, AICC2023 in blue), (b) 1σ uncertainty (AICC2012 in black, AICC2023 in blue). Crosses and slashes represent new age constraints (ice stratigraphic links in black, gas stratigraphic links in gray, $\delta^{18}\text{O}_{\text{atm}}$ in red, $\delta\text{O}_2/\text{N}_2$ in blue, TAC in orange, ^{81}Kr in green). Inset is a zoom in between 800 and 600 ka BP. Gray rectangles frame periods where the new AICC2023 uncertainty is larger than the AICC2012 uncertainty. See Fig. S13 for EDC gas age profile.

multi-site (EDC, Vostok, EDML, TALDICE, NGRIP) experiment of Paleochrono. In each of these tests, we implemented one category of new age constraints presented in this work while keeping AICC2012 parameters for other categories. Several test chronologies are thus constructed: the ^{81}Kr -, $\delta\text{O}_2/\text{N}_2$ -, TAC-, $\delta^{18}\text{O}_{\text{atm}}$ -, CH_4 -matching- and volcanic-matching-based chronologies (Fig. 7). Two additional test chronologies are obtained by implementing and modifying age constraints either on Vostok or TALDICE with respect to the AICC2012 chronology, as explained in Sect. 2.1 (Fig. 7, dotted lines). The EDC ice age difference between each test chronology and the AICC2012 timescale is represented in Fig. 7 so that it is possible to read which type of dating tool suggests shifting the background chronology towards either older or younger ages.

Although the three orbital dating tools globally agree with each other over the last 800 kyr, meaning that they all tend to shift the background chronology towards either older or younger ages over a certain period of time, they are sometimes inconsistent (Fig. 7). The three largest inconsistencies involve age differences between $\delta\text{O}_2/\text{N}_2$ -, TAC- and $\delta^{18}\text{O}_{\text{atm}}$ -based chronologies reaching 4.15 to 8.3 kyr (Table 5). At 390 ka BP, a large 8.3 kyr discrepancy is observed between $\delta\text{O}_2/\text{N}_2$ - and $\delta^{18}\text{O}_{\text{atm}}$ -based chronologies. Over this

period, the low-resolution $\delta\text{O}_2/\text{N}_2$ record variations do not match its orbital target variations (two insolation minima against one $\delta\text{O}_2/\text{N}_2$ maximum; see Fig. 1). For this reason, the $\delta\text{O}_2/\text{N}_2$ age constraints identified between 480 and 350 ka BP were attached to a 6 kyr uncertainty (quarter of a recession period; Fig. 1). In contrast, the $\delta^{18}\text{O}_{\text{atm}}$ record agrees well with $\delta^{18}\text{O}_{\text{calcite}}$ (Fig. 3), and the uncertainty attached to the $\delta^{18}\text{O}_{\text{calcite}}$ inferred tie points over this interval is smaller. Hence, the new AICC2023 chronology suggests shifting AICC2012 towards older ages by 2.2 kyr, as per the $\delta^{18}\text{O}_{\text{atm}}$ -based chronology (Fig. 7). Around 550 ka BP, the TAC- and $\delta^{18}\text{O}_{\text{atm}}$ -based chronologies strongly diverge. This may be caused by the absence of TAC tie points due to the non-coincidence of TAC and ISI375 extrema (Fig. 3), while there is good agreement between $\delta^{18}\text{O}_{\text{atm}}$ and $\delta^{18}\text{O}_{\text{calcite}}$ records. Therefore, we decide to increase the uncertainty attached to the four TAC age constraints between 600 and 550 ka BP up to 6 kyr (Fig. 2), and AICC2023 follows the $\delta^{18}\text{O}_{\text{atm}}$ -based chronology, inducing older ages than AICC2012. At 765 ka BP, the discordance between $\delta\text{O}_2/\text{N}_2$ - (and TAC-) and $\delta^{18}\text{O}_{\text{atm}}$ -based chronologies is likely due to the poor quality of the records from the lowermost part of the core. Over these oldest time periods, $\delta^{18}\text{O}_{\text{atm}}$, TAC and $\delta\text{O}_2/\text{N}_2$ were tied up, respectively, with precession, inte-

grated insolation and insolation with a large uncertainty (6 to 10 kyr). This leads to a final chronology AICC2023, suggesting a larger chronological uncertainty than AICC2012 as well as younger ages (as per TAC and $\delta\text{O}_2/\text{N}_2$ chronologies) over MIS 18 and then older ages (as per $\delta^{18}\text{O}_{\text{atm}}$ chronology) over MIS 19.

4.1.3 Final chronology and uncertainty

The new AICC2023 chronology suggests significant age shifts when compared to AICC2012 over old periods, including 3.8 and 5 kyr shifts towards older ages around 800 and 690 ka BP as well as a 2.1 kyr shift towards younger ages around 730 ka BP. The chronology is also modified over MIS 5 and MIS 11, where AICC2023 is about 2 kyr older than AICC2012. These 2 kyr shifts are induced by $\delta\text{O}_2/\text{N}_2$ and $\delta^{18}\text{O}_{\text{atm}}$ dating constraints and stratigraphic links over MIS 5 and by TAC and $\delta^{18}\text{O}_{\text{atm}}$ constraints over MIS 11. When averaged over the past 800 kyr, the chronological uncertainty is reduced from 1.7 kyr for AICC2012 to 900 years here. Still, it remains significant (above 2 kyr) over MIS 11 and in the lowermost part of the core, between 800 and 650 ka BP. Specifically, between 800 and 670 ka BP, the uncertainty associated with the new AICC2023 timescale is sometimes larger than the AICC2012 uncertainty (Fig. 8). This is caused by a larger relative error attached to $\delta\text{O}_2/\text{N}_2$ and TAC age constraints as well as by the exclusion of the two redundant ^{10}Be age constraints at 780.3 and 798.3 ka BP associated with the Matuyama–Brunhes geomagnetic reversal event.

The age difference between ice and gas timescales (Δage) is 3 kyr on average, reaching its largest values (~ 4 kyr) during the cold eras of MISs 12, 8, 6 and 4 (at 440, 260, 145 and 70 ka BP, respectively; Fig. 9). A 4 kyr Δage is obtained at around 160 ka BP (Fig. 9), consistent with the use of new $\delta^{15}\text{N}$ data of Bréant et al. (2019), leading to a background scenario of LID that is 13 m smaller than the prior LID scenario used in AICC2012 between the depths of 1900 and 2000 m (Fig. 6). Using the definition of an interglacial period implying an EDC δD value surpassing the threshold of -403‰ (EPICA Community Members, 2004), we identify 10 substages of interglacials (MISs 1, 5e, 7a, 7c, 7e, 9e, 11c, 15a, 15e and 19; Fig. 9). The average duration of these substages is reduced by 320 years with the new AICC2023 timescale in comparison with the AICC2012 chronology (Fig. 9). More specifically, MISs 5e to 15a are shorter, while only MIS 15e and MIS 19 are longer. The largest decreases in duration affect the Last Interglacial (MIS 5e) and MIS 11c, whose lengths are decreased from 16.3 to 15.1 kyr and from 31.1 to 30.1 kyr, respectively, in agreement with the durations of 14.8 and 29.7 kyr proposed by Extier et al. (2018a).

4.2 Comparison with other chronologies

4.2.1 MIS 5 (from 130 to 80 ka BP)

When Veres et al. (2013) presented the AICC2012 chronology over the last climatic cycle, they identified a disagreement with the Greenland timescale GICC05-modelext between 115 and 100 ka BP. The comparison between the Greenland $\delta^{18}\text{O}_{\text{ice}}$ record and the $\delta^{18}\text{O}_{\text{calcite}}$ from U–Th-dated Alpine speleothems showed a delay of up to 2.7 kyr during the Dansgaard–Oeschger (D–O) events 23, 24 and 25. Later, this disagreement between abrupt changes in $\delta^{18}\text{O}_{\text{ice}}$ from NGRIP (Greenland surface temperature) and $\delta^{18}\text{O}_{\text{calcite}}$ from the Alps was re-evaluated based on a different use of $\delta^{18}\text{O}_{\text{atm}}$ in ice core chronology, and Extier et al. (2018a) presented better agreement between the two records with an older NGRIP timescale than AICC2012 by ~ 2200 years for D–O 23 to 25.

In Fig. 11, the NGRIP $\delta^{18}\text{O}_{\text{ice}}$ record is represented on the AICC2023 timescale and is compared to ancient and novel records of $\delta^{18}\text{O}_{\text{calcite}}$ from speleothems that grew along the northern rim of the Alps (NALPS; Boch et al., 2011; Moseley et al., 2020). Thanks to new $\delta\text{O}_2/\text{N}_2$ and $\delta^{18}\text{O}_{\text{atm}}$ age constraints, the new AICC2023 chronology is also older than AICC2012 between 115 and 100 ka BP and leads to improved agreement between the records along with a reduction in the uncertainty. This amelioration is particularly visible over D–O warmings 23 and 24, where the difference between NALPS and NGRIP chronologies is reduced from ~ 2000 years (AICC2012) to 430 and 325 years (AICC2023), respectively (Table 6).

The Greenland Interstadial (GI) 25 can be subdivided in three substages: GI-25a, GI-25-b and GI-25-c, where GI-25a is the earliest glacial so-called “rebound event” (Capron et al., 2010). This latter consists of a brief warm–wet excursion during the slow cooling trend of the longer GI-25 period before jumping back to a cool–dry climate. The GI-25a warm–wet interval corresponds to a temperature increase in Greenland and continental Europe and is hence identified by a positive excursion in NGRIP and NALPS $\delta^{18}\text{O}$ records (D–O 25 rebound) (Boch et al., 2011; Capron et al., 2012). At lower latitudes, this rebound likely affected the rainfall amount variations, as exhibited by the abrupt decrease in the $\delta^{18}\text{O}_{\text{calcite}}$ from a U–Th-dated Sardinian stalagmite from Bue Marino Cave (BMS1; Columbu et al., 2017). The 2 kyr shift in the new AICC2023 chronology towards older ages improves the coherency between NALPS, NGRIP and BMS1 timescales over the GI-25a onset (traceable in the $\delta^{18}\text{O}$ series; Fig. 10). The age discrepancy is reduced from ~ 3600 years (between AICC2012 and BMS1 timescale) to 1640 years (between AICC2023 and BMS1 timescale; Table 6).

Between 128 and 103 ka BP, the comparison between the AICC2012 timescale and the novel Dome Fuji ice core DF2021 chronology indicates that AICC2012 is likely too

Table 5. Description of the inconsistencies between $\delta\text{O}_2/\text{N}_2$ -, TAC- and $\delta^{18}\text{O}_{\text{atm}}$ -based chronologies. The age shift suggested by each dating tool with respect to AICC2012 age is detailed. The age position of the disagreement is given as per AICC2023. We did not highlight inconsistencies between $\delta\text{O}_2/\text{N}_2$ - and TAC-based chronologies as they remain within their respective orbital uncertainty.

$\delta\text{O}_2/\text{N}_2$	$\delta^{18}\text{O}_{\text{atm}}$		
	Non-coherent	Non-coherent	Non-coherent
TAC	Coherent	Non-coherent	Non-coherent
Disagreement type	$\delta\text{O}_2/\text{N}_2$ chronology younger than AICC2012 by 4700 years	TAC (and $\delta\text{O}_2/\text{N}_2$) chronology younger than AICC2012 by 2400 (and 800) years	$\delta\text{O}_2/\text{N}_2$ (and TAC) chronology younger than AICC2012 by 2850 (and 1300) years
	$\delta^{18}\text{O}_{\text{atm}}$ chronology older than AICC2012 by 3600 years	$\delta^{18}\text{O}_{\text{atm}}$ chronology older than AICC2012 by 1700 years	$\delta^{18}\text{O}_{\text{atm}}$ chronology older than AICC2012 by 2800 years
Interval of disagreement (ka BP)	430–350 (MIS 11)	580–510 (MIS 14)	800–700 (MISs 19–18)

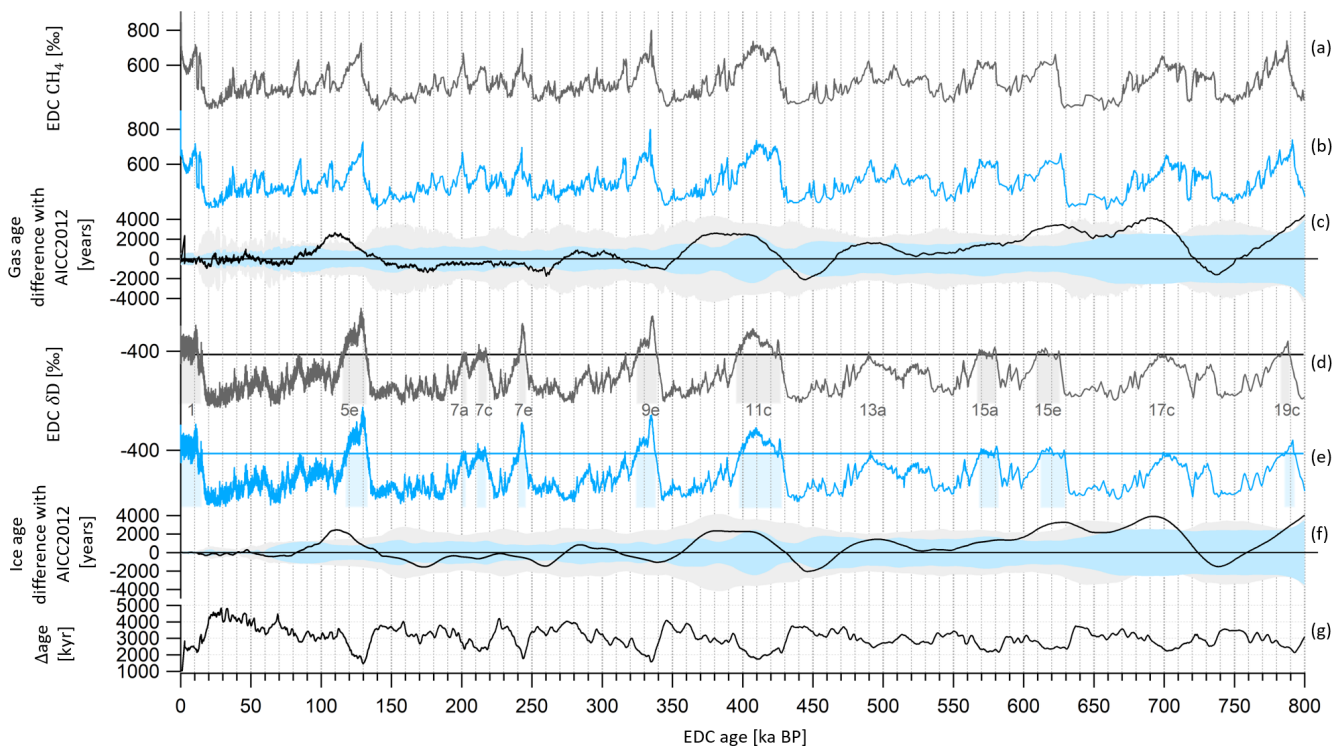


Figure 9. EDC gas and ice records on AICC2023 (blue) and AICC2012 (black) timescales over the last 800 kyr. **(a)** EDC CH_4 (Loulergue et al., 2008) on AICC2012 and **(b)** AICC2023 gas timescales. **(c)** Gas age difference AICC2023–AICC2012. Gray and blue envelopes are AICC2012 and AICC2023 chronological 1σ uncertainties, respectively. **(d)** EDC δD (Jouzel et al., 2007) on AICC2012 and **(e)** AICC2023 ice timescales. Gray and blue rectangles indicate interglacial periods defined when δD is greater than the threshold of -403‰ (horizontal lines) (EPICA Community Members, 2004). Interglacials are numbered from MISs 1 to 19 (Berger et al., 2016). **(f)** Ice age difference AICC2023–AICC2012. **(g)** Age difference between ice and gas AICC2023 timescales (Δage).

Table 6. Timing of D–O warmings 23 and 24 and D–O 25 rebound event onset. The GICC05-modelext age uncertainty is undetermined.

Event	Timing (a BP) and error (years)					
	NGRIP ice core timescale				Speleothem timescale	
	GICC05-modelext (Wolff et al., 2010)	AICC2012 (Veres et al., 2013)	Extier et al. (2018a)	AICC2023 (this study)	BMS1 (Columbu et al., 2017)	NALPS (Boch et al., 2011)
D–O 23 warming	103 995	101 850 ± 1310	104 090 ± 1200	103 980 ± 930	Not recorded	103 550 ± 375
D–O 24 warming	108 250	105 850 ± 1330	108 010 ± 1200	107 975 ± 850	Not recorded	108 300 ± 450
D–O 25 rebound onset	110 960	108 100 ± 1410	110 280 ± 1200	110 120 ± 900	111 760 ± 450	111 780 ± 630

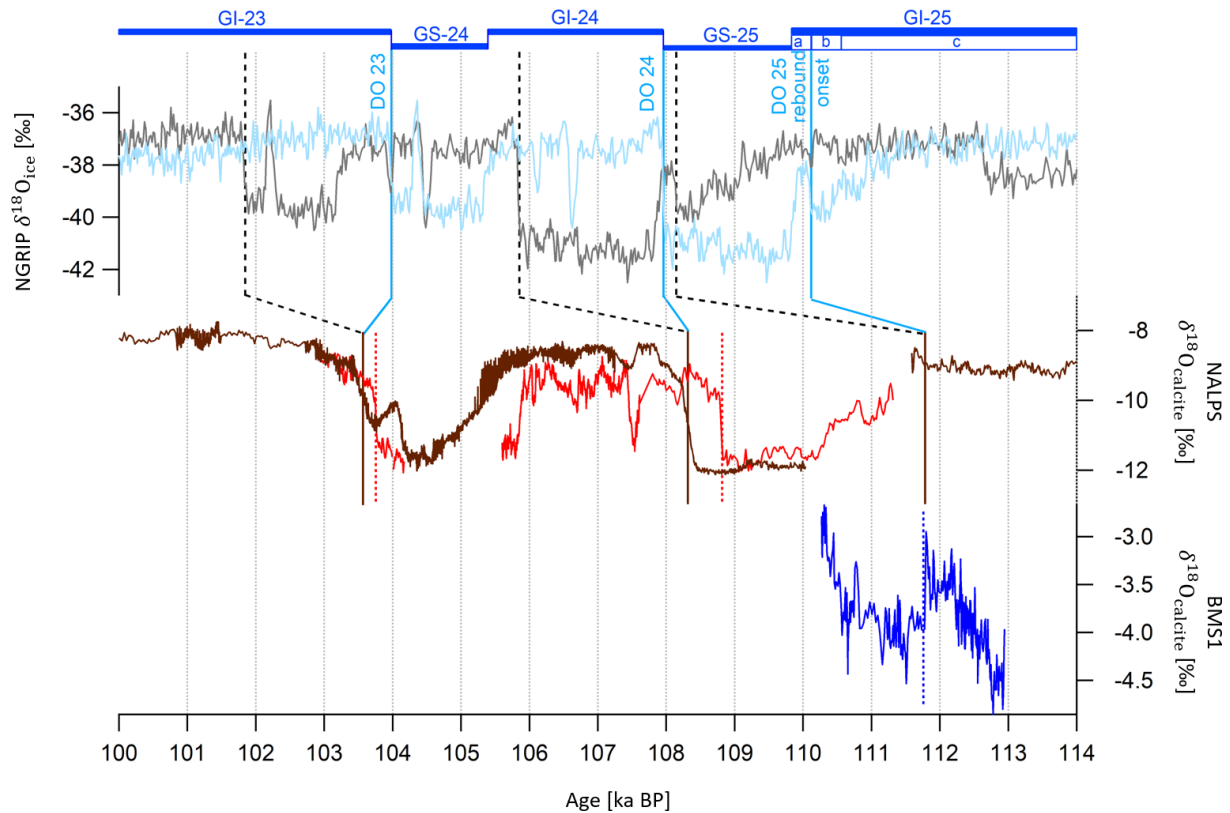


Figure 10. Northern Alpine speleothems (NALPS) and Bue Marino stalagmite (BMS1) $\delta^{18}\text{O}_{\text{calcite}}$ records and NGRIP $\delta^{18}\text{O}_{\text{ice}}$ evolution between 114 and 100 ka BP. NGRIP $\delta^{18}\text{O}_{\text{ice}}$ data by Andersen et al. (2004) on AICC2012 (gray) and AICC2023 (blue) chronologies. NALPS $\delta^{18}\text{O}_{\text{calcite}}$ data by Moseley et al. (2020) (red) and Boch et al. (2011) (brown). BMS1 $\delta^{18}\text{O}_{\text{calcite}}$ data by Columbu et al. (2017) (dark blue). Vertical bars indicate D–O 25 rebound, D–O 24 and D–O 23 warmings at the onset of the GI-25a warm-wet substage, GI-24, and GI-23. They correspond to abrupt increases in the NALPS $\delta^{18}\text{O}_{\text{calcite}}$ and NGRIP $\delta^{18}\text{O}_{\text{ice}}$ records and to a decrease in the BMS1 $\delta^{18}\text{O}_{\text{calcite}}$ series (for the GI-25a onset). Dashed black bars and blue bars show increases in $\delta^{18}\text{O}_{\text{ice}}$, respectively, on AICC2012 and AICC2023 chronologies. Brown bars and dotted red bars show increases in NALPS $\delta^{18}\text{O}_{\text{calcite}}$ datasets. The dotted blue bar indicates the decrease in BMS1 $\delta^{18}\text{O}_{\text{calcite}}$. GI–GS (Greenland stadial) boundaries and GI-25 subdivision are indicated on the new AICC2023 chronology by horizontal bars.

young by up to 4 kyr. Here, thanks to new highly resolved $\delta\text{O}_2/\text{N}_2$ data and to the alignment of $\delta^{18}\text{O}_{\text{atm}}$ and $\delta^{18}\text{O}_{\text{calcite}}$ records, we improve the consistency between AICC2023 and DF2021, now agreeing within 1.7 kyr over MIS 5e (Fig. 11). With the new chronologies, the records of $\delta^{18}\text{O}_{\text{atm}}$ and $\delta\text{O}_2/\text{N}_2$ from the Dome Fuji and EDC ice cores

show synchronous variations between 140 and 115 ka BP, although the $\delta\text{O}_2/\text{N}_2$ measurements from EDC are more scattered than DF data due to the use of smaller samples (see Sect. S1 in the Supplement). However, δD records are still slightly discordant, and the EDC record lags DF by up to 1700 years over MIS 5e and at the onset of the Antarctic

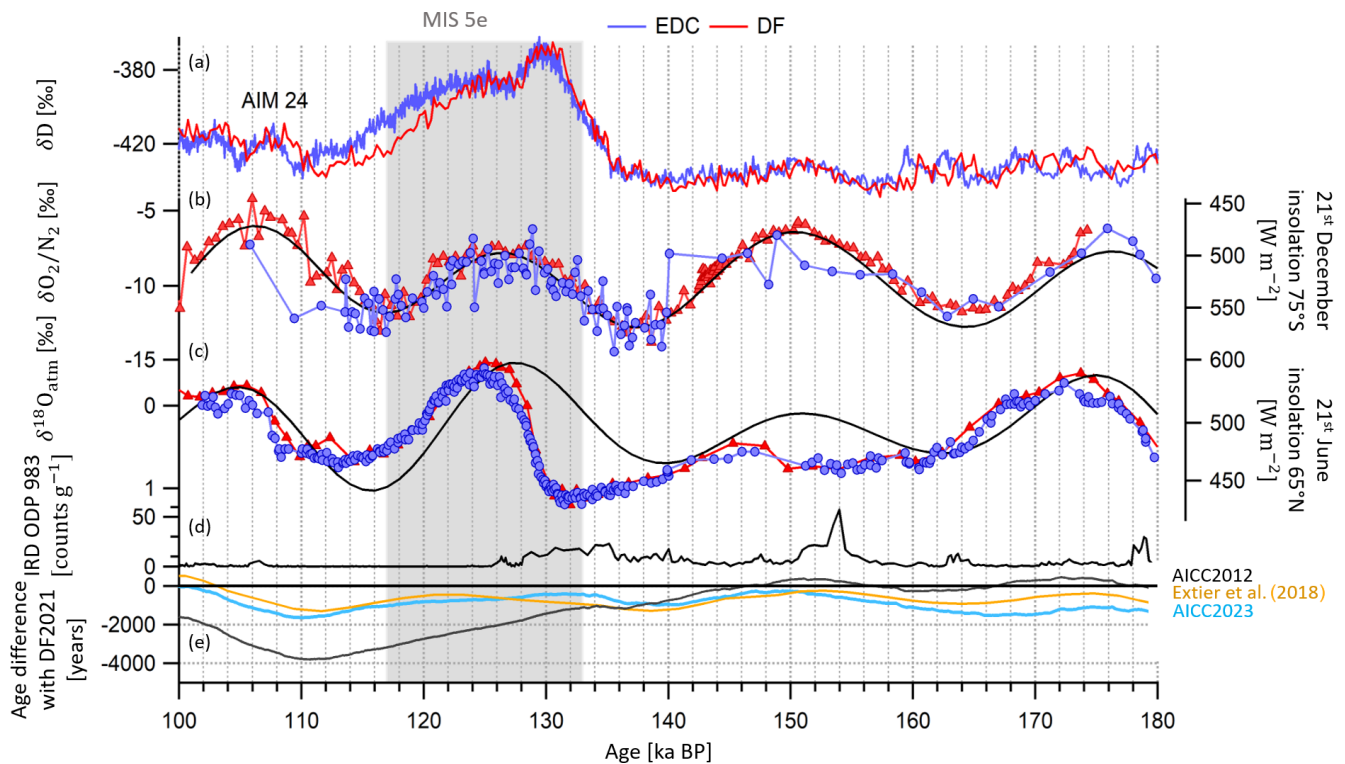


Figure 11. Evolution of EDC and DF records on AICC2023 and DF2021 chronologies between 180 and 100 ka BP. **(a)** δD records from DF (red; Uemura et al., 2018) and EDC (purple; Jouzel et al., 2007). **(b)** $\delta O_2/N_2$ records from DF (red triangles; Oyabu et al., 2022) and EDC (purple circles; this work). **(c)** $\delta^{18}O_{atm}$ records from DF (red triangles; Kawamura et al., 2007) and EDC (purple circles; this work). DF and EDC records are represented on DF2021 and AICC2023 timescales. **(d)** IRD from ODP 983 (Barker et al., 2019, 2021). **(e)** Ice age difference between DF2021 and (i) AICC2023 (blue), (ii) Extier et al. (2018a) chronology (orange) and (iii) AICC2012 (black). The age difference is calculated as per EDC age – DF2021 age. DF2021 age is transferred onto the EDC ice core via the volcanic synchronization of Fujita et al. (2015). The gray rectangle indicates MIS 5e.

Isotope Maximum (AIM) 24 (Fig. 11), suggesting some remaining chronology problems (AIM 24 onset) or regional climatic differences (δD decrease over MIS 5e). Between 180 and 150 ka BP, AICC2012 shows better agreement with the DF2021 chronology than the new AICC2023 chronology, which suggests younger ages as per TAC and $\delta^{18}O_{atm}$ dating constraints.

4.2.2 MIS 11 (from 425 to 375 ka BP)

Over the time interval from 430 to 360 ka BP, encompassing MIS 11, the new AICC2023 chronology predicts older ages than AICC2012 (by up to 2 kyr) with a diminished uncertainty (from 3.9 to 1.7 kyr). This shift towards older ages is induced by $\delta^{18}O_{atm} - \delta^{18}O_{calcite}$ (Hulu, Sambao and Dongge caves) tie points at 377.3, 385.7 and 398.5 ka BP and by the TAC age constraint at 362.1 ka BP (Figs. 7 and 12). As a result, two major rises in the EDC atmospheric CO_2 and CH_4 concentration records (corresponding to carbon dioxide jumps CDJ+ 11a.3 and 11a.4, labeled as per Nehrbass-Ahles et al., 2020) occur at 385.6 ± 1.4 and 389.8 ± 1.5 ka BP (Fig. 12). These two rapid jumps in CO_2 and CH_4 are

better aligned with two abrupt decreases in the highly resolved $\delta^{18}O_{calcite}$ record of Zhao et al. (2019) from Yongxing cave (independently dated with ^{230}Th at 386.4 ± 3.1 and 390.0 ± 3.0 ka BP) than when using the AICC2012 chronology (improvement by ~ 800 years). Such millennial-scale synchronicity is expected between CH_4 and $\delta^{18}O_{calcite}$ series from Chinese speleothems as they are both influenced by Asian monsoon area displacements (and associated methane emissions from wetlands) (Sánchez Goñi et al., 2008).

4.2.3 MIS 19 (from 780 to 760 ka BP)

The Matuyama–Brunhes event (geomagnetic field reversal) is reflected by a globally synchronous event in the ^{10}Be signal: an abrupt termination of the large ^{10}Be peak following a long-term increasing trend recorded in both ice and sedimentary cores (Giaccio et al., 2023). The $^{40}Ar/^{39}Ar$ age-constrained chronology of a lacustrine succession from Sulmona basin (Giaccio et al., 2023) gives an age of 770.9 ± 1.6 ka BP for the ^{10}Be peak termination. The new AICC2023 chronology provides an estimate of 767.3 ± 3 ka BP for the same ^{10}Be peak termination, an age which is closer to the

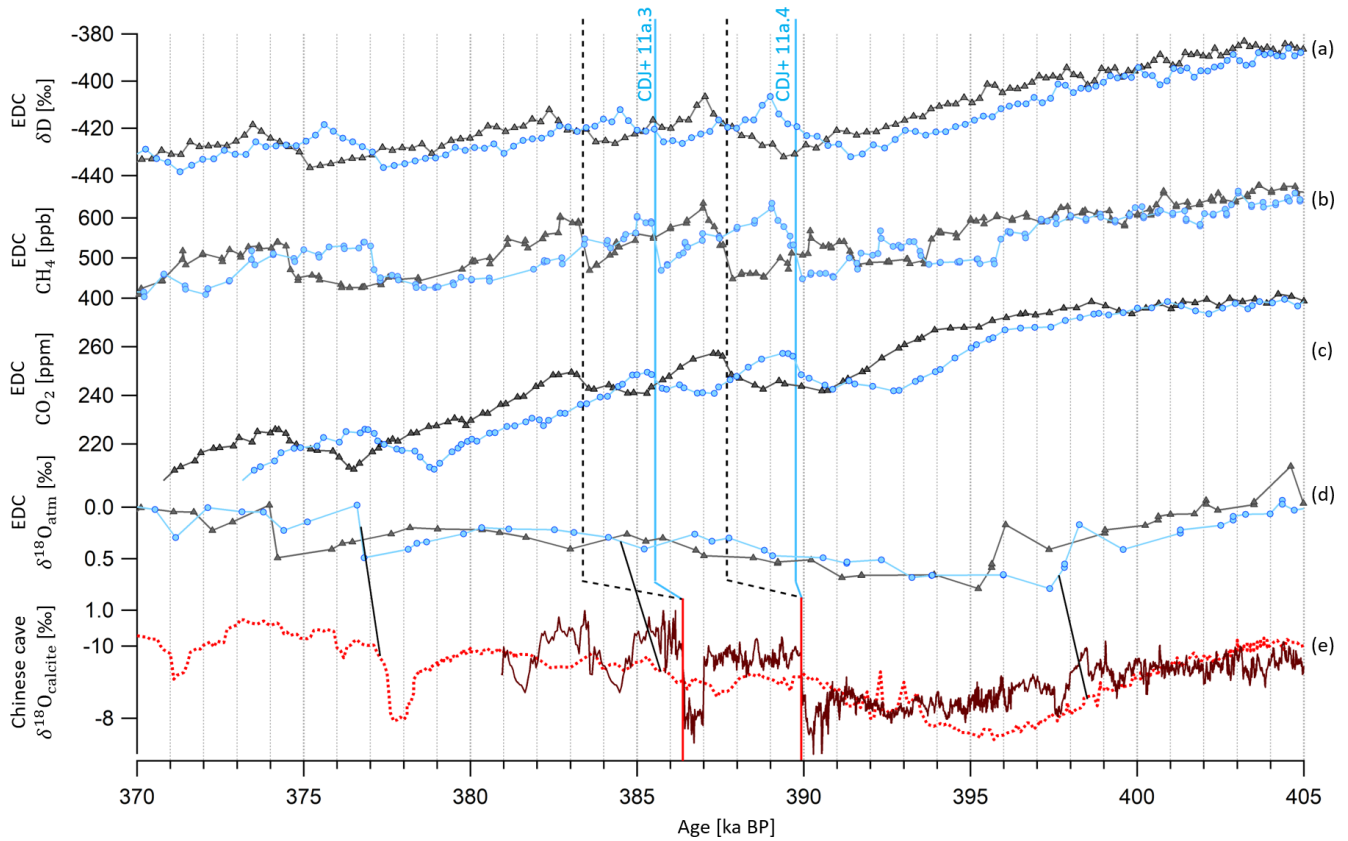


Figure 12. Evolution of climate tracers from the EDC ice core and Yongxing cave stalagmites between 405 and 370 ka BP. EDC records of (a) δD , (b) CH_4 (Nehrbass-Ahles et al., 2020), (c) CO_2 (Nehrbass-Ahles et al., 2020) and (d) $\delta^{18}O_{atm}$ on AICC2012 (gray triangles) and AICC2023 (blue circles) chronologies. (e) Speleothem $\delta^{18}O_{calcite}$ from Hulu, Dongge and Sambaog cave, used to constrain AICC2023 (dashed red curve; Cheng et al., 2016), and from Yongxing cave, independently dated with ^{230}Th dating and annual band counting (plain brown curve; Zhao et al., 2019). CDJ+ is labeled as per Nehrbass-Ahles et al. (2020). Vertical dashed black and blue bars show jumps in CO_2 on AICC2012 and AICC2023 chronologies, respectively; vertical red bars show corresponding decreases in $\delta^{18}O_{calcite}$. Black lines show the three tie points between $\delta^{18}O_{atm}$ and $\delta^{18}O_{calcite}$ (Cheng et al., 2016) used to constrain AICC2023.

$^{40}Ar/^{39}Ar$ age evaluation than the AICC2012 chronology estimate (766.2 ± 3 ka BP; Fig. 13). The new AICC2023 chronology indeed indicates an increasingly older age than AICC2012 over MIS 19 (from 790 to 761 ka BP) due to the new $\delta^{18}O_{atm}$ -based timescale (Fig. 7).

We acknowledge that the Chiba composite section also provides a high-resolution ^{10}Be record, as the Montalbano Jonico marine section (Simon et al., 2017), the Sulmona basin succession and the EDC ice core do. Although the ^{10}Be flux records of Sulmona and EDC show a similar pattern and the same asymmetrical shape (i.e., slow increase followed by an abrupt ^{10}Be peak termination), the sharp termination is less obvious in the Montalbano Jonico and Chiba records. In addition, the Chiba and Montalbano Jonico records are shallow marine deposits; hence expression of paleoclimatic proxies can be amplified and/or hampered by fluvial input (Nomade et al., 2019). Finally, substantial adjustments, up to 10.2 ± 5.5 kyr (i.e., exceeding the related uncertainty), are required to fit the millennial-scale variability in the Chiba

record within the Sulmona radioisotopic-based chronology. Giaccio et al. (2023) point out that, despite these relatively large temporal offsets for the Chiba record, the Sulmona-based age model is more linear and describes a simpler, and likely more realistic, history of sediment accumulation. Therefore, we rather use the Sulmona succession to compare with AICC2023.

5 Conclusions

In this study, we have established a new reference chronology for the EDC ice core, AICC2023, covering the last 800 kyr, which is consistent with the official GICC05 timescale over the last 60 kyr. A valuable update of the chronology construction has been the compilation of chronological and glaciological information, including new age markers from recent high-resolution measurements on the EDC ice core. As a result, the chronological uncertainty is reduced from 1.7 kyr in AICC2012 (standard deviation of 995 years) to 900 years

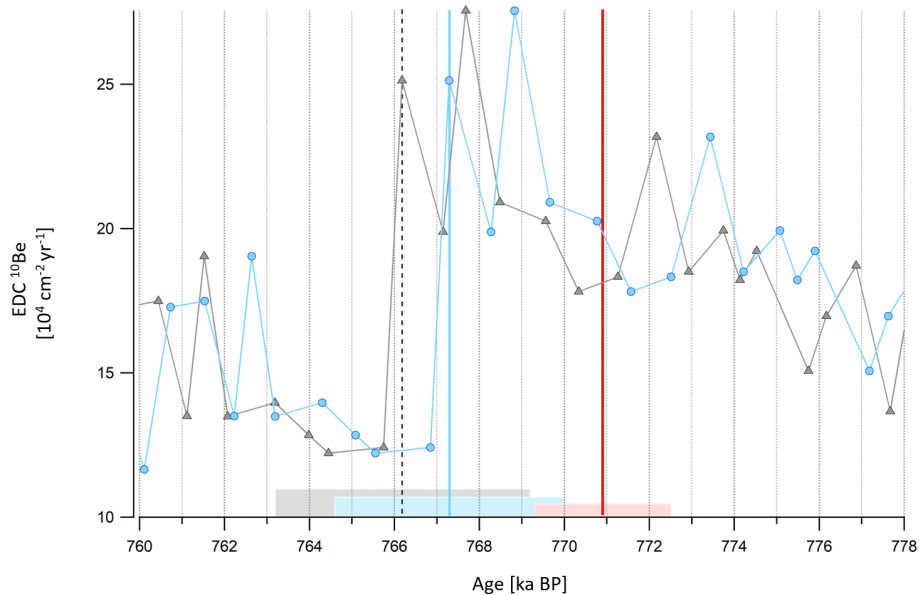


Figure 13. EDC ^{10}Be record on AICC2012 and AICC2023 chronologies between 778 and 760 ka BP. Vertical gray and blue bars indicate the age of the abrupt EDC ^{10}Be peak termination on AICC2012 (gray triangles) and AICC2023 (blue circles) chronologies, respectively. The horizontal gray and blue rectangles correspond to AICC2012 and AICC2023 2σ confidence intervals (± 3 and ± 2.7 ka, respectively). The vertical red bar and horizontal rectangle show the ^{10}Be peak termination age and its 2σ confidence interval (770.9 ± 1.6 ka BP; Giaccio et al., 2023).

on average in AICC2023 (standard deviation of 720 years). A total of 90 % of the new AICC2023 timescale is associated with an uncertainty lower than 2 kyr, compared to only 60 % in the AICC2012 chronology. First, the distinct orbital chronologies derived from $\delta\text{O}_2/\text{N}_2$, TAC and $\delta^{18}\text{O}_{\text{atm}}$ are coherent within their respective uncertainties except over three periods, including MIS 11 and MIS 19. Second, new $\delta^{15}\text{N}$ measurements along with new sensitivity tests with the firn densification model described by Bréant et al. (2017) and adapted for the EDC ice core provide the most plausible evolution of LID at EDC over the last 800 kyr.

The majority of the age disparities observed between the AICC2023 and AICC2012 chronologies are smaller than 500 years (median), hence minor given the average uncertainty in AICC2012 (1.7 kyr). Exceptions are significant age shifts reaching 3.4, 3.8 and 5 kyr towards older ages suggested over MIS 15, MIS 17 and MIS 19, respectively. However, most of these age discrepancies lead to an improved coherency between the new EDC timescale and independent absolute chronologies derived for other climate archives, especially over the following periods: MIS 5, MIS 11 and MIS 19.

We have identified time intervals where building the chronology is more complicated, such as termination VI (from 540 to 456 ka BP) and from 800 to 600 ka BP, corresponding to the lowermost section of the core, and we would like to draw attention to the requirement for new measurements over these periods. In particular, the links between the variability in $\delta\text{O}_2/\text{N}_2$ and TAC records and their orbital tar-

gets are not obvious over the 800–600 ka BP period (Fig. 1). This may be due to bad quality of the ice and/or diffusion of gases through the ice matrix (Bereiter et al., 2009). The imprecision of the signal may also be partially explained by the limited temporal resolution of the existing dataset in this deep section. To address these issues, highly resolved $\delta\text{O}_2/\text{N}_2$ and TAC measurements are needed in the lowermost section of the EDC ice core. In addition, $\delta\text{O}_2/\text{N}_2$ from ice samples over the period covering TVI should also be analyzed to investigate the mismatch between old and new datasets (Fig. 1).

A final important aspect would be to further extend the Paleochrono dating experiment by implementing other ice cores such as Dome Fuji, WAIS Divide and NEEM (North Greenland Eemian), for which a large amount of chronological and glaciological information is now available.

Code availability. The input and output files created during this study to obtain the new AICC2023 chronology are available on Zenodo (<https://doi.org/10.5281/zenodo.10091515>; Bouchet et al., 2023a). They include both updated and old age markers.

Data availability. A folder is available for each site in the PANGAEA data repository (Bouchet et al., 2023b). It includes new gas and ice age scales and their uncertainties as well as new gas data along with background and analyzed scenarios for accumulation rate, thinning function and

LID. A correspondence between AICC2023 and WD2014 age models is also given (<https://doi.org/10.1594/PANGAEA.961017>; Bouchet et al., 2023b). The new $\delta^{18}\text{O}_{\text{atm}}$ and $\delta\text{O}_2/\text{N}_2$ datasets for EDC are also available in the PANGAEA data repository (<https://doi.org/10.1594/PANGAEA.961023>; Bouchet et al., 2023c).

Supplement. The supplement related to this article is available online at: <https://doi.org/10.5194/cp-19-2257-2023-supplement>.

Author contributions. MB wrote the manuscript with the contribution of all co-authors. AL and FP contributed to the conceptualization of the study and the methodology. Measurements on the EDC ice core were performed at the LSCE by AG, FP, RJ and EF. EC, DR, VYL and MFL contributed to the collection, analysis and interpretation of the TAC record. ML provided resources. The krypton analysis was conducted by WJ, FR, ZTL and GMY. TE, AS, EL and PM contributed to the validation of the study.

Competing interests. At least one of the (co-)authors is a member of the editorial board of *Climate of the Past*. The peer-review process was guided by an independent editor, and the authors also have no other competing interests to declare.

Disclaimer. Publisher's note: Copernicus Publications remains neutral with regard to jurisdictional claims made in the text, published maps, institutional affiliations, or any other geographical representation in this paper. While Copernicus Publications makes every effort to include appropriate place names, the final responsibility lies with the authors.

Special issue statement. This article is part of the special issue "Ice core science at the three poles (CP/TC inter-journal SI)". It is a result of the IPICS 3rd Open Science Conference, Crans-Montana, Switzerland, 2–7 October 2022.

Acknowledgements. Krypton analysis has been supported by the Innovation Program for Quantum Science and Technology (2021ZD0303101) and by the National Natural Science Foundation of China (41727901). Development of the Paleochrono model was funded by CNRS/INSU/LEFE projects IceChrono and CO2Role. Emilie Capron and Etienne Legrain acknowledge financial support from the French National Research Agency under the "Programme d'Investissements d'Avenir" (ANR-19-MPGA-0001), through the Make Our Planet Great Again HOTCLIM project, as well as the financial support from the AXA research fund. We also acknowledge the assistance from the European Union FP5-EESD program (grant agreement no. EVK2-CT-2000-00077; EPICA), the French National Research Agency program "NE-ANDROOTS" (ANR-19-CE27-0011) and the French Polar Institute project no. 902 (GLACIOLOGIE CONCORDIA). Our special thanks go to Markus Grimmer, Marcel Haeberli, Daniel Baggen-

stos, Jochen Schmitt, Matthias Baumgartner, Hubertus Fischer, Kenji Kawamura and Ikumi Oyabu for sharing their thoughts and data and sustaining the discussion on the construction of new ice core age scales and to Sébastien Nomade and Alison Pereira for providing advice and expertise in geochronology.

Financial support. This research has received funding from the European Research Council under the European Union Horizon 2020 Excellent Science program (H2020/20192024)/ERC grant agreement no. 817493 (ERC ICORDA).

Review statement. This paper was edited by Christo Buizert and reviewed by two anonymous referees.

References

- Alley, R. B.: Firm densification by grain-boundary sliding: a first model, *Journal de Physique Colloque*, 48, 1–249, <https://doi.org/10.1051/JPHYSCOL:1987135>, 1987.
- Andersen, K. K., Azuma, N., Barnola, J.-M., Bigler, M., Biscaye, P., Caillon, N., Chappellaz, J., Clausen, H. B., Dahl-Jensen, D., Fischer, H., Flückiger, J., Fritzsche, D., Fujii, Y., Goto-Azuma, K., Grønvold, K., Gundestrup, N. S., Hansson, M., Huber, C., Hvidberg, C. S., Johnsen, S. J., Jonsell, U., Jouzel, J., Kipfstuhl, S., Landais, A., Leuenberger, M., Lorrain, R., Masson-Delmotte, V., Miller, H., Motoyama, H., Narita, H., Popp, T., Rasmussen, S. O., Raynaud, D., Rothlisberger, R., Ruth, U., Samyn, D., Schwander, J., Shoji, H., Siggard-Andersen, M.-L., Steffensen, J. P., Stocker, T., Sveinbjörnsdóttir, A. E., Svensson, A., Takata, M., Tison, J.-L., Thorsteinsson, Th., Watanabe, O., Wilhelms, F., White, J. W. C., and N. G. I. C. P. members: High-resolution record of Northern Hemisphere climate extending into the last interglacial period, *Nature*, 431, 147–151, <https://doi.org/10.1038/nature02805>, 2004.
- Andersen, K. K., Svensson, A., Johnsen, S. J., Rasmussen, S. O., Bigler, M., Röthlisberger, R., Ruth, U., Siggaard-Andersen, M.-L., Peder Steffensen, J., Dahl-Jensen, D., Vinther, B. M., and Clausen, H. B.: The Greenland Ice Core Chronology 2005, 15–42 ka. Part 1: constructing the time scale, *Quaternary Sci. Rev.*, 25, 3246–3257, <https://doi.org/10.1016/j.quascirev.2006.08.002>, 2006.
- Arnaud, L., Barnola, J. M., and Duval, P.: Physical modeling of the densification of snow/firm and ice in the upper part of polar ice sheets, *Physics of Ice Core Records*, 285–305, <http://hdl.handle.net/2115/32472> (last access: 9 November 2023), 2000.
- Arthern, R. J., Vaughan, D. G., Rankin, A. M., Mulvaney, R., and Thomas, E. R.: In situ measurements of Antarctic snow compaction compared with predictions of models, *J. Geophys. Res.-Earth*, 115, 3011, <https://doi.org/10.1029/2009JF001306>, 2010.
- Baglin, C. M.: Nuclear Data Sheets for $A = 81$, *Nucl. Data Sheets*, 109, 2257–2437, <https://doi.org/10.1016/J.NDS.2008.09.001>, 2008.
- Barker, S., Knorr, G., Conn, S., Lordsmith, S., Newman, D., and Thornalley, D.: Early interglacial legacy of deglacial climate instability, *Paleoceanogr. Paleoclimatol.*, 34, 1455–1475, <https://doi.org/10.1029/2019PA003661>, 2019.

- Barker, S., Zhang, X., Jonkers, L., Lordsmith, S., Conn, S., and Knorr, G.: Strengthening Atlantic inflow across the mid-Pleistocene transition, *Paleoceanogr. Paleoclimatol.*, 36, 2021e2020PA004200, <https://doi.org/10.1029/2020PA004200>, 2021.
- Barnola, J.-M., Pimienta, P., Raynaud, D., and Korotkevich, Y. S.: CO₂-climate relationship as deduced from the Vostok ice core: a re-examination based on new measurements and on a re-evaluation of the air dating, *Tellus B*, 43, 83–90, <https://doi.org/10.1034/J.1600-0889.1991.T01-1-00002.X>, 1991.
- Baumgartner, M., Kindler, P., Eicher, O., Floch, G., Schilt, A., Schwander, J., Spahni, R., Capron, E., Chappellaz, J., Leuenberger, M., Fischer, H., and Stocker, T. F.: NGRIP CH₄ concentration from 120 to 10 kyr before present and its relation to a $\delta^{15}\text{N}$ temperature reconstruction from the same ice core, *Clim. Past*, 10, 903–920, <https://doi.org/10.5194/cp-10-903-2014>, 2014.
- Bazin, L., Landais, A., Lemieux-Dudon, B., Toyé Mahamadou Kele, H., Veres, D., Parrenin, F., Martinerie, P., Ritz, C., Capron, E., Lipenkov, V., Loutre, M.-F., Raynaud, D., Vinther, B., Svensson, A., Rasmussen, S. O., Severi, M., Blunier, T., Leuenberger, M., Fischer, H., Masson-Delmotte, V., Chappellaz, J., and Wolff, E.: An optimized multi-proxy, multi-site Antarctic ice and gas orbital chronology (AICC2012): 120–800 ka, *Clim. Past*, 9, 1715–1731, <https://doi.org/10.5194/cp-9-1715-2013>, 2013.
- Bazin, L., Landais, A., Capron, E., Masson-Delmotte, V., Ritz, C., Picard, G., Jouzel, J., Dumont, M., Leuenberger, M., and Prié, F.: Phase relationships between orbital forcing and the composition of air trapped in Antarctic ice cores, *Clim. Past*, 12, 729–748, <https://doi.org/10.5194/cp-12-729-2016>, 2016.
- Bender, M. L.: Orbital tuning chronology for the Vostok climate record supported by trapped gas composition, *Earth Planet. Sc. Lett.*, 204, 275–289, [https://doi.org/10.1016/S0012-821X\(02\)00980-9](https://doi.org/10.1016/S0012-821X(02)00980-9), 2002.
- Bender, M. L., Barnett, B., Dreyfus, G., Jouzel, J., and Porcelli, D.: The contemporary degassing rate of ⁴⁰Ar from the solid Earth, *P. Natl. Acad. Sci. USA*, 105, 8232–8237, <https://doi.org/10.1073/PNAS.0711679105>, 2008.
- Bereiter, B., Schwander, J., Lüthi, D., and Stocker, T. F.: Change in CO₂ concentration and O₂/N₂ ratio in ice cores due to molecular diffusion, *Geophys. Res. Lett.*, 36, 2009L05703, <https://doi.org/10.1029/2008GL036737>, 2009.
- Berger, A.: Long-Term Variations of Daily Insolation and Quaternary Climatic Changes, *J. Atmos. Sci.*, 35, 2362–2367, [https://doi.org/10.1175/1520-0469\(1978\)035<2362:LTVODI>2.0.CO;2](https://doi.org/10.1175/1520-0469(1978)035<2362:LTVODI>2.0.CO;2), 1978.
- Berger, B., Crucifix, M., Hodell, D. A., Mangili, C., McManus, J. F., Otto-Bliesner, B., Pol, K., Raynaud, D., Skinner, L. C., Tzedakis, P. C., Wolff, E. W., Yin, Q. Z., Abe-Ouchi, A., Barbante, C., Brovkin, V., Cacho, I., Capron, E., Ferretti, P., Ganopolski, A., Girmalt, J. O., Hönisch, B., Kawamura, K. A., Landais, A., Margari, V., Martrat, B., Masson-Delmotte, V., Mokeddem, Z., Parrenin, F., Prokopenko, A. A., Rashid, H., Schulz, M., and Vazquez Riveiros, N.: Interglacials of the last 800,000 years, *Rev. Geophys.*, 54, 162–219, <https://doi.org/10.1002/2015RG000482>, 2016.
- Boch, R., Cheng, H., Spötl, C., Edwards, R. L., Wang, X., and Häuselmann, P.: NALPS: a precisely dated European climate record 120–60 ka, *Clim. Past*, 7, 1247–1259, <https://doi.org/10.5194/cp-7-1247-2011>, 2011.
- Bouchet, M., Parrenin, F., and Landais, A.: AICC2023 dating experiment using Paleochrono model, Zenodo [code], <https://doi.org/10.5281/zenodo.10091515>, 2023a.
- Bouchet, M., Landais, A., Grisart, A., Parrenin, F., Prié, F., Jacob, R., Fourné, E., Capron, E., Raynaud, D., Lipenkov, V. Y., Loutre, M.-F., Extier, T., Svensson, A. M., Martinerie, P., Leuenberger, M. C., Jiang, W., Ritterbusch, F., Lu, Z.-T., and Yang, G.-M.: The Antarctic ice core chronology (AICC2023), PANGAEA [data set], <https://doi.org/10.1594/PANGAEA.961017>, 2023b.
- Bouchet, M., Grisart, A., Landais, A., Prié, F., Jacob, R., and Fourné, E.: $\delta\text{O}_2/\text{N}_2$ and $\delta^{18}\text{O}$ of O₂ from EPICA Dome C ice core (Antarctica) (0–800 ka), PANGAEA [data set], <https://doi.org/10.1594/PANGAEA.961023>, 2023c.
- Bréant, C., Martinerie, P., Orsi, A., Arnaud, L., and Landais, A.: Modelling firn thickness evolution during the last deglaciation: constraints on sensitivity to temperature and impurities, *Clim. Past*, 13, 833–853, <https://doi.org/10.5194/cp-13-833-2017>, 2017.
- Bréant, C., Landais, A., Orsi, A., Martinerie, P., Extier, T., Prié, F., Stenni, B., Jouzel, J., Masson-Delmotte, V., and Leuenberger, M.: Unveiling the anatomy of Termination 3 using water and air isotopes in the Dome C ice core, East Antarctica, *Quaternary Sci. Rev.*, 211, 156–165, <https://doi.org/10.1016/J.QUASCIREV.2019.03.025>, 2019.
- Buizert, C.: The Ice Core Gas Age-Ice Age Difference as a Proxy for Surface Temperature, *Geophys. Res. Lett.*, 48, e2021GL094241, <https://doi.org/10.1029/2021GL094241>, 2021.
- Buizert, C., Sowers, T., and Blunier, T.: Assessment of diffusive isotopic fractionation in polar firn, and application to ice core trace gas records, *Earth Planet. Sc. Lett.*, 361, 110–119, <https://doi.org/10.1016/J.EPSL.2012.11.039>, 2013.
- Buizert, C., Baggenstos, D., Jiang, W., Purtschert, R., Petrenko, V. V., Lu, Z. T., Müller, P., Kuhl, T., Lee, J., Severinghaus, J. P., and Brook, E. J.: Radiometric ⁸¹Kr dating identifies 120,000-year-old ice at Taylor Glacier, Antarctica, *P. Natl. Acad. Sci. USA*, 111, 6876–6881, <https://doi.org/10.1073/pnas.1320329111>, 2014.
- Buizert, C., Cuffey, K. M., Severinghaus, J. P., Baggenstos, D., Fudge, T. J., Steig, E. J., Markle, B. R., Winstrup, M., Rhodes, R. H., Brook, E. J., Sowers, T. A., Clow, G. D., Cheng, H., Edwards, R. L., Sigl, M., McConnell, J. R., and Taylor, K. C.: The WAIS Divide deep ice core WD2014 chronology – Part 1: Methane synchronization (68–31 ka BP) and the gas age–ice age difference, *Clim. Past*, 11, 153–173, <https://doi.org/10.5194/cp-11-153-2015>, 2015.
- Buizert, C., Sigl, M., Severi, M., Markle, B. R., Wettstein, J. J., McConnell, J. R., Pedro, J. B., Sodemann, H., Goto-Azuma, K., Kawamura, K., Fujita, S., Motoyama, H., Hirabayashi, M., Uemura, R., Stenni, B., Parrenin, F., He, F., Fudge, T. J., and Steig, E.: Abrupt ice-age shifts in southern westerly winds and Antarctic climate forced from the north, *Nature*, 563, 681–685, <https://doi.org/10.1038/s41586-018-0727-5>, 2018.
- Capron, E., Landais, A., Chappellaz, J., Schilt, A., Buiron, D., Dahl-Jensen, D., Johnsen, S. J., Jouzel, J., Lemieux-Dudon, B., Loulergue, L., Leuenberger, M., Masson-Delmotte, V., Meyer, H., Oerter, H., and Stenni, B.: Millennial and sub-millennial scale climatic variations recorded in polar ice cores over the last glacial

- period, *Clim. Past*, 6, 345–365, <https://doi.org/10.5194/cp-6-345-2010>, 2010.
- Capron, E., Landais, A., Chappellaz, J., Buiron, D., Fischer, H., Johnsen, S. J., Jouzel, J., Leuenberger, M., Masson-Delmotte, V., and Stocker, T. F.: A global picture of the first abrupt climatic event occurring during the last glacial inception, *Geophys. Res. Lett.*, 39, L15703, <https://doi.org/10.1029/2012GL052656>, 2012.
- Capron, E., Landais, A., Buiron, D., Cauquoin, A., Chappellaz, J., Debret, M., Jouzel, J., Leuenberger, M., Martinerie, P., Masson-Delmotte, V., Mulvaney, R., Parrenin, F., and Prié, F.: Glacial-interglacial dynamics of Antarctic firn columns: Comparison between simulations and ice core air- $\delta^{15}\text{N}$ measurements, *Clim. Past*, 9, 983–999, <https://doi.org/10.5194/cp-9-983-2013>, 2013.
- Cheng, H., Edwards, R. L., Sinha, A., Spötl, C., Yi, L., Chen, S., Kelly, M., Kathayat, G., Wang, X., Li, X., Kong, X., Wang, Y., Ning, Y., and Zhang, H.: The Asian monsoon over the past 640,000 years and ice age terminations, *Nature*, 534, 640–646, <https://doi.org/10.1038/nature18591>, 2016.
- Columbu, A., Drysdale, R., Capron, E., Woodhead, J., De Waele, J., Sanna, L., Hellstrom, J., and Bajo, P.: Early last glacial intra-interstadial climate variability recorded in a Sardinian speleothem, *Quaternary Sci. Rev.*, 169, 391–397, <https://doi.org/10.1016/J.QUASCIREV.2017.05.007>, 2017.
- Crotti, I., Landais, A., Stenni, B., Bazin, L., Parrenin, F., Frezzotti, M., Ritterbusch, F., Lu, Z. T., Jiang, W., Yang, G. M., Fourré, E., Orsi, A., Jacob, R., Minster, B., Prié, F., Dreossi, G., and Barbante, C.: An extension of the TALDICE ice core age scale reaching back to MIS 10.1, *Quaternary Sci. Rev.*, 266, 107078, <https://doi.org/10.1016/J.QUASCIREV.2021.107078>, 2021.
- Dansgaard, W. and Johnsen, S. J.: A Flow Model and a Time Scale for the Ice Core from Camp Century, Greenland, *J. Glaciol.*, 8, 215–223, <https://doi.org/10.3189/S0022143000031208>, 1969.
- Dong, X. Z., Ritterbusch, F., Chu, Y. Q., Gu, J. Q., Hu, S. M., Jiang, W., Lu, Z. T., Yang, G. M., and Zhao, L.: Dual Separation of Krypton and Argon from Environmental Samples for Radioisotope Dating, *Anal. Chem.*, 91, 13576–13581, <https://doi.org/10.1021/ACS.ANALCHEM.9B02716>, 2019.
- Dreyfus, G. B., Parrenin, F., Lemieux-Dudon, B., Durand, G., Masson-Delmotte, V., Jouzel, J., Barnola, J. M., Panno, L., Spahni, R., Tisserand, A., Siegenthaler, U., and Leuenberger, M.: Anomalous flow below 2700 m in the EPICA Dome C ice core detected using $\delta^{18}\text{O}$ of atmospheric oxygen measurements, *Clim. Past*, 3, 341–353, <https://doi.org/10.5194/cp-3-341-2007>, 2007.
- Dreyfus, G. B., Raisbeck, G. M., Parrenin, F., Jouzel, J., Guyodo, Y., Nomade, S., and Mazaud, A.: An ice core perspective on the age of the Matuyama–Brunhes boundary, *Earth Planet. Sc. Lett.*, 274, 151–156, <https://doi.org/10.1016/J.EPSL.2008.07.008>, 2008.
- Dreyfus, G. B., Jouzel, J., Bender, M. L., Landais, A., Masson-Delmotte, V., and Leuenberger, M.: Firn processes and $\delta^{15}\text{N}$: potential for a gas-phase climate proxy, *Quaternary Sci. Rev.*, 29, 28–42, <https://doi.org/10.1016/j.quascirev.2009.10.012>, 2010.
- EPICA Community Members: Augustin, L., Barbante, C., Barnes, P. R. F., Barnola, J. M., Bigler, M., Castellano, E., Cattani, O., Chappellaz, J., Dahl-Jensen, D., Delmonte, B., Dreyfus, G., Durand, G., Falourd, S., Fischer, H., Flückiger, J., Hansson, M. E., Huybrechts, P., Jugie, G., Johnsen, S. J., Jouzel, J., Kaufmann, P., Kipfstuhl, J., Lambert, F., Lipenkov, V. Y., Littot, G. C., Longinelli, A., Lorrain, R., Maggi, V., Masson-Delmotte, V., Miller, H., Mulvaney, R., Oerlemans, J., Oerter, H., Orombelli, G., Parrenin, F., Peel, D. A., Petit, J. R., Raynaud, D., Ritz, C., Ruth, U., Schwander, J., Siegenthaler, U., Souchez, R., Stauffer, B., Steffensen, J. P., Stenni, B., Stocker, T. F., Tabacco, I. E., Udisti, R., van de Wal, R. S. W., van den Broeke, M., Weiss, J., Wilhelms, F., Winther, J. G., Wolff, E. W., and Zucchelli, M.: Eight glacial cycles from an Antarctic ice core, *Nature*, 429, 623–628, <https://doi.org/10.1038/nature02599>, 2004.
- Epifanio, J. A., Brook, E. J., Buizert, C., Edwards, J. S., Sowers, T. A., Kahle, E. C., Severinghaus, J. P., Steig, E. J., Winski, D. A., Osterberg, E. C., Fudge, T. J., Aydin, M., Hood, E., Kalk, M., Kreutz, K. J., Ferris, D. G., and Kennedy, J. A.: The SP19 chronology for the South Pole Ice Core – Part 2: Gas chronology, Δ age, and smoothing of atmospheric records, *Clim. Past*, 16, 2431–2444, <https://doi.org/10.5194/cp-16-2431-2020>, 2020.
- Extier, T., Landais, A., Bréant, C., Prié, F., Bazin, L., Dreyfus, G., Roche, D. M., and Leuenberger, M.: On the use of $\delta^{18}\text{O}_{\text{atm}}$ for ice core dating, *Quaternary Sci. Rev.*, 185, 244–257, <https://doi.org/10.1016/J.QUASCIREV.2018.02.008>, 2018a.
- Extier, T., Landais, A., Bréant, C., Prié, F., Bazin, L., Dreyfus, G., Roche, D. M., and Leuenberger, M. C.: $\delta^{18}\text{O}_{\text{atm}}$ records between 100–800 ka from EPICA Dome C ice core, PANGAEA [data set], <https://doi.org/10.1594/PANGAEA.887323>, 2018b.
- Extier, T., Landais, A., Bréant, C., Prié, F., Bazin, L., Dreyfus, G., Roche, D. M., and Leuenberger, M. C.: $\delta\text{O}_2/\text{N}_2$ records between 100–800 ka from EPICA Dome C ice core, PANGAEA [data set], <https://doi.org/10.1594/PANGAEA.887326>, 2018c.
- Freitag, J., Kipfstuhl, S., Laepple, T., and Wilhelms, F.: Impurity-controlled densification: a new model for stratified polar firn, *J. Glaciol.*, 59, 1163–1169, <https://doi.org/10.3189/2013JOG13J042>, 2013.
- Fujita, S., Parrenin, F., Severi, M., Motoyama, H., and Wolff, E. W.: Volcanic synchronization of Dome Fuji and Dome C Antarctic deep ice cores over the past 216 kyr, *Clim. Past*, 11, 1395–1416, <https://doi.org/10.5194/cp-11-1395-2015>, 2015.
- Giaccio, B., Zanchetta, G., Galli, P., Nomade, S., Regattieri, E., and Sagnotti, L.: The Quaternary evolution of Sulmona basin, central Italy, <https://inquinaroma2023.org/wp-content/uploads/2022/01/5-Post.pdf> (last access: 10 September 2023), 2023.
- Goujon, C., Barnola, J. M., and Ritz, C.: Modeling the densification of polar firn including heat diffusion: Application to close-off characteristics and gas isotopic fractionation for Antarctica and Greenland sites, *J. Geophys. Res.-Atmos.*, 108, 4792, <https://doi.org/10.1029/2002JD003319>, 2003.
- Grachev, A. M. and Severinghaus, J. P.: Determining the thermal diffusion factor for $^{40}\text{Ar}/^{36}\text{Ar}$ in air to aid paleoreconstruction of abrupt climate change, *J. Phys. Chem. A*, 107, 4636–4642, <https://doi.org/10.1021/JP027817U>, 2003.
- Grisart, A.: Étude à haute résolution des cycles hydrologiques et climatiques à partir d'une carotte de glace d'Antarctique avec un focus sur les déglaciations, Université Paris-Saclay, <https://theses.hal.science/tel-04042459> (last access: 9 November 2023), 2023.
- Heaton, T. J., Bard, E., Ramsey, C. B., Butzin, M., Köhler, P., Muscheler, R., Reimer, P. J., and Wacker, L.: Radiocarbon: A key tracer for studying Earth's dynamo, climate system, carbon cycle, and Sun, *Science*, 374, 6568, <https://doi.org/10.1126/SCIENCE.ABD7096>, 2021.

- Herron, M. M. and Langway, C. C.: Firn densification: an empirical model, *J. Glaciol.*, 25, 373–385, <https://doi.org/10.3189/S0022143000015239>, 1980.
- Jiang, W., Hu, S. M., Lu, Z. T., Ritterbusch, F., and Yang, G.: min: Latest development of radiokrypton dating – A tool to find and study paleogroundwater, *Quatern. Int.*, 547, 166–171, <https://doi.org/10.1016/J.QUAINT.2019.04.025>, 2020.
- Jouzel, J., Hoffmann, G., Parrenin, F., and Waelbroeck, C.: Atmospheric oxygen 18 and sea-level changes, *Quaternary Sci. Rev.*, 21, 307–314, [https://doi.org/10.1016/S0277-3791\(01\)00106-8](https://doi.org/10.1016/S0277-3791(01)00106-8), 2002.
- Jouzel, J., Masson-Delmotte, V., Cattani, O., Dreyfus, G., Falourd, S., Hoffmann, G., Minster, B., Nouet, J., Barnola, J. M., Chappellaz, J., Fischer, H., Gallet, J. C., Johnsen, S., Leuenberger, M., Loulergue, L., Luethi, D., Oerter, H., Parrenin, F., Raisbeck, G., Raynaud, D., Schilt, A., Schwander, J., Selmo, E., Souchez, R., Spahni, R., Stauffer, B., Steffensen, J. P., Stenni, B., Stocker, T. F., Tison, J. L., Werner, M., and Wolff, E. W.: Orbital and millennial antarctic climate variability over the past 800,000 years, *Science*, 317, 793–796, <https://doi.org/10.1126/SCIENCE.1141038>, 2007.
- Kawamura, K., Parrenin, F., Lisiecki, L., Uemura, R., Vimeux, F., Severinghaus, J. P., Hutterli, M. A., Nakazawa, T., Aoki, S., Jouzel, J., Raymo, M. E., Matsumoto, K., Nakata, H., Motoyama, H., Fujita, S., Goto-Azuma, K., Fujii, Y., and Watanabe, O.: Northern Hemisphere forcing of climatic cycles in Antarctica over the past 360,000 years, *Nature*, 448, 912–916, <https://doi.org/10.1038/nature06015>, 2007.
- Kuipers Munneke, P., Ligtenberg, S. R. M., Noël, B. P. Y., Howat, I. M., Box, J. E., Mosley-Thompson, E., McConnell, J. R., Steffen, K., Harper, J. T., Das, S. B., and Van Den Broeke, M. R.: Elevation change of the Greenland Ice Sheet due to surface mass balance and firn processes, 1960–2014, *The Cryosphere*, 9, 2009–2025, <https://doi.org/10.5194/tc-9-2009-2015>, 2015.
- Landais, A., Chappellaz, J., Delmotte, M., Jouzel, J., Blunier, T., Bourg, C., Caillon, N., Cherrier, S., Malaizé, B., Masson-Delmotte, V., Raynaud, D., Schwander, J., and Steffensen, J. P.: A tentative reconstruction of the last interglacial and glacial inception in Greenland based on new gas measurements in the Greenland Ice Core Project (GRIP) ice core, *J. Geophys. Res.-Atmos.*, 108, 4563, <https://doi.org/10.1029/2002JD003147>, 2003.
- Landais, A., Barnola, J. M., Kawamura, K., Caillon, N., Delmotte, M., Van Ommen, T., Dreyfus, G., Jouzel, J., Masson-Delmotte, V., Minster, B., Freitag, J., Leuenberger, M., Schwander, J., Huber, C., Etheridge, D., and Morgan, V.: Firn-air $\delta^{15}\text{N}$ in modern polar sites and glacial–interglacial ice: a model-data mismatch during glacial periods in Antarctica?, *Quaternary Sci. Rev.*, 25, 49–62, <https://doi.org/10.1016/J.QUASCIREV.2005.06.007>, 2006.
- Landais, A., Dreyfus, G., Capron, E., Masson-Delmotte, V., Sanchez-Goni, M. F., Desprat, S., Hoffmann, G., Jouzel, J., Leuenberger, M., and Johnsen, S.: What drives the millennial and orbital variations of $\delta^{18}\text{O}_{\text{atm}}$?, *Quaternary Sci. Rev.*, 29, 235–246, <https://doi.org/10.1016/J.QUASCIREV.2009.07.005>, 2010.
- Landais, A., Dreyfus, G., Capron, E., Pol, K., Loutre, M. F., Raynaud, D., Lipenkov, V. Y., Arnaud, L., Masson-Delmotte, V., Paillard, D., Jouzel, J., and Leuenberger, M.: Towards orbital dating of the EPICA Dome C ice core using $\delta\text{O}_2/\text{N}_2$, *Clim. Past*, 8, 191–203, <https://doi.org/10.5194/cp-8-191-2012>, 2012.
- Landais, A., Stenni, B., Masson-Delmotte, V., Jouzel, J., Cauquoin, A., Fourré, E., Minster, B., Selmo, E., Extier, T., Werner, M., Vimeux, F., Uemura, R., Crotti, I., and Grisart, A.: Inter-glacial Antarctic–Southern Ocean climate decoupling due to moisture source area shifts, *Nat. Geosci.*, 14, 918–923, <https://doi.org/10.1038/s41561-021-00856-4>, 2021.
- Lascu, I., Feinberg, J. M., Dorale, J. A., Cheng, H., and Edwards, R. L.: Age of the Laschamp excursion determined by U-Th dating of a speleothem geomagnetic record from North America, *Geology*, 44, 139–142, <https://doi.org/10.1130/G37490.1>, 2016.
- Laskar, J., Robutel, P., Joutel, F., Gastineau, M., Correia, A. C. M., and Levrard, B.: A long-term numerical solution for the insolation quantities of the Earth, *Astron. Astrophys.*, 428, 261–285, <https://doi.org/10.1051/0004-6361:20041335>, 2004.
- Laskar, J., Fienga, A., Gastineau, M., and Manche, H.: La2010: a new orbital solution for the long-term motion of the Earth, *Astron. Astrophys.*, 532, A89, <https://doi.org/10.1051/0004-6361/201116836>, 2011.
- Lemieux-Dudon, B., Blayo, E., Petit, J. R., Waelbroeck, C., Svensson, A., Ritz, C., Barnola, J. M., Narcisi, B. M., and Parrenin, F.: Consistent dating for Antarctic and Greenland ice cores, *Quaternary Sci. Rev.*, 29, 8–20, <https://doi.org/10.1016/J.QUASCIREV.2009.11.010>, 2010.
- Lemieux-Dudon, B., Bazin, L., Landais, A., Toyé Mahamadou Kele, H., Guillevic, M., Kindler, P., Parrenin, F., and Martinerie, P.: Implementation of counted layers for coherent ice core chronology, *Clim. Past*, 11, 959–978, <https://doi.org/10.5194/cp-11-959-2015>, 2015.
- Ligtenberg, S. R. M., Helsen, M. M., and Van Den Broeke, M. R.: An improved semi-empirical model for the densification of Antarctic firn, *The Cryosphere*, 5, 809–819, <https://doi.org/10.5194/tc-5-809-2011>, 2011.
- Lipenkov, V., Candaudap, F., Ravoire, J., Dulac, E., and Raynaud, D.: A new device for the measurement of air content in polar ice, *J. Glaciol.*, 41, 423–429, <https://doi.org/10.3189/S0022143000016294>, 1995.
- Lipenkov, V. Y., Raynaud, D., Loutre, M. F., and Duval, P.: On the potential of coupling air content and O_2/N_2 from trapped air for establishing an ice core chronology tuned on local insolation, *Quaternary Sci. Rev.*, 30, 3280–3289, <https://doi.org/10.1016/J.QUASCIREV.2011.07.013>, 2011.
- Loulergue, L., Schilt, A., Spahni, R., Masson-Delmotte, V., Blunier, T., Lemieux, B., Barnola, J. M., Raynaud, D., Stocker, T. F., and Chappellaz, J.: Orbital and millennial-scale features of atmospheric CH_4 over the past 800,000 years, *Nature*, 453, 383–386, <https://doi.org/10.1038/nature06950>, 2008.
- Lu, Z. T., Schlosser, P., Smethie, W. M., Sturchio, N. C., Fischer, T. P., Kennedy, B. M., Purtschert, R., Severinghaus, J. P., Solomon, D. K., Tanhua, T., and Yokochi, R.: Tracer applications of noble gas radionuclides in the geosciences, *Earth Sci. Rev.*, 138, 196–214, <https://doi.org/10.1016/J.EARSCIREV.2013.09.002>, 2014.
- Moseley, G. E., Spötl, C., Brandstätter, S., Erhardt, T., Luetscher, M., and Lawrence Edwards, R.: NALPS19: Sub-orbital-scale climate variability recorded in northern Alpine speleothems during the last glacial period, *Clim. Past*, 16, 29–50, <https://doi.org/10.5194/cp-16-29-2020>, 2020.
- Nehrbass-Ahles, C., Shin, J., Schmitt, J., Bereiter, B., Joos, F., Schilt, A., Schmidely, L., Silva, L., Teste, G., Grilli, R., Chappellaz, J., Hodell, D., Fischer, H., and Stocker, T. F.:

- Abrupt CO₂ release to the atmosphere under glacial and early interglacial climate conditions, *Science*, 369, 1000–1005, <https://doi.org/10.1126/SCIENCE.AAY8178>, 2020.
- Nomade, S., Bassinot, F., Marino, M., Simon, Q., Dewilde, F., Maiorano, P., Isguder, G., Blamart, D., Girone, A., Scao, V., Pereira, A., Toti, F., Bertini, A., Combourieu-Nebout, N., Peral, M., Bourlès, D. L., Petrosino, P., Gallicchio, S., and Ciaranfi, N.: High-resolution foraminifer stable isotope record of MIS 19 at Montalbano Jonico, southern Italy: A window into Mediterranean climatic variability during a low-eccentricity interglacial, *Quaternary Sci. Rev.*, 205, 106–125, <https://doi.org/10.1016/j.quascirev.2018.12.008>, 2019.
- Nye, J. F.: The motion of ice sheets and glaciers, *J. Glaciol.*, 3, 493–507, <https://doi.org/10.3189/S002214300001724X>, 1959.
- Oraschewski, F. M. and Grinsted, A.: Modeling enhanced firn densification due to strain softening, *The Cryosphere*, 16, 2683–2700, <https://doi.org/10.5194/tc-16-2683-2022>, 2022.
- Oyabu, I., Kawamura, K., Buizert, C., Parrenin, F., Orsi, A., Kitamura, K., Aoki, S., and Nakazawa, T.: The Dome Fuji ice core DF2021 chronology (0–207 kyr BP), *Quaternary Sci. Rev.*, 294, 107754, <https://doi.org/10.1016/J.QUASCIREV.2022.107754>, 2022.
- Parrenin, F., Rémy, F., Ritz, C., Siebert, M. J., and Jouzel, J.: New modeling of the Vostok ice flow line and implication for the glaciological chronology of the Vostok ice core, *J. Geophys. Res.-Atmos.*, 109, D20102, <https://doi.org/10.1029/2004JD004561>, 2004.
- Parrenin, F., Dreyfus, G., Durand, G., Fujita, S., Gagliardini, O., Gillet, F., Jouze, J., Kawamura, K., Lhomme, N., Masson-Delmotte, V., Ritz, C., Schwander, J., Shoji, H., Uemura, R., Watanabe, O., and Yoshida, N.: 1-D-ice flow modelling at EPICA Dome C and Dome Fuji, East Antarctica, *Clim. Past*, 3, 243–259, <https://doi.org/10.5194/cp-3-243-2007>, 2007a.
- Parrenin, F., Barnola, J.-M., Beer, J., Blunier, T., Castellano, E., Chappellaz, J., Dreyfus, G., Fischer, H., Fujita, S., Jouzel, J., Kawamura, K., Lemieux-Dudon, B., Loulergue, L., Masson-Delmotte, V., Narcisi, B., Petit, J.-R., Raisbeck, G., Raynaud, D., Ruth, U., Schwander, J., Severi, M., Spahni, R., Steffensen, J. P., Svensson, A., Udisti, R., Waelbroeck, C., and Wolff, E.: The EDC3 chronology for the EPICA Dome C ice core, *Clim. Past*, 3, 485–497, <https://doi.org/10.5194/cp-3-485-2007>, 2007b.
- Parrenin, F., Barker, S., Blunier, T., Chappellaz, J., Jouzel, J., Landais, A., Masson-Delmotte, V., Schwander, J., and Veres, D.: On the gas-ice depth difference (Δ_{depth}) along the EPICA Dome C ice core, *Clim. Past*, 8, 1239–1255, <https://doi.org/10.5194/cp-8-1239-2012>, 2012.
- Parrenin, F., Bazin, L., Capron, E., Landais, A., Lemieux-Dudon, B., Masson-Delmotte, V., Parrenin, F., Bazin, L., Capron, E., Landais, A., Lemieux-Dudon, B., and Masson-Delmotte, V.: IceChrono1: a probabilistic model to compute a common and optimal chronology for several ice cores, *Geosci. Model Dev.*, 8, 1473–1492, <https://doi.org/10.5194/gmd-8-1473-2015>, 2015.
- Parrenin, F., Bazin, L., Capron, É., Landais, A., Lemieux-Dudon, B., and Masson-Delmotte, V.: Icechrono1: un modèle probabiliste pour calculer une chronologie commune et optimale pour plusieurs carottes de glace, *Quaternaire*, 28, 179–184, <https://doi.org/10.4000/QUATERNAIRE.8121>, 2017.
- Parrenin, F., Bazin, L., Buizert, C., Capron, E., Chowdry Bee-man, J., Corrick, E., Drysdale, R., Kawamura, K., Landais, A., Mulvaney, R., Oyabu, I., and Rasmussen, S.: The Paleochrono probabilistic model to derive a consistent chronology for several paleoclimatic sites, EGUGA, EGU21-822, <https://doi.org/10.5194/EGUSPHERE-EGU21-822>, 2021.
- Petit, J. R., Jouzel, J., Raynaud, D., Barkov, N. I., Barnola, J. M., Basile, I., Bender, M., Chappellaz, J., Davis, M., Delaygue, G., Delmotte, M., Kotiyakov, V. M., Legrand, M., Lipenkov, V. Y., Lorius, C., Pépin, L., Ritz, C., Saltzman, E., and Stievenard, M.: Climate and atmospheric history of the past 420,000 years from the Vostok ice core, Antarctica, *Nature*, 399, 429–436, <https://doi.org/10.1038/20859>, 1999.
- Pimienta, P. and Duval, P.: Rate controlling processes in the creep of polar glacier ice, *Journal de Physique Colloques*, 48, C1-243–C1-248, <https://doi.org/10.1051/jphyscol:1987134>, 1987.
- Raisbeck, G. M., Yiou, F., Jouzel, J., and Stocker, T. F.: Direct north–south synchronization of abrupt climate change record in ice cores using Beryllium 10, *Clim. Past*, 3, 541–547, <https://doi.org/10.5194/cp-3-541-2007>, 2007.
- Raisbeck, G. M., Cauquoin, A., Jouzel, J., Landais, A., Petit, J. R., Lipenkov, V. Y., Beer, J., Synal, H. A., Oerter, H., Johnsen, S. J., Steffensen, J. P., Svensson, A., and Yiou, F.: An improved north–south synchronization of ice core records around the 41 kyr 10Be peak, *Clim. Past*, 13, 217–229, <https://doi.org/10.5194/cp-13-217-2017>, 2017.
- Raynaud, D., Lipenkov, V., Lemieux-Dudon, B., Duval, P., Loutre, M. F., and Lhomme, N.: The local insolation signature of air content in Antarctic ice. A new step toward an absolute dating of ice records, *Earth Planet. Sc. Lett.*, 261, 337–349, <https://doi.org/10.1016/J.EPSL.2007.06.025>, 2007.
- Reutenauer, C., Landais, A., Blunier, T., Bréant, C., Kageyama, M., Woillez, M. N., Risi, C., Mariotti, V., and Braconnot, P.: Quantifying molecular oxygen isotope variations during a Heinrich stadial, *Clim. Past*, 11, 1527–1551, <https://doi.org/10.5194/cp-11-1527-2015>, 2015.
- Sánchez Goñi, M. F., Landais, A., Fletcher, W. J., Naughton, F., Desprat, S., and Duprat, J.: Contrasting impacts of Dansgaard–Oeschger events over a western European latitudinal transect modulated by orbital parameters, *Quaternary Sci. Rev.*, 27, 1136–1151, <https://doi.org/10.1016/J.QUASCIREV.2008.03.003>, 2008.
- Schwander, J., Jouzel, J., Hammer, C. U., Petit, J. R., Udisti, R., and Wolff, E.: A tentative chronology for the EPICA Dome Concordia Ice Core, *Geophys. Res. Lett.*, 28, 4243–4246, <https://doi.org/10.1029/2000GL011981>, 2001.
- Severinghaus, J. P., Bender, M. L., Keeling, R. F., and Broecker, W. S.: Fractionation of soil gases by diffusion of water vapor, gravitational settling, and thermal diffusion, *Geochim. Cosmochim. Ac.*, 60, 1005–1018, [https://doi.org/10.1016/0016-7037\(96\)00011-7](https://doi.org/10.1016/0016-7037(96)00011-7), 1996.
- Shackleton, N. J.: The 100,000-year ice-age cycle identified and found to lag temperature, carbon dioxide, and orbital eccentricity, *Science*, 289, 1897–1902, <https://doi.org/10.1126/SCIENCE.289.5486.1897>, 2000.
- Sigl, M., Fudge, T. J., Winstrup, M., Cole-Dai, J., Ferris, D., McConnell, J. R., Taylor, K. C., Welten, K. C., Woodruff, T. E., Adolphi, F., Bisiaux, M., Brook, E. J., Buizert, C., Caffee, M. W., Dunbar, N. W., Edwards, R., Geng, L., Iverson, N., Koffman, B., Layman, L., Maselli, O. J., McGwire, K., Muscheler, R., Nishiizumi, K., Pasteris, D. R., Rhodes, R. H., and Sowers,

- T. A.: The WAIS Divide deep ice core WD2014 chronology – Part 2: Annual-layer counting (0–31 ka BP), *Clim. Past*, 12, 769–786, <https://doi.org/10.5194/cp-12-769-2016>, 2016.
- Simon, Q., Bourlès, D. L., Bassinot, F., Nomade, S., Marino, M., Ciaranfi, N., Girone, A., Maiorano, P., Thouveny, N., Choy, S., Dewilde, F., Scao, V., Isguder, G. and Blamart, D., Authigenic $^{10}\text{Be}/^9\text{Be}$ ratio signature of the Matuyama–Brunhes boundary in the Montalbano Jonico marine succession, *Earth Planet. Sc. Lett.*, 460, 255–267, <https://doi.org/10.1016/j.epsl.2016.11.052>, 2017.
- Suwa, M. and Bender, M. L.: Chronology of the Vostok ice core constrained by O_2/N_2 ratios of occluded air, and its implication for the Vostok climate records, *Quaternary Sci. Rev.*, 27, 1093–1106, <https://doi.org/10.1016/J.QUASCIREV.2008.02.017>, 2008.
- Svensson, A., Andersen, K. K., Bigler, M., Clausen, H. B., Dahl-Jensen, D., Davies, S. M., Johnsen, S. J., Muscheler, R., Parrenin, F., Rasmussen, S. O., Röthlisberger, R., Seierstad, I., Steffensen, J. P., and Vinther, B. M.: A 60 000 year Greenland stratigraphic ice core chronology, *Clim. Past*, 4, 47–57, <https://doi.org/10.5194/cp-4-47-2008>, 2008.
- Svensson, A., Bigler, M., Blunier, T., Clausen, H. B., Dahl-Jensen, D., Fischer, H., Fujita, S., Goto-Azuma, K., Johnsen, S. J., Kawamura, K., Kipfstuhl, S., Kohno, M., Parrenin, F., Popp, T., Rasmussen, S. O., Schwander, J., Seierstad, I., Severi, M., Steffensen, J. P., Udisti, R., Uemura, R., Vallelonga, P., Vinther, B. M., Wegner, A., Wilhelms, F., and Winstrup, M.: Direct linking of Greenland and Antarctic ice cores at the Toba eruption (74 ka BP), *Clim. Past*, 9, 749–766, <https://doi.org/10.5194/cp-9-749-2013>, 2013.
- Svensson, A., Dahl-Jensen, D., Steffensen, J. P., Blunier, T., Rasmussen, S. O., Vinther, B. M., Vallelonga, P., Capron, E., Gkinis, V., Cook, E., Kjær, H. A., Muscheler, R., Kipfstuhl, S., Wilhelms, F., Stocker, T. F., Fischer, H., Adolphi, F., Erhardt, T., Sigl, M., Landais, A., Parrenin, F., Buizert, C., McConnell, J. R., Severi, M., Mulvaney, R., and Bigler, M.: Bipolar volcanic synchronization of abrupt climate change in Greenland and Antarctic ice cores during the last glacial period, *Clim. Past*, 16, 1565–1580, <https://doi.org/10.5194/cp-16-1565-2020>, 2020.
- Tian, L., Ritterbusch, F., Gu, J. Q., Hu, S. M., Jiang, W., Lu, Z. T., Wang, D., and Yang, G. M.: ^{81}Kr Dating at the Guliya Ice Cap, Tibetan Plateau, *Geophys. Res. Lett.*, 46, 6636–6643, <https://doi.org/10.1029/2019GL082464>, 2019.
- Tison, J.-L., de Angelis, M., Littot, G., Wolff, E., Fischer, H., Hansson, M., Bigler, M., Udisti, R., Wegner, A., Jouzel, J., Stenni, B., Johnsen, S., Masson-Delmotte, V., Landais, A., Lipenkov, V., Loulergue, L., Barnola, J.-M., Petit, J.-R., Delmonte, B., Dreyfus, G., Dahl-Jensen, D., Durand, G., Bereiter, B., Schilt, A., Spahni, R., Pol, K., Lorrain, R., Souchez, R., and Samyn, D.: Retrieving the paleoclimatic signal from the deeper part of the EPICA Dome C ice core, *The Cryosphere*, 9, 1633–1648, <https://doi.org/10.5194/tc-9-1633-2015>, 2015.
- Uemura, R., Motoyama, H., Masson-Delmotte, V., Jouzel, J., Kawamura, K., Goto-Azuma, K., Fujita, S., Kuramoto, T., Hirabayashi, M., Miyake, T., Ohno, H., Fujita, K., Abe-Ouchi, A., Iizuka, Y., Horikawa, S., Igarashi, M., Suzuki, K., Suzuki, T., and Fujii, Y.: Asynchrony between Antarctic temperature and CO_2 associated with obliquity over the past 720,000 years, *Nat. Commun.*, 9, 1–11, <https://doi.org/10.1038/s41467-018-03328-3>, 2018.
- Veres, D., Bazin, L., Landais, A., Toyé Mahamadou Kele, H., Lemieux-Dudon, B., Parrenin, F., Martinerie, P., Blayo, E., Blunier, T., Capron, E., Chappellaz, J., Rasmussen, S. O., Severi, M., Svensson, A., Vinther, B., and Wolff, E. W.: The Antarctic ice core chronology (AICC2012): an optimized multi-parameter and multi-site dating approach for the last 120 thousand years, *Clim. Past*, 9, 1733–1748, <https://doi.org/10.5194/cp-9-1733-2013>, 2013.
- Wolff, E.: Recommendation of AICC2023 by EPICA SSC, <https://doi.org/10.5194/egusphere-2023-1081-CC1>, 2023.
- Wolff, E. W., Chappellaz, J., Blunier, T., Rasmussen, S. O., and Svensson, A.: Millennial-scale variability during the last glacial: The ice core record, *Quaternary Sci. Rev.*, 29, 2828–2838, <https://doi.org/10.1016/J.QUASCIREV.2009.10.013>, 2010.
- Yan, Y., Bender, M. L., Brook, E. J., Clifford, H. M., Kemeny, P. C., Kurbatov, A. v., Mackay, S., Mayewski, P. A., Ng, J., Severinghaus, J. P., and Higgins, J. A.: Two-million-year-old snapshots of atmospheric gases from Antarctic ice, *Nature*, 574, 663–666, <https://doi.org/10.1038/s41586-019-1692-3>, 2019.
- Yiou, F., Raisbeck, G. M., Baumgartner, S., Beer, J., Hammer, C., Johnsen, S., Jouzel, J., Kubik, P. W., Lestringuez, J., Stievenard, M., Suter, M., and Yiou, P.: Beryllium 10 in the Greenland Ice Core Project ice core at Summit, Greenland, *J. Geophys. Res.-Oceans*, 102, 26783–26794, <https://doi.org/10.1029/97JC01265>, 1997.
- Zappala, J. C., Baggenstos, D., Gerber, C., Jiang, W., Kennedy, B. M., Lu, Z. T., Masarik, J., Mueller, P., Purtschert, R., and Visser, A.: Atmospheric ^{81}Kr as an Integrator of Cosmic-Ray Flux on the Hundred-Thousand-Year Time Scale, *Geophys. Res. Lett.*, 47, e2019GL086381, <https://doi.org/10.1029/2019GL086381>, 2020.
- Zhao, X., Cheng, H., Sinha, A., Zhang, H., Baker, J. L., Chen, S., Kong, X., Wang, Y., Edwards, R. L., Ning, Y., and Zhao, J.: A High-Resolution Speleothem Record of Marine Isotope Stage 11 as a Natural Analog to Holocene Asian Summer Monsoon Variations, *Geophys. Res. Lett.*, 46, 9949–9957, <https://doi.org/10.1029/2019GL083836>, 2019.



Supplement of

**The Antarctic Ice Core Chronology 2023 (AICC2023)
chronological framework and associated timescale
for the European Project for Ice Coring
in Antarctica (EPICA) Dome C ice core**

Marie Bouchet et al.

Correspondence to: Marie Bouchet (marie.bouchet@lsce.ipsl.fr)

The copyright of individual parts of the supplement might differ from the article licence.

1 Supplementary Material

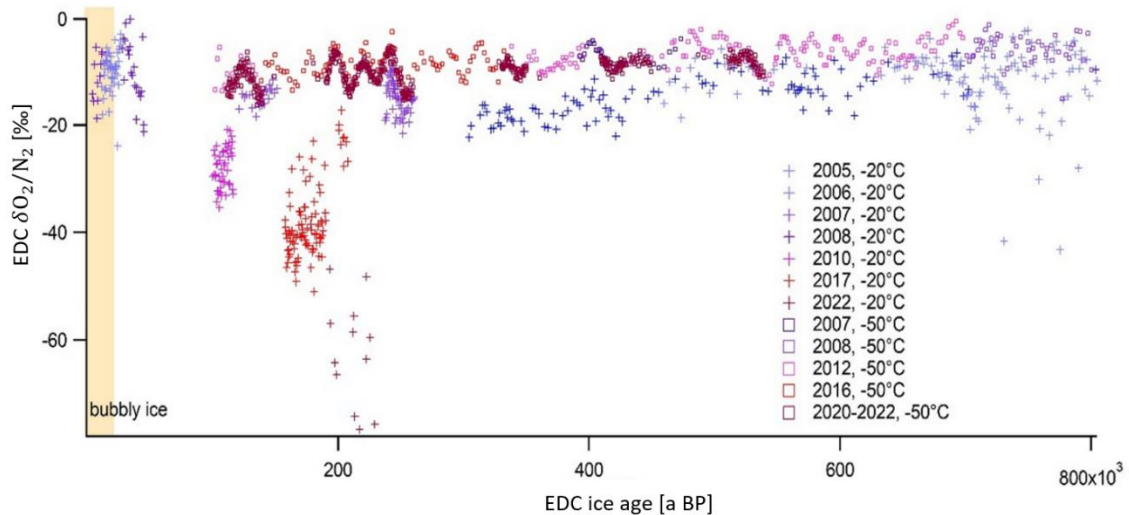
2 1. Study of the gas loss effect for the EDC $\delta\text{O}_2/\text{N}_2$ data

3 The EDC $\delta\text{O}_2/\text{N}_2$ data have been obtained from several measurement campaigns over the period 2005-2022 at
4 LSCE. We detail in Table S1 the different conditions of storage and measurements of the series.

5 **Table S1. Series of $\delta\text{O}_2/\text{N}_2$ obtained on the EDC ice cores with details on the storage and conditions of preparation.**

Age range (AICC2012, ice age, ka BP)	Date of measurements	Bubbly or clathrate ice	Storage temperature since drilling	Analytical method	Reference
11.3 – 27.06	2006	Bubbly and bubble to clathrate	-20°C	Automated melt extraction line	This study
4.05 – 11.89 & 27.82 – 44.91	2008	Bubbly and bubble to clathrate	-20°C	Automated melt extraction line	This study
100.162 – 116.238	2010	Clathrate	-20°C	Automated melt extraction line	This study
121.19 – 151.32 & 237.7 – 260.27	2007	Clathrate	-20°C	Manual extraction line	This study
157.56 – 208.66	2017	Clathrate	-20°C	Automated melt extraction line	This study
193.14 – 229.19	2022	Clathrate	-20°C	Automated melt extraction line	This study
302.32 – 800	2005	Clathrate	-20°C	Manual extraction line (LSCE)	Landais et al. (2012)
459.77 – 800	2006	Clathrate	-20°C	Manual extraction line (LSCE)	Landais et al. (2012)
392.49 – 473.31	2007	Clathrate	-50°C	Manual extraction line (LSCE)	Landais et al. (2012)
700 – 800	2008	Clathrate	-50°C	Automated melt extraction line (LSCE)	Landais et al. (2012)
103.75 – 136.47 & 338.25 – 700	2012	Clathrate	-50°C	Automated melt extraction line (LSCE)	Bazin et al. (2016)
138.76 – 332.03	2016	Clathrate	-50°C	Automated melt extraction line (LSCE)	Extier et al. (2018b)
111.39 – 148.85 & 180.34 – 259.39 & 328.08 – 360.59 & 409.29 – 449.61 & 486.98 – 539.35	2020 - 2022	Clathrate	-50°C	Automated melt extraction line (LSCE)	This study

6 A correction has been applied on the datasets obtained in 2006 and 2007 because they were obtained on a new
 7 mass spectrometer. We found that the calibration of the $\delta O_2/N_2$ data at the time has not be done correctly when
 8 switching from the old to the new mass spectrometer and that a shift of +1.5 ‰ should be applied to the $\delta O_2/N_2$
 9 data.



10 **Figure S1. $\delta O_2/N_2$ series from the EDC ice core after different storage conditions.** Note that the ice quality was very bad
 11 for the ice samples cut at the bottom of the ice core (corresponding to the age range of 800 – 700 ka BP). The orange rectangle
 12 frames the zone with only bubbly ice. The years of measurement are indicated and correspond to the different colors of the
 13 series.

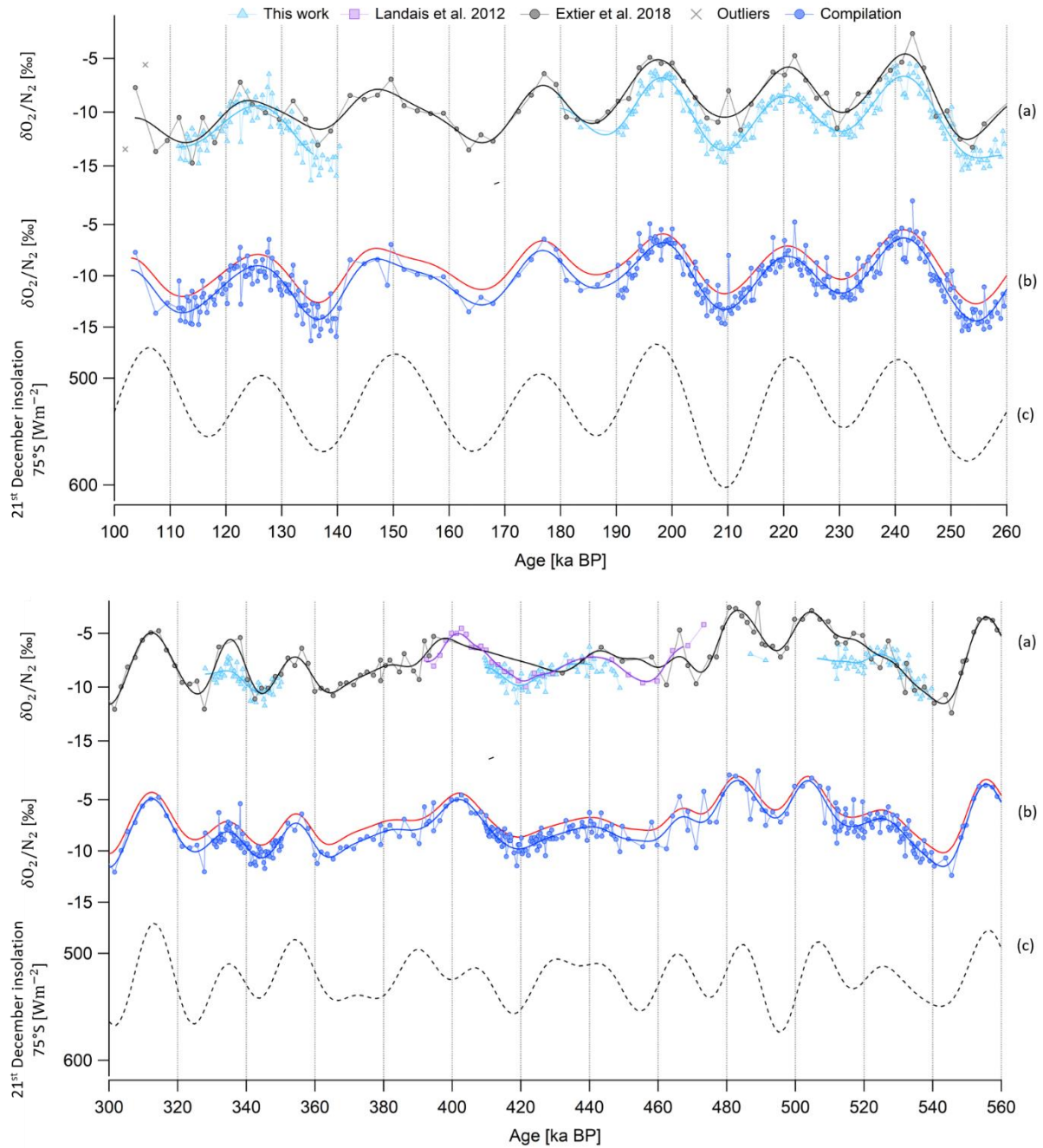
14 Figure S1 shows the evolution of the mean level of $\delta O_2/N_2$ after different storage conditions. We do not notice
 15 differences in the $\delta O_2/N_2$ mean level for the samples stored at $-50^\circ C$ even after 14 years of storage (2022 vs 2008).
 16 This result is similar to the one obtained at Dome Fuji by Oyabu et al. (2021) even if we are working with smaller
 17 sample (20-30 g before removing the outer part). On the contrary, ice storage at $-20^\circ C$ has a strong effect,
 18 especially on clathrate ice. The samples analyzed in 2022 after storage at $-20^\circ C$ during more than 18 years exhibit
 19 $\delta O_2/N_2$ values as low as -80 ‰. The bubbly ice analyzed here has been stored at $-20^\circ C$. The associated mean level
 20 of $\delta O_2/N_2$ is not significantly different from the one measured for samples stored at $-50^\circ C$ but the scattering is
 21 much larger as already observed on other series from bubbly ice (e.g. Oyabu et al., 2021).

22 2. Methods for aligning ice core records to reference curves

23

24 2.1 Study of the impact of filtering on $\delta O_2/N_2$ - insolation tie point identification

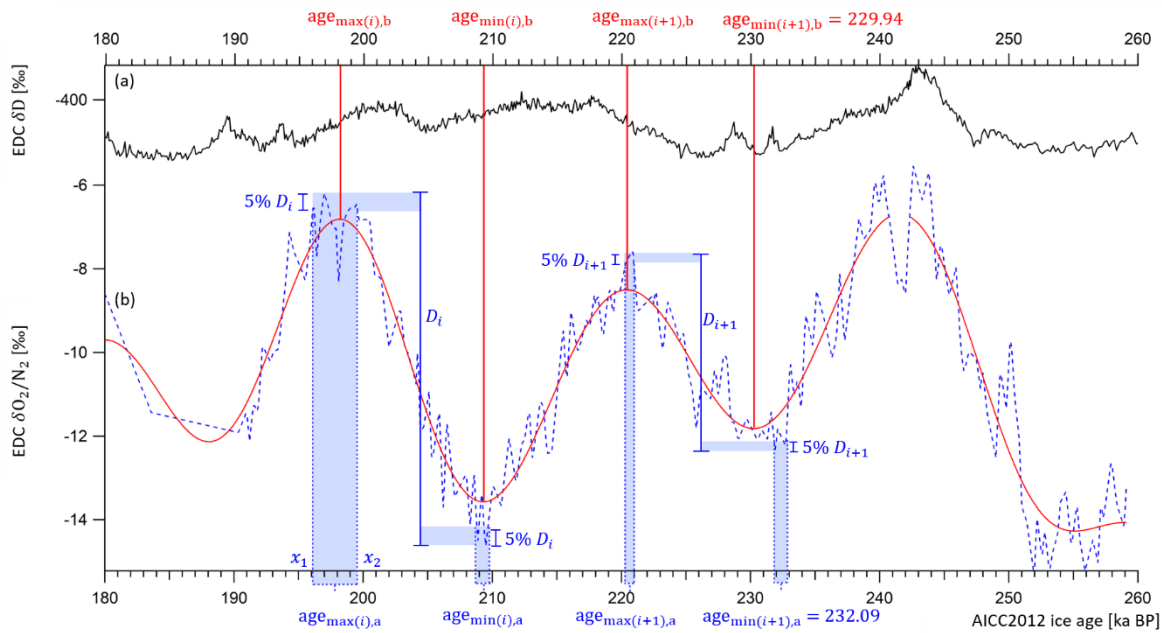
25 Figure S2 shows the smoothed $\delta O_2/N_2$ dataset using a low-pass (rejecting periods below 15 kyr) or a band-pass
 26 filter (keeping periods between 100 and 15 kyr periods, used by Bazin et al., 2013). The choice of filter does not
 27 alter the peak positions in the $\delta O_2/N_2$ curve



28 **Figure S2. Evolution of EDC $\delta\text{O}_2/\text{N}_2$ record between 260 and 100 ka BP and between 560 and 300 ka BP.** (a) EDC raw
 29 $\delta\text{O}_2/\text{N}_2$ old data between 800 and 100 ka BP (black circles for data of Extier et al., 2018b; and purple squares for data of Landais
 30 et al., 2012), outliers (grey crosses) and low-pass filtered signal (black and purple lines). EDC raw $\delta\text{O}_2/\text{N}_2$ new data (blue
 31 triangles, this study) and low-pass filtered signals (blue line). (b) Compilation of the two datasets and low-pass filtered (blue
 32 line) or band-pass filtered (red line) compiled signal. (c) 21st December insolation at 75° S on a reversed axis.

33 We compare tie point identification performed without (method a) and with (method b) filtering of the highly
 34 resolved $\delta\text{O}_2/\text{N}_2$ record between 260 and 180 ka BP (Fig. S3). The signal is first interpolated every 100 years. For
 35 the method a, we identified the mean maximum (or minimum) position $\text{age}_{\text{max}(i),a}$ (or $\text{age}_{\text{min}(i),a}$) as the middle
 36 of the age interval $[x_1; x_2]$ in which $\delta\text{O}_2/\text{N}_2$ is superior (or inferior) to a certain threshold. The threshold is defined
 37 as 95 % (or 5 %) of the amplitude difference D_i between the considered maximum and the minimum immediately
 38 preceding it (or between the considered minimum and the maximum immediately following it). The process is

39 reiterated every ~ 10 kyr (precession half period) when an extremum is reached in the $\delta O_2/N_2$ signal. For the
 40 method b (described in the main text), we detected the peak positions ($age_{max(i),b}$ and $age_{min(i),b}$) in the $\delta O_2/N_2$
 41 via an automated method using the zero values of the time derivatives of the low-pass filtered $\delta O_2/N_2$ compiled
 42 signal. After comparison of the peak positions identified by methods a and b (Table S2), we found an average
 43 disagreement of 700 years, with the largest value, 2150 years, observed between $age_{min(i+1),b}$ and $age_{min(i+1),a}$ at
 44 about 230 ka BP (Fig. S3). This period coincides with abrupt variations in the EDC δD record (Fig. S3), reflecting
 45 changes in surface climatic conditions which may have impacted high resolution variability of the $\delta O_2/N_2$ signal
 46 in addition of the insolation effect. Over periods of lower resolution of the $\delta O_2/N_2$ signal, the extrema positions
 47 are not affected by the filtering by more than 600 years (Table S2).



48 **Figure S3. Identification of peaks position in filtered or unfiltered $\delta O_2/N_2$ record between 260 and 180 ka BP.** (a) EDC
 49 δD (Jouzel et al. 2007). (b) EDC $\delta O_2/N_2$ (blue dashed curve) and low-pass filtered EDC $\delta O_2/N_2$ (red curve). Peaks position in
 50 the $\delta O_2/N_2$ record is identified as per methods a or b. Following the method a, the maximum position $age_{max(i),a}$ (on the bottom
 51 horizontal axis) is the middle of the age interval $[x_1; x_2]$ (blue vertical rectangles) in which $\delta O_2/N_2$ values are superior to 95 %
 52 of the difference D_i (vertical blue bars). The other peaks position is indicated in a similar way on the bottom horizontal axis.
 53 Following the method b, the extremum position is given by a 0 value in the temporal derivative of the filtered $\delta O_2/N_2$ record.
 54 The peak positions obtained with the method b ($age_{max(i),b}$, $age_{min(i),b}$) are indicated by red vertical bars and displayed on the
 55 top horizontal axis.

56 **Table S2. Peak positions of $\delta O_2/N_2$ identified as per method a and method b between 260 and 180 ka BP.** The age
 57 difference found between methods a and b is calculated. The average age difference is of 700 years and the standard deviation
 58 is of 250 years. EDC ice age as per AICC2012 and orbital ages as per Laskar et al. 2004.

Peak position (ka BP)			Age difference (years)
Method a	Method b	Insolation	Between methods a and b
197.64	197.94	196.8	300
209.19	209.14	210.1	50
220.69	220.24	220.8	450
232.09	229.94	231.7	2,150

241.84	241.24	240.1	600
			Average: 700
			Standard deviation: 250

59

60 2.2 Aligning EDC $\delta^{18}\text{O}_{\text{atm}}$ record and climatic precession variations

61 For the construction of the new AICC2023 chronology between 800 and 590 ka BP, the EDC $\delta^{18}\text{O}_{\text{atm}}$ record is
62 aligned with the climatic precession delayed or not by 5,000 years depending on the occurrence of Heinrich like
63 events, reflected by peaks in the IRD record from the North Atlantic Ocean (Sect 3.2.3 in the main text). Potential
64 errors may arise from aligning $\delta^{18}\text{O}_{\text{atm}}$ to precession (Oyabu et al., 2022). To support the use of our approach, we
65 test three methodologies to align $\delta^{18}\text{O}_{\text{atm}}$ and precession. Four test chronologies are built:

- 66 1) The test chronology 1 is obtained by aligning $\delta^{18}\text{O}_{\text{atm}}$ to 5-kyr-delayed precession as in Bazin et al. (2013).
- 67 2) The test chronology 2 is obtained by aligning $\delta^{18}\text{O}_{\text{atm}}$ to precession as it would be expected if only precession
68 is driving the $\delta^{18}\text{O}_{\text{atm}}$ signal.
- 69 3) The test chronology 3 is obtained by aligning $\delta^{18}\text{O}_{\text{atm}}$ to precession delayed if IRD counts are superior to 10
70 counts g^{-1} and to precession without delay if IRD counts are inferior to 10 counts g^{-1} .
- 71 4) The test chronology 4 is obtained by matching $\delta^{18}\text{O}_{\text{atm}}$ and $\delta^{18}\text{O}_{\text{calcite}}$ variations only.

72

73 2.2.1 Between 810 and 590 ka BP

74 We first evaluate the impact on the chronology whether $\delta^{18}\text{O}_{\text{atm}}$ is aligned with the precession with or without delay
75 between 810 and 590 ka BP. The age mismatch between test chronologies 1 and 2 is of 3,000 years on average,
76 reaching its maximum value of 3,700 years at 712 ± 2.6 ka BP (red arrow in Fig. S4).

77

78

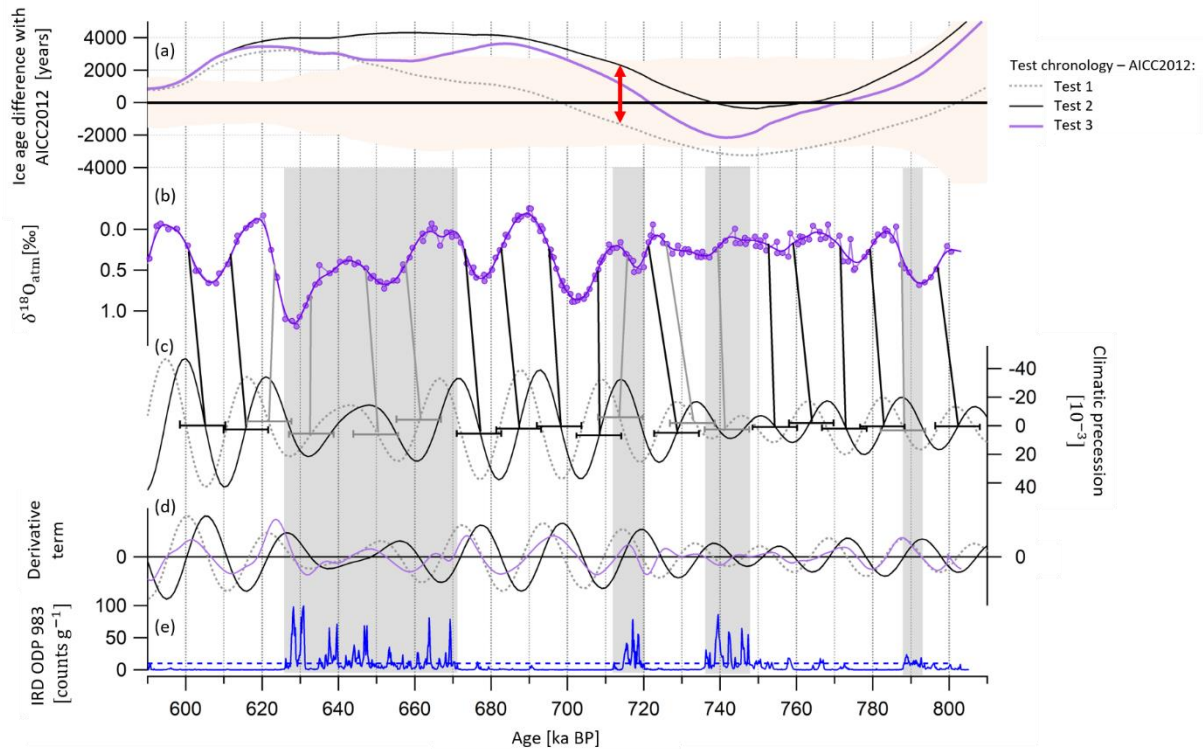
79

80

81

82

83



84 **Figure S4. Alignment of EDC $\delta^{18}\text{O}_{\text{atm}}$ and climatic precession and impact on the chronology between 810 and 590 ka**
 85 **BP.** (a) EDC ice age difference between AICC2012 and three test chronologies (1) test chronology 1 (grey dotted line), (2) test
 86 chronology 2 (black dashed line), (3) test chronology 3 (purple plain line). AICC2023 ice age 1σ uncertainty is shown by the
 87 orange area. The largest age difference between chronology 1 and 2 is indicated by the red arrow at 712.0 ± 2.6 ka BP. (b)
 88 Compiled EDC $\delta^{18}\text{O}_{\text{atm}}$ (purple circles). (c) Precession delayed by 5 kyr (grey dotted line) and not delayed (black dashed line)
 89 (Laskar et al. 2004). (d) Temporal derivative of precession (black dashed line), delayed precession (grey dotted line) and of the
 90 compiled $\delta^{18}\text{O}_{\text{atm}}$ record (purple plain line). (e) IRD (red by McManus et al. 1999; blue by Barker et al. 2019, 2021). The gray
 91 squares indicate periods where IRD counts are superior to the 10 counts g^{-1} threshold shown by the blue dotted horizontal line.
 92 Grey vertical bars illustrate new tie points between EDC $\delta^{18}\text{O}_{\text{atm}}$ and delayed precession mid-slopes (i.e. derivative extrema)
 93 when IRD counts are superior to the threshold. Black vertical bars illustrate new tie points between EDC $\delta^{18}\text{O}_{\text{atm}}$ and precession
 94 mid-slopes (i.e. derivative extrema) when no Heinrich-like events is shown by IRD record. The 12 kyr 2σ -uncertainty attached
 95 to the tie points is shown by the horizontal error-bars in panel b.

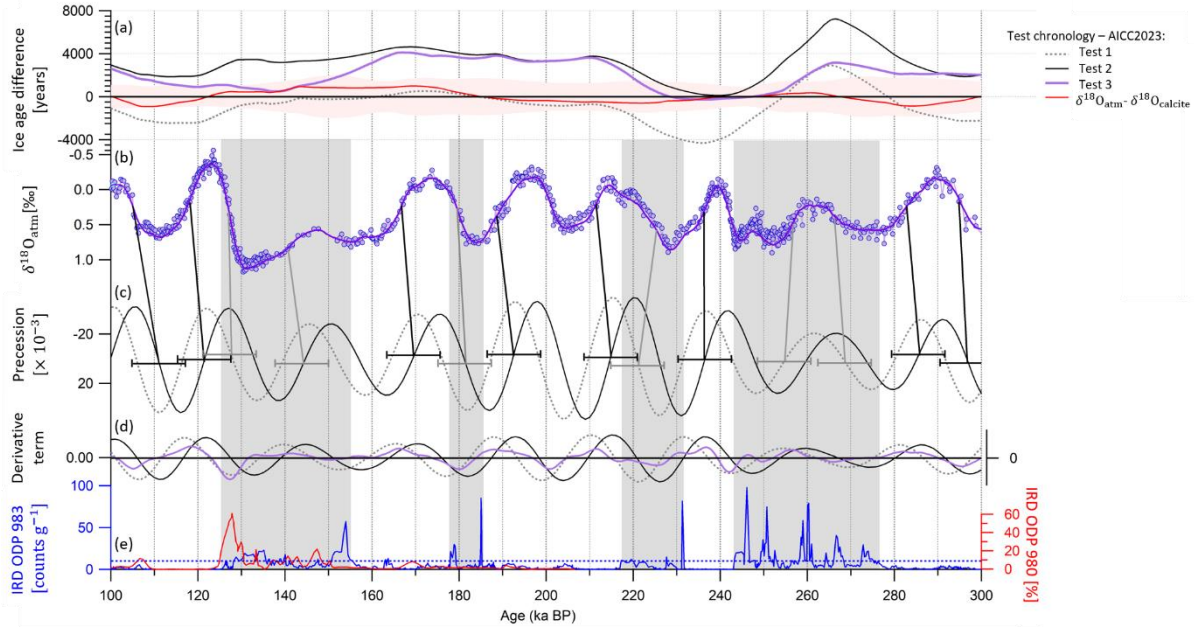
96 2.2.2 Between 300 and 100 ka BP

97 Then, we test the three methodologies to align $\delta^{18}\text{O}_{\text{atm}}$ and precession over the 100-300 ka period, where we have
 98 high confidence in our chronology.

99 Over this time interval, the test chronology 3 appears to be the best compromise as it agrees well with both the
 100 AICC2023 age model and the chronology derived from $\delta^{18}\text{O}_{\text{atm}}-\delta^{18}\text{O}_{\text{calcite}}$ matching (Fig. S5). This is why we
 101 believe that it can faithfully be applied to the bottom part of the EDC ice core while keeping large uncertainties in
 102 the tie points (1σ uncertainty of 6 kyr).

103 This agreement is particularly satisfying over the 120-160 ka BP time interval. Over this period, Oyabu et al.
 104 (2022) identified a large peak (up to 61%) in the IRD record of McManus et al. (1999) (red plain line in panel e)
 105 corresponding to HE 11 between 131 and 125 ka BP. Yet, if we consider the IRD record of Barker et al. (2019,

106 2021) used in our study because it covers the last 800 kyr (blue plain line in panel e), we observe another large
 107 peak (up to 56 counts g⁻¹) at around 150-156 ka BP. Because of this presence of IRD, to establish the test
 108 chronology 3, we tuned $\delta^{18}\text{O}_{\text{atm}}$ to the 5-kyr delayed precession over the whole period stretching from 155 to 124
 109 ka BP (gray frame), which is larger than the duration covering only HE 11.



110 **Figure S5. EDC ice age difference between test chronology and AICC2023 between 300 and 100 ka BP.** (a) EDC ice age
 111 difference between AICC2023 and 4 tests chronologies: (1) test chronology 1 (grey dotted line), (2) test chronology 2 (black
 112 dashed line), (3) test chronology 3 (purple plain line) and (4) test chronology 4 derived using only $\delta^{18}\text{O}_{\text{atm}}-\delta^{18}\text{O}_{\text{calcite}}$ matching
 113 (red plain line). AICC2023 ice age 1σ uncertainty is shown by the red area. (b) $\delta^{18}\text{O}_{\text{atm}}$ data from EDC (purple circles) and
 114 Vostok (blue circles). (c) Precession delayed by 5 kyr (grey dotted line) and not delayed (black dashed line) (Laskar et al.
 115 2004). (d) Temporal derivative of precession (black dashed line), delayed precession (grey dotted line) and of the compiled
 116 $\delta^{18}\text{O}_{\text{atm}}$ record (purple plain line). (e) IRD (red by McManus et al. 1999; blue by Barker et al. 2019, 2021). The gray squares
 117 indicate periods where IRD counts are superior to the 10 counts g⁻¹ threshold shown by the blue dotted horizontal line. Grey
 118 vertical bars illustrate new tie points between EDC $\delta^{18}\text{O}_{\text{atm}}$ and delayed precession when IRD counts are superior to the
 119 threshold. Black vertical bars illustrate new tie points between EDC $\delta^{18}\text{O}_{\text{atm}}$ and precession when no Heinrich-like event is
 120 shown by IRD record. The 12 kyr 2σ -uncertainty attached to the tie points is shown by the horizontal error-bars in panel b.

121 3. Sensitivity tests on background scenarios and associated relative uncertainties

122

123 3.1 Background lock-in-depth (LID) scenario at Dome C

124 The background LID scenario can be derived either from the $\delta^{15}\text{N}$ data (i.e. experimental LID), or from firm
 125 modeling (i.e. modeled LID). We favor the use of $\delta^{15}\text{N}$ data when there are available. Over depth intervals where
 126 no measurements of $\delta^{15}\text{N}$ were made, the LID can be deduced from firm modeling or from a synthetic $\delta^{15}\text{N}$ record
 127 using the $\delta\text{D}-\delta^{15}\text{N}$ relationship (Bazin et al., 2013). In this work, we assess the credibility of three composite LID
 128 scenario (Table S3) constructed using the firm model (Bréant et al., 2017) or the synthetic $\delta^{15}\text{N}$ record when no
 129 data are available. The credibility is defined by the criterion Δ as per:

130

$$\Delta = |(\text{analyzed LID} - \text{background LID})|$$

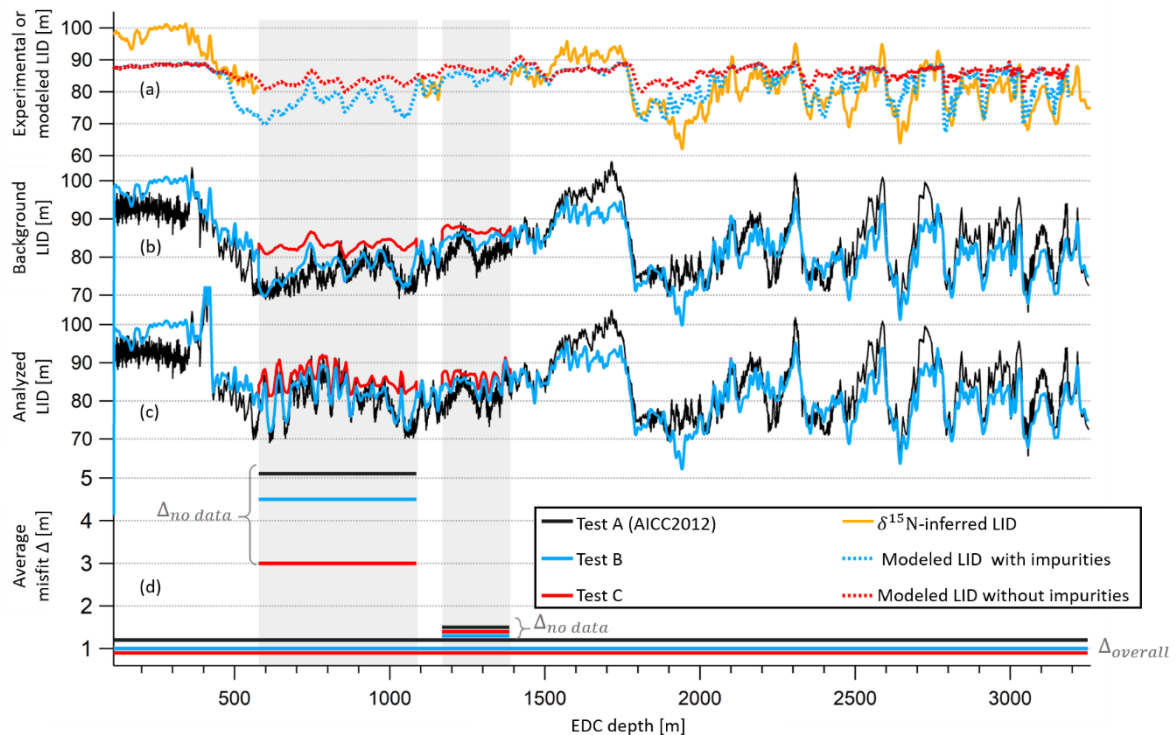
131 Δ represents the average absolute value of the mismatch between the background LID (i.e. prior LID provided in
 132 input in PaleoChrono) and analyzed LID (i.e. the posterior LID given by PaleoChrono) scenarios of LID. The
 133 weaker is Δ , the closer the background scenario is to the analyzed scenario, meaning that the background scenario
 134 is in relatively good agreement with chronological information compelling the inverse model in PaleoChrono. On
 135 the contrary, the larger is Δ , the more PaleoChrono is forced to significantly modify the background scenario which
 136 is incompatible with the chronological constraints. Therefore, the larger Δ is, the less credible is the prior LID
 137 scenario. It should be noted that the relative error in the prior LID scenario and the age constraints input in
 138 PaleoChrono are equal in each test, so that the mismatch Δ is only impacted by the value of the prior LID from one
 139 test to another. Three background scenarios of LID are tested (Table S3).

140 **Table S3. Test of three composite background LID scenarios.** Test A corresponds to the background LID used to constrain
 141 AICC2012 chronology. Test B corresponds to the background LID used in the new AICC2023 chronology. Configuration 1
 142 implies consideration of impurity concentration in the firn model. Configuration 2 implies **no** consideration of impurity
 143 concentration in the firn model.

	Test			$\delta^{15}\text{N}$ data availability	Depth interval (m)
	A (AICC2012)	B (AICC2023)	C		
LID calculation	From raw $\delta^{15}\text{N}$ data assuming a negligible thermal signal.	From $\delta^{15}\text{N}$ data corrected for thermal fractionation estimated by the firn model (configuration 1).	From $\delta^{15}\text{N}$ data corrected for thermal fractionation estimated by the firn model (configuration 2).	Yes	[345 – 578], [1086 – 1169] and [1386 – bottom]
	From $\delta^{15}\text{N}$ synthetic record (using the δD - $\delta^{15}\text{N}$ relationship).	From firn modeling (configuration 1)	From firn modeling (configuration 2)	No	[0 – 345], [578 – 1086] and [1169 – 1386]

144

145



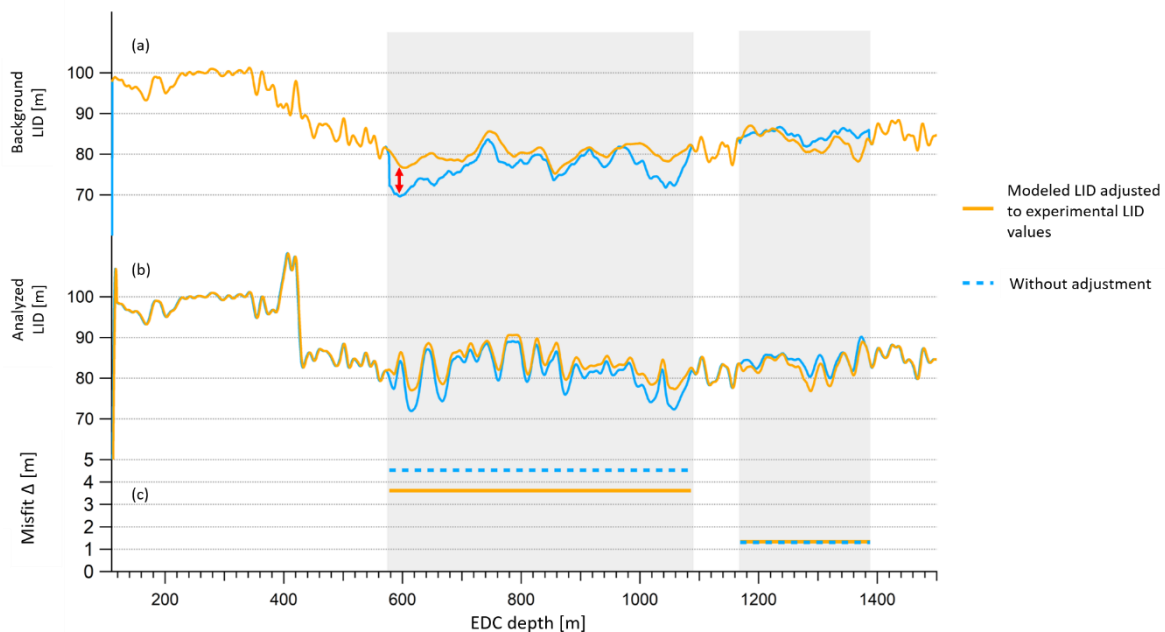
146 **Figure S6. Mismatch Δ between background and analyzed LID for EDC over the 100-3200 m depth interval.** (a)
 147 Experimental LID (orange) and modeled LID scenarios as per configuration 1 (with impurities, blue dots) and configuration 2
 148 (without impurities, red dots). (b) Composite background LID as per tests A (black), B (blue) and C (red). (c) Analyzed LID
 149 scenarios given by Paleochrono. (d) Three values of the misfit Δ are calculated for the three composite LID: $\Delta_{no\ data}$, averaged
 150 over the two depth intervals where $\delta^{15}\text{N}$ data are not available (either between 578 and 1086 m or between 1169 and 1386 m,
 151 see intervals shown by grey rectangles), and $\Delta_{overall}$, averaged over the whole 3200 m.

152 For the construction of the AICC2012 timescale, the background LID scenario at EDC was derived from a
 153 synthetic $\delta^{15}\text{N}$ record using the $\delta\text{D}-\delta^{15}\text{N}$ relationship (Bazin et al., 2013). Yet, this scenario (A, Table S3) is
 154 associated with the largest mismatch criterion over the last 800 kyr, reaching $\Delta = 5$ m over the 578-1086 m depth
 155 interval where no $\delta^{15}\text{N}$ data are available (Fig. S6). Hence it is believed to be the least pertinent among the three
 156 tested scenarios and we decided not to use the $\delta\text{D}-\delta^{15}\text{N}$ relationship to construct the prior LID scenario in this
 157 work.

158 Modeled LID scenarios (B and C, Table S3) are characterized by smaller mismatch criteria Δ than LID A regardless
 159 of the depth interval considered (Fig. S6), hence we believe that firm modeling estimates reproduce well the
 160 evolution of past LID at EDC site. In the firm model, the creep factor can be either dependent on impurity inclusion
 161 inducing firm softening (giving LID B) or not (giving LID C). The LID sensitivity to the impurity parameter is
 162 evaluated by comparing LID B and LID C performances. Even though LID B is associated with a smaller criterion
 163 Δ between 578 and 1086 m, LID B and LID C show comparable values for Δ over the last 800 kyr (Fig. S6).
 164 Bréant et al. (2017) argued that implementing the impurity dependence in the model reduces the $\delta^{15}\text{N}$ data-model
 165 mismatch at Dome C. This is particularly verified over deglaciations where significant LID augmentations inferred
 166 from $\delta^{15}\text{N}$ are well reproduced by the modeled LID when the impurity parameter is included (panel a in Fig. S6).
 167 We thus follow the recommendation of Bréant et al. (2017) and use the composite LID B scenario to constrain the
 168 new AICC2023 chronology.

169 Discontinuities are visible when switching from experimental to modeled values when no data are
 170 available (grey rectangles on Fig. S7). To avoid these discontinuities, we test a LID scenario where the modeled
 171 LID is fitted to experimental LID values (orange curve in Fig. S7). In other words, the firm modeling estimates are
 172 adjusted, by standard normalization, to the scale of LID values derived from $\delta^{15}\text{N}$ data. Adjusting the modeled
 173 LID to experimental LID values induces a modification of 4.7 m at most (see red arrow) which remains within the
 174 background relative uncertainty (20%).

175 On the depth interval from 578 to 1086 m, the modeled scenario without any fitting to $\delta^{15}\text{N}$ -inferred LID (blue
 176 curve, Fig. S7) is almost as effective as the one that was fitted (orange curve, Fig. S7) (i.e., close Δ values). On the
 177 second depth interval of interest, from 1169 to 1386 m, both scenarios show equal Δ values.



178 **Figure S7. Mismatch Δ between background and analyzed LID for EDC over the 100-1500 m depth interval.** (a)
 179 Background LID with and without adjusting the modeled LID to experimental LID values (orange and blue curves
 180 respectively). (b) Analyzed LID. (c) The averaged value of the misfit, Δ , is calculated for the two LID over the two depth
 181 intervals where $\delta^{15}\text{N}$ data are not available (either between 578 and 1086 m or between 1169 and 1386 m, see intervals shown
 182 by grey rectangles).

183 We thus conclude that we can keep the scenario combining $\delta^{15}\text{N}$ -inferred LID and modeled LID in the construction
 184 of AICC2023.

185 3.2 Background uncertainties for LID, accumulation rate and thinning scenarios

186 Although there is no objective way to assign specific prior uncertainties, the values chosen by Bazin et al. (2013)
 187 seem unrealistic (i.e. 80 % of uncertainty for the LID during some glacial periods at EDC whereas firn modeling
 188 and $\delta^{15}\text{N}$ agree within a 20 %-margin at most). That is why we believe the prior uncertainties should be reduced
 189 in AICC2023 and implement the following major changes (blue plain line in Fig. S8 and S9):

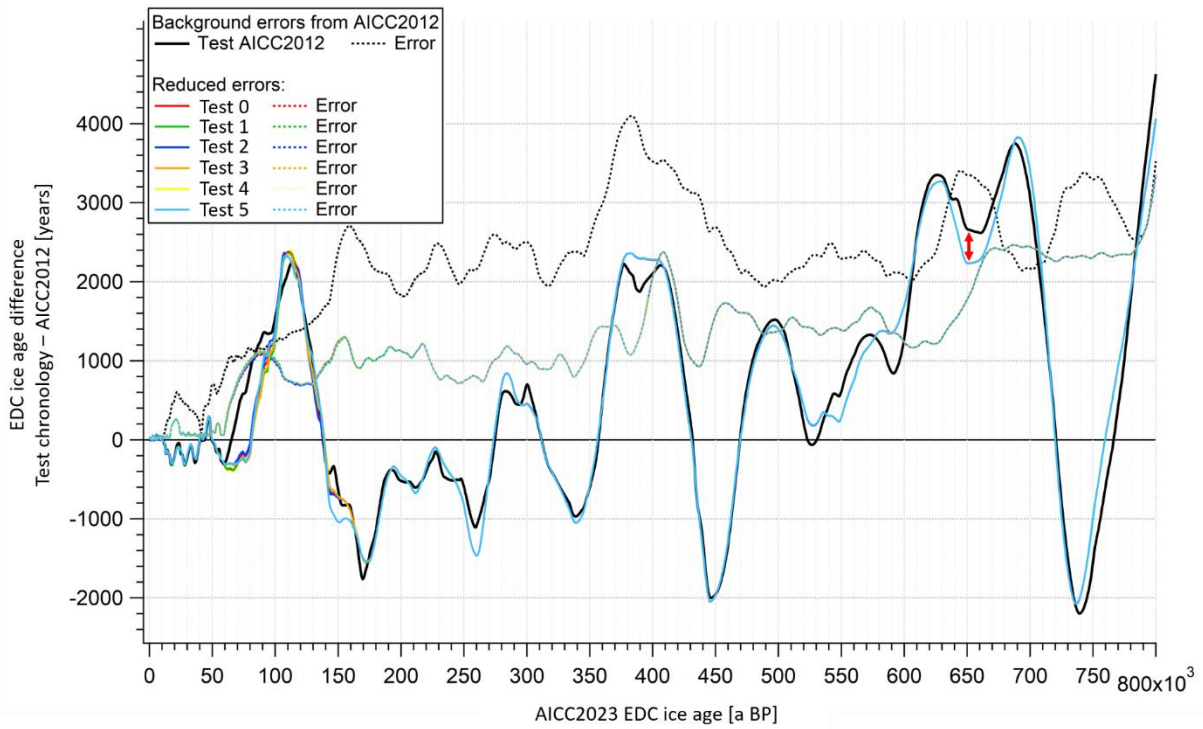
- 190 - The LID background relative uncertainty is reduced to values oscillating between 10 and 20 % at most,
 191 excluding values reaching 80 % used in AICC2012. The reason for this modification is that in 2012, the
 192 mismatch between firn model outputs and $\delta^{15}\text{N}$ -inferred LID was not understood. In the meantime, much
 193 progresses have been made, confirming that the $\delta^{15}\text{N}$ -inferred LID was correct and firn models or their
 194 forcing have been adapted (Parrenin et al., 2012; Bréant et al., 2017; Buizert et al., 2021).
- 195 - The thinning relative uncertainty is evolving linearly, rather than exponentially as it was done in
 196 AICC2012. The linear uncertainty permits to have a significant uncertainty at intermediate depth levels
 197 while with the exponential shape, the uncertainty was essentially located at lower depth levels, which was
 198 not realistic.
- 199 - The accumulation relative uncertainty is decreased to 20 %, as opposed to 60 % used in AICC2012. This
 200 choice is motivated by the study of Parrenin et al. (2007) who counted event duration in EDC and DF ice
 201 cores and found out an offset of 20 % on average.

202 We build different test chronologies by keeping the same age constraints and background scenarios as in
 203 AICC2023 but varying the background errors (Table S4). The largest age offset is observed between the test
 204 AICC2012 and the other test chronologies at around 650 ka BP. It reaches 400 years (see red arrow in Fig. S8),
 205 which is not significant considering the uncertainty associated with the test chronologies over this period (ranging
 206 from 1,800 to 3,400 years). Since varying the background uncertainties has no significant impact on the final age
 207 model and the background uncertainties of AICC2012 seem unrealistic, we reduce the background errors with
 208 respect to AICC2012 and we use the Test 5 configuration from Table S4 to construct AICC2023.

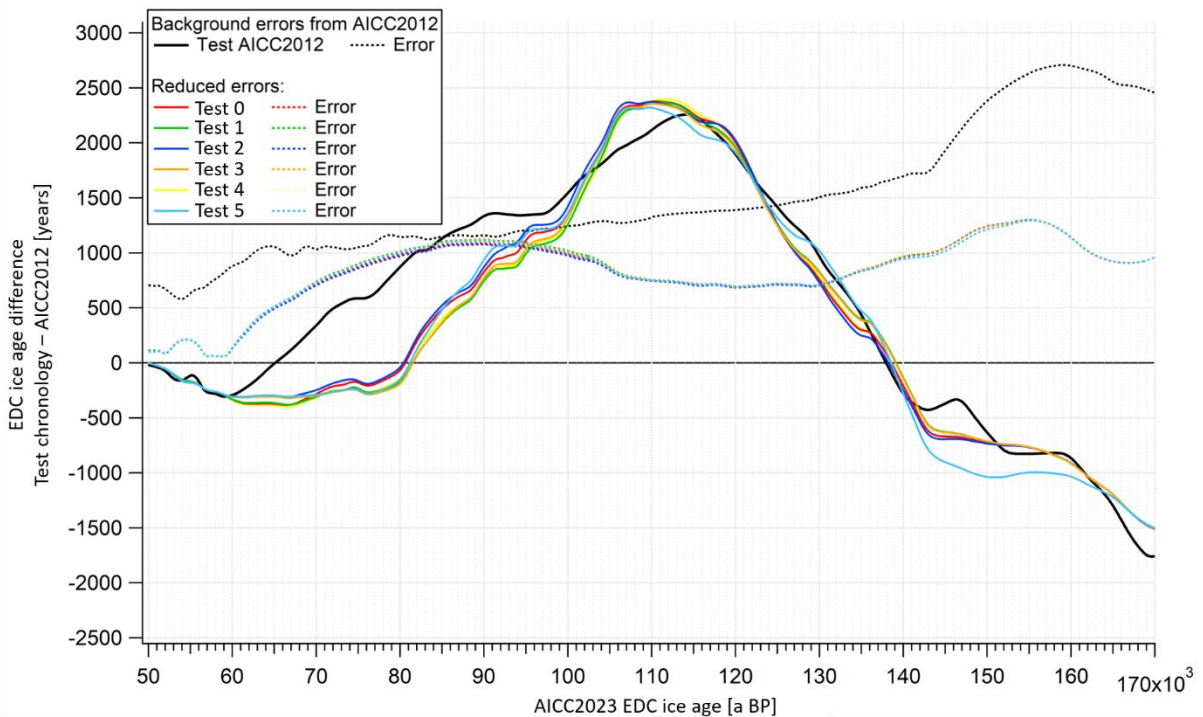
209 **Table S4. The different prior relative uncertainties tested for LID, thinning and accumulation.** The LID prior relative
 210 uncertainty is set between 0.1 or 0.2 whether $\delta^{15}\text{N}$ data are available or not.

Test	Sites	LID	Thinning	Accumulation
Test AICC2012	EDC			
	EDML			
	VK			
	TALDICE			
	NGRIP			
Test 0	EDC	0.1 (data) or 0.2 (no data)	Linear from 0 to 0.5	0.2
	EDML	0.1 (data) or 0.2 (no data)	Linear from 0 to 0.5	From AICC2012 (between 0.2 and 0.8)
	VK	0.1 (data) or 0.2 (no data)	Linear from 0 to 0.5	Linear from 0.2 to 0.7
	TALDICE	0.2	From AICC2012 (exponential from 0 to 2.4)	0.2
	NGRIP	0.2	Linear from 0 to 0.5	0.2
Test 1	EDC	0.1 (data) or 0.2 (no data)	Linear from 0 to 0.5	0.2
	EDML	0.1 (data) or 0.2 (no data)	Linear from 0 to 1	From AICC2012 (between 0.2 and 0.8)
	VK	0.1 (data) or 0.2 (no data)	Linear from 0 to 0.5	Linear from 0.2 to 0.7
	TALDICE	0.2	From AICC2012	0.2

			(exponential from 0 to 2.4)	
	NGRIP	0.2	Linear from 0 to 0.5	0.2
Test 2	EDC	0.1 (data) or 0.2 (no data)	Linear from 0 to 0.5	0.2
	EDML	0.1 (data) or 0.2 (no data)	Linear from 0 to 0.5	0.2
	VK	0.1 (data) or 0.2 (no data)	Linear from 0 to 0.5	Linear from 0.2 to 0.7
	TALDICE	0.2	From AICC2012 (exponential from 0 to 2.4)	0.2
	NGRIP	0.2	Linear from 0 to 0.5	0.2
Test 3	EDC	0.1 (data) or 0.2 (no data)	Linear from 0 to 0.5	0.2
	EDML	0.1 (data) or 0.2 (no data)	Linear from 0 to 1	0.2
	VK	0.1 (data) or 0.2 (no data)	Linear from 0 to 0.5	Linear from 0.2 to 0.7
	TALDICE	0.2	From AICC2012 (exponential from 0 to 2.4)	0.2
	NGRIP	0.2	Linear from 0 to 0.5	0.2
Test 4	EDC	0.1 (data) or 0.2 (no data)	Linear from 0 to 0.5	0.2
	EDML	0.1 (data) or 0.2 (no data)	Linear from 0 to 0.5	Linear from 0.2 to 0.7
	VK	0.1 (data) or 0.2 (no data)	Linear from 0 to 0.5	Linear from 0.2 to 0.7
	TALDICE	0.2	From AICC2012 (exponential from 0 to 2.4)	0.2
	NGRIP	0.2	Linear from 0 to 0.5	0.2
Test 5 (AICC2023)	EDC	0.1 (data) or 0.2 (no data)	Linear from 0 to 0.5	0.2
	EDML	0.1 (data) or 0.2 (no data)	Linear from 0 to 1	0.2
	VK	0.1 (data) or 0.2 (no data)	Linear from 0 to 0.5	Linear from 0.2 to 0.7
	TALDICE	0.2	Linear from 0 to 1	0.2
	NGRIP	0.2	Linear from 0 to 0.5	0.2



211 **Figure S8. EDC ice age difference between each test chronology and AICC2012 timescale between 800 and 0 ka BP.** The
 212 ice age uncertainty (1σ) obtained for each test is shown by the dotted lines. The red arrow indicates the largest age mismatch
 213 between the test chronologies.



214 **Figure S9. EDC ice age difference between each test chronology and AICC2012 timescale between 170 and 50 ka BP.**
 215 The ice age uncertainty (1σ) obtained for each test is shown by dotted lines.

216

217 **4 The new AICC2023 chronology**

218

219 **4.1 New age constraints**

220

221 **4.1.1 $\delta^{18}\text{O}_{\text{atm}}$, $\delta\text{O}_2/\text{N}_2$ and TAC age constraints for EDC**

222 **Table S5. $\delta^{18}\text{O}_{\text{atm}}$, $\delta\text{O}_2/\text{N}_2$ and TAC age constraints used for EDC in AICC2023.** Sources: A (this work), B (Bazin et al.,
223 2013) and C (Extier et al., 2018a).

$\delta^{18}\text{O}_{\text{atm}}$				$\delta\text{O}_2/\text{N}_2$				TAC			
EDC depth (m)	Gas age (ka BP)	Uncertainty (years)	Source	EDC depth (m)	Ice age (ka BP)	Uncertainty (years)	Source	EDC depth (m)	Ice age (ka BP)	Uncertainty (years)	Source
1465.61	108.50	1303.84	C	1495.96	117.4	3000	A	645.31	30.95	3000	A
1585.2	120.90	1303.84	C	1652.39	125.8	3000	A	782.86	47.95	3000	A
1706.92	128.80	1303.84	C	1772.83	138.1	3000	A	1337.51	93.85	3000	A
1903.01	160.40	1860.11	C	1823.08	150.1	3000	A	1453.56	107.15	3000	A
1921.37	163.00	1860.11	C	1915.39	164.6	3000	A	1588.23	118.35	3000	A
1931.13	165.20	1860.11	C	1964.71	176	3000	A	1650.52	124.75	3000	A
1997.19	178.30	1860.11	C	2008.15	187.2	3000	A	1747.64	135.95	3000	A
2050.18	191.80	2282.54	C	2065.72	196.8	3000	A	1853.73	150.05	3000	A
2096.02	199.00	2282.54	C	2128.92	210.1	3000	A	1938.82	165.35	3000	A
2139.91	207.90	2282.54	C	2196.61	220.8	3000	A	2121.53	210.05	3000	A
2160.01	209.3	2282.54	A	2232.66	231.7	3000	A	2205.70	222.85	3000	A
2229.99	225.3	1303.84	C	2281.09	240.1	3000	A	2237.52	230.45	3000	A
2232.88	227.60	1253	A	2336.71	253.4	3000	A	2274.72	238.9	3000	A
2258.68	233.2	1486.61	A	2374.24	268	3000	A	2318.83	252.55	3000	A
2300.06	242.20	1140.18	C	2406.67	281.1	3000	A	2383.34	268.95	3000	A
2332.74	248.4	1140.18	A	2438.00	290.4	3000	A	2505.82	313.35	3000	A
2363.62	258.70	1140.18	C	2469.99	302.2	3000	A	2623.99	353.65	3000	A
2376.66	264.40	1140.18	C	2502.46	312.8	3000	A	2633.73	362.125	3000	A
2409.39	279.00	2459.67	C	2536.47	325.1	3000	A	2759.45	417.15	6000	A
2451.16	289.00	2459.67	C	2572.12	334.6	3000	A	2792.11	434.15	6000	A
2466.27	293.90	2459.67	C	2603.71	344.2	3000	A	2815.91	467.05	6000	A
2475.81	301.30	1941.65	C	2622.61	354.1	6000	A	2823.81	475.4	6000	A
2490.37	304.90	1941.65	C	2639.97	366.6	6000	A	2831.30	483.55	3000	A
2522.11	316.60	1303.84	C	2677.69	372.5	6000	A	2850.57	495.45	3000	A
2582.63	334.30	1303.84	C	2685.82	377.8	6000	A	2931.35	556.25	6000	A
2599.92	337.90	1253	C	2763.95	418.1	6000	A	2962.01	569.25	6000	A
2664.62	377.30	1421.27	C	2805.78	454.9	6000	A	2986.85	578.35	6000	A
2679.89	385.70	1627.88	C	2815.83	465.7	6000	A	3000.24	587.95	6000	A
2707.22	398.50	3008.32	C	2820.37	475.4	6000	A	3013.99	599.85	3000	A
2776.91	425.9	1702.94	A	2833.08	484.2	3000	A	3020.93	611.65	3000	A
2784.70	428.8	1702.94	A	2849.73	496	3000	A	3029.38	621.55	3000	A

2791.70	434.5	1702.94	A	2863.56	506.5	3000	A	3035.80	629.75	3000	A
2793.91	440.3	1702.94	A	2880.63	517.3	3000	A	3043.28	642.85	3000	A
2838.23	483.90	4632.49	C	2892.99	525.5	3000	A	3068.47	682.75	10000	A
2857.55	500.60	4632.49	C	2914.24	542.5	3000	A	3078.07	691.55	10000	A
2873.92	504.10	7382.41	C	2929.86	556.2	3000	A	3094.01	703	10000	A
2894.57	521.00	3008.32	A	2951.86	568.4	3000	A	3120.55	715.35	10000	A
2904.64	531.3	3195.31	A	2986.64	577.8	3000	A	3139.92	730.75	10000	A
2909.14	534.90	3195.31	C	3003.49	589.5	3000	A	3148.15	742.55	10000	A
2917.53	549.10	4245	C	3013.24	599.3	3000	A	3160.38	767.45	10000	A
2930.36	555.60	4341.66	C	3021.40	611.3	3000	A	3169.76	779.75	10000	A
2937.72	559.10	3668.79	C	3029.95	620.6	3000	A	3179.04	787.75	10000	A
3002.71	583.00	4632.49	C	3039.12	631.7	6000	A				
3009.86	590.00	4341.66	C	3043.84	644.8	6000	A				
3018.09	602.7	5805.17	C	3052.27	660.7	10000	A				
3017.25	605.08	6000	A	3059.61	671.7	10000	A				
3027.54	615.88	6000	A	3065.69	682.9	10000	A				
3027.9	615.20	8471.72	C	3082.61	691.9	10000	A				
3035.41	622.07	6000	B	3101.62	703.9	10000	A				
3038.00	627.5	6888.4	C	3123.67	714.4	10000	A				
3040.00	633	6888.4	C	3133.92	724.9	10000	A				
3043.01	634.42	6000	B	3141.52	732.5	10000	A				
3043.26	638.2	7481.31	C	3148.60	742.9	10000	A				
3048.51	649.06	6000	B	3155.83	752.1	10000	A				
3056.77	660.79	6000	B	3160.42	758.3	10000	A				
3065.93	676.70	6000	A	3165.19	767.7	10000	A				
3077.74	687.33	6000	A	3172.00	778.8	10000	A				
3093.51	698.16	6000	A	3181.00	787.5	10000	A				
3112.43	708.96	6000	A								
3119.57	714.37	6000	B								
3124.27	729.38	6000	A								
3131.02	733.95	6000	B								
3143.2	741.94	6000	B								
3152.25	754.18	6000	A								
3158.91	763.07	6000	A								
3166.87	772.68	6000	A								
3174.81	782.61	6000	A								
3180.6	797.74	6000	B								
3189.83	802.46	6000	A								

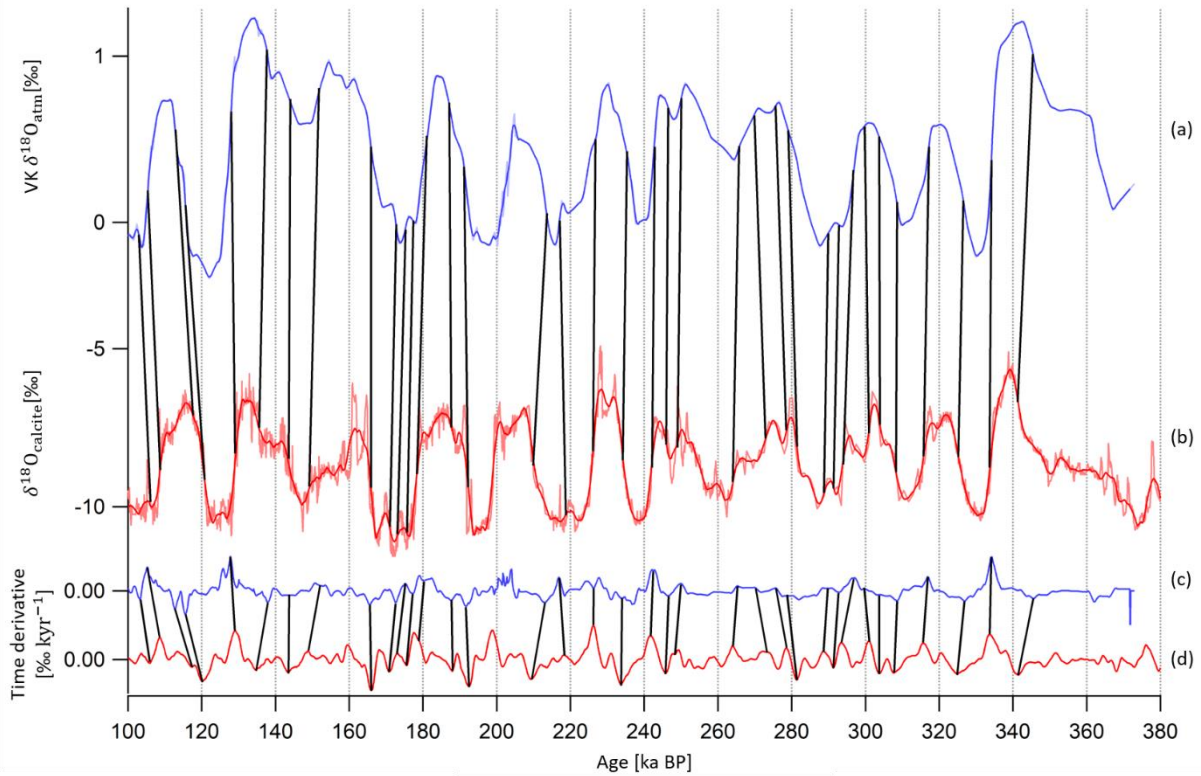
224

225 **4.1.2 $\delta^{18}\text{O}_{\text{atm}}$ age constraints for Vostok**

226 Following the dating approach proposed by Extier et al. (2018a), $\delta^{18}\text{O}_{\text{atm}}$ from Vostok ice core and $\delta^{18}\text{O}_{\text{calcite}}$ from

227 Chinese speleothems (Cheng et al., 2016) are aligned using mid-slopes of their variations between 370 and 100 ka

228 BP (Fig. S10). To do so, the Vostok $\delta^{18}\text{O}_{\text{atm}}$ record and the Chinese $\delta^{18}\text{O}_{\text{calcite}}$ signal are linearly interpolated every
 229 100 years, smoothed (25 points Savitzky-Golay) and extrema in their temporal derivative are aligned. 35 new tie
 230 points are identified and attached to a 1σ -uncertainty between 2.3 and 3.5 kyr. They replace the 35 age constraints
 231 obtained by aligning $\delta^{18}\text{O}_{\text{atm}}$ and delayed precession, associated with a 6 kyr 1σ -uncertainty and used to construct
 232 AICC2012.



233 **Figure S10. Alignment of Vostok $\delta^{18}\text{O}_{\text{atm}}$ and $\delta^{18}\text{O}_{\text{calcite}}$ records between 370 and 100 ka BP.** (a) Vostok (VK) $\delta^{18}\text{O}_{\text{atm}}$ raw
 234 (light blue) and smoothed (dark blue, Savitzky-Golay 25 points) record (Petit et al., 1999). (b) Raw (light red) and smoothed
 235 (red) composite $\delta^{18}\text{O}_{\text{calcite}}$ from speleothems from Sambaio, Hulu and Dongge caves (Cheng et al., 2016). (c) Temporal derivative
 236 of smoothed VK $\delta^{18}\text{O}_{\text{atm}}$ (blue). (d) Temporal derivative of smoothed $\delta^{18}\text{O}_{\text{calcite}}$ (red). Extrema in temporal derivatives are
 237 aligned. New tie points used to constrain AICC2023 are represented by black vertical bars.

238 4.2 New background scenarios

239 4.2.1 LID scenario for Vostok using $\delta^{15}\text{N}$ and $\delta^{40}\text{Ar}$ data

240 When $\delta^{15}\text{N}$ measurements are not available, Bazin et al. (2013) used a synthetic $\delta^{15}\text{N}$ signal based on the
 241 correlation between $\delta^{15}\text{N}$ and δD to estimate the background LID scenario at Vostok and to constrain the
 242 AICC2012 timescale. In this work, the background LID scenario is modified (Table S6). It is estimated from $\delta^{15}\text{N}$
 243 data or $\delta^{40}\text{Ar}$ data (which also reflects evolution of the firm thickness) and corrected for thermal fractionation. The
 244 thermal fractionation term is estimated by the firm model running in the same configuration as for calculating the
 245 modeled LID at EDC (i.e. firm densification activation energy depending on the temperature and impurity
 246 concentration). The final LID scenario has been smoothed using a Savitzky-Golay algorithm (25 points), and then
 247 provided as an input file to Paleochrono (Fig. S11).

248 **Table S6. Method of determination of LID background scenario according to Vostok depth range.** The thermal
 249 fractionation term is estimated by the firm model running in configuration 1: Firm densification activation energy depending on
 250 the temperature and impurity concentration.

Depth range (m)	0 – 150	150 – 2737	2737 – 2847	2847 – Bottom
data availability	No	$\delta^{15}\text{N}$ (Sowers et al., 1992)	$\delta^{40}\text{Ar}$ (Caillon et al., 2003)	$\delta^{15}\text{N}$ (Sowers et al., 1992)
LID	From constant $\delta^{15}\text{N}$ (measured at 150 m) and corrected for thermal fractionation.	From $\delta^{15}\text{N}$ data, corrected for thermal fractionation and smoothed.	From $\delta^{40}\text{Ar}$ data, corrected for thermal fractionation and smoothed.	From $\delta^{15}\text{N}$ data, corrected for thermal fractionation and smoothed.

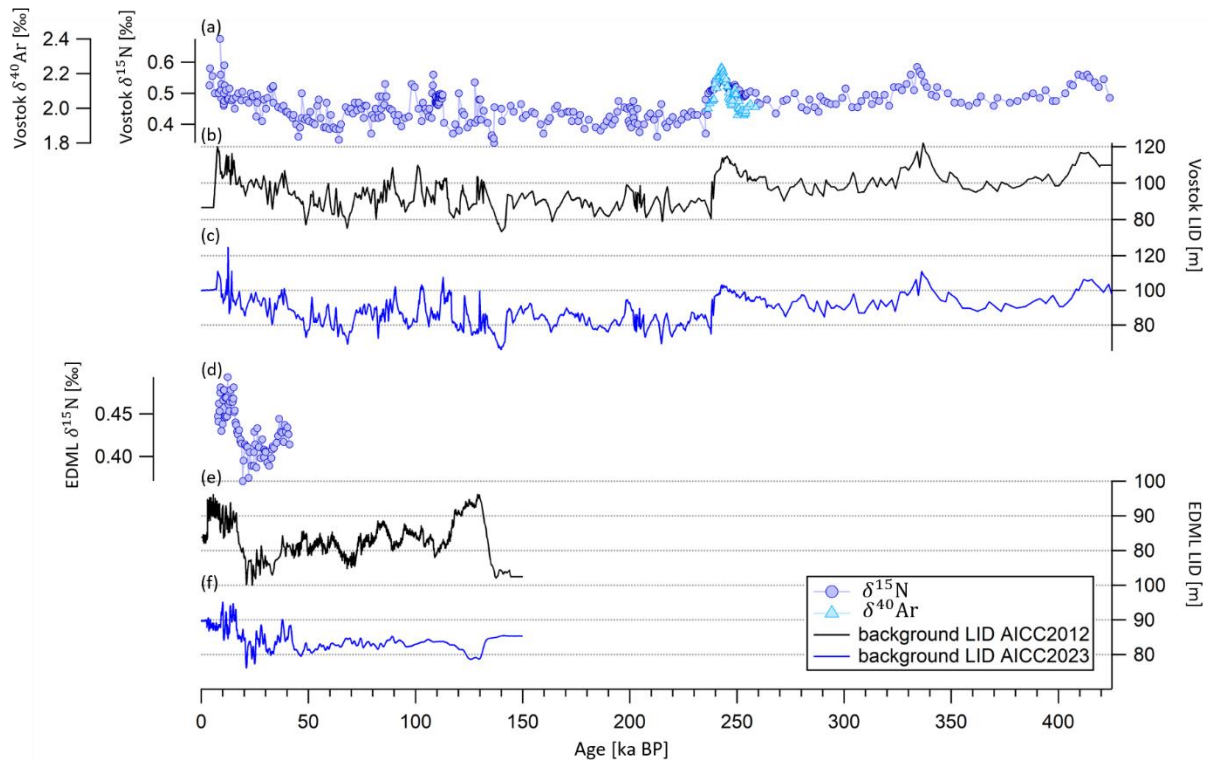
251

252 4.2.2 LID scenario for EDML using $\delta^{15}\text{N}$ data and firn model estimates

253 When $\delta^{15}\text{N}$ measurements are not available, Bazin et al. (2013) used a synthetic $\delta^{15}\text{N}$ signal based on the
 254 correlation between $\delta^{15}\text{N}$ and δD to estimate the background LID scenario at EDML and to constrain the
 255 AICC2012 timescale. In this work, the background LID scenario at EDML is estimated from $\delta^{15}\text{N}$ data (when
 256 available), which is corrected for thermal fractionation. The thermal fractionation term is estimated by the firn
 257 model. Otherwise, the background LID is calculated by the firn model running in the same configuration as for
 258 calculating the modeled LID at EDC (i.e. firn densification activation energy depending on the temperature and
 259 impurity concentration). The final LID scenario has been smoothed using a Savitzky-Golay algorithm (25 points),
 260 and then provided as an input file to Paleochrono (Fig. S11).

261 **Table S7. Method of determination of LID background scenario according to EDML depth range.** The thermal
 262 fractionation term is estimated by the firn model running in the same configuration as for calculating the modeled LID, i.e. firn
 263 densification activation energy depending on the temperature and impurity concentration.

Depth range (m)	0 – 548	548 – 1398.2	1398.2 – Bottom
$\delta^{15}\text{N}$ data availability	No	Yes (Landais et al., 2006)	No
LID	From constant $\delta^{15}\text{N}$ (measured at 548 m) and corrected for thermal fractionation.	From $\delta^{15}\text{N}$ data, corrected for thermal fractionation and smoothed.	From firn modeling.



264 **Figure S11. Records of $\delta^{40}\text{Ar}$ and $\delta^{15}\text{N}$ and LID scenarios at Vostok and EDML.** (a) $\delta^{40}\text{Ar}$ and $\delta^{15}\text{N}$ records of Vostok ice
 265 core (Sowers et al., 1992; Caillon et al., 2003) and (d) $\delta^{15}\text{N}$ record of EDML ice core (Landais et al., 2006) on AICC2023 age
 266 scale. (b) Background LID at Vostok and (e) EDML used to constrain AICC2012 (Bazin et al. 2013). (c) Background LID at
 267 Vostok and (f) EDML used to constrain AICC2023 (this study).

268 Such modifications of the background LID scenarios have a negligible impact on the new AICC2023
 269 chronology. Indeed, choosing the scenarios described in this section for EDML and Vostok rather than the
 270 scenarios that were used to constrain AICC2012 induces maximum age shifts of 200 and 350 years in the
 271 chronology of EDML and Vostok ice cores respectively, which is minor considering the chronological uncertainty
 272 of several hundreds of years.

273

274

275

276

277

278

279

280

281

282

283 4.2.3 Background scenarios and relative errors for the construction of AICC2023

284 With respect to the AICC2012 chronology, the background LID scenarios for EDC, Vostok, EDML and
 285 TALDICE ice cores are revised in AICC2023 (Table S8). We also reduce the background relative uncertainties
 286 associated with the LID, thinning and accumulation functions at the five sites (see Sect. 3.2 in the Supplementary
 287 Material).

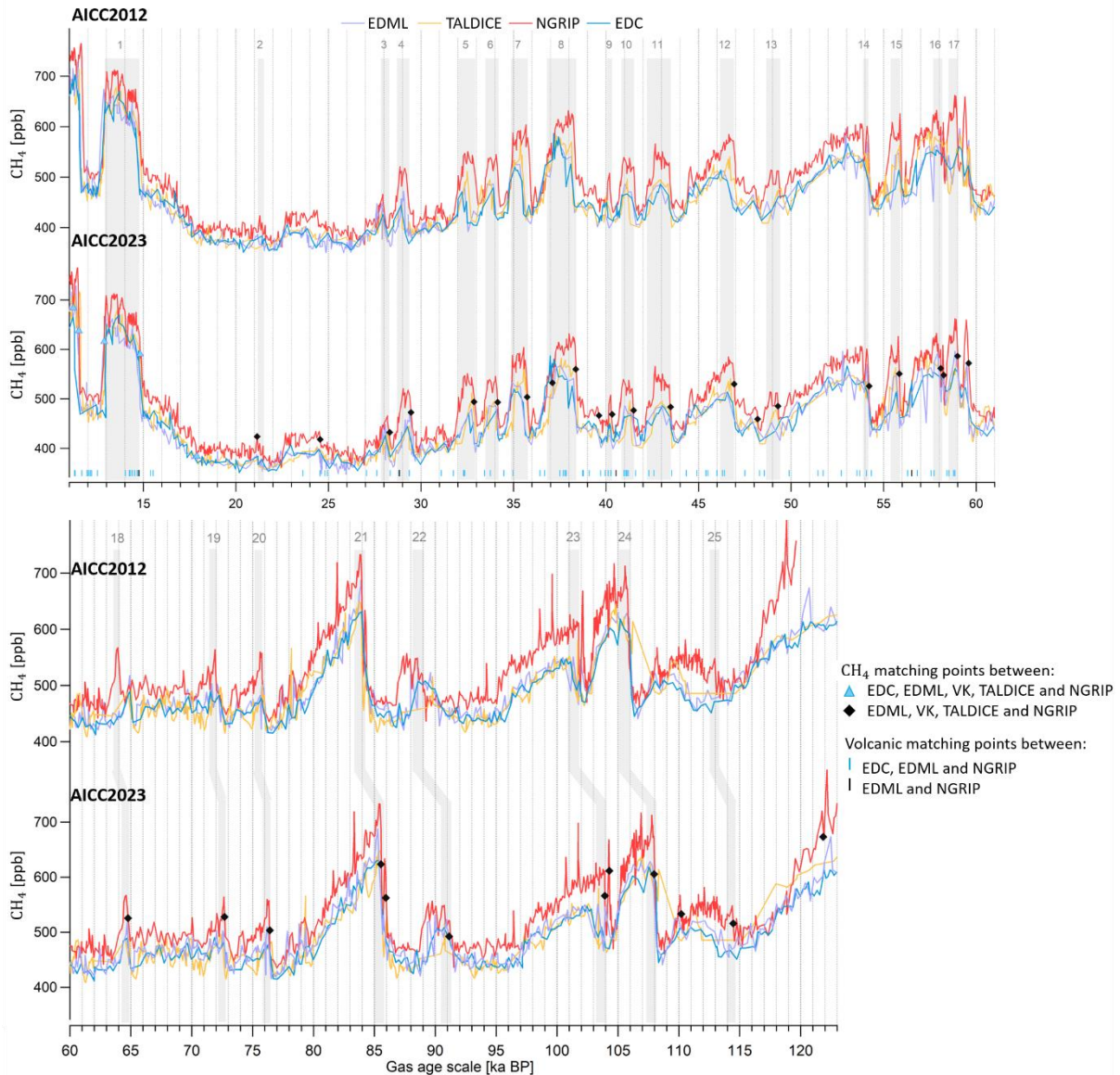
288 **Table S8. Origin of the background scenarios of LID, thinning and accumulation for EDC, EDML, Vostok, TALDICE**
 289 **and NGRIP and associated relative errors used in AICC2023.** The LID prior relative uncertainty is set between 0.1 or 0.2
 290 whether $\delta^{15}\text{N}$ data are available or not. The mention ‘‘AICC2012’’ means that the scenario is the same than in AICC2012 (Bazin
 291 et al., 2013).

	LID		Thinning		Accumulation	
	Scenario	Relative error	Scenario	Relative error	Scenario	Relative error
EDC	$\delta^{15}\text{N}$	0.1 (data)	AICC2012	Linear from 0 to 0.5	AICC2012	0.2
	Firn model	0.2 (no data)				
EDML	$\delta^{15}\text{N}$	0.1 (data)	AICC2012	Linear from 0 to 1	AICC2012	0.2
	Firn model	0.2 (no data)				
Vostok	$\delta^{15}\text{N}$, $\delta^{40}\text{Ar}$	0.1 (data) 0.2 (no data)	AICC2012	Linear from 0 to 0.5	AICC2012	Linear from 0.2 to 0.7
TALDICE	TALDICE-deep1 (Crotti et al., 2021) $\delta^{15}\text{N}$	0.2	AICC2012	Linear from 0 to 1	AICC2012	0.2
NGRIP	AICC2012 (Firn model)	0.2	AICC2012	Linear from 0 to 0.5	AICC2012	0.2

292

293 4.3 The new AICC2023 age scale over the last 120 kyr

294 With respect to the AICC2012 chronology, new stratigraphic links between ice and gas series are used to constrain
 295 AICC2023 over the past 120 kyr. They include tie points between CH_4 series from EDC, EDML, Vostok,
 296 TALDICE and NGRIP ice cores (Baumgartner et al., 2014) as well as volcanic matching points between EDC,
 297 EDML and NGRIP ice cores (Svensson et al., 2020) (Fig. S12). The gas stratigraphic links used to construct
 298 AICC2012 over the last glacial period come from matching CH_4 and $\delta^{18}\text{O}_{\text{atm}}$ variations between ice cores. Still, an
 299 offset of several centuries is observed between Antarctic and Greenland CH_4 records during the rapid increases
 300 associated with Dansgaard-Oeschger (D-O) events in AICC2012 (Fig. S12). Baumgartner et al. (2014)
 301 substantially extended the NGRIP CH_4 dataset and provided accurate tie points between NGRIP, EDML, EDC,
 302 Vostok and TALDICE CH_4 records. By implementing these new gas stratigraphic links in AICC2023, we improve
 303 the alignment between the CH_4 records by several centuries, up to 500 and 840 years for the North Atlantic abrupt
 304 warming associated with D-O 5 and 18 respectively.



305 **Figure S12. CH₄ records from Antarctic and NGRIP sites over the last 122 kyr.** CH₄ from EDML, TALDICE, NGRIP and
 306 EDC ice cores on the AICC2012 gas timescale (top panel). CH₄ from EDML, TALDICE, NGRIP and EDC ice cores on the
 307 AICC2023 gas timescale (bottom panel). Stratigraphic links between CH₄ series from EDC, EDML, Vostok, TALDICE and
 308 NGRIP ice cores (blue triangles and black squares, Baumgartner et al., 2014) and between volcanic sulfate patterns from EDC,
 309 EDML and NGRIP ice cores (vertical bars, Svensson et al., 2020) are used to constrain AICC2023 over the last 122 kyr. Abrupt
 310 D-O events are shown by grey rectangles and numbered from the youngest to the oldest (1-25) (Barbante et al., 2006).

311

312

313

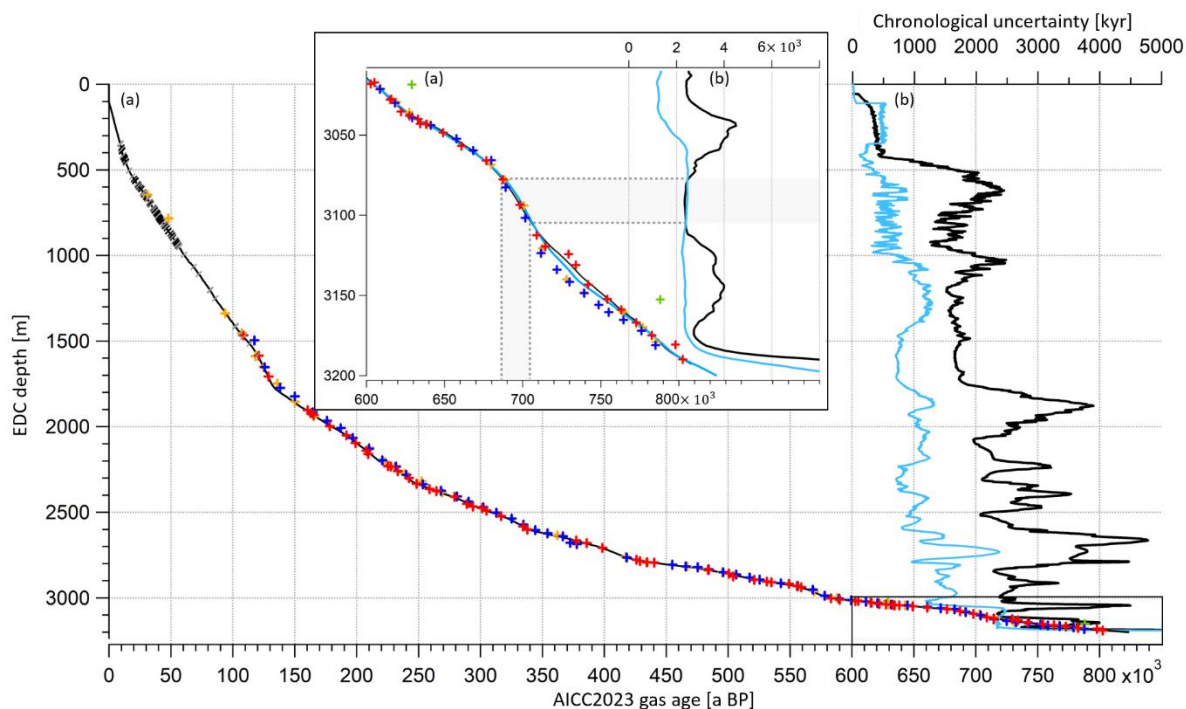
314

315

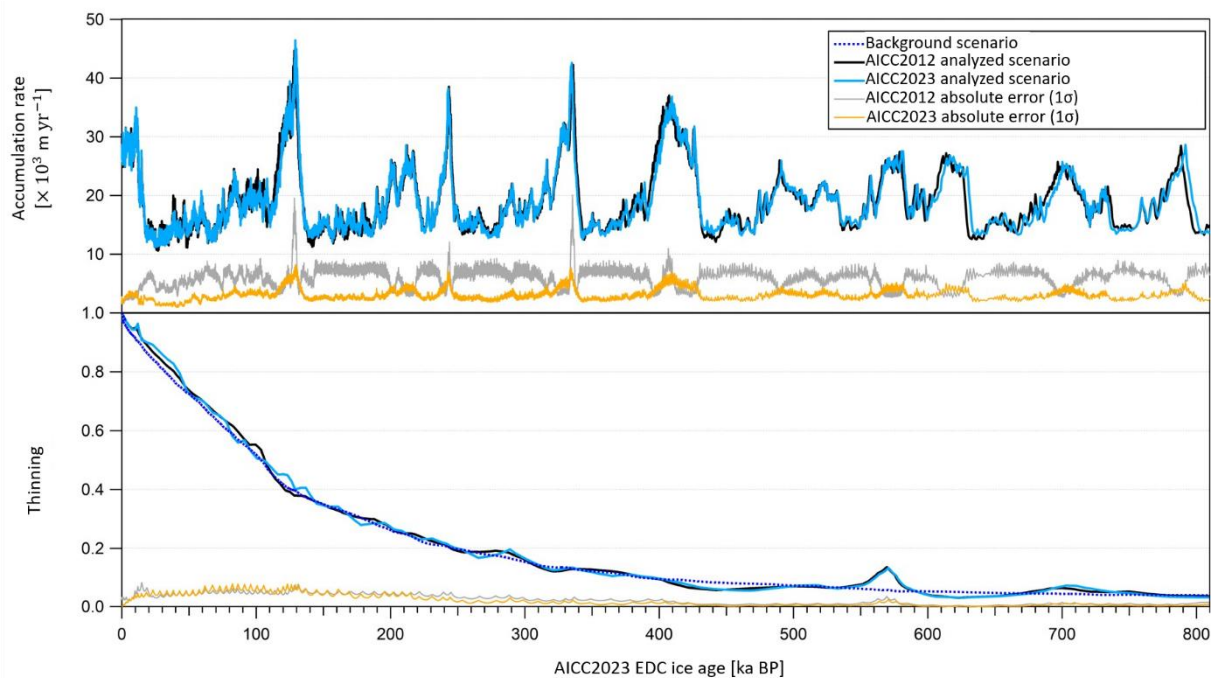
316

317

318 **4.4 The new AICC2023 age scale for EDC over the last 800 kyr**



319 **Figure S13. EDC gas age and uncertainty as a function of the depth.** (a) EDC gas age (AICC2012 in black, AICC2023 in
320 blue). (b) 1σ uncertainty (AICC2012 in black, AICC2023 in blue). Crosses and slashes represent new age constraints (ice
321 stratigraphic links in black, gas stratigraphic links in grey, $\delta^{18}\text{O}_{\text{atm}}$ in red, $\delta\text{O}_2/\text{N}_2$ in blue, TAC in orange, ^{81}Kr in green). Inset
322 is a zoom in between 800 and 600 ka BP. Grey rectangles frame periods where the new AICC2023 uncertainty is larger than
323 AICC2012 uncertainty.



324 **Figure S14. Analyzed accumulation and thinning functions for EDC over the last 800 kyr.** They are provided by AICC2012
325 and AICC2023 (black and blue plain lines respectively) along with their absolute uncertainties (gray and yellow respectively).
326 The background thinning function is the same for AICC2012 and AICC2023 (dark blue dotted line).

328 **References**

- 329 Barbante, C., Barnola, J.-M., Becagli, S., Beer, J., Bigler, M., Boutron, C., Blunier, T., Castellano, E., Cattani, O.,
 330 Chappellaz, J., Dahl-Jensen, D., Debret, M., Delmonte, B., Dick, D., Falourd, S., Faria, S., Federer, U., Fischer,
 331 H., Freitag, J., Frenzel, A., Fritzsche, D., Fundel, F., Gabrielli, P., Gaspari, V., Gersonde, R., Graf, W., Grigoriev,
 332 D., Hamann, I., Hansson, M., Hoffmann, G., Hutterli, M. A., Huybrechts, P., Isaksson, E., Johnsen, S., Jouzel, J.,
 333 Kaczmarek, M., Karlin, T., Kaufmann, P., Kipfstuhl, S., Kohno, M., Lambert, F., Lambrecht, A., Lambrecht, A.,
 334 Landais, A., Lawer, G., Leuenberger, M., Littot, G., Loulergue, L., Lüthi, D., Maggi, V., Marino, F., Masson-
 335 Delmotte, V., Meyer, H., Miller, H., Mulvaney, R., Narcisi, B., Oerlemans, J., Oerter, H., Parrenin, F., Petit, J.-R.,
 336 Raisbeck, G., Raynaud, D., Röthlisberger, R., Ruth, U., Rybak, O., Severi, M., Schmitt, J., Schwander, J.,
 337 Siegenthaler, U., Siggaard-Andersen, M.-L., Spahni, R., Steffensen, J. P., Stenni, B., Stocker, T. F., Tison, J.-L.,
 338 Traversi, R., Udasti, R., Valero-Delgado, F., van den Broeke, M. R., van de Wal, R. S. W., Wagenbach, D., Wegner,
 339 A., Weiler, K., Wilhelms, F., Winther, J.-G., Wolff, E., and Members, E. C.: One-to-one coupling of glacial climate
 340 variability in Greenland and Antarctica, *Nature*, 444, 195–198, DOI:10.1038/nature05301, 2006.
- 341 Barker, S., Knorr, G., Conn, S., Lordsmith, S., Newman, D., & Thornalley, D.: Early interglacial legacy of
 342 deglacial climate instability, *Paleoceanogr. Paleoclimatol.*, 34, 1455-1475, DOI:10.1029/2019PA003661, 2019.
- 343 Barker, S., Zhang, X., Jonkers, L., Lordsmith, S., Conn, S., & Knorr, G.: Strengthening Atlantic inflow across the
 344 mid-Pleistocene transition, *Paleoceanogr. Paleoclimatol.*, 36, DOI:10.1029/2020PA004200, 2021.
- 345 Baumgartner, M., Kindler, P., Eicher, O., Floch, G., Schilt, A., Schwander, J., Spahni, R., Capron, E., Chappellaz,
 346 J., Leuenberger, M., Fischer, H., and Stocker, T. F.: NGRIP CH₄ concentration from 120 to 10 kyr before present
 347 and its relation to a $\delta^{15}\text{N}$ temperature reconstruction from the same ice core, *Clim. Past*, 10, 903–920,
 348 DOI:10.5194/CP-10-903-2014, 2014.
- 349 Bazin, L., Landais, A., Lemieux-Dudon, B., Toyé Mahamadou Kele, H., Veres, D., Parrenin, F., Martinerie, P.,
 350 Ritz, C., Capron, E., Lipenkov, V., Loutre, M.-F., Raynaud, D., Vinther, B., Svensson, A., Rasmussen, S. O.,
 351 Severi, M., Blunier, T., Leuenberger, M., Fischer, H., Masson-Delmotte, V., Chappellaz, J., and Wolff, E.: An
 352 optimized multi-proxy, multi-site Antarctic ice and gas orbital chronology (AICC2012): 120–800 ka, *Clim. Past*,
 353 9, 1715–1731, DOI:10.5194/cp-9-1715-2013, 2013.
- 354 Bazin, L., Landais, A., Capron, E., Masson-Delmotte, V., Ritz, C., Picard, G., Jouzel, J., Dumont, M., Leuenberger,
 355 M., and Prié, F.: Phase relationships between orbital forcing and the composition of air trapped in Antarctic ice
 356 cores, *Clim. Past*, 12, 729–748, DOI:10.5194/cp-12-729-2016, 2016.
- 357 Bréant, C., Martinerie, P., Orsi, A., Arnaud, L., and Landais, A.: Modelling firn thickness evolution during the last
 358 deglaciation: constraints on sensitivity to temperature and impurities, *Clim. Past*, 13, 833–853, DOI:10.5194/cp-
 359 13-833-2017, 2017.
- 360 Buizert, C.: The Ice Core Gas Age-Ice Age Difference as a Proxy for Surface Temperature, *Geophys. Res. Lett.*,
 361 48, e2021GL094241, DOI:10.1029/2021GL094241, 2021.
- 362 Caillon, N., Jouzel, J., Severinghaus, J. P., Chappellaz, J., and Blunier, T.: A novel method to study the phase
 363 relationship between Antarctic and Greenland climate, *Geophys. Res. Lett.*, 30, DOI:10.1029/2003GL017838,
 364 2003.
- 365 Crotti, I., Landais, A., Stenni, B., Bazin, L., Parrenin, F., Frezzotti, M., Ritterbusch, F., Lu, Z. T., Jiang, W., Yang,
 366 G. M., Fourré, E., Orsi, A., Jacob, R., Minster, B., Prié, F., Dreossi, G., and Barbante, C.: An extension of the
 367 TALDICE ice core age scale reaching back to MIS 10.1, *Quat. Sci. Rev.*, 266, 107078,
 368 DOI:10.1016/J.QUASCIREV.2021.107078, 2021.
- 369 Dreyfus, G. B., Parrenin, F., Lemieux-Dudon, B., Durand, G., Masson-Delmotte, V., Jouzel, J., Barnola, J. M.,
 370 Panno, L., Spahni, R., Tisserand, A., Siegenthaler, U., and Leuenberger, M.: Anomalous flow below 2700 m in

371 the EPICA Dome C ice core detected using $\delta^{18}\text{O}$ of atmospheric oxygen measurements, *Clim. Past*, 3, 341–353,
372 DOI:10.5194/CP-3-341-2007, 2007.

373 Extier, T., Landais, A., Bréant, C., Prié, F., Bazin, L., Dreyfus, G., Roche, D. M., and Leuenberger, M.: On the
374 use of $\delta^{18}\text{O}_{\text{atm}}$ for ice core dating, *Quat. Sci. Rev.*, 185, 244–257, DOI:10.1016/J.QUASCIREV.2018.02.008,
375 2018a.

376 Extier, T., Landais, A., Bréant, C., Prié, F., Bazin, L., Dreyfus, G., Roche, D. M., and Leuenberger, M. C.: $\delta\text{O}_2/\text{N}_2$
377 records between 100–800 ka from EPICA Dome C ice core, *PANGAEA*, DOI:10.1594/PANGAEA.887326,
378 2018b.

379 Landais, A., Barnola, J.M., Kawamura, K., Caillon, N., Delmotte, M., Van Ommen, T., Dreyfus, G., Jouzel, J.,
380 Masson-Delmotte, V., Minster, B., Freitag, J., Leuenberger, M., Schwander, J., Huber, C., Etheridge, D. and
381 Morgan, V., Firn-air $\delta^{15}\text{N}$ in modern polar sites and glacial–interglacial ice: a model-data mismatch during glacial
382 periods in Antarctica?, *Quat. Sci. Rev.*, 25, 49–62, DOI:10.1016/j.quascirev.2005.06.007, 2006.

383 Landais, A., Dreyfus, G., Capron, E., Pol, K., Loutre, M. F., Raynaud, D., Lipenkov, V. Y., Arnaud, L., Masson-
384 Delmotte, V., Paillard, D., Jouzel, J., and Leuenberger, M.: Towards orbital dating of the EPICA Dome C ice core
385 using $\delta\text{O}_2/\text{N}_2$, *Clim. Past*, 8, 191–203, DOI:10.5194/CP-8-191-2012, 2012.

386 Laskar, J., Robutel, P., Joutel, F., Gastineau, M., Correia, A. C. M., and Levrard, B.: A long-term numerical
387 solution for the insolation quantities of the Earth, *Astron. Astrophys.*, 428, 261–285, DOI:10.1051/0004-
388 6361:20041335, 2004.

389 Oyabu, I., Kawamura, K., Uchida, T., Fujita, S., Kitamura, K., Hirabayashi, M., Aoki, S., Morimoto, S., Nakazawa,
390 T., Severinghaus, J. P., and Morgan, J. D.: Fractionation of O_2/N_2 and Ar/N_2 in the Antarctic ice sheet during
391 bubble formation and bubble–clathrate hydrate transition from precise gas measurements of the Dome Fuji ice
392 core, *Cryosphere*, 15, 5529–5555, DOI:10.5194/tc-15-5529-2021, 2021.

393 Oyabu, I., Kawamura, K., Buizert, C., Parrenin, F., Orsi, A., Kitamura, K., Aoki, S., and Nakazawa, T.: The Dome
394 Fuji ice core DF2021 chronology (0–207 kyr BP), *Quat. Sci. Rev.*, 294, 107754,
395 DOI:10.1016/J.QUASCIREV.2022.107754, 2022.

396 Parrenin, F., Rémy, F., Ritz, C., Siebert, M. J., and Jouzel, J.: New modeling of the Vostok ice flow line and
397 implication for the glaciological chronology of the Vostok ice core, *J. Geophys. Res. Atmos.*, 109, D20102,
398 DOI:10.1029/2004JD004561, 2004.

399 Parrenin, F., Dreyfus, G., Durand, G., Fujita, S., Gagliardini, O., Gillet, F., Jouze, J., Kawamura, K., Lhomme, N.,
400 Masson-Delmotte, V., Ritz, C., Schwander, J., Shoji, H., Uemura, R., Watanabe, O., and Yoshida, N.: 1-D-ice
401 flow modelling at EPICA Dome C and Dome Fuji, East Antarctica, *Clim. Past*, 3, 243–259, DOI:10.5194/CP-3-
402 243-2007, 2007.

403 Parrenin, F., Barker, S., Blunier, T., Chappellaz, J., Jouzel, J., Landais, A., Masson-Delmotte, V., Schwander, J.,
404 and Veres, D.: On the gas-ice depth difference (Δdepth) along the EPICA Dome C ice core, *Clim. Past*, 8, 1239–
405 1255, DOI:10.5194/CP-8-1239-2012, 2012.

406 Petit, J. R., Jouzel, J., Raynaud, D., Barkov, N. I., Barnola, J. M., Basile, I., Bender, M., Chappellaz, J., Davis, M.,
407 Delaygue, G., Delmotte, M., Kotiyakov, V. M., Legrand, M., Lipenkov, V. Y., Lorius, C., Pépin, L., Ritz, C.,
408 Saltzman, E., and Stievenard, M.: Climate and atmospheric history of the past 420,000 years from the Vostok ice
409 core, Antarctica, *Nature*, 399, 429–436, DOI:10.1038/20859, 1999.

410 Sowers, T., Bender, M., Raynaud, D., and Korotkevich, Y. S.: $\delta^{15}\text{N}$ of N_2 in air trapped in polar ice: A tracer of
411 gas transport in the firn and a possible constraint on ice age–gas age differences, *J. Geophys. Res. Atmos.*, 97,
412 15683–15697, DOI:10.1029/92JD01297, 1992.

413 Svensson, A., Dahl-Jensen, D., Steffensen, J. P., Blunier, T., Rasmussen, S. O., Vinther, B. M., Vallenga, P.,
414 Capron, E., Gkinis, V., Cook, E., Kjær, H. A., Muscheler, R., Kipfstuhl, S., Wilhelms, F., Stocker, T. F., Fischer,
415 H., Adolphi, F., Erhardt, T., Sigl, M., Landais, A., Parrenin, F., Buizert, C., McConnell, J. R., Severi, M.,

416 Mulvaney, R., and Bigler, M.: Bipolar volcanic synchronization of abrupt climate change in Greenland and
417 Antarctic ice cores during the last glacial period, *Clim. Past*, 16, 1565–1580, DOI:10.5194/cp-16-1565-2020, 2020.

4.2 LIMITATIONS AND PERSPECTIVES

4.2.1 On the next coherent Antarctic ice core chronology

4.2.1.1 Corrections of AICC2023

The last 60 kyr

In order to prevent any confusion with reference ice core timescales, the new AICC2023 chronology for NGRIP is compelled to respect exactly the layer-counted GICC05 timescale through absolute dated horizons placed at one-meter intervals over the last 60 kyr (Svensson et al., 2005). For this reason, we did not use the methodology described by Lemieux-Dudon et al. (2015) which rather implemented layer counting as a constraint on the duration of events in the dating tool. In practice, we used GICC05 age constraints as dated horizons listed in the *age_horizons.txt* input file for NGRIP site in the Paleochrono-1.1 experiment. Lemieux-Dudon et al. (2015) rather used dated intervals prescribed in the *ice_age_intervals.txt* input file.

Although this alternative method has no significant impact on the chronology (410 years at most), it provides more plausible uncertainty estimates for the chronology over the past 60 kyr.

Gas age inversions

In AICC2012, many gas age inversions (i.e. gas age decreases with increasing depth) were observed because of the too important variability of the analyzed LID scenario that was transferred to the Δ depth, itself driven by the high relative uncertainty associated with the background LID (between 20 and 70% in AICC2012). To address this problem in AICC2023, we revised the background LID scenario using firn modeling (reducing the uncertainty to 20%) and $\delta^{15}\text{N}$ data when available (reducing the uncertainty to 10%). We also used a smoothing function on the $\delta^{15}\text{N}$ -inferred LID. The less variable LID scenario obtained in AICC2023 resulted in less gas age inversion.

However, as noticed by J. Schmitt, some gas age reversals occur in the gas age scale of the top 600 m of EDC ice core. They can be shown by calculating the gas age increment at each depth z as: gas age ($z + 0.55$ m) – gas age (z) (blue curve in Fig. 4.2). A negative gas age increment indicates a gas age reversal. The age reversals are only present if the AICC2023 experiment is run with the LID calculated at high resolution (< 1 m; blue curve in Fig. 4.2). Although it was demonstrated that gas age reversals are possible at a very fine scale (Fourteau et al., 2020), our aim was to provide a smoothed age scale and to avoid these gas age reversals in the younger section of the core, which was not the focus of our study. Indeed, our aim was to refine the dating of the deeper section (prior to 60 ka BP).

Smoothing the prior LID scenario enables removal of the age inversion at ~ 580 m (red curve in Fig. 4.2) caused by a discontinuity in the prior LID due to an abrupt transition from $\delta^{15}\text{N}$ -inferred values to modeled LID values. However, the gas age inversion present at ~ 590 m remains. It may be due to an abrupt decrease observed in the posterior LID, itself likely due to an incoherence between prior LID (which may be underestimated by firn modeling) and volcanic matching points linking EDC to EDML ice core (Svensson et al., 2020). We have less confidence in the prior LID given by the firn model than in stratigraphic links established by

Svensson et al. (2020). Indeed, this age inversion occurs during glacial conditions while the firn densification model is calibrated for present-day conditions and might not be as performant during extremely cold conditions. To remove this gas age inversion at ~590 m, we increase the *lambda_lid* parameter (from 1000 years in the AICC2023 experiment to 2000, see the black curve in Fig. 4.2) in the *parameters_all_sites.yml* file in the Paleochrono-1.1 model. This parameter permits to authorize more or less variability in the posterior LID scenario with respect to the initial prior scenario. The *parameters_all_sites.yml* file is composed of the site parameters that are the same for all sites (e.g. the resolution of the vertical grid and the lambda to calculate the posterior scenarios of LID, thinning and snow accumulation rate). Here, this operation forces the posterior LID to show a variability of lesser magnitude than the prior LID.

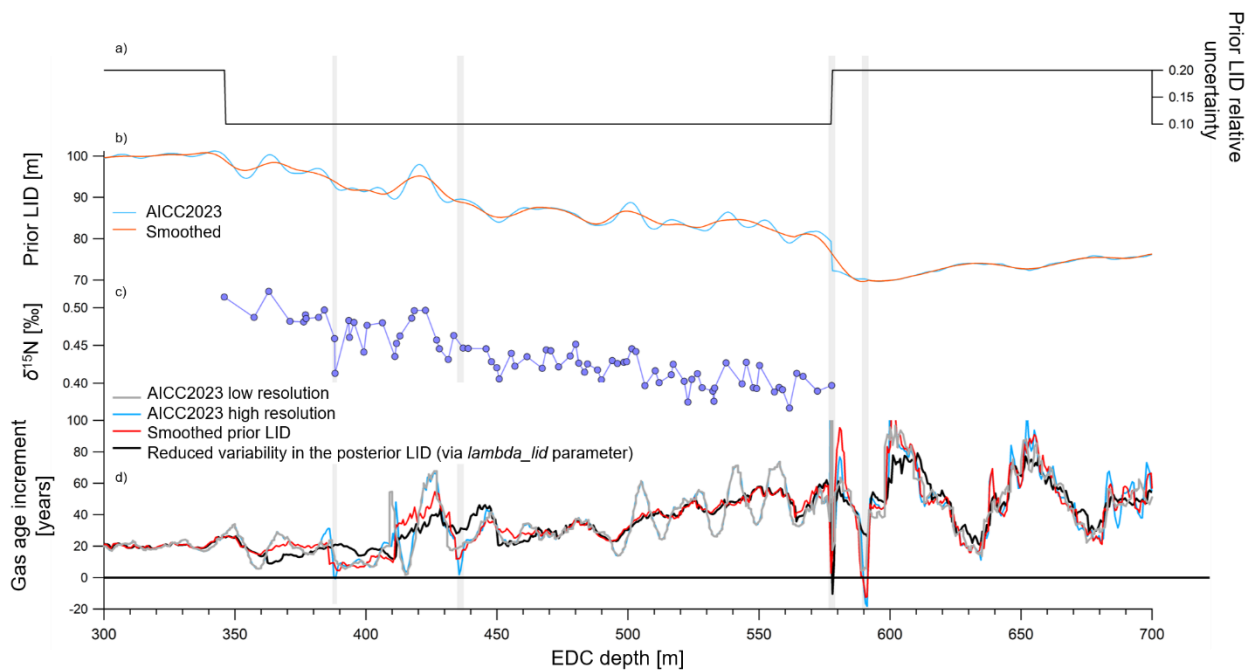


Figure 4.2 Gas age inversions in the top 700 m of the EDC ice core. a) Prior uncertainty attached to the background LID scenario. b) Background LID scenario used in AICC2023 and smoothed with respect to AICC2023 (blue and orange curves). c) $\delta^{15}\text{N}$ data used to calculate the background LID in AICC2023. d) The gas age increment calculated at each depth z as gas age ($z + 0.55$ m) – gas age (z). A negative gas age increment indicates a gas age reversal. The blue curve shows the gas age increment if the LID is calculated at high resolution (blue curve; AICC2023) or low resolution (gray curve). The gray bars highlight the gas age reversal occurring in AICC2023. The red curve is obtained using a smoothed prior LID with respect to AICC2023. The black curve is obtained by increasing the *lambda_lid* parameter from 1000 in AICC2023 to 2000 in the Paleochrono-1.1 model. This operation increases the regularity of the posterior LID with respect to the prior LID.

No gas age scale before the top meters

As pointed out by P. Köhler, the EDC gas age scale in AICC2023 published on PANGAEA starts at 111.1 m depth, but the most recent CO_2 samples (Monnin et al., 2004) are measured for a depth of ~100 m, so there are five EDC- CO_2 samples without an official AICC2023 gas age.

We believe this issue comes from the 0-value assigned to the background LID scenario in the firn (between 0 and 111.1 m). However, we should have assigned the present-day value of the LID (~98.5 m) to the background scenario in the firn before the depth of 111.1 m. I modified

as such the input file and launched a new Paleochrono experiment with this update. The resulting gas age scale starts at the depth of 98.5 m (corresponding to the age of - 44 a BP, i.e. 1994 CE). The rest of the gas age scale is not significantly changed (at most 6 years at the depth of ~3100m where the gas age uncertainty is of 2500 years).

CH₄ synchronization involving the Vostok ice core

In AICC2023, the five ice cores are synchronized using the matching of their CH₄ records established by (Baumgartner et al., 2014). The residuals method of Parrenin et al. (2024) indicates that the stratigraphic link established at the depth of 228.7 m in Vostok ice core is not coherent with the rest of the background chronological information.

Baumgartner et al. (2014) tied this point to a maximum in the CH₄ record from EDML (see dashed line in Fig. 4.3). However, we believe that the low resolution of the Vostok methane record in this section (30 to 50 m) prevents from identifying without ambiguity a minimum and/or maximum in the CH₄ record. For instance, matching the CH₄ records with the plain line in Fig. 4.3, i.e. at the depth of 303.8 m in the Vostok ice core, also appears as a reasonable choice.

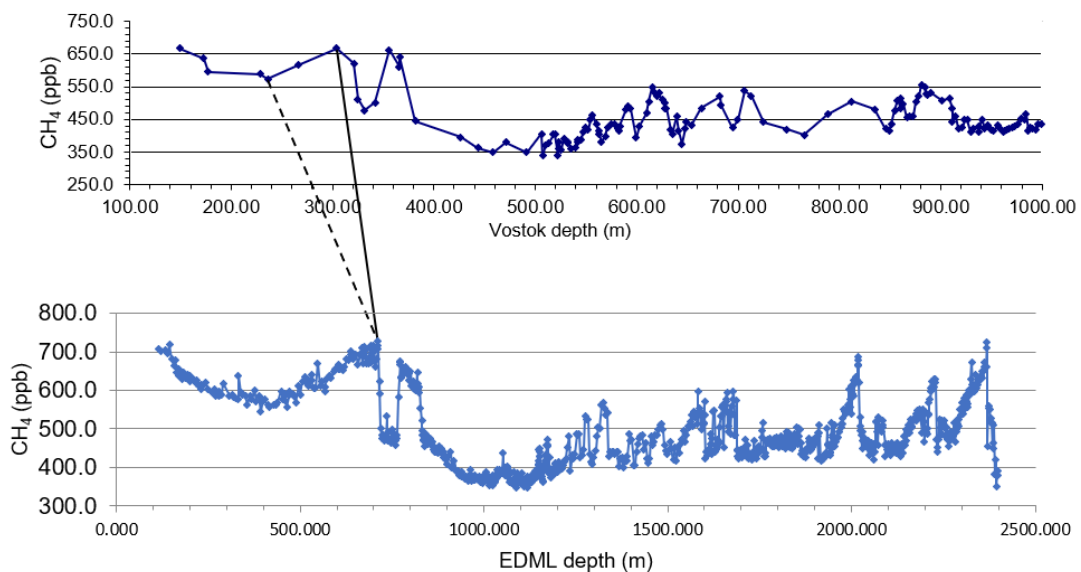


Figure 4.3 Matching EDML and Vostok CH₄ records around 11.3 ka BP. CH₄ records of Vostok and EDML ice cores are tied at the depths of (i) 228.7 and 703.6 m (respectively in Vostok and EDML), as per Baumgartner et al. (2014) (dashed line); and at the depths of (ii) 303.8 and 703.6 m, as per an alternative matching choice (plain line).

Summary

In the next coherent dating effort, we thus suggest to bring the following corrections:

- (i) Use the methodology described by Lemieux-Dudon et al. (2015), consisting in integrating the layer counting of GICC05 as dated intervals in the *ice_age_intervals.txt* input file to constrain NGRIP age rather than as dated horizons in the *ice_age_horizons.txt* file
- (ii) Increase the regularity of the posterior LID with respect to the prior LID (increasing the *lambda_lid* parameter in the *parameters_all_sites.yml* file to 2000 for example; Fig. 4.2)
- (iii) Smooth the prior LID scenario
- (iv) Calculate the analyzed LID with a depth resolution of 2000 points (out of ~3200 m) or less (setting the *nb_steps* variable to 2000 in the *corr_lid_grid* in the *parameters_all_sites.yml* file for example).
- (v) Make use of recently published high-resolution CH₄ records to synchronize the five ice cores (Nehrbass-Ahles et al., 2020b; Shin et al., 2020).

4.2.1.2 Suggestions for the next coherent Antarctic ice core chronology

Integration of the WAIS Divide and Dome Fuji sites

The WAIS Divide and Dome Fuji ice cores have been recently dated using high resolution data (Buizert, Cuffey, et al., 2015; Oyabu et al., 2022; Sigl et al., 2016). These studies provide *dated horizons* that could be used to integrate the two ice cores to the next coherent chronology AICC-. Relative *stratigraphic links* are also provided between EDC and WAIS Divide and between EDC and Dome Fuji by the studies of Buizert et al. (2018) and Fujita et al. (2015) respectively.

The NGRIP site

The recent study of Davies et al. (2014) provides a precise tephrostratigraphical framework that connects the NGRIP ice core to marine sediment cores located in the Northern Atlantic sector. The dating of some tephras used in their study to synchronize the different sites have been more accurately refined using ⁴⁰Ar/³⁹Ar dating (Guillou et al., 2019). The links given by Davies et al. (2014) and recently refined by Guillou et al. (2019) could be used as absolute *dated horizons* for the NGRIP ice core in the development of the next AICC- dating effort. They could also serve as *stratigraphic links* between NGRIP and the Northern Atlantic cores for the building of a chronology coherent for ice and marine cores using the Paleochrono-1.1 model. The methodology for constructing such coherent chronologies over the past glacial-interglacial cycles is explored in the Chapter 5. For now, the study described in the Chapter 5 does not rely on the studies of Davies et al. (2014) and Guillou et al. (2019) which are limited to the last glacial period.

4.2.2 On the development of the Paleochrono-tuning tool

For now, the Paleochrono-1.1 model considers discrete chronological information, i.e. discrete sets of *dated horizons* and *stratigraphic links*. F. Parrenin recently developed an automatic tuning functionality in the Paleochrono dating tool which enables to perform orbital dating via continuous synchronization of orbital proxies (e.g. ice core record of $\delta O_2/N_2$) to their orbital targets (e.g. local summer solstice insolation). Together with H. Guilluy, whose PhD project is co-supervised by E. Capron and F. Parrenin, we performed preliminary tests to evaluate the agreement between the discrete and continuous matching approaches. Further work is needed in this direction to assess whether this continuous synchronization method could be employed for next dating efforts as an added functionality to the Paleochrono-1.1 model.

4.3 IMPLICATIONS

4.3.1 On the use of the AICC2023 chronology as a tool

For evaluating paleo reconstructions of snow accumulation rate, LID and thinning function

In the Section 3.1 of the Supplementary Material (in Section 4.1), we assessed the compatibility of the modeled LID scenarios with the background chronological information of EDC. It is possible to apply the same approach, i.e. confronting prior and posterior scenarios given by the Paleochrono-1.1 model parameterized with AICC2023 chronological information, to evaluate the plausibility of the tested prior scenarios. Indeed, among the different pairs of prior/posterior scenarios, the prior scenario that is closer to its posterior scenario is the more compatible with the rest of the background chronological constraints. A perspective is to employ this method for the evaluation of any paleo reconstruction of snow accumulation rate, LID or thinning function for the sites included in AICC2023 by confronting them to the background chronological information.

For multi-archive paleo-data synthesis and climate modeling studies

The synthesis of paleo-data from multiple archives over past interglacials can serve as a test bed for evaluating climate model feedbacks in warmer-than-present high latitude regions (Legrain, 2023; Capron et al., 2014). Such syntheses are contingent upon the chronological framework employed for aligning paleoclimatic records. The uncertainty associated with the compiled surface temperature records can be reduced by using a more precise chronology of reference. Ongoing work led by Stevenard et al. uses AICC2023 as a chronological framework for building a multi-archive data synthesis over MISs 7, 9 and 11.

For understanding the bipolar seesaw mechanism

Barker et al. (2011) assumes that the bipolar seesaw mechanism (described in the Section 1.2.2.3; Stocker and Johnsen, 2003) was at play during past glacial periods. If this is correct, we expect abrupt rises in atmospheric CH₄ concentration reflecting northern hemispheric abrupt warming (D-O warmings) to occur synchronously with Antarctic ice- δ D maxima (AIM). Using the new high-resolution δ^{15} N record of EDC ice core along with new firn modeling estimates, we reduced the posterior uncertainty of the Δ age yielded by the AICC2023 experiment to 450 years on average (blue curve in Fig. 4.4). The uncertainty was of 3200 years on average in AICC2012 (gray curve in Fig. 4.4). The uncertainty in the Δ age remains large (above 450 years) over the past glacial period as no δ^{15} N data are available for EDC ice core.

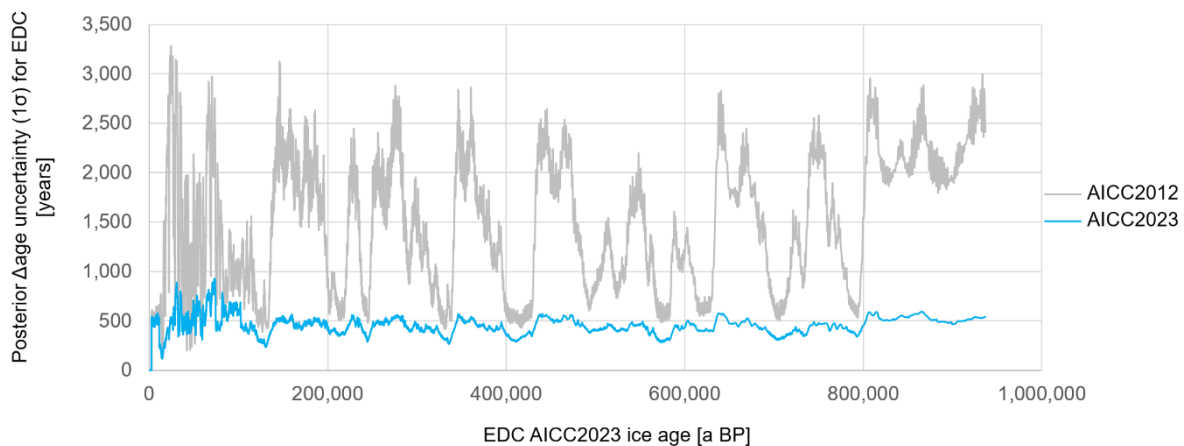


Figure 4.4 Uncertainty (1σ) yielded by the Paleochrono-1.1 model for Δ age estimates given by the AICC2012 (gray) and AICC2023 (blue) tests.

Using the posterior Δ age yielded by the AICC2023 experiment, it is possible to examine more precisely the temporal phasing between EDC records of CH₄ and δ D on their respective gas and ice age scales. Figure 4.5 is a zoom on the 200-150 ka BP time interval of the penultimate glacial period. In turn, it is possible to assess whether the hypothesis of Barker et al. (2011), implying the synchronicity of δ D maxima and abrupt increases in CH₄, is reliable. In Fig. 4.5, we designate by yellow bars AIM that do correspond to abrupt increases in CH₄ on the new AICC2023 chronology, thus supporting the theory of Barker et al. (2011). By contrast, red dashed bars point out AIM that do not correspond to an abrupt increase in CH₄ on the new AICC2023 chronology but rather to a gradual increase or no increase (opposite to what is expected from the bipolar seesaw and the theory of Barker et al, 2011).

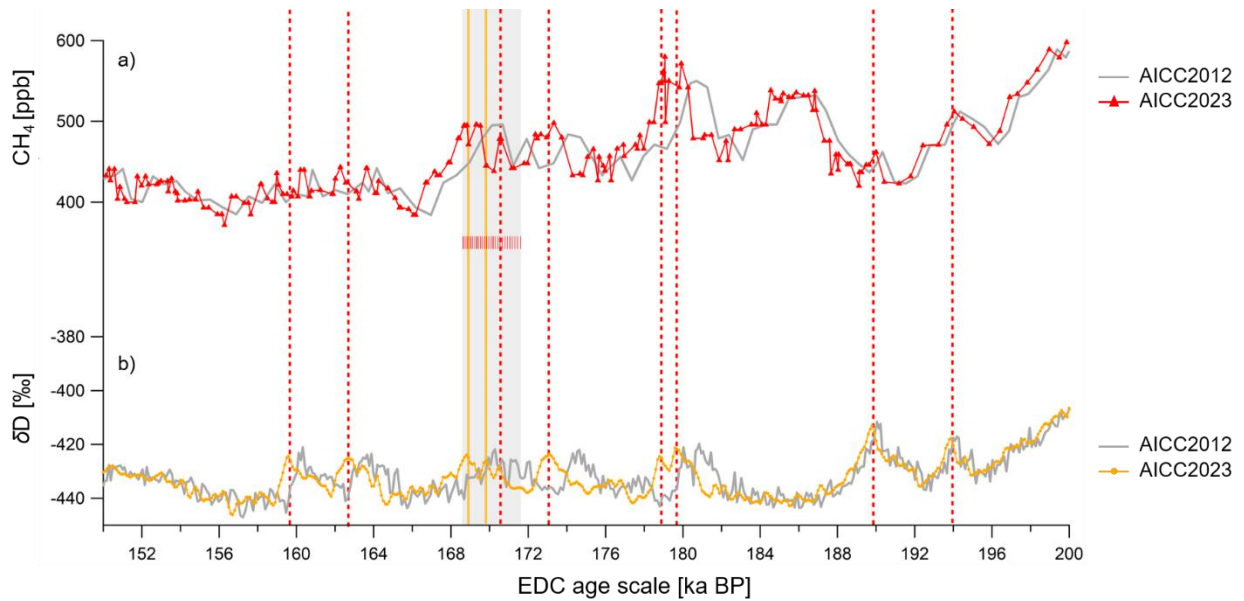


Figure 4.5 EDC records of CH_4 and δD over the 200-150 ka BP time interval. a) CH_4 data of Loulergue et al. (2008) (red triangles on AICC2023; gray curve on AICC2012). b) δD data of Landais and Stenni (2021) (yellow dots on AICC2023; gray curve on AICC2012). Yellow bars show AIM that do correspond to abrupt increases in CH_4 . Red dashed bars show AIM that do not correspond to an abrupt increase in CH_4 on AICC2023. The gray rectangle frames the interval on which 21 samples (indicated by red vertical markers) will provide new CH_4 measurements.

Over the specific MIS 6 glacial period (191-123 ka BP), several AIM do not match abrupt increases in CH_4 . Over this period, we also notice a significant disagreement between modeled and $\delta^{15}\text{N}$ -based Δage reconstructions (Chapter 3; black and blue curves respectively in Fig. 5.6). This is intriguing as there is, in general, a good agreement between modeled and $\delta^{15}\text{N}$ -inferred Δage over glacial Terminations and interglacial periods. The offset between both Δage estimates reaches 500 years between 170 and 160 ka BP (red arrow in Fig. 4.6), which is equivalent to the 1σ uncertainty over this period (Fig. 4.4).

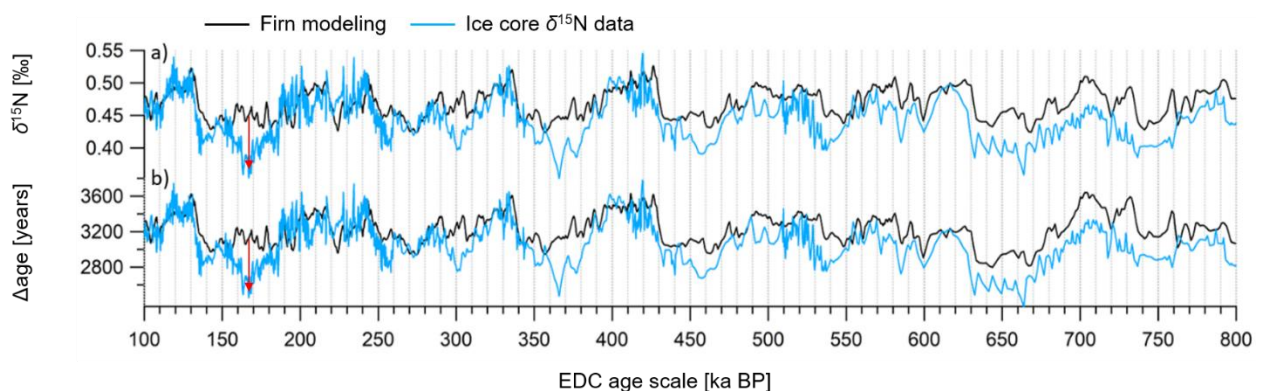


Figure 4.6 $\delta^{15}\text{N}$ model-data mismatch over the 800-100 ka BP period. a) EDC $\delta^{15}\text{N}$ record provided in the Chapter 3 (blue) and modeled scenario (black). b) Δage estimated using $\delta^{15}\text{N}$ data (blue) and Δage yielded by the firn model (black). The latest model-data disagreement is outlined by red arrows at ~ 170 ka BP.

The study of Margari et al. (2010) examined foraminiferal isotope and pollen records from the

Portuguese margin and argued that the bipolar seesaw mechanism was at play during the MIS 6 glacial period. We could possibly expect abrupt rises in CH₄ to occur synchronously with δD maxima at around 170 ka BP. However, it is not obvious to identify rapid augmentation in the methane record over this period because the temporal resolution of the existing dataset is too low (300-400 years) (Fig. 4.5). We believe new CH₄ measurements at higher resolution (~100 years) in the EDC ice core could help us detecting more precisely the expected rapid augmentations over the 172-168 ka BP time interval (red frame in Fig. 4.5). To obtain a higher resolution CH₄ record, I contributed to the writing of a sample request sent to the EPICA science steering committee. They approved our request to use 21 samples to perform CH₄ measurements. The samples should be measured by H. Guilluy at IGE by the end of 2024.

Further study would be required to assess whether these preliminary observations challenge the hypothesis of Barker et al. (2011) or whether they are an artefact due to the low resolution in the CH₄ record of EDC ice core.

4.3.2 On the use of the AICC2023 chronology for determining the temporal sequence of events over glacial Terminations

The synchronization of the EDC ice core with the U/Th-dated Chinese speleothem composite used to develop the AICC2023 chronology yields an absolute age scale for the EDC ice core. In AICC2012, the EDC age scale was relative to that of insolation curves because it was solely derived using the orbital approach (i.e. synchronization of ice core records with the orbital curves). As a result, the AICC2023 EDC age scale is less dependent on tuning to insolation. The AICC2023 chronology thus provides valuable insights for comparing the respective timings of changes in the external forcing of climate (e.g. insolation) and of the internal climatic response (e.g. changes in the GHGs concentration and in other EDC climate proxies) compared with AICC2012 that is solely based on the orbital dating approach.

The glacial Terminations prior to 600 ka BP

Figure 4.7 shows the EDC records of CH₄ as well as of δD and $\delta^{15}N$ tracing local climate change over the nine most recent glacial Terminations on both AICC2012 and AICC2023 chronologies. Starting points of the deglacial increases in the respective records are indicated by vertical dashed bars. In the majority of the Terminations, the new AICC2023 chronology suggests that EDC climatic records start increasing when the boreal summer solstice insolation (yellow curve) is also rising. Exceptions are the Terminations IX and VII (~805 and 630 ka BP) which are dated older as per AICC2023 than per AICC2012. In these cases, the CH₄, δD and $\delta^{15}N$ EDC records start increasing during the decreasing phase of the boreal summer insolation.

A more precise examination of the sequences of climatic events across these two Terminations would be required for a better comprehension of the mechanisms involved. It would permit to assess whether this result is reliable or whether it is an artefact induced by the significant uncertainty (>3kyr) related to AICC2023 over these intervals (see red double-headed arrows in Fig. 4.7).

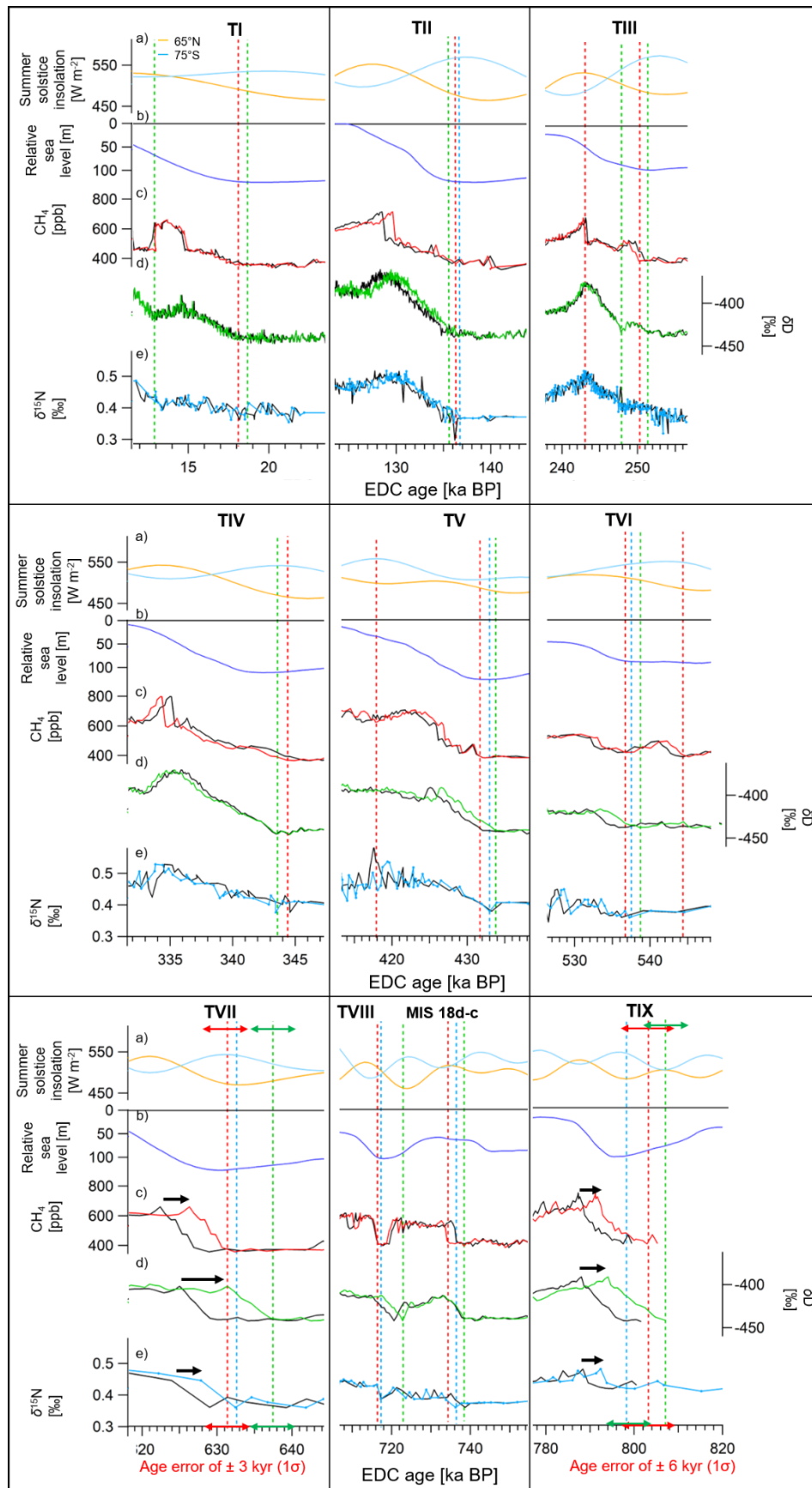


Figure 4.7 EDC records of CH_4 as well as of δD and $\delta^{15}N$ tracing local climate change over glacial

Terminations (TIX-TI) on AICC2012 (black curves) and AICC2023 chronologies (red, green and blue curves respectively). a) Summer solstice insolation at 65°N and at 75°S (yellow and blue curves; Laskar et al., 2004). b) Relative sea level with respect to present-day (Bintanja et al., 2005b). c) CH₄ data (Loulergue et al., 2008). d) δD data (Landais & Stenni, 2021). e) $\delta^{15}N$ data presented in the Chapter 3. Starting points of the increase in the three records are indicated by vertical dashed bars. Significant shift towards older ages suggested by AICC2023 with respect to AICC2012 are indicated by black arrows for TVII and TIX. The corresponding 1 σ error given by the Paleochrono-1.1 model are illustrated by the red and green double-headed arrows.

Figure 4.8 shows the comparison of EDC records on the AICC2023 timescale to other paleo records from various regions across the Earth on their independent timescales (e.g. pollen records) or to global climatic reconstructions (e.g. sea level and global surface temperature). From this comparison arises an interesting feature on the MIS 18d-c transition and over the Termination VIII (~740 and 720 ka BP). The abrupt increases in EDC record of CO₂ on AICC2023 (brown dashed bars) lag the increases in sea level documented by the benthic stack of Spratt and Lisiecki (2016) represented on its own age scale (blue plain bars). This lag of CO₂ behind the global sea level change deserves to be further studied as it differs from the CO₂ lead that is classically observed over the most recent Terminations (this study; Shakun et al., 2012).

To summarize, we observe three exceptional features for the oldest Terminations recorded in EDC between 800 and 600 ka BP (TIX-TVII). However, the chronology of the EDC ice core record remains a challenge over this period as no dated speleothem record can serve as a reference prior to 640 ka BP yet and because the orbital tuning records exhibit an important noise. The dating of EDC ice core could be refined using new high-resolution measurements of $\delta^{15}N$, $\delta O_2/N_2$ and $\delta^{18}O_{atm}$ collected between 800 and 600 ka BP by A. Klüssendorf since the beginning of her PhD (October 2023) supervised by A. Landais at LSCE.

Over the past 800 kyr, we suggest three leads for further work for improving the chronology using $\delta^{15}N$, $\delta O_2/N_2$ and $\delta^{18}O_{atm}$ measurements:

(i) $\delta^{15}N$

The $\delta^{15}N$ measurements could be used to constrain both background scenarios for the LID and for the snow accumulation rate (as suggested in Chapter 3).

(ii) $\delta O_2/N_2$

During her PhD supervised by A. Landais (LSCE) and P. Martinerie (IGE), R. Harris-Stuart concentrated on the understanding of insolation-driven $\delta O_2/N_2$ variability due to physical processes occurring within the firn column. In a comparative study of the $\delta O_2/N_2$ records from 18 Antarctic sites, including Dome C, she demonstrated the additional influence of local climate parameters (such as the snow accumulation rate) on the near-surface snow properties that determine the $\delta O_2/N_2$ value. She proposes a first step towards the decomposition of the $\delta O_2/N_2$ signal into its constituent contributions. Further work could focus integrating her findings to improve the precision of the $\delta O_2/N_2$ as an orbital dating tool.

(iii) $\delta^{18}O_{atm}$

In addition, further work could be done in the wake of the studies of Extier et al. (2018a) and Landais et al. (2010) for understanding the millennial and orbital variability of the $\delta^{18}\text{O}_{\text{atm}}$ signal in ice core. In the context of orbital dating, different methodologies exist for synchronizing $\delta^{18}\text{O}_{\text{atm}}$ to precession. For example, it is possible to consider complementary climatic proxies (as IRDs, atmospheric CH_4 or the *Greenland synthetic temperature* proposed by Barker et al., 2011) that could indicate the occurrence of millennial-scale events affecting the hydrological cycle and hence $\delta^{18}\text{O}_{\text{atm}}$. Depending on which methodology is used, it is possible to yield distinct set of *dated horizons* from the $\delta^{18}\text{O}_{\text{atm}}$ record. Confronting these different sets of $\delta^{18}\text{O}_{\text{atm}}$ -derived constraints to other sources of chronological information (glaciological modeling, $\delta\text{O}_2/\text{N}_2$, TAC and $\delta^{15}\text{N}$) could help us to understand the $\delta^{18}\text{O}_{\text{atm}}$ variability. An improved understanding of the $\delta^{18}\text{O}_{\text{atm}}$ will help to better (i) constrain the ice core chronology, in particular for the most ancient glacial Terminations, and (ii) to precisely identify the past climatic mechanisms that could have driven the variability recorded in the $\delta^{18}\text{O}_{\text{atm}}$.

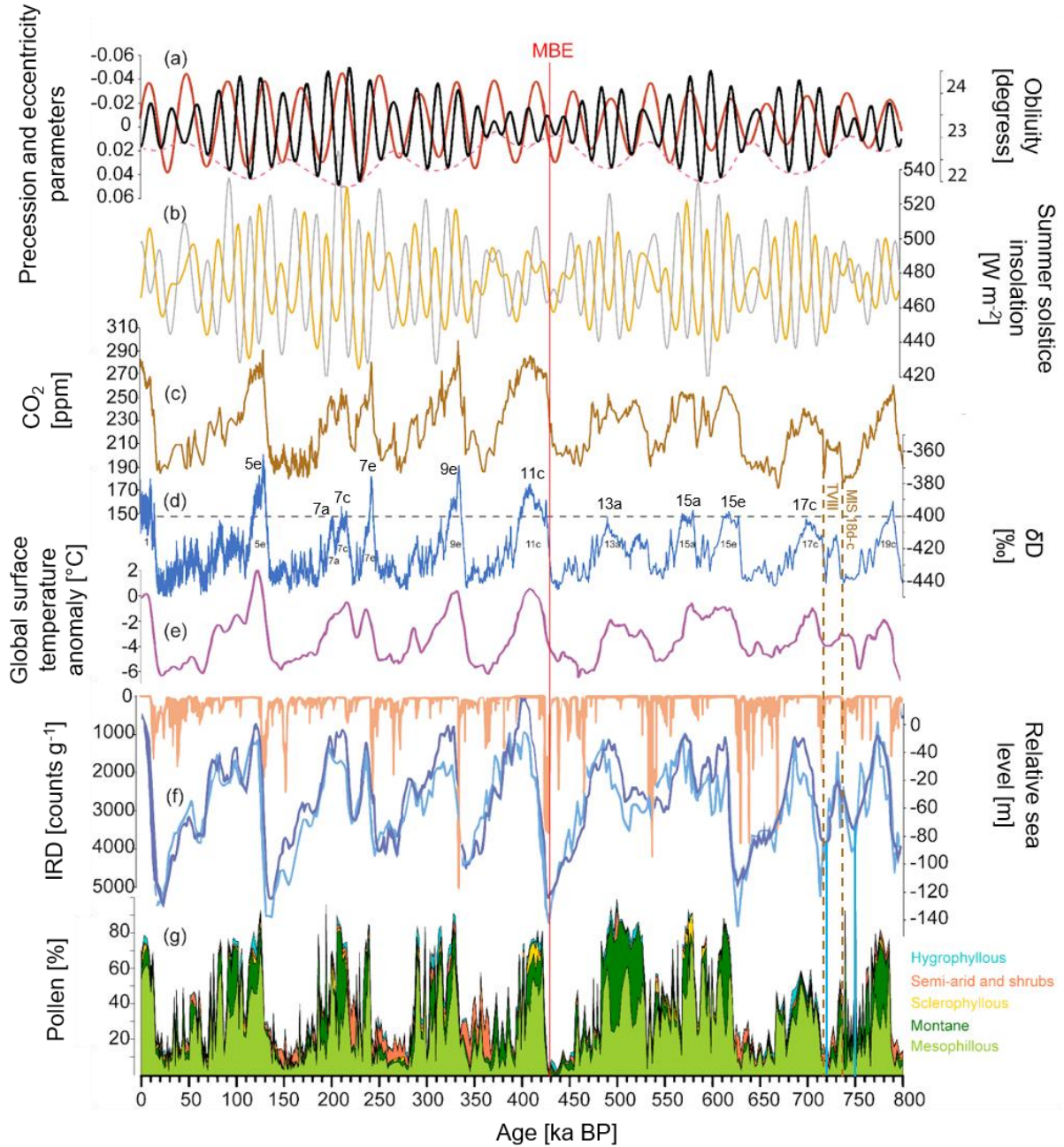


Figure 4.8 Paleoclimate reconstructions over the last 800 kyr (from Bouchet et al., 2024; modified from Tzedakis et al., 2022). (a) Eccentricity (red dashed), precession (black), obliquity (red solid), and (b) summer solstice insolation at 65°N and 65°S (yellow and grey curves). Antarctic EDC ice-core records of (c) CO₂ (Bereiter et al., 2015) and of (d) δD of ice on AICC2023. A 400‰-threshold (dashed line) separates pre- and post-MBE (Mid-Brunhes Event) interglacials. On their own and independent timescales are represented: (e) global average surface temperature anomaly vs. present-day (Snyder, 2016); (f) left axis: IRD in North Atlantic ODP Site 983 (Barker, 2021); right axis: two reconstructions of relative sea level (light and dark blue; Shakun et al., 2015; Spratt & Lisiecki, 2016); (g) pollen from Lake Ohrid (Donders et al., 2021). Vertical dashed brown bars and blue plain bars respectively indicate increases in CO₂ and sea level corresponding to the MIS 18d-c transition and TVIII.

The Termination V followed by the MIS 11c interglacial

The unusual MIS 11c interglacial is known for its prolonged high sea-level and atmospheric CO₂ concentrations, despite weak summer insolation forcing (Tzedakis et al. 2022). This specific interglacial does not align with the astronomical theory of ice ages because it exhibits an anti-correlation between minimum precession and maximum obliquity, which are typically observed at the onset of an interglacial. In this instance, we observe a prolonged period of maximum boreal insolation, over two precessional cycles. This results in a very long interglacial period, which is associated with high CO₂ and sea level (Fig. 4.8).

The study of this interglacial is of particular interest, as it represents a pivotal stage in the evolution of humans in Europe and a departure from the past. Following the severe MIS 12 glacial stage, showing one of the largest northern ice sheets extent (Batchelor et al., 2019), the number of occupations increased. This was accompanied by the emergence of new subsistence behaviors and technical innovations, as well as the regionalization of traditions. This break corresponds to the end of the Lower Paleolithic (and Acheulean) and the beginning of the Middle Paleolithic. These changes coincide with the emergence of the Neanderthal among hominid groups. One might hypothesize that the observed changes in human evolution were the result of adaptation to environmental changes brought about by altered climatic cycles. The aim of the project NEANDROOTS coordinated by M. Moncel (<https://anr.fr/Projet-ANR-19-CE27-0011>) was to evaluate the validity of this hypothesis combining the anthropological, archeological and paleoclimate approaches. Indeed, the MIS 11 is an exceptionally long interglacial period distinguished by unusual warmth in the polar regions, relatively low winter precipitation, expansion of grasslands in southern Europe, and high biomass availability, which may have facilitated the proliferation of large herbivore populations. These factors may have encouraged the Neanderthal population to increase (Moncel & Schreve, 2016; Sánchez-Goñi, 2020).

During my PhD, I was able to attend two workshops organized in the framework of the NEANDROOTS project to present the implications of the new AICC2023 chronology for the timing of the glacial Termination V that marked the transition from the MIS 12 glacial to the MIS 11 interglacial. In AICC2023, the chronology of EDC ice core was refined over the MIS 11 with respect to AICC2012. Firstly, using new $\delta\text{O}_2/\text{N}_2$ data (blue triangles and purple squares in Fig. 4.9), we determined a new matching point with insolation around 415 ka BP (blue link in Fig. 4.9) and we refined the position of the two tie points initially used in AICC2012 between 470 and 440 ka BP (gray links replaced by blue links in Fig. 4.9).

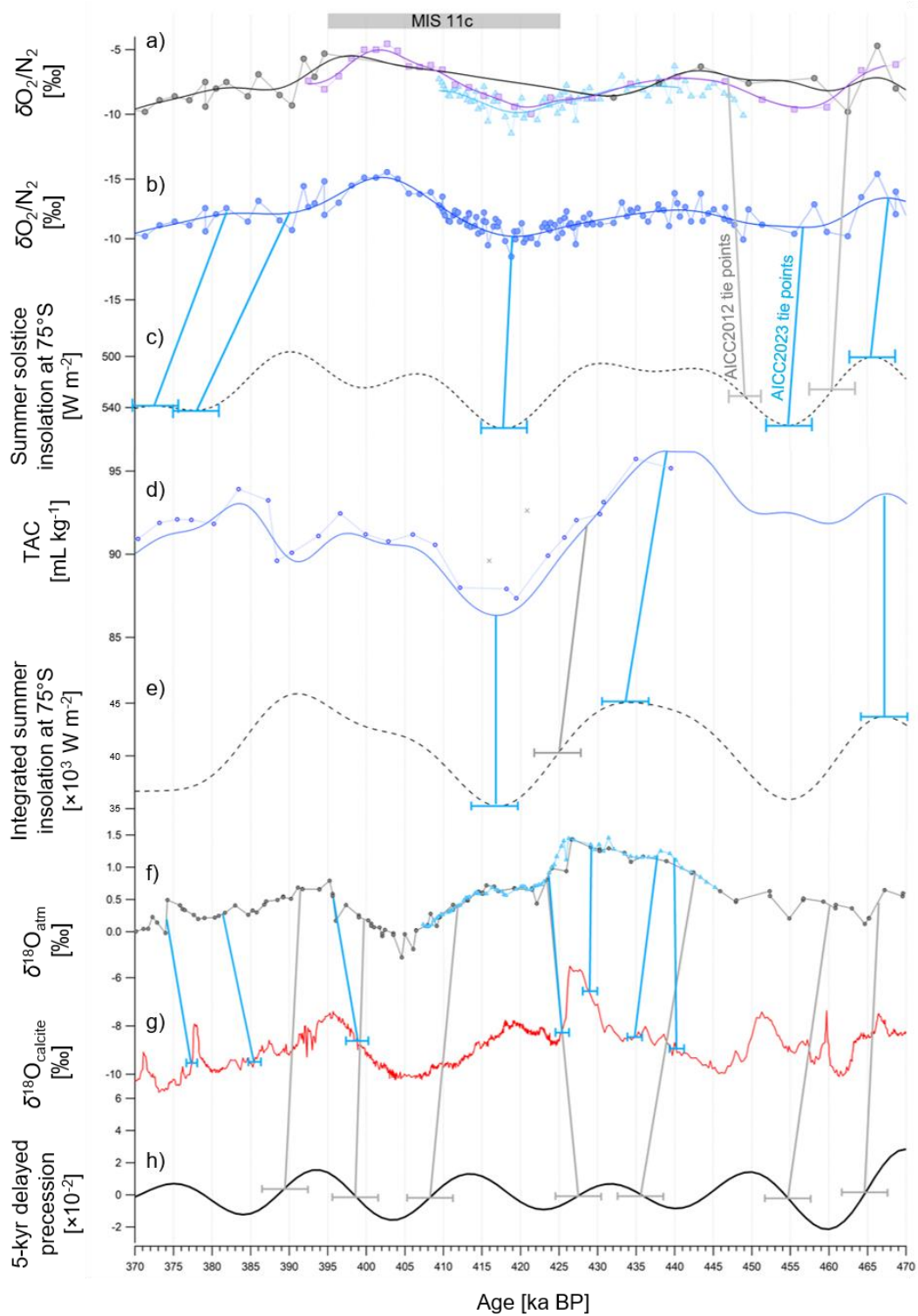


Figure 4.9 Alignment of EDC records of $\delta O_2/N_2$, TAC and $\delta^{18}O_{atm}$ to their orbital targets and to the Chinese speleothem record of $\delta^{18}O_{calcite}$ between 470 and 370 ka BP. a) Raw and filtered $\delta O_2/N_2$ old data (black circles and curve for data of Extier et al., 2018b; purple squares and curve for data of Landais et al., 2012) and new data (blue triangles and curve; Bouchet et al., 2023). b) Maxima/minima in the compiled filtered $\delta O_2/N_2$ dataset (blue plain line) are respectively matched to minima/maxima in the c) 21st December insolation at 75°S. d) Raw and filtered TAC record (purple circles and curve; Raynaud et al., 2007) and outliers (gray crosses). Maxima/minima in the filtered TAC record are matched to maxima/minima in the e) integrated summer insolation at 75°S. f) Raw and filtered $\delta^{18}O_{atm}$ old data (black circles and curve; Extier et al., 2018b) and new data (blue triangles and curve; Grisart, 2023). In AICC2023, the $\delta^{18}O_{atm}$ is matched (blue links) to the g)

$\delta^{18}\text{O}_{\text{calcite}}$ composite record from the Chinese speleothems (red curve; Cheng et al., 2016). The speleothem record is shown on the U/Th age scale. In AICC2012, the $\delta^{18}\text{O}_{\text{atm}}$ is matched to the h) 5-kyr delayed precession. EDC data are plotted on AICC2012. Tie points used in AICC2012 or AICC2023 are indicated by gray or blue lines and their prior uncertainty (1σ) is shown by horizontal error bars.

However, the $\delta\text{O}_2/\text{N}_2$ and insolation variation do not resemble each other over this period and it is difficult to match them. For instance, two peaks in the insolation curve only correspond to one peak in the $\delta\text{O}_2/\text{N}_2$ data. This could be explained by a low eccentricity inducing a smaller magnitude in the variations of insolation target and hence in $\delta\text{O}_2/\text{N}_2$ signal over MIS 11. The same issue concerns the TAC record which displays two peaks while the integrated summer insolation only shows one peak. As a result, only a few tie points were established over this time interval. Still, the new TAC record allowed us to determine three tie points that we used in AICC2023 over MIS 11 whereas only one was used to constrain AICC2012. The major chronological improvement over MIS 11c lies in the synchronization of the highly resolved record of $\delta^{18}\text{O}_{\text{atm}}$ from EDC with the precisely dated Chinese speleothem composite record of $\delta^{18}\text{O}_{\text{calcite}}$ of Cheng et al. (2016). The resulting tie points are associated with a smaller uncertainty than the tie points used in AICC2012 that were established between $\delta^{18}\text{O}_{\text{atm}}$ and delayed precession.

As a result, the new EDC chronology is shifted by up to 2,300 years towards older ages with respect to AICC2012 over the MIS 11 (blue plain line in Fig. 4.10). Before MIS 11, prior to 430 ka BP, the new EDC chronology suggests a shift of 2,000 years towards younger ages with respect to AICC2012. The resulting age uncertainty is reduced from 3,500 years to 2,400 years on average over MIS 11c, as indicated by the black arrow in Fig. 4.10. The duration of the Antarctic warming documented by δD associated with glacial Termination V is shortened in AICC2023 with respect to AICC2012 (Fig. 4.11). The overall duration of the MIS 11c interglacial (defined when ice core- δD is superior to the threshold of -403‰ ; EPICA Community members, 2004) is reduced by $\sim 2,000$ years in the new chronology (Fig. 4.11).

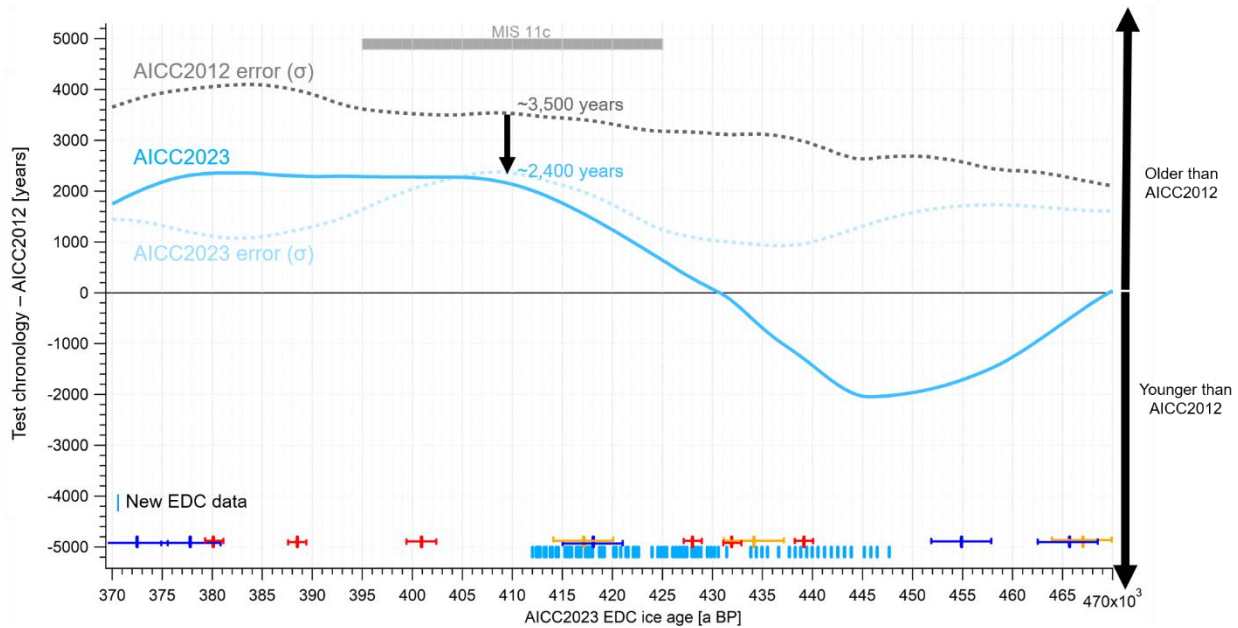


Figure 4.10 The age difference for EDC between the AICC2023 and AICC2012 chronologies between 470 and 370 ka BP (blue plain line). Posterior age uncertainty (1σ) associated with AICC2012 and AICC2023 are shown by gray and blue dashed lines respectively. Crosses indicate age markers derived from $\delta O_2/N_2$ (dark blue), TAC (orange) and $\delta^{18}O_{atm}$ (red) and blue vertical bars show new high-resolution EDC data published along with the study presented in Section 4.1.

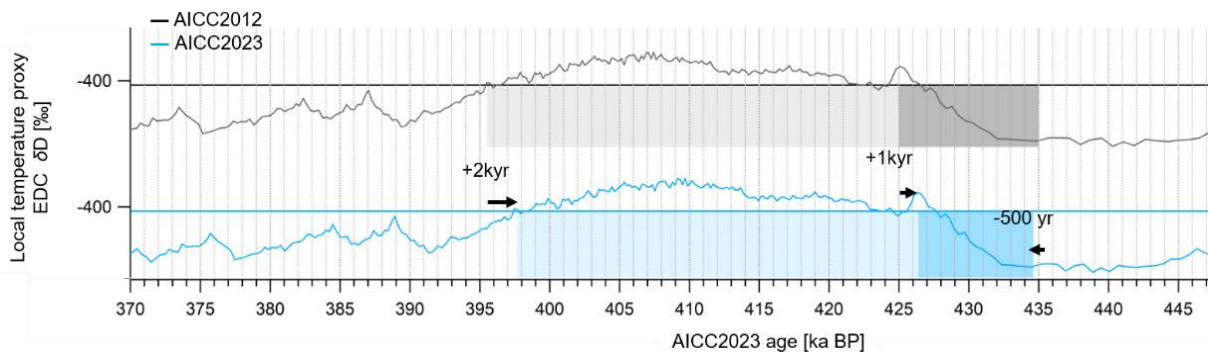


Figure 4.11 EDC δD record on AICC2012 and AICC2023 chronologies. The Antarctic warming associated with TV is reflected by the increase in the EDC δD record (Landais & Stenni, 2021). It is framed by the dark-colored boxes. Light-colored rectangles indicate interglacial periods defined when δD is superior to the threshold of -403‰ (horizontal lines) (EPICA members, 2004). Arrows indicate the age shift suggested by AICC2023 with respect to AICC2012.

After Tzedakis et al. (2022), the specificity of MIS 11c may be due to three parameters: the weak boreal insolation forcing, the preceding large ice sheet extent (MIS 12) and high atmospheric concentration in CO_2 from the start of MIS 11c. However, the detailed sequence of climatic events over the MIS 12-11 transition still remains controversial. This question was discussed at the workshop of the Quaternary Interglacial working group to which I participated in September 2023. I coordinated the writing of the report summarizing the discussions that took place at the workshop in a short paper published in the Past Global Changes Magazine (Bouchet et al., 2024; Appendix 7.1). The necessity to develop a coordinated modeling protocol over the Termination V-MIS 11c time period was raised during the discussion. In this framework, the group agreed on the importance of constraining the volume and extent of the

MIS 12 ice sheet, and of developing a coherent temporal framework for the rate of sea-level rise, and for various paleoclimate proxies representative of different parts of the Earth System across the deglaciation.

Indeed, separate dating efforts have been independently led for ice cores which recorded past changes in atmospheric concentration of GHGs (Bouchet, Landais, Grisart, et al., 2023) and marine cores which document sea level changes (Hobart et al., 2023).

In the wake of the workshop, together with A. Landais (LSCE), we co-supervised the master thesis of E. Auriol on the establishment of a coherent chronology for glacial and marine cores over the past 640 kyr. This study was conducted with the help of E. Wolff (University of Cambridge), S. Barker (Cardiff University), E. Capron (IGE) and F. Parrenin (IGE). This work is the subject of the following Chapter.

5 CHAPTER 5

BUILDING COHERENT CHRONOLOGICAL FRAMEWORK FOR MARINE AND GLACIAL ARCHIVES OVER THE PAST GLACIAL-INTERGLACIAL TRANSITIONS

Foreword

For understanding the cause-effect relationships between the orbital forcing and the climate response (atmospheric concentration in GHGs, sea level and temperature) over the past glacial Terminations, it is necessary to develop a **coherent** and **absolute** temporal framework for the rate of sea-level rise, for the variations in atmospheric CO₂ concentrations as well as for various paleoclimate proxies representative of different parts of the Earth System.

However, glacial archives providing atmospheric CO₂ record and marine archives providing proxies of sea level have been dated independently over the past glacial-interglacial cycles (Fig. 5.1). As their age models are not coherent, the respective timing of deglacial rises in sea level and in atmospheric concentration in CO₂ cannot be compared. In addition, the age models of glacial and marine archives are relative since they mainly rely on the alignment of their records to orbital curves (orbital dating, see Sections 2.3.4 and 4.1). Thus, they do not provide a calendar or absolute age but a relative age with large uncertainties (several thousand years).

This chapter is thus dedicated to the development of a coherent, relative and absolute, timescale for marine and glacial archives over the past 640 kyr. It relates the work undertaken by E. Auriol in the framework of her master project that I co-supervised from February to the end of July 2024. I reviewed her Master Thesis which has been returned in June.

In the first section of this chapter, the context as well as the state-of-the-art of research relative to this work is presented. In the second section, the dating methodology is explained. This includes a description of the Paleochrono-1.1 dating tool as well as of the different approaches that can be used to align marine cores, ice cores and speleothems. The sensitivity of the coherent chronology to the dating methodology is evaluated in the third section. The resulting coherent age model and its implications for identifying the sequence of climatic events during glacial Terminations are depicted in the fourth section. The perspectives of this work are outlined in the fifth section.

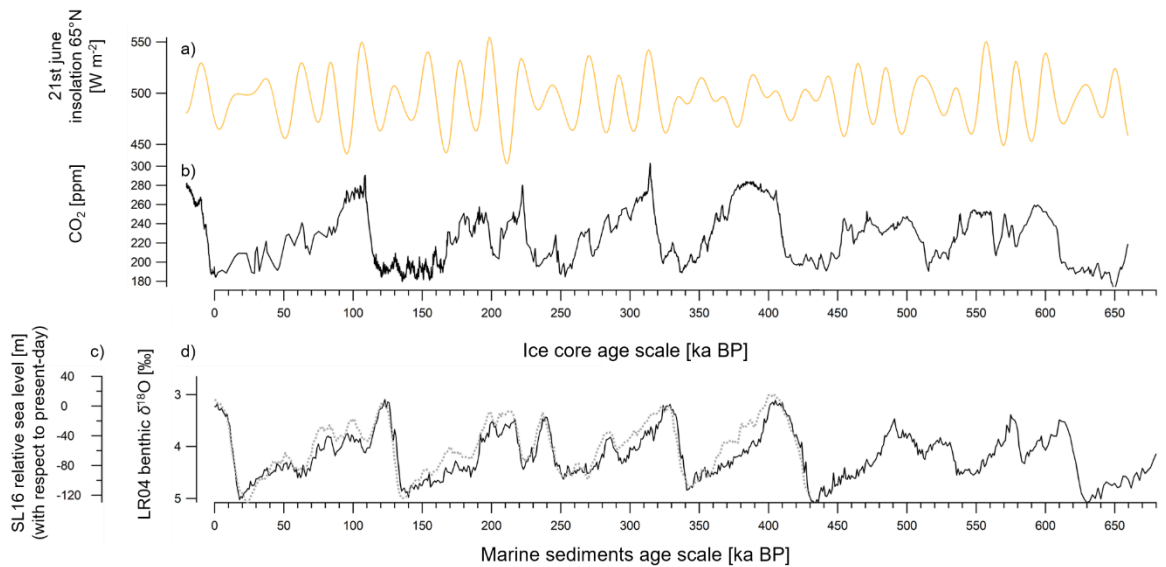


Figure 5.1 Evolution of climatic forcing and response over the past 680 kyr. a) Summer solstice insolation at 65°N (Laskar et al., 2004). b) EDC record of atmospheric CO₂ concentration (Lüthi et al., 2008; Shin et al., 2020; Siegenthaler et al., 2005). c) SL16 reconstruction of relative sea level (with respect to present-day) (gray dashed curve; Spratt & Lisiecki, 2016). d) The LR04 stack of globally distributed benthic $\delta^{18}\text{O}$ records which can be considered as a proxy for sea level (black curve; Lisiecki & Raymo, 2005). Each paleorecord is represented on its independent age scale.

Objectives

The objectives of this chapter are:

- ✓ To provide a coherent, relative and absolute chronological framework for marine and glacial records over the past 640 kyr
- ✓ To assess the sensitivity of the coherent age model to the dating methodology employed and to provide solid error bars for the chronology
- ✓ To identify the temporal sequence of changes in the orbital forcing, in atmospheric CO₂ and sea level over the seven most recent glacial Terminations

Methods

To achieve the above-mentioned objectives, we employed the following methods:

- Q We have compiled existing chronological information for each archive and novel stratigraphic links between marine cores, ice cores and speleothems in the Paleochrono-1.1 Bayesian dating tool
- Q With my help, E. Auriol performed sensitivity experiments with the Paleochrono-1.1 model using varying prior uncertainties, choices of tie points and alignment methods.
- Q We used the model described by Mudelsee (2000) for fitting ramp functions to the rises observed in sea level proxy and atmospheric CO₂ content over the glacial Terminations so that it is possible to identify the timing of their onset/end in the two records on the same age scale.

Highlights

- We detect the timing of the onset/end of glacial Terminations in the two records using the coherent chronological framework. The timings obtained sometimes disagree (by more than 1 σ) with the timings estimated using the independent chronologies. This result emphasizes the need for using a chronological framework that is coherent for all climatic records considered for identifying correct temporal sequence of events.
- We observe a constant lead of a few kyr (from 1 to 5.5 kyr) of the deglacial rise in atmospheric CO₂ with respect to the increase in benthic $\delta^{18}\text{O}$ record of IODP site U1308 (assumed in this study to be a proxy for sea level) in the majority of the onset and end of the past seven Terminations. This result agrees what was advocated in precedent studies.
- We find that the confidence interval of the temporal phasing between CO₂ and the benthic $\delta^{18}\text{O}$ record of U1308 estimated using a coherent chronology ranges from 6 kyr (onset of TVII) to 25 kyr (end of TV and TVII).
- One exception is the Termination VI, for which the atmospheric CO₂ lags the benthic $\delta^{18}\text{O}$ record of IODP site U1308, although the chronological error bar does not exclude a lead of the CO₂.

5.1 INTRODUCTION AND CONTEXT

Understanding the cause-effect relationships between the orbital forcing and the climate internal response (atmospheric concentration in GHGs, sea level and temperature) over the past glacial Terminations has been the subject of numerous studies (Broecker & Henderson, 1998; Clark et al., 2012; Ganopolski & Brovkin, 2017; Köhler et al., 2005; Shakun et al., 2012b, 2015). However, the exact temporal sequence of climatic events observed during glacial Terminations (rises in sea level and atmospheric CO₂ concentration as well as in various paleotemperature reconstructions) remains uncertain. This is partly due to the lack of a coherent temporal framework to determine the lead-lag relationship between the different paleorecords. Indeed, it is typical to date archives independently. As result, marine archives provide an age scale for sea level variations that is not comparable with that given by ice cores for observing changes in the atmospheric CO₂.

Significant efforts have been made to date marine sediments of the Northern Atlantic (Hobart et al., 2023) and Antarctic ice cores (Bouchet et al., 2023). These studies are based on the synchronization of these respective archives to the Chinese speleothems which are absolutely and precisely dated using Uranium-Thorium techniques. As a result, two respective relative and absolute chronologies were derived for marine and glacial archives with reduced uncertainties over the past 640 and 800 kyr.

Although Antarctic ice cores and Northern Atlantic marine cores cannot be straightforwardly synchronized, they can be connected via stratigraphic matching with an archive representing an intermediate region, i.e. the Chinese speleothems. The objective of this chapter is twofold: firstly, to present a new, coherent, relative and absolute chronology for marine sediments, ice cores and speleothems over the past 640 kyr; and secondly, to provide robust uncertainty estimates.

5.2 DATING METHODOLOGY

5.2.1 Bayesian approach: Paleochrono-1.1

The chronological information related to each archive (inferred from modeling and/or data) is integrated into the statistical dating tool Paleochrono-1.1 (Parrenin et al., 2024). The underlying assumption is that each site possesses independent information. The background information is used by the model to calculate the *prior* age model. The model then statistically adjusts the age scale so that it gives the most optimal compromise between all chronological constraints and that it is coherent for all sites. The resulting age scale is referred to as the *posterior* age model and is given by Paleochrono-1.1 along with the *posterior* 1σ uncertainty.

The model is designed to accommodate two distinct types of archives which are referred to as:

- (i) The *ice-core archives*, which are associated with two age scales (one for the ice matrix and one for the enclosed air), variable density, and are affected by post-depositional thinning of the annual horizontal layers.
- (ii) The so-called *simple archives*, which have one unique depth-age relationship, constant density, and no post-depositional thinning of the annual horizontal layers.

Both speleothems and marine cores are considered as *simple archives*. Incrementing them in the Paleochrono-1.1 experiment is a relatively straightforward process. It necessitates identifying the ages corresponding to the top and bottom extremities of the core/speleothem. The sedimentation rate is assumed constant and can be calculated.

The background information of each site is composed of its sedimentation scenario as well as its own *dated horizons*, which are depth levels at which the absolute age has been independently estimated from measurements with a certain degree of accuracy. In addition, *stratigraphic links* can be made between the depth levels of two or more archives of same age (Fig. 5.2).

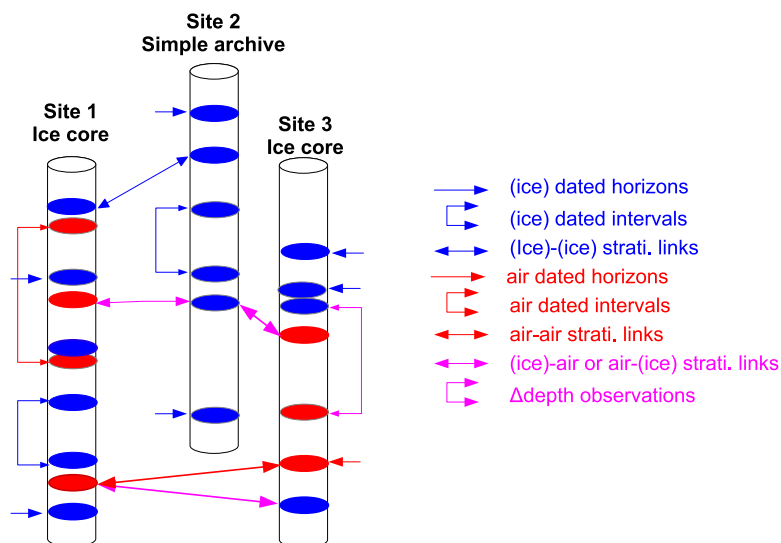


Fig. 5.2 Scheme illustrating the different kinds of observations used to constrain the chronologies

of the paleoclimatic sites in the Paleochrono-1.1 probabilistic dating model (from Parrenin et al., 2024). Different types of archives can be integrated into the dating experiment: ice-core archives (with two distinct age scales for the ice and gas phases, e.g. sites 1 and 3) or simple archives (e.g. site 2).

5.2.2 Experiment construction

Paleochrono-1.1 was employed to construct the AICC2023 dating experiment for the EDC, EDML, Vostok, TALDICE and NGRIP ice cores (see Section 4.1; Bouchet et al., 2023). AICC2023 is an incremental advancement of AICC2012 (Bazin et al., 2013; Veres et al., 2013) that incorporated novel measurements on the EDC ice core.

Parrenin et al. (2024) incorporated two speleothems, MSL and MSD, from the Hulu Cave in China (Y. J. Wang et al., 2001), to create the AICC2023-Hulu experiment. The two speleothems are precisely dated using published U/Th dated horizons on the 18-55 kyr ka BP interval (Cheng et al., 2018). Adolphi et al. (2018) and Corrick et al. (2020) assert that millennial-scale D-O events featuring the last glacial period are synchronously archived in the $\delta^{18}\text{O}_{\text{ice}}$ record of NGRIP ice core, in the $\delta^{18}\text{O}_{\text{calcite}}$ records of MSD and MSL speleothems and in the global atmospheric CH_4 record. This synchronicity involves teleconnections between Greenland temperature, latitudinal displacement of the ITCZ and monsoon area and CH_4 emission from tropical wetland over D-O events respectively (Section 1.2.2.3). The climatic processes involved are more precisely described subsequently (Section 5.2.3.2).

Parrenin et al. (2024) follow the findings of Adolphi et al. (2018) and Corrick et al. (2020) and linked the following records:

- (i) the NGRIP $\delta^{18}\text{O}_{\text{ice}}$ to the MSD $\delta^{18}\text{O}_{\text{calcite}}$
- (ii) the MSD $\delta^{18}\text{O}_{\text{calcite}}$ to the MSL $\delta^{18}\text{O}_{\text{calcite}}$
- (iii) the MSL $\delta^{18}\text{O}_{\text{calcite}}$ to the EDC CH_4

at the onset of each abrupt D-O event. A mid-slope approach is used, assuming a global synchronicity in the timing of the rapid warming transitions and of the $\delta^{18}\text{O}_{\text{calcite}}$ changes. A constant uncertainty (1σ) of 100 years is assigned to these stratigraphic links prior to Paleochrono-1.1 input. It is a rough approximation of the synchronization error during D-O transitions.

The AICC2023-Hulu experiment served as the foundation for this study. The stratigraphic links and other chronological constraints used in the AICC2023-Hulu experiment can be viewed at the Github of F. Parrenin (<https://github.com/parrenin/paleochrono/tree/master/AICC2023-Hulu>). For the study described here, we implemented one marine core and one composite speleothem to the existing AICC2023-Hulu experiment. The following list details the archives included in our Paleochrono-1.1 experiment (along with their reference name used in the model provided in brackets):

- The MSD speleothem (*MSD*) (Parrenin et al., 2024)

- The MSL speleothem (*MSL*) (Parrenin et al., 2024)
- The EDML ice core (*EDML*) (Bouchet et al., 2023)
- The TALDICE ice core (*TALDICE*) (Bouchet et al., 2023)
- The Vostok ice core (*VK*) (Bouchet et al., 2023)
- The NGRIP ice core (*NGRIP*) (Bouchet et al., 2023)
- The EDC ice core (*EDC*) (Bouchet et al., 2023)
- **The Chinese speleothem composite composed of speleothems from Smbao, Hulu and Dongge caves (*speleocomposite*) (this study)**
- **The IODP U1308 marine core (*U1308*) (this study)**

The location of the sites included in the new dating experiment (or mentioned in Sections 4.4 and 4.6) is indicated in Fig. 5.3.

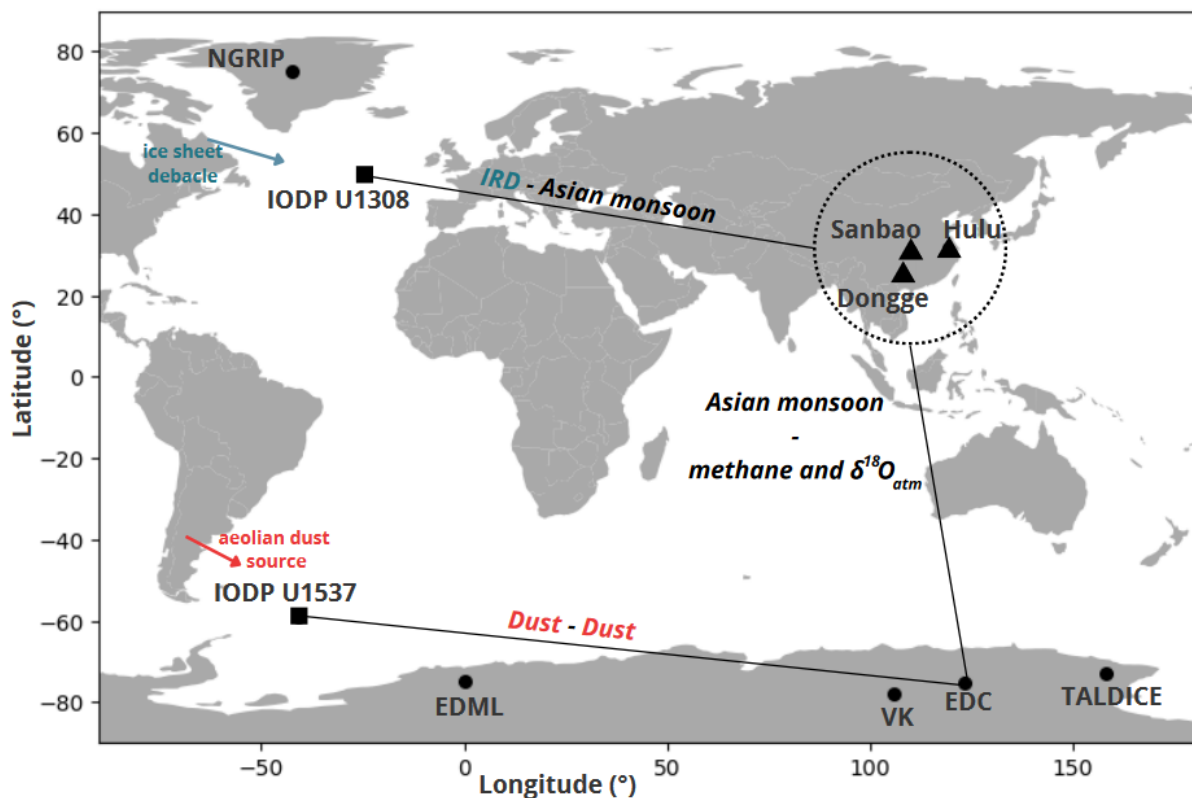


Figure 5.3 Location of the sites included in the new dating experiment or mentioned in the perspectives. Polar ice cores are indicated by dots, marine cores are indicated by squares and the three Chinese caves are shown by triangles. The MSD and MSL speleothems come from the Hulu cave. The Chinese composite of (Cheng et al., 2016) is composed of speleothem records from the Smbao, Hulu and Dongge caves. The lines connecting the different sites symbolize the stratigraphic matching that can be established. For each stratigraphic matching, the underlying climatic assumptions are indicated. For example, it is possible to connect the Chinese speleothem composite to the IODP U1308 marine core assuming that IRD event coincide with abrupt variability of the Asian Monsoon (Hobart et al., 2023).

In the list above, I highlighted in bold the new archives integrated in the dating experiment in the framework of the Master project of E. Auriol. For each of them, we built from scratch the

background input files for Paleochrono-1.1. We also implemented stratigraphic ties linking EDC to the new archives. We thus slightly updated the background information related to EDC with respect to the experiment that provided the reference AICC2023 chronology. The following sections detail the approach employed to determine the new background chronological information assigned to the new archives and to EDC.

5.2.3 Background chronological information related to the archives newly integrated in the dating experiment

5.2.3.1 Dated horizons

Chinese speleothem composite

The study of Cheng et al. (2016) provides a $\delta^{18}\text{O}_{\text{calcite}}$ composite record from speleothems from Hulu, Dongge and Sambaos caves in China (Fig. 5.3), reaching back to 640 ka BP. The Chinese speleothem composite was dated using 8353 absolute ages inferred from U/Th radiometric dating over the past 640 kyr. The uncertainty of this dating approach increases with increasing age and is comprised between 400 years and 10 kyr. We integrated the Chinese speleothem composite as one unique *simple archive* to the dating experiment along with the 8353 absolute *dated horizons* given by Cheng et al. (2016).

IODP U1308 marine core

The U1308 marine core was drilled in the eastern North Atlantic Ocean (Fig. 5.3) in the framework of the Integrated Ocean Drilling Program (IODP). This sedimentary core provides records of sea level proxy (benthic $\delta^{18}\text{O}$) as well as of IRDs proxy (bulk carbonate $\delta^{18}\text{O}$) over the past 1.4 million years (Hodell et al., 2008). The age model of the U1308 core was initially constructed by correlating the benthic $\delta^{18}\text{O}$ record to the stacked $\delta^{18}\text{O}$ LR04 record. We calculate the sedimentation rate (assumed constant) using the age of the core top and bottom extremities given by its initial age model. We integrated the U1308 core to the dating experiment along with its background sedimentation scenario but with no absolute *dated horizons*.

5.2.3.2 Stratigraphic links

Connecting the Northern Atlantic marine core to the Chinese speleothem composite

Centennial- to millennial-scale climate oscillations were detected via occurrence of layers rich in IRDs in Northern Atlantic marine sediments (Heinrich, 1988b) (Section 1.2.2.3.1). IRDs are continuously released from various sources, but when they are identified in the Ruddiman belt (between 40° and 55°N), they serve as proxies for Heinrich events (Ruddiman et al., 1977). The IODP U1308 marine core is situated in the Ruddiman belt and provides a record of bulk carbonate $\delta^{18}\text{O}$, a proxy for IRDs. The Heinrich events coincide with southward shift of the ITCZ,

which is displaced away from Asia, thus reducing the intensity of the Asian monsoon (Section 1.2.2.3.2). The Chinese speleothem composite record of $\delta^{18}\text{O}_{\text{calcite}}$ documented the millennial-scale dynamics of Asian monsoon, referred to as Abrupt Asian Monsoon Variability (AAMV) (Section 1.2.2.1). A larger $\delta^{18}\text{O}_{\text{calcite}}$ value indicates a reduced spatially integrated monsoon rainfall between the tropical monsoon sources and the cave site, as well as potentially weaker summer monsoon rainfall in the cave region. The term “Weak Monsoon Intervals” (WMI) is used to refer to high $\delta^{18}\text{O}_{\text{calcite}}$ values.

Hobart et al. (2023) posit that the aforementioned events occur synchronously and suggest correlating IRD layers from North Atlantic cores to AAMV recorded in Chinese speleothem record. They used a stack of eight Northern Atlantic marine cores, which are not all located in the Ruddiman belt. In this study, we utilize solely the sediment core from the stack of Hobart et al. (2023) that is situated within the Ruddiman belt, i.e. IODP U1308, thereby increasing the probability that its IRD record is linked with the Asian monsoon variability.

We use the discrete matching proposed by Hobart et al. (2023) between the AAMV recorded in the Chinese speleothem composite and the IRDs traced in the IODP U1308 marine core over the past 640 kyr. An example of possible matching at ~ 130 ka BP is represented by two vertical lines in Fig. 5.4. These stratigraphic links complement the background chronological information related to the pair of sites: speleocomposite-U1308. We performed additional experiments with the Paleochrono-1.1 model to evaluate the sensitivity of the resulting chronology to the choice of tie points and assigned background uncertainty. The sensitivity tests and resulting chronological uncertainty are presented in the Section 5.3.1.

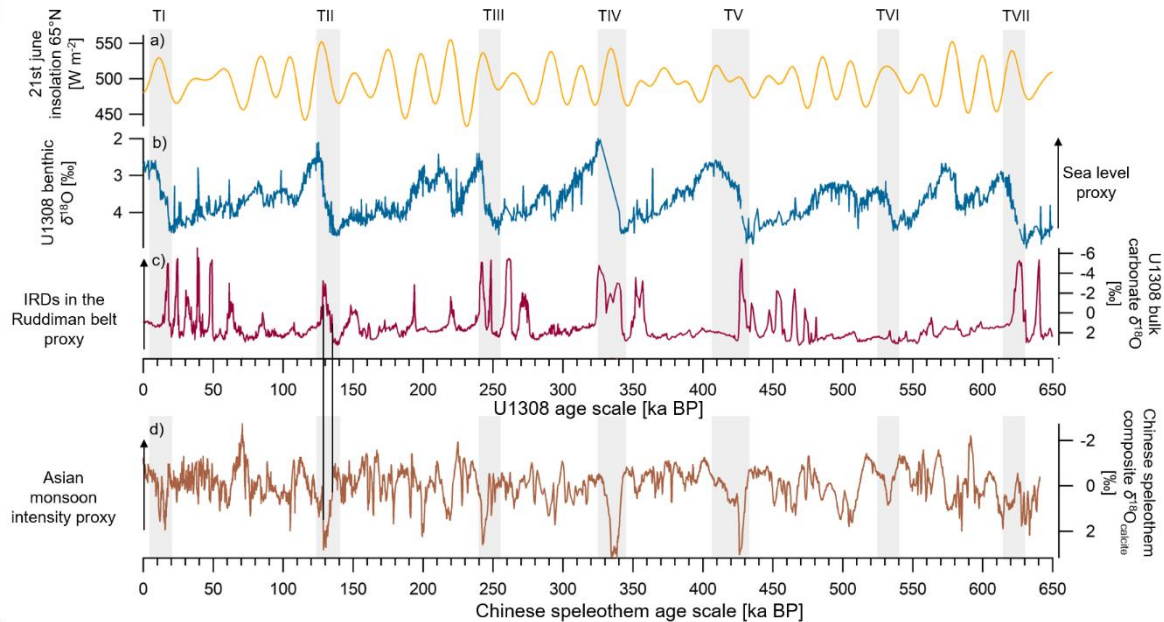


Figure 5.4 Connecting the IODP U1308 marine core with the Chinese speleothem composite via synchronization of IRD and AAMV events. a) Summer solstice insolation at 65°N (Laskar et al., 2004). The IODP U1308 records of b) $\delta^{18}\text{O}$ of benthic foraminifera as a proxy for sea level and of c) $\delta^{18}\text{O}$ of bulk carbonate as an IRD proxy in the Ruddiman belt (Hodell et al., 2008). IODP U1308 records are represented on their initial age model. d) The Chinese speleothem detrended record of $\delta^{18}\text{O}_{\text{calcite}}$ (Cheng et al., 2016). The gray frames show the deglacial rises observed in the benthic $\delta^{18}\text{O}$ record and corresponding Terminations are numbered from TI to TVII. An example of two stratigraphic links are represented at ~ 130 ka BP linking the IRD onset/end in the U1308 record with the AAMV onset/end in the Chinese speleothem composite (vertical lines) (Hobart et al., 2023).

Connecting the EDC ice core to the Chinese speleothem composite

Extier et al. (2018) and Bouchet et al. (2023) synchronize the $\delta^{18}\text{O}_{\text{atm}}$ data from EDC ice core with the $\delta^{18}\text{O}_{\text{calcite}}$ from the Chinese speleothem composite, based on their common sensitivity to millennial and orbital changes in the hydrological cycle. Examples of such matching are illustrated by black vertical dotted lines in Fig. 5.5.

Here we explore whether this dating strategy agrees with a complementary method consisting in aligning increases in atmospheric CH_4 concentration with intensification of the Asian monsoon activity. This method has already been used for dating ice cores (Buizert, Cuffey, et al., 2015). Indeed, the intensification of the Asian monsoon results in the expansion of wetland areas, representing a significant source of methane emissions, and thus to an increase in atmospheric CH_4 . The seven most recent Terminations are featured by a WMI, evidenced by an elevated $\delta^{18}\text{O}_{\text{calcite}}$ of the Chinese speleothem composite. The abrupt end of the WMI is accompanied by an abrupt increase in atmospheric methane evidenced in Antarctic ice core records (Cheng et al., 2006, 2016).

Cheng et al. (2016) identified endings of WMIs during the past seven Terminations as well as during two similar events: the MISs 4-3 and 5b-a transitions occurring at around 60 ka BP and 85 ka BP. They also detect ends of WMIs during the periods noted TIIIa and TVIIa which are referred to as “extra Terminations” as they exhibit a pattern of events similar to the main Terminations, along with significant and comparable changes in benthic records of $\delta^{18}\text{O}$. The WMIs detected by Cheng et al. (2009, 2016) are framed by orange vertical rectangles in Fig. 5.5. Stratigraphic links can be determined by matching WMI endings detected by significant decreases in the Chinese speleothem composite record of $\delta^{18}\text{O}_{\text{calcite}}$ to abrupt increases detected in the CH_4 record of EDC ice core. An example of such stratigraphic links is indicated by the red vertical plain line in Fig. 5.5.

As Heinrich events coincide with abrupt changes in the Asian monsoon intensity (Barker et al., 2011; Cheng et al., 2009), one could expect to detect IRD peaks in marine sediments situated in the Ruddiman belt at the end of WMIs. It is possible to use this hypothesis as a criterion for establishing additional stratigraphic links between the EDC ice core and the Chinese speleothem composite. In other words, additional stratigraphic links can be determined by matching increases in CH_4 of EDC to decreases in $\delta^{18}\text{O}_{\text{calcite}}$ of the Chinese speleothem composite when an IRD peak tracing a parallel Heinrich event is detected in the IODP U1308 (Hodell et al., 2008) or in the IRD proxies of the ODP 983 cores (Barker et al., 2019). Examples of such links are represented by the red vertical dashed lines in Fig. 5.5 and corresponding IRD peaks are outlined by dashed circles.

We performed additional experiments with the Paleochrono-1.1 model to evaluate the sensitivity of the resulting chronology to the choice of tie points and assigned background uncertainty. The sensitivity tests along with the resulting chronological uncertainty are presented in Section 5.3.2.

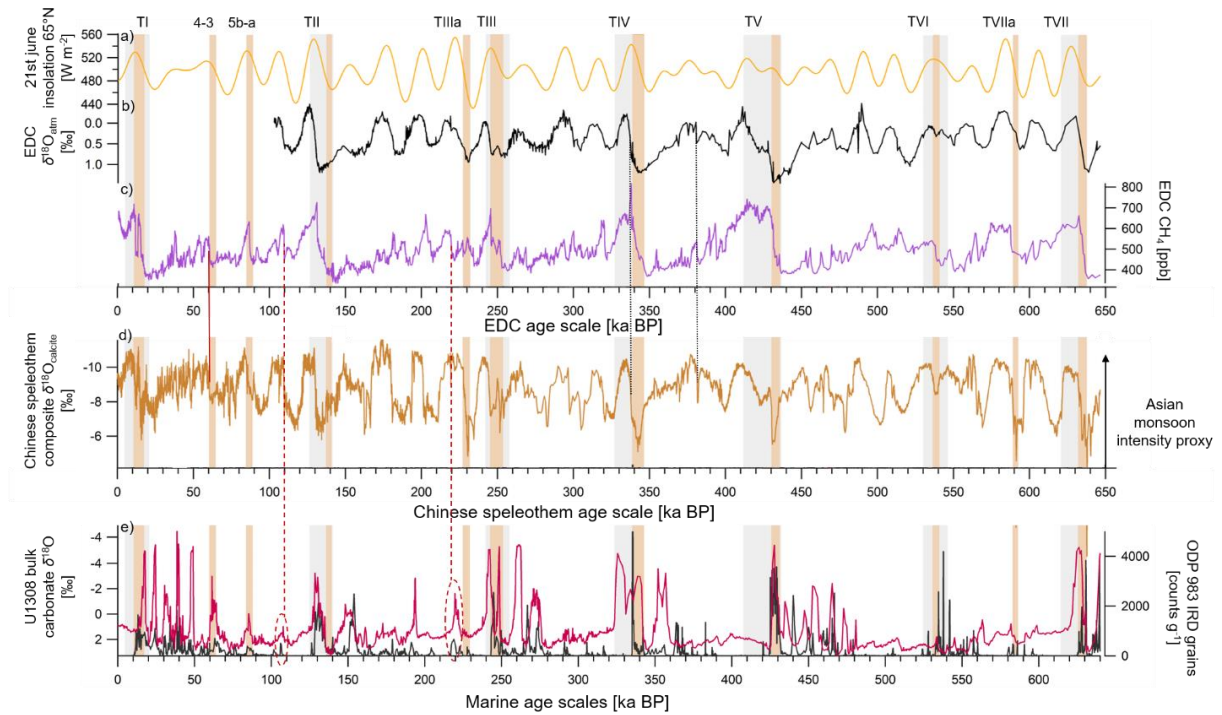


Figure 5.5 Connecting the EDC ice core with the Chinese speleothem composite via synchronization of $\delta^{18}\text{O}_{\text{atm}}$ or CH_4 to $\delta^{18}\text{O}_{\text{calcite}}$. a) Summer solstice insolation at 65°N (Laskar et al., 2004). EDC records of b) $\delta^{18}\text{O}_{\text{atm}}$ (Bouchet, Grisart, Landais, et al., 2023a) and c) atmospheric CH_4 (Loulergue et al., 2008). d) Chinese speleothem composite record of $\delta^{18}\text{O}_{\text{calcite}}$ (Cheng et al., 2016). e) IODP U1308 and ODP 983 IRDs proxies (pink and black curves respectively; Barker et al., 2019; Hodell et al., 2008). The gray rectangles frame the deglacial rises observed in the benthic $\delta^{18}\text{O}$ record (Hodell et al., 2008) and corresponding Terminations are numbered from TI to TVII. The orange vertical bars frame WMIs corresponding to high $\delta^{18}\text{O}_{\text{calcite}}$ levels identified by Cheng et al. (2009, 2016). Two possible stratigraphic links between $\delta^{18}\text{O}_{\text{atm}}$ and $\delta^{18}\text{O}_{\text{calcite}}$ are shown at ~ 380 and 340 ka BP (black dotted lines). One possible stratigraphic link between WMI end and CH_4 abrupt increase is represented at ~ 60 ka BP (red vertical plain line). Two possible stratigraphic links between $\delta^{18}\text{O}_{\text{calcite}}$ and CH_4 are represented (red vertical dashed lines). They do not occur at WMI endings as identified by Cheng et al. (2016) but coincide with IRD events (red dashed circles).

5.3 ASSESS THE SENSITIVITY OF THE COHERENT AGE MODEL TO THE DATING METHODOLOGY

5.3.1 Speleocomposite – U1308

Sensitivity tests description

Hobart et al. (2023) defined the start of the AAMV as the onset of the abrupt increase in the detrended $\delta^{18}\text{O}_{\text{calcite}}$ record, and the AAMV end as the point where the detrended $\delta^{18}\text{O}_{\text{calcite}}$ value returns to the level at which the AAMV began. The detrended record is obtained by removing the component of the Asian monsoon that correlates with insolation, thus enabling the examination of residual suborbital variation across the entire record. In practice, the detrended record is calculated by subtracting the modeled insolation at 65°N on the 21st of July (Laskar et al., 2004) to the $\delta^{18}\text{O}_{\text{calcite}}$.

Hobart et al. (2023) correlate the start/end of AAMV to start/end of IRD events identified by the increase/decrease detected in the $\delta^{18}\text{O}$ of bulk carbonate of site U1308. The stratigraphic links established between IODP U1308 and the Chinese composite by Hobart et al. (2023) along with their uncertainties are used to generate an initial experiment speleo-marine 1 (SM1). The links used in SM1 are illustrated by green triangles linked by dotted lines in Fig. 5.6.

We propose an alternative set of stratigraphic links between IODP U1308 and the Chinese composite. These new links are tested in an experiment noted SM2. We correlate AAMV to IRD events identified when peaks are detected in more than one IRD proxies for the IODP U1308 site. These IRD proxies include the $\delta^{18}\text{O}$ of bulk carbonate, the ratio of calcium or silicon to strontium, the magnetic susceptibility or the bulk density (Hodell et al., 2008). To determine the tie point position in the marine core we take the average position of all the starting/ending points visually detected in each IRD proxy records. We slightly shift the position of the start/end of the AAMV events detected in the $\delta^{18}\text{O}_{\text{calcite}}$ record with respect with what was proposed by Hobart et al. (2023) when we disagree with the choice made in their study. Figure 5.6 shows the 450-300 ka BP interval where Hobart et al. (2023) suggest to link the green triangles while we propose to link the pink dots. We also get rid of some matches from Hobart et al. (2023) that we find ambiguous, such as the link at ~440 ka BP.

We come up with a third set of tie points by keeping all the tie points determined in SM2 except for an ambiguous link at the end of TIV (~335 ka BP; see Fig. 5.6). These new links are tested in an experiment noted SM3. Identifying the endpoints of the IRD and AAMV events is not straightforward over this period, making it a perfect context for evaluating the sensitivity of the chronology to the choice of tie points. The IRD proxy exhibit three distinct decreases between 342 and 323 ka BP (black arrows in panel b of Fig. 5.6). In the SM2 experiment, the first local minimum in IRD proxy is connected to the first plateau encountered in the abrupt $\delta^{18}\text{O}_{\text{calcite}}$ decrease (pink dots at ~335 ka BP in Fig. 5.6). In SM3, we remove this tie point and rather align the end points of AAMV and IRD events at ~325 ka BP (maroon squares linked by the plain line in Fig. 5.6) when both $\delta^{18}\text{O}_{\text{calcite}}$ and $\delta^{18}\text{O}$ of bulk carbonate return to a value that is closer to their value before the beginning of the millennial-scale event.

Ultimately, we perform additional tests by keeping the set of tie points used in SM2 and SM3

but varying the background uncertainty (in years) attached to the stratigraphic links. The uncertainty of the tie points was either set up to 0.5, 2 or 4 kyr. These complementary tests aim at assessing the sensitivity of the chronology to the choice of prior uncertainty attached to the tie points. The configuration of each tests is reported in Table 5.1.

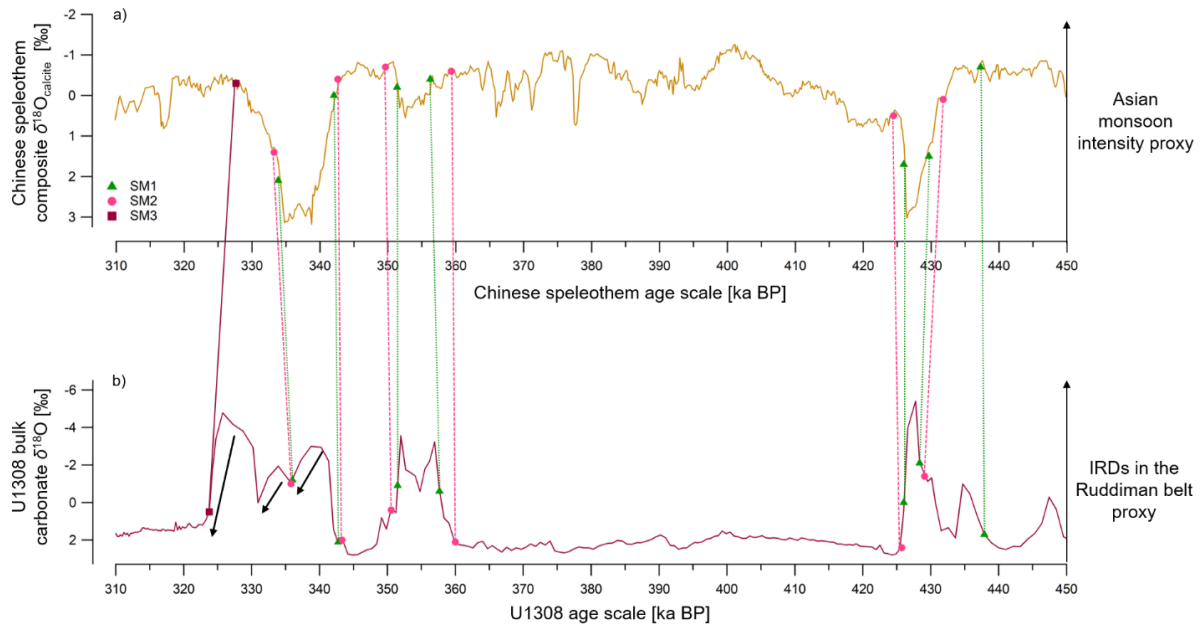


Figure 5.6 Stratigraphic matching of the IODP U1308 marine core to the Chinese speleothem composite via synchronization of IRD and AAMV events over the 450–310 ka BP interval. a) The Chinese speleothem detrended record of $\delta^{18}\text{O}_{\text{calcite}}$ (Cheng et al., 2016). b) The IODP U1308 $\delta^{18}\text{O}$ of bulk carbonate as an IRD proxy in the Ruddiman belt (Hodell et al., 2008). Green triangles linked with dotted lines show tie points of Hobart et al. (2023) used in SM1. Pink dots linked with dashed lines show tie points established in this study and used in SM2. The maroon squares linked with a plain line shows one alternative stratigraphic links considered in SM3. Three black arrows in panel b indicate distinct decreases in the IRD proxy between 342 and 323 ka BP.

Table 5.1 Parameterizations of the different speleocomposite-marine (SM) synchronization tests. We either vary the set of stratigraphic links (between SM1, SM2 and SM3) or the prior uncertainty attached to the links (between SM2-0.5, SM2-2 and SM2-4). All SM experiments were performed using the S11 configuration defined in the next section so that all test chronologies are coherent for the three types of archives.

Experiment	Alignment approach	Prior uncertainty	Source
		(years)	
SM1	AAMV onset/end in $\delta^{18}\text{O}_{\text{calcite}}$ – IRD onset/end in $\delta^{18}\text{O}$ of bulk carbonate	465 – 4,780	Hobart et al. (2023)
SM2-0.5	AAMV onset/end in $\delta^{18}\text{O}_{\text{calcite}}$ – IRD onset/end in $\delta^{18}\text{O}$ of bulk carbonate	500	This study
SM2-2	//	2,000	This study
SM2-4	//	4,000	This study

SM3-0.5	SM2 with the replacement by the link at ~335 ka BP by another link at ~325 ka BP	500	This study
SM3-2	//	2,000	This study
SM3-4	//	4,000	This study

Results of the sensitivity tests

We remind that the objective is not to ascertain which tie points are correct or to produce a reference chronology for the IODP U1308 site. We rather use the model PaleoChrono-1.1 to evaluate the margins of error that can be induced by the dating methodology in the building process of the coherent age model for IODP U1308, EDC and the Chinese speleothem composite. In this section, we focus on the sensitivity of the marine chronology for two reasons: (i) since it is the least constrained, it shows a greater sensitivity and (ii) it is of interest to determine the temporal rate of evolution of sea level.

Figure 5.7 shows the age difference between the initial chronology of IODP U1308 and the new coherent chronologies resulting from SM1 (green line), SM2 (pink lines) and SM3 (maroon lines) experiments. Only the past 650 kyr are represented as it corresponds to the interval where the IODP U1308 marine core can be synchronized with the absolutely dated Chinese speleothem composite. The new tests agree to shift the initial age model towards the same direction, either younger or older ages, over the majority of the past 650 kyr. This means that, during the majority of the time interval, the synchronization of site U1308 to the Chinese speleothem composite results in a consistent shift in the age model regardless of the stratigraphic links employed. Some exceptions are indicated by the vertical frames in Fig. 5.7.

The discrepancies between SM1 and SM2 chronologies are indicated by red vertical bars and between SM2 and SM3 by the gray vertical bar. The removal of the SM1 link established by Hobart et al. (2023) at ~440 ka BP results in a ~4.8 kyr age offset between SM1 and SM2 (red arrows in Fig. 5.7). The replacement of one tie point in SM2 by another match in SM3 at ~330 ka BP induces an age offset reaching 4 kyr between SM2 and SM3 tests (gray arrow in Fig. 5.7).

At each time step, we calculate the magnitude of the age offset among the IODP U1308 chronologies yielded by the different tests. The offset magnitude is of 1.7 kyr on average (past 650 kyr) and reaches a maximum of ~4.8 kyr at around 440 ka BP (red arrows in Fig. 5.7). This age discrepancy obtained among the new coherent age models originates from the fact that only one set of discrete tie points is used for synchronizing the IODP U1308 to the Chinese speleothem composite while various possibilities exist.

We conclude that the choice of matching links affects the resulting age model of U1308 which can be expected to vary in a ± 2.5 kyr envelop. This envelop is the minimal uncertainty estimate permitting to encompass the maximum offset of almost 5 kyr observed at ~440 ka BP and 600 ka BP.

A few-hundred years age offset is observed on average between SM2-0.5, SM2-2 and SM2-4 tests (as for SM3-0.5, SM3-2 and SM3-4 tests) undertaken with a range of various uncertainties

attached to the tie points. This indicates that the age model of IODP U1308 is relatively less affected by the choice of prior uncertainty attached to the tie points than by the choice of tie points itself. The only exception is at ~340 ka BP where the age offset between SM2-0.5, SM2-2 and SM2-4 tests (various pink lines in Fig. 5.7) reaches 2 kyr (pink arrow in Fig. 5.7) whereas it is of 420 years at most for SM3-0.5, SM3-2 and SM3-4 tests (maroon lines in Fig. 5.7). This suggests that the tie point in SM2 (TP2) might be less reliable than the tie point in SM3 (TP3). A possible interpretation is that TP2 is evaluated less plausible by the probabilistic tool than the rest of the chronological information. We argue that performing such two-step sensitivity tests:

- (i) testing two sets of stratigraphic links by replacing the tie point n°1 by an alternative tie point n°2 (SM2 versus SM3);
- (ii) and testing various prior uncertainties for this specific tie point in both set of stratigraphic links (SM2-0.5, SM2-2 and SM2-4 versus SM3-0.5, SM3-2 and SM3-4),

may give clues to evaluate whether the tie point n°1 or the tie point n°2 is the most coherent with the rest of the background chronological information.

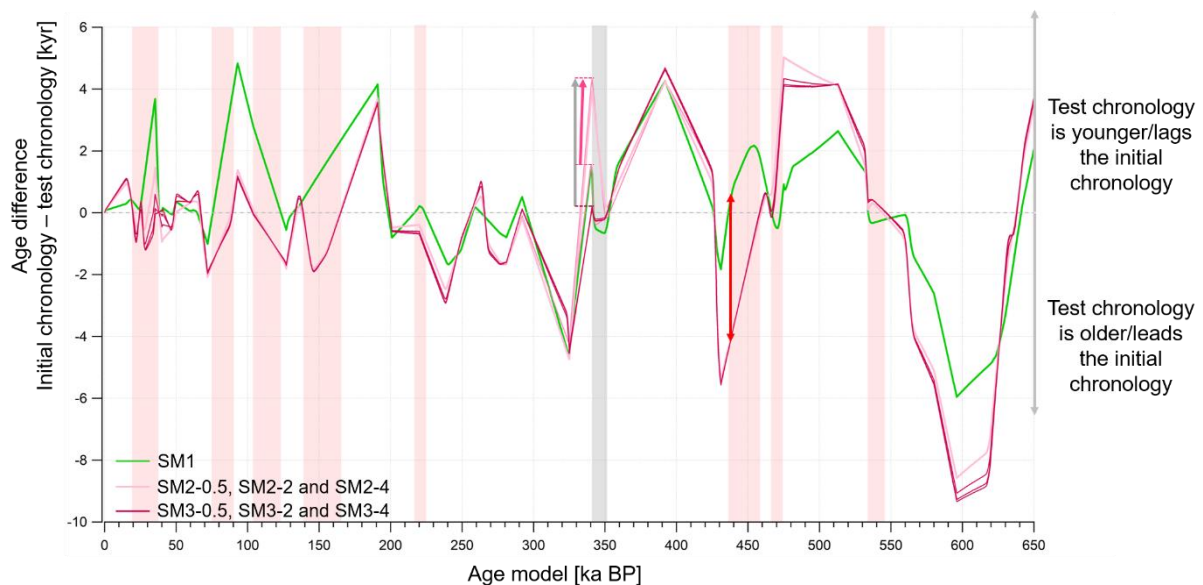


Figure 5.7 Age difference between the initial IODP U1308 age scale and the test chronologies. A positive difference indicates that the test chronologies are younger than (or lag) the initial one. The test chronologies are obtained by varying either (i) the tie points as per SM1 (green curve), SM2 (pink curves) and SM3 (maroon curves); either (ii) the prior uncertainty attached to the tie points between 500 years and 4 kyr for SM2 (pink curves) and SM3 (maroon curves). Vertical red frames show disagreement intervals between SM1 and SM2 and the gray vertical bar frames the disagreement between SM2 and SM2. Gray arrow indicates the largest offset between SM2 and SM3 and red arrows indicate the largest offset among all test chronologies.

We acknowledge that the posterior age scale yielded for the IODP U1308 site appears quite sharp (as shown by the sharp angles followed by the curves in Fig. 5.7). Further work would be needed on the configuration of the parameters related to the background marine chronology in the Paleochrono-1.1 model. As a perspective, the marine sediment posterior chronology

could be adjusted more smoothly to comply with the chronological constraints.

5.3.2 Speleocomposite – EDC

Sensitivity tests description

Some studies synchronized ice core records of atmospheric CH₄ concentration to $\delta^{18}\text{O}_{\text{calcite}}$ of Chinese speleothems (Buizert, Cuffey, et al., 2015; Parrenin et al., 2024; Shackleton et al., 2004). While this approach may be appropriate for millennial-scale events of the last glacial period, Extier et al. (2018) argue for caution during deglaciations. Indeed, during the WMI occurring in the first phase of a Termination marked by a Heinrich event, CH₄ shows a strong increase, probably induced by high-latitude emissions. This CH₄ pattern during deglaciations is inconsistent with the $\delta^{18}\text{O}_{\text{calcite}}$ variations. Similarly, the orbital variations of the Chinese speleothem record of $\delta^{18}\text{O}_{\text{calcite}}$ are not seen in the CH₄ record. Therefore, Extier et al. (2018) call for the synchronization of ice core record of $\delta^{18}\text{O}_{\text{atm}}$ to the $\delta^{18}\text{O}_{\text{calcite}}$ of Chinese speleothems when considering multiple glacial-interglacial cycles. In the paper presented in the Section 4.1, we followed the methodology prescribed by Extier et al. (2018). We integrated the EDC $\delta^{18}\text{O}_{\text{atm}}$ – Chinese speleothem $\delta^{18}\text{O}_{\text{calcite}}$ synchronization as absolute *dated horizons* for EDC to construct the AICC2023 chronology. In this Chapter, we confront the two approaches based respectively on EDC records of CH₄ or $\delta^{18}\text{O}_{\text{atm}}$.

For the CH₄ – $\delta^{18}\text{O}_{\text{calcite}}$ synchronization, we either align the mid-points (SI1 experiment) or starting points (SI2 experiment) of abrupt increases in methane and decreases in $\delta^{18}\text{O}_{\text{calcite}}$ (Fig. 5.8). We connect $\delta^{18}\text{O}_{\text{calcite}}$ and CH₄ when an IRD peak tracing a parallel Heinrich event is detected in the IODP U1308 (Hodell et al., 2008) and in the ODP 983 cores (Barker et al., 2019). This results in identifying tie points over the WMIs identified by Cheng et al. (2009, 2016) (orange vertical frames in Fig. 5.5) as well as over additional periods of weak monsoon associated with IRD peaks that we identified here.

We also use the set of $\delta^{18}\text{O}_{\text{atm}} - \delta^{18}\text{O}_{\text{calcite}}$ tie points proposed by Extier et al. (2018) to align EDC to the Chinese speleothem (Fig. 5.8). This set of tie points constitutes the SI3 experience. Figure 5.8 shows a zoom in the 460-350 ka BP interval and illustrates the three synchronization methodologies used in the SI1, SI2 and SI3 tests. The configuration of each test is reported in Table 5.2.

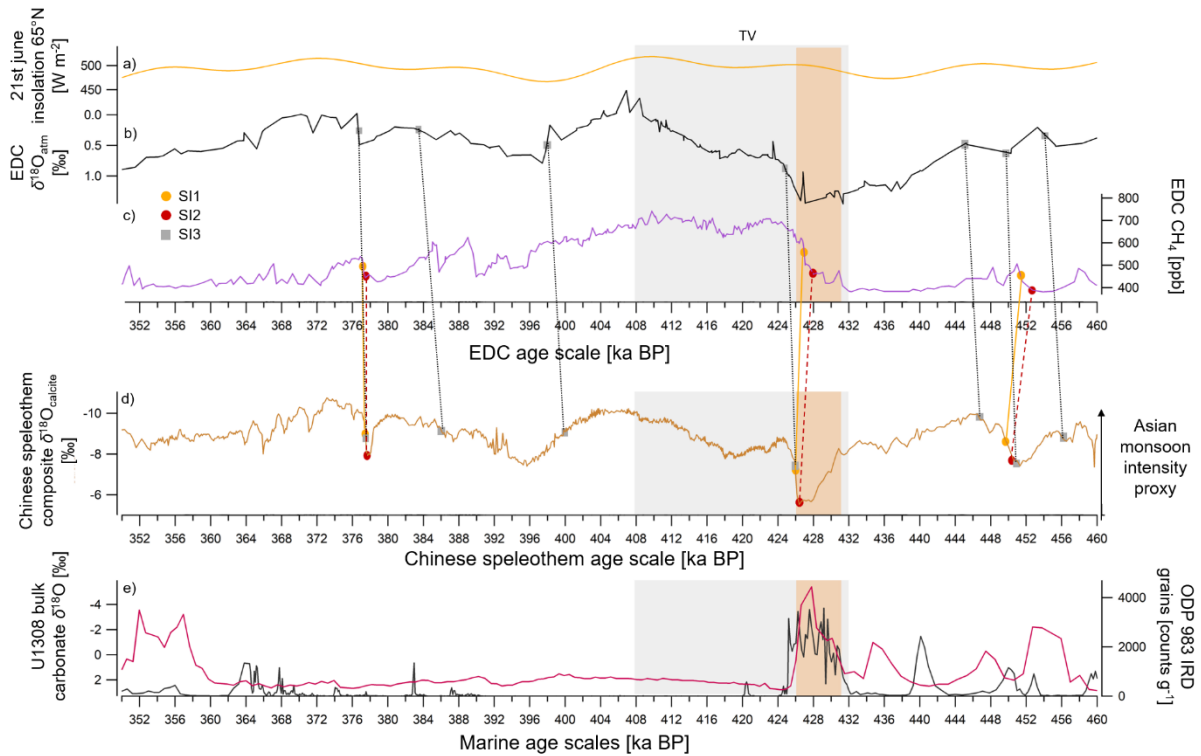


Figure 5.8 Connecting the EDC ice core with the Chinese speleothem composite via synchronization of $\delta^{18}\text{O}_{\text{atm}}$ or CH_4 to $\delta^{18}\text{O}_{\text{calcite}}$. a) Summer solstice insolation at 65°N (Laskar et al., 2004). EDC records of b) $\delta^{18}\text{O}_{\text{atm}}$ (Bouchet, Grisart, Landais, et al., 2023a) and c) atmospheric CH_4 concentration (Louergue et al., 2008). d) Chinese speleothem composite record of $\delta^{18}\text{O}_{\text{calcite}}$ (Cheng et al., 2016). e) IODP U1308 and ODP 983 IRDs proxies (pink and black curves respectively; (Barker et al., 2019; Hodell et al., 2008). The gray rectangle frames the deglacial rise observed in the benthic $\delta^{18}\text{O}$ record (Hodell et al., 2008) over TV. The orange dots linked by plain lines show the midpoints connected in SI1. The maroon dots linked by dashed lines show the starting points connected in SI2. The gray squares linked by dotted lines show the $\delta^{18}\text{O}_{\text{atm}} - \delta^{18}\text{O}_{\text{calcite}}$ defined in Extier et al. (2018) and used in SI3.

Table 5.2 Parameterizations of the different speleo-ice core (SI) synchronization tests. We vary the set of stratigraphic links between SI1, SI2 and SI3. All SI experiments were performed using the SM1 configuration defined in the preceding section so that all test chronologies are coherent for the three types of archives. We note WMI the intervals of weak Asian monsoon defined by (Cheng et al., 2009, 2016) complemented by intervals identified in this study, i.e. periods of weak Asian monsoon coinciding with peaks in the IRD proxies of IODP U1308 and ODP 983 sites.

Experiment	Alignment approach	Prior uncertainty (years)	Source

SI1	Midpoint of decrease in $\delta^{18}\text{O}_{\text{calcite}}$ (WMI end) – midpoint of increase in CH_4 (when IRDs are identified in IRDs proxies)	3,000	This study
SI2	Start point of decrease in $\delta^{18}\text{O}_{\text{calcite}}$ (WMI end) – start point of increase in CH_4 (when IRDs are identified in IRDs proxies)	3,000	This study
SI3	Midpoint of increase/decrease in $\delta^{18}\text{O}_{\text{calcite}}$ – midpoint of increase/decrease in $\delta^{18}\text{O}_{\text{atm}}$	1,140 – 8,471	Extier et al. (2018)

Results of the sensitivity tests

We use the model PaleoChrono-1.1 to evaluate the margins of error that can be induced by the dating methodology in the building process of the EDC age model. We focus on the sensitivity of the ice core chronology for two reasons: (i) it is less constrained than the one of speleothem and (ii) it is of interest to determine the temporal rate of evolution of atmospheric CO_2 concentration.

Figure 5.9 shows the age difference between the AICC2012 chronology of EDC ice core and the new chronologies resulting from SI1, SI2 and SI3 experiments. Only the most recent 650 kyr are displayed as they correspond to the interval where EDC can be synchronized with the absolutely dated Chinese speleothem composite.

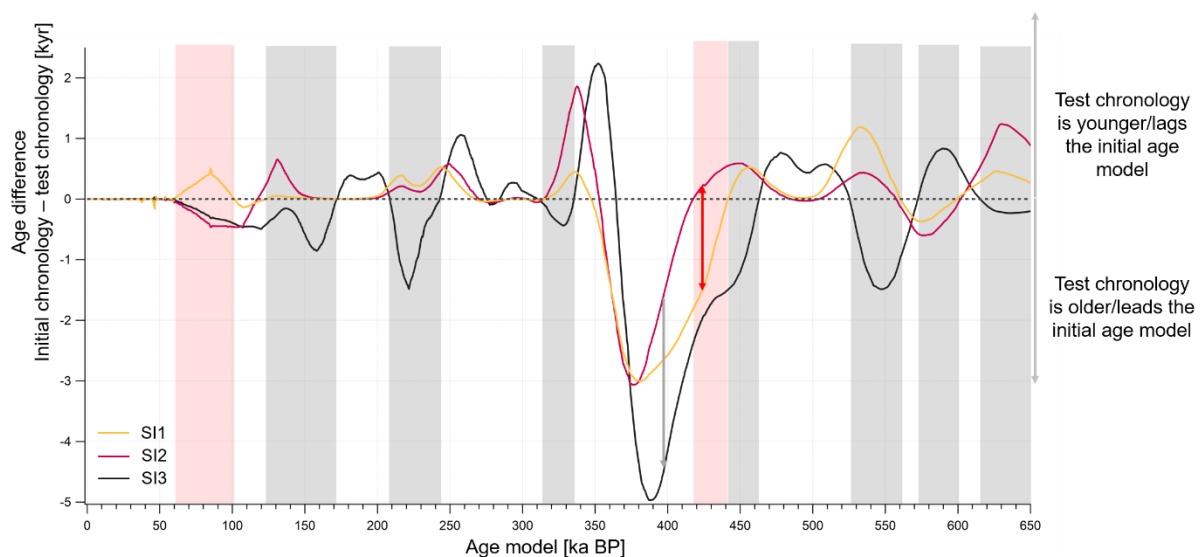


Figure 5.9 Age discrepancies between the initial EDC age scale (AICC2012) and the test chronologies. A positive difference indicates that the test chronologies are younger than (or lag) the initial one. The test chronologies are obtained by linking midpoints (SI1, orange line) or start points (SI2, red line) of CH_4 increase and $\delta^{18}\text{O}_{\text{calcite}}$ decrease. The SI3 test (black line) is obtained using the midpoints $\delta^{18}\text{O}_{\text{calcite}} - \delta^{18}\text{O}_{\text{atm}}$ synchronization of Extier et al. (2018). Vertical red frames show disagreement intervals between SI1 and SI2. The gray vertical frames show disagreement between SI1 or SI2 and SI3. The gray arrow indicates the largest offset between the three tests and the red arrow indicates the largest offset among SI1 and SI2 chronologies.

The $\text{CH}_4 - \delta^{18}\text{O}_{\text{calcite}}$ alignments (tests SI1 and SI2 in orange and maroon respectively) agree to shift the initial age model towards the same direction, either younger or older ages, over the majority of the past 650 kyr. Two exceptions are indicated by vertical red frames in Fig. 5.9. SI1 is younger than the initial age scale while SI2 is older between 100 and 50 ka BP and the situation is reversed between 440 and 420 ka BP. The age offset between SI1 and SI2 reaches a maximum of ~ 1.8 kyr at around 425 ka BP (red arrows in Fig. 5.9). The choice of matching point between CH_4 and $\delta^{18}\text{O}_{\text{calcite}}$ affects the resulting age model of EDC. This effect can account for a ± 0.9 kyr variability, with the maximum offset of ~ 1.8 kyr observed at ~ 425 ka BP corresponding to the extremities of the uncertainty envelop.

It is therefore of particular interest to compare the chronology obtained using the $\text{CH}_4 - \delta^{18}\text{O}_{\text{calcite}}$ alignments to the chronology obtained using the $\delta^{18}\text{O}_{\text{atm}} - \delta^{18}\text{O}_{\text{calcite}}$ alignment over this specific period. Figures 5.8 and 5.9 reveal that the $\text{CH}_4 - \delta^{18}\text{O}_{\text{calcite}}$ mid-point synchronization (SI1) better agrees with the $\delta^{18}\text{O}_{\text{atm}} - \delta^{18}\text{O}_{\text{calcite}}$ alignment (SI3) than the $\text{CH}_4 - \delta^{18}\text{O}_{\text{calcite}}$ start-point synchronization (SI2) at ~ 425 ka BP.

Over the majority of the past 650 kyr, the possible discrete matching of EDC to the Chinese speleothem composite via $\text{CH}_4 - \delta^{18}\text{O}_{\text{calcite}}$ (tests SI1 and SI2) or $\delta^{18}\text{O}_{\text{atm}} - \delta^{18}\text{O}_{\text{calcite}}$ (test SI3) alignments yield coherent results. Major exceptions are indicated by the gray vertical frames in Fig. 5.9, with the maximum offset between the three tests reaching almost 3 kyr at ~ 395 ka BP (gray arrows in Fig. 5.9). Thus, depending on the choice of alignment method (either $\text{CH}_4 - \delta^{18}\text{O}_{\text{calcite}}$ or $\delta^{18}\text{O}_{\text{atm}} - \delta^{18}\text{O}_{\text{calcite}}$), the resulting age model of EDC can be expected to vary in a ± 1.5 kyr envelop. This envelop is the minimal uncertainty estimate permitting to encompass the maximum offset of 3 kyr observed at ~ 395 ka BP.

Over the 460-380 ka BP period, where is observed the largest disagreement between the discrete matching approaches, it is difficult to match the $\delta^{18}\text{O}_{\text{atm}}$ to the $\delta^{18}\text{O}_{\text{calcite}}$ without ambiguity because of the low resolution of the EDC $\delta^{18}\text{O}_{\text{atm}}$ record (Fig. 5.8). In addition, the magnitude of the $\delta^{18}\text{O}_{\text{atm}}$ variations may be attenuated due to the low eccentricity in the Earth orbit, which induces a variability of lesser amplitude in the northern hemispheric insolation forcing. Hence, we emphasize on the necessity to combine the synchronization of $\delta^{18}\text{O}_{\text{atm}}$ or CH_4 EDC records to the $\delta^{18}\text{O}_{\text{calcite}}$ of the Chinese speleothem composite as complementary approaches.

5.3.3 Confidence intervals evaluated from the sensitivity tests

The SM1, SM2 and SM3 tests yield a confidence interval of ± 2.5 kyr for the IODP U1308 – Chinese speleothem composite synchronization via alignment of IRD proxies and AAMV traced by $\delta^{18}\text{O}_{\text{calcite}}$.

The SI1, SI2 and SI3 tests yield a confidence interval of ± 1.8 kyr ($\sqrt{1.5^2 + 0.9^2}$) for the EDC ice core – Chinese speleothem composite synchronization via alignment of millennial and/or orbital variability of the ice core records of $\delta^{18}\text{O}_{\text{atm}}$ or CH_4 to the $\delta^{18}\text{O}_{\text{calcite}}$ variations.

5.4 SEQUENCES OF CLIMATIC EVENTS OVER GLACIAL TERMINATIONS

We perform three additional tests in this section. For these tests we use the stratigraphic links published in Bouchet et al. (2023) to connect the $\delta^{18}\text{O}_{\text{calcite}}$ record of the Chinese speleothem composite and the $\delta^{18}\text{O}_{\text{atm}}$ record of the EDC ice core. A prior uncertainty of ± 1.8 kyr (1σ) is assigned to the tie points if the published uncertainty employed in Bouchet et al. (2023) was inferior to 1.8 kyr. Otherwise, the prior uncertainty published in Bouchet et al. (2023) is conserved. For connecting the IODP U1308 marine core to the Chinese speleothem composite, we either use the set of stratigraphic links defined for the SM1, SM2 or SM3 tests. A prior uncertainty of ± 2.5 kyr (1σ) is assigned to the tie points for the IODP U1308 – Chinese speleothem composite synchronization via alignment of IRD proxies and AAMV traced by $\delta^{18}\text{O}_{\text{calcite}}$. The three additional tests are referred to as SM1', SM2' and SM3' and yield three coherent, relative and absolute chronologies for the IODP U1308 marine core and the EDC ice core.

It is thus possible to plot the past evolution of atmospheric CO_2 concentration and of the global sea level traced by the benthic $\delta^{18}\text{O}$ record of IODP U1308 site on a common timescale (yellow, orange and brown curves in Fig. 5.10). The three test chronologies frame a possible time interval within which the respective changes in atmospheric CO_2 recorded in EDC and in the global sea level traced by the benthic $\delta^{18}\text{O}$ record of IODP U1308 likely occurred. The lead-lag relationship between CO_2 and sea level variations during glacial Terminations is studied in this section.

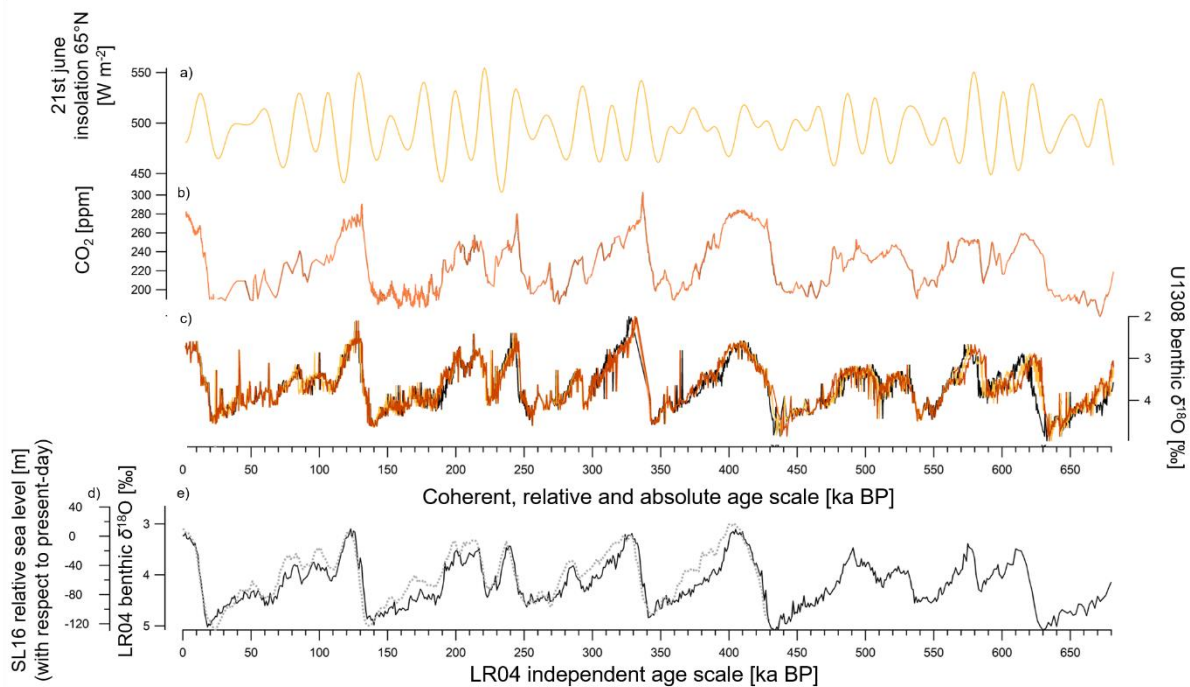


Figure 5.10 Evolution of climatic forcing and response over the past 680 kyr. a) Summer solstice insolation at 65°N (Laskar et al., 2004). b) EDC record of atmospheric CO_2 concentration (Lüthi et al., 2008; Shin et al., 2020; Siegenthaler et al., 2005). c) $\delta^{18}\text{O}$ of benthic foraminifera as a proxy for sea level (Hodell et al., 2008). The paleorecords are represented on their individual age scale (black curves) and on the common, relative and absolute age scales yielded by the SM1', SM2' and SM3' tests (yellow, orange and brown curves respectively). d) The SL16 reconstruction of relative sea level (with respect to present-day) (gray dashed curve; Spratt & Lisiecki, 2016) and e) the LR04 stack of globally distributed benthic $\delta^{18}\text{O}$ records which can be considered as a proxy for sea level (black

curve; Lisiecki & Raymo, 2005) are represented on their individual age scales that are not coherent with that of EDC or IODP U1308.

5.4.1 Methods

For each Termination, the timing of the start (t_1) and end (t_2) of the increase in atmospheric CO₂ concentration and in the benthic $\delta^{18}\text{O}$ record is determined using the Rampfit method (Mudelsee, 2000). This method has already been used for the detection of the onset and end of glacial-interglacial transitions. For example, it was used by Landais et al. (2013) to examine the relative changes in atmospheric CO₂, Antarctic temperature and global climate during Termination II.

The Rampfit method involves fitting a "ramp function" $f(t)$ to a given time series. The function $f(t)$ is continuous and segmented into three distinct intervals (Fig. 5.11):

$$f(t) = f_1 \text{ if } t < t_1$$

$$f(t) = f_2 \text{ if } t > t_2$$

$f(t)$ evolves linearly from f_1 to f_2 if $t_1 < t < t_2$

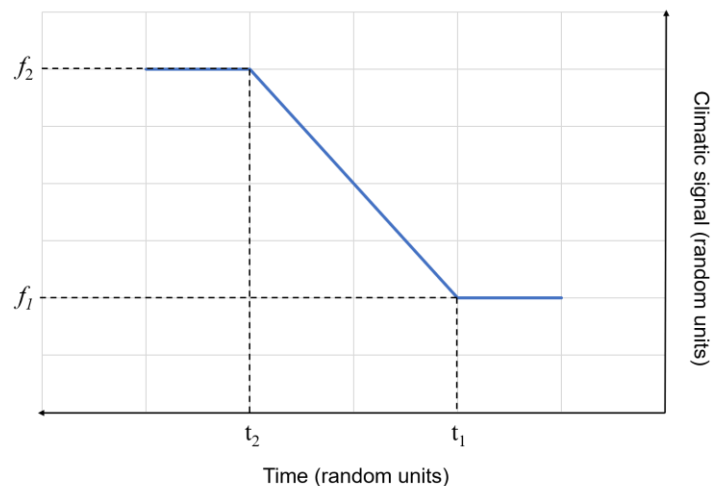


Figure 5.11 Ramp function regression model (adapted from Mudelsee, 2000).

The Rampfit model is particularly robust against noise in the data, which is crucial for analyzing geophysical series that can be affected by random fluctuations. However, notable drawbacks of the methods in our specific case include that it requires that we assume that (i) the sea level and atmospheric CO₂ concentration increase linearly in time and that (ii) both climatic variables shift from a stable level to another stable level over glacial Terminations.

5.4.2 Preliminary discussion of limitations

We insist on the fact that the interpretations drawn here are preliminary and subject to significant limitations. The main goal of our study is treated in the preceding sections (5.1-5.3), i.e. developing a solid methodology, as well as testing its robustness, for building a coherent temporal framework for speleothems, marine archives and ice cores over the past glacial-interglacial transitions. From now on, we propose tracks for interpreting the resulting coherent age scale once it is built. We acknowledge that these possible interpretations are hampered by the following limitations.

On the representativeness of the climate proxies integrated to the chronology

Sea level and benthic $\delta^{18}\text{O}$

In addition to its sensitivity to sea level variations, the benthic $\delta^{18}\text{O}$ record of the IODP U1308 site may be strongly affected by changes in deep ocean temperature. A point of inflection in the sole benthic $\delta^{18}\text{O}$ record of IODP site U1308 may reflect a regional temperature signal rather than a global change in sea level. In addition, the benthic $\delta^{18}\text{O}$ data of IODP U1308 sometimes are scarce (such as over TIV; Fig. 1.10), making it unclear to detect the real inflection point in the record. Detecting the deglacial sea level rise using only this record is thus associated with significant drawbacks. Ideally, multiple benthic records from both hemispheres and various oceans could be aligned to glacial archives through dust fluxes or to speleothems through Heinrich-like event proxies for example. Stacking the multiple benthic records on the coherent age scale would permit to smooth out the regional temperature effects.

A perspective would be to integrate the ODP 1090 site (Martínez-García et al., 2011) that is part of the LR04 stack to the coherent chronology by aligning its dust flux to the one of the EDC ice core. The 4-Myr-long dust record of ODP 1090 was indeed proposed as a stratigraphic template for dating Oldest Ice (Wolff et al., 2022). However, the unavailability of the dust record of ODP 1090 site on the same scale than its benthic $\delta^{18}\text{O}$ record prevents us from yielding the temporal evolutions of the benthic $\delta^{18}\text{O}$ record on a coherent age model. We hope that the ongoing discussion with Martínez-García et al. will lead to the integration of ODP 1090 to the coherent chronology so that its benthic $\delta^{18}\text{O}$ record can be stacked to the IODP U1308 record for further interpretation of sea level variability.

On the definition of a glacial Termination

To reach a precision of 1 kyr in the synchronization of records or in the identification of onset and end timings of Termination we bump into the question: how is defined a glacial Termination?

For detecting the timings of onset and end of sea level and CO_2 increases, we make the hypothesis of the ramp function to model the Terminations. This assumption can be questioned, in particular for detecting the end of Termination IV in the CO_2 record. This Termination is featured by a distinct phenomenon known as the CO_2 overshoot, i.e. a jump of +14 ppm within a few centuries followed by a gradual decrease comparable in rate with the

increase preceding the jump (Fig. 1.10; Nehrbass-Ahles et al., 2020). The question of whether the overshoot should be considered part of the interglacial climate or the deglaciation remains a subject of debate (Bouchet et al., 2024).

The subjectivity of these choices induces uncertainty in the chronology and raises the question of the potential circular reasoning. For instance, in the process of understanding the mechanisms of the glacial Terminations, we first model Terminations as we expect them to be, i.e. logarithmical or linear increase followed by an overshoot, and then we draw conclusions from that assumption. It is important to keep in mind that this way of reasoning introduces logical fallacy as our reasoning starts with the hypothesis we may want to verify.

It is also important to consider that glacial Terminations differ from one to another (Bréant et al., 2019; Past Interglacials Working Group of PAGES, 2016) and should be studied independently. The shape of a specific Termination also varies depending on the climatic proxy or archive considered. Hence the need for intercomparing as much reliable proxies as possible for understanding of climatic mechanisms at play during Terminations.

5.4.3 Temporal phasing estimates

We calculate the temporal phasing between inflection point in the benthic $\delta^{18}\text{O}$ of U1308 and atmospheric CO_2 of EDC at the onset ($t_{1, \delta^{18}\text{O}} - t_{1, \text{CO}_2}$) and end ($t_{2, \delta^{18}\text{O}} - t_{2, \text{CO}_2}$) for each Termination using the Rampfit model. The temporal phasing estimates are displayed in Fig. 5.12 using a scatter plot to visualize the time interval within which the respective changes in CO_2 and in the benthic $\delta^{18}\text{O}$ record of IODP U1308 likely occurred during past deglaciations. A negative/positive phasing posits that the onset or end of the deglacial increase in CO_2 leads/lags the change in the benthic $\delta^{18}\text{O}$ record of IODP U1308. The temporal phasing estimates provided by the three coherent test chronologies are indicated by green (SM1'), pink (SM2'), and maroon dots (SM3') in Fig. 5.12. For each temporal phasing estimate, a vertical bar indicates the 1σ posterior uncertainty yielded by the Paleochrono-1.1 model (calculated as $\sqrt{(1\sigma \text{ posterior uncertainty on EDC age})^2 + (1\sigma \text{ posterior uncertainty on IODP U1308 age})^2}$ for each timing).

For comparison, the temporal phasing is calculated using independent and incoherent chronologies. We use the Rampfit model to detect onset/end of deglacial rise in CO_2 of EDC on the AICC2023 age scale and:

- (i) in benthic $\delta^{18}\text{O}$ U1308 record on the independent age scale of Hodell et al. (2008). The resulting $\text{CO}_2 - \text{benthic } \delta^{18}\text{O}$ phasing is shown by blue squares in Fig. 5.12.
- (ii) in LR04 benthic $\delta^{18}\text{O}$ stack on the independent age scale of Lisiecki & Raymo (2005). The resulting $\text{CO}_2 - \text{benthic } \delta^{18}\text{O}$ phasing is shown by red squares in Fig. 5.12.

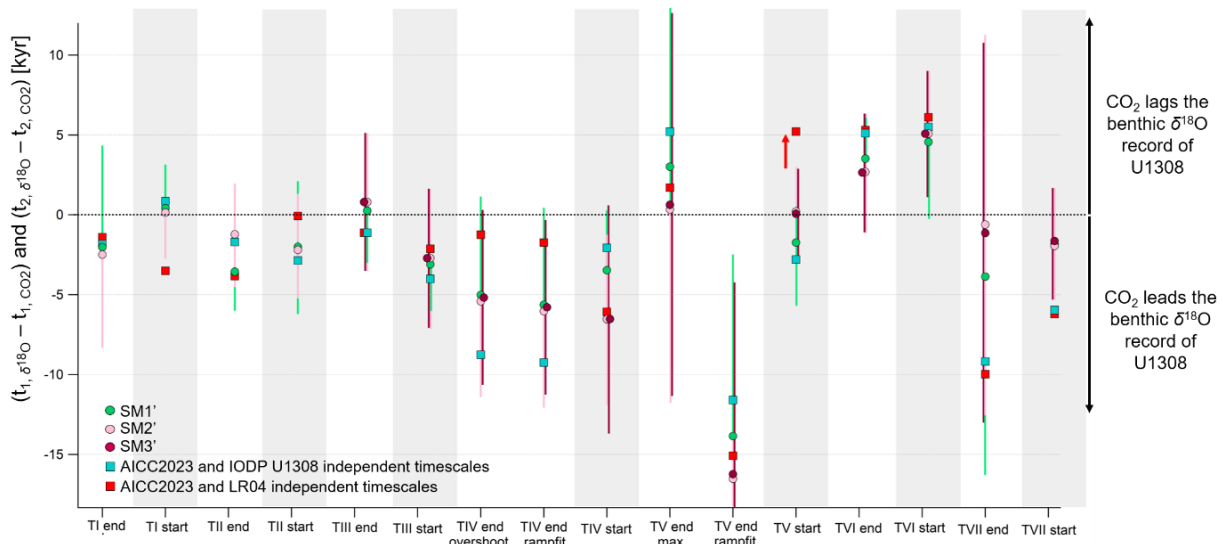


Figure 5.12 Temporal phasing at the onset ($t_1, \delta^{18}\text{O} - t_1, \text{CO}_2$) and end ($t_2, \delta^{18}\text{O} - t_2, \text{CO}_2$) for the past seven Terminations. The timings of end/onset are identified by the Rampfit model as well as visually for the end of TV and TIV for which a pronounced overshoot is observed in the CO_2 . A negative/positive phasing posits that the onset or end of the deglacial increase in atmospheric CO_2 concentration leads/lags the change in the benthic $\delta^{18}\text{O}$ record of U1308. The temporal phasing estimates provided by the coherent chronologies SM1', SM2' and SM3' are shown by green, pink and maroon dots respectively. The vertical green, pink and maroon bars indicate the posterior uncertainty yielded by the Paleochrono-1.1 model for the SM1', SM2' and SM3' tests. The temporal phasing that can be estimated using independent chronologies are also depicted by blue squares (EDC age on AICC2023 vs. U1308 age by Hodell et al., 2008) and red squares (EDC age on AICC2023 vs. LR04 stack age by Lisiecki & Raymo, 2005). The red arrow indicates the disagreement between methodologies using coherent versus incoherent age scales.

5.4.4 Results

This preliminary study yields three major results of interest.

Firstly, combining the time interval spanned by the three estimates given by the coherent chronologies to their error bars, we estimate the confidence interval of the $\text{CO}_2 - \text{benthic } \delta^{18}\text{O}$ temporal phasing calculated using a coherent chronology. This confidence interval is ranging from 6,000 years (TI) to 15,000 years (TIV) at the onset of the deglacial rise and from 6,000 years (TVI) to 25,000 years (TV and TVII) at the end of the deglacial rise.

Secondly, the temporal phasing estimated using independent and incoherent chronologies (squares in Fig. 5.12) disagree with the estimates provided using the coherent chronologies established in our study (dots in Fig. 5.12) at the onset of TI, TV and TVII. For instance, at the onset of TV, the temporal phasing yielded by comparing LR04 and AICC2023 age models disagrees by up to 7 kyr with the estimate given by SM1'. As result, the phasing estimate is located ~2,500 years away from the extremity of the 1σ error bar yielded by the Paleochrono-1.1 model (red arrow in Fig. 5.12). These outliers identified at the start of TV and TVII highlight significant ($>1\sigma$) disagreement between incoherent and coherent chronologies. This result emphasizes the **need for using a chronological framework that is coherent for all climatic records considered** for identifying as accurately as possible the temporal sequence of events.

Finally, a consistent trend seems to arise from the inter-comparison between the past seven Terminations and the inter-comparison between the three coherent chronologies. The onset of the deglacial rise in CO₂ leads the increase in benthic δ¹⁸O record of IODP U1308 by ~1 kyr for TV, 1.8 kyr for TVII, 2.3 kyr for TII, 3 kyr for TIII and 5 kyr for TIV (averages of SM1', SM2 and SM3'). The end of the deglacial rise in CO₂ leads the increase in benthic δ¹⁸O record of IODP U1308 by ~2.5 kyr for TI, TII, TVII to ~5.5 kyr for TIV (averages of SM1', SM2 and SM3').

An exception is the Termination VI for which the Rampfit model suggests that the onset and end of CO₂ increase lags that of the benthic record by $5 \pm \frac{4}{5}$ kyr and 3 ± 3.5 kyr respectively. Further work would be helpful to investigate whether this exceptional feature is an artefact due to the dating method used in this study or whether it is a reliable result. In the latter case, it would be valuable to study this specific Termination.

5.5 CONCLUSIONS

We integrated existing chronological information for the EDC ice core, for the Chinese speleothem composite and for the IODP U1308 marine core along with novel stratigraphic links connecting the different sites in the Paleochrono-1.1 model. A coherent chronological framework is obtained for the different archives over the past 640 kyr.

Sensitivity experiments are performed using varying prior uncertainties as well as multiple discrete matching methods to assess the sensitivity of the coherent age model to the dating methodology employed. Solid error bars are provided for the chronology and for the lead-lag relationship estimated between climatic records at the glacial Termination onset and end.

Specifically, we make strong climatic hypotheses and apply the ramp fitting model of Mudelsee (2000) to detect a deglacial signal in the benthic $\delta^{18}\text{O}$ record of IODP U1308 and in the atmospheric CO_2 content over the past seven glacial Terminations. We show that it is possible to identify the temporal phasing between the two climatic signals within a confidence interval ranging from 6 to 25 kyr at the onset/end of glacial Terminations.

5.6 PERSPECTIVES

5.6.1 Refine the implications of the *speleocomposite* – EDC sensitivity tests

It would be of particular interest to investigate why the two methods for synchronizing EDC to the Chinese speleothem that were tested here, i.e. aligning either the $\delta^{18}\text{O}_{\text{atm}}$ or CH_4 to the $\delta^{18}\text{O}_{\text{calcite}}$, sometimes disagree. A first step for exploring this disagreement would be to compare the paleorecords over the 450-350 ka BP time interval, where the largest disagreements occur (Figures 5.8 and 5.9).

5.6.2 Integrate additional archives to the coherent chronology

The Chinese speleothem composite

One advantage of the Paleochrono-1.1 model is to combine multiple archives. A potential perspective could be to integrate each speleothem constituting the Chinese composite as a single archive in the Paleochrono-1.1 experiment rather than implementing the composite as a single archive. To this extent, stratigraphic links could be determined between the speleothems by matching their respective $\delta^{18}\text{O}_{\text{calcite}}$ records on overlapping time intervals.

The IODP U1537 marine core

The IODP U1537 marine core is situated in the southern Scotia Sea between Antarctica and Patagonia, (59°6.65'S, 40°54.37'W; Fig. 5.3; Weber et al., 2022). It does not provide a benthic record to trace past changes in sea level. However, it can be synchronized with the EDC ice core via their dust flux proxies. By employing a variety of alignment approaches, we can gain valuable insights into potential synchronization methods between ice and marine cores.

Major sources of dust deposition in the Southern Ocean include South America (e.g., Patagonia), New Zealand and Australia (Neff & Bertler, 2015).

With the exception of small, intermittent contributions from local volcanoes, the dust measured in Antarctic ice originates from the same terrestrial sources than dust deposited in Southern Ocean. Some dust is deposited in the Southern Ocean before reaching Antarctica.

Glacial conditions are characterized by enhanced dust production in the Southern Hemisphere. Lower sea level exposes low continental shelves, prolonging Southern America and increased wind strength enhances the erosion of a relatively dry continental plateau. However, reduced washout due to weakened precipitation, as well as increased storminess and aridity, results in increased dust transport and deposition to both sub-Antarctic marine sediments and Antarctic ice (Markle et al., 2018; McGee et al., 2010).

Antarctic ice and Southern Ocean dust seem to have the same source and the same transport pathways leading to washout, therefore it is possible to assume that changes in dust deposition

associated with glacial-interglacial transitions occur nearly synchronously across in these two regions.

The Southern Ocean marine dust proxies have been correlated to the EDC dust record to build relative chronologies for the Pacific (Lamy et al., 2014), the Atlantic (Martínez-García et al., 2011) and the Scotia Sea (Weber et al., 2022) over the past 800 kyr. More recently, Ng et al. (2024) investigated the relationship between Antarctic ice dust records and well-dated marine dust records from sediment cores in the southern Atlantic and Pacific oceans, including the IODP U1537 site. They assessed the representativeness of these marine records with respect to Antarctic dust and found that the record from Site U1537 near South America, which spans 1.5 million years, is likely the most robust predictor of the Antarctic ice dust signal.

We started a preliminary study on the discrete matching of the dust records of IODP U1537 and EDC (respectively orange and green curves in Fig. 5.13).

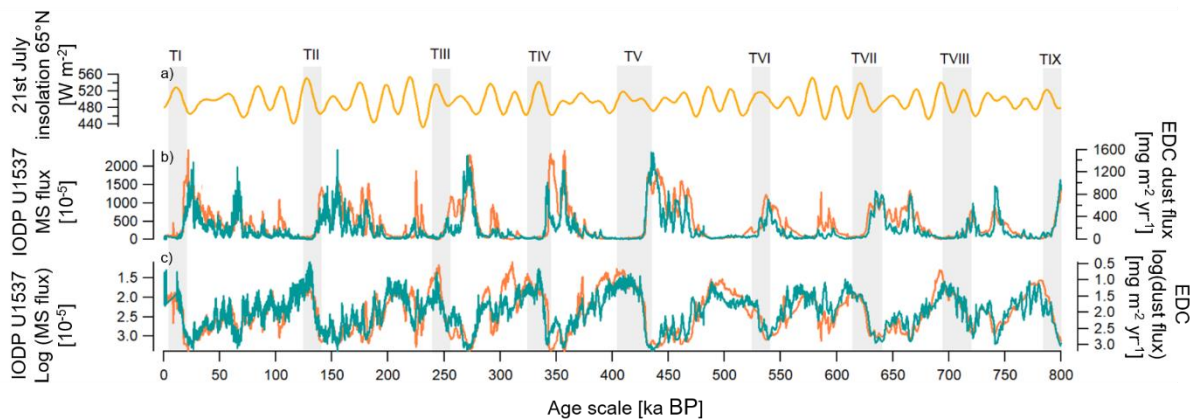


Figure 5.13 Paleoreconstructions of dust flux deposited at EDC and IODP U1537 sites over the past 800 kyr. a) 21st July insolation at 65°N (Laskar et al., 2004). b) Dust flux proxies: magnetic susceptibility (MS) from IODP U1537 (Weber et al., 2022; orange) and dust flux from EDC (Lambert et al., 2008; green). c) Logarithms of the MS from IODP U1537 (orange) and of the dust flux from EDC (green). Gray rectangles frame increases in the benthic $\delta^{18}\text{O}$ record of IODP U1308 associated with deglaciations.

Such synchronization is highly dependent on the climatic assumptions on which the synchronization strategy is based, and on the synchronization method itself. For example, let's build a hypothetical Termination inspired from what is observed in the fluxes at EDC and U1537 sites for some Terminations (Fig. 5.13). It could be characterized by a change in the atmospheric circulation and in the position of the polar front that causes simultaneous decrease in dust emissions from South America and increase in precipitation over the Southern Ocean (leading to dust washout) over a period of 5,000 years. The reduction in dust fluxes could thus be explained by (i) a reduction in dust emission and (ii) dust washout leading to further reduction in dust reaching IODP U1537 and even further reduction in dust reaching EDC site. The exact shape of this alleged reduction is unknown, but it is physically reasonable to assume that it is logarithmic, i.e. that the emitted dust decreases by some percent each year. An additional argument to represent the dust flux variations in a logarithmical way is that the logarithm of the dust flux of IODP U1537 show similarities with the evolution of the global sea level.

Figure 5.14 schematically represents four possible shapes of dust signal archived in the IODP U1537 site versus in the EDC ice core during a generic glacial Termination. If the change really occurs in a logarithmic way then both proxies should be aligned in logarithmic plots to get a good match at the mid-point (Fig. 5.14). If either one of the proxy records is represented linearly, then its apparent midpoint is younger and it may also be more ambiguous to detect where the position mid-point is. Figure 5.14 shows that different reasonable choices of mid-points for aligning the two records induce a significant change in the match by up to ~2kyr. This age offset between the mid-points also gives an approximation of the uncertainty in the case that the change does not follow a logarithmic trend. The age uncertainty seems less significant if we match starting and ending points of the change in dust records.

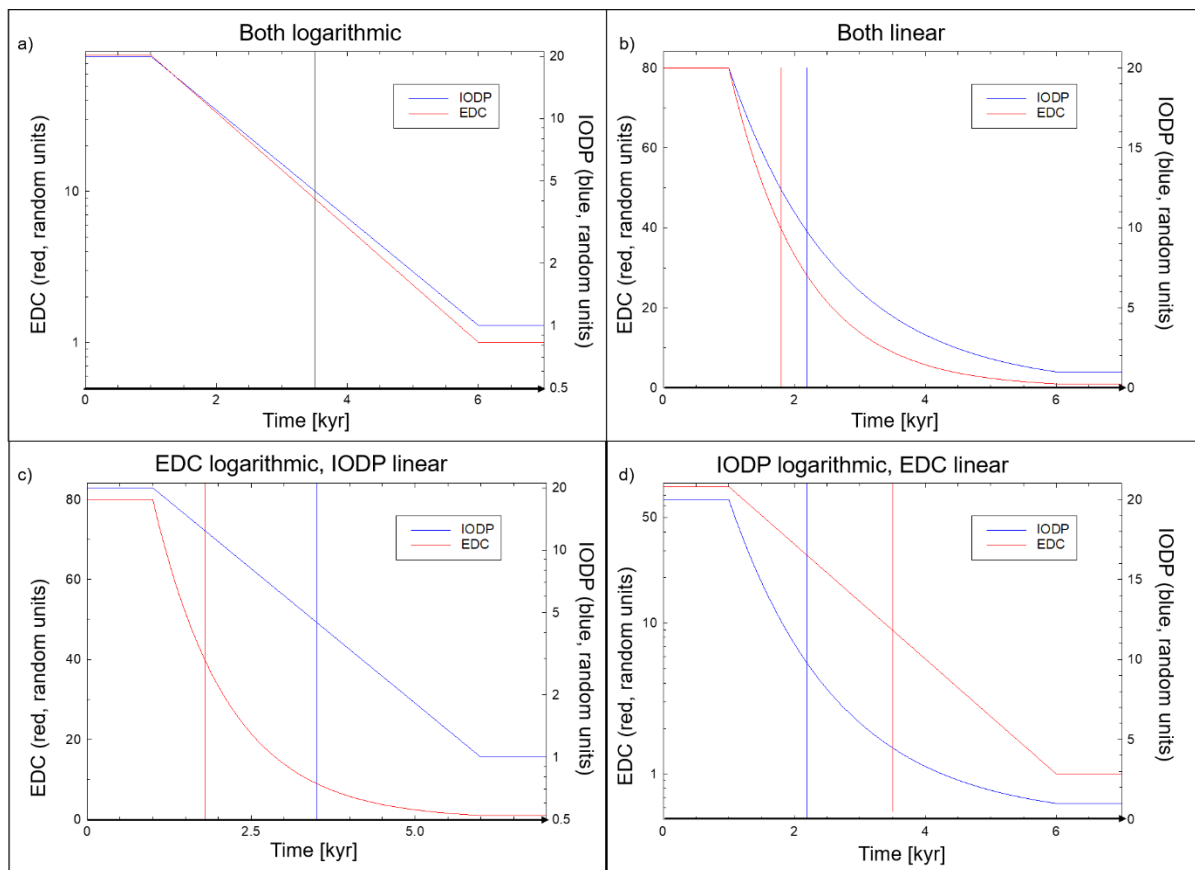


Figure 5.14 Schematic representations of the possible shapes of dust signal observed in IODP cores (blue) vs EDC ice core (red) during a generic glacial Termination. The Termination is triggered at 1 kyr and lasts 5 kyr. The age position of the mid-point is indicated by a vertical bar in the two hypothetical signals. a) If both logarithmic, start, end, midpoint all aligned between EDC and IODP. b) With both linear, there is a small mismatch in mid-point. c) With EDC linear, its midpoint is earlier than the IODP logarithmic and d) vice-versa (reproduced with the authorization of E. Wolff).

The question whether to align the start, midpoint or end of a transition depending on its shape to synchronize dust records remains a subject of vigorous discussion whether it is over glacial Terminations or D-O transitions (Adolphi et al., 2018; Corrick et al., 2020). Therefore, further work could focus on performing several tests similar to those described in the Section 5.3 to assess the sensitivity of the chronology (i) to the assumptions that make the foundation of our

synchronization strategy and (ii) to the synchronization method itself. The various tests could include synchronization of either the logarithmic or linear dust fluxes as well as matching mid-points or starting/ending points of the transitions. A further perspective could be to apply such methodology for synchronizing the EDC ice core with a marine core located between Patagonia and Antarctica that provides records of dust flux as well as of benthic $\delta^{18}\text{O}$ on one same depth scale.

When it comes to the synchronization of paleorecords over long events such as glacial Terminations ($\sim 5\text{kyr}$), we emphasize the importance of asking the following questions:

- What can be the different hypothetical shapes of the climatic transition?
- What is the nature of the signal archived in each proxy record?
- How should the alignment be made: at the start, midpoint or end of a transition?
- What uncertainty results from the incremental steps of the alignment methodology?

Multiple benthic records from various regions

Another perspective to develop would be the integration of multiple benthic records from various regions to the coherent chronology via synchronization to the Chinese speleothem (IRD- $\delta^{18}\text{O}_{\text{calcite}}$ alignment) or to the EDC ice core (dust fluxes alignment). It is essential that the benthic $\delta^{18}\text{O}$ record be measured in the same core as the dust flux and/or the IRD proxies in order to permit synchronization. This allows all marine records from a single site to be input on the same depth scale into the Paleochrono-1.1 model, which is necessary for integration into the coherent chronology. By examining multiple benthic records from various regions, we can eliminate the regional temperature effect and enhance the representativeness of the sea level.

Multiple speleothems from other regions than Asia

The Chinese speleothem composite was chosen as alignment target rather than speleothems tracing African or Southern American monsoon for different reasons. First, the Chinese speleothems present the highest resolution and oldest records so far. They are more accurately dated than their counterparts in other regions due to the important presence of uranium, which allows for the use of the U/Th method. Since the work of Chiang et al. (2003), multiple studies evidenced the correlation between glacial extent in the Northern Hemisphere and the Asian monsoon. There are fewer modeling studies that have examined the relationship between the northern hemispheric ice sheet, the polar front displacement and the South American monsoon. However, if one invokes the ITCZ, there is no reason why this approach cannot be employed. Therefore, speleothem records representative of monsoon from other regions (south America or Africa) could be the focus of further studies and integrated in the age model.

5.6.3 Test various fitting functions for detecting the Termination onset and end

In addition to the Rampfit model, different linear fitting functions could be tested to detect the inflection points in the records of CO₂ and benthic $\delta^{18}\text{O}$ over past Terminations. For example, Legrain et al. (Appendix 7.4) compared three linear fit methods from Caillon et al. (2003), Chowdhry Beeman et al. (2019) and Parrenin et al. (2013b) to constrain the lead-lag relationship between Antarctic climate and CO₂ over the last five deglaciations. The fitting function of Parrenin et al. (2013) provides an optimized decomposition of the signal into a chosen number of linear segments. The linear fit obtained is closer to the record than the ramp fit used in our study. Further work could focus on the comparison of various automatic methods with more or less freedom allowed in the fitting process for the purpose of better constraining the phasing between the sea level proxy and the CO₂.

5.6.4 Refine the interpretation of the climatic processes at play during glacial Terminations

Another perspective is to examine the Termination VI for which we found an exceptional lag of CO₂ behind the $\delta^{18}\text{O}$ benthic record of IODP U1308 (Fig. 5.12). This Termination led to the interglacial of MIS 13 which is notable for its unique combination of warm conditions in the Northern Hemisphere and relatively cool conditions in the Southern Hemisphere (Fig. 5.15). Additionally, it was preceded by a relatively mild glaciation (MIS 14) with lower ice volume and higher CO₂ levels than the two preceding glacial maxima (Fig. 5.15). The coherent and absolute chronology developed in this work could help deciphering the complex relationships between global ice volume and atmospheric CO₂ during this specific Termination-interglacial sequence, such as investigated by Lisiecki et al. (2016).

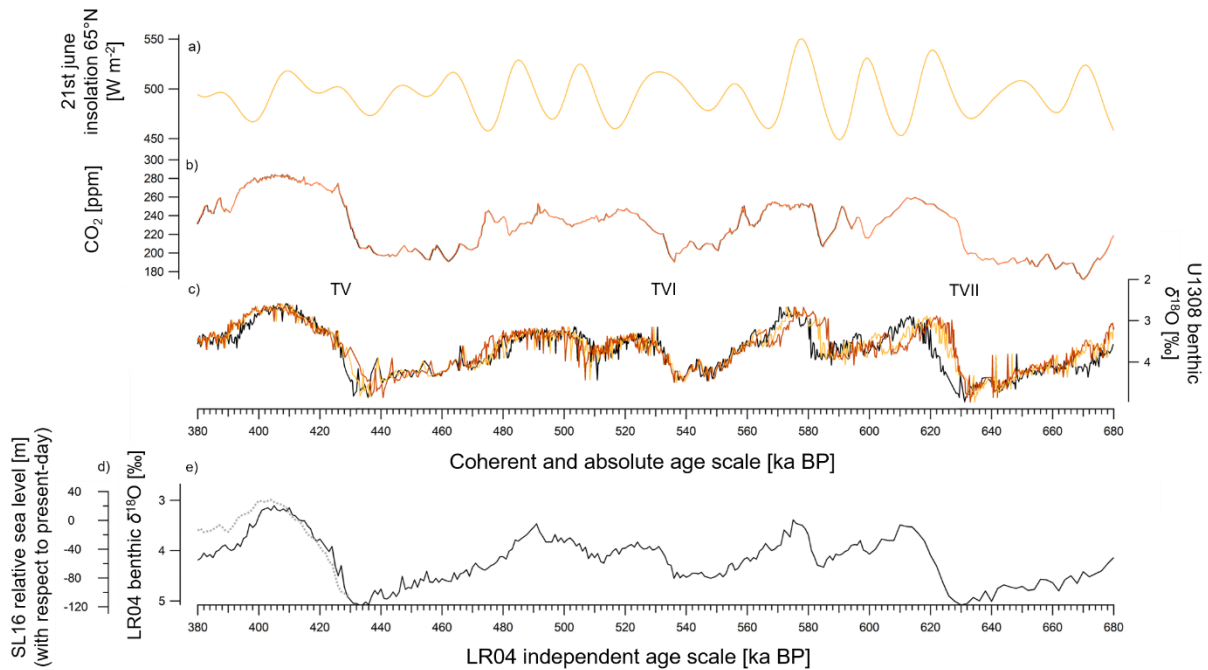


Figure 5.15 Evolution of climatic forcing and response over the 680–380 ka BP interval. a) Summer solstice insolation at 65°N (Laskar et al., 2004). b) EDC records of atmospheric CO₂ concentration (Lüthi et al., 2008; Shin et al., 2020; Siegenthaler et al., 2005). c) δ¹⁸O of benthic foraminifera as a proxy for sea level (Hodell et al., 2008). The paleorecords are represented on their individual age scale (black curves) and on a common and absolute age scales yielded by the SM1', SM2' and SM3' tests (yellow, orange and brown curves respectively). d) The SL16 reconstruction of relative sea level (with respect to present-day) (gray dashed curve; Spratt & Lisiecki, 2016) and e) the LR04 stack of globally distributed benthic δ¹⁸O records which can be considered as a proxy for sea level (black curve; Lisiecki & Raymo, 2005) are represented on their individual age scales that is not coherent with that of EDC or IODP U1308.

5.6.5 On the use of the coherent chronological framework for developing a modeling protocol over TV-MIS 11c

During the workshop of the Quaternary Interglacial working group (September 2023), the group agreed on the importance of developing a coherent temporal framework for the rate of sea-level rise, and for various paleoclimate proxies representative of different parts of the Earth System across the Termination V-MIS 11c. In this study, we present a first step towards the building of such coherent chronology for marine archives, tracing past sea level, and glacial archives, documenting changes in atmospheric concentration in greenhouse gases and local climate. Further work could focus on the use of such coherent age model for developing forcing scenarios of sea level and CO₂ changes to drive climate models. Such modeling experiment could help (i) evaluating the climate model performances by confronting the model to paleo data and (ii) understanding climatic mechanisms at play during glacial Terminations, which are potential analogue to ongoing global warming, and during past interglacials, which are possible analogue to a future warmer world.

6 CHAPTER 6

CONCLUSION AND PERSPECTIVES

In the first section of this chapter is presented the research strategy of my PhD (Section 6.1). The main findings of my research are described (Section 6.2) and perspectives for future work are developed (Section 6.3). An opening to other disciplines is proposed in Section 6.4.

6.1 RESEARCH STRATEGY

Because my PhD took place in a diverse and collaborative environment, our research strategy combined various approaches which are described in this section.

As first aspect of this multi-approach strategy is the experimental approach as I participated to the gas extraction from samples of the Skytrain Ice Rise ice core for Krypton analysis (which is not detailed in this manuscript) as well as to the measure of $\delta^{15}\text{N}$ of N_2 from air trapped in the EDC ice core at LSCE.

A second aspect is the multi-proxy approach since I played (compilation and analysis) with multi-proxy datasets including ice core records of total air content, $\delta^{15}\text{N}$ of N_2 , $\delta^{18}\text{O}_{\text{atm}}$, $\delta\text{O}_2/\text{N}_2$ and ^{81}Kr measured on the gas phase as well as of dust concentration, calcium content, ^{10}Be and water isotopic ratios measured on the ice phase.

A third aspect is a multi-site approach as these records were originating from five polar ice cores from Greenland and Antarctic. Each site is associated with a distinct local climate (temperature and snow accumulation) so that the interpretation of the same tracer can change from one site to the other.

A fourth aspect is a multi-archive approach because I connected Antarctic ice core datasets with proxies from other climatic archives such as to the $\delta^{18}\text{O}_{\text{calcite}}$ of calcite from Chinese speleothems, the ^{10}Be record of an Italian lacustrine succession and to the dust flux recorded in marine sediments between Patagonia and Antarctica. I also worked on the synchronization of Northern Atlantic marine cores to the Chinese speleothems via alignment of IRD proxies with the $\delta^{18}\text{O}_{\text{calcite}}$.

A fifth aspect is a model-data approach as I connected ice core datasets with modeling outputs that I obtained (insolation curves, firn densification model) or that I have been given (ice sheet model, ESM) to gain insight into past climate variability (Chapter 3) and/or to ameliorate the precision of multi-archive chronologies (Chapters and 5).

This multi-approach strategy provides various information constraining (i) the age of the

different archives as well as (i) the past evolution of glaciologic and climatic variables (such as LID, temperature and snow accumulation rate). All these sources of information are combined and integrated as probability densities in the statistical tool Paleochrono-1.1 based on Bayesian inference.

The forward approach consisted in combining all the information derived from paleo-data in the probabilistic model which yielded an optimized chronology along with posterior scenarios for the glaciological and climatic variables mentioned above.

However, it is possible to think the other way around and to use hypothetical and/or uncertain sources of chronological, glaciological and/or climatic information as input to the probabilistic model. By analyzing the magnitude of the adjustment performed by the model it is possible to evaluate the compatibility between the distinct sources of constraints. This inverse approach was employed in Chapter 4 for evaluating the (i) the consistency between the orbital dating methods based on different ice core records (total air content, $\delta^{15}\text{N}$ of N_2 , $\delta^{18}\text{O}_{\text{atm}}$ and $\delta\text{O}_2/\text{N}_2$) and (ii) the compatibility of the LID scenario yielded by the firn model at Dome C with the rest of the chronological information.

This multi-approach strategy was conducted in the framework of the EPICA community and of my respective research teams at LSCE and IGE. This helped me gain expertise on multi-proxy and multi-sites approaches for analyzing and interpreting ice core records through regular meetings and numerous discussions. My PhD monitoring committee was composed of A. Svensson (NBI, Univ. of Copenhagen) and M. Baroni (CEREGE, Univ. of Aix-Marseilles). Thanks to annual meetings and more frequent exchanges, they provide me with insights on the multi-proxy and multi-site approach as per their respective points of view: the volcanic signal in Greenland and Antarctic ice cores (A. Svensson) and the cosmogenic isotopes from Antarctic near-coastal sites (M. Baroni). By discussing with the wider Quaternary climate community at LSCE, during conferences (EGU 2022, INQUA 2023, EGU 2024) and workshops (e.g. the Quaternary interglacials, QUIGS, workshop in 2023), I received feedbacks on the multi-site chronology as well as advice for developing multi-archive chronologies that integrates both model and paleo data.

6.2 MAIN RESULTS

In this section are provided the main results of my PhD organized per Chapters.

6.2.1 Ameliorating paleoclimatic reconstruction

While water isotopes are classically used to infer past temperature and accumulation rate when measured in ice cores, we show that $\delta^{15}\text{N}$ of N_2 measured in air bubbles trapped in ice core can be used as a complementary tool. $\delta^{15}\text{N}$ indeed reflects the depth of bubble enclosure in the ice sheet, itself driven by surface temperature and snow accumulation rate at surface. A new record of $\delta^{15}\text{N}$ over the last 800 kyr is presented and provides an accurate identification of the lead-lag relationship between atmospheric CO_2 and Antarctic climate over deglaciations. The peak atmospheric CO_2 concentration is found to lag Antarctic climate change by

approximately 500 years at the end of Terminations I, II, III and V.

The local paleoclimate reconstruction inferred from $\delta^{15}\text{N}$ and from δD disagrees over glacial periods at maximum obliquity. Over these specific periods, the $\delta^{15}\text{N}$ -based temperature is higher than inferred from δD and the $\delta^{15}\text{N}$ -based snow accumulation rate is lower than inferred from δD . By confronting climate and firn modeling outputs to δD and $\delta^{15}\text{N}$ records, we show that these disagreements can be caused by obliquity-driven variations in East Antarctic climate during glacial periods, which affect differently the δD and $\delta^{15}\text{N}$ signals (notably via changes in precipitation intermittency). To reconstruct more accurately past climate, we use the scenarios inferred from δD records to drive the firn densification model to calculate $\delta^{15}\text{N}$. We then adjust the climatic scenarios so that they enable to reproduce the $\delta^{15}\text{N}$ record. This approach suggests higher temperature and lower snow accumulation rate than classical reconstructions in East Antarctica over glacial periods during obliquity maxima.

6.2.2 Ameliorating the precision of deep polar ice core chronology over the past 800 kyr

The new reference AICC2023 chronology is provided for the EDC ice core over the past 800 kyr. The average uncertainty is reduced from 1.7 to 0.9 kyr with respect to the former AICC2012 chronology. Significant shifts toward older ages are suggested with respect to AICC2012 over MISs 19 (+5 kyr), 17 (+3.8 kyr), 15 (+3.4 kyr) and 5 (+2.5 kyr). The duration of the TV-MIS 11c pair is shortened by ~3 kyr. We find that these modifications lead to a coherency improved by 1000 to 2000 years with independent absolute chronologies of other climate archives over MISs 19, 11 and 5 (Italian Lacustrine succession from Sulmona Basin, Dome Fuji ice core and northern Alpine speleothems).

The distinct orbital chronologies derived from EDC records of $\delta\text{O}_2/\text{N}_2$, total air content, and $\delta^{18}\text{O}_{\text{atm}}$ are consistent within their respective uncertainties except for three periods, including MISs 19 and 11. The new $\delta^{15}\text{N}$ measurements together with firn densification modeling experiments provide the most plausible evolution of the lock-in-depth at Dome C over the past 800 kyr.

For the majority of the past eight glacial Terminations, the new AICC2023 chronology suggests that EDC records of atmospheric CH_4 , δD and $\delta^{15}\text{N}$ start increasing when the boreal summer solstice insolation is also rising. Exceptions are the Terminations IX and VII (~805 and 630 ka BP) which are dated older as per AICC2023 than per AICC2012. In these cases, the EDC climatic records start increasing during the decreasing phase of the boreal summer insolation.

6.2.3 Developing a coherent, relative and absolute chronology for glacial and marine archives over the past 640 kyr

The resulting coherent chronology covers the seven most recent glacial Terminations. It

enabled a more accurate identification of the lead-lag relationships between the insolation forcing and the climatic responses, including changes in atmospheric CO₂ and sea level, across glacial Terminations than using independent chronologies. By fitting ramp functions to the deglacial rises observed in sea level proxy and atmospheric CO₂ content, we found a lead of a few kyr (from 1 to 5.5 kyr) of atmospheric CO₂ with respect to the sea level proxy in most of the glacial Terminations studied. One exception is the Termination VI, although the age error bar does not exclude a lead of the CO₂.

Indeed, we assessed the sensitivity of the coherent chronology to the methodology used. This provided us with robust error bars that can reach several thousand years so that the confidence interval of the temporal phasing between CO₂ and the sea level proxy ranges from 6 kyr to 25 kyr. This interval varies among Terminations depending on the uncertainty of the chronological constraints used to build the age model. The sources of uncertainty include the strong climatic hypotheses assumed to stratigraphically link the different paleo sites as well as the choice of discrete stratigraphic matching for connecting the sites which can be ambiguous or subjective. We emphasize the need for performing several tests similar to those described in our study to assess the sensitivity of the chronology (i) to the climatic assumptions that make the foundation of the synchronization strategy and (ii) to the synchronization method itself.

The lead-lag relationships identified in our study sometimes disagree (by more than 1 σ) with the timings estimated using independent and thus incomparable chronologies. This is the case for example for Terminations V and I. This result emphasizes the need for using a chronological framework that is coherent for all climatic records considered for identifying correct temporal sequence of events.

6.3 PERSPECTIVES

In this section are provided the perspectives of my PhD. They are grouped into two themes: (i) the perspectives for further research on orbital dating and climatic interpretation (Section 6.3.1), and (ii) the perspectives for future work based on multi-approach strategies (Section 6.3.2).

6.3.1 Orbital dating and climatic interpretation

On the need for new $\delta^{15}\text{N}$ measurements on the EDC and BE-OIC ice cores over the last two glacial periods

New high-resolution $\delta^{15}\text{N}$ measurements on the EDC ice core and upcoming Beyond EPICA-oldest ice core (BE-OI, which aims at retrieving 1.5 Myr of climatic records, <https://www.beyondepica.eu/en/>) would be of interest during past glacial periods, in particular over the two most recent ones. These new data could help investigating whether a $\delta^{15}\text{N}$ model-data decoupling analogous to what is described in Chapter 3 is also observed over the last glacial period. The classically assumed relationship between temperature and snow accumulation rate could be further examined. This will help to understand the drivers of local climatic variability, which might differ from glacial to interglacial conditions, and to refine East

Antarctic climate reconstructions.

New high-resolution measurements of $\delta^{15}\text{N}$ have already been collected on the EDC ice core between 800 and 600 ka BP by A.-M. Klussendorf since the beginning of her PhD (October 2023) at LSCE. The analysis of such data will improve the precision of the Δage estimate, essential for constraining ice core chronologies and accurately identifying lead-lag relationships between different ice core records. This is crucial for understanding climate variability. For example, it permits to identify the lead-lag relationship between D-O warmings and AIM, which characterizes the inter-hemispheric connections at play during past glacial periods (Section 4.3.1).

On the need for $\delta\text{O}_2/\text{N}_2$, $\delta^{18}\text{O}_{\text{atm}}$ and total air content measurements on the EDC and BE-OIC ice cores between 540 and 460 ka BP and prior to 600 ka BP

For the past 640 kyr, the AICC2023 chronology is partly based on the synchronization to the absolute U/Th age scale of Chinese speleothems. Therefore, it provides valuable insights for comparing the respective timings of changes in the external forcing of climate (e.g. insolation) and of the internal climatic response (e.g. changes in the GHGs concentration and in other EDC climate proxies) with respect to the former ice core chronology which was solely based on the orbital dating approach. However, we identified in Chapter 4 time periods where building the chronology is more complicated. An example is from 540 to 460 ka BP time interval, encompassing Termination VI, where the $\delta\text{O}_2/\text{N}_2$ and total air content-based chronologies disagree with that of $\delta^{18}\text{O}_{\text{atm}}$ (Fig. 7 of Section 4.1). In addition, the new $\delta\text{O}_2/\text{N}_2$ dataset presented in Chapter 4 significantly disagrees with the old dataset (Fig. 1 in Section 4.1). We call for the need for new high-resolution $\delta\text{O}_2/\text{N}_2$, total air content and $\delta^{18}\text{O}_{\text{atm}}$ data from the EDC and BE-OIC ice cores over the 540-460 ka BP period. These new data should be analyzed to investigate the mismatch between old and new $\delta\text{O}_2/\text{N}_2$ datasets and to ameliorate the ice core chronology over this period. This last point is all the more essential as an exceptional lag of atmospheric CO_2 with respect to the sea level proxy is found over the Termination VI in Chapter 5. The new data would permit to refine the coherent chronology developed in Chapter 5, thus permitting to assess whether this exceptional lag of CO_2 is an artefact of the uncertain chronology or not. Precise identification of lead-lag relationship is crucial for deciphering the complex relationships between global ice volume and atmospheric CO_2 during the particular TVI-MIS 13 interglacial sequence.

In Chapter 4, we also highlighted that building the ice core chronology is difficult prior to 600 ka BP, which corresponds to the lowermost section of the EDC ice core. We would like to draw attention to the requirement for new measurements on the EDC and BE-OIC ice cores over these periods. Firstly, no dated speleothem record can serve as a reference for the $\delta^{18}\text{O}_{\text{atm}}$ prior to 640 ka BP yet. In addition, the links between the variability in $\delta\text{O}_2/\text{N}_2$, $\delta^{18}\text{O}_{\text{atm}}$ and total air content records and their orbital targets are not obvious prior to 600 ka BP (Figures 1 and 5 in Section 4.1). This may be due to bad quality of the ice and/or diffusion of gases through the ice matrix (Bereiter et al., 2009). The imprecision of the signal may also be partially explained by the limited temporal resolution of the existing dataset in this deep section.

In the framework of their PhDs which started in October 2023 at IGE and LSCE, H. Guilluy and A.-M. Klussendorf are collecting high-resolution measurements of total air content and of $\delta\text{O}_2/\text{N}_2$ and $\delta^{18}\text{O}_{\text{atm}}$ on the EDC ice core between 800 and 600 ka BP. The new data that they are collecting should be analyzed for refining the orbital dating of the EDC ice core prior to 600 ka BP. In addition, new highly resolved $\delta\text{O}_2/\text{N}_2$, $\delta^{18}\text{O}_{\text{atm}}$ and total air content measurements should be performed on the BE-OIC ice core prior 600 ka BP.

These new data will be of particular interest as the chronology developed in Chapter 4 suggests unusual timings of the oldest Terminations recorded in EDC ice core (TIX-TVII) with respect to orbital changes. Indeed, the EDC records of local climate proxies ($\delta^{15}\text{N}$, δD) and of atmospheric CH_4 start increasing while the boreal summer insolation is decreasing. This is different from what is observed for recent Terminations (TVI-TI).

On the developing of dating tools

During her PhD supervised by A. Landais (LSCE) and P. Martinerie (IGE) and which started in October 2021, R. Harris-Stuart showed that both insolation and snow accumulation rates affect the $\delta\text{O}_2/\text{N}_2$ variability due to physical processes occurring within the firn column. Her findings could be considered for correcting the $\delta\text{O}_2/\text{N}_2$ from the accumulation-driven variability for ameliorating the precision of orbital dating of ice cores.

Finally, absolute dating constraints can be obtained from the measurements of $\delta^{40}\text{Ar}_{\text{atm}}$ in the air trapped in ice core because of the progressive radioactive decay of ^{40}K leading to ^{40}Ar outgassing in the atmosphere (Section 2.3.2.3). Because of the small increase in $\delta^{40}\text{Ar}_{\text{atm}}$ with time (0.066 ‰ / million of years), this method is useful for old periods and requires a very high analytical precision for the $\delta^{40}\text{Ar}_{\text{atm}}$ measurements. However, a relatively large uncertainty (0.02 ‰) is currently associated to the analytical measure of $\delta^{40}\text{Ar}_{\text{atm}}$ at LSCE and the measured signal can also be significantly affected by gas loss during ice storage (Landais et al., 2022). In addition, some studies noticed an anomalous enrichment of the measured $\delta^{40}\text{Ar}_{\text{atm}}$ in the deepest sections of the Greenland ice sheet (DYE3 in Bender et al., 2010; and GISP2 in Yau et al., 2016) and of the Antarctic ice sheet (EDC, TALDICE, Vostok; A. Landais and A. Orsi).

After my PhD, I will work eight months at the LSCE in the framework of the ERC ICORDA project coordinated by A. Landais (<https://cordis.europa.eu/project/id/817493>). I will perform and analyze $\delta^{40}\text{Ar}_{\text{atm}}$ measurements on the basal ice from Greenland ice cores (NEEM, DYE 3) and from Antarctic ice cores (SkyTrain, EDC and Vostok). The aim is to improve the precision of the measurements and to investigate the reasons of the excess Argon found in deeper part of the ice sheets. The ages that will be derived from $\delta^{40}\text{Ar}_{\text{atm}}$ measurements on the Skytrain ice samples could be compared to the three ^{81}Kr -ages inferred from the samples that I measured during my PhD (Section 2.2.5.2, Table 6.1).

Table 6.1 ^{81}Kr ages of the three Skytrain samples (A, B and C) measured during my PhD.

Sample No.	Start depth (m)	Stop depth (m)	^{81}Kr age (ka BP)	Error + (kr)	Error – (kyr)	Error (^{81}Kr half-life) (kyr)
A	634.8	637.99	189	31	30	9
B	638.54	642.28	273	39	36	13
C	643.99	647.21	408	34	28	20

6.3.2 On further use of the multi-approach strategy

In this section, we emphasize the need for combining multiple approaches to ameliorate climatic reconstructions as well as chronologies, which is crucial for understanding climate variability and predict future climate change.

Improving paleoclimate reconstruction and coherent chronologies

We insist on the need for combining multiple proxies and approaches such as what we did in Chapter 3 with combination of climate modeling, water stables isotopes data as well as firn modeling and $\delta^{15}\text{N}$ data, to refine East Antarctic climate reconstructions. Such methodology could be systematically applied to East Antarctic sites, such as the upcoming BE-OI ice core for obtaining a precise reconstruction of orbital-scale variability of local climate over the past million years.

An important aspect would be to further extend the polar ice core chronology presented in Chapter 4 by implementing other ice cores such as Dome F, WAIS Divide and NEEM (North Greenland Eemian), for which a large amount of chronological and glaciological information is now available. A wider perspective would be to integrate additional marine sites to the coherent chronology presented in Chapter 5 for increasing the representativeness of the paleorecords considered for detecting deglacial climate change. More specifically, suggestions are given for integrating the IODP U1537 and the ODP 1090 marine cores to the chronology.

Understanding climate tracers and climatic mechanisms

Using Bayesian dating tools allows to confront different source of information and determine whether they are compatible with each other. For example, we could confront the various potential dating methodologies based on $\delta^{18}\text{O}_{\text{atm}}$ to other sources of chronological information (glaciological modeling, $\delta\text{O}_2/\text{N}_2$, total air content, ^{81}Kr and $\delta^{15}\text{N}$) in various ice core dating experiments with the Paleochrono-1.1 model. These tests would designate the most adapted synchronization target for the $\delta^{18}\text{O}_{\text{atm}}$ (e.g. among the precession, the delayed precession, IRD events, ...). Such study would be useful for understanding the $\delta^{18}\text{O}_{\text{atm}}$ variability.

Using Bayesian dating tools also enables to emancipate the chronology from strong climatic

assumptions made for establishing chronologies based on a single approach. The more a chronology is constrained by various proxies, sites, archives and approaches, the more it is suited for testing climatic assumptions. For example, our multi-approach methodology permits to elucidate with more confidence whether the bipolar seesaw feature can be traced in Antarctic ice core records during glacial intervals prior to the last glacial period. Using the Δ age estimate yielded by AICC2023 with reduced uncertainties (450 years on average), we show that over the penultimate glacial period, several AIM do not match D-O warmings detected in CH₄. This preliminary observation disagrees with the hypothesis of a bipolar seesaw feature persisting beyond the last glacial period. To reinforce this observation, new CH₄ measurements at higher resolution in the EDC ice core will be performed by H. Guilluy at IGE over this period (MIS 6).

Improving the relationship between external forcing and climatic response

The combined analyses of global climatic tracers (e.g. atmospheric CO₂, sea level, productivity), regional climate proxies (e.g. temperature, precipitation, ice sheet extent) as well as of climate modeling experiments are needed. For example, I co-authored a model-data study led by Legrain et al. (submitted to *Nature Geosciences*; Appendix 7.5) in which are identified significant releases of carbon dioxide during deglaciation, glacial periods and interglacial contexts over the past 500 kyr. New simulations show that the continental biosphere and the Southern Ocean are the main carbon sources during these significant releases that are connected to Heinrich events in the Northern Hemisphere. Such studies help investigating the role of external forcing (e.g. variations in the Earth's orbital parameters) on the relationships between atmospheric CO₂ concentration and Antarctic climate. Notably, Legrain et al. demonstrated that the continental biosphere is the obliquity-dependent CO₂ source for these rapid events. For the first time, the long-term external forcing is shown to directly impact past centennial-scale atmospheric CO₂ variations. A similar methodology could be employed to study the obliquity influence on the CO₂ over the glacial inceptions from MIS 7e to MIS 7d and from 5e to 5d. Indeed, in Section 3.4.1, we highlighted two gradual declines in atmospheric CO₂ and EDC $\delta^{15}\text{N}$ record which contrast with the more abrupt decreases observed in the EDC record of δD at ~245 and 130 ka BP (Fig. 3.2 in Section 3.4.1). These two periods correspond to relatively important obliquity decrease which could explain the $\delta^{15}\text{N}$ - δD mismatch (see Chapter 3). We believe further study is needed for investigating the influence of obliquity on atmospheric CO₂ over these cooling intervals.

For developing and testing a climate modeling protocol

Finally, the new AICC2023 chronology suggests to shorten the length of the TV-MIS 11c sequence. The necessity to develop a coordinated modeling protocol over this specific time period was raised at the workshop of the Quaternary Interglacial working group in September 2023. To this extent, the group agreed on the importance of developing a coherent temporal framework for the rate of sea-level rise, and for various paleoclimate proxies representative of different parts of the Earth System across TV. We present a first step towards the building of a coherent chronology for marine archives and glacial archives in Chapter 5. Such coherent

temporal framework for sea level and CO₂ changes could be used to drive climate models. These climate simulations could in turn help:

- (i) evaluating the climate model performances by confronting the simulated climate to paleo data,
- (ii) and understanding climatic mechanisms at play during glacial Terminations, which can be considered as analogue to the ongoing global warming, and during past interglacials, which are possible analogue to a future warmer world.

6.4 OPENING

The combination of coherent chronologies built over the last 800 thousand years with accurate Antarctic climate reconstruction enables a better understanding of the complex interactions between the internal components of the Earth system in response to external perturbation. It also provides tools to assess climate models and to estimate the climate sensitivity to radiative forcing and its potential variability through time. A better understanding of past climate response to external and internal radiative forcing is imperative for accurately predicting future climate and undertaking the adaptation of our societies to the ongoing and future climate change.

Although the impact of abrupt past climate change on ancient human societies is an ongoing debate, the combination of natural and archeological records shows that important climatic crises highlighted the vulnerability of human societies and questioned their adaptability (Finné et al., 2017; Hazell et al., 2022).

REFERENCES

- Abe-Ouchi, A., Saito, F., Kawamura, K., Raymo, M. E., Okuno, J., Takahashi, K., & Blatter, H. (2013). Insolation-driven 100,000-year glacial cycles and hysteresis of ice-sheet volume. *Nature*, *500*(7461), 190–193. <https://doi.org/10.1038/nature12374>
- Adolphi, F., Bronk Ramsey, C., Erhardt, T., Lawrence Edwards, R., Cheng, H., Turney, C. S. M., Cooper, A., Svensson, A., Rasmussen, S. O., Fischer, H., & Muscheler, R. (2018). Connecting the Greenland ice-core and U/Th timescales via cosmogenic radionuclides: Testing the synchronicity of Dansgaard-Oeschger events. *Climate of the Past*, *14*(11), 1755–1781. <https://doi.org/10.5194/CP-14-1755-2018>
- Ahn, J., Brook, E. J., Schmittner, A., & Kreutz, K. (2012). Abrupt change in atmospheric CO₂ during the last ice age. *Geophysical Research Letters*, *39*(18). <https://doi.org/https://doi.org/10.1029/2012GL053018>
- Ai, X. E., Studer, A. S., Sigman, D. M., Martínez-García, A., Fripiat, F., Thöle, L. M., Michel, E., Gottschalk, J., Arnold, L., Moretti, S., Schmitt, M., Oleynik, S., Jaccard, S. L., & Haug, G. H. (2020). Southern Ocean upwelling, Earth's obliquity, and glacial-interglacial atmospheric CO₂ change. *Science*, *370*(6522), 1348–1352. <https://doi.org/10.1126/science.abd2115>
- Alley, R. B. (1987). FIRN DENSIFICATION BY GRAIN-BOUNDARY SLIDING: A FIRST MODEL. *Le Journal de Physique Colloques*, *48*(C1), C1-249. <https://doi.org/10.1051/JPHYSCOL:1987135>
- Andersen, K. K., Azuma, N., Barnola, J. M., Bigler, M., Biscaye, P., Caillon, N., Chappellaz, J., Clausen, H. B., Dahl-Jensen, D., Fischer, H., Flückiger, J., Fritzsche, D., Fujii, Y., Goto-Azuma, K., Grønvold, K., Gundestrup, N. S., Hansson, M., Huber, C., Hvidberg, C. S., ... White, J. W. C. (2004). High-resolution record of Northern Hemisphere climate extending into the last interglacial period. *Nature*, *431*(7005), 147–151. <https://doi.org/10.1038/NATURE02805>
- Andersen, K. K., Svensson, A., Johnsen, S. J., Rasmussen, S. O., Bigler, M., Röthlisberger, R., Ruth, U., Siggaard-Andersen, M.-L., Peder Steffensen, J., Dahl-Jensen, D., Vinther, B. M., & Clausen, H. B. (2006). The Greenland Ice Core Chronology 2005, 15–42ka. Part 1: constructing the time scale. *Quaternary Science Reviews*, *25*(23), 3246–3257. <https://doi.org/https://doi.org/10.1016/j.quascirev.2006.08.002>
- Anderson, D. L., & Benson, C. S. (1963). The densification and diagenesis of snow. In *Ice and snow: properties, processes and applications* (pp. 391–411). MIT Press Cambridge.
- Arnaud, L., Barnola, J. M., & Duval, P. (2000). *Physical modeling of the densification of snow/firn and ice III the upper part of polar ice sheets*.
- Arthern, R. J., Vaughan, D. G., Rankin, A. M., Mulvaney, R., & Thomas, E. R. (2010). In situ measurements of Antarctic snow compaction compared with predictions of models. *Journal of Geophysical Research: Earth Surface*, *115*(F3), 3011. <https://doi.org/10.1029/2009JF001306>

- Arzt, E. (1982). The influence of an increasing particle coordination on the densification of spherical powders. *Acta Metallurgica*, 30(10), 1883–1890. [https://doi.org/10.1016/0001-6160\(82\)90028-1](https://doi.org/10.1016/0001-6160(82)90028-1)
- Ashby, M. F. (1974). A first report on sintering diagrams. *Acta Metallurgica*, 22(3), 275–289. [https://doi.org/10.1016/0001-6160\(74\)90167-9](https://doi.org/10.1016/0001-6160(74)90167-9)
- Augustin, L., Barbante, C., Barnes, P. R. F., Barnola, J. M., Bigler, M., Castellano, E., Cattani, O., Chappellaz, J., Dahl-Jensen, D., Delmonte, B., Dreyfus, G., Durand, G., Falourd, S., Fischer, H., Flückiger, J., Hansson, M. E., Huybrechts, P., Jugie, G., Johnsen, S. J., ... Zucchelli, M. (2004). Eight glacial cycles from an Antarctic ice core. *Nature* 2004 429:6992, 429(6992), 623–628. <https://doi.org/10.1038/nature02599>
- Barker, S. (2021). *Planktic foraminiferal and Ice Rafted Debris (IRD) counts from ODP Site 983*. <https://doi.pangaea.de/10.1594/PANGAEA.929721>
- Barker, S., Diz, P., Vautravers, M. J., Pike, J., Knorr, G., Hall, I. R., & Broecker, W. S. (2009). Interhemispheric Atlantic seesaw response during the last deglaciation. *Nature*, 457(7233), 1097–1102. <https://doi.org/10.1038/nature07770>
- Barker, S., Knorr, G., Conn, S., Lordsmith, S., Newman, D., & Thornalley, D. (2019). Early Interglacial Legacy of Deglacial Climate Instability. *Paleoceanography and Paleoclimatology*, 34(8), 1455–1475. <https://doi.org/10.1029/2019PA003661>
- Barker, S., Knorr, G., Edwards, R. L., Parrenin, F., Putnam, A. E., Skinner, L. C., Wolff, E., & Ziegler, M. (2011). 800,000 Years of abrupt climate variability. *Science*, 334(6054), 347–351. https://doi.org/10.1126/SCIENCE.1203580/SUPPL_FILE/BARKER.SOM.PDF
- Barker, S., Starr, A., van der Lubbe, J., Doughty, A., Knorr, G., Conn, S., Lordsmith, S., Owen, L., Nederbragt, A., Hemming, S., Hall, I., & Levay, L. (2022). Persistent influence of precession on northern ice sheet variability since the early Pleistocene. *Science*, 376(6596). https://doi.org/10.1126/SCIENCE.ABM4033/SUPPL_FILE/SCIENCE.ABM4033_MATLAB_FILES.ZIP
- Barnes, P., Tabor, D., & Walker, J. C. F. (1971). The friction and creep of polycrystalline ice. *Proceedings of the Royal Society of London. A. Mathematical and Physical Sciences*, 324(1557), 127–155. <https://doi.org/10.1098/RSPA.1971.0132>
- Barnola, J. -M, Pimienta, P., Raynaud, D., & Korotkevich, Y. S. (1991). CO₂-climate relationship as deduced from the Vostok ice core: a re-examination based on new measurements and on a re-evaluation of the air dating. *Tellus B*, 43(2), 83–90. <https://doi.org/10.1034/J.1600-0889.1991.T01-1-00002.X>
- Barnola, J. M., Raynaud, D., Korotkevich, Y. S., & Lorius, C. (1987). Vostok ice core provides 160,000-year record of atmospheric CO₂. *Nature* 1987 329:6138, 329(6138), 408–414. <https://doi.org/10.1038/329408a0>
- Batchelor, C. L., Margold, M., Krapp, M., Murton, D. K., Dalton, A. S., Gibbard, P. L., Stokes, C. R., Murton, J. B., & Manica, A. (2019). The configuration of Northern Hemisphere ice sheets

- through the Quaternary. *Nature Communications* 2019 10:1, 10(1), 1–10. <https://doi.org/10.1038/s41467-019-11601-2>
- Battle, M., Bender, M., Sowers, T., Tans, P. P., Butler, J. H., Elkins, J. W., Ellis, J. T., Conway, T., Zhang, N., Lang, P., & Clarke, A. D. (1996). Atmospheric gas concentrations over the past century measured in air from firn at the South Pole. *Nature* 1996 383:6597, 383(6597), 231–235. <https://doi.org/10.1038/383231a0>
- Baumgartner, M., Kindler, P., Eicher, O., Floch, G., Schilt, A., Schwander, J., Spahni, R., Capron, E., Chappellaz, J., Leuenberger, M., Fischer, H., & Stocker, T. F. (2014). NGRIP CH₄ concentration from 120 to 10 kyr before present and its relation to a $\delta^{15}\text{N}$ temperature reconstruction from the same ice core. *Climate of the Past*, 10(2), 903–920. <https://doi.org/10.5194/CP-10-903-2014>
- Bauska, T. K., Marcott, S. A., & Brook, E. J. (2021). Abrupt changes in the global carbon cycle during the last glacial period. *Nature Geoscience*, 14(2), 91–96. <https://doi.org/10.1038/s41561-020-00680-2>
- Bazin, L., Landais, A., Capron, E., Masson-Delmotte, V., Ritz, C., Picard, G., Jouzel, J., Dumont, M., Leuenberger, M., & Prié, F. (2016). Phase relationships between orbital forcing and the composition of air trapped in Antarctic ice cores. *Clim. Past*, 12, 729–748. <https://doi.org/10.5194/cp-12-729-2016>
- Bazin, L., Landais, A., Lemieux-Dudon, B., Toyé Mahamadou Kele, H., Veres, D., Parrenin, F., Martinerie, P., Ritz, C., Capron, E., Lipenkov, V., Loutre, M.-F., Raynaud, D., Vinther, B., Svensson, A., Rasmussen, S. O., Severi, M., Blunier, T., Leuenberger, M., Fischer, H., ... Wolff, E. (2013). An optimized multi-proxy, multi-site Antarctic ice and gas orbital chronology (AICC2012): 120–800 ka. *Climate of the Past*, 9(4), 1715–1731. <https://doi.org/10.5194/cp-9-1715-2013>
- Becagli, S., Proposito, M., Benassai, S., Flora, O., Genoni, L., Gragnani, R., Largiuni, O., Pili, S. L., Severi, M., Stenni, B., Traversi, R., Udisti, R., & Frezzotti, M. (2004). Chemical and isotopic snow variability in East Antarctica along the 2001/02 ITASE traverse. *Annals of Glaciology*, 39, 473–482. <https://doi.org/10.3189/172756404781814636>
- Bender, M. L. (2002). Orbital tuning chronology for the Vostok climate record supported by trapped gas composition. *Earth and Planetary Science Letters*, 204(1–2), 275–289. [https://doi.org/10.1016/S0012-821X\(02\)00980-9](https://doi.org/10.1016/S0012-821X(02)00980-9)
- Bender, M. L., Barnett, B., Dreyfus, G., Jouzel, J., & Porcelli, D. (2008). The contemporary degassing rate of ⁴⁰Ar from the solid Earth. *Proceedings of the National Academy of Sciences*, 105(24), 8232–8237. <https://doi.org/10.1073/PNAS.0711679105>
- Bender, M. L., Burgess, E., Alley, R. B., Barnett, B., & Clow, G. D. (2010). On the nature of the dirty ice at the bottom of the GISP2 ice core. *Earth and Planetary Science Letters*, 299(3–4), 466–473. <https://doi.org/10.1016/J.EPSL.2010.09.033>
- Bender, M., Sowers, T., & Labeyrie, L. (1994). The Dole Effect and its variations during the last 130,000 years as measured in the Vostok Ice Core. *Global Biogeochemical Cycles*, 8(3),

363–376. <https://doi.org/10.1029/94GB00724>

- Bereiter, B., Eggleston, S., Schmitt, J., Nehrbass-Ahles, C., Stocker, T. F., Fischer, H., Kipfstuhl, S., & Chappellaz, J. (2015). Revision of the EPICA Dome C CO₂ record from 800 to 600-kyr before present. *Geophysical Research Letters*, *42*(2), 542–549. <https://doi.org/10.1002/2014GL061957>
- Bereiter, B., Schwander, J., Lüthi, D., & Stocker, T. F. (2009). Change in CO₂ concentration and O₂/N₂ ratio in ice cores due to molecular diffusion. *Geophysical Research Letters*, *36*(5). <https://doi.org/10.1029/2008GL036737>
- Berends, C. J., Köhler, P., Lourens, L. J., & van de Wal, R. S. W. (2021). On the Cause of the Mid-Pleistocene Transition. *Reviews of Geophysics*, *59*(2), e2020RG000727. <https://doi.org/https://doi.org/10.1029/2020RG000727>
- Berger, A. (1980). The Milankovitch astronomical theory of paleoclimates: A modern review. *Vistas in Astronomy*, *24*(PART 2), 103–122. [https://doi.org/10.1016/0083-6656\(80\)90026-4](https://doi.org/10.1016/0083-6656(80)90026-4)
- Berger, André L. (1978). Long-term variations of caloric insolation resulting from the earth's orbital elements. *Quaternary Research*, *9*(2), 139–167. [https://doi.org/https://doi.org/10.1016/0033-5894\(78\)90064-9](https://doi.org/https://doi.org/10.1016/0033-5894(78)90064-9)
- Bergeron, T. (1935). On the physics of clouds and precipitation. *Proc. 5th Assembly UGGI*.
- Bintanja, R., Van De Wal, R. S. W., & Oerlemans, J. (2005). Modelled atmospheric temperatures and global sea levels over the past million years. *Nature*, *437*(7055), 125–128. <https://doi.org/10.1038/NATURE03975>
- Birner, B., Hodell, D. A., Tzedakis, P. C., & Skinner, L. C. (2016). Similar millennial climate variability on the Iberian margin during two early Pleistocene glacials and MIS 3. *Paleoceanography*, *31*(1), 203–217. <https://doi.org/https://doi.org/10.1002/2015PA002868>
- Blackford, J. R. (2007). Sintering and microstructure of ice: a review. *Journal of Physics D: Applied Physics*, *40*(21), R355. <https://doi.org/10.1088/0022-3727/40/21/R02>
- Blunier, T., Barnett, B., Bender, M. L., & Hendricks, M. B. (2002). Biological oxygen productivity during the last 60,000 years from triple oxygen isotope measurements. *Global Biogeochemical Cycles*, *16*(3), 3-1-3–13. <https://doi.org/https://doi.org/10.1029/2001GB001460>
- Blunier, T., & Brook, E. J. (2001). Timing of millennial-scale climate change in Antarctica and Greenland during the last glacial period. *Science (New York, N.Y.)*, *291*(5501), 109–112. <https://doi.org/10.1126/SCIENCE.291.5501.109>
- Bohm, E., Lippold, J., Gutjahr, M., Frank, M., Blaser, P., Antz, B., Fohlmeister, J., Frank, N., Andersen, M. B., & Deininger, M. (2014). Strong and deep Atlantic meridional overturning circulation during the last glacial cycle. *Nature* *2014* *517*:7532, *517*(7532), 73–76. <https://doi.org/10.1038/nature14059>

- Bond, G. C., & Lotti, R. (1995). Iceberg Discharges into the North Atlantic on Millennial Time Scales During the Last Glaciation. *Science*, 267(5200), 1005–1010. <https://doi.org/10.1126/science.267.5200.1005>
- Bouchet, M., Donner, A., Grimmer, M., Jasper, C., Krauss, F., Legrain, E., & Vera Polo, P. (2024). The atypical interglacial of MIS 11c and the long-term change in interglacial intensity over the past 800 kyr. *Past Global Changes Magazine*, 32(1), 55–55. <https://doi.org/10.22498/PAGES.32.1.55>
- Bouchet, M., Grisart, A., Landais, A., Prié, F., Jacob, R., & Fourré, E. (2023a). $\delta^{18}O$ of O_2 from EPICA Dome C ice core (Antarctica) (0–800 ka). PANGAEA. <https://doi.org/10.1594/PANGAEA.961024>
- Bouchet, M., Grisart, A., Landais, A., Prié, F., Jacob, R., & Fourré, E. (2023b). $\delta^{18}O/N_2$ from EPICA Dome C ice core (Antarctica) (0–800 ka). <https://doi.org/10.1594/PANGAEA.961025>
- Bouchet, M., Landais, A., Grisart, A., Parrenin, F., Prié, F., Jacob, R., Fourré, E., Capron, E., Raynaud, D., Lipenkov, V. Y., Loutre, M. F., Extier, T., Svensson, A., Legrain, E., Martinerie, P., Leuenberger, M., Jiang, W., Ritterbusch, F., Lu, Z. T., & Yang, G. M. (2023). The Antarctic Ice Core Chronology 2023 (AICC2023) chronological framework and associated timescale for the European Project for Ice Coring in Antarctica (EPICA) Dome C ice core. *Climate of the Past*, 19(11), 2257–2286. <https://doi.org/10.5194/CP-19-2257-2023>
- Bouchet, M., Landais, A., & Parrenin, F. (2023). Dive into the timescales of deep ice cores. *Past Global Changes Magazine*, 31(2), 104–105. <https://doi.org/10.22498/PAGES.31.2.104>
- Bouttes, N., Roche, D. M., & Paillard, D. (2012). Systematic study of the impact of fresh water fluxes on the glacial carbon cycle. *Climate of the Past*, 8(2), 589–607. <https://doi.org/10.5194/cp-8-589-2012>
- Boyle, E. A. (2000). Is ocean thermohaline circulation linked to abrupt stadial/interstadial transitions? *Quaternary Science Reviews*, 19(1), 255–272. [https://doi.org/https://doi.org/10.1016/S0277-3791\(99\)00065-7](https://doi.org/https://doi.org/10.1016/S0277-3791(99)00065-7)
- Bréant, C. (2017). *Variabilité régionale de la densification de la neige polaire lors des grandes transitions climatiques*.
- Bréant, C., Landais, A., Orsi, A., Martinerie, P., Extier, T., Prié, F., Stenni, B., Jouzel, J., Masson-Delmotte, V., & Leuenberger, M. (2019). Unveiling the anatomy of Termination 3 using water and air isotopes in the Dome C ice core, East Antarctica. *Quaternary Science Reviews*, 211, 156–165. <https://doi.org/10.1016/J.QUASCIREV.2019.03.025>
- Bréant, C., Martinerie, P., Orsi, A., Arnaud, L., & Landais, A. (2017). Modelling firn thickness evolution during the last deglaciation: constraints on sensitivity to temperature and impurities. *Climate of the Past*, 13(7), 833–853. <https://doi.org/10.5194/cp-13-833-2017>
- Broecker, W. S. (1997). Thermohaline Circulation, the Achilles Heel of Our Climate System: Will Man-Made CO_2 Upset the Current Balance? *Science*, 278(5343), 1582–1588. <https://doi.org/10.1126/science.278.5343.1582>

- Broecker, W. S., Clark, E., McCorkle, D. C., Peng, T.-H., Hajdas, I., & Bonani, G. (1999). Evidence for a reduction in the carbonate ion content of the deep sea during the course of the Holocene. *Paleoceanography*, *14*(6), 744–752. <https://doi.org/https://doi.org/10.1029/1999PA900038>
- Broecker, W. S., & Denton, G. H. (1989). The role of ocean-atmosphere reorganizations in glacial cycles. *Geochimica et Cosmochimica Acta*, *53*(10), 2465–2501. [https://doi.org/https://doi.org/10.1016/0016-7037\(89\)90123-3](https://doi.org/https://doi.org/10.1016/0016-7037(89)90123-3)
- Broecker, W. S., & Henderson, G. M. (1998). The sequence of events surrounding Termination II and their implications for the cause of glacial-interglacial CO₂ changes. *Paleoceanography*, *13*(4), 352–364. <https://doi.org/10.1029/98PA00920>
- Buizert, C. (2021). The Ice Core Gas Age-Ice Age Difference as a Proxy for Surface Temperature. *Geophysical Research Letters*, *48*(20), e2021GL094241. <https://doi.org/10.1029/2021GL094241>
- Buizert, C. (2023). The thermal bipolar seesaw during abrupt climate change. In *Reference Module in Earth Systems and Environmental Sciences*. Elsevier. <https://doi.org/https://doi.org/10.1016/B978-0-323-99931-1.00119-7>
- Buizert, C., Adrian, B., Ahn, J., Albert, M., Alley, R. B., Baggenstos, D., Bauska, T. K., Bay, R. C., Bencivengo, B. B., Bentley, C. R., Brook, E. J., Chellman, N. J., Clow, G. D., Cole-Dai, J., Conway, H., Cravens, E., Cuffey, K. M., Dunbar, N. W., Edwards, J. S., ... Members, W. D. P. (2015). Precise inter-polar phasing of abrupt climate change during the last ice age. *Nature*, *520*(7549), 661–665. <https://doi.org/10.1038/nature14401>
- Buizert, C., Baggenstos, D., Jiang, W., Purtschert, R., Petrenko, V. V., Lu, Z. T., Müller, P., Kuhl, T., Lee, J., Severinghaus, J. P., & Brook, E. J. (2014). Radiometric ⁸¹Kr dating identifies 120,000-year-old ice at Taylor Glacier, Antarctica. *Proceedings of the National Academy of Sciences of the United States of America*, *111*(19), 6876–6881. https://doi.org/10.1073/PNAS.1320329111/SUPPL_FILE/PNAS.1320329111.SD01.XLS
- Buizert, C., Cuffey, K. M., Severinghaus, J. P., Baggenstos, D., Fudge, T. J., Steig, E. J., Markle, B. R., Winstrup, M., Rhodes, R. H., Brook, E. J., Sowers, T. A., Clow, G. D., Cheng, H., Edwards, R. L., Sigl, M., McConnell, J. R., & Taylor, K. C. (2015). The WAIS Divide deep ice core WD2014 chronology – Part 1: Methane synchronization (68–31 ka BP) and the gas age-ice age difference. *Climate of the Past*, *11*(2), 153–173. <https://doi.org/10.5194/CP-11-153-2015>
- Buizert, C., Fudge, T. J., Roberts, W. H. G., Steig, E. J., Sherriff-Tadano, S., Ritz, C., Lefebvre, E., Edwards, J., Kawamura, K., Oyabu, I., Motoyama, H., Kahle, E. C., Jones, T. R., Abe-Ouchi, A., Obase, T., Martin, C., Corr, H., Severinghaus, J. P., Beaudette, R., ... Schwander, J. (2021). Antarctic surface temperature and elevation during the Last Glacial Maximum. *Science*, *372*(6546), 1097–1101. <https://doi.org/10.1126/SCIENCE.ABD2897>
- Buizert, C., Sigl, M., Severi, M., Markle, B. R., Wettstein, J. J., McConnell, J. R., Pedro, J. B., Sodemann, H., Goto-Azuma, K., Kawamura, K., Fujita, S., Motoyama, H., Hirabayashi, M., Uemura, R., Stenni, B., Parrenin, F., He, F., Fudge, T. J., & Steig, E. J. (2018). Abrupt ice-age

- shifts in southern westerly winds and Antarctic climate forced from the north. *Nature* 2018 563:7733, 563(7733), 681–685. <https://doi.org/10.1038/s41586-018-0727-5>
- Caillon, N., Jouzel, J., Severinghaus, J. P., Chappellaz, J., & Blunier, T. (2003). A novel method to study the phase relationship between Antarctic and Greenland climate. *Geophysical Research Letters*, 30(17). <https://doi.org/10.1029/2003GL017838>
- Caillon, N., Severinghaus, J. P., Barnola, J.-M., Chappellaz, J., Jouzel, J., & Parrenin, F. (2001). Estimation of temperature change and of gas age-ice age difference, 108 kyr B.P., at Vostok, Antarctica. *Journal of Geophysical Research: Atmospheres*, 106(D23), 31893–31901. <https://doi.org/https://doi.org/10.1029/2001JD900145>
- Calder, N. (1974). Arithmetic of ice ages. *Nature* 1974 252:5480, 252(5480), 216–218. <https://doi.org/10.1038/252216a0>
- Capron, E. (2010). *L'air piégé dans les glaces polaires: contraintes chronologiques et caractérisation de la variabilité climatique rapide*. <http://www.theses.fr/2010VERS0064>
- Capron, E., Govin, A., Stone, E. J., Masson-Delmotte, V., Mulitza, S., Otto-Bliesner, B., Rasmussen, T. L., Sime, L. C., Waelbroeck, C., & Wolff, E. W. (2014). Temporal and spatial structure of multi-millennial temperature changes at high latitudes during the Last Interglacial. *Quaternary Science Reviews*, 103, 116–133. <https://doi.org/10.1016/J.QUASCIREV.2014.08.018>
- Capron, E., Landais, A., Buiron, D., Cauquoin, A., Chappellaz, J., Debret, M., Jouzel, J., Leuenberger, M., Martinerie, P., Masson-Delmotte, V., Mulvaney, R., Parrenin, F., & Prié, F. (2013). Glacial-interglacial dynamics of Antarctic firn columns: Comparison between simulations and ice core air- $\delta^{15}\text{N}$ measurements. *Climate of the Past*, 9(3), 983–999. <https://doi.org/10.5194/CP-9-983-2013>
- Capron, E., Landais, A., Chappellaz, J., Schilt, A., Buiron, D., Dahl-Jensen, D., Johnsen, S. J., Jouzel, J., Lemieux-Dudon, B., Loulergue, L., Leuenberger, M., Masson-Delmotte, V., Meyer, H., Oerter, H., & Stenni, B. (2010). Millennial and sub-millennial scale climatic variations recorded in polar ice cores over the last glacial period. *Climate of the Past*, 6(3), 345–365. <https://doi.org/10.5194/CP-6-345-2010>
- Carroll, L., & Tenniel, J. (1871). *Through the Looking-Glass*. Macmillan.
- Casado, M., Hébert, R., Faranda, D., & Landais, A. (2023). The quandary of detecting the signature of climate change in Antarctica. *Nature Climate Change*, 13(10), 1082–1088. <https://doi.org/10.1038/s41558-023-01791-5>
- Casado, M., Landais, A., Picard, G., Münch, T., Laepple, T., Stenni, B., Dreossi, G., Ekaykin, A., Arnaud, L., Genthon, C., Touzeau, A., Masson-Delmotte, V., & Jouzel, J. (2018). Archival processes of the water stable isotope signal in East Antarctic ice cores. *Cryosphere*, 12(5), 1745–1766. <https://doi.org/10.5194/TC-12-1745-2018>
- Casado, M., Münch, T., & Laepple, T. (2020). Climatic information archived in ice cores: impact of intermittency and diffusion on the recorded isotopic signal in Antarctica. *Climate of the*

Past, 16(4), 1581–1598. <https://doi.org/10.5194/cp-16-1581-2020>

- Cauquoin, A., Landais, A., Raisbeck, G. M., Jouzel, J., Bazin, L., Kageyama, M., Peterschmitt, J. Y., Werner, M., Bard, E., & Team, A. (2015). Comparing past accumulation rate reconstructions in East Antarctic ice cores using ^{10}Be , water isotopes and CMIP5-PMIP3 models. *Climate of the Past*, 11(3), 355–367. <https://doi.org/10.5194/CP-11-355-2015>
- Cheng, H., Edwards, R. L., Broecker, W. S., Denton, G. H., Kong, X., Wang, Y., Zhang, R., & Wang, X. (2009). Ice age terminations. *Science*, 326(5950), 248–252. https://doi.org/10.1126/SCIENCE.1177840/SUPPL_FILE/CHENG-SOM.PDF
- Cheng, H., Edwards, R. L., Sinha, A., Spötl, C., Yi, L., Chen, S., Kelly, M., Kathayat, G., Wang, X., Li, X., Kong, X., Wang, Y., Ning, Y., & Zhang, H. (2016). The Asian monsoon over the past 640,000 years and ice age terminations. *Nature* 2016 534:7609, 534(7609), 640–646. <https://doi.org/10.1038/nature18591>
- Cheng, H., Edwards, R. L., Wang, Y., Kong, X., Ming, Y., Kelly, M. J., Wang, X., Gallup, C. D., & Liu, W. (2006). A penultimate glacial monsoon record from Hulu Cave and two-phase glacial terminations. *Geology*, 34(3), 217–220. <https://doi.org/10.1130/G22289.1>
- Cheng, H., Lawrence Edwards, R., Southon, J., Matsumoto, K., Feinberg, J. M., Sinha, A., Zhou, W., Li, H., Li, X., Xu, Y., Chen, S., Tan, M., Wang, Q., Wang, Y., & Ning, Y. (2018). Atmospheric $^{14}\text{C}/^{12}\text{C}$ changes during the last glacial period from hulu cave. *Science*, 362(6420), 1293–1297. https://doi.org/10.1126/SCIENCE.AAU0747/SUPPL_FILE/AAU0747_TABLE_S2.XLSX
- Cheng, H., Sinha, A., Wang, X., Cruz, F. W., & Edwards, R. L. (2012). The Global Paleomonsoon as seen through speleothem records from Asia and the Americas. *Climate Dynamics* 2012 39:5, 39(5), 1045–1062. <https://doi.org/10.1007/S00382-012-1363-7>
- Chiang, J. C. H., Biasutti, M., & Battisti, D. S. (2003). Sensitivity of the Atlantic Intertropical Convergence Zone to Last Glacial Maximum boundary conditions. *Paleoceanography*, 18(4). <https://doi.org/10.1029/2003PA000916>
- Chowdhry Beeman, J., Gest, L., Parrenin, F., Raynaud, D., Fudge, T. J., Buizert, C., & Brook, E. J. (2019). Antarctic temperature and CO_2 : near-synchrony yet variable phasing during the last deglaciation. *Climate of the Past*, 15(3), 913–926. <https://doi.org/10.5194/cp-15-913-2019>
- Ciais, P., & Jouzel, J. (1994). Deuterium and oxygen 18 in precipitation: Isotopic model, including mixed cloud processes. *Journal of Geophysical Research: Atmospheres*, 99(D8), 16793–16803. <https://doi.org/https://doi.org/10.1029/94JD00412>
- Clark, P. U., Hostetler, S. W., Pisias, N. G., Schmittner, A., & Meissner, K. J. (2007). Mechanisms for an ~7-Kyr Climate and Sea-Level Oscillation During Marine Isotope Stage 3. In *Ocean Circulation: Mechanisms and Impacts—Past and Future Changes of Meridional Overturning* (pp. 209–246). <https://doi.org/https://doi.org/10.1029/173GM15>
- Clark, P. U., Shakun, J. D., Baker, P. A., Bartlein, P. J., Brewer, S., Brook, E., Carlson, A. E., Cheng, H., Kaufman, D. S., Liu, Z., Marchitto, T. M., Mix, A. C., Morrill, C., Otto-Bliesner, B. L., Pahnke,

- K., Russell, J. M., Whitlock, C., Adkins, J. F., Blois, J. L., ... Williams, J. W. (2012). Global climate evolution during the last deglaciation. *Proceedings of the National Academy of Sciences of the United States of America*, 109(19), E1134–E1142. https://doi.org/10.1073/PNAS.1116619109/SUPPL_FILE/APPENDIX.PDF
- Clement, A., Bellomo, K., Murphy, L. N., Cane, M. A., Mauritsen, T., Rädcl, G., & Stevens, B. (2015). The Atlantic Multidecadal Oscillation without a role for ocean circulation. *Science*, 350(6258), 320–324. https://doi.org/10.1126/SCIENCE.AAB3980/SUPPL_FILE/AAB3980-CLEMENT-SM.PDF
- Colbeck, S. C. (1983). Theory of metamorphism of dry snow. *Journal of Geophysical Research: Oceans*, 88(C9), 5475–5482. <https://doi.org/10.1029/JC088IC09P05475>
- Colbeck, S. C. (1989). Air Movement in Snow Due to Windpumping. *Journal of Glaciology*, 35(120), 209–213. <https://doi.org/10.3189/S0022143000004524>
- Colleoni, F., Krinner, G., & Jakobsson, M. (2010). The role of an Arctic ice shelf in the climate of the MIS 6 glacial maximum (140 ka). *Quaternary Science Reviews*, 29(25), 3590–3597. <https://doi.org/https://doi.org/10.1016/j.quascirev.2010.06.023>
- CONNOLLEY, W. M. (1996). THE ANTARCTIC TEMPERATURE INVERSION. *International Journal of Climatology*, 16(12), 1333–1342. [https://doi.org/https://doi.org/10.1002/\(SICI\)1097-0088\(199612\)16:12<1333::AID-JOC96>3.0.CO;2-6](https://doi.org/https://doi.org/10.1002/(SICI)1097-0088(199612)16:12<1333::AID-JOC96>3.0.CO;2-6)
- Corrick, E. C., Drysdale, R. N., Hellstrom, J. C., Capron, E., Rasmussen, S. O., Zhang, X., Fleitmann, D., Couchoud, I., & Wolff, E. (2020). Synchronous timing of abrupt climate changes during the last glacial period. *Science*, 369(6506), 963–969. https://doi.org/10.1126/SCIENCE.AAY5538/SUPPL_FILE/AAY5538-CORRICK-SM.PDF
- Craig, H., Gordon, L. I., & Tongiorgi, E. (1965). Stable isotopes in oceanographic studies and paleotemperatures. V. *Lischi e Figli, Pisa*, 122.
- Craig, H., Horibe, Y., & Sowers, T. (1988). Gravitational Separation of Gases and Isotopes in Polar Ice Caps. *Science*, 242(4886), 1675–1678. <https://doi.org/10.1126/SCIENCE.242.4886.1675>
- Crivellari, S. (n.d.). *Effects of abrupt changes in the Atlantic meridional overturning circulation over the Amazon Basin: an isotopic and elemental approach*. Retrieved May 23, 2024, from https://www.researchgate.net/publication/341909781_Effects_of_abrupt_changes_in_the_Atlantic_meridional_overturning_circulation_over_the_Amazon_Basin_an_isotopic_and_elemental_approach?channel=doi&linkId=5ed901784585152945315398&showFulltext=true
- Crotti, I. (2022). *Datation et étude de la variabilité climatique à partir de la carotte de glace antarctique de TALDICE*.
- Dahl-Jensen, D., Mosegaard, K., Gundestrup, N., Clow, G. D., Johnsen, S. J., Hansen, A. W., & Balling, N. (1998). Past Temperatures Directly from the Greenland Ice Sheet. *Science*, 282(5387), 268–271. <https://doi.org/10.1126/SCIENCE.282.5387.268>
- Dansgaard, W. (1964). Stable isotopes in precipitation. *Tellus*, 16(4), 436–468.

<https://doi.org/https://doi.org/10.1111/j.2153-3490.1964.tb00181.x>

- Davies, S. M., Abbott, P. M., Meara, R. H., Pearce, N. J. G., Austin, W. E. N., Chapman, M. R., Svensson, A., Bigler, M., Rasmussen, T. L., Rasmussen, S. O., & Farmer, E. J. (2014). A North Atlantic tephrostratigraphical framework for 130–60 ka b2k: new tephra discoveries, marine-based correlations, and future challenges. *Quaternary Science Reviews*, *106*, 101–121. <https://doi.org/10.1016/J.QUASCIREV.2014.03.024>
- Dee, S., Bailey, A., Conroy, J. L., Atwood, A., Stevenson, S., Nusbaumer, J., & Noone, D. (2023). Water isotopes, climate variability, and the hydrological cycle: recent advances and new frontiers. *Environmental Research: Climate*, *2*(2), 022002. <https://doi.org/10.1088/2752-5295/ACCBE1>
- Denton, G. H., Alley, R. B., Comer, G. C., & Broecker, W. S. (2005). The role of seasonality in abrupt climate change. *Quaternary Science Reviews*, *24*(10–11), 1159–1182. <https://doi.org/10.1016/J.QUASCIREV.2004.12.002>
- Deplazes, G., Lückge, A., Peterson, L. C., Timmermann, A., Hamann, Y., Hughen, K. A., Röhl, U., Laj, C., Cane, M. A., Sigman, D. M., & Haug, G. H. (2013). Links between tropical rainfall and North Atlantic climate during the last glacial period. *Nature Geoscience* *2013* 6:3, *6*(3), 213–217. <https://doi.org/10.1038/ngeo1712>
- Deplazes, G., Lückge, A., Stuut, J.-B. W., Pätzold, J., Kuhlmann, H., Husson, D., Fant, M., & Haug, G. H. (2014). Weakening and strengthening of the Indian monsoon during Heinrich events and Dansgaard-Oeschger oscillations. *Paleoceanography*, *29*(2), 99–114. <https://doi.org/https://doi.org/10.1002/2013PA002509>
- Donders, T., Panagiotopoulos, K., Koutsodendris, A., Bertini, A., Mercuri, A. M., Masi, A., Combourieu-Nebout, N., Joannin, S., Kouli, K., Kousis, I., Peyron, O., Torri, P., Florenzano, A., Francke, A., Wagner, B., & Sadori, L. (2021). 1.36 million years of Mediterranean forest refugium dynamics in response to glacial-interglacial cycle strength. *Proceedings of the National Academy of Sciences of the United States of America*, *118*(34), e2026111118. https://doi.org/10.1073/PNAS.2026111118/SUPPL_FILE/PNAS.2026111118.SD01.XLSX
- Dreyfus, G. B., Jouzel, J., Bender, M. L., Landais, A., Masson-Delmotte, V., & Leuenberger, M. (2010). Firn processes and $\delta^{15}\text{N}$: potential for a gas-phase climate proxy. *Quaternary Science Reviews*, *29*(1–2), 28–42. <https://doi.org/10.1016/J.QUASCIREV.2009.10.012>
- Dreyfus, G. B., Parrenin, F., Lemieux-Dudon, B., Durand, G., Masson-Delmotte, V., Jouzel, J., Barnola, J. M., Panno, L., Spahni, R., Tisserand, A., Siegenthaler, U., & Leuenberger, M. (2007). Anomalous flow below 2700 m in the EPICA Dome C ice core detected using $\delta^{18}\text{O}$ of atmospheric oxygen measurements. *Climate of the Past*, *3*(2), 341–353. <https://doi.org/10.5194/CP-3-341-2007>
- Ebinuma, T., & Maeno, N. (1985). Experimental Studies on Densification and Pressure-Sintering of Ice. *Annals of Glaciology*, *6*, 83–86. <https://doi.org/10.3189/1985AOG6-1-83-86>
- Ekeykin, A. (2003). *Meteorological regime of central Antarctica and its role in the formation of isotope composition of snow thickness*. <https://theses.hal.science/tel-00701466>

- Elliot, M., Labeyrie, L., & Duplessy, J. C. (2002). Changes in North Atlantic deep-water formation associated with the Dansgaard–Oeschger temperature oscillations (60–10 ka). *Quaternary Science Reviews*, 21(10), 1153–1165. [https://doi.org/10.1016/S0277-3791\(01\)00137-8](https://doi.org/10.1016/S0277-3791(01)00137-8)
- Elmore, D., Conard, N. J., Kubik, P. W., Gove, H. E., Wahlen, M., Beer, J., & Suter, M. (1987). ^{36}Cl and ^{10}Be profiles in greenland ice: Dating and production rate variations. *Nuclear Instruments and Methods in Physics Research Section B: Beam Interactions with Materials and Atoms*, 29(1–2), 207–210. [https://doi.org/10.1016/0168-583X\(87\)90237-0](https://doi.org/10.1016/0168-583X(87)90237-0)
- Emiliani, C. (1955). Pleistocene Temperatures. *The Journal of Geology*, 63(6), 538–578. <http://www.jstor.org.insu.bib.cnrs.fr/stable/30080906>
- EPICA Community members. (2004). Eight glacial cycles from an Antarctic ice core. *Nature* 2004 429:6992, 429(6992), 623–628. <https://doi.org/10.1038/nature02599>
- EPICA Community Members. (2006). One-to-one coupling of glacial climate variability in Greenland and Antarctica. *Nature*, 444(7116), 195–198. <https://doi.org/10.1038/nature05301>
- Erb, K.-H., Kastner, T., Plutzer, C., Bais, A. L. S., Carvalhais, N., Fetzel, T., Gingrich, S., Haberl, H., Lauk, C., Niedertscheider, M., Pongratz, J., Thurner, M., & Luysaert, S. (2018). Unexpectedly large impact of forest management and grazing on global vegetation biomass. *Nature*, 553(7686), 73–76. <https://doi.org/10.1038/nature25138>
- Extier, T., Landais, A., Bréant, C., Prié, F., Bazin, L., Dreyfus, G., Roche, D. M., & Leuenberger, M. (2018a). On the use of $\delta^{18}\text{O}_{\text{atm}}$ for ice core dating. *Quaternary Science Reviews*, 185, 244–257. <https://doi.org/10.1016/J.QUASCIREV.2018.02.008>
- Extier, T., Landais, A., Bréant, C., Prié, F., Bazin, L., Dreyfus, G., Roche, D. M., & Leuenberger, M. C. (2018b). $\delta^{18}\text{O}_{\text{atm}}$ records between 100–800 ka from EPICA Dome C ice core. PANGAEA. <https://doi.org/10.1594/PANGAEA.887323>
- Extier, T., Landais, A., Bréant, C., Prié, F., Bazin, L., Dreyfus, G., Roche, D. M., & Leuenberger, M. C. (2018c). $\delta\text{O}_2/\text{N}_2$ records between 100–800 ka from EPICA Dome C ice core. PANGAEA. <https://doi.org/10.1594/PANGAEA.887326>
- Faber, A. K., Vinther, B. M., Sjolte, J., & Pedersen, R. A. (2017). How does sea ice influence $\delta^{18}\text{O}$ of Arctic precipitation? *Atmospheric Chemistry and Physics*, 17(9), 5865–5876. <https://doi.org/10.5194/ACP-17-5865-2017>
- Finné, M., Holmgren, K., Shen, C.-C., Hu, H.-M., Boyd, M., & Stocker, S. (2017). Late Bronze Age climate change and the destruction of the Mycenaean Palace of Nestor at Pylos. *PLOS ONE*, 12(12), e0189447. <https://doi.org/10.1371/journal.pone.0189447>
- Fohlmeister, J., Luetscher, M., Spötl, C., Schröder-Ritzrau, A., Schröder, B., Frank, N., Eichstädter, R., Trüssel, M., Skiba, V., & Boers, N. (2023). The role of Northern Hemisphere summer insolation for millennial-scale climate variability during the penultimate glacial. *Communications Earth & Environment* 2023 4:1, 4(1), 1–8. <https://doi.org/10.1038/s43247-023-00908-0>

- Forçage externe du climat: variation des paramètres orbitaux de la Terre - Jean-Baptiste Madeleine | Canal U.* (n.d.). Retrieved May 23, 2024, from <https://www.canal-u.tv/chaines/ipsl/variation-des-parametres-orbitaux-de-la-terre/forçage-externe-du-climat-variation-des>
- Fourteau, K., Martinerie, P., Faïn, X., Ekaykin, A. A., Chappellaz, J., & Lipenkov, V. (2020). Estimation of gas record alteration in very low-accumulation ice cores. *Climate of the Past*, 16(2), 503–522. <https://doi.org/10.5194/CP-16-503-2020>
- Freitag, J., Kipfstuhl, S., Laepple, T., & Wilhelms, F. (2013). Impurity-controlled densification: a new model for stratified polar firn. *Journal of Glaciology*, 59(218), 1163–1169. <https://doi.org/10.3189/2013JOG13J042>
- Frezzotti, M., Urbini, S., Proposito, M., Scarchilli, C., & Gandolfi, S. (2007). Spatial and temporal variability of surface mass balance near Talos Dome, East Antarctica. *Journal of Geophysical Research: Earth Surface*, 112(F2). <https://doi.org/https://doi.org/10.1029/2006JF000638>
- Fujita, S., Parrenin, F., Severi, M., Motoyama, H., & Wolff, E. W. (2015). Volcanic synchronization of Dome Fuji and Dome C Antarctic deep ice cores over the past 216 kyr. *Climate of the Past*, 11(10), 1395–1416. <https://doi.org/10.5194/CP-11-1395-2015>
- Galewsky, J., Steen-Larsen, H. C., Field, R. D., Worden, J., Risi, C., & Schneider, M. (2016). Stable isotopes in atmospheric water vapor and applications to the hydrologic cycle. *Reviews of Geophysics*, 54(4), 809–865. <https://doi.org/https://doi.org/10.1002/2015RG000512>
- Ganopolski, A., & Brovkin, V. (2017). Simulation of climate, ice sheets and CO₂ evolution during the last four glacial cycles with an Earth system model of intermediate complexity. *Climate of the Past*, 13(12), 1695–1716. <https://doi.org/10.5194/CP-13-1695-2017>
- Ganopolski, A., & Rahmstorf, S. (2001). Rapid changes of glacial climate simulated in a coupled climate model. *Nature*, 409(6817), 153–158. <https://doi.org/10.1038/35051500>
- Genthon, C., Six, D., Scarchilli, C., Ciardini, V., & Frezzotti, M. (2016). Meteorological and snow accumulation gradients across Dome C, East Antarctic plateau. *International Journal of Climatology*, 36(1), 455–466. <https://doi.org/10.1002/JOC.4362>
- Geuskens, G. (2020). *L'effet de serre et le bilan énergétique de la Terre | Science, climat et énergie.* <https://www.science-climat-energie.be/2020/12/11/leffet-de-serre-et-le-bilan-energetique-de-la-terre/>
- Gildor, H., Tziperman, E., Nienow, P. W., Shepherd, J. G., Alley, R. B., Lawton, J. H., Mahadevan, A., & Lenton, T. M. (2003). Sea-ice switches and abrupt climate change. *Philosophical Transactions of the Royal Society of London. Series A: Mathematical, Physical and Engineering Sciences*, 361(1810), 1935–1944. <https://doi.org/10.1098/RSTA.2003.1244>
- Goosse, H., Brovkin, V., Fichefet, T., Haarsma, R., Huybrechts, P., Jongma, J., Mouchet, A., Selten, F., Barriat, P. Y., Campin, J. M., Deleersnijder, E., Driesschaert, E., Goelzer, H., Janssens, I., Loutre, M. F., Morales Maqueda, M. A., Opsteegh, T., Mathieu, P. P., Munhoven, G., ...

- Weber, S. L. (2010). Description of the Earth system model of intermediate complexity LOVECLIM version 1.2. *Geoscientific Model Development*, 3(2), 603–633. <https://doi.org/10.5194/GMD-3-603-2010>
- Goujon, C., Barnola, J. M., & Ritz, C. (2003). Modeling the densification of polar firn including heat diffusion: Application to close-off characteristics and gas isotopic fractionation for Antarctica and Greenland sites. *Journal of Geophysical Research: Atmospheres*, 108(D24), 4792. <https://doi.org/10.1029/2002JD003319>
- Grachev, A. M., & Severinghaus, J. P. (2003). Laboratory determination of thermal diffusion constants for $^{29}\text{N}_2/^{28}\text{N}_2$ in air at temperatures from -60 to 0°C for reconstruction of magnitudes of abrupt climate changes using the ice core fossil–air paleothermometer. *Geochimica et Cosmochimica Acta*, 67(3), 345–360. [https://doi.org/https://doi.org/10.1016/S0016-7037\(02\)01115-8](https://doi.org/https://doi.org/10.1016/S0016-7037(02)01115-8)
- Grachev, A. M., & Severinghaus, J. P. (2005). A revised $+10\pm 4^\circ\text{C}$ magnitude of the abrupt change in Greenland temperature at the Younger Dryas termination using published GISP2 gas isotope data and air thermal diffusion constants. *Quaternary Science Reviews*, 24(5–6), 513–519. <https://doi.org/10.1016/J.QUASCIREV.2004.10.016>
- Grisart, A. (2023). *Étude à haute résolution des cycles hydrologiques et climatiques à partir d'une carotte de glace d'Antarctique avec un focus sur les déglaciations*. <https://theses.hal.science/tel-04042459>
- Grootes, P. M., Stuiver, M., White, J. W. C., Johnsen, S., & Jouzel, J. (1993). Comparison of oxygen isotope records from the GISP2 and GRIP Greenland ice cores. *Nature*, 366(6455), 552–554. <https://doi.org/10.1038/366552a0>
- Guillevic, M., Bazin, L., Landais, A., Kindler, P., Orsi, A., Masson-Delmotte, V., Blunier, T., Buchardt, S. L., Capron, E., Leuenberger, M., Martinerie, P., Prié, F., & Vinther, B. M. (2013). Spatial gradients of temperature, accumulation and $\delta^{18}\text{O}$ - ice in Greenland over a series of Dansgaard-Oeschger events. *Climate of the Past*, 9(3), 1029–1051. <https://doi.org/10.5194/CP-9-1029-2013>
- Guillou, H., Scao, V., Nomade, S., Van Vliet-Lanoë, B., Liorzou, C., & Guðmundsson, Á. (2019). $^{40}\text{Ar}/^{39}\text{Ar}$ dating of the Thorsmork ignimbrite and Icelandic sub-glacial rhyolites. *Quaternary Science Reviews*, 209, 52–62. <https://doi.org/https://doi.org/10.1016/j.quascirev.2019.02.014>
- Guillou, H., Singer, B. S., Laj, C., Kissel, C., Scaillet, S., & Jicha, B. R. (2004). On the age of the Laschamp geomagnetic excursion. *Earth and Planetary Science Letters*, 227(3), 331–343. <https://doi.org/https://doi.org/10.1016/j.epsl.2004.09.018>
- Haneda, Y., Okada, M., Suganuma, Y., & Kitamura, T. (2020). A full sequence of the Matuyama–Brunhes geomagnetic reversal in the Chiba composite section, Central Japan. *Progress in Earth and Planetary Science*, 7(1), 1–22. <https://doi.org/10.1186/S40645-020-00354-Y/FIGURES/12>
- Harris Stuart, R., Faber, A. K., Wahl, S., Hörhold, M., Kipfstuhl, S., Vasskog, K., Behrens, M., Zühr,

- A. M., & Steen-Larsen, H. C. (2023). Exploring the role of snow metamorphism on the isotopic composition of the surface snow at EastGRIP. *Cryosphere*, 17(3), 1185–1204. <https://doi.org/10.5194/TC-17-1185-2023>
- Harris Stuart, R., Landais, A., Arnaud, L., Buizert, C., Capron, E., Dumont, M., Libois, Q., Mulvaney, R., Orsi, A., Picard, G., Prié, F., Severinghaus, J., Stenni, B., & Martinerie, P. (2023). Towards an understanding of the controls on $\delta O_2/N_2$ variability in ice core records. *EGUsphere*, 2023, 1–35. <https://doi.org/10.5194/egusphere-2023-2585>
- Hays, J. D., Imbrie, J., & Shackleton, N. J. (1976). Variations in the Earth's Orbit: Pacemaker of the Ice Ages. *Science*, 194(4270), 1121–1132. <https://doi.org/10.1126/SCIENCE.194.4270.1121>
- Hazell, C. J., Pound, M. J., & Hocking, E. P. (2022). High-resolution Bronze Age palaeoenvironmental change in the Eastern Mediterranean: exploring the links between climate and societies. *Palynology*, 46(4), 1–20. <https://doi.org/10.1080/01916122.2022.2067259>
- Heinrich, H. (1988a). Origin and Consequences of Cyclic Ice Rafting in the Northeast Atlantic Ocean During the Past 130,000 Years. *Quaternary Research*, 29(2), 142–152. [https://doi.org/DOL:10.1016/0033-5894\(88\)90057-9](https://doi.org/DOL:10.1016/0033-5894(88)90057-9)
- Heinrich, H. (1988b). Origin and consequences of cyclic ice rafting in the Northeast Atlantic Ocean during the past 130,000 years. *Quaternary Research*, 29(2), 142–152. [https://doi.org/10.1016/0033-5894\(88\)90057-9](https://doi.org/10.1016/0033-5894(88)90057-9)
- Hemming, S. R. (2004). Heinrich events: Massive late Pleistocene detritus layers of the North Atlantic and their global climate imprint. *Reviews of Geophysics*, 42(1). <https://doi.org/https://doi.org/10.1029/2003RG000128>
- Herron, M. M., & Langway, C. C. (1980). Firn densification: an empirical model. *Journal of Glaciology*, 25(93). <https://doi.org/10.3189/S0022143000015239>
- Hobart, B., Lisiecki, L. E., Rand, D., Lee, T., & Lawrence, C. E. (2023). Late Pleistocene 100-kyr glacial cycles paced by precession forcing of summer insolation. *Nature Geoscience* 2023 16:8, 16(8), 717–722. <https://doi.org/10.1038/s41561-023-01235-x>
- Hodell, D. A., Channeil, J. E. T., Curtis, J. H., Romero, O. E., & Röhl, U. (2008). Onset of "Hudson Strait" Heinrich events in the eastern North Atlantic at the end of the middle Pleistocene transition (~640 ka)? *Paleoceanography*, 23(4). <https://doi.org/10.1029/2008PA001591>
- Hoefs, J. (2015). *Stable Isotope Geochemistry*. Springer International Publishing. <https://doi.org/10.1007/978-3-319-19716-6>
- Hoffmann, G., Jouzel, J., & Masson, V. (2000). Stable water isotopes in atmospheric general circulation models. *Hydrological Processes*, 14(8), 1385–1406. [https://doi.org/https://doi.org/10.1002/1099-1085\(20000615\)14:8<1385::AID-HYP989>3.0.CO;2-1](https://doi.org/https://doi.org/10.1002/1099-1085(20000615)14:8<1385::AID-HYP989>3.0.CO;2-1)
- Holme, C., Gkinis, V., & Vinther, B. M. (2018). Molecular diffusion of stable water isotopes in

- polar firn as a proxy for past temperatures. *Geochimica et Cosmochimica Acta*, 225, 128–145. <https://doi.org/10.1016/J.GCA.2018.01.015>
- Hönisch, B., Royer, D. L., Breecker, D. O., Polissar, P. J., Bowen, G. J., Henehan, M. J., Cui, Y., Steinthorsdottir, M., McElwain, J. C., Kohn, M. J., Pearson, A., Phelps, S. R., Uno, K. T., Ridgwell, A., Anagnostou, E., Austermann, J., Badger, M. P. S., Barclay, R. S., Bijl, P. K., ... Zhang, L. (2023). Toward a Cenozoic history of atmospheric CO₂. *Science*, 382(6675). https://doi.org/10.1126/SCIENCE.ADI5177/SUPPL_FILE/SCIENCE.ADI5177_SM.PDF
- Hörhold, M. W., Laepple, T., Freitag, J., Bigler, M., Fischer, H., & Kipfstuhl, S. (2012). On the impact of impurities on the densification of polar firn. *Earth and Planetary Science Letters*, 325–326, 93–99. <https://doi.org/10.1016/J.EPSL.2011.12.022>
- Horita, J., Rozanski, K., & Cohen, S. (2008). Isotope effects in the evaporation of water: a status report of the Craig–Gordon model. *Isotopes in Environmental and Health Studies*, 44(1), 23–49. <https://doi.org/10.1080/10256010801887174>
- Horiuchi, K., Uchida, T., Sakamoto, Y., Ohta, A., Matsuzaki, H., Shibata, Y., & Motoyama, H. (2008). Ice core record of ¹⁰Be over the past millennium from Dome Fuji, Antarctica: A new proxy record of past solar activity and a powerful tool for stratigraphic dating. *Quaternary Geochronology*, 3(3), 253–261. <https://doi.org/10.1016/J.QUAGEO.2008.01.003>
- Huber, C., Beyerle, U., Leuenberger, M., Schwander, J., Kipfer, R., Spahni, R., Severinghaus, J. P., & Weiler, K. (2006). Evidence for molecular size dependent gas fractionation in firn air derived from noble gases, oxygen, and nitrogen measurements. *Earth and Planetary Science Letters*, 243(1–2), 61–73. <https://doi.org/10.1016/J.EPSL.2005.12.036>
- Humboldt, A. V. (1884). *Cosmos: a sketch of the physical description of the universe: Vol. II* (E.W. Sawyer). George Bell & Sons.
- Huybers, P. (2011). Combined obliquity and precession pacing of late Pleistocene deglaciations. *Nature* 2011 480:7376, 480(7376), 229–232. <https://doi.org/10.1038/nature10626>
- Huybers, P., & Wunsch, C. (2005). Obliquity pacing of the late Pleistocene glacial terminations. *Nature* 2005 434:7032, 434(7032), 491–494. <https://doi.org/10.1038/nature03401>
- Intergovernmental Panel on Climate Change (IPCC). (2023a). *AR6 Synthesis Report: Summary for Policymakers Headline Statements*. <https://www.ipcc.ch/report/ar6/syr/resources/spm-headline-statements/>
- Intergovernmental Panel on Climate Change (IPCC). (2023b). The Earth's Energy Budget, Climate Feedbacks and Climate Sensitivity. *Climate Change 2021 – The Physical Science Basis*, 923–1054. <https://doi.org/10.1017/9781009157896.009>
- Jacka, T. H., & Li, J. (1994). The steady-state crystal size of deforming ice. *Annals of Glaciology*, 20, 13–18. <https://doi.org/10.3189/1994AOG20-1-13-18>
- Jiang, W., Hu, S. M., Lu, Z. T., Ritterbusch, F., & Yang, G. min. (2020). Latest development of radiokrypton dating – A tool to find and study paleogroundwater. *Quaternary*

International, 547, 166–171. <https://doi.org/10.1016/J.QUAINT.2019.04.025>

- Johnsen, S. J., Clausen, H. B., Cuffey, K. M., Hoffmann, G., Schwander, J., & Creyts, T. (2000). Diffusion of stable isotopes in polar firn and ice: the isotope effect in firn diffusion. *Physics of Ice Core Records*, 121–140.
- Johnsen, S. J., Clausen, H. B., Dansgaard, W., Fuhrer, K., Gundestrup, N., Hammer, C. U., Iversen, P., Jouzel, J., Stauffer, B., & Steffensen, J. P. (1992). Irregular glacial interstadials recorded in a new Greenland ice core. *Nature*, 359(6393), 311–313. <https://doi.org/10.1038/359311a0>
- Johnsen, S. J., & Dansgaard, W. (1992). On flow model dating of stable isotope records from Greenland ice cores. In E. Bard & W. S. Broecker (Eds.), *NATO ASI Series* (Springer-Verlag GmbH, Vol. 12, pp. 13–24).
- Jomelli, V., Schimmelpfennig, I., Favier, V., Mokadem, F., Landais, A., Rinterknecht, V., Brunstein, D., Verfaillie, D., Legentil, C., Aumaitre, G., Bournès, D. L., & Keddadouche, K. (2018). Glacier extent in sub-Antarctic Kerguelen archipelago from MIS 3 period: Evidence from ³⁶Cl dating. *Quaternary Science Reviews*, 183, 110–123. <https://doi.org/https://doi.org/10.1016/j.quascirev.2018.01.008>
- Jouzel, J., Masson-Delmotte, V., Cattani, O., Dreyfus, G., Falourd, S., Hoffmann, G., Minster, B., Nouet, J., Barnola, J. M., Chappellaz, J., Fischer, H., Gallet, J. C., Johnsen, S., Leuenberger, M., Loulergue, L., Luethi, D., Oerter, H., Parrenin, F., Raisbeck, G., ... Wolff, E. W. (2007). Orbital and millennial antarctic climate variability over the past 800,000 years. *Science*, 317(5839), 793–796. https://doi.org/10.1126/SCIENCE.1141038/SUPPL_FILE/JOUZEL.SOM.PDF
- Jouzel, J., & Merlivat, L. (1984). Deuterium and oxygen 18 in precipitation: Modeling of the isotopic effects during snow formation. *Journal of Geophysical Research: Atmospheres*, 89(D7), 11749–11757. <https://doi.org/https://doi.org/10.1029/JD089iD07p11749>
- Jouzel, J., Vimeux, F., Caillon, N., Delaygue, G., Hoffmann, G., Masson-Delmotte, V., & Parrenin, F. (2003). Magnitude of isotope/temperature scaling for interpretation of central Antarctic ice cores. *Journal of Geophysical Research: Atmospheres*, 108(D12), 4361. <https://doi.org/10.1029/2002JD002677>
- Jung, K. H., Park, S. C., Kim, J. H., & Kang, H. (2004). Vertical diffusion of water molecules near the surface of ice. *The Journal of Chemical Physics*, 121(6), 2758–2764. <https://doi.org/10.1063/1.1770518>
- Kawamura, K., Parrenin, F., Lisiecki, L., Uemura, R., Vimeux, F., Severinghaus, J. P., Hutterli, M. A., Nakazawa, T., Aoki, S., Jouzel, J., Raymo, M. E., Matsumoto, K., Nakata, H., Motoyama, H., Fujita, S., Goto-Azuma, K., Fujii, Y., & Watanabe, O. (2007). Northern Hemisphere forcing of climatic cycles in Antarctica over the past 360,000 years. *Nature* 2007 448:7156, 448(7156), 912–916. <https://doi.org/10.1038/nature06015>
- Kawamura, K., Severinghaus, J. P., Ishidoya, S., Sugawara, S., Hashida, G., Motoyama, H., Fujii, Y., Aoki, S., & Nakazawa, T. (2006). Convective mixing of air in firn at four polar sites. *Earth*

and Planetary Science Letters, 244(3), 672–682.
<https://doi.org/https://doi.org/10.1016/j.epsl.2006.02.017>

- Khodri, M., Leclalnche, Y., Ramstein, G., Braconnot, P., Marti, O., & Cortijo, E. (2001). Simulating the amplification of orbital forcing by ocean feedbacks in the last glaciation. *Nature*, 410(6828), 570–574. <https://doi.org/10.1038/35069044>
- Kindler, P., Guillevic, M., Baumgartner, M., Schwander, J., Landais, A., & Leuenberger, M. (2014). Temperature reconstruction from 10 to 120 kyr b2k from the NGRIP ice core. *Climate of the Past*, 10(2), 887–902. <https://doi.org/10.5194/CP-10-887-2014>
- Kious, W. J., & Tilling, R. I. (1996). This dynamic earth: the story of plate tectonics. *General Interest Publication*. <https://doi.org/10.3133/7000097>
- Köhler, P., Fischer, H., Munhoven, G., & Zeebe, R. E. (2005). Quantitative interpretation of atmospheric carbon records over the last glacial termination. *Global Biogeochemical Cycles*, 19(4). <https://doi.org/10.1029/2004GB002345>
- Köhler, P., Nehrbass-Ahles, C., Schmitt, J., Stocker, T. F., & Fischer, H. (2017). A 156kyr smoothed history of the atmospheric greenhouse gases CO₂, CH₄, and N₂O and their radiative forcing. *Earth System Science Data*, 9(1), 363–387. <https://doi.org/10.5194/essd-9-363-2017>
- Kojima, K. (1967). Densification of seasonal snow cover. *Physics of Snow and Ice: Proceedings*, 1(2), 929–952.
- Kuipers Munneke, P., Ligtenberg, S. R. M., Noël, B. P. Y., Howat, I. M., Box, J. E., Mosley-Thompson, E., McConnell, J. R., Steffen, K., Harper, J. T., Das, S. B., & Van Den Broeke, M. R. (2015). Elevation change of the Greenland Ice Sheet due to surface mass balance and firn processes, 1960-2014. *Cryosphere*, 9(6), 2009–2025. <https://doi.org/10.5194/TC-9-2009-2015>
- Kukla, G., & Gavin, J. (2004). Milankovitch climate reinforcements. *Global and Planetary Change*, 40(1), 27–48. [https://doi.org/https://doi.org/10.1016/S0921-8181\(03\)00096-1](https://doi.org/https://doi.org/10.1016/S0921-8181(03)00096-1)
- Kuniyoshi, Y., Abe-Ouchi, A., Sherriff-Tadano, S., Chan, W. Le, & Saito, F. (2022). Effect of Climatic Precession on Dansgaard-Oeschger-Like Oscillations. *Geophysical Research Letters*, 49(6), e2021GL095695. <https://doi.org/10.1029/2021GL095695>
- Kutzbach, J. E. (1974). Fluctuations of climate-monitoring and modelling. *World Meteorol. Organ. Bull*, 23, 155–163.
- Labeyrie, L. D., Pichon, J. J., Labracherie, M., Ippolito, P., Duprat, J., & Duplessy, J. C. (1986). Melting history of Antarctica during the past 60,000 years. *Nature*, 322(6081), 701–706. <https://doi.org/10.1038/322701a0>
- Laepple, T., Werner, M., & Lohmann, G. (2011). Synchronicity of Antarctic temperatures and local solar insolation on orbital timescales. *Nature*. <https://doi.org/10.1038/nature09825>
- Lambert, F., Bigler, M., Steffensen, J. P., Hutterli, M., & Fischer, H. (2012). Centennial mineral

- dust variability in high-resolution ice core data from Dome C, Antarctica. *Climate of the Past*, 8(2), 609–623. <https://doi.org/10.5194/CP-8-609-2012>
- Lambert, F., Delmonte, B., Petit, J. R., Bigler, M., Kaufmann, P. R., Hutterli, M. A., Stocker, T. F., Ruth, U., Steffensen, J. P., & Maggi, V. (2008). Dust-climate couplings over the past 800,000 years from the EPICA Dome C ice core. *Nature* 2008 452:7187, 452(7187), 616–619. <https://doi.org/10.1038/nature06763>
- Lamy, F., Gersonde, R., Winckler, G., Esper, O., Jaeschke, A., Kuhn, G., Ullermann, J., Martinez-Garcia, A., Lambert, F., & Kilian, R. (2014). Increased dust deposition in the Pacific Southern Ocean during glacial periods. *Science*, 343(6169), 403–407. https://doi.org/10.1126/SCIENCE.1245424/SUPPL_FILE/LAMY.SM.PDF
- Landais, A., Barnola, J. M., Kawamura, K., Caillon, N., Delmotte, M., Van Ommen, T., Dreyfus, G., Jouzel, J., Masson-Delmotte, V., Minster, B., Freitag, J., Leuenberger, M., Schwander, J., Huber, C., Etheridge, D., & Morgan, V. (2006). Firn-air $\delta^{15}\text{N}$ in modern polar sites and glacial-interglacial ice: a model-data mismatch during glacial periods in Antarctica? *Quaternary Science Reviews*, 25(1–2), 49–62. <https://doi.org/10.1016/J.QUASCIREV.2005.06.007>
- Landais, A., Barnola, J. M., Masson-Delmotte, V., Jouzel, J., Chappellaz, J., Caillon, N., Huber, C., Leuenberger, M., & Johnsen, S. J. (2004). A continuous record of temperature evolution over a sequence of Dansgaard-Oeschger events during Marine Isotopic Stage 4 (76 to 62 kyr BP). *Geophysical Research Letters*, 31(22). <https://doi.org/https://doi.org/10.1029/2004GL021193>
- Landais, A., Chappellaz, J., Delmotte, M., Jouzel, J., Blunier, T., Bourg, C., Caillon, N., Cherrier, S., Malaizé, B., Masson-Delmotte, V., Raynaud, D., Schwander, J., & Steffensen, J. P. (2003). A tentative reconstruction of the last interglacial and glacial inception in Greenland based on new gas measurements in the Greenland Ice Core Project (GRIP) ice core. *Journal of Geophysical Research: Atmospheres*, 108(D18). <https://doi.org/10.1029/2002JD003147>
- Landais, A., Dreyfus, G., Capron, E., Jouzel, J., Masson-Delmotte, V., Roche, D. M., Prié, F., Caillon, N., Chappellaz, J., Leuenberger, M., Laurantou, A., Parrenin, F., Raynaud, D., & Teste, G. (2013). Two-phase change in CO₂, Antarctic temperature and global climate during Termination II. *Nature Geoscience* 2013 6:12, 6(12), 1062–1065. <https://doi.org/10.1038/ngeo1985>
- Landais, A., Dreyfus, G., Capron, E., Masson-Delmotte, V., Sanchez-Goñi, M. F., Desprat, S., Hoffmann, G., Jouzel, J., Leuenberger, M., & Johnsen, S. (2010). What drives the millennial and orbital variations of $\delta^{18}\text{O}_{\text{atm}}$? *Quaternary Science Reviews*, 29(1–2), 235–246. <https://doi.org/10.1016/J.QUASCIREV.2009.07.005>
- Landais, A., Dreyfus, G., Capron, E., Pol, K., Loutre, M. F., Raynaud, D., Lipenkov, V. Y., Arnaud, L., Masson-Delmotte, V., Paillard, D., Jouzel, J., & Leuenberger, M. (2012). Towards orbital dating of the EPICA Dome C ice core using $\delta\text{O } 2/\text{N } 2$. *Climate of the Past*, 8(1), 191–203. <https://doi.org/10.5194/CP-8-191-2012>
- Landais, A., Masson-Delmotte, V., Combourieu Nebout, N., Jouzel, J., Blunier, T., Leuenberger,

- M., Dahl-Jensen, D., & Johnsen, S. (2007). Millennial scale variations of the isotopic composition of atmospheric oxygen over Marine Isotopic Stage 4. *Earth and Planetary Science Letters*, 258(1), 101–113. <https://doi.org/https://doi.org/10.1016/j.epsl.2007.03.027>
- Landais, A., Masson-Delmotte, V., Jouzel, J., Raynaud, D., Johnsen, S., Huber, C., Leuenberger, M., Schwander, J., & Minster, B. (2006). The glacial inception as recorded in the NorthGRIP Greenland ice core: Timing, structure and associated abrupt temperature changes. *Climate Dynamics*, 26(2–3), 273–284. <https://doi.org/10.1007/S00382-005-0063-Y/METRICS>
- Landais, A., Masson-Delmotte, V., Stenni, B., Selmo, E., Roche, D. M., Jouzel, J., Lambert, F., Guillevic, M., Bazin, L., Arzel, O., Vinther, B., Gkinis, V., & Popp, T. (2015). A review of the bipolar see-saw from synchronized and high resolution ice core water stable isotope records from Greenland and East Antarctica. *Quaternary Science Reviews*, 114, 18–32. <https://doi.org/10.1016/J.QUASCIREV.2015.01.031>
- Landais, A., Orsi, A. O., Fourré, E. F., Jacob, R., Crotti, I., Ritterbusch, F., Lu, Z.-T., Yang, G.-M., & Jiang, W. (2022). Absolute dating of deep ice cores with argon and krypton isotopes. *EGU22*. <https://doi.org/10.5194/EGUSPHERE-EGU22-13260>
- Landais, A., & Stenni, B. (2021). *Water stable isotopes (dD, d18O) from EPICA Dome C ice core (Antarctica) (0-800 ka)*. PANGAEA. <https://doi.org/10.1594/PANGAEA.934094>
- Landais, A., Stenni, B., Masson-Delmotte, V., Jouzel, J., Cauquoin, A., Fourré, E., Minster, B., Selmo, E., Extier, T., Werner, M., Vimeux, F., Uemura, R., Crotti, I., & Grisart, A. (2021). Interglacial Antarctic–Southern Ocean climate decoupling due to moisture source area shifts. *Nature Geoscience* 2021 14:12, 14(12), 918–923. <https://doi.org/10.1038/s41561-021-00856-4>
- Laskar, J., Robutel, P., Joutel, F., Gastineau, M., Correia, A. C. M., & Levrard, B. (2004). A long-term numerical solution for the insolation quantities of the Earth. *Astronomy & Astrophysics*, 428(1), 261–285. <https://doi.org/10.1051/0004-6361:20041335>
- Lee, S.-Y., & Poulsen, C. J. (2008). Amplification of obliquity forcing through mean annual and seasonal atmospheric feedbacks. *Climate of the Past*, 4(4), 205–213. <https://doi.org/10.5194/cp-4-205-2008>
- Legrain, E., Parrenin, F., & Capron, E. (2023). A gradual change is more likely to have caused the Mid-Pleistocene Transition than an abrupt event. *Communications Earth & Environment*, 4(1), 90. <https://doi.org/10.1038/s43247-023-00754-0>
- Lemieux-Dudon, B., Bazin, L., Landais, A., Toyé Mahamadou Kele, H., Guillevic, M., Kindler, P., Parrenin, F., & Martinerie, P. (2015). Implementation of counted layers for coherent ice core chronology. *Climate of the Past*, 11(6), 959–978. <https://doi.org/10.5194/CP-11-959-2015>
- Li, C., & Born, A. (2019). Coupled atmosphere-ice-ocean dynamics in Dansgaard-Oeschger events. *Quaternary Science Reviews*, 203, 1–20. <https://doi.org/10.1016/J.QUASCIREV.2018.10.031>

- Ligtenberg, S. R. M., Helsen, M. M., & Van Den Broeke, M. R. (2011). An improved semi-empirical model for the densification of Antarctic firn. *Cryosphere*, 5(4), 809–819. <https://doi.org/10.5194/TC-5-809-2011>
- Lisiecki, L. E., Herrero, C., García-Olivares, A., Lisiecki, L. E., Herrero, C., & García-Olivares, A. (2016). Insight to Marine Isotope Stage 13 using Late Pleistocene relaxation models of ice volume and carbon cycle change. *AGUFM*, 2016, PP31B-2281. <https://ui.adsabs.harvard.edu/abs/2016AGUFMPP31B2281L/abstract>
- Lisiecki, L. E., & Raymo, M. E. (2005). A Pliocene-Pleistocene stack of 57 globally distributed benthic $\delta^{18}\text{O}$ records. *Paleoceanography*, 20(1), 1–17. <https://doi.org/10.1029/2004PA001071>
- Liu, Z., Zhu, J., Rosenthal, Y., Zhang, X., Otto-Bliesner, B. L., Timmermann, A., Smith, R. S., Lohmann, G., Zheng, W., & Timm, O. E. (2014). The Holocene temperature conundrum. *Proceedings of the National Academy of Sciences of the United States of America*, 111(34), E3501–E3505. https://doi.org/10.1073/PNAS.1407229111/SUPPL_FILE/PNAS.201407229SI.PDF
- Lliboutry, L. (1979). *A Critical Review of Analytical Approximate Solutions for Steady State Velocities and Temperature in Cold Ice-sheets*.
- Loosli, H. H., Oeschger, H., & Wiest, W. (1970). Argon 37, argon 39, and krypton 81 in the atmosphere and tracer studies based on these isotopes. *Journal of Geophysical Research (1896-1977)*, 75(15), 2895–2900. <https://doi.org/https://doi.org/10.1029/JC075i015p02895>
- Lorius, C., Jouzel, J., Ritz, C., Merlivat, L., Barkov, N. I., Korotkevich, Y. S., & Kotlyakov, V. M. (1985). A 150,000-year climatic record from Antarctic ice. *Nature* 1985 316:6029, 316(6029), 591–596. <https://doi.org/10.1038/316591a0>
- Lorius, C., & Merlivat, L. (1975). *Distribution of mean surface stable isotopes values in east Antarctica; observed changes with depth in coastal area*. http://inis.iaea.org/search/search.aspx?orig_q=RN:07242101
- Loulergue, L., Schilt, A., Spahni, R., Masson-Delmotte, V., Blunier, T., Lemieux, B., Barnola, J. M., Raynaud, D., Stocker, T. F., & Chappellaz, J. (2008). Orbital and millennial-scale features of atmospheric CH₄ over the past 800,000 years. *Nature* 2008 453:7193, 453(7193), 383–386. <https://doi.org/10.1038/nature06950>
- Lundin, J. M. D., Stevens, C. M., Arthern, R., Buizert, C., Orsi, A., Ligtenberg, S. R. M., Simonsen, S. B., Cummings, E., Essery, R., Leahy, W., Harris, P., Helsen, M. M., & Waddington, E. D. (2017). Firn Model Intercomparison Experiment (FirnMICE). *Journal of Glaciology*, 63(239), 401–422. <https://doi.org/10.1017/JOG.2016.114>
- Lüthi, D., Le Floch, M., Bereiter, B., Blunier, T., Barnola, J. M., Siegenthaler, U., Raynaud, D., Jouzel, J., Fischer, H., Kawamura, K., & Stocker, T. F. (2008). High-resolution carbon dioxide concentration record 650,000–800,000 years before present. *Nature* 2008 453:7193, 453(7193), 379–382. <https://doi.org/10.1038/nature06949>

- Luz, B., & Barkan, E. (2011). The isotopic composition of atmospheric oxygen. *Global Biogeochemical Cycles*, *25*(3), 3001. <https://doi.org/10.1029/2010GB003883>
- Luz, B., Barkan, E., Bender, M. L., Thieme, M. H., & Boering, K. A. (1999). Triple-isotope composition of atmospheric oxygen as a tracer of biosphere productivity. *Nature* *1999* *400*:6744, *400*(6744), 547–550. <https://doi.org/10.1038/22987>
- Lu, Z. T., Schlosser, P., Smethie, W. M., Sturchio, N. C., Fischer, T. P., Kennedy, B. M., Purtschert, R., Severinghaus, J. P., Solomon, D. K., Tanhua, T., & Yokochi, R. (2014). Tracer applications of noble gas radionuclides in the geosciences. *Earth-Science Reviews*, *138*, 196–214. <https://doi.org/10.1016/J.EARSCIREV.2013.09.002>
- Lynch-Stieglitz, J. (2017). The Atlantic Meridional Overturning Circulation and Abrupt Climate Change. *Annual Review of Marine Science*, *9*(Volume 9, 2017), 83–104. <https://doi.org/https://doi.org/10.1146/annurev-marine-010816-060415>
- Macrì, P., Capraro, L., Ferretti, P., & Scarponi, D. (2018). A high-resolution record of the Matuyama-Brunhes transition from the Mediterranean region: The Valle di Manche section (Calabria, Southern Italy). *Physics of the Earth and Planetary Interiors*, *278*, 1–15. <https://doi.org/10.1016/J.PEPI.2018.02.005>
- Maeno, N., & Ebinuma, T. (1983). Pressure sintering of ice and its implication to the densification of snow at polar glaciers and ice sheets. *Journal of Physical Chemistry*, *87*(21), 4103–4110. https://doi.org/10.1021/J100244A023/ASSET/J100244A023.FP.PNG_V03
- Malaizé, B., Paillard, D., Jouzel, J., & Raynaud, D. (1999). The Dole effect over the last two glacial-interglacial cycles. *Journal of Geophysical Research: Atmospheres*, *104*(D12), 14199–14208. <https://doi.org/10.1029/1999JD900116>
- Manabe, S., & Stouffer, R. J. (1980). Sensitivity of a global climate model to an increase of CO₂ concentration in the atmosphere. *Journal of Geophysical Research: Oceans*, *85*(C10), 5529–5554. <https://doi.org/10.1029/JC085IC10P05529>
- Marchal, O. (2005). Optimal estimation of atmospheric ¹⁴C production over the Holocene: Paleoclimate implications. *Climate Dynamics*, *24*(1), 71–88. <https://doi.org/10.1007/S00382-004-0476-Z/METRICS>
- Marcott, S. A., Clark, P. U., Padman, L., Klinkhammer, G. P., Springer, S. R., Liu, Z., Otto-Bliesner, B. L., Carlson, A. E., Ungerer, A., Padman, J., He, F., Cheng, J., & Schmittner, A. (2011). Ice-shelf collapse from subsurface warming as a trigger for Heinrich events. *Proceedings of the National Academy of Sciences of the United States of America*, *108*(33), 13415–13419. https://doi.org/10.1073/PNAS.1104772108/SUPPL_FILE/PNAS.1104772108_SI.PDF
- Marcott, S. A., Shakun, J. D., Clark, P. U., & Mix, A. C. (2013). A reconstruction of regional and global temperature for the past 11,300 years. *Science*, *339*(6124), 1198–1201. https://doi.org/10.1126/SCIENCE.1228026/SUPPL_FILE/MARCOTT.SM.PDF
- Margari, V., Skinner, L. C., Tzedakis, P. C., Ganopolski, A., Vautravers, M., & Shackleton, N. J. (2010). The nature of millennial-scale climate variability during the past two glacial

- periods. *Nature Geoscience* 2010 3:2, 3(2), 127–131. <https://doi.org/10.1038/ngeo740>
- Mariotti, A. (1983). Atmospheric nitrogen is a reliable standard for natural ¹⁵N abundance measurements. *Nature* 1983 303:5919, 303(5919), 685–687. <https://doi.org/10.1038/303685a0>
- Markle, B. R., Steig, E. J., Buizert, C., Schoenemann, S. W., Bitz, C. M., Fudge, T. J., Pedro, J. B., Ding, Q., Jones, T. R., White, J. W. C., & Sowers, T. (2017). Global atmospheric teleconnections during Dansgaard–Oeschger events. *Nature Geoscience*, 10(1), 36–40. <https://doi.org/10.1038/ngeo2848>
- Markle, B. R., Steig, E. J., Roe, G. H., Winckler, G., & McConnell, J. R. (2018). Concomitant variability in high-latitude aerosols, water isotopes and the hydrologic cycle. *Nature Geoscience* 2018 11:11, 11(11), 853–859. <https://doi.org/10.1038/s41561-018-0210-9>
- Martinerie, P., Lipenkov, V. Y., Raynaud, D., Chappellaz, J., Barkov, N. I., & Lorius, C. (1994). Air content paleo record in the Vostok ice core (Antarctica): A mixed record of climatic and glaciological parameters. *Journal of Geophysical Research: Atmospheres*, 99(D5), 10565–10576. <https://doi.org/https://doi.org/10.1029/93JD03223>
- Martinerie, P., Raynaud, D., Etheridge, D. M., Barnola, J. M., & Mazaudier, D. (1992). Physical and climatic parameters which influence the air content in polar ice. *Earth and Planetary Science Letters*, 112(1–4), 1–13. [https://doi.org/10.1016/0012-821X\(92\)90002-D](https://doi.org/10.1016/0012-821X(92)90002-D)
- Martínez-García, A., Rosell-Melé, A., Jaccard, S. L., Geibert, W., Sigman, D. M., & Haug, G. H. (2011). Southern Ocean dust–climate coupling over the past four million years. *Nature* 2011 476:7360, 476(7360), 312–315. <https://doi.org/10.1038/nature10310>
- Martin, J. H. (1990). Glacial-interglacial CO₂ change: The Iron Hypothesis. *Paleoceanography*, 5(1), 1–13. <https://doi.org/10.1029/PA0051001P00001>
- Martrat, B., Grimalt, J. O., Shackleton, N. J., De Abreu, L., Hutterli, M. A., & Stocker, T. F. (2007). Four climate cycles of recurring deep and surface water destabilizations on the Iberian margin. *Science*, 317(5837), 502–507. https://doi.org/10.1126/SCIENCE.1139994/SUPPL_FILE/MARTRAT.SOM.PDF
- Masson-Delmotte, V., Buiron, D., Ekaykin, A., Frezzotti, M., Gallée, H., Jouzel, J., Krinner, G., Landais, A., Motoyama, H., Oerter, H., Pol, K., Pollard, D., Ritz, C., Schlosser, E., Sime, L. C., Sodemann, H., Stenni, B., Uemura, R., & Vimeux, F. (2011). A comparison of the present and last interglacial periods in six Antarctic ice cores. *Climate of the Past*, 7(2), 397–423. <https://doi.org/10.5194/CP-7-397-2011>
- Masson-Delmotte, V., Stenni, B., & Jouzel, J. (2004). Common millennial-scale variability of Antarctic and Southern Ocean temperatures during the past 5000 years reconstructed from the EPICA Dome C ice core. *The Holocene*, 14(2), 145–151. <https://doi.org/10.1191/0959683604hl697ft>
- Masson-Delmotte, V., Stenni, B., Pol, K., Braconnot, P., Cattani, O., Falourd, S., Kageyama, M., Jouzel, J., Landais, A., Minster, B., Barnola, J. M., Chappellaz, J., Krinner, G., Johnsen, S.,

- Röthlisberger, R., Hansen, J., Mikolajewicz, U., & Otto-Bliesner, B. (2010). EPICA Dome C record of glacial and interglacial intensities. *Quaternary Science Reviews*, 29(1–2), 113–128. <https://doi.org/10.1016/J.QUASCIREV.2009.09.030>
- McGee, D., Broecker, W. S., & Winckler, G. (2010). Gustiness: The driver of glacial dustiness? *Quaternary Science Reviews*, 29(17–18), 2340–2350. <https://doi.org/10.1016/J.QUASCIREV.2010.06.009>
- McKinney, C. R., McCrea, J. M., Epstein, S., Allen, H. A., & Urey, H. C. (1950). Improvements in Mass Spectrometers for the Measurement of Small Differences in Isotope Abundance Ratios. *Review of Scientific Instruments*, 21(8), 724–730. <https://doi.org/10.1063/1.1745698>
- Mellor, M. (1964). *Snow and Ice on the Earth's surface* (Vol. 2). U.S.Army Materiel Command, Cold Regions Research & Engineering Laboratory.
- Menviel, L., Capron, E., Govin, A., Dutton, A., Tarasov, L., Abe-Ouchi, A., Drysdale, R. N., Gibbard, P. L., Gregoire, L., He, F., Ivanovic, R. F., Kageyama, M., Kawamura, K., Landais, A., Otto-Bliesner, B. L., Oyabu, I., Tzedakis, P. C., Wolff, E., & Zhang, X. (2019). The penultimate deglaciation: protocol for Paleoclimate Modelling Intercomparison Project (PMIP) phase 4 transient numerical simulations between 140 and 127ka, version 1.0. *Geoscientific Model Development*, 12(8), 3649–3685. <https://doi.org/10.5194/gmd-12-3649-2019>
- Metcalf, B. (2013). *Planktonic Foraminifera: From production to preservation of the oceanographic signal*. <https://research.vu.nl/en/publications/planktonic-foraminifera-from-production-to-preservation-of-the-oc>
- Milankovitch, M. (1941). Kanon der Erdbestrahlung und seine Anwendung auf das Eiszeitenproblem. *Royal Serbian Academy Special Publication*, 133, 1–633. https://doi.org/10.14825/KASEKI.75.0_54
- Mitsui, T., Tzedakis, P. C., & Wolff, E. W. (2022). Insolation evolution and ice volume legacies determine interglacial and glacial intensity. *Climate of the Past*, 18(9), 1983–1996. <https://doi.org/10.5194/cp-18-1983-2022>
- Moncel, M. hélène, & Schreve, D. (2016). The Acheulean in Europe: Origins, evolution and dispersal. *Quaternary International*, 411, 1–8. <https://doi.org/10.1016/J.QUAINT.2016.08.039>
- Monnin, E., Steig, E. J., Siegenthaler, U., Kawamura, K., Schwander, J., Stauffer, B., Stocker, T. F., Morse, D. L., Barnola, J. M., Bellier, B., Raynaud, D., & Fischer, H. (2004). Evidence for substantial accumulation rate variability in Antarctica during the Holocene, through synchronization of CO₂ in the Taylor Dome, Dome C and DML ice cores. *Earth and Planetary Science Letters*, 224(1–2), 45–54. <https://doi.org/10.1016/J.EPSL.2004.05.007>
- Morgan, J. D., Buizert, C., Fudge, T. J., Kawamura, K., Severinghaus, J. P., & Trudinger, C. M. (2022). Gas isotope thermometry in the South Pole and Dome Fuji ice cores provides evidence for seasonal rectification of ice core gas records. *Cryosphere*, 16(7), 2947–2966. <https://doi.org/10.5194/TC-16-2947-2022>

- Morgan, V. I. (1991). High-temperature ice creep tests. *Cold Regions Science and Technology*, 19(3), 295–300. [https://doi.org/10.1016/0165-232X\(91\)90044-H](https://doi.org/10.1016/0165-232X(91)90044-H)
- Mudelsee, M. (2000). Ramp function regression: a tool for quantifying climate transitions. *Computers & Geosciences*, 26(3), 293–307. [https://doi.org/10.1016/S0098-3004\(99\)00141-7](https://doi.org/10.1016/S0098-3004(99)00141-7)
- Mulitza, S., Prange, M., Stuut, J.-B., Zabel, M., von Dobeneck, T., Itambi, A. C., Nizou, J., Schulz, M., & Wefer, G. (2008). Sahel megadroughts triggered by glacial slowdowns of Atlantic meridional overturning. *Paleoceanography*, 23(4). <https://doi.org/https://doi.org/10.1029/2008PA001637>
- Mulvaney, R., Rix, J., Polfrey, S., Grieman, M., Martin, C., Nehrbass-Ahles, C., Rowell, I., Tuckwell, R., & Wolff, E. (2021). Ice drilling on Skytrain Ice Rise and Sherman Island, Antarctica. *Annals of Glaciology*, 62(85–86), 311–323. <https://doi.org/10.1017/AOG.2021.7>
- Neff, P. D., & Bertler, N. A. N. (2015). Trajectory modeling of modern dust transport to the Southern Ocean and Antarctica. *Journal of Geophysical Research: Atmospheres*, 120(18), 9303–9322. <https://doi.org/10.1002/2015JD023304>
- Nehrbass-Ahles, C., Shin, J., Schmitt, J., Bereiter, B., Joos, F., Schilt, A., Schmidely, L., Silva, L., Teste, G., Grilli, R., Chappellaz, J., Hodell, D., Fischer, H., & Stocker, T. F. (2020a). Abrupt CO₂ release to the atmosphere under glacia and early interglacial climate conditions. *Science*, 369(6506), 1000–1005. https://doi.org/10.1126/SCIENCE.AAY8178/SUPPL_FILE/AAY8178_TABLES2.XLSX
- Nehrbass-Ahles, C., Shin, J., Schmitt, J., Bereiter, B., Joos, F., Schilt, A., Schmidely, L., Silva, L., Teste, G., Grilli, R., Chappellaz, J., Hodell, D., Fischer, H., & Stocker, T. F. (2020b). Abrupt CO₂ release to the atmosphere under glacia and early interglacial climate conditions. *Science*, 369(6506), 1000–1005. https://doi.org/10.1126/SCIENCE.AAY8178/SUPPL_FILE/AAY8178_TABLES2.XLSX
- Ng, J., Severinghaus, J., Bay, R., & Tosi, D. (2024). Evaluating marine dust records as templates for optical dating of Oldest Ice. *Climate of the Past*, 20(7), 1437–1449. <https://doi.org/10.5194/cp-20-1437-2024>
- Nie, S., Bartelt, N. C., & Thürmer, K. (2009). Observation of surface self-diffusion on ice. *Physical Review Letters*, 102(13), 136101. <https://doi.org/10.1103/PHYSREVLETT.102.136101/FIGURES/4/MEDIUM>
- Obase, T., & Abe-Ouchi, A. (2019). Abrupt Bølling-Allerød Warming Simulated under Gradual Forcing of the Last Deglaciation. *Geophysical Research Letters*, 46(20), 11397–11405. <https://doi.org/10.1029/2019GL084675>
- Obase, T., Abe-Ouchi, A., Saito, F., Tsutaki, S., Fujita, S., Kawamura, K., & Motoyama, H. (2023). A one-dimensional temperature and age modeling study for selecting the drill site of the oldest ice core near Dome Fuji, Antarctica. *The Cryosphere*, 17(6), 2543–2562. <https://doi.org/10.5194/tc-17-2543-2023>

- Ollivier, I., Steen-Larsen, H. C., Stenni, B., Arnaud, L., Casado, M., Cauquoin, A., Dreossi, G., Genthon, C., Minster, B., Picard, G., Werner, M., & Landais, A. (2024). Surface processes and drivers of the snow water stable isotopic composition at Dome C, East Antarctica – a multi-datasets and modelling analysis. *EGUsphere*, 2024, 1–39. <https://doi.org/10.5194/egusphere-2024-685>
- Ooms, A., Casado, M., Picard, G., Arnaud, L., Hörhold, M., Spolaor, A., Traversi, R., Savarino, J., & Masson-Delmotte, V. (2024, March 7). Study of local accumulation patterns from a snow trench at Dome C. *EGU24*. <https://doi.org/10.5194/EGUSPHERE-EGU24-15612>
- Oraschewski, F. M., & Grinsted, A. (2022). Modeling enhanced firn densification due to strain softening. *Cryosphere*, 16(7), 2683–2700. <https://doi.org/10.5194/TC-16-2683-2022>
- Oyabu, I., Kawamura, K., Buizert, C., Parrenin, F., Orsi, A., Kitamura, K., Aoki, S., & Nakazawa, T. (2022). The Dome Fuji ice core DF2021 chronology (0–207 kyr BP). *Quaternary Science Reviews*, 294, 107754. <https://doi.org/10.1016/J.QUASCIREV.2022.107754>
- Paillard, D. (2001). Glacial cycles: Toward a new paradigm. *Reviews of Geophysics*, 39(3), 325–346. <https://doi.org/https://doi.org/10.1029/2000RG000091>
- Paillard, D. (2015). Quaternary glaciations: from observations to theories. *Quaternary Science Reviews*, 107, 11–24. <https://doi.org/https://doi.org/10.1016/j.quascirev.2014.10.002>
- Paillard, D., & Parrenin, F. (2004). The Antarctic ice sheet and the triggering of deglaciations. *Earth and Planetary Science Letters*, 227(3), 263–271. <https://doi.org/https://doi.org/10.1016/j.epsl.2004.08.023>
- Parrenin, F., Barker, S., Blunier, T., Chappellaz, J., Jouzel, J., Landais, A., Masson-Delmotte, V., Schwander, J., & Veres, D. (2012). On the gas-ice depth difference (Δ depth) along the EPICA Dome C ice core. *Climate of the Past*, 8(4), 1239–1255. <https://doi.org/10.5194/CP-8-1239-2012>
- Parrenin, F., Barnola, J.-M., Beer, J., Blunier, T., Castellano, E., Chappellaz, J., Dreyfus, G., Fischer, H., Fujita, S., Jouzel, J., Kawamura, K., Lemieux-Dudon, B., Loulergue, L., Masson-Delmotte, V., Narcisi, B., Petit, J.-R., Raisbeck, G., Raynaud, D., Ruth, U., ... Wolff, E. (2007). The EDC3 chronology for the EPICA Dome C ice core. *Climate of the Past*, 3(3), 485–497. <https://doi.org/10.5194/cp-3-485-2007>
- Parrenin, F., Bouchet, M., Buizert, C., Capron, E., Corrick, E., Drysdale, R., Kawamura, K., Landais, A., Mulvaney, R., Oyabu, I., & Rasmussen, S. (2024). The Paleochrono-1.1 probabilistic model to derive optimized and consistent chronologies for several paleoclimatic sites. *EGUsphere*, 2024, 1–33. <https://doi.org/10.5194/egusphere-2023-2911>
- Parrenin, F., Dreyfus, G., Durand, G., Fujita, S., Gagliardini, O., Gillet, F., Jouze, J., Kawamura, K., Lhomme, N., Masson-Delmotte, V., Ritz, C., Schwander, J., Shoji, H., Uemura, R., Watanabe, O., & Yoshida, N. (2007). 1-D-ice flow modelling at EPICA Dome C and Dome Fuji, East Antarctica. *Climate of the Past*, 3(2), 243–259. <https://doi.org/10.5194/CP-3-243-2007>
- Parrenin, F., Masson-Delmotte, V., Köhler, P., Raynaud, D., Paillard, D., Schwander, J., Barbante,

- C., Landais, A., Wegner, A., & Jouzel, J. (2013a). Synchronous Change of Atmospheric CO₂ and Antarctic Temperature During the Last Deglacial Warming. *Science*, 339(6123), 1060–1063. <https://doi.org/10.1126/science.1226368>
- Parrenin, F., Masson-Delmotte, V., Köhler, P., Raynaud, D., Paillard, D., Schwander, J., Barbante, C., Landais, A., Wegner, A., & Jouzel, J. (2013b). Synchronous change of atmospheric CO₂ and antarctic temperature during the last deglacial warming. *Science*, 339(6123), 1060–1063. https://doi.org/10.1126/SCIENCE.1226368/SUPPL_FILE/PARRENIN.SM.PDF
- Past Interglacials Working Group of PAGES. (2016). Interglacials of the last 800,000 years. *Reviews of Geophysics*, 54(1), 162–219. <https://doi.org/10.1002/2015RG000482>
- Pausata, F. S. R., & Löfverström, M. (2015). On the enigmatic similarity in Greenland $\delta^{18}O$ between the Oldest and Younger Dryas. *Geophysical Research Letters*, 42(23), 10, 410–470, 477. <https://doi.org/https://doi.org/10.1002/2015GL066042>
- Pedro, J. B., Andersson, C., Vettoretti, G., Voelker, A. H. L., Waelbroeck, C., Dokken, T. M., Jensen, M. F., Rasmussen, S. O., Sessford, E. G., Jochum, M., & Nisancioglu, K. H. (2022). Dansgaard-Oeschger and Heinrich event temperature anomalies in the North Atlantic set by sea ice, frontal position and thermocline structure. *Quaternary Science Reviews*, 289, 107599. <https://doi.org/10.1016/J.QUASCIREV.2022.107599>
- Pedro, J. B., Rasmussen, S. O., & van Ommen, T. D. (2012). Tightened constraints on the time-lag between Antarctic temperature and CO₂ during the last deglaciation. *Climate of the Past*, 8(4), 1213–1221. <https://doi.org/10.5194/cp-8-1213-2012>
- Peltier, W. R., & Vettoretti, G. (2014). Dansgaard-Oeschger oscillations predicted in a comprehensive model of glacial climate: A “kicked” salt oscillator in the Atlantic. *Geophysical Research Letters*, 41(20), 7306–7313. <https://doi.org/10.1002/2014GL061413>
- Persson, A., Langen, P. L., Ditlevsen, P., & Vinther, B. M. (2011). The influence of precipitation weighting on interannual variability of stable water isotopes in Greenland. *Journal of Geophysical Research: Atmospheres*, 116(D20). <https://doi.org/https://doi.org/10.1029/2010JD015517>
- Petit, J. R., Jouzel, J., Raynaud, D., Barkov, N. I., Barnola, J. M., Basile, I., Bender, M., Chappellaz, J., Davis, M., Delaygue, G., Delmotte, M., Kotiyakov, V. M., Legrand, M., Lipenkov, V. Y., Lorius, C., Pépin, L., Ritz, C., Saltzman, E., & Stievenard, M. (1999). Climate and atmospheric history of the past 420,000 years from the Vostok ice core, Antarctica. *Nature* 399:6735, 399(6735), 429–436. <https://doi.org/10.1038/20859>
- Pimienta, P., & Duval, P. (1987). RATE CONTROLLING PROCESSES IN THE CREEP OF POLAR GLACIER ICE CONTROLLING PROCESSES IN THE CREEP OF POLAR GLACIER ICE. *Journal de Physique Colloques*, 48(C1). <https://doi.org/10.1051/jphyscol:1987134i>
- Quiquet, A., Dumas, C., Ritz, C., Peyaud, V., & Roche, D. M. (2018). The GRISLI ice sheet model (version 2.0): calibration and validation for multi-millennial changes of the Antarctic ice sheet. *Geoscientific Model Development*, 11(12), 5003–5025. <https://doi.org/10.5194/gmd-11-5003-2018>

- Railsback, L. B., Gibbard, P. L., Head, M. J., Voarintsoa, N. R. G., & Toucanne, S. (2015). An optimized scheme of lettered marine isotope substages for the last 1.0 million years, and the climatostratigraphic nature of isotope stages and substages. *Quaternary Science Reviews*, *111*, 94–106. <https://doi.org/10.1016/J.QUASCIREV.2015.01.012>
- Raisbeck, G. M., Yiou, F., Jouzel, J., & Stocker, T. F. (2007). Direct north-south synchronization of abrupt climate change record in ice cores using Beryllium 10. *Climate of the Past*, *3*(3), 541–547. <https://doi.org/10.5194/CP-3-541-2007>
- Ramseier, R. O. (1967). Self-Diffusion of Tritium in Natural and Synthetic Ice Monocrystals. *Journal of Applied Physics*, *38*(6), 2553–2556. <https://doi.org/10.1063/1.1709948>
- Rasmussen, S. O., Dahl-Jensen, D., Fischer, H., Fuhrer, K., Hansen, S. B., Hansson, M., Hvidberg, C. S., Jonsell, U., Kipfstuhl, S., Ruth, U., Schwander, J., Siggaard-Andersen, M. L., Sinnl, G., Steffensen, J. P., Svensson, A. M., & Vinther, B. M. (2023). Ice-core data used for the construction of the Greenland Ice-Core Chronology 2005 and 2021 (GICC05 and GICC21). *Earth System Science Data*, *15*(8), 3351–3364. <https://doi.org/10.5194/ESSD-15-3351-2023>
- Raynaud, D., Lipenkov, V., Lemieux-Dudon, B., Duval, P., Loutre, M. F., & Lhomme, N. (2007). The local insolation signature of air content in Antarctic ice. A new step toward an absolute dating of ice records. *Earth and Planetary Science Letters*, *261*(3–4), 337–349. <https://doi.org/10.1016/J.EPSL.2007.06.025>
- Raynaud, D., Yin, Q., Capron, E., Wu, Z., Parrenin, F., Berger, A., & Lipenkov, V. (2024). Local summer temperature changes over the past 440 ka revealed by the total air content in the Antarctic EPICA Dome C ice core. *Climate of the Past*, *20*(6), 1269–1282. <https://doi.org/10.5194/CP-20-1269-2024>
- Reimer, P. J., Bard, E., Bayliss, A., Beck, J. W., Blackwell, P. G., Ramsey, C. B., Buck, C. E., Cheng, H., Edwards, R. L., Friedrich, M., Grootes, P. M., Guilderson, T. P., Hafliðason, H., Hajdas, I., Hatté, C., Heaton, T. J., Hoffmann, D. L., Hogg, A. G., Hughen, K. A., ... Plicht, J. van der. (2013). IntCal13 and Marine13 Radiocarbon Age Calibration Curves 0–50,000 Years cal BP. *Radiocarbon*, *55*(4), 1869–1887. https://doi.org/10.2458/AZU_JS_RC.55.16947
- Reutenauer, C., Landais, A., Blunier, T., Bréant, C., Kageyama, M., Woillez, M. N., Risi, C., Mariotti, V., & Braconnot, P. (2015). Quantifying molecular oxygen isotope variations during a Heinrich stadial. *Climate of the Past*, *11*(11), 1527–1551. <https://doi.org/10.5194/CP-11-1527-2015>
- Rhodes, R. H., Brook, E. J., Chiang, J. C. H., Blunier, T., Maselli, O. J., McConnell, J. R., Romanini, D., & Severinghaus, J. P. (2015). Enhanced tropical methane production in response to iceberg discharge in the North Atlantic. *Science*, *348*(6238), 1016–1019. <https://doi.org/10.1126/science.1262005>
- Risi, C., Bony, S., Vimeux, F., & Jouzel, J. (2010). Water-stable isotopes in the LMDZ4 general circulation model: Model evaluation for present-day and past climates and applications to climatic interpretations of tropical isotopic records. *Journal of Geophysical Research: Atmospheres*, *115*(D12), 12118. <https://doi.org/10.1029/2009JD013255>

- Ritter, F., Christian Steen-Larsen, H., Werner, M., Masson-Delmotte, V., Orsi, A., Behrens, M., Birnbaum, G., Freitag, J., Risi, C., & Kipfstuhl, S. (2016). Isotopic exchange on the diurnal scale between near-surface snow and lower atmospheric water vapor at Kohnen station, East Antarctica. *Cryosphere*, *10*(4), 1647–1663. <https://doi.org/10.5194/TC-10-1647-2016>
- Ritz, C. (1992). *Un modèle thermo-mécanique d'évolution pour le bassin glaciaire Antarctique Vostok-Glacier Byrd: Sensibilité aux valeurs des paramètres mal connus*. <https://theses.hal.science/tel-00693923>
- Ritz, C., Rommelaere, V., & Dumas, C. (2001). Modeling the evolution of Antarctic ice sheet over the last 420,000 years: Implications for altitude changes in the Vostok region. *Journal of Geophysical Research: Atmospheres*, *106*(D23), 31943–31964. <https://doi.org/https://doi.org/10.1029/2001JD900232>
- Roe, G. H., & Steig, E. J. (2004). Characterization of Millennial-Scale Climate Variability. *Journal of Climate*, *17*, 1929–1944. <https://api.semanticscholar.org/CorpusID:51792773>
- Röthlisberger, R., Mudelsee, M., Bigler, M., De Angelis, M., Fischer, H., Hansson, M., Lambert, F., Masson-Delmotte, V., Sime, L., Udisti, R., & Wolff, E. W. (2008). The Southern Hemisphere at glacial terminations: Insights from the Dome C ice core. *Climate of the Past*, *4*(4), 345–356. <https://doi.org/10.5194/CP-4-345-2008>
- Ruddiman, W. F., McIntyre, A., & Doherty, L. (1977). Late Quaternary surface ocean kinematics and climatic change in the high-latitude North Atlantic. *Journal of Geophysical Research*, *82*(27), 3877–3887. <https://doi.org/10.1029/JC082I027P03877>
- Rudolph, E. M., Hedding, D. W., Hodgson, D. A., Fabel, D., Gheorghiu, D. M., Shanks, R., & Nel, W. (2024). A glacial chronology for sub-Antarctic Marion Island from MIS 2 and MIS 3. *Quaternary Science Reviews*, *325*, 108485. <https://doi.org/https://doi.org/10.1016/j.quascirev.2023.108485>
- Sagnotti, L., Giaccio, B., Liddicoat, J. C., Nomade, S., Renne, P. R., Scardia, G., & Sprain, C. J. (2016). How fast was the Matuyama–Brunhes geomagnetic reversal? A new subcentennial record from the Sulmona Basin, central Italy. *Geophysical Journal International*, *204*(2), 798–812. <https://doi.org/10.1093/gji/ggv486>
- Salamatin, A. N., & Ritz, C. (1996). A simplified multi-scale model for predicting climatic variations of the ice-sheet surface elevation in central Antarctica. *Ann. Glaciol.*, *23*, 28–35.
- Sánchez-Goñi, M. F. (2020). Regional impacts of climate change and its relevance to human evolution. *Evolutionary Human Sciences*, *2*, e55. <https://doi.org/10.1017/EHS.2020.56>
- Schmittner, A., Saenko, O. A., & Weaver, A. J. (2003). Coupling of the hemispheres in observations and simulations of glacial climate change. *Quaternary Science Reviews*, *22*(5), 659–671. [https://doi.org/https://doi.org/10.1016/S0277-3791\(02\)00184-1](https://doi.org/https://doi.org/10.1016/S0277-3791(02)00184-1)
- Schwander, J. (1989). The transformation of snow to ice and the occlusion of gases. In H. Oeschger & C. C. Langway (Eds.), *The environmental record in glaciers and ice sheets*. (Vol. 8, pp. 53–67). John Wiley & Sons.

- Severinghaus, J. P., & Battle, M. O. (2006). Fractionation of gases in polar ice during bubble close-off: New constraints from firn air Ne, Kr and Xe observations. *Earth and Planetary Science Letters*, 244(1–2), 474–500. <https://doi.org/10.1016/J.EPSL.2006.01.032>
- Severinghaus, J. P., Beaudette, R., Headly, M. A., Taylor, K., & Brook, E. J. (2009). Oxygen-18 of O₂ records the impact of abrupt climate change on the terrestrial biosphere. *Science*, 324(5933), 1431–1434. https://doi.org/10.1126/SCIENCE.1169473/SUPPL_FILE/SEVERINGHAUS_SOM.PDF
- Severinghaus, J. P., Bender, M. L., Keeling, R. F., & Broecker, W. S. (1996). Fractionation of soil gases by diffusion of water vapor, gravitational settling, and thermal diffusion. *Geochimica et Cosmochimica Acta*, 60(6), 1005–1018. [https://doi.org/10.1016/0016-7037\(96\)00011-7](https://doi.org/10.1016/0016-7037(96)00011-7)
- Severinghaus, J. P., & Brook, E. J. (1999). Abrupt climate change at the end of the last glacial period inferred from trapped air in polar ice. *Science (New York, N.Y.)*, 286(5441), 930–934. <https://doi.org/10.1126/SCIENCE.286.5441.930>
- Severinghaus, J. P., Grachev, A., & Battle, M. (2001). Thermal fractionation of air in polar firn by seasonal temperature gradients. *Geochemistry, Geophysics, Geosystems*, 2(7). <https://doi.org/10.1029/2000GC000146>
- Severinghaus, J. P., Grachev, A., Luz, B., & Caillon, N. (2003). A method for precise measurement of argon 40/36 and krypton/argon ratios in trapped air in polar ice with applications to past firn thickness and abrupt climate change in Greenland and at Siple Dome, Antarctica. *Geochimica et Cosmochimica Acta*, 67(3), 325–343. [https://doi.org/10.1016/S0016-7037\(02\)00965-1](https://doi.org/10.1016/S0016-7037(02)00965-1)
- Shackleton, N. J. (1969). The Last Interglacial in the Marine and Terrestrial Records. *Proceedings of the Royal Society of London. Series B, Biological Sciences*, 174(1034), 135–154. <http://www.jstor.org/insu.bib.cnrs.fr/stable/75756>
- Shackleton, N. J., Fairbanks, R. G., Chiu, T. C., & Parrenin, F. (2004). Absolute calibration of the Greenland time scale: implications for Antarctic time scales and for $\Delta^{14}\text{C}$. *Quaternary Science Reviews*, 23(14–15), 1513–1522. <https://doi.org/10.1016/J.QUASCIREV.2004.03.006>
- Shackleton, N. J., Sánchez-Goñi, M. F., Pailler, D., & Lancelot, Y. (2003). Marine Isotope Substage 5e and the Eemian Interglacial. *Global and Planetary Change*, 36(3), 151–155. [https://doi.org/10.1016/S0921-8181\(02\)00181-9](https://doi.org/10.1016/S0921-8181(02)00181-9)
- Shakun, J. D., Clark, P. U., He, F., Marcott, S. A., Mix, A. C., Liu, Z., Otto-Bliesner, B., Schmittner, A., & Bard, E. (2012). Global warming preceded by increasing carbon dioxide concentrations during the last deglaciation. *Nature* 2012 484:7392, 484(7392), 49–54. <https://doi.org/10.1038/nature10915>
- Shakun, J. D., Lea, D. W., Lisiecki, L. E., & Raymo, M. E. (2015). An 800-kyr record of global surface ocean $\delta^{18}\text{O}$ and implications for ice volume-temperature coupling. *Earth and Planetary Science Letters*, 426, 58–68. <https://doi.org/10.1016/J.EPSL.2015.05.042>

- Sharp, Z. (2017). Principles of Stable Isotope Geochemistry, 2nd Edition. *Open Textbooks*. <https://doi.org/10.25844/h9q1-0p82>
- Shin, J., Nehrbass-Ahles, C., Grilli, R., Beeman, J. C., Parrenin, F., Teste, G., Landais, A., Schmidely, L., Silva, L., Schmitt, J., Bereiter, B., Stocker, T. F., Fischer, H., & Chappellaz, J. (2020). Millennial-scale atmospheric CO₂ variations during the Marine Isotope Stage 6 period (190–135 ka). *Climate of the Past*, 16(6), 2203–2219. <https://doi.org/10.5194/CP-16-2203-2020>
- Siddall, M., Rohling, E. J., Thompson, W. G., & Waelbroeck, C. (2008). Marine isotope stage 3 sea level fluctuations: Data synthesis and new outlook. *Reviews of Geophysics*, 46(4). <https://doi.org/10.1029/2007RG000226>
- Siegenthaler, U., Stocker, T. F., Monnin, E., Lüthi, D., Schwander, J., Stauffer, B., Raynaud, D., Barnola, J. M., Fischer, H., Masson-Delmotte, V., & Jouzel, J. (2005). Atmospheric science: Stable carbon cycle-climate relationship during the late pleistocene. *Science*, 310(5752), 1313–1317. https://doi.org/10.1126/SCIENCE.1120130/SUPPL_FILE/SIEGENTHALER.SOM.PDF
- Sigl, M., Fudge, T. J., Winstrup, M., Cole-Dai, J., Ferris, D., McConnell, J. R., Taylor, K. C., Welten, K. C., Woodruff, T. E., Adolphi, F., Bisiaux, M., Brook, E. J., Buizert, C., Caffee, M. W., Dunbar, N. W., Edwards, R., Geng, L., Iverson, N., Koffman, B., ... Sowers, T. A. (2016). The WAIS Divide deep ice core WD2014 chronology – Part 2: Annual-layer counting (0–31 ka BP). *Climate of the Past*, 12(3), 769–786. <https://doi.org/10.5194/cp-12-769-2016>
- Sigl, M., McConnell, J. R., Toohey, M., Curran, M., Das, S. B., Edwards, R., Isaksson, E., Kawamura, K., Kipfstuhl, S., Krüger, K., Layman, L., Maselli, O. J., Motizuki, Y., Motoyama, H., Pasteris, D. R., & Severi, M. (2014). Insights from Antarctica on volcanic forcing during the Common Era. *Nature Climate Change* 2014 4:8, 4(8), 693–697. <https://doi.org/10.1038/nclimate2293>
- Sime, L. C., Marshall, G. J., Mulvaney, R., & Thomas, E. R. (2009). Interpreting temperature information from ice cores along the Antarctic Peninsula: ERA40 analysis. *Geophysical Research Letters*, 36(18). <https://doi.org/10.1029/2009GL038982>
- Sime, L. C., Tindall, J. C., Wolff, E. W., Connolley, W. M., & Valdes, P. J. (2008). Antarctic isotopic thermometer during a CO₂ forced warming event. *Journal of Geophysical Research: Atmospheres*, 113(D24). <https://doi.org/10.1029/2008JD010395>
- Simon, M. H., Ziegler, M., Bosmans, J., Barker, S., Reason, C. J. C., & Hall, I. R. (2015). Eastern South African hydroclimate over the past 270,000 years. *Scientific Reports*, 5(1), 18153. <https://doi.org/10.1038/srep18153>
- Sinnl, G., Winstrup, M., Erhardt, T., Cook, E., Jensen, C. M., Svensson, A., Vinther, B. M., Muscheler, R., & Rasmussen, S. O. (2022). A multi-ice-core, annual-layer-counted Greenland ice-core chronology for the last 3800 years: GICC21. *Climate of the Past*, 18(5), 1125–1150. <https://doi.org/10.5194/cp-18-1125-2022>
- Snyder, C. W. (2016). Evolution of global temperature over the past two million years. *Nature* 2016 538:7624, 538(7624), 226–228. <https://doi.org/10.1038/NATURE19798>

- Sodemann, H., Schwierz, C., & Wernli, H. (2008). Interannual variability of Greenland winter precipitation sources: Lagrangian moisture diagnostic and North Atlantic Oscillation influence. *Journal of Geophysical Research: Atmospheres*, 113(D3). <https://doi.org/https://doi.org/10.1029/2007JD008503>
- Sowers, T., Bender, M., & Raynaud, D. (1989). Elemental and isotopic composition of occluded O₂ and N₂ in polar ice. *Journal of Geophysical Research: Atmospheres*, 94(D4), 5137–5150. <https://doi.org/10.1029/JD094ID04P05137>
- Sowers, T., Bender, M., Raynaud, D., & Korotkevich, Y. S. (1992). $\delta^{15}\text{N}$ of N₂ in air trapped in polar ice: A tracer of gas transport in the firn and a possible constraint on ice age-gas age differences. *Journal of Geophysical Research: Atmospheres*, 97(D14), 15683–15697. <https://doi.org/10.1029/92JD01297>
- Spratt, R. M., & Lisiecki, L. E. (2016). A Late Pleistocene sea level stack. *Climate of the Past*, 12(4), 1079–1092. <https://doi.org/10.5194/CP-12-1079-2016>
- Steen-Larsen, H. C., Sveinbjörnsdóttir, A. E., Peters, A. J., Masson-Delmotte, V., Guishard, M. P., Hsiao, G., Jouzel, J., Noone, D., Warren, J. K., & White, J. W. C. (2014). Climatic controls on water vapor deuterium excess in the marine boundary layer of the North Atlantic based on 500 days of in situ, continuous measurements. *Atmospheric Chemistry and Physics*, 14(15), 7741–7756. <https://doi.org/10.5194/ACP-14-7741-2014>
- Stenni, B., Masson-Delmotte, V., Selmo, E., Oerter, H., Meyer, H., Röthlisberger, R., Jouzel, J., Cattani, O., Falourd, S., Fischer, H., Hoffmann, G., Iacumin, P., Johnsen, S. J., Minster, B., & Udisti, R. (2010). The deuterium excess records of EPICA Dome C and Dronning Maud Land ice cores (East Antarctica). *Quaternary Science Reviews*, 29(1–2), 146–159. <https://doi.org/10.1016/J.QUASCIREV.2009.10.009>
- Stocker, T. F., & Johnsen, S. J. (2003). A minimum thermodynamic model for the bipolar seesaw. *Paleoceanography*, 18(4). <https://doi.org/https://doi.org/10.1029/2003PA000920>
- Stocker, T. F., & Wright, D. G. (1991). Rapid transitions of the ocean's deep circulation induced by changes in surface water fluxes. *Nature*, 351(6329), 729–732. <https://doi.org/10.1038/351729a0>
- Stolper, D. A., Bender, M. L., Dreyfus, G. B., Yan, Y., & Higgins, J. A. (2016). A Pleistocene ice core record of atmospheric O₂ concentrations. *Science*, 353(6306), 1427–1430. https://doi.org/10.1126/SCIENCE.AAF5445/SUPPL_FILE/AAF5445-STOLPER-SM.PDF
- Svensson, A., Andersen, K. K., Bigler, M., Clausen, H. B., Dahl-Jensen, D., Davies, S. M., Johnsen, S. J., Muscheler, R., Parrenin, F., Rasmussen, S. O., Röthlisberger, R., Seierstad, I., Steffensen, J. P., & Vinther, B. M. (2008). A 60 000 year Greenland stratigraphic ice core chronology. *Climate of the Past*, 4(1), 47–57. <https://doi.org/10.5194/CP-4-47-2008>
- Svensson, A., Andersen, K. K., Clausen, H. B., Johnsen, S. J., Rasmussen, S. O., Steffensen, J. P., Vinther, B., Svensson, A., Andersen, K. K., Clausen, H. B., Johnsen, S. J., Rasmussen, S. O., Steffensen, J. P., & Vinther, B. (2005). The Greenland Ice Core Chronology 2005 (GICC05). *AGUFM*, 2005, PP22B-05.

<https://ui.adsabs.harvard.edu/abs/2005AGUFMPP22B..05S/abstract>

- Svensson, A., Dahl-Jensen, D., Steffensen, J. P., Blunier, T., Rasmussen, S. O., Vinther, B. M., Vallelonga, P., Capron, E., Gkinis, V., Cook, E., Kjær, H. A., Muscheler, R., Kipfstuhl, S., Wilhelms, F., Stocker, T. F., Fischer, H., Adolphi, F., Erhardt, T., Sigl, M., ... Bigler, M. (2020). Bipolar volcanic synchronization of abrupt climate change in Greenland and Antarctic ice cores during the last glacial period. *Climate of the Past*, 16(4), 1565–1580. <https://doi.org/10.5194/cp-16-1565-2020>
- Tian, L., Ritterbusch, F., Gu, J. Q., Hu, S. M., Jiang, W., Lu, Z. T., Wang, D., & Yang, G. M. (2019). 81Kr Dating at the Guliya Ice Cap, Tibetan Plateau. *Geophysical Research Letters*, 46(12), 6636–6643. <https://doi.org/10.1029/2019GL082464>
- Timmermann, A., Friedrich, T., Timm, O. E., Chikamoto, M. O., Abe-Ouchi, A., & Ganopolski, A. (2014). Modeling Obliquity and CO₂ Effects on Southern Hemisphere Climate during the Past 408 ka. *Journal of Climate*, 27(5), 1863–1875. <https://doi.org/https://doi.org/10.1175/JCLI-D-13-00311.1>
- Tzedakis, P. C., Crucifix, M., Mitsui, T., & Wolff, E. W. (2017). A simple rule to determine which insolation cycles lead to interglacials. *Nature*, 542(7642), 427–432. <https://doi.org/10.1038/nature21364>
- Tzedakis, P. C., Hodell, D. A., Nehrbass-Ahles, C., Mitsui, T., & Wolff, E. W. (2022). Marine Isotope Stage 11c: An unusual interglacial. *Quaternary Science Reviews*, 284, 107493. <https://doi.org/10.1016/J.QUASCIREV.2022.107493>
- Tzedakis, P. C., Roucoux, K. H., De Abreu, L., & Shackleton, N. J. (2004). The duration of forest stages in southern Europe and interglacial climate variability. *Science*, 306(5705), 2231–2235. https://doi.org/10.1126/SCIENCE.1102398/SUPPL_FILE/TZEDAKIS_SOM.PDF
- Uemura, R., Masson-Delmotte, V., Jouzel, J., Landais, A., Motoyama, H., & Stenni, B. (2012). Ranges of moisture-source temperature estimated from Antarctic ice cores stable isotope records over glacial-interglacial cycles. *Climate of the Past*, 8(3), 1109–1125. <https://doi.org/10.5194/CP-8-1109-2012>
- Uemura, R., Motoyama, H., Masson-Delmotte, V., Jouzel, J., Kawamura, K., Goto-Azuma, K., Fujita, S., Kuramoto, T., Hirabayashi, M., Miyake, T., Ohno, H., Fujita, K., Abe-Ouchi, A., Iizuka, Y., Horikawa, S., Igarashi, M., Suzuki, K., Suzuki, T., & Fujii, Y. (2018). Asynchrony between Antarctic temperature and CO₂ associated with obliquity over the past 720,000 years. *Nature Communications*, 9(1), 961. <https://doi.org/10.1038/s41467-018-03328-3>
- Usoskin, I. G., & Kromer, B. (2000). RECONSTRUCTION OF THE 14 C PRODUCTION RATE FROM MEASURED RELATIVE ABUNDANCE. *RADIOCARBON*, 47(1), 31–37. <https://doi.org/10.1017/S0033822200052176>
- Vautravers, M. J., & Shackleton, N. J. (2006). Centennial-scale surface hydrology off Portugal during marine isotope stage 3: Insights from planktonic foraminiferal fauna variability. *Paleoceanography*, 21(3). <https://doi.org/https://doi.org/10.1029/2005PA001144>

- Veres, D., Bazin, L., Landais, A., Toyé Mahamadou Kele, H., Lemieux-Dudon, B., Parrenin, F., Martinerie, P., Blayo, E., Blunier, T., Capron, E., Chappellaz, J., Rasmussen, S. O., Severi, M., Svensson, A., Vinther, B., & Wolff, E. W. (2013). The Antarctic ice core chronology (AICC2012): an optimized multi-parameter and multi-site dating approach for the last 120 thousand years. *Climate of the Past*, 9(4), 1733–1748. <https://doi.org/10.5194/cp-9-1733-2013>
- Vettoretti, G., Ditlevsen, P., Jochum, M., & Rasmussen, S. O. (2022). Atmospheric CO₂ control of spontaneous millennial-scale ice age climate oscillations. *Nature Geoscience* 2022 15:4, 15(4), 300–306. <https://doi.org/10.1038/s41561-022-00920-7>
- Vidal, L., Schneider, R. R., Marchal, O., Bickert, T., Stocker, T. F., & Wefer, G. (1999). Link between the North and South Atlantic during the Heinrich events of the last glacial period. *Climate Dynamics*, 15(12), 909–919. <https://doi.org/10.1007/s003820050321>
- Vimeux, F., Masson, V., Jouzel, J., Stievenard, M., & Petit, J. R. (1999). Glacial–interglacial changes in ocean surface conditions in the Southern Hemisphere. *Nature* 1999 398:6726, 398(6726), 410–413. <https://doi.org/10.1038/18860>
- Wang, X., Auler, A. S., Edwards, R. L., Cheng, H., Cristalli, P. S., Smart, P. L., Richards, D. A., & Shen, C.-C. (2004). Wet periods in northeastern Brazil over the past 210 kyr linked to distant climate anomalies. *Nature*, 432(7018), 740–743. <https://doi.org/10.1038/nature03067>
- Wang, X., Auler, A. S., Edwards, R. L., Cheng, H., Ito, E., & Solheid, M. (2006). Interhemispheric anti-phasing of rainfall during the last glacial period. *Quaternary Science Reviews*, 25(23–24), 3391–3403. <https://doi.org/10.1016/J.QUASCIREV.2006.02.009>
- Wang, Y., Cheng, H., Edwards, R. L., Kong, X., Shao, X., Chen, S., Wu, J., Jiang, X., Wang, X., & An, Z. (2008). Millennial- and orbital-scale changes in the East Asian monsoon over the past 224,000 years. *Nature* 2008 451:7182, 451(7182), 1090–1093. <https://doi.org/10.1038/nature06692>
- Wang, Y. J., Cheng, H., Edwards, R. L., An, Z. S., Wu, J. Y., Shen, C. C., & Dorale, J. A. (2001). A high-resolution absolute-dated late pleistocene monsoon record from Hulu Cave, China. *Science*, 294(5550), 2345–2348. <https://doi.org/10.1126/SCIENCE.1064618/ASSET/F012425E-B1A9-4311-999E-0DD76B7FE297/ASSETS/GRAPHIC/SE4810025003.JPEG>
- Weber, M. E., Bailey, I., Hemming, S. R., Martos, Y. M., Reilly, B. T., Ronge, T. A., Brachfeld, S., Williams, T., Raymo, M., Belt, S. T., Smik, L., Vogel, H., Peck, V. L., Armbrecht, L., Cage, A., Cardillo, F. G., Du, Z., Fauth, G., Fogwill, C. J., ... Zheng, X. (2022). Antiphased dust deposition and productivity in the Antarctic Zone over 1.5 million years. *Nature Communications* 2022 13:1, 13(1), 1–18. <https://doi.org/10.1038/s41467-022-29642-5>
- Weiler, K., Schwander, J., Leuenberger, M., Blunier, T., Mulvaney, R., Anderson, P. S., Salmon, R., & Sturges, W. T. (2009). Seasonal Variations of Isotope Ratios and CO₂ Concentrations in Firn Air. *低温科学*, 68(Supplement), 247–272. <http://hdl.handle.net/2115/45452>

- Wendt, K. A., Nehrbass-Ahles, C., Niezgodna, K., Noone, D., Kalk, M., Menviel, L., Gottschalk, J., Rae, J. W. B., Schmitt, J., Fischer, H., Stocker, T. F., Muglia, J., Ferreira, D., Marcott, S. A., Brook, E., & Buizert, C. (2024). Southern Ocean drives multidecadal atmospheric CO₂ rise during Heinrich Stadials. *Proceedings of the National Academy of Sciences*, *121*(21), e2319652121. <https://doi.org/10.1073/pnas.2319652121>
- Werner, M., Jouzel, J., Masson-Delmotte, V., & Lohmann, G. (2018). Reconciling glacial Antarctic water stable isotopes with ice sheet topography and the isotopic paleothermometer. *Nature Communications* *2018 9:1*, *9*(1), 1–10. <https://doi.org/10.1038/s41467-018-05430-y>
- Werner, M., Langebroek, P. M., Carlsen, T., Herold, M., & Lohmann, G. (2011). Stable water isotopes in the ECHAM5 general circulation model: Toward high-resolution isotope modeling on a global scale. *Journal of Geophysical Research: Atmospheres*, *116*(D15). <https://doi.org/https://doi.org/10.1029/2011JD015681>
- Werner, M., Mikolajewicz, U., Heimann, M., & Hoffmann, G. (2000). Borehole versus isotope temperatures on Greenland: Seasonality does matter. *Geophysical Research Letters*, *27*(5), 723–726. <https://doi.org/https://doi.org/10.1029/1999GL006075>
- Westerhold, T., Marwan, N., Drury, A. J., Liebrand, D., Agnini, C., Anagnostou, E., Barnett, J. S. K., Bohaty, S. M., De Vleeschouwer, D., Florindo, F., Frederichs, T., Hodell, D. A., Holbourn, A. E., Kroon, D., Laurentino, V., Littler, K., Lourens, L. J., Lyle, M., Pälike, H., ... Zachos, J. C. (2020). An astronomically dated record of Earth's climate and its predictability over the last 66 million years. *Science*, *369*(6509), 1383–1388. https://doi.org/10.1126/SCIENCE.ABA6853/SUPPL_FILE/ABA6853_TABLES_S8_S34.XLSX
- Wheeler, J. A. (1990). Information, Physics, Quantum: The search for links. *THE PROCEEDINGS OF THE WORKSHOP ON COMPLEXITY, ENTROPY, AND THE PHYSICS OF INFORMATION, VIII*.
- Wilhelms, F., Miller, H., Gerasimoff, M. D., Drücker, C., Frenzel, A., Fritzsche, D., Grobe, H., Hansen, S. B., Hilmarsson, S. Æ., Hoffmann, G., Hörnby, K., Jaeschke, A., Jakobsdóttir, S. S., Juckschat, P., Karsten, A., Karsten, L., Kaufmann, P. R., Karlin, T., Kohlberg, E., ... Wilhelms-Dick, D. (2014). The EPICA Dronning Maud Land deep drilling operation. *Annals of Glaciology*, *55*(68), 355–366. <https://doi.org/DOI: 10.3189/2014AoG68A189>
- Wilkinson, D. S., & Ashby, M. F. (1975). Pressure sintering by power law creep. *Acta Metallurgica*, *23*(11), 1277–1285. [https://doi.org/10.1016/0001-6160\(75\)90136-4](https://doi.org/10.1016/0001-6160(75)90136-4)
- Winski, D. A., Fudge, T. J., Ferris, D. G., Osterberg, E. C., Fegyveresi, J. M., Cole-Dai, J., Thundercloud, Z., Cox, T. S., Kreutz, K. J., Ortman, N., Buizert, C., Epifanio, J., Brook, E. J., Beaudette, R., Severinghaus, J., Sowers, T., Steig, E. J., Kahle, E. C., Jones, T. R., ... McConnell, J. R. (2019). The SP19 chronology for the South Pole Ice Core - Part 1: Volcanic matching and annual layer counting. *Climate of the Past*, *15*(5), 1793–1808. <https://doi.org/10.5194/CP-15-1793-2019>
- Witrant, E., Martinerie, P., Hogan, C., Laube, J. C., Kawamura, K., Capron, E., Montzka, S. A., Dlugokencky, E. J., Etheridge, D., Blunier, T., & Sturges, W. T. (2012). A new multi-gas

- constrained model of trace gas non-homogeneous transport in firn: Evaluation and behaviour at eleven polar sites. *Atmospheric Chemistry and Physics*, 12(23), 11465–11483. <https://doi.org/10.5194/ACP-12-11465-2012>
- Wolff, E. W., Fischer, H., van Ommen, T., & Hodell, D. A. (2022). Stratigraphic templates for ice core records of the past 1.5 Myr. *Climate of the Past*, 18(7), 1563–1577. <https://doi.org/10.5194/cp-18-1563-2022>
- Woodhead, J., & Petrus, J. (2019). Exploring the advantages and limitations of in situ U-Pb carbonate geochronology using speleothems. *Geochronology*, 1(1), 69–84. <https://doi.org/10.5194/GCHRON-1-69-2019>
- Yan, H. (2020). Daily growth bands of giant clam shell: A potential paleoweather recorder. *Solid Earth Sciences*, 5(4), 249–253. <https://doi.org/10.1016/J.SESCI.2020.10.001>
- Yan, Y., Brook, E. J., Kurbatov, A. V., Severinghaus, J. P., & Higgins, J. A. (2021). Ice core evidence for atmospheric oxygen decline since the Mid-Pleistocene transition. *Science Advances*, 7(51), 9341. https://doi.org/10.1126/SCIADV.ABJ9341/SUPPL_FILE/SCIADV.ABJ9341_DATASETS_S1_A_ND_S2.ZIP
- Yau, A. M., Bender, M. L., Blunier, T., & Jouzel, J. (2016). Setting a chronology for the basal ice at Dye-3 and GRIP: Implications for the long-term stability of the Greenland Ice Sheet. *Earth and Planetary Science Letters*, 451, 1–9. <https://doi.org/10.1016/J.EPSL.2016.06.053>
- Yin, Q. Z., & Berger, A. (2012). Individual contribution of insolation and CO₂ to the interglacial climates of the past 800,000 years. *Climate Dynamics*, 38(3–4), 709–724. <https://doi.org/10.1007/S00382-011-1013-5/FIGURES/13>

7 APPENDIXES

The Appendix is composed of:

- two first-authored short articles published in the *Past Global Changes Magazine*: (7.1) Bouchet et al. (2024) and (7.2) Bouchet et al. (2023a)
- as well as co-authored papers related to the PhD project: (7.3) Parrenin et al. (2024), (7.4) Legrain et al. (in preparation), (7.5) Legrain et al. (submitted to *Nature Geosciences*) and (7.6) Paul et al. (in preparation).

APPENDIX 7.1

First-author publication:

Bouchet, M., Donner, A., Grimmer, M., Jasper, C., Krauss, F., Legrain, E. and Vera Polo, P., The atypical interglacial of MIS 11c and the long-term change in interglacial intensity over the past 800 kyr, Past Global Changes Magazine, 32 (1), 55, <https://doi.org/10.22498/pages.32.1.55>, 2024.

The atypical interglacial of MIS 11c and the long-term change in interglacial intensity over the past 800 kyr

Marie Bouchet¹, A. Donner², M. Grimmer³, C. Jasper⁴, F. Krauss³, E. Legrain⁵ and P. Vera Polo^{6,7}

Final QUIGS workshop, Grenoble, France, and online, 19-22 September 2023



Eleven interglacials have been identified in the past 800 kyr (Past Interglacials Working Group of PAGES 2016). Around 430 kyr BP, a change in interglacial strength, known as the Mid-Brunhes Event (MBE), was observed in atmospheric CO₂ levels, and in proxy records of Antarctic and global surface temperatures, marking a transition to stronger interglacials, such as Marine Isotope Stages (MISs) 5e and 11c (Fig. 1). While the onset of interglacials seems linked to an increased Northern Hemisphere summer insolation, uncertainties persist due to complex interactions involving astronomical forcing, ice volume, CO₂ levels, and temperature.

Active research areas in Late Pleistocene interglacials focus on those not aligning with the astronomical theory of ice ages, and on long-term changes in interglacial intensity over the past 800 kyr. To address these topics, the PAGES working group on Quaternary Interglacials (QUIGS) convened in Grenoble, France. Here we highlight some of the topics covered, and a few of the presentations that led to particular areas of discussion.

The unusual MIS 11c interglacial is known for its prolonged high sea-level and atmospheric CO₂ concentrations, despite weak summer-insolation forcing (Tzedakis et al. 2022). The prolonged Termination V was suggested to be associated with the largest sea-level contribution from the Greenland Ice Sheet over the last 800 kyr. Alessio Rovere showed how large ice sheets may drive high sea-level stands, with MIS 12 believed to have featured one of the most extensive glaciations (Batchelor et al. 2019). Claire Jasper's study of iceberg rafted debris (IRD) in the Southern Ocean's Atlantic sector, during Termination V and MIS 11c, indicated a protracted period of Antarctic Ice Sheet iceberg discharge and melt. Steve Barker suggested that the asynchronous phasing of obliquity and precession during Termination V (Fig. 1) may explain the prolonged nature of this deglaciation.

The necessity to develop a coordinated modeling protocol over the Termination V-MIS 11c time period was discussed. In this framework, the group agreed on the importance of constraining the volume and extent of the MIS 12 ice sheet, and developing a coherent temporal framework for the rate of sea-level rise, and for various paleoclimate proxies representative of different parts of the Earth System across the deglaciation.

The second part of the discussions delved into the MBE, addressing challenges related to the metrics of interglacial intensity. Mean

Ocean Temperature reconstructed by Markus Grimmer emerged as a potential metric for distinguishing between strong and weak interglacials. A debate arose regarding the classification of early interglacial peaks in CO₂, known as overshoots, and whether they are part of the interglacial or termination. Takahito Mitsui presented a model predicting interglacial intensity based on the previous glacial strength and summer insolation, received at both northern and southern high latitudes during deglaciation. According to Mitsui et al. (2022), the increase in interglacial intensities after the MBE is related to the amplitude increase in obliquity cycles. Finally, Quizhen Yin pointed out that in some records, such as Chinese loess, there is no discernable increase in interglacial strength across MBE. This observation gave rise to the alternative suggestion: can we use records where MBE is not detectable to understand what causes the observation of MBE in other records? In conclusion, an outline for a short position paper effort was defined on our current knowledge of interglacial intensity, incorporating both paleoclimate records and modeling.

The QUIGS leadership team thanks all the participants who engaged in this final workshop, and throughout the QUIGS adventure, extending thanks to PAGES for their continuous support.

ACKNOWLEDGEMENTS

We thank PAGES, the LABEX-OSUG and the AXA Research Fund for financially supporting the last QUIGS workshop.

AFFILIATIONS

- ¹Laboratoire des Sciences du Climat et de l'Environnement, LSCE-IPSL, CEA-CNRS-UVSQ, Univ. Paris-Saclay, Gif-sur-Yvette, France
²Institute of Geology, University of Innsbruck, Austria
³Climate and Environmental Physics and Oeschger Center for Climate Research, University of Bern, Switzerland
⁴Columbia University, Lamont-Doherty Earth Observatory, Palisades, NY, USA
⁵University of Grenoble Alpes, CNRS, INRAE, IRD, Grenoble INP, IGE, Grenoble, France
⁶Dipartimento di Biologia Ambientale, Sapienza University of Rome, Italy
⁷Departamento de Estratigrafía y Paleontología, University of Granada, Spain

CONTACT

Marie Bouchet: marie.bouchet@lscce.ipsl.fr

REFERENCES

- Batchelor CL et al. (2019) *Nat Commun* 10: 3713
 Bouchet M et al. (2023) *Clim Past* 19: 2257-2286
 Donders T et al. (2021) *Proc Natl Acad Sci* 118: e2026111118
 Mitsui T et al. (2022) *Clim Past* 18: 1983-1996
 Past Interglacials Working Group of PAGES (2016) *Rev Geophys* 54: 162-219
 Tzedakis PC et al. (2022) *Quat Sci Rev* 284: 107493

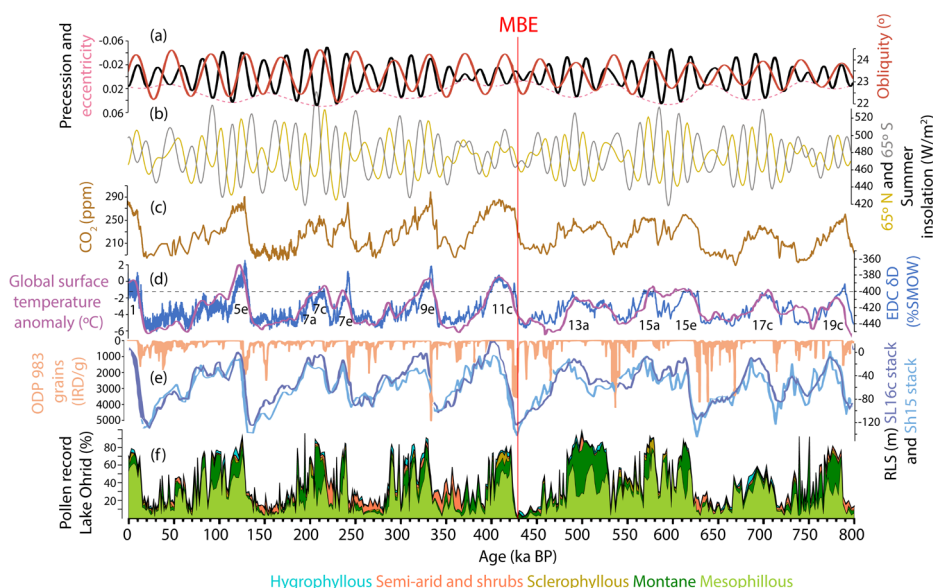


Figure 1: Paleoclimate reconstructions over the last 800 kyr (modified from Tzedakis et al. 2022). **(A)** Eccentricity (red dashed), precession (black), obliquity (red solid), and **(B)** summer solstice insolation at 65°N (orange) and 65°S (gray). Antarctic EDC ice-core records of **(C)** atmospheric CO₂ and **(D)** δD of ice (blue) on AICC2023 timescale (Bouchet et al. 2023). A 400‰-threshold (dashed line) separates pre- and post-MBE interglacials. Global average surface temperature (anomaly vs. present) (purple). **(E)** IRD in North Atlantic ODP Site 983 (salmon); two reconstructions of relative sea level (dark and light blue). **(F)** Pollen from Lake Ohrid (Donders et al. 2021).

APPENDIX 7.2

First-author publication:

Bouchet, M., Landais, A. and Parrenin, F., Dive into the timescales of deep ice cores, Past Global Changes Magazine, 31(2), 104-105, <https://doi.org/10.22498/pages.31.2.104>, 2023.

Dive into the timescales of deep ice cores

Marie Bouchet¹, A. Landais¹ and F. Parrenin²

We review some of the possible methods for building optimized and coherent timescales of deep polar ice cores. We focus on drilling sites characterized by a low temporal resolution due to minimal accumulation of snow at the ice-sheet surface.

Deep-polar ice cores are unique archives of past climate. Their investigation is valuable to study mechanisms governing the Earth's climate variations during the glacial-interglacial cycles of the late Quaternary. Precise ice-core chronologies are essential to determine the sequences and durations of climatic events, as well as questioning phase relationships between the external forcings and the climatic responses. One example of climate forcings are the orbital parameters governing the amount of solar energy received at the Earth's surface.

Three challenges are associated with the dating of deep ice cores:

- A coat of unpacked snow (50–120 m), the firn, covers the ice sheet. The atmospheric air circulates freely within the firn. At the firn-ice transition, the air is enclosed in bubbles and no longer diffuses. Hence, the construction of two separate chronologies is required: one for the ice and one for the younger air.
- Most of the paleoclimatic information is recorded within the deepest part of the ice core, due to the thinning of ice layers from their deposition at the surface to the bottom

of the ice sheet. Improving the timescales of deep ice cores is therefore of great concern for the ice-core community, along with extending them further back in time.

iii. Ice cores drilled at sites characterized by high accumulation rates of snow at the surface (10–30 cm/year) are dated by counting annual layers via identification of a seasonal cycle in some records (Sigl et al. 2016). Conversely, some East Antarctic sites show comparatively low accumulation rates (1–5 cm/year), which prevent annual layers from being identified and counted. Chronologies of deep ice cores therefore involve other strategies, summarized below.

Glaciological modeling

Glaciological models simulate the flow and thinning of annual layers over time, from surface deposition down to the bedrock, thus providing the ice age-depth relationship (Parrenin et al. 2004). The model inputs are past scenarios of snow accumulation and temperature at the surface, estimated from water isotope measurements, together with a calculated temperature-depth profile in the ice sheet. This strategy is highly dependent on poorly known boundary conditions and physical constants. Glaciological

modeling is thus combined with dating constraints, which are depths with a known ice or gas age.

Dating constraints

Absolute dating constraints in ice cores can be determined using radioactive isotope records. The ^{10}Be production rate in the atmosphere relates to the geomagnetic field and solar activities. The Laschamp Excursion, a rapid drop in the Earth's geomagnetic field intensity, is visible as a peak in the ice-core ^{10}Be records, and is independently dated with different series at 41 kyr BP (thousand years before 1950) (Raisbeck et al. 2017). Ice-core ^{40}Ar records reflect past atmospheric concentration modulated by the radioactive decay of ^{40}K in the Earth's crust (Yan et al. 2019). Recently, ^{81}Kr measurements on ice samples of a few kilograms provided age estimates between 1,300 and 300 kyr BP (Buizert et al. 2014).

Another approach, called "orbital dating", consists in synchronizing ice-core proxies to the Earth orbital parameters (or targets), whose variations are precisely modeled in time. The alignment of the proxy with its target gives ice- or gas-age constraints (Fig. 1). Three orbital proxies are used: $\delta^{18}\text{O}_{\text{atm}}$,

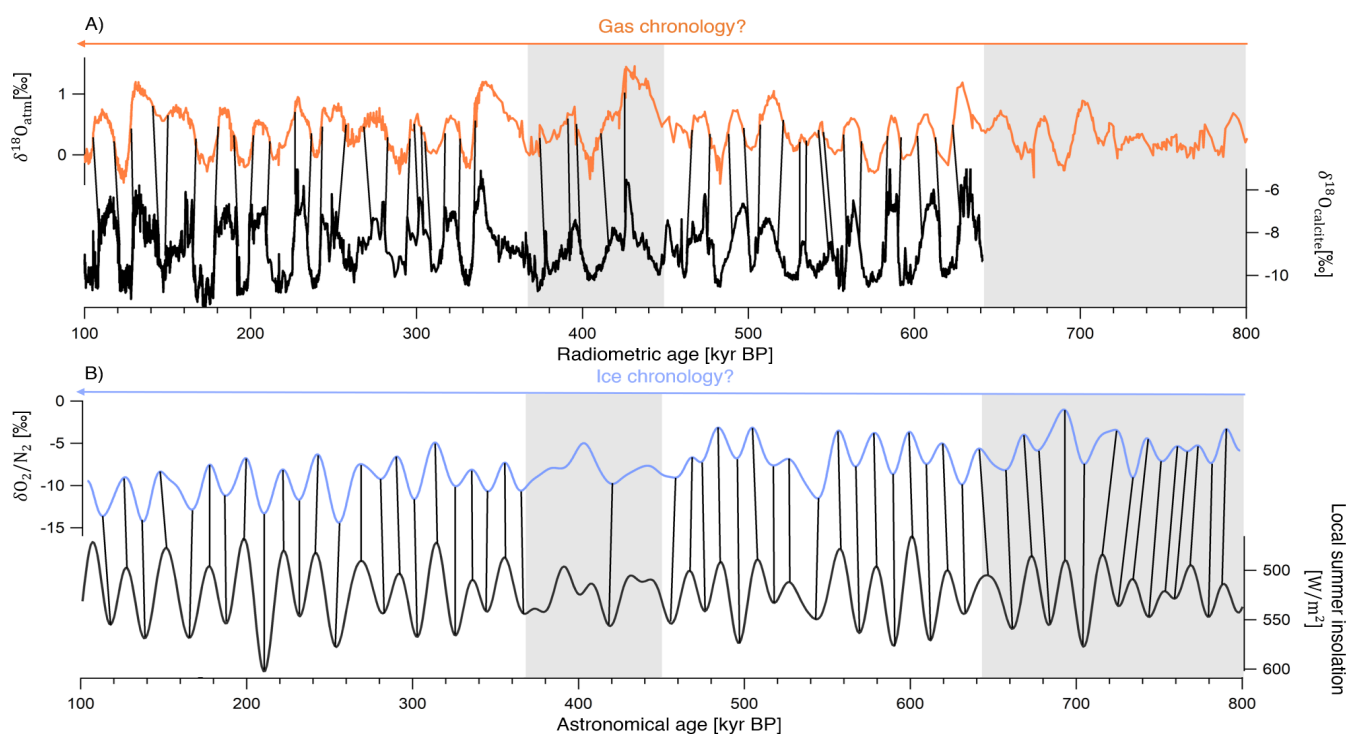


Figure 1: Synchronization of ice-core records with well dated series. Alignment of EPICA Dome C records of (A) $\delta^{18}\text{O}_{\text{atm}}$ and (B) $\delta\text{O}_2/\text{N}_2$ (Extier et al. 2018) to $\delta^{18}\text{O}_{\text{calcite}}$ from East Asian speleothems and local summer insolation, respectively. $\delta\text{O}_2/\text{N}_2$ is filtered in the insolation frequency band. Gray areas indicate time intervals of large dating uncertainty.

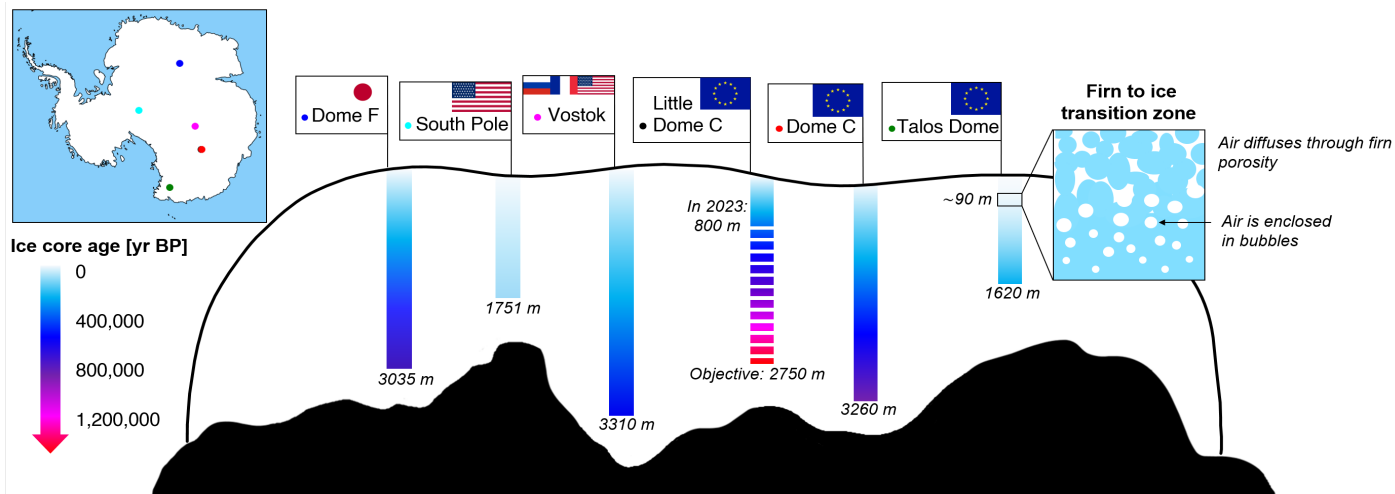


Figure 2: Deep East Antarctic ice cores and age scale. The numbers at the bottom of each ice core indicates the maximum depth drilled. Dome F (720 kyr BP), South Pole (54 kyr BP), Vostok (420 kyr BP), Dome C (800 kyr BP) and Talos Dome (340 kyr BP). The Little Dome C drilling aims to reach 2750 m, and 1.5 Myr BP.

$\delta\text{O}_2/\text{N}_2$, and total air content. The oxygen in air bubbles ($\delta^{18}\text{O}_{\text{atm}}$) is sensitive to ocean water $\delta^{18}\text{O}$ (and, therefore, to the global ice volume), as well as to the biosphere productivity and the low latitude water cycle. Conversely, the oxygen in precipitation ($\delta^{18}\text{O}_{\text{ice}}$) depends on local temperature changes, and, thus, not used for orbital dating. $\delta^{18}\text{O}_{\text{atm}}$ was synchronized to the Earth's axial precession, delayed by 5,000 years, because such a delay was observed during the last deglaciation. However, the lag of $\delta^{18}\text{O}_{\text{atm}}$ behind precession fluctuates. Rapid climatic instabilities linked to breakdowns of the Northern Canadian ice sheet (Heinrich-like events) occur during deglaciations, which could be responsible for occasionally delaying the response of $\delta^{18}\text{O}_{\text{atm}}$ to orbital forcing via changes in the water cycle (Extier et al. 2018). The variability of this delay induces a lack of confidence in the $\delta^{18}\text{O}_{\text{atm}}$ - precession synchronization, associated with an uncertainty of 6,000 years, which corresponds to the quarter period of a precession cycle. Further, the ice core $\delta^{18}\text{O}_{\text{atm}}$ and Chinese speleothems $\delta^{18}\text{O}_{\text{calcite}}$ signals display identical features. The two series' show orbital-scale (induced by the precession forcing) and millennial-scale oscillations, both types of variations being associated with changes in the low latitude water cycle imprinted in $\delta^{18}\text{O}_{\text{atm}}$ and $\delta^{18}\text{O}_{\text{calcite}}$ (Fig. 1a). To improve the precision of the gas chronology, it is preferable to synchronize the $\delta^{18}\text{O}_{\text{atm}}$ variations with the $\delta^{18}\text{O}_{\text{calcite}}$ record from Uranium-series-dated Asian speleothems (Cheng et al. 2016). In addition, Bender (2002) and Lipenkov et al. (2011) observed that the $\delta\text{O}_2/\text{N}_2$ and total air content records simultaneously oscillate with the local summer insolation (Fig. 1b). They formulated the subsequent hypothesis: insolation modulates near-surface snow properties (grain size and shape). This imprint is preserved as snow densifies in the firn and, later, affects the ratio $\delta\text{O}_2/\text{N}_2$ and the total air content in deep ice. The total air content variations share more similarities with Earth's axial obliquity than $\delta\text{O}_2/\text{N}_2$, hence its insolation target is integrated over an extended summer interval. Wiggle-matching between $\delta\text{O}_2/\text{N}_2$ and total air content, and their insolation targets gives dating constraints with a relative uncertainty varying between 1,000 and 7,000 years

(Bazin et al. 2013). The orbital dating accuracy is liable to:

- The choice of the well-suited orbital target;
- its synchronization with the orbital proxy, which can be ambiguous when Earth's orbit is nearly circular; and
- the poor quality of measurements in the deepest sections of the cores (gray areas in Fig. 1).

Other tracers supplying relative dating constraints, or stratigraphic links, improve the consistency between timescales of different ice cores over the last glacial-interglacial cycle. The synchronization of globally well-mixed atmospheric-methane records from Greenland and Antarctic ice cores brings in stratigraphic links with an accuracy of 60 to 500 years (Epifanio et al. 2020). Climate independent constraints, such as large volcanic eruptions, leave singular sulfate patterns in ice cores from both hemispheres. The detection of these deposits results in highly precise (within 5 to 150 years) stratigraphic tie points between cores (Svensson et al. 2020).

Connecting ice and gas timescales

The lock-in depth, indicating the depth threshold where the air is trapped in enclosed bubbles and no longer diffuses (Fig. 2), determines the age difference between the ice and gas phases at each depth. Through the diffusion column (the interval between the surface and the lock-in depth), the preferential downward diffusion of heavy isotopes increases the $\delta^{15}\text{N}$ fraction of N_2 . Measurements of $\delta^{15}\text{N}$ in air trapped in ice cores yields a first estimate of the diffusion column thickness, and, therefore, of the lock-in depth. This depth can also be calculated with firn densification modeling (Bréant et al. 2017).

Bayesian dating tools

To build consistent ice-core chronologies combining independent synchronization, absolute and relative dating constraints, as well as glaciological modeling, Bayesian dating tools have been developed. Now, they have

gained improved mathematical, numerical, and programming capacities (Parrenin et al. 2021). Prior estimates of gas and ice timescales built by glaciological models are statistically adjusted by the Bayesian tools to comply with the dating constraints. These probabilistic tools use an inverse method, integrating all dating information and associated relative uncertainty, to produce a coherent timescale for distinct ice cores.

Perspectives

Deep ice-core chronologies strongly rely on gas measurements. To improve the chronological precision, it is crucial to collect highly resolved data from ice samples stored at cold temperatures (-50°C) to avoid gas diffusion and loss of signal for $\delta^{18}\text{O}_{\text{atm}}$ and $\delta\text{O}_2/\text{N}_2$. The dating accuracy is soon to be challenged by the upcoming Beyond EPICA ice core, expected to provide much more paleoclimatic information within a shallower depth range than present ice-core drillings (1.5 Myr BP zipped in ~ 2750 m, Fig. 2) (Fischer et al. 2013).

AFFILIATIONS

¹Laboratory for Sciences of Climate and Environment, University of Paris-Saclay, Gif-sur-Yvette, France
²Institute of Environmental Geosciences, University of Grenoble-Alpes, France

CONTACT

Marie Bouchet: marie.bouchet@lscce.ipsl.fr

REFERENCES

- Bazin L et al. (2013) *Clim Past* 9: 1715-1731
 Bender ML (2002) *Earth Planet Sci Lett* 204: 275-289
 Bréant C et al. (2017) *Clim Past* 13: 833-853
 Buizert C et al. (2014) *Proc Natl Acad Sci* 111: 6876-6881
 Cheng H et al. (2016) *Nature* 534: 640-646
 Epifanio JA et al. (2020) *Clim Past* 16: 2431-2444
 Extier T et al. (2018) *Quat Sci Rev* 185: 244-257
 Fischer H et al. (2013) *Clim Past* 9: 2489-2505
 Lipenkov VY et al. (2011) *Quat Sci Rev* 30: 3280-3289
 Parrenin F et al. (2004) *J Geophys Res Atmos* 109: D20102
 Parrenin F et al. (2021) EGU General Assembly 2021, Vienna, Austria
 Raisbeck GM et al. (2017) *Clim Past* 13: 217-229
 Sigl M et al. (2016) *Clim Past* 12: 769-786
 Svensson A et al. (2020) *Clim Past* 16: 1565-1580
 Yan Y et al. (2019) *Nature* 574: 663-666

APPENDIX 7.3

Co-authored study in discussion in *EGUsphere*:

Parrenin, F., Bouchet, M., Buizert, C., Capron, E., Corrick, E., Drysdale, R., Kawamura, K., Landais, A., Mulvaney, R., Oyabu, I., and Rasmussen, S.: The Paleochrono-1.1 probabilistic model to derive optimized and consistent chronologies for several paleoclimatic sites, EGUsphere [preprint], <https://doi.org/10.5194/egusphere-2023-2911>, 2024.

I contributed to this study as a co-author by providing input files relative to AICC2023 dating experiment.



The Paleochrono-1.1 probabilistic model to derive optimized and consistent chronologies for several paleoclimatic sites

Frédéric Parrenin¹, Marie Bouchet², Christo Buizert³, Emilie Capron¹, Ellen Corrick⁴, Russell Drysdale⁵, Kenji Kawamura⁶, Amaëlle Landais², Robert Mulvaney⁷, Ikumi Oyabu⁶, Sune Rasmussen⁸

5 ¹Univ. Grenoble Alpes, CNRS, INRAE, IRD, Grenoble INP, IGE, 38000 Grenoble, France

²UMR8212, CEA–CNRS–UVSQ–UPS, Laboratoire des Sciences du Climat et de l’Environnement (IPSL), Gif-sur-Yvette, France

³College of Earth, Ocean and Atmospheric Sciences, Oregon State University (OSU), Corvallis, OR, USA

⁴School of Earth, Atmosphere and Environment, Monash University, Clayton, Victoria, Australia

10 ⁵School of Geography, The University of Melbourne, Melbourne, Victoria, Australia.

⁶National Institute of Polar Research, Research Organizations of Information and Systems, 10-3 Midori-cho, Tachikawa, Tokyo 190-8518, Japan

⁷British Antarctic Survey, Madingley Road, High Cross, Cambridge, CB3 0ET, UK

15 ⁸Physics of Ice, Climate and Earth, Niels Bohr Institute, University of Copenhagen, Copenhagen, Denmark.

Correspondence to: Frédéric Parrenin (frederic.parrenin@univ-grenoble-alpes.fr)

Abstract Past climate and environmental changes can be reconstructed using paleoclimate archives such as ice cores, lake and marine sediment cores, speleothems, tree rings and corals. The dating of these natural archives is crucial for deciphering the temporal sequence of events and rates of change during past climate changes. It is also essential to provide quantified estimates of the absolute and relative errors associated with the inferred chronologies. However, this task is complex since it involves combining different dating approaches at different paleoclimatic sites and often on different types of archives. Here we present *Paleochrono-1.1*, a new probabilistic model to derive a common and optimised chronology for several paleoclimatic sites with potentially different types of archives. Paleochrono-1.1 is based on the inversion of an archiving model: a varying deposition rate (also named growth rate, sedimentation rate or accumulation rate) and also, for ice cores, a lock-in-depth of air (since, in the absence of significant surface melt, the air is trapped in the ice at about 50-120 m below the surface) and a thinning function (since glacier ice undergoes flow). Paleochrono-1.1 integrates several types of chronological information: prior knowledge of the archiving process, independently dated horizons, depth intervals of known duration, undated stratigraphic links between records, and, for ice cores, Δ depth observations (depth

20
25
30



differences between events recorded synchronously in the gas and solid phases of a certain core). The optimization is formulated as a least-squares problem, assuming that all probability densities are near-Gaussian and that the model is nearly linear in the vicinity of the best solution. Paleochrono-1.1 is the successor of IceChrono, which produces common and optimized chronologies for ice-cores. Paleochrono-1.1 outperforms IceChrono in terms of computational efficiency, ease of use, and accuracy. We demonstrate the ability of Paleochrono-1.1 in a new ice-core–speleothem dating experiment, which combines the Antarctic Ice Core Chronology 2023 dating experiment, based on records from five polar ice cores, with data from two speleothems dated using uranium/thorium radiometric techniques from Hulu Cave (China). We analyse the performance of Paleochrono-1.1 in terms of computing time and memory usage in various dating experiments. Paleochrono-1.1 is freely available under the MIT open-source license.

1 Introduction

Numerous natural archives provide records of the past evolution of climate and environment. Continuous paleoclimate archives require a continuous deposition process. Examples are: ice cores (e.g., NorthGRIP project members, 2004; EPICA community members et al., 2004; EPICA Community Members et al., 2006; NEEM community Members, 2013; WAIS Divide Project Members, 2013; Dome Fuji Ice Core Project Members et al., 2017), marine sediment cores (e.g., Lisiecki and Raymo, 2005; Elderfield et al., 2012; Shackleton, 2000; Shackleton et al., 2000), lake sediment cores (e.g., Williams et al., 1997; Hodell et al., 1999) and speleothems (e.g., Wang et al., 2001; Cheng et al., 2018; Corrick et al., 2020). Such archives can directly record or more indirectly reflect various climatic parameters, such as local atmospheric or oceanic temperature, precipitation amount and seasonality, sedimentation or precipitation rate, atmospheric composition, sea level, ocean circulation intensity, insolation or biosphere activity. For paleoclimate archives to provide precise insight into past climate change, it is a prerequisite to be able to derive the age of the archive at each depth level, i.e. to derive an associated chronology. This is, however, a complex task which involves different dating methods (Brauer et al., 2014), depending on the



archive type and the temporal coverage. We will not go into the detail of each method for every archive, but we list here the different types of chronological information:

1) **Modelling of the archiving process:** it is often possible to model deposition through time. For an ice core, this is complicated by the fact that air bubbles are trapped at depth and not at the surface, hence the air is systematically younger than the surrounding ice by a non-constant amount. Moreover, ice layers thin with time due to ice flow. For some archives, the sedimentation or growth rate may vary abruptly due to climatic or local environmental factors, making it a challenge to accurately describe the deposition/growth.

2) **Dated horizons:** some horizons in the archive can be dated using an independent method. Examples include a volcanic ash layer that is dated either from historical records or by radiometric dating of the ash, a paleomagnetic or solar event identified by variations in the ^{10}Be concentration or remanent magnetization, or an event dated by radiometric analysis such as U/Th, ^{14}C or ^{81}Kr .

3) **Intervals of known duration:** sometimes, a section of an archive is of known duration (typically, a section where annual layers can be counted), although the absolute age of the section may not be known accurately.

4) **Stratigraphic links:** links can be derived between the depths of several paleoclimate sites that are known (or assumed) to have the same age. Typically, this can be the same volcanic event recognized at different sites, or an abrupt Dansgaard-Oeschger event seen in multiple proxy records which is assumed to be synchronously recorded within a given margin.

5) **Δ_{depth} observations:** can be seen as stratigraphic links between ice and air phases of a single ice-core site (Parrenin et al., 2012).

Each dating method and paleoclimate archive has strengths and weaknesses in terms of chronological construction. For example, ice cores have robust archiving models, which accurately describe the processes of snow deposition, densification and ice flow (e.g., Parrenin et al., 2004, 2007) and at some sites, the annual layers can be counted over long sections (e.g., Sigl et al., 2016; Svensson et al., 2008). However, ice cores generally do not have strong constraints on absolute ages beyond the last millenia. Speleothems can be dated very accurately and precisely using uranium-thorium (U-Th) dating methods (e.g., Cheng et al., 2018). However, speleothem records are often less continuous than ice or marine



85 sediment records due to hiatuses in calcite precipitation, which can be related to drier or colder conditions
above the cave but may also be unrelated to climate (e.g. due to changes in the percolation path of the
source waters). Marine sediment cores have the longest temporal extent (e.g., Lisiecki and Raymo, 2005).
However, prior to the radiocarbon dating limit (~50 kyr BP, thousands of years before 1950 A.D.), their
chronologies rely on tuning to different reference records such as those based on the calculation of Earth's
orbital parameters (Laskar et al., 2004). In palaeoclimatology, it is typical to treat individual records
90 independently, making difficult the comparisons between chronologies. Combining chronological data
from multiple archives, across various archive types, has the potential to improve our chronological
framework. An appropriate strategy is to combine the results from the different dating methods and
paleoclimatic sites using a probabilistic framework in order to make the best out of the different archives
and records.

95 A probabilistic framework was originally developed for polar ice cores using the Bayesian model *Datice*
(Lemieux-Dudon et al., 2010b, 2015). *Datice* produces an optimal chronology using different types of
chronological information from multiple ice cores. Using this method, the ice-core chronology is derived
from an archiving model that relies on the three canonical glaciological quantities of the ice-core dating
problem: the deposition rate also called accumulation rate, the lock-In depth (LID) of air and the thinning
100 function,(i.e. ratio of the present-day thickness of an annual layer to its initial thickness when it was
deposited at the surface. In Bayesian terminology, the initial estimate of this archive model is called the
prior scenario.

Datice then seeks an optimal scenario, which is the best compromise between the prior scenario of the
archiving process and the various chronological data. *Datice* was used in the construction of the reference
105 chronology Antarctic Ice Core Chronology 2012 (hereafter AICC2012), combining archiving models and
chronological information from four Antarctic and one Greenland ice cores (Bazin et al., 2013; Veres et
al., 2013). *Datice* was entirely coded in Fortran and, although a powerful tool in terms of performance,
was difficult to use and to modify.

The *IceChrono* dating model (Parrenin et al., 2015) was developed, based on the same principles as
110 *Datice*, providing improvements and simplifications in the mathematical, numerical and programming
aspects with respect to *Datice*. However, *IceChrono* is sometimes slower than *Datice* depending on the



resolution chosen, in particular because IceChrono performs a numerical gradient calculation while Datice has a more efficient analytical gradient calculation. IceChrono is coded in Python 2.

Both Datice and IceChrono were initially developed for ice core studies. Technically, it is possible to use these dating tools to combine chronological information from other paleoclimatic archives by fixing the thinning function at unity and by discarding the air bubbles variable (Bazin et al., 2019), but the models are not designed for this purpose.

In this paper, we present a new probabilistic model, named *Paleochrono-1.1*, which is the successor of IceChrono. Paleochrono-1.1 is specifically designed to combine chronological information from multiple types of archives. Paleochrono-1.1 is coded in Python 3 and is more efficient, easier to use and more accurate than IceChrono. We first detail the Paleochrono-1.1 methodology (section 2) and demonstrate its utility with a dating experiment that combines ice cores and speleothems (section 3). We then present the computing resources used by Paleochrono-1.1 in various dating experiments (section 4) and discuss our results (section 5).

2 Method

Paleochrono-1.1 is designed to work with paleoclimatic archives where it can be assumed that the deposition rate is strictly positive at any time. Paleochrono-1.1 does not integrate information regarding hiatuses, working at a temporal resolution where this assumption is valid (because, for example, it does not snow everyday on an ice sheet). We use the term *site*, to refer to one individual archive; we do not use the term record since it can mean a particular proxy within a site. We use *depth* in a broader sense to refer to the distance along the archive, from the youngest to the oldest section. The age along the archive is therefore continuous and strictly increasing. If there is a known hiatus in the archive, the sections before and after the hiatus should be considered as two different sites in Paleochrono-1.1.

Paleochrono-1.1 is set up for two types of archives: the so-called *simple archives*, with one unique depth-age relationship, constant density, and no post-depositional thinning (e.g., speleothems, marine sediments), and *ice-core archives*, where we deal with two ages (one for the ice matrix and one for the enclosed air), variable density, and where post-depositional thinning occurs.



2.1 Method summary

The true chronology of a paleoclimate site is a function of the deposition rate. In the case of ice cores, two additional variables must also be considered: the LID of the air bubbles and the thinning function. These variables form what we call the forward model, and they are unknown. To find the optimal chronology, they must be estimated based on:

- Prior information about their values at each site;
- Chronological observations (Figure 1) such as: ages at certain depths, the time elapsed between two depths, the synchronicity of events recorded at two different sites that are assumed capable of recording events simultaneously, or the depth difference of air and ice levels of the same age within the same ice core (Δ_{depth}).

All these different types of information, which can be mathematically described as probability density functions (PDF), are assumed to be independent and are combined together using a Bayesian framework to obtain posterior estimates of the input variables (deposition rate and, for an ice core, LID, and thinning) and of the resulting chronologies. Uncertainties on the prior estimates and on the observations are assumed to be Gaussian and the forward model is linearized, allowing this problem to be solved as a least-square optimization.

2.2 The forward model

2.2.1 For a simple archive

For a simple archive, the archiving model is:

$$\chi(z) = \chi_0 + \int_{z_0}^z \frac{dz'}{a(z')} \quad (1)$$

where z is the depth along the paleoclimatic record, $\chi(z)$ is the age at depth z , χ_0 is the age at the top depth $z = z_0$ (i.e. the age of the youngest material at the site), and a is the depth-dependent deposition rate at the site of deposition.

This equation integrates along the depth axis the number of annual layers per unit depth from the surface.



2.2.2 For an ice-core archive

For an ice-core site, the archiving model is slightly more complicated, since we need to account for the age of the air inside the ice and for the vertical thinning of ice layers:

$$\chi(z) = \chi_0 + \int_{z_0}^z \frac{D(z')}{a(z')\tau(z')} dz', \quad (2)$$

$$\psi(z) = \chi(z - \Delta_{\text{depth}}(z)), \quad (3)$$

$$\int_{z - \Delta_{\text{depth}}(z)}^z \frac{D(z')}{\tau(z')} dz' = l(z) \times \left. \frac{D}{\tau} \right|_{\text{firn}}^0, \quad (4)$$

where z is the depth along the ice core, $\chi(z)$ is the age of the ice at depth z , χ_0 is the age of the ice at the top (with depth $z = z_0$), a is the deposition rate along the ice core, D is the (dimensionless) relative density of the snow/ice material, τ is the vertical thinning function (also dimensionless), ψ is the age of the air, Δ_{depth} is the depth difference between air and ice of the same age, l is the lock-in-depth of air bubbles and $\left. \frac{D}{\tau} \right|_{\text{firn}}^0$ is the average value of $\frac{D}{\tau}$ in the firn when the air particle was at the lock-in-depth (this parameter is usually ~ 0.7 for most firns, see Parrenin et al., 2012).

Equation 2 integrates along the depth axis the number of annual layers per unit depth from the surface. Equation 3 describes that the air age at depth z is equal to the ice age at depth $z - \Delta_{\text{depth}}$, which is the definition of Δ_{depth} . Equation 4 describes that if one corrects a depth interval between an ice depth and the depth of air of the same age for thinning, one gets the initial firn thickness in ice-equivalent units.

2.2.3 Numerical aspects

The parameters a , τ and l are discretized onto a fine depth grid called the *age-equation grid*. Equation (1) (for a simple archive) or Equation (2) (for an ice-core archive) are solved using a cumulative sum. Then Equation (4) for the Δ_{depth} is solved to deduce the air age from Equation (3). To solve Equation (4), we first integrate $\frac{D}{\tau}$ from the surface down to every depth in the age-equation grid, i.e. we have a correspondence table between real depths and unthinned-ice-equivalent (UIE) depths. Then, for every



180 actual air depth in the age-equation grid, we obtain the air UIE depth from the table. We then subtract the
right-hand side of Equation (4) from this air UIE depth to get the ice UIE depth. Finally, we use the
correspondence table to obtain the real ice depth and the Δ_{depth} . When we need to compute the age of the
ice or air or Δ_{depth} at depths which are not nodes of the age-equation grid (for example when comparing
the model with observations, see below), we use a linear interpolation.

185 **2.3 The probabilistic problem**

2.3.1 General probabilistic consideration

The general idea of Paleochrono-1.1 is to combine different sources of chronological information: prior
knowledge on the archiving process, together with various chronological observations (e.g. radiometric
ages). The assumption is that each site and each site pair (used for stratigraphic links) have independent
190 information. Moreover, within each site and within each site pair, the various types of chronological
information are assumed to be independent. For example, for a given site, the prior scenario of the
deposition rate, the dated horizons and the dated intervals are all assumed to be independent. It is only
within each type of information for a certain site or a certain site pair that it is possible to define the
correlation of the information. For prior archiving scenarios of deposition rate (and thinning and LID for
195 an ice core), we do this by defining correlation matrices which have a triangular form, that is, the
correlation matrix has ones along its diagonal and the correlation linearly decreases to zero when the age
difference (for the deposition rate and LID) or the depth difference (for the thinning function) reaches a
user-defined λ value. Setting these correlation matrices for the prior allows to have a weighting which
does not depend on the resolution chosen for the inversion grids. As a consequence, the cost function
200 converges towards a single value when the resolution is increased.

In mathematical terms (Tarantola, 2005), combining different sources of information corresponds to
multiplying the probability density functions (PDFs) of the prior and of the observations. The result of
this multiplication is called the likelihood function. Here, we assume the PDFs to be independent
multivariate Gaussian distributions. Multiplying the PDFs therefore corresponds to adding least squares
205 terms.



2.3.2 The least-squares cost function

We write the cost function as follows:

$$J = \sum_k J_k + \sum_{k < m} J_{k,m}, \quad (5)$$

where J_k is the term related to site number k and $J_{k,m}$ is the term related to site pair (k, m) .

For a simple archive, the cost function term is the sum of terms related to the age at the top of the sequence χ_0 , deposition prior information, dated horizons, and dated intervals. For an ice-core archive, the cost function term is the sum of terms related to the age at the top of the site χ_0 , the prior information (for deposition, thinning, and LID), dated horizons (in ice or air), dated intervals (in ice or air), and Δ_{depth} observations.

For a site pair of simple archives, the cost function term simply contains a term related to the stratigraphic links. For a site pair of ice-core archives, the cost function term is the sum of four terms related to ice-ice, ice-air, air-ice and air-air stratigraphic links. For a mixed site pair of a simple archive and an ice-core archive, the cost function term is the sum of two terms related to ice and air stratigraphic links.

Each of additive components of the J_k and $J_{k,m}$ terms described above is written as:

$$J = \mathbf{R}^T \mathbf{C}^{-1} \mathbf{R} \quad (6)$$

where \mathbf{R} is a residual vector, i.e. a vector containing the differences between the model values and the observations/prior values divided by the uncertainty of the observations/prior, and \mathbf{C} is a correlation matrix. This correlation matrix can be Cholesky-decomposed as $\mathbf{C} = \mathbf{L} \mathbf{L}^T$, so that Equation (6) can be rewritten:

$$\mathbf{J} = (\mathbf{L}^{-1} \mathbf{R})^T (\mathbf{L}^{-1} \mathbf{R}) \quad (7)$$

At the end, we therefore have the sum of independent scalar residuals.

2.3.3 The input variables

The general idea is to adjust the age of the top of the record and the deposition rate (as well as the thinning function and LID for an ice-core archive) so as to minimize the cost function. We call these variables the *inverted variables*. The prior estimates of deposition rate (and thinning and LID for an ice core) are transferred by interpolation onto the age-equation grid. A first approach could be to adjust these variables



on the same age-equation grid, as is done in the Datice software (Lemieux-Dudon, 2009; Lemieux-Dudon
230 et al., 2010b, a, 2015). This requires the inversion of many variables, hence considerable computing
resources. Here we follow the same approach as in IceChrono (Parrenin et al., 2015), where we define a
multiplicative correction function onto a coarser grid, called the *inversion grid*. These correction functions
are defined as a function of the age for the deposition rate and LID and as a function of the depth for the
thinning function. We then transfer these correction functions on the age-equation grid by a linear
235 interpolation, using the prior age (the age calculated from the prior scenario of deposition, LID and
thinning) for the deposition rate and the LID. A basic assumption of our method is that the inverted
variables are always strictly positive, otherwise the Equations (1-4) have a singularity for a value of zero
for deposition rate and thinning. The correction function should therefore stay strictly positive as well.
Such variables are called *Jeffreys variables* and are generally described by log-normal distributions
240 (Tarantola, 2005). Through the application of a change of variable using the logarithm function, Jeffreys
variables become Cartesian and are then described by Gaussian probabilities.

2.3.4 The optimization method

This least-squares problem is solved iteratively using a *trust region* algorithm (Byrd et al., 1988; Branch
et al., 1999), which converges toward a minimum of the cost function and stops when a convergence
245 criterion is met (the default value is 10^{-5} but it can easily be changed). At each iteration, the model is
linearized, that is, we consider the linear operator which is tangent to the model. This linear system is
solved and the solution is then used as the base of the next iteration.

Contrary to IceChrono, the Jacobian operator is calculated analytically. For each site and each site pair,
the Jacobian matrix is derived for the residuals. For additional efficiency, the linear tangent operator and
250 its adjoint are derived for the multi-site logic. Indeed, when using the linear solver, one does not need to
calculate the Jacobian matrix, but just the effect of this matrix or its transpose on a vector. The linear
tangent and adjoint operators are therefore an efficient way to solve a least-squares problem, especially
when the Jacobian matrix is sparse because this Jacobian matrix does not need to be fully formed.

The initial value of the input vectors is set either as the prior, randomly or from the result of a previous
255 dating experiment. The latter option is possible even if a previous experiment did not have the same depth



or age resolutions. It is therefore possible to use a bootstrap method, starting from a fast, low-resolution experiment to spin and following up with a high-resolution experiment.

The trust region algorithm provides optimized values of the input vectors. At the solution, the product of the transpose Jacobian matrix with itself gives an approximate value of the Hessian matrix, that is, the inverse of the posterior covariance matrix. From there, the covariance matrix of the input variables for each site is calculated. Then, the covariance matrix for the output variables for each site is calculated.

2.4 Programming aspects

Paleochrono-1.1 is coded in the Python 3 programming language with several scientific packages (numpy, scipy, matplotlib). Paleochrono-1.1 both solves the optimization problem and displays the results as figures. For a simple archive, the figures show deposition rate and age. For an ice-core archive, the figures depict deposition rate, thinning function, LID, ice age, air age, Δ_{depth} , Δ_{age} , and ice layer thickness.

We use the trust region algorithm as implemented in the `scipy.optimize.least_squares` function. Compared to IceChrono, several coding optimizations have also been made.

The core of the code is entirely separated from the dating experiment directory which also contains the results of the run and which is composed of general parameter files, a directory for each site (which contains the parameters and observations for the given site) and a directory for each site pair (which contains the observations for the given site pair). Parameters that are common to all sites or site pairs can be set directly in a single file. All the parameter files follow the YAML format (Paleochrono-1.1 uses the `pyaml` module), which, contrary to IceChrono, allows one to make a clear separation between the main code and the parameters. The input data are given in text files. With respect to IceChrono, all files are given more straightforward names. It is not necessary to understand Python to run the code. Documentation on how to use Paleochrono-1.1 is available within the code. The output figures have also been improved with respect to IceChrono.

There are outputs at each steps of the code, including the initialisations, the optimization, the computing of the confidence intervals and the construction of the graphs, so that the user can inspect the process and estimate how much time is needed for completion. In particular, during the optimization by the trust region algorithm, the value of the cost function and its reduction is displayed at each iteration.



There are no fixed units in the code, so it is possible to use any unit system, but the units must be consistent. For example, it is possible to use kyr as the age unit instead of yr, but then this unit has to be used everywhere. Also, for a particular site, the depth can be expressed in another unit system (e.g., mm for speleothems), but then the deposition rate is expressed using the derived unit (e.g., mm/yr for speleothems).

3. Example dating experiment

IceChrono (Parrenin et al., 2015) was used on the AICC2012 dating experiment, a chronology that combines the EPICA Dome C (EDC), Vostok (VK), Talos Dome (TALDICE) and EPICA Dronning Maud Land (EDML) Antarctic ice cores and the NorthGRIP (NGRIP) Greenland ice core (Bazin et al., 2013; Veres et al., 2013).

Paleochrono-1.1 was already used on the AICC2023 dating experiment (Bouchet et al., 2023), an incremental improvement of AICC2012, with updated prior scenarios and dated horizons for the EDC ice core over the last 800 kyr. For this experiment, we increased the resolution until the cost function converges towards a single value. This value is ~ 196 , which is small with respect to the number of observations (2,139), highlighting the good general match of the posterior scenario with respect to the observations.

Here, to test and demonstrate the ability of Paleochrono-1.1 to date simple archives in combination with ice cores, we incorporate into this AICC2023 experiment two last glacial speleothems (MSD and MSL) from Hulu Cave (Wang et al., 2001), that have U/Th dated horizons (Cheng et al., 2018) on a 18-55 ka BP time interval. We caution readers that this dating experiment has been constructed to test the Paleochrono-1.1 model and to illustrate its abilities, and as such the resulting chronology presented here is *not* intended to be used for paleoclimatic studies. A future effort to update the AICC2023 chronology with information from speleothems is planned, but this is beyond the scope of the current study.

We set the prior deposition scenario to constant for both speleothems with an relative uncertainty (1σ) set to 1 (that is, the deposition is allowed to vary by an exponential factor). This value of 1 was defined by an *a posteriori* analysis of the reconstructed deposition rate and its variations. We assume also a



310 correlation length of 1,000 yr for the deposition rate of both speleothems, assuming higher frequency
variations are absent. For each speleothem, we use published U/Th dated horizons (Cheng et al., 2018).
Then, we define stratigraphic links between (1) the NGRIP $\delta^{18}\text{O}_{\text{ice}}$ and the MSD $\delta^{18}\text{O}_{\text{calcite}}$, (2) the MSD
and MSL $\delta^{18}\text{O}_{\text{calcite}}$ and (3) the MSL $\delta^{18}\text{O}_{\text{calcite}}$ and the EDC CH_4 records. To do so, we take advantage of
the fact that the abrupt climate variability characterising the last glacial period (NorthGRIP project
members, 2004; Corrick et al., 2020) is clearly expressed in each of these records. We link the records at
315 the onset of each abrupt Dansgaard-Oeschger (DO) events (Figure 2) using a mid-slope approach by
assuming a global synchronicity in the timing of the rapid warming transitions and of the $\delta^{18}\text{O}_{\text{calcite}}$ changes
(Corrick et al., 2020). We assign a constant uncertainty (1σ) of 100 yr to these synchronisation horizons.
100 yr is a rough estimate of the synchronisation error during DO transitions. A more careful analysis
would be needed to refine these estimates individually, but this is beyond the scope of the current
320 manuscript.

We call this experiment *AICC2023-Hulu*. Figure 2 shows the NGRIP $\delta^{18}\text{O}_{\text{ice}}$ record, Hulu/MSD and
Hulu/MSL $\delta^{18}\text{O}_{\text{calcite}}$ records and EDC CH_4 record onto this common and optimized age scale. Figure 3
are automatically generated by the Paleochrono-1.1 software and represent the chronology and deposition
rate for the MSL speleothem as well as the synchronisation for the NGRIP-MSD site pair, respectively.

325 We can observe in Figure 3 that the posterior chronology for the MSL speleothem is in better agreement
with the dated horizons than the prior chronology (which is expected since a constant growth rate is
assumed in the prior case) and generally fits the U-Th ages within their confidence interval. Paleochrono-
1.1 is also able to interpolate in-between age horizons when they are less dense. The uncertainty of the
posterior chronology ranges from 50 to 400 yr (1σ), increasing when the age horizons are less dense or
330 less precise.

Figure 4 shows that Paleochrono-1.1 is able to reconstruct a variable deposition rate from the
chronological information, in particular the dated horizons along the MSL speleothem. It is also able to
estimate an uncertainty on this posterior reconstruction, which will depend mainly on the uncertainty of
the U/Th dated horizons, the depth resolution of the U/Th dates and the assumed growth-rate variation
335 that affects interpolation uncertainty.



In Figure 5, we observe that Paleochrono-1.1 starts with a prior scenario based on archiving models with asynchronous stratigraphic links and that this new tool is able to come up with a solution where these stratigraphic links are respected.

4. Benchmarks

340 We now test the computing performance of Paleochrono-1.1 (computing time, memory used) in various dating experiments and configurations. We use a computing server with a Bi pro Xeon 2.10 GHz (48 cores and 96 threads) and 256 Gb of RAM. We use the Anaconda distribution of Python, which contains the Intel MKL (Math Kernel Library), providing parallel algorithms for common mathematical operations.

345 4.1 Comparison to IceChrono

We perform a test of computing performances on the AICC2012-VHR (Very High Resolution) experiment as defined in Parrenin et al. (2015). In this experiment, there are 10,520 variables to be inverted and 1,939 observations.

The experiment took about 24h and used 4.8 GB of RAM using IceChrono. The same experiment took 2
350 m and used 3.6 GB of RAM using Paleochrono-1.1. This is a factor ~700 difference in computing time and 25% less memory. This improvement in terms of computing resources will allow users to increase the number of sites in a dating experiment, increase the resolution within a paleoclimatic site, and/or run the software on their desktop computer rather than on a server.

4.2 Computing time as a function of the number of computing cores

355 We now test the Paleochrono-1.1 software with different numbers of computing cores. We use the AICC2023 dating experiment as defined in section 3. We test with 1, 2, 4, 6, 8, 12, 16, 24, 32 and 48 computing cores. Figure 6 shows the result of this experiment. The total computing time (resp. optimization time) ranges from 3 m 50 s (resp. 1 m 51 s) for 48 computing cores, to 24 mn (resp. 2 m 55 s) for one computing core. In this dating experiment, the Paleochrono-1.1 software therefore scales quite
360 well from one core to 16 cores (with a scaling factor of ~6), but after 16 cores the computing time



stagnates. In this experiment, 16 therefore seems to be the optimal number of computing cores, but this result might depend on the number of inverted parameters in the dating experiment.

4.3 Resources as a function of the number of inverted parameters

We now test the resources required by Paleochrono-1.1 as a function of the number of inverted parameters. We use the AICC2023 dating experiment (Bouchet et al., 2023). Starting from a low-resolution experiment, we multiply the resolution of deposition rate, LID and thinning in this experiment by factors of: 1, 2, 5 and 10. As a result, the number of inverted parameters is: 6,478, 12,944, 32,332 and 64,644. The third experiment corresponds to the official AICC2023 experiment (Bouchet et al., 2023). The results are shown on Figure 7 (on a log scales). The computing time ranges from ~0.7 m to ~14.2 m. The memory used ranges from ~2.1 GB to ~107.3 GB. We can observe that the memory evolves roughly quadratically as a function of the number of inverted parameters. For the computing time, the evolution is close to linear for a small number of parameters and then becomes quadratic for a large number of parameters.

5 Discussion and perspectives

5.1 On the use of probabilistic dating methods

First, we discuss why we should combine chronologies in the first place and what “optimal” means in this context. Common chronologies with internally-consistent sources of chronological information have the advantage to be more accurate because they incorporate more data and their uncertainties. A probabilistic method can capitalize on the fact that each dating method has its own strengths and they are complementing each other. In the example employed here, the speleothems provide very accurate absolute ages via radiometric U/Th dating, whereas the NGRIP ice core provides very accurate relative ages (i.e., durations) from counting of annual layers across intervals. Combining these two archives could therefore provide a chronology that is more accurate than the age scale of each archive dated in isolation. Moreover, common chronologies allow to decipher temporal sequence of climate and environmental changes



385 between different archives as lead and lags are not originating from chronology differences (assuming the synchronization links are realistic).

Second, we enumerate several applications of probabilistic dating models. Datice, the predecessor of Paleochrono-1.1, was used to create a coherent chronology of the EDC, EDML and NGRIP ice cores during the last deglaciation (Lemieux-Dudon et al., 2010b). Later, Datice was used to build AICC2012
390 (Bazin et al., 2013; Veres et al., 2013), a common chronology for 4 Antarctic ice cores (EDC, VK, EDML, TALDICE) and one Greenland ice core (NGRIP), taking into account many different types of absolute or relative chronological constraints. AICC2012 was used to discuss the comparison and phasing of EDC, EDML, TALDICE and NGRIP during the DO events of the last deglaciation (Landais et al., 2015). Datice was also used in a multi-archives context to build a coherent chronological scenario in the Mediterranean
395 region during the last deglaciation for 3 lake-sediments cores, 2 speleothems and one marine core (Bazin et al., 2019). More recently, Paleochrono-1.1 was used to build the DF2021 chronology for the Dome Fuji ice core (Oyabu et al., 2022), taking into account dated horizons and Δ depth constraints from various methods. Paleochrono-1.1 was also used to reconstruct the temporal variations of surface mass balance around Dome Fuji (Antarctica) for the last 5,000 years using shallow ice cores and snow pits (Oyabu et
400 al., 2023) synchronized using volcanic horizons. The ST22 chronology of the Skytrain ice core was constructed by matching its stratigraphy to EDC through various ice and air records and by using Paleochrono-1.1 to obtain a best fit. Finally, AICC2023, an update of AICC2012 with in-particular more accurate orbital-tuning records, was recently build using Paleochrono-1.1 (Bouchet et al., 2023).

Third, we discuss the limitation of probabilistic dating methods. Common chronologies are also attached
405 to drawbacks: they may mask systematic differences between dating methods that should be investigated and solved rather than forced into the same framework. In this case, the optimal solution in probabilistic terms may actually represent a compromise that is less physically meaningful. Additionally, the models for combining all the information may grow to be so comprehensive that most users will not be able to maintain an overview of the data employed, and operating the model will entail sometimes implicit and
410 important choices, e.g. on how to estimate the error bars of the prior and of the observations, how to set the correlation lengths for the prior, etc.



Another limitation of the method is that it requires errors to be both independent and have Gaussian distribution. Radiocarbon calendar ages typically do not have a Gaussian uncertainty, as they are a convolution of the measurement uncertainty and a calibration curve taking into account the variable atmospheric ^{14}C history. Likewise, volcanic ties have a complex uncertainty: if the tie correctly links the same layer in two records, the uncertainty of the synchronization will usually be no more than a few years, determined by data resolution and the shape of the signal matched. However, if the tie is incorrect, the error can be any number, and the error will rarely be described well by a Gaussian distribution with a width of e.g. 200 years. Furthermore, errors in any type of age constraint will be correlated in case of systematic biases. For example, when a sequence of closely spaced volcanic layers (forming a recognizable pattern due to their similar spacing) are matched between two ice cores, the tie points are likely all correct or all erroneous, making their uncertainties highly correlated. In the experiment performed here, there may be temporal lags in the climate system between the various parameters that are stratigraphically linked, the annual layer counting could systematically over- or under-count layers beyond what is included in the counting uncertainties, and the U/Th dating may have systematic biases related to for example the detrital Th correction.

In conclusion, optimal chronologies are practical for users who want to use the best possible common chronology, but it absolutely does not replace the need to compare and improve the chronologies of individual sites. The compromises involved in the modelling entail a risk that wrong chronological information or insufficiently quantified uncertainties will influence the resulting time scale negatively in a non-transparent way.

5.2 Comparison with IceChrono

Paleochrono-1.1 is an evolution of IceChrono (Parrenin et al., 2015), since it started as the same code base. But Paleochrono-1.1 improves several aspects of IceChrono. The first improvement to note is that Paleochrono-1.1 can handle continuous paleoclimatic archives other than ice cores. We showed here a test with two speleothems from Hulu Cave and multiple ice cores from Greenland and Antarctica. Other improvements include:



- **Efficiency:** Paleochrono-1.1 uses significantly less computing resources, in particular computing time. This is thanks to:

- the new trust region algorithm which can use an iterative solver at each linear iteration
- the per-site analytical Jacobian matrix
- the prior and multi-sites linear tangent and adjoint operators
- the ability to define the convergence criterion
- various python optimizations

On a AICC2012-VHR dating experiment identical to the one shown in Parrenin et al. (2015), the gain in computation time is a factor ~ 700 , which is huge. Therefore, Paleochrono-1.1 is more adapted for high-resolution runs than IceChrono. The memory reduction is less significant, with only a 25% reduction.

- **Ease of use:** Paleochrono-1.1 is easier to use than IceChrono thanks to several improvements:

- Paleochrono-1.1 now uses parameters files in the YAML format instead of the python format. This makes it easier to work with these parameter files and creates a clear separation between the main code and the parameters.
- Paleochrono-1.1 now uses a simpler naming of parameters and input/output files.
- Paleochrono-1.1 now has pre-defined grid types. Apart from the ‘regular’ type with a constant step, there is a ‘quadratic’ type with a linearly increasing step. It is also easy to add new grid types. This makes it easier to have, for example, age grids which are refined for present times and coarse for past times, or depths grids for ice cores which are more refined near the bedrock.
- There is an interactive output during the optimization process that displays the evolution of the cost function at each iteration. This makes it easier to inspect the optimization process and estimate the time that is still needed for the run to complete.
- The output figures have been greatly improved. In particular, the resolution is displayed on the deposition rate, LID and thinning figures. Moreover, it is possible to define the units used and the figures will respect these units.



- 465 • **Accuracy:** Paleochrono-1.1 is more accurate than IceChrono because of the following
improvements:
- Paleochrono-1.1 now inverts χ_0 , the age at the top of the sequence, while it was prescribed
in IceChrono. This is an improvement since it is not always possible to accurately
determine the age of the top of the sequence, in which case it needs to be estimated within
470 the optimization process.
 - The forward model is more accurate, thanks to several inaccuracies which have been
corrected.
 - Paleochrono-1.1 does not estimate the thinning in the firn for Equation (4) but directly
prescribes $\frac{D}{T}\Big|_{firn}^0$. This allows Equation (4) to be exact instead of being an approximation.
 - 475 ○ Thanks to the analytical Jacobian, the optimization finds a better minimum, that is, in closer
agreement with the observations.

In summary, Paleochrono-1.1 is a considerable improvement with respect to IceChrono and we highly
recommend the use of Paleochrono-1.1 to any existing and interested users of IceChrono. Indeed, the
future maintenance of IceChrono will be discontinued.

480 **5.3 Computing resources**

In the AICC2023 dating experiment, we have tested the computed time needed by Paleochrono-1.1 as a
function of the number of computing cores used. We find that 16 seems to be the optimal number of
computing cores, with a code which scales with a factor ~ 6 with respect to one unique computing core.
We have successfully tested the Paleochrono-1.1 software in the AICC2023 experiment with $\sim 65,000$
485 inverted parameters and $\sim 2,000$ observations. We find that the resource requirement (computing time,
memory) evolves roughly quadratically as a function of the number of inverted parameters. In this
experiment, the limiting factor is the memory. Indeed, the most demanding run takes only 14 mn, which
is acceptable but the memory used (107 GB) is on the upper range of what can be found in a workstation.
Using a computing node with ~ 1 TB of memory, which is at the edge of what can be done currently with
490 shared memory, would allow one to invert for $\sim 200,000$ parameters.



5.4 Possible future improvements

Paleochrono-1.1 only deals with continuous depth-age models. It could be interesting in the future to include possible hiatuses.

495 Paleochrono-1.1 does not support the automatic detection of outliers in the original site and site pair chronological information, e.g. information that is incompatible (within uncertainty) with the remaining constraints. A posterior visual check is necessary to detect them, and the irrelevant chronological observations should be manually removed.

Regarding resources, the most memory-demanding part in this run is not the optimization itself, but rather the construction of the posterior covariance matrix, which is required to evaluate the uncertainty of the posterior scenario. Another possibility to decrease the memory used and further increase the number of inverted parameters would be to not form the whole posterior covariance matrix, but only subsets of it, as seems possible using the LSQR linear solver (Kostina et al., 2009).

Conclusions

Here we describe a new probabilistic dating model for continuous climate archives, called *Paleochrono-1.1*. Paleochrono-1.1 is an evolution of the IceChrono model originally dedicated to ice cores, but it can now handle other continuous climate archives based on a varying deposition rate, such as lake and marine sediment cores or speleothems, and produce a coherent age scale between these multiple records and archives. Paleochrono-1.1 is more efficient, easier to use and more accurate than IceChrono. We demonstrate the ability of Paleochrono-1.1 in an AICC2023-Hulu dating experiment where we add two radiometrically-dated speleothems from Hulu Cave to the AICC2023 dating experiment (Bouchet et al., 2023). We then benchmark the computing resources needed to run Paleochrono-1.1. We observe that the code scales with up to 16 cores with a gain factor ~ 6 . We also show that the computing time and memory evolve roughly quadratically with respect to the number of inverted parameters. Finally, we test an AICC2023 dating experiment with $\sim 65,000$ parameters, where the limiting factor is the memory used. Going beyond 200,000 inverted parameters would require rewriting some sections of the model, in

particular with respect to the computation of the posterior covariance matrix needed to compute the uncertainty of the posterior scenario.

Paleochrono-1.1 has already been used in several published studies, either on one unique ice-core site but with multiple age constrains (Oyabu et al., 2022) or with multiple ice-core sites and multiple age
520 constrains (Oyabu et al., 2023; Mulvaney et al., 2023; Bouchet et al., 2023). Many other applications of Paleochrono-1.1 would be possible for various time periods and using various paleoclimatic records.

Code availability

Paleochrono-1.1 is an open source model available under the MIT license. It is hosted on the github facility (<https://github.com/parrenin/paleochrono>) and the version corresponding to the submission of this
525 manuscript has been published on Zenodo (<https://doi.org/10.5281/zenodo.10580279>). The main author (F. Parrenin) can provide support for people wanting to use the software.

Author contribution

FP developed the model code. MB, AL, KK, IO and RM tested the software. FP ran the simulations which were discussed between all co-authors. FP prepared the manuscript with contributions from all co-authors.

530 Competing interests

The authors declare they have no conflict of interest.

Acknowledgements.

We thank Lucie Bazin for helpful discussions and for testing the Paleochrono-1.1 software. This work was supported by the Fondation Ars et Cuttoli CO2Role project and by the LEFE IceChrono and CO2Role
535 projects. Some preliminary computations presented in this paper were performed using the GRICAD infrastructure (<https://gricad.univ-grenoble-alpes.fr>), which is supported by Grenoble research communities. EC acknowledges the financial support from the French National Research Agency under



the “Programme d’Investissements d’Avenir” through the Make Our Planet Great Again HOTCLIM project (ANR-19-MPGA-0001). SOR gratefully acknowledges the support from the Carlsberg
540 Foundation to the ChronoClimate project . CB acknowledges financial support from the US National Science Foundation (grants 1643394 and 1702920). We are thankful to Anders Svensson for helpful discussions.

References

- 545 Bazin, L., Landais, A., Lemieux-Dudon, B., Toyé Mahamadou Kele, H., Veres, D., Parrenin, F., Martinerie, P., Ritz, C., Capron, E., Lipenkov, V., Loutre, M.-F., Raynaud, D., Vinther, B., Svensson, A., Rasmussen, S. O., Severi, M., Blunier, T., Leuenberger, M., Fischer, H., Masson-Delmotte, V., Chappellaz, J., and Wolff, E.: An optimized multi-proxy, multi-site Antarctic ice and gas orbital chronology (AICC2012): 120–800 ka, *Clim Past*, 9, 1715–1731, <https://doi.org/10.5194/cp-9-1715-2013>, 2013.
- 550 Bazin, L., Lemieux-Dudon, B., Siani, G., Govin, A., Landais, A., Genty, D., Michel, E., and Nomade, S.: Construction of a tephra-based multi-archive coherent chronological framework for the last deglaciation in the Mediterranean region, *Quat. Sci. Rev.*, 216, 47–57, <https://doi.org/10.1016/j.quascirev.2019.05.018>, 2019.
- 555 Bouchet, M., Landais, A., Grisart, A., Parrenin, F., Prié, F., Jacob, R., Fourré, E., Capron, E., Raynaud, D., Lipenkov, V. Y., Loutre, M.-F., Extier, T., Svensson, A., Legrain, E., Martinerie, P., Leuenberger, M., Jiang, W., Ritterbusch, F., Lu, Z.-T., and Yang, G.-M.: The Antarctic Ice Core Chronology 2023 (AICC2023) chronological framework and associated timescale for the European Project for Ice Coring in Antarctica (EPICA) Dome C ice core, *Clim. Past*, 19, 2257–2286, <https://doi.org/10.5194/cp-19-2257-2023>, 2023.
- 560 Branch, M. A., Coleman, T. F., and Li, Y.: A Subspace, Interior, and Conjugate Gradient Method for Large-Scale Bound-Constrained Minimization Problems, *SIAM J. Sci. Comput.*, 21, 1–23, <https://doi.org/10.1137/S1064827595289108>, 1999.
- 565 Brauer, A., Hajdas, I., Blockley, S. P. E., Bronk Ramsey, C., Christl, M., Ivy-Ochs, S., Moseley, G. E., Nowaczyk, N. N., Rasmussen, S. O., Roberts, H. M., Spötl, C., Staff, R. A., and Svensson, A.: The importance of independent chronology in integrating records of past climate change for the 60–8 ka INTIMATE time interval, *Quat. Sci. Rev.*, 106, 47–66, <https://doi.org/10.1016/j.quascirev.2014.07.006>, 2014.



- 570 Byrd, R. H., Schnabel, R. B., and Shultz, G. A.: Approximate solution of the trust region problem by minimization over two-dimensional subspaces, *Math. Program.*, 40, 247–263, <https://doi.org/10.1007/BF01580735>, 1988.
- Cheng, H., Edwards, R. L., Southon, J., Matsumoto, K., Feinberg, J. M., Sinha, A., Zhou, W., Li, H., Li, X., Xu, Y., Chen, S., Tan, M., Wang, Q., Wang, Y., and Ning, Y.: Atmospheric $^{14}\text{C}/^{12}\text{C}$ changes during the last glacial period from Hulu Cave, *Science*, 362, 1293–1297, <https://doi.org/10.1126/science.aau0747>, 2018.
- 575 Corrick, E. C., Drysdale, R. N., Hellstrom, J. C., Capron, E., Rasmussen, S. O., Zhang, X., Fleitmann, D., Couchoud, I., and Wolff, E.: Synchronous timing of abrupt climate changes during the last glacial period, *Science*, 369, 963–969, <https://doi.org/10.1126/science.aay5538>, 2020.
- 580 Dome Fuji Ice Core Project Members, Kawamura, K., Abe-Ouchi, A., Motoyama, H., Ageta, Y., Aoki, S., Azuma, N., Fujii, Y., Fujita, K., Fujita, S., Fukui, K., Furukawa, T., Furusaki, A., Goto-Azuma, K., Greve, R., Hirabayashi, M., Hondoh, T., Hori, A., Horikawa, S., Horiuchi, K., Igarashi, M., Iizuka, Y., Kameda, T., Kanda, H., Kohno, M., Kuramoto, T., Matsushi, Y., Miyahara, M., Miyake, T., Miyamoto, A., Nagashima, Y., Nakayama, Y., Nakazawa, T., Nakazawa, F., Nishio, F., Obinata, I., Ohgaito, R., Oka, A., Okuno, J., Okuyama, J., Oyabu, I., Parrenin, F., Pattyn, F., Saito, F., Saito, T., Saito, T., Sakurai, T., Sasa, K., Seddik, H., Shibata, Y., Shinbori, K., Suzuki, K., Suzuki, T., Takahashi, A., Takahashi, K.,
585 Takahashi, S., Takata, M., Tanaka, Y., Uemura, R., Watanabe, G., Watanabe, O., Yamasaki, T., Yokoyama, K., Yoshimori, M., and Yoshimoto, T.: State dependence of climatic instability over the past 720,000 years from Antarctic ice cores and climate modeling, *Sci. Adv.*, 3, e1600446, <https://doi.org/10.1126/sciadv.1600446>, 2017.
- 590 Elderfield, H., Ferretti, P., Greaves, M., Crowhurst, S., McCave, I. N., Hodell, D., and Piotrowski, A. M.: Evolution of Ocean Temperature and Ice Volume Through the Mid-Pleistocene Climate Transition, *Science*, 337, 704–709, <https://doi.org/10.1126/science.1221294>, 2012.
- 595 EPICA community members, Augustin, L., Barbante, C., Barnes, P. R. F., Marc Barnola, J., Bigler, M., Castellano, E., Cattani, O., Chappellaz, J., Dahl-Jensen, D., Delmonte, B., Dreyfus, G., Durand, G., Falourd, S., Fischer, H., Flückiger, J., Hansson, M. E., Huybrechts, P., Jugie, G., Johnsen, S. J., Jouzel, J., Kaufmann, P., Kipfstuhl, J., Lambert, F., Lipenkov, V. Y., Littot, G. C., Longinelli, A., Lorrain, R., Maggi, V., Masson-Delmotte, V., Miller, H., Mulvaney, R., Oerlemans, J., Oerter, H., Orombelli, G., Parrenin, F., Peel, D. A., Petit, J.-R., Raynaud, D., Ritz, C., Ruth, U., Schwander, J., Siegenthaler, U., Souchez, R., Stauffer, B., Peder Steffensen, J., Stenni, B., Stocker, T. F., Tabacco, I. E., Udisti, R., van de Wal, R. S. W., van den Broeke, M., Weiss, J., Wilhelms, F., Winther, J.-G., Wolff, E. W., and
600 Zucchelli, M.: Eight glacial cycles from an Antarctic ice core, *Nature*, 429, 623–628, <https://doi.org/10.1038/nature02599>, 2004.
- EPICA Community Members, Barbante, C., Barnola, J.-M., Becagli, S., Beer, J., Bigler, M., Boutron, C., Blunier, T., Castellano, E., Cattani, O., Chappellaz, J., Dahl-Jensen, D., Debret, M., Delmonte, B., Dick, D., Falourd, S., Faria, S., Federer, U., Fischer, H., Freitag, J., Frenzel, A., Fritzsche, D., Fundel, F.,



- 605 Gabrielli, P., Gaspari, V., Gersonde, R., Graf, W., Grigoriev, D., Hamann, I., Hansson, M., Hoffmann, G., Hutterli, M. A., Huybrechts, P., Isaksson, E., Johnsen, S., Jouzel, J., Kaczmarek, M., Karlin, T., Kaufmann, P., Kipfstuhl, S., Kohno, M., Lambert, F., Lambrecht, A., Landais, A., Lawer, G., Leuenberger, M., Littot, G., Loulergue, L., Lüthi, D., Maggi, V., Marino, F., Masson-Delmotte, V., Meyer, H., Miller, H., Mulvaney, R., Narcisi, B., Oerlemans, J., Oerter, H., Parrenin, F., Petit, J.-R., Raisbeck, G., Raynaud, D., Röthlisberger, R., Ruth, U., Rybak, O., Severi, M., Schmitt, J., Schwander, J., Siegenthaler, U., Siggaard-Andersen, M.-L., Spahni, R., Steffensen, J. P., Stenni, B., Stocker, T. F., Tison, J.-L., Traversi, R., Udisti, R., Valero-Delgado, F., van den Broeke, M. R., van de Wal, R. S. W., Wagenbach, D., Wegner, A., Weiler, K., Wilhelms, F., Winther, J.-G., and Wolff, E.: One-to-one coupling of glacial climate variability in Greenland and Antarctica, *Nature*, 444, 195–198, <https://doi.org/10.1038/nature05301>, 2006.
- 610
- Hodell, D. A., Brenner, M., Kanfoush, S. L., Curtis, J. H., Stoner, J. S., Xueliang, S., Yuan, W., and Whitmore, T. J.: Paleoclimate of Southwestern China for the Past 50,000 yr Inferred from Lake Sediment Records, *Quat. Res.*, 52, 369–380, <https://doi.org/10.1006/qres.1999.2072>, 1999.
- Kostina, E. A., Saunders, M. A., and Schierle, I.: Computation of covariance matrices for constrained parameter estimation problems using LSQR, *Univ.*, 2009.
- 620
- Landais, A., Masson-Delmotte, V., Stenni, B., Selmo, E., Roche, D. M., Jouzel, J., Lambert, F., Guillevic, M., Bazin, L., Arzel, O., Vinther, B., Gkinis, V., and Popp, T.: A review of the bipolar see-saw from synchronized and high resolution ice core water stable isotope records from Greenland and East Antarctica, *Quat. Sci. Rev.*, 114, 18–32, <https://doi.org/10.1016/j.quascirev.2015.01.031>, 2015.
- 625
- Laskar, J., Robutel, P., Joutel, F., Gastineau, M., Correia, A. C. M., and Levrard, B.: A long-term numerical solution for the insolation quantities of the Earth, *Astron. Astrophys.*, 428, 261–285, <https://doi.org/10.1051/0004-6361:20041335>, 2004.
- Lemieux-Dudon, B.: Conjonction de données et de modèles pour la datation des forages profonds d’Antarctique et du Groenland, PhD thesis, Université Joseph Fourier, 2009.
- 630
- Lemieux-Dudon, B., Parrenin, F., and Blayo, E.: A Probabilistic Method to Construct an Optimal Ice Chronology for Ice Cores, in: *Physics of Ice Core Records 2*, 233–245, 2010a.
- Lemieux-Dudon, B., Blayo, Petit, J. R. E., Waelbroeck, C., Svensson, A., Ritz, C., Barnola, J.-M., Narcisi, B. M., and Parrenin, F.: Consistent dating for Antarctica and Greenland ice cores, *Quat Sci Rev*, 29, 8–20, 2010b.
- 635
- Lemieux-Dudon, B., Bazin, L., Landais, A., Toyé Mahamadou Kele, H., Guillevic, M., Kindler, P., Parrenin, F., and Martinerie, P.: Implementation of counted layers for coherent ice core chronology, *Clim. Past*, 11, 959–978, <https://doi.org/10.5194/cp-11-959-2015>, 2015.



Lisiecki, L. E. and Raymo, M. E.: A Plio-Pleistocene Stack of 57 Globally Distributed Benthic $\delta^{18}\text{O}$ Records, *Paleoceanography*, 20, PA1003, <https://doi.org/10.1029/2004PA001071>, 2005.

640 Mulvaney, R., Wolff, E. W., Grieman, M. M., Hoffmann, H. H., Humby, J. D., Nehrbass-Ahles, C., Rhodes, R. H., Rowell, I. F., Parrenin, F., Schmidely, L., Fischer, H., Stocker, T. F., Christl, M., Muscheler, R., Landais, A., and Prié, F.: The ST22 chronology for the Skytrain Ice Rise ice core – Part 2: An age model to the last interglacial and disturbed deep stratigraphy, *Clim. Past*, 19, 851–864, <https://doi.org/10.5194/cp-19-851-2023>, 2023.

645 NEEM community Members: Eemian interglacial reconstructed from a Greenland folded ice core, *Nature*, 493, 489–494, <https://doi.org/10.1038/nature11789>, 2013.

NorthGRIP project members: High-resolution record of Northern Hemisphere climate extending into the last interglacial period, *Nature*, 431, 147–151, 2004.

650 Oyabu, I., Kawamura, K., Buizert, C., Parrenin, F., Orsi, A., Kitamura, K., Aoki, S., and Nakazawa, T.: The Dome Fuji ice core DF2021 chronology (0–207 kyr BP), *Quat. Sci. Rev.*, 294, 107754, <https://doi.org/10.1016/j.quascirev.2022.107754>, 2022.

655 Oyabu, I., Kawamura, K., Fujita, S., Inoue, R., Motoyama, H., Fukui, K., Hirabayashi, M., Hoshina, Y., Kurita, N., Nakazawa, F., Ohno, H., Sugiura, K., Suzuki, T., Tsutaki, S., Abe-Ouchi, A., Niwano, M., Parrenin, F., Saito, F., and Yoshimori, M.: Temporal variations of surface mass balance over the last 5000 years around Dome Fuji, Dronning Maud Land, East Antarctica, *Clim. Past*, 19, 293–321, <https://doi.org/10.5194/cp-19-293-2023>, 2023.

Parrenin, F., Rémy, F., Ritz, C., Siegert, M., and Jouzel, J.: New modelling of the Vostok ice flow line and implication for the glaciological chronology of the Vostok ice core, *J Geophys Res*, 109, D20102, <https://doi.org/10.1029/2004JD004561>, 2004.

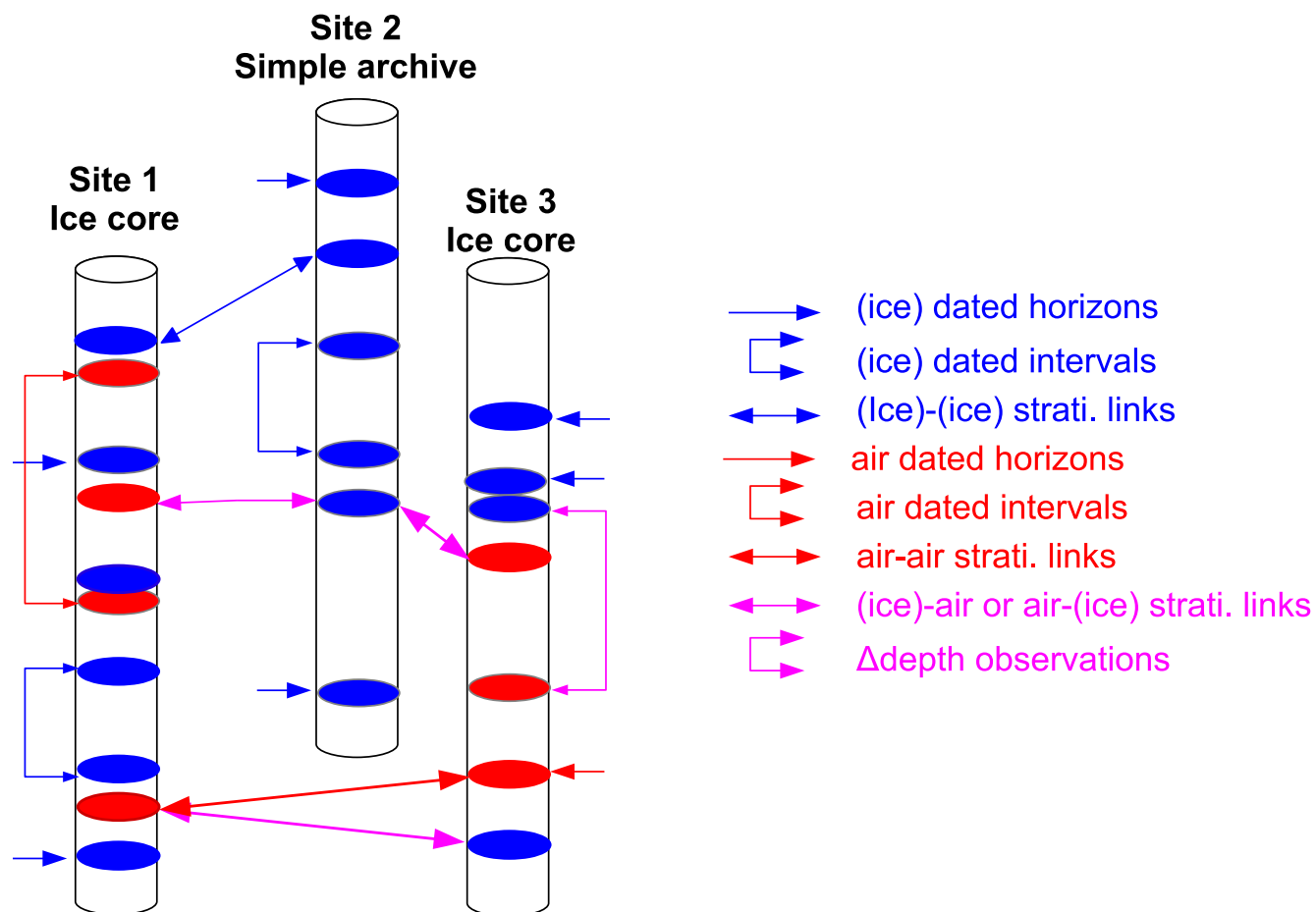
660 Parrenin, F., Dreyfus, G., Durand, G., Fujita, S., Gagliardini, O., Gillet, F., Jouzel, J., Kawamura, K., Lhomme, N., Masson-Delmotte, V., Ritz, C., Schwander, J., Shoji, H., Uemura, R., Watanabe, O., and Yoshida, N.: 1-D-ice flow modelling at EPICA Dome C and Dome Fuji, East Antarctica, *Clim Past*, 3, 243–259, <https://doi.org/10.5194/cp-3-243-2007>, 2007.

665 Parrenin, F., Barker, S., Blunier, T., Chappellaz, J., Jouzel, J., Landais, A., Masson-Delmotte, V., Schwander, J., and Veres, D.: On the gas-ice depth difference (Δdepth) along the EPICA Dome C ice core, *Clim Past*, 8, 1239–1255, <https://doi.org/10.5194/cp-8-1239-2012>, 2012.

Parrenin, F., Bazin, L., Capron, E., Landais, A., Lemieux-Dudon, B., and Masson-Delmotte, V.: IceChrono1: a probabilistic model to compute a common and optimal chronology for several ice cores, *Geosci Model Dev*, 8, 1473–1492, <https://doi.org/10.5194/gmd-8-1473-2015>, 2015.

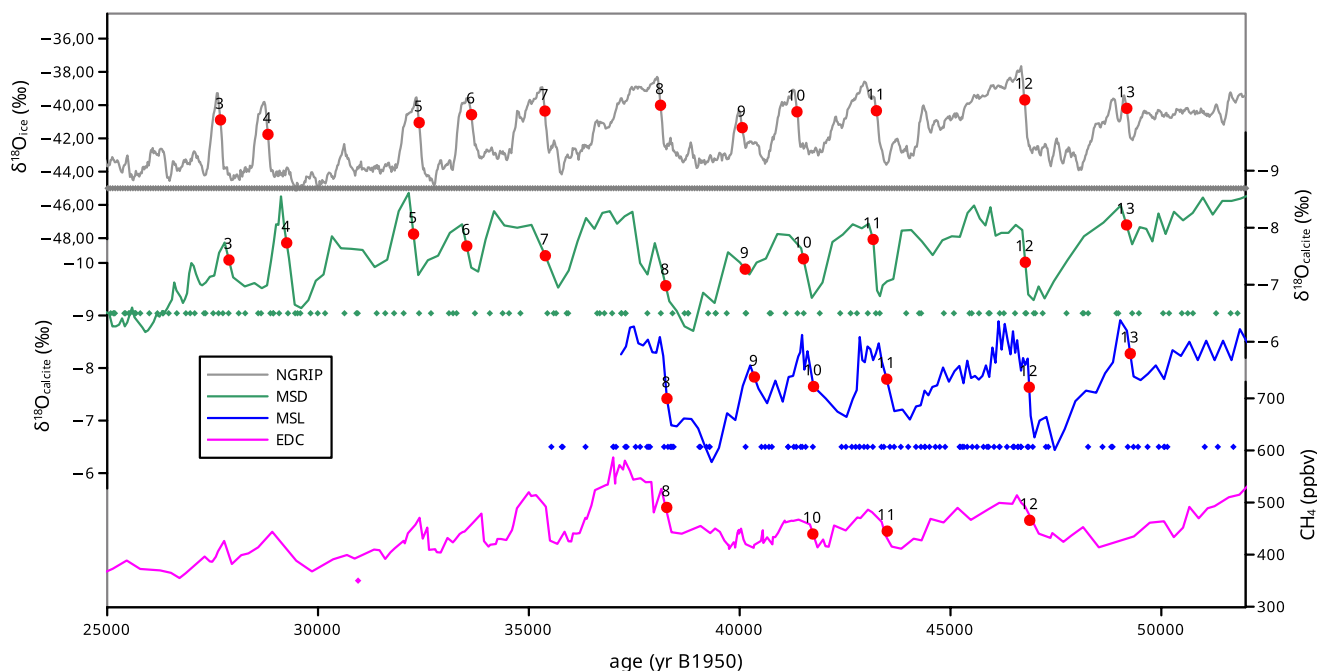


- 670 Shackleton, N. J.: The 100,000-Year Ice-Age Cycle Identified and Found to Lag Temperature, Carbon Dioxide, and Orbital Eccentricity, *Science*, 289, 1897–1902, 2000.
- Shackleton, N. J., Hall, M. A., and Vincent, E.: Phase relationships between millennial-scale events 64,000–24,000 years ago, *Paleoceanography*, 15, 565–569, 2000.
- 675 Sigl, M., Fudge, T. J., Winstrup, M., Cole-Dai, J., Ferris, D., McConnell, J. R., Taylor, K. C., Welten, K. C., Woodruff, T. E., Adolphi, F., Bisiaux, M., Brook, E. J., Buizert, C., Caffee, M. W., Dunbar, N. W., Edwards, R., Geng, L., Iverson, N., Koffman, B., Layman, L., Maselli, O. J., McGwire, K., Muscheler, R., Nishiizumi, K., Pasteris, D. R., Rhodes, R. H., and Sowers, T. A.: The WAIS Divide deep ice core WD2014 chronology – Part 2: Annual-layer counting (0–31 ka BP), *Clim Past*, 12, 769–786, <https://doi.org/10.5194/cp-12-769-2016>, 2016.
- 680 Svensson, A., Andersen, K. K., Bigler, M., Clausen, H. B., Dahl-Jensen, D., Davies, S. M., Johnsen, S. J., Muscheler, R., Parrenin, F., Rasmussen, S. O., Röthlisberger, R., Seierstad, I., Steffensen, J. P., and Vinther, B. M.: A 60 000 year Greenland stratigraphic ice core chronology, *Clim Past*, 4, 47–57, 2008.
- Tarantola, A.: Inverse problem theory and methods for model parameter estimation, *Society for Industrial Mathematics*, 2005.
- 685 Veres, D., Bazin, L., Landais, A., Toyé Mahamadou Kele, H., Lemieux-Dudon, B., Parrenin, F., Martinerie, P., Blayo, E., Blunier, T., Capron, E., Chappellaz, J., Rasmussen, S. O., Severi, M., Svensson, A., Vinther, B., and Wolff, E. W.: The Antarctic ice core chronology (AICC2012): an optimized multi-parameter and multi-site dating approach for the last 120 thousand years, *Clim Past*, 9, 1733–1748, <https://doi.org/10.5194/cp-9-1733-2013>, 2013.
- 690 WAIS Divide Project Members: Onset of deglacial warming in West Antarctica driven by local orbital forcing, *Nature*, 500, 440–444, <https://doi.org/10.1038/nature12376>, 2013.
- Wang, Y. J., Cheng, H., Edwards, R. L., An, Z. S., Wu, J. Y., Shen, C. C., and Dorale, J. A.: A high-resolution absolute-dated late Pleistocene Monsoon record from Hulu Cave, China., *Science*, 294, 2345–2348, 2001.
- 695 Williams, D. F., Peck, J., Karabanov, E. B., Prokopenko, A. A., Kravchinsky, V., King, J., and Kuzmin, M. I.: Lake Baikal record of continental climate response to orbital insolation during the past 5 million years, *Science*, 278, 1114–1117, 1997.

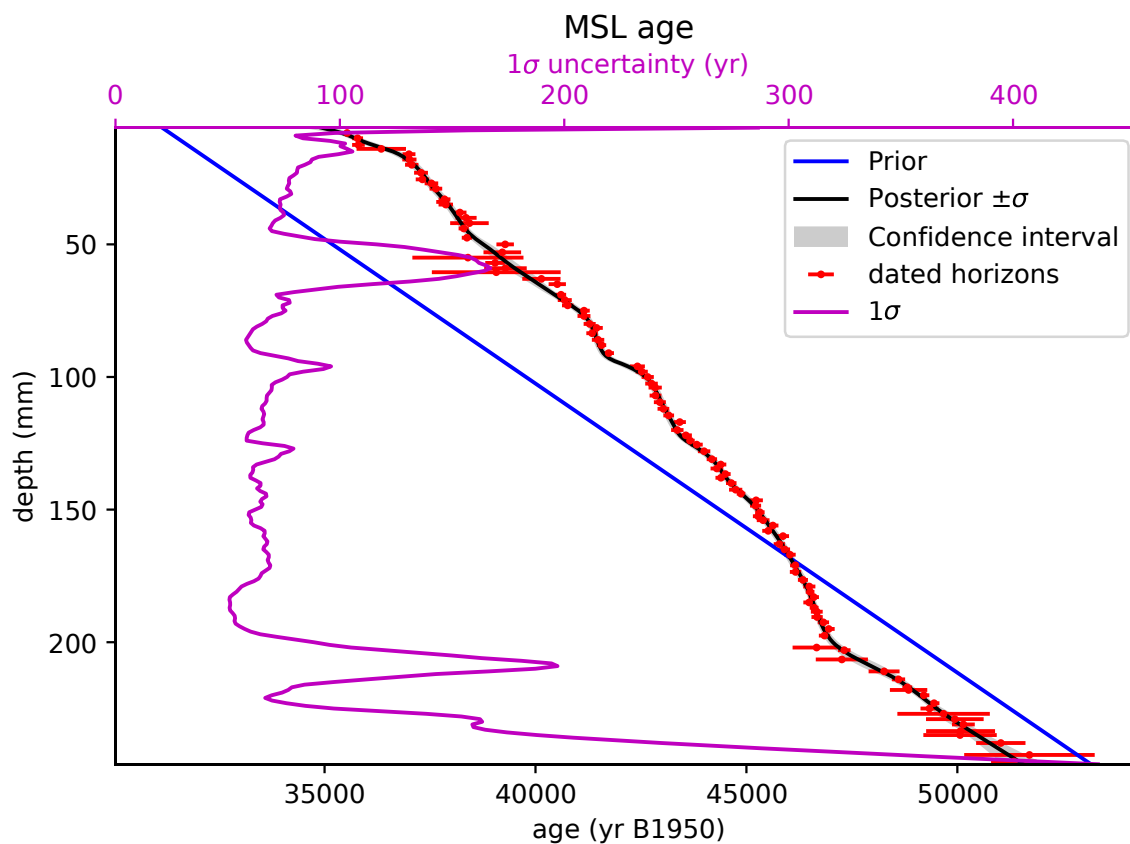


700

Figure 1: Scheme illustrating the different kinds of observations used to constrain the chronologies of the paleoclimatic sites in the Paleochrono-1.1 probabilistic dating model.

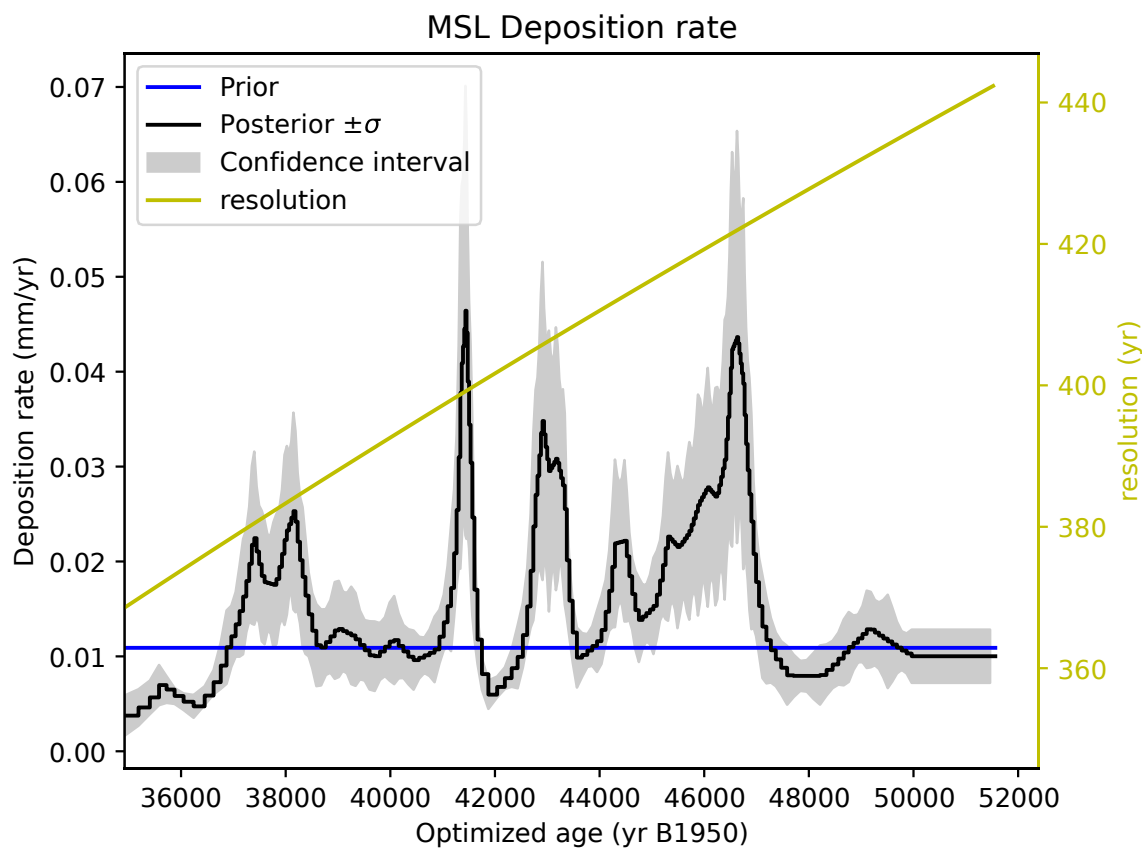


705 **Figure 2: Illustration of the synchronized and optimized chronology AICC2023-Hulu. From Top to bottom: NGRIP $\delta^{18}\text{O}_{\text{ice}}$ record; Hulu/MSD and Hulu/MSL $\delta^{18}\text{O}_{\text{calcite}}$ records; EDC CH_4 record. The red dots indicate the mid-points of DO onsets where the stratigraphic links are placed for the NGRIP-MSD, MSD-MSL and MSL-EDC site pairs and the labels indicate the DO numbers. The diamonds at the bottom of each panel represent the dated horizons used for each site.**

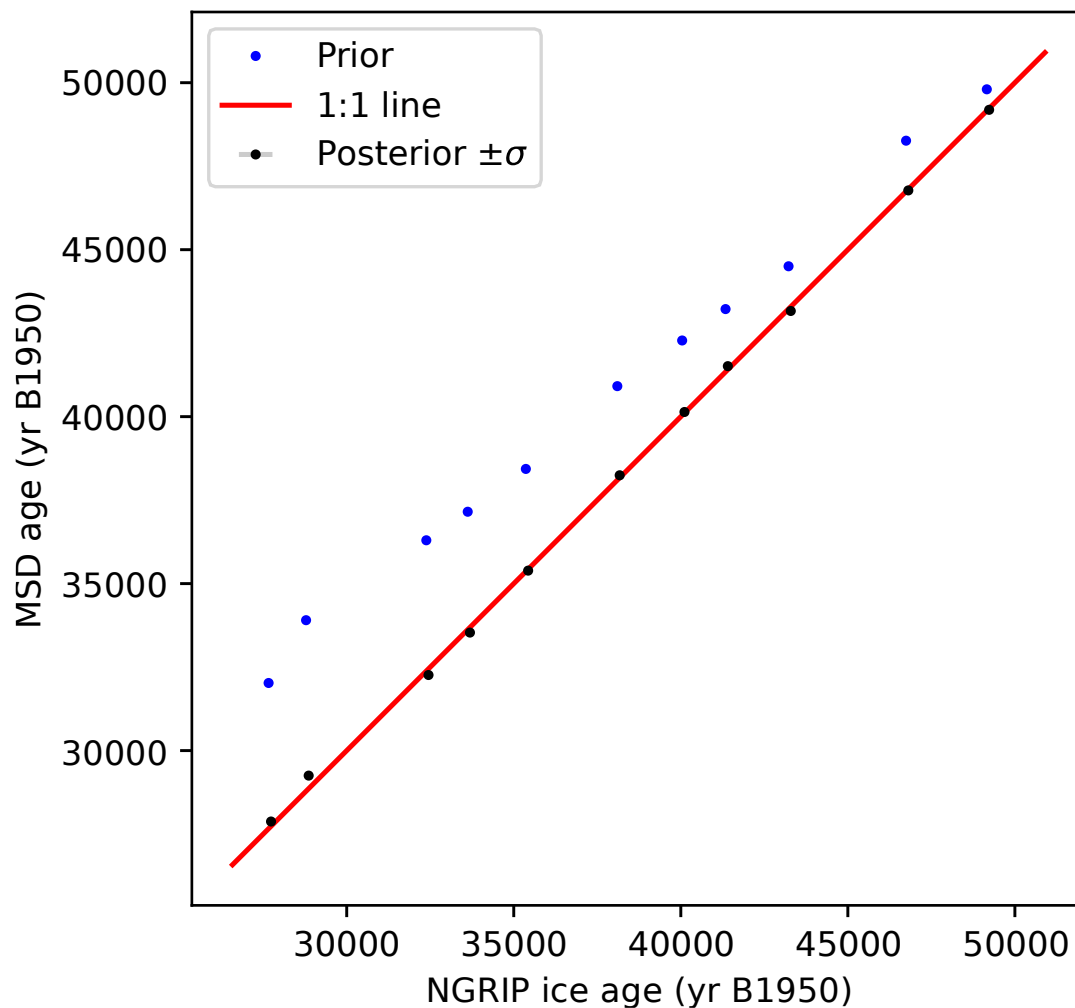


710

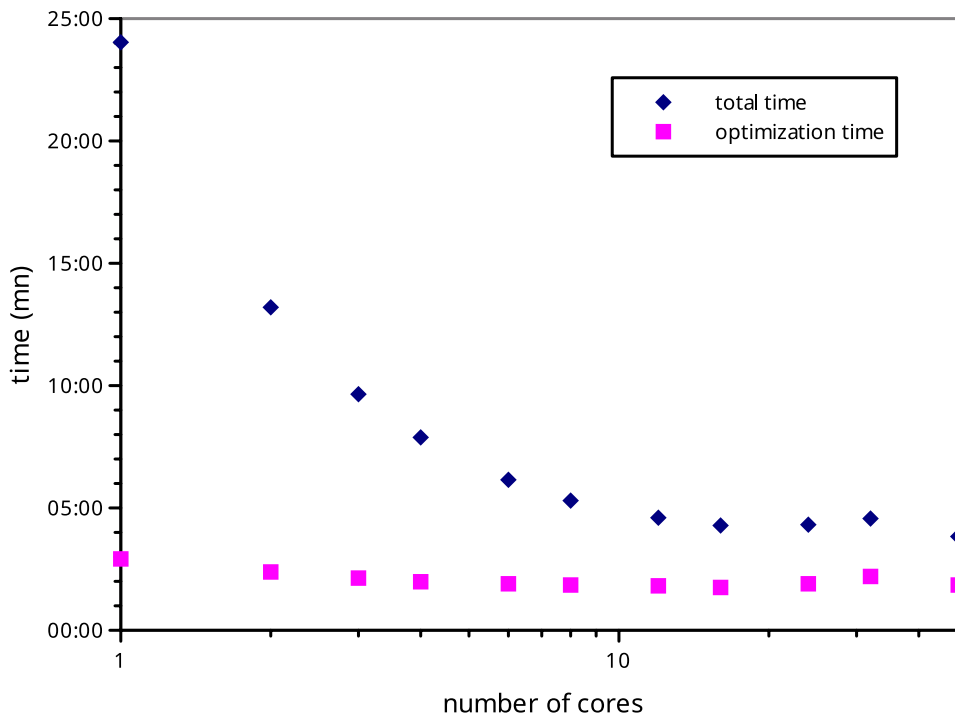
Figure 3: Age graph for the MSL speleothem as produced by Paleochrono-1.1 in the AICC2023-Hulu dating experiment. Blue: prior chronology based on the sedimentation scenario. Black and grey: posterior chronology and its confidence interval after optimization by Paleochrono-1.1. Red: dated horizons used in the dating experiment. Pink: 1sigma uncertainty of the posterior chronology.



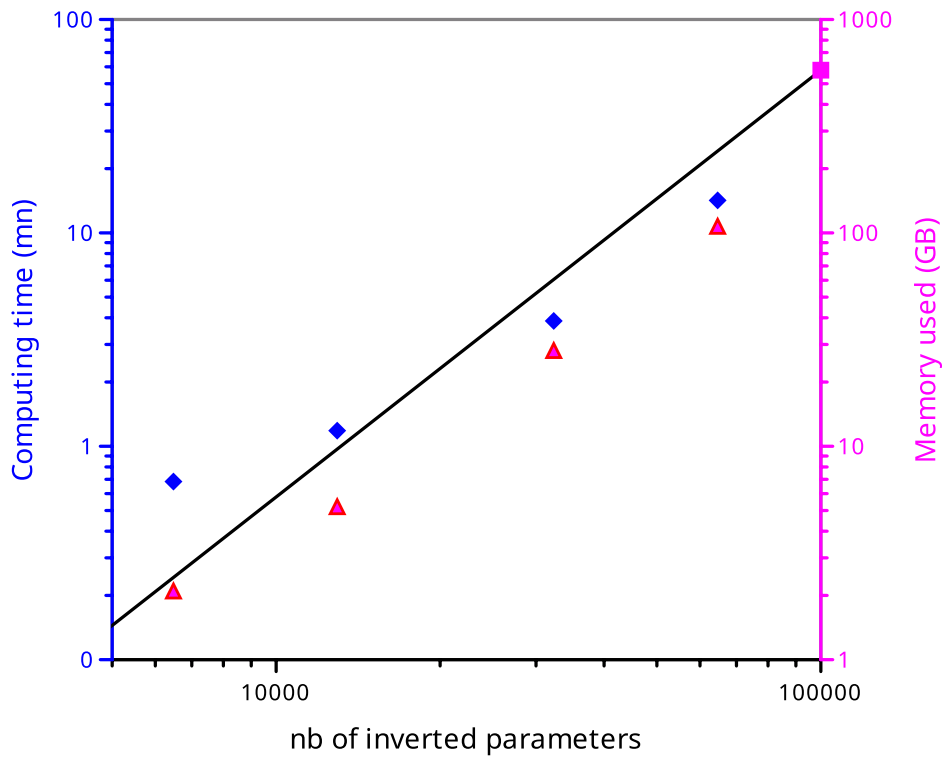
715 **Figure 4:** Deposition/growth rate graph for the MSL speleothem as produced by Paleochrono-1.1 in the AICC2023-Hulu dating experiment. Blue: prior scenario. Black and grey: posterior scenario and its confidence interval after optimization by Paleochrono-1.1. Yellow: time resolution of the deposition rate in the inversion grid.



720 **Figure 5: Synchronisation graph for the NGRIP-MSD site pair as produced by Paleochrono-1.1 in the AICC2023-Hulu dating experiment. Blue: prior scenario. Black: posterior scenario after optimization by Paleochrono-1.1. Red: the 1:1 line for comparison.**



725 **Figure 6: Computing time of the AICC2023 dating experiment using Paleochrono-1.1, as a function of the number of computing cores.**



730 **Figure 7: Computing time and memory used by Paleochrono-1.1 in the AICC2023 dating experiment, as a function of the number of inverted parameters. The X- and Y-axes are logarithmic. The black line represent a quadratic evolution of the resources with respect to the number of parameters.**

APPENDIX 7.4

Co-authored study submitted to PNAS:

Legrain, E., Capron, E., Bouchet, M., Landais, A., Parrenin, F., Caillon, N., Grisart, A., Prié, F. and Landais, A., Evolution of the Antarctic climate-atmospheric CO₂ phasing over the past five glacial Terminations, submitted to the Proceedings of the National Academy of Sciences (PNAS) journal in July 2024.

My contribution as a co-author to this study consisted in the reviewing of the article as well as in the questioning the interpretation of the overall research outputs.

1 **Evolution of the Antarctic climate-atmospheric CO₂ phasing over the past five glacial** 2 **Terminations**

3 Etienne Legrain^{1,2,3*}, Emilie Capron¹, Marie Bouchet⁴, Frédéric Parrenin¹, Nicolas Caillon¹, Antoine
4 Grisart⁴, Frédéric Prié⁴, Amaëlle Landais⁴

5 *1 Université Grenoble Alpes, CNRS, IRD, Grenoble INP, IGE, Grenoble, France*

6 *2 Laboratoire de Glaciologie, Université libre de Bruxelles, Brussels, Belgium.*

7 *3 Department of Water and Climate, Vrije Universiteit Brussel, Brussels, Belgium*

8 *4 Laboratoire des Sciences du Climat et de l'Environnement, LSCE/IPSL, CEA-CNRS-UVSQ,*
9 *Université Paris-Saclay, Gif-sur-Yvette, France*

10 **Corresponding author: etienne.legrain@ulb.be*

11

12 **Abstract**

13 The phasing between Antarctic climate and atmospheric CO₂ was quantified across the large
14 glacial terminations of the Quaternary to refine the processes responsible for carbon cycle changes
15 during global warming transitions. Previous studies have revealed heterogeneous results across the past
16 three glacial terminations. However, they rely on (i) paleoclimate reconstructions of multi-decadal to
17 thousand years of temporal resolutions, (ii) Antarctic ice cores drilled at different locations, (iii) climate
18 proxies measured either on the ice or the gas phase and (iv) heterogeneous statistical methods used to
19 quantify the phasing. These method-related differences prevent unambiguous climatic interpretations.
20 Here, we quantify the phasing evolution between Antarctic climate and atmospheric CO₂ across the past
21 five glacial terminations using new and existing high-resolution records of atmospheric CO₂ and the
22 isotopic composition of nitrogen ($\delta^{15}\text{N}$) measured on the EPICA Dome C ice core that is used as a gas-
23 phase proxy of Antarctic surface climate during terminations. Our analysis comparing three statistical
24 methods reveal that the phasing at the termination onsets depends on the considered methodology and
25 termination. Reversely, peak atmospheric CO₂ concentrations lag Antarctic climate change by ~ 500
26 years at the end of Terminations regardless of the methodology used. Combined with a multi-proxy
27 analysis, these results illustrate similarities between the end of Terminations and the last glacial
28 millennial-scale variability. Our results suggest that glacial terminations are ultimately ended by a
29 millennial-scale event occurring under favourable orbital conditions.

30

31

32 **Significance**

33 Glacial terminations represent the largest global warming transitions of the Quaternary. We
34 quantify the evolution of the Antarctic climate-atmospheric CO₂ phasing over the past five glacial

35 terminations with several statistical methods. While the phase relationship at the onset of terminations
36 seems to be method-dependent, the multi-centennial lag of atmospheric CO₂ decrease over the Antarctic
37 climate change is a recurrent climatic feature at the end of terminations. We interpret this lag as a
38 consequence of a millennial-scale climatic event leading to the end of the terminations.

39

40 **Introduction**

41 Glacial cycles of the Pleistocene are paced by small periodic variations in the astronomical
42 forcing (1–3). During this epoch, the most prominent climatic changes are the transitions from a glacial
43 state to an interglacial state, also known as glacial terminations (4). The timing of occurrences of these
44 major climatic transitions is driven by insolation forcing, itself determined by the orbital variations of
45 the Earth, and the global ice volume (e.g. 1, 5). How the relatively small variations in insolation forcing
46 translate into these major climatic variations remains unclear. During a termination, the warming is
47 initiated in the Southern Hemisphere, with an Antarctic temperature increase of 4-7°C (6, 7) and it is
48 systematically coupled with an atmospheric CO₂ concentration increase of 60-100 ppm (8–10). The
49 atmospheric CO₂ concentrations are controlled by sinks and sources of carbon in the Earth System that
50 act on centennial to orbital timescales. The oceanic reservoir and the continental biosphere are the two
51 main active drivers of atmospheric CO₂ concentrations during the Pleistocene, through changes in
52 oceanic circulation and high sensitivity to changes in surface climatic conditions respectively (8, 11,
53 12). A millennial-scale variability superimposed onto the orbital-scale changes has also been identified
54 during some of the past terminations in both Antarctic temperature and atmospheric CO₂ records ((10,
55 13); Legrain et al., in revision). This millennial-scale variability is superimposed onto the linear increase
56 of Antarctic temperature and atmospheric CO₂ (13) and is even suspected to play a role in the termination
57 occurrences itself (14, 15). The close coupling between atmospheric CO₂ and the warming in Antarctic
58 temperature leads to the following questions: what is the role of carbon cycle in glacial terminations?
59 Does the carbon cycle act as a driver or as an amplifier of the Antarctic warming? Determining which
60 of Antarctic climate or the carbon cycle first reacts at the onset of a termination would allow to establish
61 a causality link between these two drivers and to propose a sequence of changes starting from the initial
62 insolation variations to the resulting observed major climatic transitions. During the past three decades,
63 efforts have been led to produce high-resolution atmospheric CO₂((11, 12, 17); Legrain et al. in revision)
64 and surface Antarctic temperature records (7, 17). In addition, numerous statistical approaches for lead-
65 lag analysis have been developed to investigate the phasing between carbon cycle and surface Antarctic
66 climate across the last three terminations and the 650-430 ka interval (e.g. 14, 19–23).

67 The phasing between atmospheric CO₂ and Antarctic temperature during Termination I (TI) was
68 studied in several ice cores, using distinct statistical methodologies and temperature reconstruction
69 approaches (e.g. 14, 21, 23–27) (Table S1). With time, temporal resolution of both atmospheric CO₂

70 and Antarctic temperature records increased, better age models have been built and more complex
71 statistical methods have been developed while all these studies rely on the water isotopes composition
72 of ice as a proxy for surface Antarctic temperature (27). However, analysing the phasing between
73 atmospheric CO₂ and Antarctic temperature, which are measured in the gas phase on one hand and on
74 the ice phase on the other hand is subject to uncertainties associated with the relative age difference
75 between ice and air at a same depth level (the so-called delta age). To estimate this age difference, most
76 studies investigating TI estimate the gas lock-in-depth (LID) using a firn densification model (e.g. (24,
77 25)). However, the model is associated with large uncertainties for East Antarctic sites (up to ~1,000
78 years and ~550 years during glacial periods in Ref. (24) and Ref. (25), respectively) . To minimize these
79 uncertainties, some studies used ice cores drilled at sites characterised by high accumulation rate (20,
80 26). Another approach is to use the isotopic composition of nitrogen ($\delta^{15}\text{N}$ of N₂) and argon ($\delta^{40}\text{Ar}$).
81 Indeed, these air isotopes are considered to reflect variations in the forcings of firnification occurring at
82 orbital timescale, especially in East Antarctica, as their value is related to the LID through gravitational
83 molecular fractionation occurring in the firn before the bubble close-off (13, 28, 29). Using the $\delta^{15}\text{N}$ as
84 a proxy of LID, Ref. (13) has developed independent proxy of ice-gas age difference to investigate the
85 Antarctic temperature/CO₂ phasing across the entire TI. The studies investigating the Antarctic
86 temperature/CO₂ phasing across the entire TI suggests that Antarctic temperature leads CO₂ from -56
87 up to 410 years (20, 25, 26). Reversely, studies focusing on the end and onset of terminations reveal an
88 Antarctic temperature lead from 337 up to 1000 years and from synchronous up to 1000 years,
89 respectively (13, 22, 24, 25)(Table S1). A potential cause for this heterogeneity in results is likely related
90 to the fact that the water isotopic records inferred from ice cores drilled in different parts of Antarctica
91 can also reflect asynchronous regional climatic changes (e.g. 29, 30). For instance, the Siple Dome ice
92 core was retrieved at a coastal site from West Antarctica (32) while the EDC ice core was drilled on the
93 high plateau in East Antarctica (33).

94 The Antarctic temperature-CO₂ phase relationships across TII and TIII were investigated
95 originally using water isotopes as Antarctic temperature proxy (23, 24). However, these studies only
96 rely on a visual identification of the phasing due to the low resolution of the records, and the large
97 uncertainties related to the delta age are too large to identify significant sub-millennial-scale phasing. In
98 fact, the gas age computation is highly related to the LID, itself computed through firn densification
99 modelling. Beyond the TI, the uncertainty associated with such modelling is superior to estimate
100 potential phasing between Antarctic temperature and CO₂ concentration.

101 To circumvent this limitation, TII and TIII were investigated using the air isotopes as a direct
102 proxy of Antarctic climate. In the East Antarctic plateau, the LID is driven by changes in surface air
103 temperature and snow accumulation rate during terminations. The variations of $\delta^{15}\text{N}$ and $\delta^{40}\text{Ar}$ are thus
104 strongly related with surface climate conditions in the East Antarctic plateau through gravitational
105 fractionation (21, 34, 35). At the end of terminations, a significant thermal fractionation of air isotopes

106 is superimposed on the gravitational fractionation. The thermal fractionation is induced by a gradient of
107 temperature in the firn (36). A diminution of the gradient would have for consequence to lower the air
108 isotopes signal. The peak of air isotopes at the end of a termination is thus influenced by a lowering of
109 surface air temperature, or a slowdown of the surface air temperature increase. We can thus consider
110 that air isotopes variations are closely correlated with surface temperature and accumulation variations
111 on the Antarctic eastern plateau during glacial Terminations (21, 34).

112

113 Since air isotopes are directly measured in the gas-phase of the EDC and Vostok ice cores, it
114 circumvent all relative age uncertainty with the CO₂ concentration records (18, 21) (Table S1). Using
115 this approach based on the isotopic composition of argon ($\delta^{40}\text{Ar}$), an 800 ± 200 years lag of atmospheric
116 CO₂ over Antarctic temperature was calculated when considering the whole TIII. Indeed, the used
117 statistical methodology only provides a single phasing value calculated for the entire termination
118 interval. In other words, this approach does not allow exploring potential phasing changes across the
119 termination (19; Table S1). For TII, the use of the $\delta^{15}\text{N}$ variations as a proxy of Antarctic temperature
120 and the analysis based on a ramp fitting method revealed a two-step phasing, including a synchronous
121 rise of CO₂ and Antarctic surface temperature at the onset of the termination and a multi-centennial lag
122 of CO₂ at the end of the termination (21). While TII and TIII studies are both based on air-isotopes
123 Antarctic temperature proxy and East Antarctic ice cores, they differ by the statistical approach of lead-
124 lag quantification applied (see Methods). It is thus hard to conclude if this phasing difference is due to
125 the specificity of each Termination (e.g. the occurrence of millennial-scale event at the onset of TIII),
126 or if it is the due to the heterogeneity of statistical approaches.

127 The Antarctic temperature-CO₂ concentrations phasing studies aim to progress on the
128 understanding of the mechanisms at play during terminations. Especially, the near-synchronous to sub-
129 millennial lag of atmospheric CO₂ vs Antarctic temperature during terminations has confirmed the
130 Southern Ocean as the main source of carbon at orbital-scale and millennial-scale (13, 20, 25). However,
131 interpreting the phasing at a specific period of the Termination, e.g. onset or end, is more subject to
132 discussion. Especially, the large range of phasing results among TI studies and from a Termination to
133 another yields a critical question: does the observed differences in the phasing between Antarctic
134 Temperature and atmospheric CO₂ concentrations during the last three terminations represent a real
135 climatic signal or do they result from the heterogeneity of the chosen approaches (temperature proxy,
136 statistical method and location of the site)?

137 To address this question, a systematic evaluation of the phasing between atmospheric CO₂ and
138 Antarctic climate during terminations based on the same ice core, same statistical method, and same
139 Antarctic climate proxy is necessary. Also, due to the diversity in term of structure that is associated
140 with glacial terminations as observed in paleoclimatic archives (4), an extension of the Antarctic

141 climate-CO₂ phasing study beyond the last three terminations would provide useful insights. Here we
142 combine new and recently published sub-millennial-scale $\delta^{15}\text{N}$ of N₂ and atmospheric CO₂ records to
143 analyse the Antarctic climate-CO₂ phasing over the past five terminations (17, 22, 33, 34; Legrain et al.,
144 in revision). These analyses, the first conducted over TIV and TV, are performed using records from the
145 same ice core (EDC) and a similar Antarctic climate proxy ($\delta^{15}\text{N}$ of N₂). In addition, we base our
146 approach on several methods of phasing identification that are representative of the large diversity of
147 phasing method used (14, 19, 23; Supplementary materials). Based on this original approach, we are
148 now able to distinguish the climatic pervasive pattern of terminations from the approach-dependent
149 results. Finally, the results are integrated in a broader context using other paleoclimate records to explore
150 the climatic implications of our results on the evolution of the Antarctic climate-CO₂ phase relationship
151 over the past five glacial terminations.

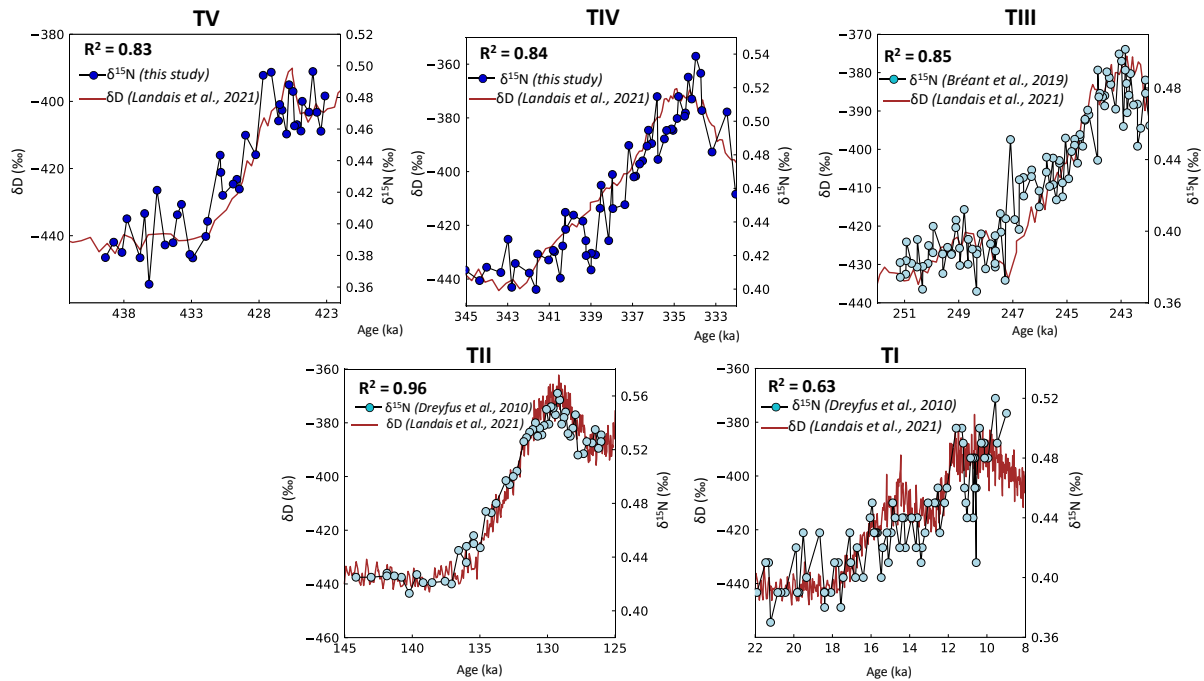
152

153 **Results**

154 *$\delta^{15}\text{N}$ records across TIV and TV*

155 We measured the $\delta^{15}\text{N}$ values on 37 new ice samples from the Antarctic EPICA Dome C (EDC)
156 ice core over TIV and TV using the melt-refreeze extraction system coupled with a mass spectrometer
157 at LSCE. A complete description of the experimental set-up and analyses is available in Ref. (35).
158 Combining these new measurements with published ones (34, 35), the average temporal resolution over
159 TIV and TV is 200 and 480 years, respectively. Measurements are associated with an uncertainty of
160 0.01‰. The amplitude of change is similar to the one registered during the last three terminations with
161 a $\delta^{15}\text{N}$ increase from the onset to the end of TIV and TV of ~0.10-0.15‰ (21, 34, 35). The increase
162 occurs in parallel to the δD record, an ice-phase proxy of Antarctic temperature (7). The correlation
163 found between δD and $\delta^{15}\text{N}$ over the TII, TIII, TIV and TV terminations is very strong ($R^2 > 0.8$; Fig.
164 1; Supplementary materials). The coefficient of determination R^2 is of 0.6 during TI. We explain this
165 lower R^2 by the fact that TI falls within a depth interval in the EDC ice core characterised by brittle ice
166 (34). This led to poor quality ice samples (i.e. associated with multiple cracks), and hence to a noisy
167 $\delta^{15}\text{N}$ profile across this period. Considering the values of the coefficient of determination, we propose
168 here to use the $\delta^{15}\text{N}$ variations as a proxy of Antarctic surface climate variations during glacial
169 terminations, following the approach of Refs. (21, 34, 35).

170



171

172 **Fig. 1: Comparison of $\delta^{15}\text{N}$ and δD records from the EDC ice core across the past five glacial terminations.** The $\delta^{15}\text{N}$
 173 record (light blue dots: (34, 35); black blue dots: this study) and the δD (brown lines (17)) on the AICC2023 timescale (37).
 174 The correlation between the two records is quantified using the coefficient of determination R^2 .

175

176 ***Phasing between Antarctic climate and atmospheric CO_2***

177 In this section, the phasing between Antarctic climate and CO_2 concentrations over the past five
 178 terminations is quantified using the three distinct methods from Caillon et al. (2003), Parrenin et al.
 179 (2013) and Chowdhry Beeman et al. (2019). First, the method of Caillon et al. (2003) calculates an
 180 average phasing between Antarctic climate and atmospheric CO_2 across the entire Termination,
 181 preventing the investigation of whether the phasing has evolved through time ((20, 24–26), see
 182 Supplementary Materials). Second, Parrenin et al. (2013) developed a method based on a piecewise
 183 linear function to quantify the phasing between Antarctic climate and atmospheric CO_2 concentrations
 184 at multiple stages during TI. Hence, they could investigate the evolution of the Antarctic climate- CO_2
 185 phasing across this termination. Third, the method of Chowdhry Beeman et al. (2019) also uses a
 186 piecewise linear function to distinguish the phasing at various stages across TI. Nevertheless, instead of
 187 providing a single “best fit” such as in Parrenin et al. (2013), it analyses the ensemble of fits accepted
 188 by the routine and provides probabilistic locators of changes in slope (22). Methodologies are described
 189 in details in the original papers (13, 18, 22) and are also discussed in the Methods section and in the
 190 Supplementary Materials.

191 Figure 2 presents our new analyses of the Antarctic climate- CO_2 phase relationship across the
 192 past five terminations (all results are given with the 1σ uncertainty). Based on the approach from Caillon

193 et al. (2003), our results show that on average, the Antarctic climate significantly leads the atmospheric
194 CO₂ concentrations by 560 ± 176 and 390 ± 102 years during TI and TIII respectively (Table S1).
195 However, no significant phase relationship can be identified during TII, TIV and TV (140 ± 345 , 170
196 ± 223 , 120 ± 509 years).

197 Following the approach of Parrenin et al. (2013), the onsets of TI, TIV and TV do not exhibit
198 significant asynchronicity between the Antarctic climate and atmospheric CO₂ increases: -320 ± 425 , $-$
199 180 ± 1335 and 80 ± 690 years respectively. In contrast, atmospheric CO₂ lags Antarctic climate at the
200 onset of TII (2110 ± 452 years) (Figs. 2 and 3). The millennial-scale event at the onset of TIII prevents
201 a clear identification of the start of this termination in both the CO₂ and the $\delta^{15}\text{N}$ records. The results for
202 the termination onsets obtained with the Chowdhry Beeman et al. (2019) method are different as a
203 significant lag of the Antarctic climate over the CO₂ is identified at the onset of TIV (-1863 ± 241 years).
204 Reversely, a significant lead of the Antarctic climate over the CO₂ is identified at the onset of TI (651
205 ± 535 years) (Fig. 2, Table S1). Phasing results at the onset of the terminations are thus heterogeneous
206 and differ among the statistical methods used. The heterogeneity could be explained by slow increase
207 rate registered in the two gas records. For instance, the CO₂ increase at the onset of TIV is characterized
208 by a two-step ~ 10 ppm increase, with the second one occurring at a larger increasing rate. While the
209 method from Chowdhry identifies the first small increase as the start of TIV, the Parrenin method makes
210 a compromise between the two steps and identifies for the CO₂ concentration increase a younger start
211 by ($\sim 2,000$ years) start.

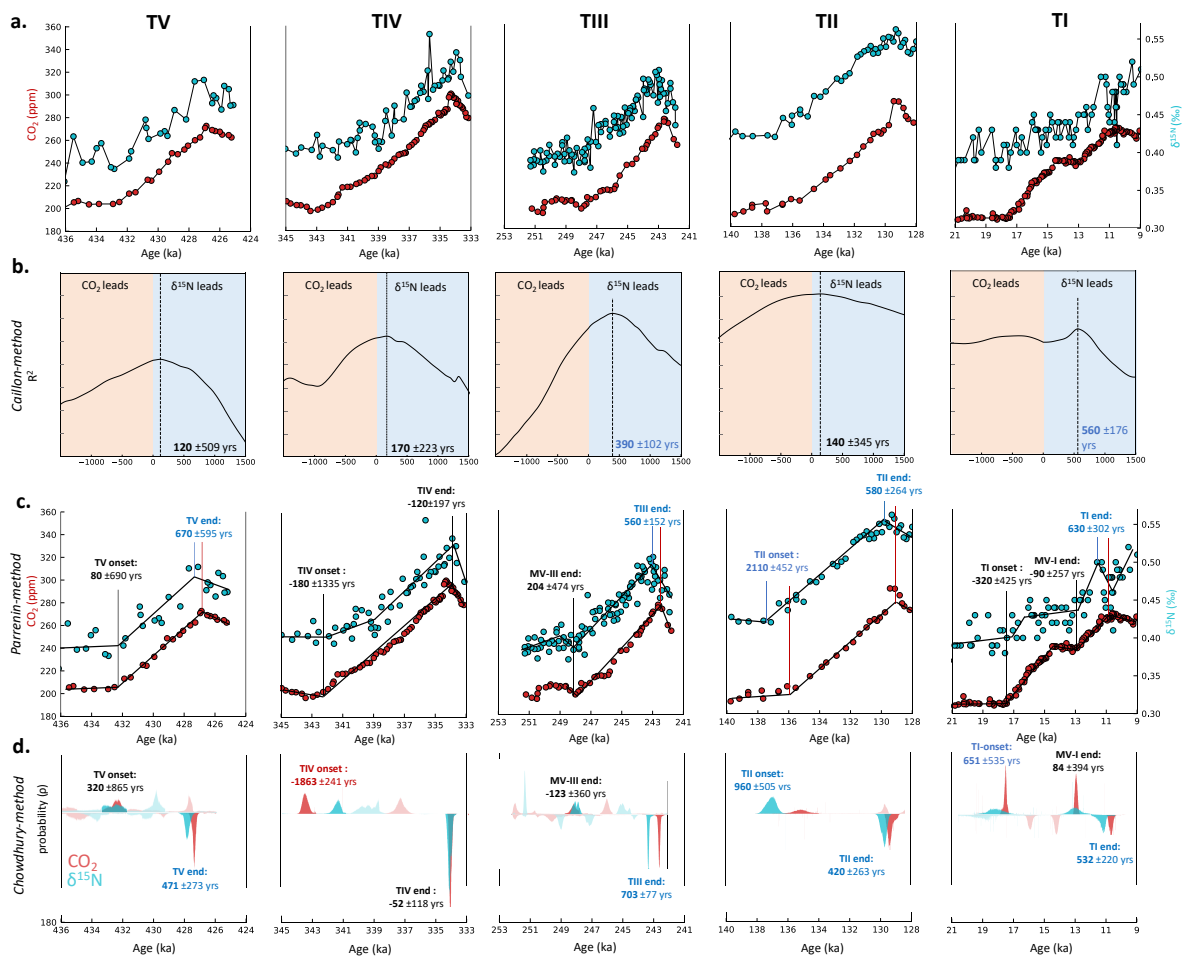
212 Looking now at the results at the end of TI, TII, TIII and TV, our analysis using the Parrenin et
213 al. (2013) method reveals a systematic lag of the CO₂ peak (i.e. the onset of the CO₂ concentrations
214 decreases) over Antarctic climate of 630 ± 302 , 580 ± 264 , 560 ± 152 , 670 ± 595 years (Figs 2 and 3).
215 Similarly, our results based on the Chowdhry Beeman et al. (2019) method identify a CO₂ lag over
216 Antarctic climate of 532 ± 220 , 420 ± 263 , 703 ± 77 , 471 ± 273 years at the end TI, TII, TIII and TV,
217 respectively. The only exception occurs at the end of TIV, while the Parrenin et al. (2013) and Chowdhry
218 Beeman et al. (2019) methods both reveal a near synchronous decrease (-120 ± 128 years and -52 ± 118
219 years respectively) (Table S1). Phasing results at the end of the terminations thus illustrates a significant
220 lead of Antarctic climate over CO₂ concentrations as inferred using both statistical methods, apart for
221 TIV.

222 Beyond the end and the onset of terminations, other slope breakpoints are revealed by the
223 Parrenin et al. (2013) and the Chowdhry Beeman et al. (2019) methods. Most of these breakpoints are
224 identified during intervals associated with low-resolution $\delta^{15}\text{N}$ and CO₂ records (see Supplementary
225 Materials). Thus, we decided to interpret only the breakpoints coinciding with already-identified
226 millennial-scale variability in both records and with both methods. The end of the millennial-scale event
227 occurring during TI ends is synchronous in both records using the Parrenin et al. (2013) method (90

228 ± 257 years) and the Chowdhry Beeman et al. (2019) method (84 ± 394 years) (Fig. 2, Table S1).
 229 Similarly, the end of the millennial-scale event occurring at the onset of TIII occurs synchronously in
 230 both records with the Parrenin et al., 2013 method (204 ± 474 years respectively) and the Chowdhry
 231 Beeman et al. (2019) method (-123 ± 360 years).

232 To conclude, the phasing results at the onset of Terminations are method- and Termination-
 233 dependent. Reversely, there is a significant lead of Antarctic climate change over CO₂ concentrations
 234 decrease at the end of four of the past five Terminations regardless of the statistical method used.

235



236

237 **Fig. 2: Phasing analysis of the $\delta^{15}\text{N}$ and atmospheric CO₂ records during the past five terminations.** a. Blue and red
 238 curves are respectively the $\delta^{15}\text{N}$ (33, 34; this study) and atmospheric CO₂ records from the EDC ice core on the AICC2023 gas
 239 timescale (37). b. Quantification of the average phasing over the entire termination following the method from Caillon et al.
 240 (2003). The vertical dash line corresponds to the time shift that needs to be made between the two datasets to obtain the best
 241 correlation (R^2). c. Quantification of the phasing at different stages of the termination (end, onset, end of millennial-variability)
 242 using the method from Parrenin et al. (2013). The interpreted changes are the ones marked with vertical lines. The number of
 243 breakpoints used corresponds to the number of different slopes and can vary from a Termination to another. d. Quantification
 244 of the phasing at different stages of the termination (end, onset, end of millennial-variability) using the method from Chowdhry
 245 Beeman et al. (2019). Blue and red curves are the normalized histograms of probable changes for $\delta^{15}\text{N}$ and atmospheric CO₂,

246 respectively. Histograms are downward-oriented when the rate of change decreases and upward-oriented when it increases.
247 The only interpreted changes are the ones marked with plain colours. Blue and red text represent a lead of $\delta^{15}\text{N}$ and CO_2 ,
248 respectively, while a black text represents no significant lag of one of the parameters. MV: Millennial-scale Variability.

249

250 **Discussion**

251 The analyses performed with the Parrenin et al. (2013) and Chowdhry Beeman et al. (2019)
252 statistical methods reveal an evolution of the Antarctic climate- CO_2 phasing during terminations: among
253 a single Termination, the phasing could differ between the onset and the end of the Termination. As a
254 result, it appears evident that the method from Caillon et al. (2003) oversimplified the phasing results.
255 Hence, we do not discuss further the results inferred from the Caillon et al. (2003) method in this section.

256 *Antarctic climate- CO_2 phasing at the onset and end of terminations*

257 Quantifying the Antarctic climate- CO_2 phasing at the onset of terminations can help deciphering
258 whether the carbon cycle acts (i) as a trigger of the climatic transition or (ii) as an amplifier of a climatic
259 transition. Previous studies have provided conclusions that either demonstrate a synchronous rise of both
260 parameters, or a multi-centennial lag of atmospheric CO_2 over Antarctic climate (Table S1). Here our
261 new approach has allowed to investigate this phasing without any bias due to the use of different ice
262 core sites, Antarctic climate proxies and statistical methods. Especially, we identify that the phasing at
263 the onset of a termination is highly dependent of the statistical method used. For instance, our results
264 applying the statistical method from Parrenin et al. (2013) reveal a millennial-scale lead of Antarctic
265 climate over atmospheric CO_2 at the onset of TII while the study of Ref. (21), that used the Ramp Fit
266 statistical method (38), proposes a synchronous increase. This heterogeneity is already observed by
267 comparing studies based on ice-phase Antarctic climate proxy focusing on phasing during TI. However,
268 these differences could also come from the use of distinct ice cores between these studies (13, 26).

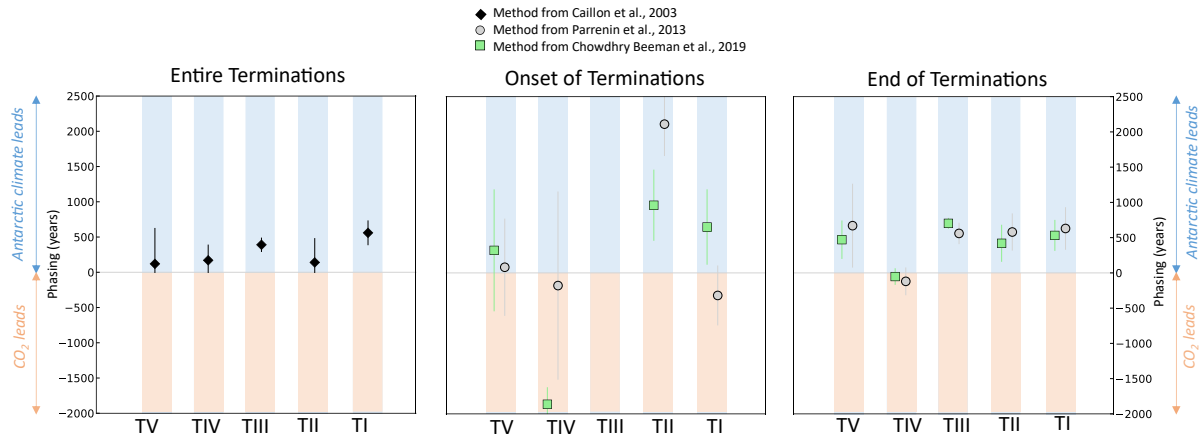
269 Precisely quantifying the phasing at the onset of a termination is challenging for two main
270 reasons. First, the onset of a termination is characterized by a relatively slow rate of increase in both
271 CO_2 and $\delta^{15}\text{N}$ records, making it hard to distinguish proxy-induced or measurement-induced variability
272 from the real climatic signal. Second, the onset of a termination occurred in a full glacial condition,
273 characterized by a larger short-term variability than during interglacial periods (7). Especially, the
274 occurrence of large millennial-scale events (such as the Antarctic Isotope Maximum 1 during TI),
275 sometimes nearly synchronous to the onset of the termination (such as the millennial-scale event at the
276 start of TIII) makes it challenging to identify precisely the timing of the variation onsets in the proxies.

277 Reversely, at the EDC drilling site, the multi-centennial scale lead of the Antarctic climate over
278 atmospheric CO_2 observed at the end of TI, TII, TIII and TV does not depend on the identification
279 method used. Nevertheless, the representativeness of the EDC drilling site as an indicator of the timing

280 of Antarctic climate variations can be questioned. Previous studies focusing on the millennial-scale
281 climate variability deduced from water isotopes measurements evidenced a multi-centennial scale
282 asynchronicity in the climatic variations at different locations of Antarctica (6, 30). To check this result,
283 we compared the timing of Antarctic temperature variations as represented by the $\delta^{18}\text{O}$ records from
284 spatially scattered Antarctic ice cores (EDML, TALDICE and WD) and the EDC ice core records using
285 the method from Parrenin et al. (2013) at the end of Termination I (Fig. S2). For this period, the dating
286 of the ice cores is mostly estimated through ice annual layers counting (WD, (39)) or through volcanic
287 tephra or sulfate markers (WD, EDML, TALDICE and EDC, (37, 40)). The relative timing of water
288 isotopes variations at the end of TI is thus not biased by a synchronization of the ice cores relying on a
289 climatic hypothesis. At the end of TI, the change in water isotopes composition is first registered at the
290 WD site, which is located in the Western Antarctic ice sheet. Then, the isotopic composition varies at
291 the EDML and TALDICE sites, approximately ~200 years before the EDC site (Fig. S2). These results
292 suggest that the observed ~500 years lead of Antarctic climate as recorded at the EDC site over
293 atmospheric CO_2 concentrations likely represents a minimum value of the average Antarctic climate
294 lead over CO_2 concentrations change at the end of a Termination.

295 The lead of Antarctic climate over atmospheric CO_2 at the end of Terminations was previously
296 evidenced during TI and TII (13, 21, 22, 24, 38). These studies rely on an ice-phase climatic proxy for
297 TI and on the Rampfit statistical methodology for TII (38). Here we confirm these results for the last
298 two terminations and evidence a similar pattern at the end of TIII and TV, making the multi-centennial
299 lag of atmospheric CO_2 over Antarctic temperature a pervasive pattern of four of the five past
300 terminations. Towards the end of a termination, the atmospheric CO_2 and $\delta^{15}\text{N}$ signal undergoes an
301 abrupt increase followed by a decrease (Fig. 2). This morphology probably explains why it is easier to
302 quantify the phasing at the end of a termination compared to its onset. Indeed, the associated change in
303 slope can be easily detected through statistical method due to its abruptness.

304 Over the past five terminations, the only exception of phasing between atmospheric CO_2
305 concentrations and Antarctic climate occurred during the end of TIV. The multi-phasing method of
306 analysis could be biased since different types of climate variabilities occurring at different timescales
307 are superimposed. The end of this termination is characterised by an increase rate of 26.2 ± 17.6 ppm per
308 century and an amplitude of 15.8 ± 1.1 ppm in the CO_2 record which is the fastest and most amplified
309 centennial-scale event in the atmospheric CO_2 record of the last 500 ka ((16); Legrain et al. in revision).
310 This event is not associated with any counterparts in the water isotopic record from Antarctica ((17);
311 Fig. 1). We hypothesise that this event would have provoked an early maximum in CO_2 concentrations
312 that consequently disturbed the CO_2 - Antarctic temperature phasing at the end of the Termination.



313

314 **Fig. 3: Quantification of the Antarctic climate-CO₂ phasing during the different stages of the past five terminations.**

315 **Left:** phasing along the termination using the Caillon et al., 2003 methodology (black diamonds). **Middle:** Phasing results at
 316 the onset of the terminations using the method from Parrenin et al., 2013 (pink circles) and the one from Chowdhry Beeman et
 317 al., 2019 (grey squares). **Right:** Phasing results at the end of the terminations using the method from Parrenin et al., 2013 (pink
 318 circles) and the one from Chowdhry Beeman et al., 2019 (grey squares). At the onset of TIII (both methods), the statistical
 319 methods do not converge to provide a timing of slope change for at least of one the two records. For the three panels, a positive
 320 value implies a lead of Antarctic climate over atmospheric CO₂.

321

322 *The end of glacial terminations as millennial-scale climate event*

323 The occurrence of millennial-scale events and its manifestation in the Southern Hemisphere
 324 with the Antarctic Isotope Maxima (AIM) was systematically associated with a delayed peak response
 325 of atmospheric CO₂ concentrations respectively to the Antarctic climate (12). The lag observed during
 326 AIM is of similar amplitude to the one identified at the end of terminations (Fig. 2) (~500 years).
 327 Similarly to the last glacial period, we consider that our lag value is a minimum value as the water
 328 isotopic variations at the EDC site occurs later compared to other Antarctic sites at the end of a glacial
 329 termination (Fig. S2). Thus, our study evidenced a similarity in phasing between atmospheric CO₂
 330 concentrations and Antarctic climate variations during the last glacial period and the end of terminations
 331 that suggests a common mechanism occurring at the end of these two climatic features.

332 Based on various climatic proxies, we explore the role of Northern and low latitudes at the end
 333 of glacial Terminations to investigate the mechanisms at play during these periods. In the ice core record,
 334 the millennial-scale events occurring during the last glacial period are characterized by an abrupt
 335 increase of CH₄ concentrations of at least 50 ppb (41). This variability in CH₄ concentrations can be
 336 attributed to a shift of Intertropical Convergence Zone (ITCZ) and subsequent release of CH₄ from
 337 Northern Hemisphere wetlands (41). A carbon cycle box model analysis of the carbon sources during
 338 the last glacial period has revealed that a combination of both Southern and Northern hemisphere
 339 processes contributed to the observed variations in atmospheric CO₂ concentrations (12). While the

340 Southern hemisphere mechanisms acted as a background forcing shaping the first order dynamics of
341 carbon cycle, the Northern hemisphere would play a key role in centennial-scale variability observed at
342 the end of each millennial-scale event.

343 To compare these mechanisms initially described for the last glacial period with the end of
344 Termination, we perform a phasing analysis between atmospheric CO₂ concentrations and two gas-
345 phase proxies reflecting the dynamics of Northern and low-latitudes: the atmospheric CH₄
346 concentrations (42, 43) and the $\delta^{18}\text{O}_{\text{atm}}$ of O₂ (21, 44–46) (Fig. 4). The end of the past five terminations
347 is characterized by a sharp increase in CH₄ concentrations of at least 100 ppb. This abrupt CH₄ release
348 is interpreted as reflecting a perturbation of the low-to-mid latitude of Northern Hemisphere continental
349 CH₄ sources (41, 43). We quantify the phasing of the onset of CH₄ concentrations relatively to the CO₂
350 concentrations peak using the Parrenin et al. (2013) method (Table S2). The analysis reveals a lead of
351 CH₄ concentrations during TI (382 ± 197 years) and TIII (597 ± 39 years), while the phasing during TII,
352 TIV, and TV is not significantly distinct from a synchronous variation (1σ).

353 In addition, the $\delta^{18}\text{O}_{\text{atm}}$ is interpreted as a complex tracer integrating changes in global sea level,
354 hydrological cycle and biosphere productivity (21, 47, 48). Over the past 800 ka, strong similarities are
355 observed between $\delta^{18}\text{O}_{\text{atm}}$ and Chinese speleothem calcite $\delta^{18}\text{O}$ tracking the East Asian monsoon change
356 at millennial and orbital scale (46, 49). This correlation suggests that the low-to-mid latitude
357 hydrological cycle of the Northern hemisphere is thought to be the dominant driver of $\delta^{18}\text{O}_{\text{atm}}$ variations
358 at these timescales. A decrease of the $\delta^{18}\text{O}_{\text{atm}}$ signal is identified at the end of the past five Terminations
359 (Fig. 4). As the residence time of O₂ in the atmosphere is ~1,000 to 1,200 years (47, 48), we focus on
360 inflexion points to identify trend variations. The timing of variation of the decreasing rate of $\delta^{18}\text{O}_{\text{atm}}$ is
361 precisely determined using the Parrenin et al. (2013) method for TI, TII, TIII and TIV (Table S2). As
362 the $\delta^{18}\text{O}_{\text{atm}}$ during TV is poorly resolved, the method of Parrenin et al. (2013) could not be applied and
363 the timing of change as well as the associated uncertainty is visually estimated. Our analysis reveals that
364 the change in $\delta^{18}\text{O}_{\text{atm}}$ rate of decrease coincides at centennial scale with the peak of CO₂ concentrations
365 at the end of a termination for the past five terminations (Fig. 4) (Table S2). The Chinese speleothem
366 $\delta^{18}\text{O}$ record also provides interesting insights to understand the Northern latitude carbon cycle dynamics
367 as they track the variations in the hydrological cycle of the East Asian monsoon (50). This record also
368 registered a peak around the period of CO₂ maximum concentrations although the relative age
369 uncertainty associated with different timescales makes it difficult to discuss the synchronicity of these
370 events at centennial-scale (51) (Fig. 4). The CH₄ concentrations, the $\delta^{18}\text{O}_{\text{atm}}$ and the speleothem calcite
371 $\delta^{18}\text{O}$ illustrate a major perturbation of the hydrological cycle potentially affecting the carbon cycle of
372 the North hemisphere and low latitude at the end of the Terminations.

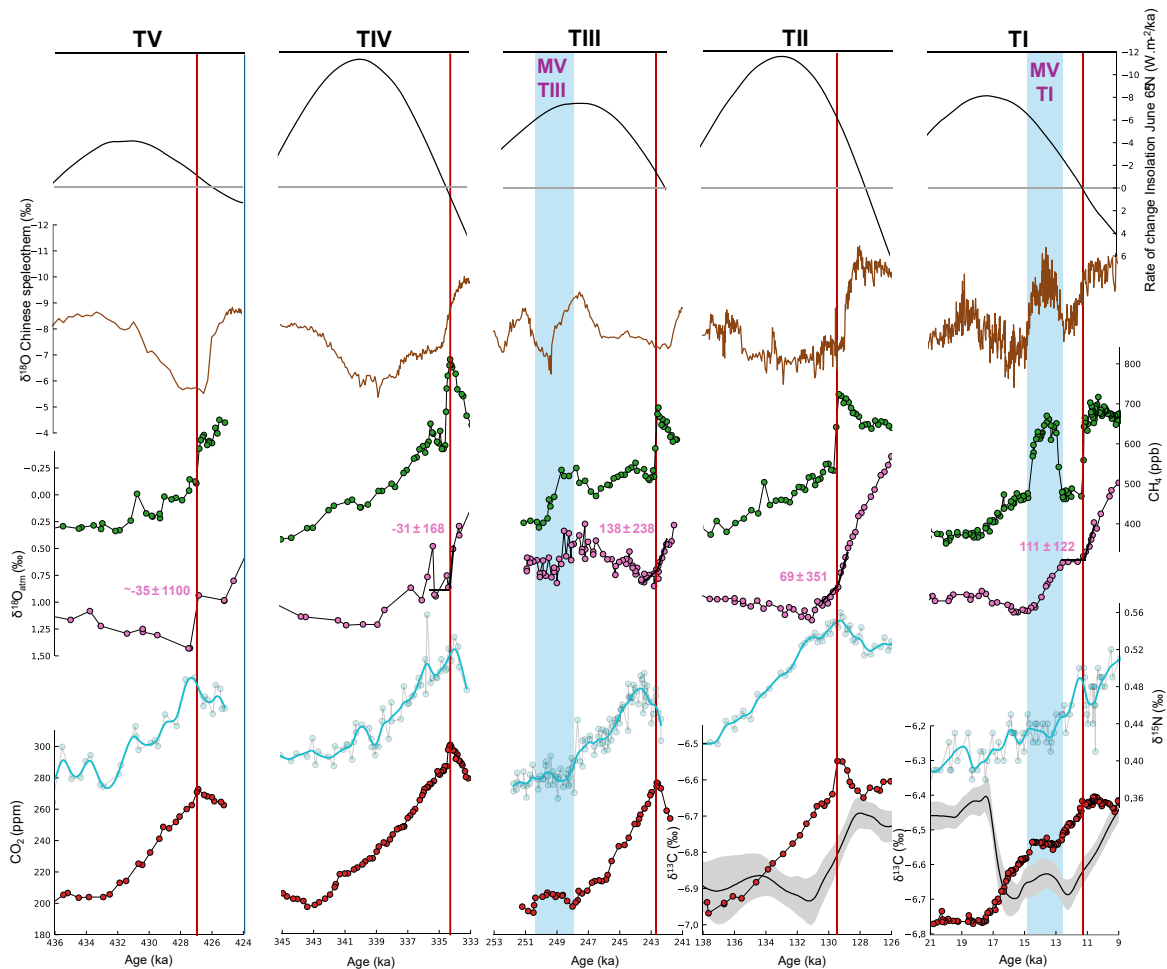
373 Finally, a $\delta^{13}\text{C}$ -CO₂ record is available for the last two terminations (52–55). Strong differences
374 are observed at the onset and over the course of terminations, partly due to the occurrence of the

375 millennial-scale event occurring during TI (56) (Fig. 4). Reversely, a similar increase occurred at ~ 131
376 and 12 ka during both Terminations, probably explained by the progressive regrowth of the terrestrial
377 biosphere due to the ice sheet retreat and the establishment of warmer conditions (54, 57). Nevertheless,
378 the onset of CO₂ decrease right after the peak occurring at the end of both terminations is not associated
379 with a corresponding change in the δ¹³C-CO₂. Indeed, the δ¹³C-CO₂ continues to increase for at least a
380 millennium, potentially due to compensating effect between different carbon sources (Fig. 4).
381 Disentangling the δ¹³C-CO₂ sources and sinks at the exact timing of the end of termination would require
382 (i) some dedicated carbon cycle modeling as performed during the last glacial period and TI (12, 55)
383 and (ii) to extend the δ¹³C-CO₂ records during terminations older than TII.

384 To conclude, the dynamics of CO₂ atmospheric concentrations at the end of a termination appear
385 to result from changes in the carbon cycle dynamics in the Northern Hemisphere and low-latitudes of
386 both hemispheres, such as observed during the centennial-scale climate variability during the last glacial
387 period. Consequently, we propose that the late decrease in atmospheric CO₂ concentrations starting right
388 after the peak of terminations is decoupled from the Antarctic surface climate, which starts cooling
389 several hundreds of years before.

390 Ref. (14) proposed that the onset of terminations is initiated by a Southern Hemisphere
391 millennial-scale climate event that does not propagate to the Northern Hemisphere. They argue that the
392 terminations are ended by the delayed response to the initial Southern Hemisphere perturbation in the
393 North hemisphere. Thus, they hypothesize the termination as a potential single millennial-scale event,
394 that initiates the warming in the Southern Hemisphere. After several millennia of muted bipolar see-
395 saw, the initial heat is finally propagated to the Northern Hemisphere, causing the end of the
396 Termination. In a perspective study, (15) described the glacial Terminations as the ultimate interaction
397 between millennial and orbital timescale variability and highlight the key role played by AMOC in these
398 terminations. In support to this hypothesis, a high-resolution record of Ice Rafted Debris (IRD) revealed
399 the occurrence of Heinrich-like events over the course of the past five Terminations (58). While the
400 AMOC slowdown is likely not initiated by the massive iceberg discharges itself, the final Laurentide
401 massive iceberg discharge would contribute to maintain this slow AMOC and would thus be related to
402 this ultimate millennial-scale event ending the termination (59).

403



404

405 **Fig. 4: Sequence of events of climatic records over the past five terminations.** From top to bottom: Rate of change of the
 406 June Insolation at 65°N (black). Horizontal light grey lines illustrate a null rate of change. $\delta^{18}\text{O}$ composite of the Chinese
 407 speleothem (51). Gas-phase proxies measured on the EDC ice core: CH_4 (green) (41, 43), $\delta^{18}\text{O}_{\text{atm}}$ (pink) (46), $\delta^{15}\text{N}$ (blue) (22,
 408 33, 34; this study), CO_2 (red) (10, 17, 22; Legrain et al., in revision) and $\delta^{13}\text{C}$ (60) records displayed on the AICC2023 timescale
 409 (37). Blue line is a smoothing spline of the $\delta^{15}\text{N}$ used to highlight the global trend of the $\delta^{15}\text{N}$ record. Red vertical lines indicate
 410 the CO_2 concentration maxima recorded during the terminations. Black lines were inferred following the Parrenin et al. (2013)
 411 method and illustrate the change in rate of $\delta^{18}\text{O}_{\text{atm}}$ variations that coincides with the CO_2 concentration peaks (values are in
 412 years). Vertical blue areas highlight the millennial-scale variabilities (noted MV) occurring during terminations.

413

414 Our phasing analysis between atmospheric CO_2 concentrations and Antarctic climate variations
 415 evidences the similarity between the millennial-scale variability of the last glacial period and the end of
 416 terminations. Similarities in the dynamics of carbon cycle in the Northern and low latitudes confirmed
 417 this parallel. However, if the end of a termination is associated with a millennial-scale event, a remaining
 418 question is why the occurrence of a millennial-scale event over the course of a termination does not
 419 systematically trigger its end. Ref. (14) propose to consider the entire Termination as a southern
 420 hemisphere perturbation with a delayed control of the Northern hemisphere. However, the occurrence
 421 of millennial-scale events in the course of TI and TIII does not argue in favour of considering a

422 termination as a single delayed millennial-scale event (Fig. 4). Instead, it would rather suggest that the
423 delayed response of Northern Hemisphere to the Southern Hemisphere warming can occur before the
424 end of the Termination and not systematically trigger the end of the Termination.

425 Especially, Antarctic warming and atmospheric CO₂ concentrations continue to rise after the
426 end of the millennial-scale events during TI and TIII. The millennial-scale events occurring during TI
427 and TIII are ended by synchronous changes in the Antarctic climate and atmospheric CO₂, indicating a
428 different dominant mechanism than during the end of terminations and the last glacial period. In
429 addition, we observe that the onset of the atmospheric CO₂ decrease at the end of a termination occurs
430 under a relatively stable orbital forcing (Fig. 4). In particular, the millennial-scale climate events
431 triggering the end of the past five Terminations occur under a low rate of change in the 65°N June
432 Insolation. Reversely, the average rate of change in the 65°N June Insolation is higher during the
433 millennial-scale events occurring in the middle of TI and TIII (Fig. 4). Hence, it suggests that at this
434 stage of the Termination, the impact of the orbital forcing is dominant over the millennial-scale
435 variability explaining the continuing atmospheric CO₂ and Antarctic temperature increase after the
436 millennial-scale event occurring during TI and TIII. Also, we argue that in opposite, the occurrence of
437 a millennial-scale event in a context of low-variability of the orbital forcing could end a Termination.
438 Our results highlight the importance of the orbital context during millennial-scale variations in
439 determining whether the orbital- or millennial-scale processes affecting the carbon cycle will be
440 dominant.

441

442 **Conclusions**

443 To estimate the Antarctic climate-CO₂ concentrations phasing during the past five glacial
444 terminations, we developed an approach using (i) high resolution records of the EDC ice core, (ii) the
445 $\delta^{15}\text{N}$ as a proxy of the Antarctic climate variations (iii) several statistical approaches. We identify a
446 robust multi-centennial lag (~ 500 years) of atmospheric CO₂ over the Antarctic climate at the end of
447 TI, TII, TIII and TV. We highlight that this phasing is similar than the one observed during the
448 millennial-scale climate variability of the last glacial period. We also illustrate that the end of a
449 Termination is driven by Northern Hemisphere and low latitude processes, explaining the observed
450 decoupling between local Antarctic climate change and global atmospheric CO₂ concentrations. Lastly,
451 we show that the strength of the orbital forcing, tracked by the rate of change of the 65°N June Insolation,
452 is key for the millennial-scale event to cause the end of the termination. Our new results highlight the
453 close interplay between millennial-scale climate variability and the orbital forcing to shape glacial
454 terminations. In the future, modelling effort should be conducted (i) to test quantitatively how the orbital
455 forcing modulates the ability of a millennial-scale event to end a glacial termination, (ii) to extend the
456 carbon isotope record on terminations older than TII and (iii) to perform carbon cycle modelling to

457 identify the sources and sinks of carbon and their respective contributions to modulate atmospheric CO₂
458 concentration changes across glacial terminations.

459

460

461

462

463

464

465

466

467

468

469

470

471

472 **Methods**

473 *EDC $\delta^{15}N$ measurements*

474 New measurements of $\delta^{15}N$ of N₂ have been performed across TIV and TV on the EDC ice core
475 at LSCE using a semi-automated wet extraction line (Fig. 1). The method used is a melt refreeze air
476 extraction technique and the extracted air is then analysed on a dual inlet Delta 220 V plus (Thermo
477 Electron Corporation) mass spectrometer (see Ref. (61) for the detailed analytical procedure). Results
478 are expressed as an anomaly to atmospheric air. The results have been corrected from chemical
479 interferences of $\delta O_2/N_2$ and CO₂ (62). In total, 37 duplicate samples were measured at the depth interval
480 of 2580.9 – 2609.5 m and 2776.8 – 2793.2 m corresponding to the time intervals 333.7 - 342.8 ka and
481 424.8 - 437.8ka on the AICC2023 time scale. The final average temporal resolution over TIV and TV
482 is 200 and 480 years respectively.

483 *Statistical methods to analyse the Antarctic climate-CO₂ phasing*

484 In the present study, the evolution of the timing of $\delta^{15}N$ vs CO₂ changes across the past five
485 terminations has been investigated using EDC ice core records. Since both records are measured in the

486 air-phase of the ice core, there is no inherent relative age uncertainty between them. However, we argue
487 that the choice of the methodology of phasing quantification could impact the results. Hence, we propose
488 in this study to use and compare three different statistical approaches.

489 (i) *Method from Caillon et al. (2003)*. This approach is a statistical method based on least
490 squares. It operates under the assumption of a constant phasing between two curves
491 throughout a defined time window (e.g. time interval covering the entire glacial
492 termination). In this method, one of the two curves is shifted from a minimum to an
493 extremum time value, with a step defined by the user. At each step, the sum of the square
494 of the residuals is computed. The fit that corresponds to the highest value for the coefficient
495 of determination R^2 is considered as the best solution and the corresponding age shift
496 represents the relative lag of the moving record over the fixed one. In this study, we
497 performed the R^2 computation between -1500 and +1500 years from the original age scale
498 at a time step of 10 years. Results are shown in Fig. 2b.

499 (ii) *Method from Parrenin et al. (2013)*. The LinearFit code is a piecewise linear function that
500 enables the investigation of the phasing at specific break points in a given dataset. The
501 number of break points n in the linear function is determined arbitrary by the user. Starting
502 from an initial position of the n break points determined by the user, the function explores
503 the entire temporal range of the time series to find their optimal locations. The best fit
504 associated with the position of the n break points is quantified using a cost function that
505 minimizes the total sum of residuals (Fig. 2c). The uncertainty associated with each break
506 point is evaluated by calculating the standard deviation of the residuals of the data value to
507 a first best n points linear function (13). This function provides the single best fit solution
508 that has been identified.

509 (iii) *Method from Chowdhry Beeman et al. (2019)*. They developed a method for detecting break
510 points in paleorecords building upon the approach of Parrenin et al. (2013). However, they
511 enhanced the methodology by employing a Monte Carlo analysis to explore the parameter
512 space and to estimate the likely timing of these changes. The key technique used in this
513 method is the Metropolis-Hastings algorithm that is a Markov chain Monte Carlo method
514 (63). Eventually, the method generates an ensemble of fits accepted by the routine, which
515 are then depicted as histograms (Fig. 2d). These histograms are used as probabilistic
516 indicators of the locations where changes in slope occur within the records. The uncertainty
517 attached to the break point locations is obtained by fitting the histogram to a normal
518 distribution, which allows to quantify the uncertainty at a 1σ level. A detailed description
519 of the code can be found in Ref. (22).

520

521
522
523
524
525
526
527
528
529
530
531
532
533
534
535
536
537
538
539
540
541
542
543
544
545
546
547
548
549
550

Supplementary Materials

On the use of $\delta^{15}\text{N}$ as a surface Antarctic climate proxy at the EDC site

The water isotopes measured on the ice-phase of Antarctic ice cores have been widely used as proxies of Antarctic surface temperature (7, 17). The aim of our study is to compare the Antarctic climate with atmospheric CO_2 variations measured in the gas-phase of ice cores. However, the age of the air bubbles trapped in the ice is always younger than the age of the surrounding ice matrix. Consequently, a difference of age (Δage) exists between ice and gas at the same depth. The uncertainty associated with this Δage depends on the ability to reconstruct the evolution through time of the Lock-in-Depth, which is the depth at which air is trapped in the ice (13). This uncertainty that can reached up to 20% of the delta age itself is an important limiting factor when comparing the timing of changes between ice-phase and gas-phase proxies. To overcome this challenge, three approaches can be used:

- (i) The LID is constrained using the variations of the $\delta^{15}\text{N}$ records making the assumption that $\square^{15}\text{N}$ is dominated by gravitational fractionation in sites of the East Antarctic plateau (eg. (13)). The LID is then converted into a difference of depth (Δdepth) using a modeled vertical thinning function and assuming a constant firn average density. The methodology of phasing identification between ice-phase and

551 gas-phase proxy has been essentially used during the TI (13, 22) and during the last
552 glacial period (12).

553 (ii) The use of a high-accumulation site (typically Siple Dome: 10-20 cm.yr⁻¹; (64))
554 reduces the uncertainty on Δ_{age} , as a Δ_{depth} value would correspond to a smaller
555 Δ_{age} value for a high accumulation site. Consequently, using ice-core records from
556 high-accumulation sites, the Antarctic climate-CO₂ phasing could be investigated
557 using an ice-phase temperature proxy across TI (20, 26) with small uncertainties
558 linked to Δ_{age} .

559 (iii) The air isotopes of the gas-phase of ice cores, especially $\delta^{15}N$ and $\delta^{40}Ar$, are affected
560 by two main processes: the thermal fractionation and the gravitational fractionation
561 (65). Both fractionations may lead to variations of $\delta^{15}N$ on the Dome C site during
562 specific phase of the Terminations (34, 35). On the one hand, the variations of $\delta^{15}N$
563 due to gravitational fractionation reflect changes in the firnification process which
564 depends to the surface temperature and the accumulation process (35). In the East
565 Antarctic Plateau and for large climate change, accumulation rate is linked to
566 surface air temperature variations (18, 21, 34). On the other hand, the variations of
567 $\delta^{15}N$ due to thermal fractionation reflects directly changes in the temperature
568 gradient in the firn, and thus the surface temperature. It has thus been proposed that
569 changes in air isotopes can be used in investigating the phasing between Antarctic
570 surface temperature and atmospheric CO₂ during TII in the EDC ice core (21) and
571 TIII in the Vostok ice core (18).

572 In our study, we focus on the EDC site from the East Antarctic plateau that is characterized by
573 an average accumulation rate of 1-5 cm/yr (35). We investigate the phasing during terminations for
574 periods as old as ~440 ka. Given the limitations associated with the low-accumulation nature of the EDC
575 site and the age range of our study, the Δ_{age} is associated with an uncertainty of several centuries that
576 would prevent us discussing phasing between Antarctic climate and atmospheric CO₂ (37). Hence, we
577 propose here to follow the strategy of Refs. (18, 21). It has been demonstrated that the $\delta^{15}N$ variations
578 at the EDC site would be a combined signal of both accumulation and temperature processes (35). In
579 addition, it is likely that accumulation processes are directly linked with temperature changes in the East
580 Antarctic plateau (13, 35, 43). As a consequence, we consider here the $\delta^{15}N$ as a proxy of the Antarctic
581 climate variations (accounting for both the surface temperature and accumulation rate changes) rather
582 than a purely temperature-driven proxy.

583 The strong correlation ($R^2 > 0.8$ apart from TI) observed between the δD and $\delta^{15}N$ confirms the
584 $\delta^{15}N$ during the last five terminations as a reliable proxy for Antarctic climate changes. The lower R^2
585 during TI ($R^2=0.63$) can be explained by the fact that this period falls with a depth interval where the
586 EDC ice is brittle, leading to a degraded quality of the $\delta^{15}N$ data affected by the presence of multiple

587 cracks in the ice samples. For the TI period, reliable quantification of the phasing between Antarctic
588 temperature and CO₂ concentrations have been established through water isotopes-based temperature
589 reconstruction (13, 22). Our results during TI, i.e. a lag of atmospheric CO₂ over Antarctic climate
590 variations at the end of the termination and the synchronous end of the Antarctic Cold Reversal, are
591 consistent with those of Refs. (13, 22).

592 The hypothesis of a delayed response of $\delta^{15}\text{N}$ to changes in temperature or accumulation at the
593 surface cannot be excluded. Indeed, it could be caused by the response time in the firn to surface climatic
594 changes. In the context of our study, we evidenced in particular a multi-centennial lead of Antarctic
595 climate changes over CO₂ concentrations at the end of the terminations. If the response of $\delta^{15}\text{N}$ is indeed
596 delayed compared to the real climate signal, this implies that the estimated lead of Antarctic climate
597 changes is likely a minimal value and may be even larger. Reversely, an anticipated response of the firn
598 compared to surface climatic changes seems physically very unlikely.

599

600 *Comparison across TIII of the EDC $\delta^{15}\text{N}$ and CO₂ records with the Vostok $\delta^{40}\text{Ar}$ and CO₂ records*

601

602 The phasing between the Antarctic climate and atmospheric CO₂ during TIII was initially
603 investigated based on Vostok ice core records (18). The Antarctic climate proxy used was the $\delta^{40}\text{Ar}$,
604 which is driven by the same physical processes in the firn column that controls the $\delta^{15}\text{N}$ variations (65).
605 The EDC $\delta^{15}\text{N}$ and Vostok $\delta^{40}\text{Ar}$ records appear visually correlated in their global trend, as they both
606 increase during the deglaciation (Figure S1). In addition, the peak associated with the end of the
607 termination occurs synchronously at centennial-scale. The major visual difference between the two
608 records is the most pronounced bump in the $\delta^{40}\text{Ar}$ record during the millennial-scale event occurring at
609 ~250 ka. Regarding the CO₂ records, the morphology of the two records are similar, with a synchronous
610 maximum of concentrations reached at the end of TIII. However, the low resolution at the onset of TIII
611 in the Vostok record does not allow to identify the millennial-scale event observed in the EDC CO₂
612 record (Fig. S1). This global similarity combined with a difference in resolution and in sub-orbital-scale
613 variability observed in the record explains the qualitative similarity in the observed CO₂ lag over
614 Antarctic climate using the Caillon et al., (2003) method. However, differences in the lag of CO₂
615 concentration values are observed: 800 ± 200 years using the Vostok records and 390 ± 120 years using
616 the EDC records. When using a statistical approach allowing an evolution of the Antarctic climate-CO₂
617 phasing through the glacial termination, the results reveal that the end of millennial event occurs
618 synchronously, during the first part of the Termination, while the end of the termination is characterized
619 by a significant lag of atmospheric CO₂ over Antarctic climate. Hence, TIII is a good case-study to
620 illustrate the importance in the choice of the methodology to determine the Antarctic climate-CO₂
621 phasing during past deglaciations.

622

623 *Statistical methods to quantify the Antarctic climate-CO₂ phasing during past terminations.*

624

625 Various methods have been used to constrain the phasing between the Antarctic climate and the
626 atmospheric CO₂ concentrations during glacial terminations (13, 18, 20–26, 54, 66).

627 One family of statistical methods relies on the assumption that the phasing is constant along a
628 glacial termination. Under this assumption, a simple answer could be provided for each Termination.
629 An example is the study of Ref. (18) that evidenced a constant lag of 800 ± 200 years of atmospheric
630 CO₂ over Antarctic temperature during the entire TIII. Following this study, more complex approaches
631 have been investigated on TI and TII questioning this result (13, 21, 22). However, the hypothetical
632 specificity of TIII could not be excluded from inter-termination differences (13). Our analysis here
633 reveals that the phasing of TIII is more complex than a constant lag of atmospheric CO₂ over Antarctic
634 climate ((18); Fig. 2). Nevertheless, we consider that this type of methods can provide a good estimate
635 of the approximate average phasing. This is why we propose to apply the methodology from Caillon et
636 al. (2003) to the past five terminations.

637 The second family of statistical method implies piecewise linear function that allows to
638 investigate the temporal evolution of the Antarctic climate-CO₂ phasing at different periods of a
639 Termination. As these methods focus on shorter time windows, they require the use of relatively high-
640 resolution records, explaining why these more complex methods have not been used initially (18, 23,
641 66). TII has been studied based on a rampfitting method (21). The Rampfit tool (38) find the best fit
642 between the record and a constant-linear-constant piecewise function. It thus allows us to identify
643 phasing during two periods of the Termination, e.g. the onset and the end of a Termination. However,
644 this approach has two main characteristics: (i) The ramp is fitted between what are assumed to be two
645 stable states (ii) the breakpoints are by definition limited to two. We consider that this model is more
646 adapted to compute the amplitude of glacial terminations rather than the phase relationship during such
647 events. In addition, the rampfitting tool is very sensitive to the time window considered for the search
648 of the ramp fit, which in turns influences strongly the timing of -the identified breakpoints characterising
649 the onset and the end of the ramp across the Termination. The Linearfit fit function from Parrenin et al.
650 (2013) is an alternative of Rampfit that differs for two main points: (i) all segments of the function are
651 linear function (ii) more than two breakpoints are allowed and the number of breakpoints is fixed by the
652 user after a visual inspection of the considered glacial termination. Thus, we propose here to use this
653 model rather than the Rampfit approach in our phasing analysis study.

654 Finally, a recent study has developed a more rigorous statistical tool based on Metropolis
655 Algorithm (22). This method provides more complex estimate of uncertainty, and the number of
656 breakpoints is not fixed by the user. We consider that this method is the most reliable for the highly
657 resolved records of TI used in the source study (22). However, the convergence of such method requires

658 noiseless and highly-resolved records. We thus considered that this method is not superior to the method
659 of Parrenin et al. (2013) for TII, TIII, TIV and TV, where the records are less resolved than during TI.
660 Reversely, we consider that a complementary use of Parrenin et al. (2013) method and Chowdhry
661 Beeman et al. (2019) particularly efficient for the older glacial terminations.

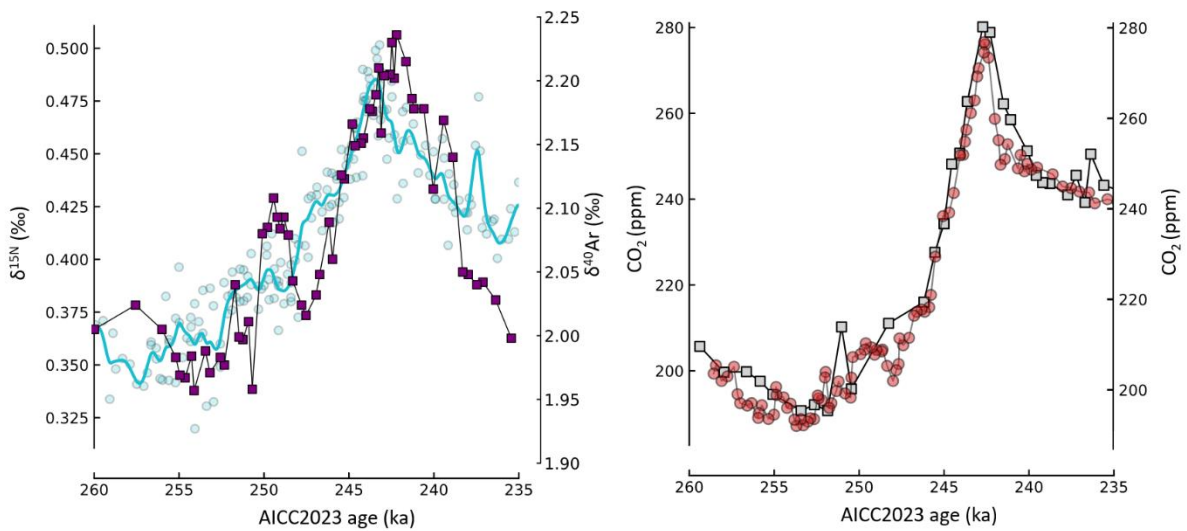
662 Based on our results, we would recommend the combine use of several methods to distinguish
663 method-dependent results from pervasive climatic signal. And even with this recommendation, the
664 quantified phase relationships with different statistical methods should be carefully interpreted, taking
665 into account the fact that the methods are sensitive to (i) the dataset on which it is applied: for instance,
666 heterogeneity reveal at the onset of TI between the Parrenin et al. (2013) and Chowdry Beeman et al.
667 (2019) are mainly due to the use of EDC CO₂ record vs WAIS Divide CO₂ record (ii) the time windows
668 considered for the search of the optimal fit (iii) the chosen complexity of such a fit (especially for Refs.
669 (13, 22)). A visual inspection of the results is systematically necessary to identify the potential aberrant
670 results produced by objective methodologies.

671 *On the use of smoothed $\delta^{15}N$ records*

672
673 In Antarctic, the $\delta^{15}N$ records are noisier compared to the δD records due (i) to the complexity
674 of processes governing the $\delta^{15}N$ variations (ii) the lower signal of $\delta^{15}N$ compared to δD for a same ice
675 quantity (35). As discussed in the last section, the use of the Chowdhry Beeman et al. (2019) method
676 and, in a smaller extent the one from Parrenin et al. (2013), requires low-noise records to converge.
677 Hence, in order to use efficiently the method of Chowdhry Beeman et al. (2019), we applied a Savitzky-
678 Golay filter with an approximate cutoff periodicity of 500 years to the $\delta^{15}N$ record. Ref. (22)
679 demonstrated that smoothing the data does not significantly impact the final results of the study. When
680 using the Parrenin et al. (2013) methodology, only the $\delta^{15}N$ record over TI was smoothed.

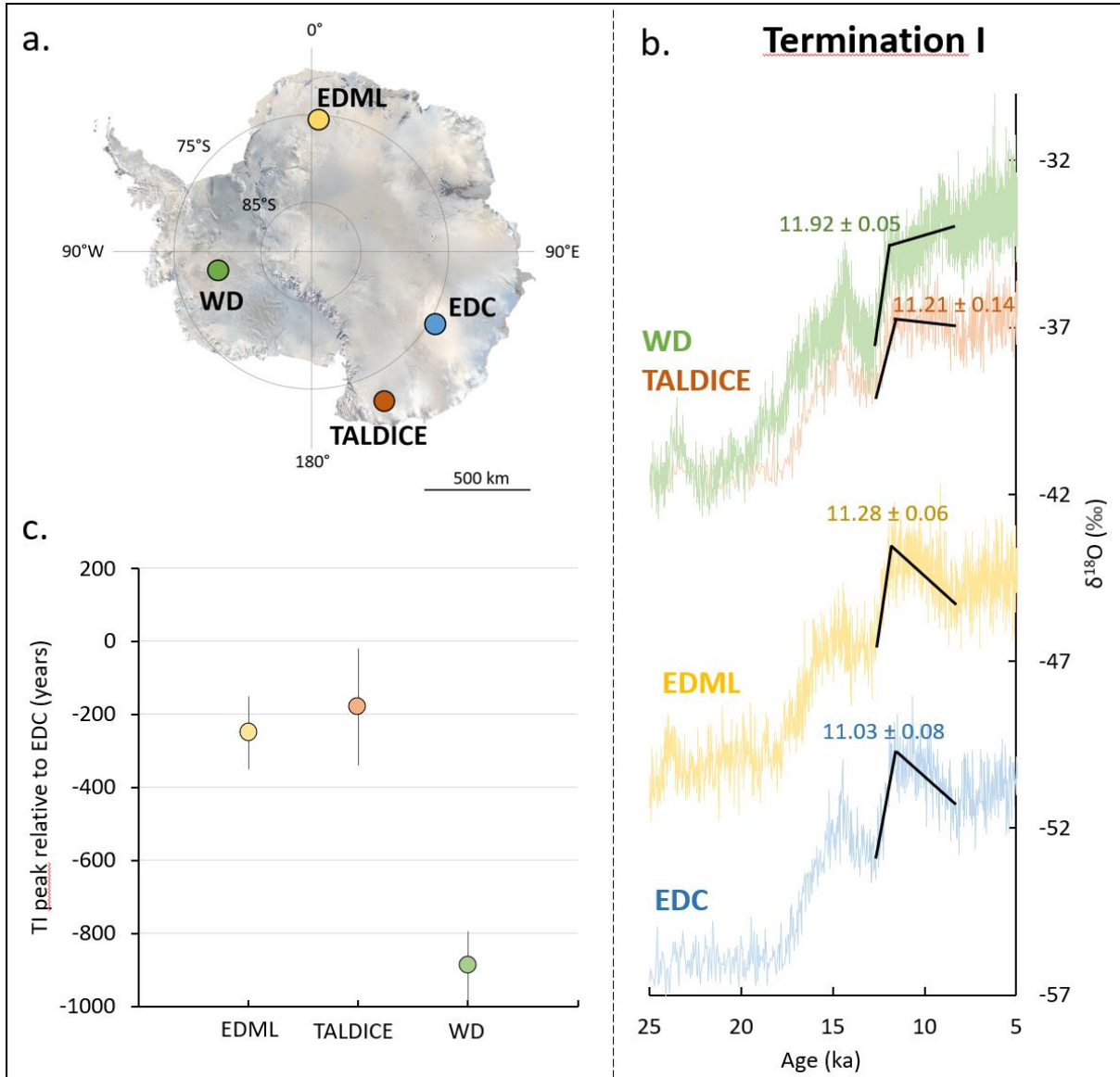
681
682
683
684
685
686
687
688
689
690
691

692
693
694
695
696
697
698
699
700
701
702
703
704
705
706
707
708
709 **Supplementary Figures**



710
711
712
713
714

Fig. S1: Comparison of the records used in the phasing analysis from this study and the from Ref. (18). Left: EDC $\delta^{15}\text{N}$ record (blue dots, (35)). Vostok $\delta^{40}\text{Ar}$ record (purple squares, (18)). Right: EDC CO_2 record (red dots, Legrain et al., in revision). Vostok CO_2 record (grey squares, (18)). All records are plotted on the AICC2023 gas timescale (37).



716
 717 Fig S2: Phasing of Antarctic isotopes variations over the last termination. a) Location of EDML, TALDICE, EDC and WD ice
 718 cores. b. TI δ¹⁸O records from the EDML (yellow), TALDICE (orange) EDC (blue) ice cores on the AICC2023 timescale (37).
 719 TI δ¹⁸O record from the WD ice cores on the WD2014 timescale (39). The colored ages (ka) correspond to the timing of the
 720 end of TI and their associated 1σ uncertainty using the method from Parrenin et al. (2013). c. Phasing between TI δ¹⁸O peaks
 721 in the EDML, TALDICE and EDC ice cores relatively to the EDC ice core using the method from Parrenin et al. (2013).

722
 723
 724
 725
 726
 727
 728
 729
 730

731 **Table S1: Compilation of studies investigating the phasing between atmospheric CO₂ and Antarctic climate over the past five terminations.** MV: Millennial-scale Variability. C: Caillon,
 732 P :Parrenin, CB : Chowdhury Beeman.

733

	Termination I								
<i>Reference</i>	<i>Raynaud and Barnola 1985</i>	<i>Fischer et al., 1999</i>	<i>Monin et al., 2001</i>	<i>Ahn et al., 2004</i>	<i>Pedro et al., 2012</i>	<i>Parrenin et al., 2013</i>	<i>Chowdhury et al., 2019</i>	<i>This study</i>	
<i>Ice core</i>	Dome C	Taylor dome / Byrd	EDC	Siple dome	Byrd Dome / Siple dome CO ₂ , Antarctic Temperature stack	EDC CO ₂ , Antarctic temperature stack	Wais Divide CO ₂ , Antarctic temperature stack	EDC	
<i>Antarctic climate proxy</i>	Water isotopes based	Water isotopes based	Water isotopes based	Water isotopes based	Water isotopes based	Water isotopes based	Water isotopes based	Air isotopes based ($\delta^{15}N$)	
Δ age estimation	Rough approximation	Firn model	Firn model	Firn model	Synchronization to GICC05	use of $\delta^{15}N$	Firn model	/	
<i>Statistical method</i>	Visual inspection	Visual inspection	Linear fit (onset) and R2 correlation (global)	R2 correlation applied on derivative and smoothed records	R2 correlation with Montecarlo analysis	Piecewise linear fit	Bayesian analysis with piecewise linear fit	R2 correlation / piecewise linear fit / Bayesian analysis with piecewise linear fit	
<i>Results (if > 0, Antarctic climate leads CO₂)</i>	Global: Synchronous	Onset: ~1000 yrs MV: 300-500 yrs End: 600 - 1000 yrs	Onset: 800 ±600 yrs Global: ~410 yrs	Global: ~150-400 yrs	Global: -56 to 381 yrs	Onset: 10 ±160 yrs MV onset: 260 ±130 yrs MV end: -60 ±120 yrs End: 500 ±90 yrs	Onset: 127 - 751 yrs MV onset: -136 - 376 yrs MV end: -211 - -117 yrs End: 337 - 629 yrs	C-method: Global : 560 ±176 yrs P-method: Onset: -320± 425 MV end: -90 ±257 yrs End: 630 ±302 yrs CB-method: Onset: 651 ±535 yrs MV end: 84 ±394 yrs End: 532 ±220 yrs	
	Termination II				Termination III			Termination IV	Termination V
<i>Reference</i>	<i>Barnola et al., 1991</i>	<i>Landais et al., 2013</i>	<i>Fischer et al., 1999</i>	<i>This study</i>	<i>Fischer et al., 1999</i>	<i>Caillon et al., 2003</i>	<i>This study</i>	<i>This study</i>	<i>This study</i>
<i>Ice core</i>	Vostok	EDC	Vostok	EDC	Vostok	Vostok	EDC	EDC	EDC
<i>Antarctic climate proxy</i>	Water isotopes based	Air isotopes based ($\delta^{15}N$)	Water isotopes based	Air isotopes based ($\delta^{15}N$)	Water isotopes based	Air isotopes based ($\delta^{40}Ar$)	Air isotopes based ($\delta^{15}N$)	Air isotopes-based ($\delta^{15}N$)	Air isotopes-based ($\delta^{15}N$)
Δ age estimation	Firn model	/	Firn model	/	/	/	/	/	/
<i>Statistical method</i>	Visual inspection	Ramp fit	Visual inspection	R2 correlation / piecewise linear fit / Bayesian analysis with piecewise linear fit	Visual inspection	R2 correlation	R2 correlation / piecewise linear fit / Bayesian analysis with piecewise linear fit	R2 correlation / piecewise linear fit / Bayesian analysis with piecewise linear fit	R2 correlation / piecewise linear fit / Bayesian analysis with piecewise linear fit
<i>Results (if > 0, Antarctic climate leads CO₂)</i>	Onset : less than 1000 yrs	Onset: synchronous Mid-slope: 900 ±325 yrs	Onset: undetermined End: 400 ±200 yrs	C-method: Global : 140 ±345 yrs P-method: Onset: 2110 ± 452 yrs End: 580 ±264 yrs CB-method: Onset: 960 ± 505 yrs End: 420 ±263 yrs	Onset: undetermined End: 600 ±200 yrs	Global: 800 ±200 yrs	C-method: Global : 390 ±102 yrs P-method: Onset: undetermined MV end: 204 ±474 yrs End: 560 ±152 yrs CB-method: Onset: undetermined MV end: -123 ±360 yrs End: 703 ±77 yrs	C-method: Global : 170 ±223 yrs P-method: Onset: -180 ± 1335 yrs End: -120 ±197 yrs CB-method: Onset: -1863 ±241 yrs End: -52 ±118 yrs	C-method: Global : 120 ±509 yrs P-method: Onset: 80 ±690 yrs End: 670 ±595 yrs CB-method: Onset: 320 ± 865 yrs End: 471 ±273 yrs

734

735

736

737 **Table S2: Phasing analysis of CH₄ peak and $\delta^{18}\text{O}_{\text{atm}}$ compared to the atmospheric CO₂ concentrations peak at the end**
738 **of the past five terminations.** Results are in years, and are computed using the method from Parrenin et al. (2013). A
739 positive value indicates a lead of the CH₄ or $\delta^{18}\text{O}_{\text{atm}}$ over CO₂.

740

	TI	TII	TIII	TIV	TV
CH₄	597	228	382	263	118
<i>1σ</i>	39	385	197	52	355
$\delta^{18}\text{O}_{\text{atm}}$	111	69	138	-31	-35
<i>1σ</i>	122	351	238	168	1140

741

742

743

744

745

746

747

748

749

750

751

752

753

754

755

756

757

758

759

760

761

762

763

764

765 **References**

766

- 767 1. P. C. Tzedakis, M. Crucifix, T. Mitsui, E. W. Wolff, A simple rule to determine which insolation
768 cycles lead to interglacials. *Nature* **542**, 427–432 (2017).
- 769 2. N. J. Shackleton, N. D. Opdyke, Oxygen isotope and palaeomagnetic evidence for early
770 Northern Hemisphere glaciation. *Nature* **270**, 216–219 (1977).
- 771 3. M. Milankovitch, Canon of insolation and the iceage problem. *Koniglich Serbische Akademie*
772 *Beograd Special Publication* **132** (1941).
- 773 4. Past Interglacials Working Group of PAGES, Interglacials of the last 800,000 years. *Rev.*
774 *Geophys.* **54**, 162–219 (2016).
- 775 5. F. Parrenin, D. Paillard, Terminations VI and VIII (~ 530 and ~ 720 kyr BP) tell us the
776 importance of obliquity and precession in the triggering of deglaciations. *Clim. Past* **8**, 2031–
777 2037 (2012).
- 778 6. C. Buizert, *et al.*, Antarctic surface temperature and elevation during the Last Glacial Maximum.
779 *Science* **372**, 1097–1101 (2021).
- 780 7. J. Jouzel, *et al.*, Orbital and Millennial Antarctic Climate Variability over the Past 800,000
781 Years. *Science* **317**, 793–796 (2007).
- 782 8. J. R. Petit, *et al.*, Climate and atmospheric history of the past 420,000 years from the Vostok ice
783 core, Antarctica. **399**, 10 (1999).
- 784 9. J. M. Barnola, D. Raynaud, Y. S. Korotkevitch, C. Lorius, Vostok ice core provides 160,000-
785 year record of atmospheric CO₂. *Nature* **329**, 408–414 (1987).
- 786 10. S. A. Marcott, *et al.*, Centennial-scale changes in the global carbon cycle during the last
787 deglaciation. *Nature* **514**, 616–619 (2014).
- 788 11. B. Bereiter, *et al.*, Revision of the EPICA Dome C CO₂ record from 800 to 600 kyr before
789 present: Analytical bias in the EDC CO₂ record. *Geophys. Res. Lett.* **42**, 542–549 (2015).
- 790 12. T. K. Bauska, S. A. Marcott, E. J. Brook, Abrupt changes in the global carbon cycle during the
791 last glacial period. *Nat. Geosci.* **14**, 91–96 (2021).
- 792 13. F. Parrenin, *et al.*, Synchronous Change of Atmospheric CO₂ and Antarctic Temperature During
793 the Last Deglacial Warming. *Science* **339**, 1060–1063 (2013).
- 794 14. E. W. Wolff, H. Fischer, R. Röthlisberger, Glacial terminations as southern warmings without
795 northern control. *Nature Geosci* **2**, 206–209 (2009).
- 796 15. S. Barker, G. Knorr, Millennial scale feedbacks determine the shape and rapidity of glacial
797 termination. *Nat Commun* **12**, 2273 (2021).
- 798 16. C. Nehrbaß-Ahles, *et al.*, Abrupt CO₂ release to the atmosphere under glacial and early
799 interglacial climate conditions. *Science* **369**, 1000–1005 (2020).
- 800 17. A. Landais, *et al.*, Interglacial Antarctic–Southern Ocean climate decoupling due to moisture
801 source area shifts. *Nat. Geosci.* **14**, 918–923 (2021).
- 802 18. N. Caillon, *et al.*, Timing of Atmospheric CO₂ and Antarctic Temperature Changes Across
803 Termination III. *Science* **299**, 1728–1731 (2003).

- 804 19. U. Siegenthaler, *et al.*, Stable Carbon Cycle/Climate Relationship During the Late Pleistocene.
805 *Science* **310**, 1313–1317 (2005).
- 806 20. J. B. Pedro, S. O. Rasmussen, T. D. Van Ommen, Tightened constraints on the time-lag between
807 Antarctic temperature and CO₂; during the last deglaciation. *Clim. Past*
808 **8**, 1213–1221 (2012).
- 809 21. A. Landais, *et al.*, Two-phase change in CO₂, Antarctic temperature and global climate during
810 Termination II. *Nature Geosci* **6**, 1062–1065 (2013).
- 811 22. J. Chowdhry Beeman, *et al.*, Antarctic temperature and CO₂;: near-
812 synchrony yet variable phasing during the last deglaciation. *Clim. Past* **15**, 913–926 (2019).
- 813 23. J.-M. Barnola, P. Pimienta, D. Raynaud, Y. S. Korotkevich, CO₂-climate relationship as
814 deduced from the Vostok ice core: a re-examination based on new measurements and on a re-
815 evaluation of the air dating. *Tellus B* **43**, 83–90 (1991).
- 816 24. H. Fischer, M. Wahlen, J. Smith, D. Mastroianni, B. Deck, Ice Core Records of Atmospheric CO
817 ₂ Around the Last Three Glacial Terminations. *Science* **283**, 1712–1714 (1999).
- 818 25. E. Monnin, *et al.*, Atmospheric CO₂ Concentrations over the Last Glacial Termination. *Science*
819 **291**, 112–114 (2001).
- 820 26. J. Ahn, *et al.*, A record of atmospheric CO₂ during the last 40,000 years from the Siple Dome,
821 Antarctica ice core. *J. Geophys. Res.* **109**, 2003JD004415 (2004).
- 822 27. J. Jouzel, *et al.*, Magnitude of isotope/temperature scaling for interpretation of central Antarctic
823 ice cores. *J. Geophys. Res.* **108**, 2002JD002677 (2003).
- 824 28. T. Sowers, M. Bender, D. Raynaud, Y. S. Korotkevich, δ¹⁵N of N₂ in air trapped in polar ice: A
825 tracer of gas transport in the firn and a possible constraint on ice age-gas age differences. *J.*
826 *Geophys. Res.* **97**, 15683–15697 (1992).
- 827 29. E. Capron, *et al.*, Glacial–interglacial dynamics of Antarctic firn columns: comparison between
828 simulations and ice core air-δ¹⁵N measurements. *Clim. Past* **9**, 983–999
829 (2013).
- 830 30. A. Landais, *et al.*, A review of the bipolar see–saw from synchronized and high resolution ice
831 core water stable isotope records from Greenland and East Antarctica. *Quaternary Science*
832 *Reviews* **114**, 18–32 (2015).
- 833 31. WAIS Divide Project Members, Onset of deglacial warming in West Antarctica driven by local
834 orbital forcing. *Nature* **500**, 440–444 (2013).
- 835 32. E. J. Brook, *et al.*, Timing of millennial-scale climate change at Siple Dome, West Antarctica,
836 during the last glacial period. *Quaternary Science Reviews* **24**, 1333–1343 (2005).
- 837 33. B. Stauffer, J. Flückiger, E. Wolff, P. Barnes, The EPICA deep ice cores: first results and
838 perspectives. *Ann. Glaciol.* **39**, 93–100 (2004).
- 839 34. G. B. Dreyfus, *et al.*, Firn processes and δ¹⁵N: potential for a gas-phase climate proxy.
840 *Quaternary Science Reviews* **29**, 28–42 (2010).
- 841 35. C. Bréant, *et al.*, Unveiling the anatomy of Termination 3 using water and air isotopes in the
842 Dome C ice core, East Antarctica. *Quaternary Science Reviews* **211**, 156–165 (2019).

- 843 36. A. M. Grachev, J. P. Severinghaus, Determining the Thermal Diffusion Factor for $^{40}\text{Ar}/^{36}\text{Ar}$ in
844 Air To Aid Paleoreconstruction of Abrupt Climate Change. *J. Phys. Chem. A* **107**, 4636–4642
845 (2003).
- 846 37. M. Bouchet, *et al.*, The Antarctic Ice Core Chronology 2023 (AICC2023) chronological
847 framework and associated timescale for the European Project for Ice Coring in Antarctica
848 (EPICA) Dome C ice core. *Clim. Past* **19**, 2257–2286 (2023).
- 849 38. M. Mudelsee, Ramp function regression: a tool for quantifying climate transitions p. (2000).
- 850 39. M. Sigl, *et al.*, The WAIS Divide deep ice core WD2014 chronology – Part 2: Annual-layer
851 counting (0–31 ka BP). *Clim. Past* **12**, 769–786 (2016).
- 852 40. C. Buizert, *et al.*, Abrupt Ice Age Shifts in Southern Westerlies and Antarctic Climate Forced
853 from the North. (2018). <https://doi.org/10.7892/BORIS.142480>.
- 854 41. R. H. Rhodes, *et al.*, Enhanced tropical methane production in response to iceberg discharge in
855 the North Atlantic. *Science* **348**, 1016–1019 (2015).
- 856 42. R. Spahni, *et al.*, Atmospheric Methane and Nitrous Oxide of the Late Pleistocene from
857 Antarctic Ice Cores. *Science* **310**, 1317–1321 (2005).
- 858 43. L. Louergue, *et al.*, Orbital and millennial-scale features of atmospheric CH₄ over the past
859 800,000 years. *Nature* **453**, 383–386 (2008).
- 860 44. G. B. Dreyfus, *et al.*, Anomalous flow below 2700 m in the EPICA Dome C ice core detected
861 using $\delta^{18}\text{O}$ of atmospheric oxygen measurements. *Clim. Past* (2007).
- 862 45. L. Bazin, *et al.*, Phase relationships between orbital forcing and the composition of air trapped in
863 Antarctic ice cores. *Clim. Past* **12**, 729–748 (2016).
- 864 46. T. Extier, *et al.*, On the use of $\delta^{18}\text{O}_{\text{atm}}$ for ice core dating. *Quaternary Science Reviews* **185**,
865 244–257 (2018).
- 866 47. A. Landais, *et al.*, What drives the millennial and orbital variations of $\delta^{18}\text{O}_{\text{atm}}$? *Quaternary
867 Science Reviews* **29**, 235–246 (2010).
- 868 48. M. Bender, *et al.*, Climate correlations between Greenland and Antarctica during the past
869 100,000 years. *Nature* **372**, 663–666 (1994).
- 870 49. Y. Wang, *et al.*, Millennial- and orbital-scale changes in the East Asian monsoon over the past
871 224,000 years. *Nature* **451**, 1090–1093 (2008).
- 872 50. H. Cheng, *et al.*, Ice Age Terminations. *Science* **326**, 248–252 (2009).
- 873 51. H. Cheng, *et al.*, The Asian monsoon over the past 640,000 years and ice age terminations.
874 *Nature* **534**, 640–646 (2016).
- 875 52. A. Lourantou, J. Chappellaz, J.-M. Barnola, V. Masson-Delmotte, D. Raynaud, Changes in
876 atmospheric CO₂ and its carbon isotopic ratio during the penultimate deglaciation. *Quaternary
877 Science Reviews* **29**, 1983–1992 (2010).
- 878 53. J. Schmitt, *et al.*, Carbon Isotope Constraints on the Deglacial CO₂ Rise from Ice Cores. *Science*
879 **336**, 711–714 (2012).

- 880 54. R. Schneider, J. Schmitt, P. Köhler, F. Joos, H. Fischer, A reconstruction of atmospheric carbon
881 dioxide and its stable carbon isotopic composition from the penultimate glacial maximum to the
882 last glacial inception. *Clim. Past* **9**, 2507–2523 (2013).
- 883 55. T. K. Bauska, *et al.*, Carbon isotopes characterize rapid changes in atmospheric carbon dioxide
884 during the last deglaciation. *Proc. Natl. Acad. Sci. U.S.A.* **113**, 3465–3470 (2016).
- 885 56. P. Köhler, H. Fischer, Simulating low frequency changes in atmospheric
886 CO₂ during the last 740 000 years. *Clim. Past* **2**, 57–78 (2006).
- 887 57. P. Köhler, H. Fischer, G. Munhoven, R. E. Zeebe, Quantitative interpretation of atmospheric
888 carbon records over the last glacial termination. *Global Biogeochemical Cycles* **19**,
889 2004GB002345 (2005).
- 890 58. S. Barker, *et al.*, Persistent influence of precession on northern ice sheet variability since the
891 early Pleistocene. *Science* **376**, 961–967 (2022).
- 892 59. S. Barker, *et al.*, Icebergs not the trigger for North Atlantic cold events. *Nature* **520**, 333–336
893 (2015).
- 894 60. S. Eggleston, J. Schmitt, B. Bereiter, R. Schneider, H. Fischer, Evolution of the stable carbon
895 isotope composition of atmospheric CO₂ over the last glacial cycle. *Paleoceanography* **31**, 434–
896 452 (2016).
- 897 61. E. Capron, L'air piégé dans les glaces polaires: Contraintes chronologiques et caractérisation de
898 la variabilité climatique rapide. (2010).
- 899 62. A. Landais, N. Caillon, J. P. Severinghaus, J. Jouzel, V. Masson-Delmotte, Analyses isotopiques
900 à haute précision de l'air piégé dans les glaces polaires pour la quantification des variations
901 rapides de température: méthode et limites. (2003).
- 902 63. D. Foreman-Mackey, D. W. Hogg, D. Lang, J. Goodman, emcee : The MCMC Hammer.
903 *Publications of the Astronomical Society of the Pacific* **125**, 306–312 (2013).
- 904 64. G. S. Hamilton, Mass balance and accumulation rate across Siple Dome, West Antarctica. *Ann.*
905 *Glaciol.* **35**, 102–106 (2002).
- 906 65. J. P. Severinghaus, T. Sowers, E. J. Brook, R. B. Alley, M. L. Bender, fractionated gases in polar
907 ice. **391** (1998).
- 908 66. M. Mudelsee, The phase raelnadtioognlosbaaml
909 iocnegvoatlummoespohveerrichCeOp_ascto4n2te0nkt,atemperature. *Quaternary Science*
910 *Reviews* (2001).

911

912

913

914

915

APPENDIX 7.5

Co-authored study submitted to *Nature Geosciences*:

Legrain, E., Capron, E., Menviel, L., Wohleber, A., Parrenin, F., Teste, G., Landais, A., Bouchet, M., Grilli, R., Nehrbass-Ahles, C., Silva, L., Fischer, H. and Stocker, T. F., Centennial-scale variations in the carbon cycle enhanced by high obliquity, submitted to Nature Geosciences in July 2024.

My contribution as a co-author to this study consisted in the reviewing of the article as well as in the questioning the interpretation of the overall research outputs.

1 **Title:** Centennial-scale variations in the carbon cycle enhanced by high obliquity

2

3 **Authors:** Etienne Legrain^{1,2,3*}, Emilie Capron¹, Laurie Menviel^{4,5}, Axel Wohleber¹, Frédéric
4 Parrenin¹, Grégory Teste¹, Amaëlle Landais⁶, Marie Bouchet⁶, Roberto Grilli¹, Christoph
5 Nehrbass-Ahles^{7,8}, Lucas Silva⁹, Hubertus Fischer⁹, Thomas F. Stocker⁹

6 **Affiliations:**

7 *1 Université Grenoble Alpes, CNRS, IRD, Grenoble INP, IGE, Grenoble, France*

8 *2 Laboratoire de Glaciologie, Université libre de Bruxelles, Brussels, Belgium.*

9 *3 Department of Water and Climate, Vrije Universiteit Brussel, Brussels, Belgium*

10 *4 Climate Change Research Centre, University of New South Wales, Sydney, Australia*

11 *5 The Australian Centre for Excellence in Antarctic Science, University of New South Wales,*
12 *Sydney, Australia*

13 *6 Laboratoire des Sciences du Climat et de l'Environnement, LSCE/IPSL, CEA-CNRS-UVSQ,*
14 *Université Paris-Saclay, Gif-sur-Yvette, France*

15 *7 Department of Earth Sciences, University of Cambridge, Cambridge, UK*

16 *8 National Physical Laboratory, Teddington, UK*

17 *9 Climate and Environmental Physics, Physics Institute, and Oeschger Centre for Climate*
18 *Change Research, University of Bern, Bern, Switzerland*

19 *Corresponding author: etienne.legrain@ulb.be

20

21 *Text length: 2994 words. Nb references: 50. Online methods length: 2807 words. Nb Figures: 4.*

22

23 **Abstract:** Centennial-scale releases of atmospheric carbon dioxide (Carbon Dioxide Jumps,
24 CDJs) are identified during deglacial, glacial and interglacial periods and linked to the Northern
25 Hemisphere abrupt climate variability. However, the limited number of identified CDJs
26 prevents investigating the role of orbital background conditions on the different components of
27 the global carbon cycle that may lead to such rapid atmospheric CO₂ releases. Here, we present
28 a new high-resolution CO₂ record measured on an Antarctic ice core between 260 and 190
29 thousand years ago which reveals seven new CDJs. 18 of the 22 CDJs identified over the past
30 500 thousand years occurred under a context of high obliquity. New simulations performed
31 with an Earth system model of intermediate complexity point toward both the continental
32 biosphere and the Southern Ocean as the two main carbon sources during CDJs connected to
33 Heinrich events. Notably, the continental biosphere appears to be the obliquity-dependent CO₂

34 source for these rapid events. For the first time, we demonstrate that the long-term external
35 forcing directly impacts past abrupt atmospheric CO₂ variations.

36 **Main text:** Understanding the mechanisms of natural centennial-scale changes in the carbon
37 cycle is a major challenge under the ongoing anthropogenic CO₂-driven climate change. Recent
38 efforts to produce high-resolution atmospheric CO₂ records from Antarctic ice cores
39 demonstrated the pervasive character of centennial-scale atmospheric CO₂ increases (Carbon
40 Dioxide Jumps, CDJs) in the global climate system over the last 500 ka (thousand years before
41 present) ¹. These CDJs consist of an atmospheric CO₂ increase of varying magnitude, from ~5
42 ppm up to ~ 16 ppm, that occurs in a few decades to centuries at estimated rates of up to 26
43 ppm/century in the atmosphere ¹. The CDJs represent the strongest of the abrupt events in
44 centennial-scale variability of atmospheric CO₂ concentrations, and they are identified through
45 thresholds applied on detrended ice core CO₂ records (amplitude larger than 5 ppm and growth
46 rate equal or above 1.5 ppm/century after removing the orbital trend) ¹. Two types of Northern
47 Hemisphere (NH) climatic events are associated with the CDJs: (i) the so-called Dansgaard-
48 Oeschger (DO) events which are identified during the last glacial period in Greenland ^{2,3} and
49 North Atlantic ⁴ archives. Each DO event is characterized by an abrupt transition from cold -
50 *stadial* - to milder - *interstadial*- conditions associated with a Greenland surface temperature
51 increase of 5 to 16°C in less than a century ⁵. We stress that a CDJ with a minimum amplitude
52 of 5 ppm cannot be detected for all DO warmings; (ii) the maximum intensity of Heinrich events
53 (HE) within the so-called Heinrich stadials (HS), i.e. cold stadial periods in glacial times during
54 which Heinrich iceberg discharge events occurred, as reflected in peaks of Ice Rafted Debris
55 (IRD) in North Atlantic sediment cores ⁶. The CDJs that occurred at the onset of a DO event
56 (hereafter CDJ+) ¹ are associated with an increase in atmospheric methane (CH₄) concentrations
57 larger than 50 ppb ⁷. The CDJs that occurred within a HS (hereafter CDJ-) ¹ are associated with
58 a short and smaller CH₄ increase ¹ (<50 ppb) happening within the HS and likely when
59 maximum iceberg discharge led to further reduction of the AMOC (Atlantic Meridional
60 Overturning Circulation). Proposed hypotheses to explain how these rapid atmospheric CO₂
61 increases relate to DO events or HE involve both terrestrial ^{8,9} and marine CO₂ sources ^{10,11}, but
62 overall the underlying mechanisms remain poorly understood (Supplementary Materials).

63 Here, we argue that the orbital-scale climatic background conditions modulate the intensity of
64 the centennial-scale carbon cycle response to the Northern Hemisphere climatic perturbations.
65 To test this hypothesis, we extend the time frame covered by high-resolution atmospheric CO₂
66 reconstructions to allow the identification of additional potential CDJs under varying orbital

67 configurations. Then, we investigate the impact of orbital-scale changes in the climatic
68 background on centennial-scale CO₂ increases through new simulations performed with an
69 Earth system model of intermediate complexity.

70 **New sub-millennial-scale atmospheric CO₂ record**

71 We measured 203 new samples on the Antarctic EPICA Dome C (EDC) ice core over the
72 interval 260 – 190 ka using the dry-extraction system coupled to a gas chromatograph at the
73 Institute of Environmental Geosciences (IGE, Grenoble, France; ¹²; see methods). Our new CO₂
74 record is in general agreement with published data ¹³, but we increase the mean temporal
75 resolution by a factor of three to an average of 340 years (Fig. 1, Fig. S1). Owing to the high-
76 resolution data, we identify seven new events of centennial-scale CO₂ release to the atmosphere.
77 These CDJs have been identified using the detection methodology described in ref. ¹. In
78 summary, we first remove the orbital-scale (i.e. deglaciation and glaciation) and millennial-
79 scale (i.e., Antarctic Isotope Maximum events) imprint in the CO₂ record using cubic smoothing
80 splines ¹⁴. Second, we calculate the rate of change of the detrended CO₂ record and third, we
81 apply thresholds of 1.5 ppm/century for the minimum rate of increase and 5 ppm for the
82 minimum amplitude from ref. ¹ to identify CDJs (see methods; Figs. S2, S3). In our new record,
83 we identify two CDJ+ associated with atmospheric CH₄ increases higher than 50 ppb in less
84 than 300 years (CDJ+7e and CDJ+7a), three CDJ- that are not associated with a detectable
85 increase in atmospheric CH₄ in the ice core record and that can be linked to a IRD peak in the
86 oceanic record (CDJ-8a.1, CDJ-8a.2, CDJ-8a.3), and two CDJ that are not associated with either
87 of these two markers (CDJ 7c, CDJ 7b) (Figs. 1, S3, S4). Two CDJs occurred during interglacial
88 conditions¹⁵ (CDJ 7b, CDJ+7a) when Northern Hemisphere ice sheets had shrunk to a size
89 approaching the Holocene value, confirming the occurrence of CDJs during periods of
90 relatively small global ice sheet volume ¹ (Figs. 1, S5). Hence, combining published and newly-
91 described events we find in total 22 CDJs occurring under a wide range of climatic and orbital
92 boundary conditions over the past 500 ka (Fig. 2, Fig. S6, Table S1).

93 **Carbon cycle variability and obliquity state**

94 The sources and mechanisms behind centennial-scale releases of atmospheric CO₂ have been
95 previously investigated based on carbon isotope measurements on Antarctic ice and carbon
96 cycle modelling ^{8,16}. Two main hypotheses have been discussed: (i) the role of a terrestrial
97 carbon source due to a southward shift in the intertropical convergence zone ^{8,17} and (ii) an
98 increase of upwelling activity in the Southern Ocean and/or the North Pacific Ocean possibly

99 due to enhanced intensity or location relative to the sea-ice edge of winds ^{10,18}. However, the
100 role played by long-term forcing on the centennial-scale CO₂ variability has not yet been
101 assessed.

102 Here we investigate the potential role of the long-term forcing, e.g. the global ice volume and
103 the orbital forcing, on the occurrence of CDJs. We show that 18 of the 22 CDJs occurred at
104 times above the average obliquity value (23.33°) of the 12 obliquity cycles of the last 500 ka
105 (Fig. 2; Fig. S5). We note that seven of the eight obliquity maxima between 416 and 9 ka
106 covered by high-resolution CO₂ and CH₄ data that allows the identification of CDJ occurrences
107 show at least one CDJ. Reversely, only two out of the seven obliquity minima covered by high-
108 resolution CO₂ data are linked to a CDJ (Fig. 2). We investigate the hypothesis of a coincidental
109 origin of this specific pattern of CDJs relative to obliquity changes performing a statistical chi-
110 square test (see Methods). According to our analysis, the null hypothesis that centennial-scale
111 release of CO₂ is independent of the obliquity state can be rejected with 90% confidence
112 ($p < 0.1$). Vice versa, the occurrence of CDJs is not significantly coupled to the changes in
113 climatic precession, eccentricity, and global ice volume (Fig. S5; Table S2). Note that our
114 results are independent from the ice-core gas chronology used to display the CO₂ record ^{19–22}
115 and the choice of orbital solutions ^{23,24} (Supplementary Materials, Fig. S7, Table S3). In
116 addition, while our results are obtained using the threshold detection values from ref. ¹,
117 sensitivity tests show that obliquity dependence of the CDJ occurrence is robust regardless of
118 the specific threshold values considered (Supplementary Material, Fig. S8, Table S4). Finally,
119 the AMOC variability itself, at the origin of the CDJs, seems not directly related to obliquity.
120 Indeed, most of AMOC variability occurs under a CO₂ concentration window of 190–225
121 ppm²⁵, which corresponds to periods equally distributed between high (50.7%) and low (49.3%)
122 obliquity over the past 500 ka.

123 **Modelling assessment of CO₂ sources during CDJ- events**

124 CDJs- are most likely associated with a complete AMOC shutdown that occurs sometime
125 within the HS¹. To study the impact of such an AMOC shutdown on the centennial-scale
126 atmospheric CO₂ response, we perform a suite of sensitivity experiments to mimic the carbon
127 cycle response to a HS under both high and low obliquity boundary conditions with the Earth
128 System Model LOVECLIM ²⁶. We find that HS 5 is the most appropriate HS to use as a case
129 study since the corresponding CDJ occurs during a period characterised by the highest obliquity
130 value (24.3°).

131 We perform four simulations under 49 ka boundary conditions, i.e., with realistic orbital
132 parameters, including an obliquity of 24.3° , as well as an estimate of northern hemispheric ice-
133 sheet extent, topography and associated albedo²⁶ (Methods, Table S5). We also perform four
134 simulations under the same boundary conditions except for an obliquity value of 22.1° , i.e. the
135 lowest value of the last 500 ka (Table S5). In all experiments, an idealized HE is simulated by
136 adding 0.3 Sverdrup (Sv) of freshwater to the North Atlantic ($60\text{-}10^\circ\text{W}$, $50\text{-}60^\circ\text{N}$) during 1000
137 years, to induce an Atlantic Meridional Overturning Circulation (AMOC) shutdown (Fig. S9).
138 The sequence of changes during HS is still debated and especially the role of freshwater flux in
139 the observed AMOC weakening^{7,27}. Nevertheless, previous modelling studies have shown that
140 the simulated climatic response to an AMOC weakening was similar whether the freshwater
141 flux had an active (hosed) or passive (unhosed) role²⁸.

142 The simulation conducted under 49 ka climatic conditions (*HighObl*) reveals a centennial-scale
143 response of the carbon cycle to the induced freshwater perturbation (Fig. 3a), characterised by
144 a ~ 9.5 ppm increase in atmospheric CO_2 over the first 400 years of the simulation (Fig. 3a, Fig.
145 3c, Table S5, Fig. S10, Supplementary Materials). A similar simulation performed under low
146 obliquity (*LowObl*), only leads to a ~ 3.3 ppm CO_2 increase over the first 400 years following
147 the freshwater perturbation (Fig. 3c, Table S5). In both experiments, the CO_2 increase is due to
148 a terrestrial carbon release brought about by climatic changes induced by the AMOC weakening
149 (Fig. 3d, Fig. S9). Surface air temperature is lower under low obliquity, particularly in the
150 Northern Hemisphere (-1.4°C north of 20°N), thus impacting the precipitation patterns (Fig.
151 4a). As a result, the terrestrial carbon reservoir is smaller under low than high obliquity (-105
152 Gigatons of carbon, GtC; Fig. 4b). The decrease of precipitation and the lower temperature over
153 the Northern high-latitudes during the freshwater input thus leads to a smaller terrestrial carbon
154 release under low obliquity compared to high obliquity.

155 To investigate the role of terrestrial carbon release, two freshwater experiments are performed
156 in which carbon fluxes between the continental biosphere and the atmosphere are suppressed.
157 Under such conditions, neither the experiment performed under high obliquity
158 (*HighObl_noVeg*) nor the one performed under low obliquity (*LowObl_NoVeg*) produce a
159 centennial-scale CO_2 event (i.e. ~ 0 ppm CO_2 change at year 400, Fig. 3c, Fig. S11, Table S5).
160 Those results highlight that the obliquity no longer has an influence on the centennial-scale CO_2
161 variability if the continental biosphere is muted. They point to the continental biosphere as the
162 variable source of carbon at centennial-scale for CDJ- events, which appears strongly controlled
163 by Earth's obliquity.

164 A stronger CO₂ release in the Southern Ocean, potentially resulting from enhanced Southern
165 Ocean upwelling has been suggested as a process leading to CDJ+ during Termination I¹⁰.
166 Enhanced upwelling of CO₂ rich waters in SO could result from a poleward shift of the sea-ice
167 edge¹⁰ or intensified (and/or poleward shifted) Southern Hemisphere Westerlies (SHW) during
168 HS²⁹. The robustness of the modelled responses to such wind changes was tested by conducting
169 two additional simulations with an imposed ~40% increase of the SHW windstress, one under
170 49 ka conditions (*HighObl_SHW*) and one under low obliquity conditions (*LowObl_SHW*)
171 (Table S5). This leads to a stronger CO₂ release during both high and low obliquity conditions.
172 However, the difference in total CO₂ release between high and low obliquity conditions persists
173 and again only exists if the terrestrial biosphere exchanges CO₂ with the atmosphere. These
174 results reinforce the idea that the SHW play a role in centennial-scale carbon cycle increases
175 (Fig. 3a, Table S5). However, larger CO₂ changes are simulated when terrestrial vegetation and
176 enhanced SHW (*HighObl_SHW* and *LowObl_SHW*) are considered. Our results show that the
177 terrestrial biosphere reservoir is the main source of the higher carbon release during high
178 obliquity conditions for CDJ- events due to its apparent sensitivity to the obliquity context.

179 Now, we compare the centennial-scale atmospheric CO₂ variations recorded in the WAIS
180 Divide ice core across HS 5 (~49 ka) and those modelled in the LOVECLIM simulations that
181 include terrestrial carbon fluxes in term of magnitude and duration. In particular, we look at the
182 CO₂ difference between the high- and low-obliquity simulations (ΔCO_2 , Fig. 3b). The ΔCO_2
183 value allows to identify the difference of amplitude of the observed centennial-scale response
184 of atmospheric CO₂ concentrations in the high-obliquity vs low-obliquity simulations. ΔCO_2
185 increases at centennial-scale and reaches a maximum around year 400 (Fig. 3b, Supplementary
186 Materials). In terms of magnitude, this ΔCO_2 partially explains the recorded centennial-scale
187 variability in the WAIS Divide CO₂ record. This comparison illustrates a similar temporal
188 structure between the measured and simulated CO₂ changes. After year 1000, the WAIS Divide
189 CO₂ changes are decoupled from the variations of the simulated ΔCO_2 , revealing a change in
190 the dynamics of the carbon cycle from centennial-scale to millennial-scale most likely not
191 related to obliquity state. While this model-data comparison is limited by the modelling design,
192 it supports our hypothesis that the orbital-scale obliquity changes influence centennial-scale
193 carbon cycle variations through the terrestrial carbon reservoir.

194 **Drivers of centennial-scale atmospheric CO₂ increases**

195 Previous studies have demonstrated an acidification of the Southern Ocean^{10,11} and of the North
196 Pacific Ocean¹⁸ at the exact timing of the CDJ+ occurring at the onsets of the Bolling Allerød

197 and of the Holocene. This would be consistent with an enhanced CO₂ outgassing in the Southern
198 Ocean resulting from the interplay between the location of the SHW and the sea ice edge, that
199 could have also contributed to previous CDJ+ events ¹⁰. Our modelling results show that
200 variations in SHW can act as a key driver of centennial-scale carbon cycle. However, the SHW
201 changes resulting from an AMOC shutdown could also be modulated by obliquity. Hence, we
202 cannot exclude the hypothesis that the Southern Ocean is an obliquity-dependent source of CO₂
203 and additional simulations investigating the link between SHW and obliquity should be
204 performed with alternative models (Supplementary Materials).

205 Our simulations indicate that the continental biosphere provides an additional source of carbon
206 to the atmosphere during CDJ- events, as already inferred by modelling or carbon-isotope
207 approaches ^{8,30,31} and reveals the obliquity-dependence of this carbon source at centennial-scale.
208 Especially, the region between 8°N and 40°N appears as the additional source of terrestrial
209 carbon under a high-obliquity phase (Fig. 4c). Previous studies revealed an orbital- and
210 millennial-scale control of obliquity on vegetation changes based on pollen ^{32,33} and sediment
211 records ^{34,35}, as well as through modelling approaches ³⁶. This obliquity control modulates the
212 carbon stock available to be released during centennial-scale increases through the extent and
213 type of vegetation. In the low-latitude regions, the induced southward shift of the Inter Tropical
214 Convergence Zone (ITCZ) and changes in latitudinal insolation gradients ³⁶ cause an obliquity-
215 paced vegetation change especially for subtropical biomes and tree coverage ^{32,35}. Depending
216 on the area considered in the mid-latitudes regions, both precession and obliquity forcing seem
217 to be the main drivers of the Asian monsoon system, and hence of the induced summer
218 precipitation that controls the vegetation coverage in the area ³⁴. At higher latitudes, the
219 predominance of trees and shrubs over grasses and herbs is favoured under high obliquity due
220 to lower local ice extent ³³. Our study suggests that the expansion of continental biomass in the
221 high latitudes and the change of vegetation at low latitudes in high obliquity phases could thus
222 provide a large amount of carbon to be released during CDJ- (Fig. 3d). In principle, this
223 additional carbon is also available for enhanced terrestrial carbon release during CDJ+ under
224 high obliquity conditions. However, our model experiments by design only test the terrestrial
225 release during an AMOC shutdown (HE, hence equivalent to CDJ- events) and not for a
226 resumption of the AMOC into interstadial conditions (which would correspond to CDJ+
227 events). With respect to the opposite latitudinal shift of the ITCZ between DO and HE, a similar
228 obliquity dependence on the terrestrial biosphere carbon release is also possible, but additional
229 model experiments would need to be performed to corroborate the influence of obliquity on

230 CDJ+ events. To conclude, our study confirms a joint contribution of terrestrial and oceanic
231 carbon release during CDJ- events and points toward the terrestrial carbon reservoir as a
232 variable sensitive to obliquity in this centennial-scale response.

233 Under the conditions of the glacial-interglacial cycles during the last 600 ka, a strong imprint
234 of both obliquity^{32,33,35,36} and precession^{37,38} was demonstrated for regional variability of
235 vegetation and climate. Our CDJ compilation reveals no direct correlation between precession
236 and CDJ occurrences over the past 500 ka (Fig. S5), and our new simulations confirm the
237 quantitative impact of obliquity on centennial-scale variability of terrestrial carbon fluxes
238 during CDJ- (Fig. 4). Future simulations investigating the precession influence on centennial-
239 scale CO₂ release would be useful to investigate the potential role of precession changes in
240 driving CDJs.

241 Our results reinforce the importance of producing carbon isotope and oceanic pH records during
242 CDJ periods to confirm the processes leading to the atmospheric CO₂ increase during
243 centennial-scale events. In addition, further modelling studies of both CDJ+ and CDJ- events
244 should be conducted to confirm the pervasive character of the identified mechanism. Here we
245 show that past centennial-scale increases of atmospheric CO₂ concentrations with associated
246 AMOC disruption were more likely to happen during high-obliquity phases. Five of the past
247 CDJs occurred under an obliquity value that is close to the current one (± 5 % of the range of
248 the obliquity value variability of the last 500 ka). While a 15% weakening of the AMOC since
249 the mid-twentieth century has been estimated³⁹, large uncertainties remain on the potential
250 occurrence of a large AMOC disruption at multi-centennial-scale in the future^{40,41}. If such
251 AMOC disruption occurs, the current relatively high-obliquity phase is favourable to a
252 measurable release of carbon into the atmosphere which could be superimposed on the
253 anthropogenic-sourced perturbation. This release, which could last from a few decades to a few
254 centuries, would be equivalent to ~ 4 years of CO₂ anthropogenic emission at the 2010-2019
255 emission rate.

256

257 **Acknowledgments:** This study is an outcome of the Make Our Planet Great Again HOTCLIM
258 project, it received the financial support from the French National Research Agency under the
259 “Programme d’Investissements d’Avenir” (ANR-19-MPGA-0001). This publication was also
260 generated in the frame of the Beyond EPICA Oldest Ice Core (BE-OI) project. The BE-OI
261 project has received funding from the European Union’s Horizon 2020 research and innovation

262 programme under grant agreement no. 815384 (Oldest Ice Core). It is supported by national
263 partners and funding agencies in Belgium, Denmark, France, Germany, Italy, Norway, Sweden
264 (through the Crafoord Foundation), and Switzerland, The Netherlands and the United Kingdom.
265 Logistic support is mainly provided by ENEA and IPEV through the Concordia Station system.
266 The opinions expressed and arguments employed herein do not necessarily reflect the official
267 views of the European Union funding agency or other national funding bodies. This is Beyond
268 EPICA publication number XX. LM acknowledges funding from the Australian Research
269 Council (ARC) grants FT180100606 and SR200100008. The research leading to these results
270 has received funding from the French National Research Agency (ANR HUM117 and ANR
271 NEANDROOT), and the European Research Council under the European Union Horizon 2020
272 Programme (ERC ICORDA, grant number 817493). TFS and HF gratefully acknowledge
273 funding by the Swiss National Science Foundation (grants 200020_200492 and
274 200020_200328, respectively).

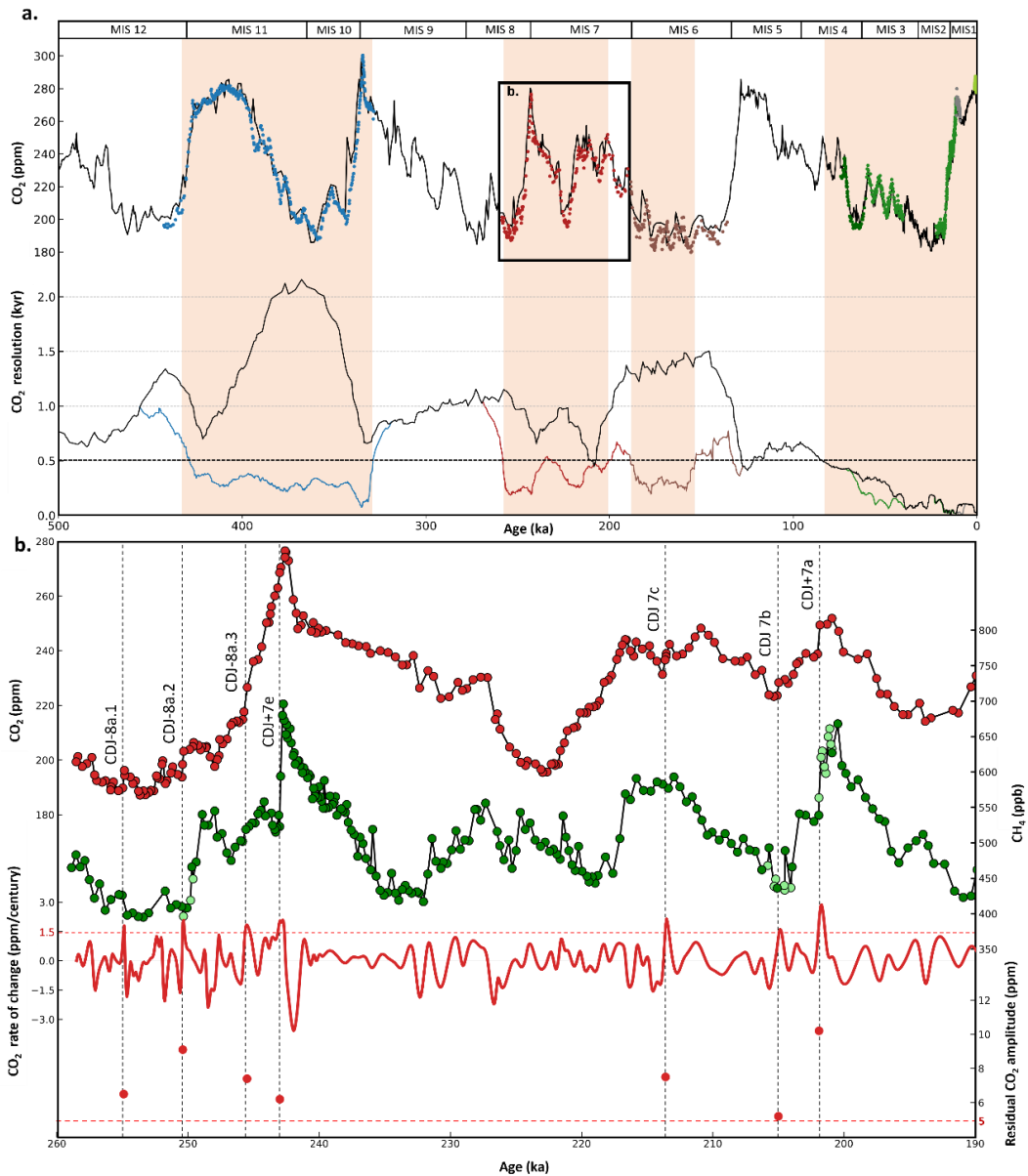
275 **Author contributions:** EC, EL and LM designed research. EL, GT and AW performed the
276 experimental analyses. LM performed the modelling work. EL and EC wrote a draft with
277 subsequent inputs from all co-authors.

278 **Competing interests:** Authors declare that they have no competing interests

279 **Data availability:** The new dataset used in this study and the model outputs are available to
280 download at – *a link to the PANGEA repository will be available before publication* –

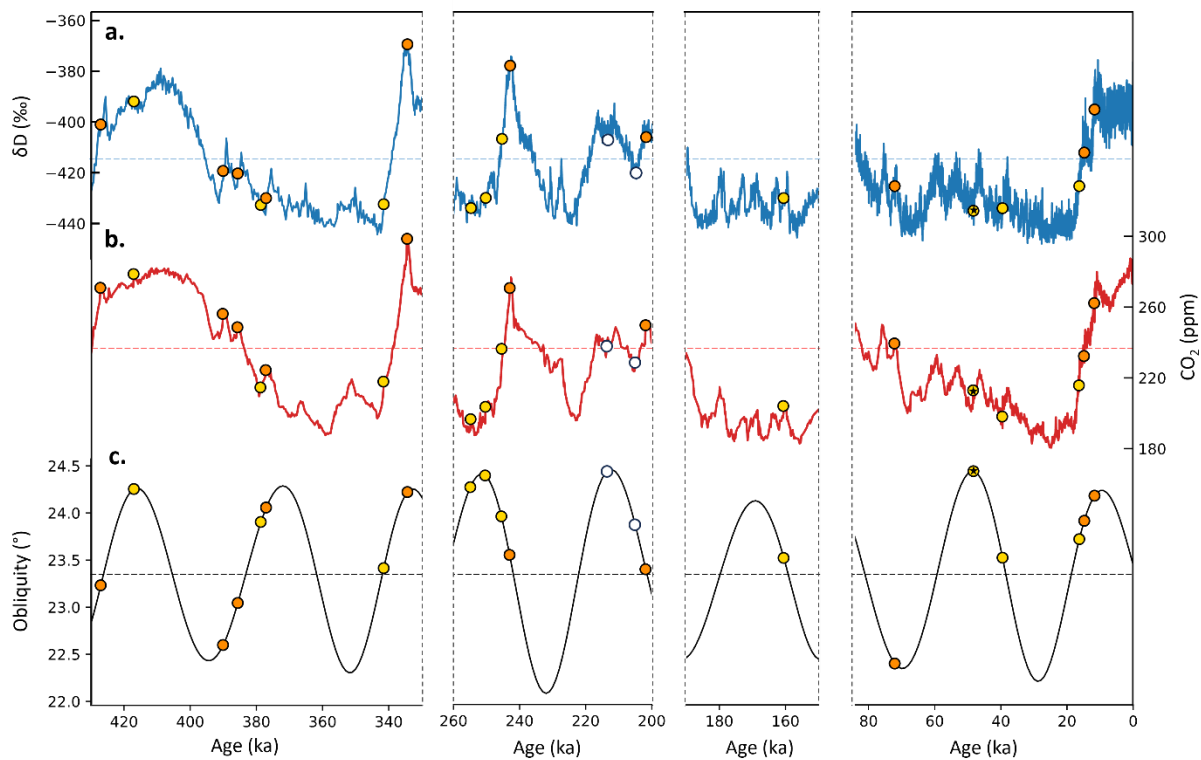
281

282 **Figures**



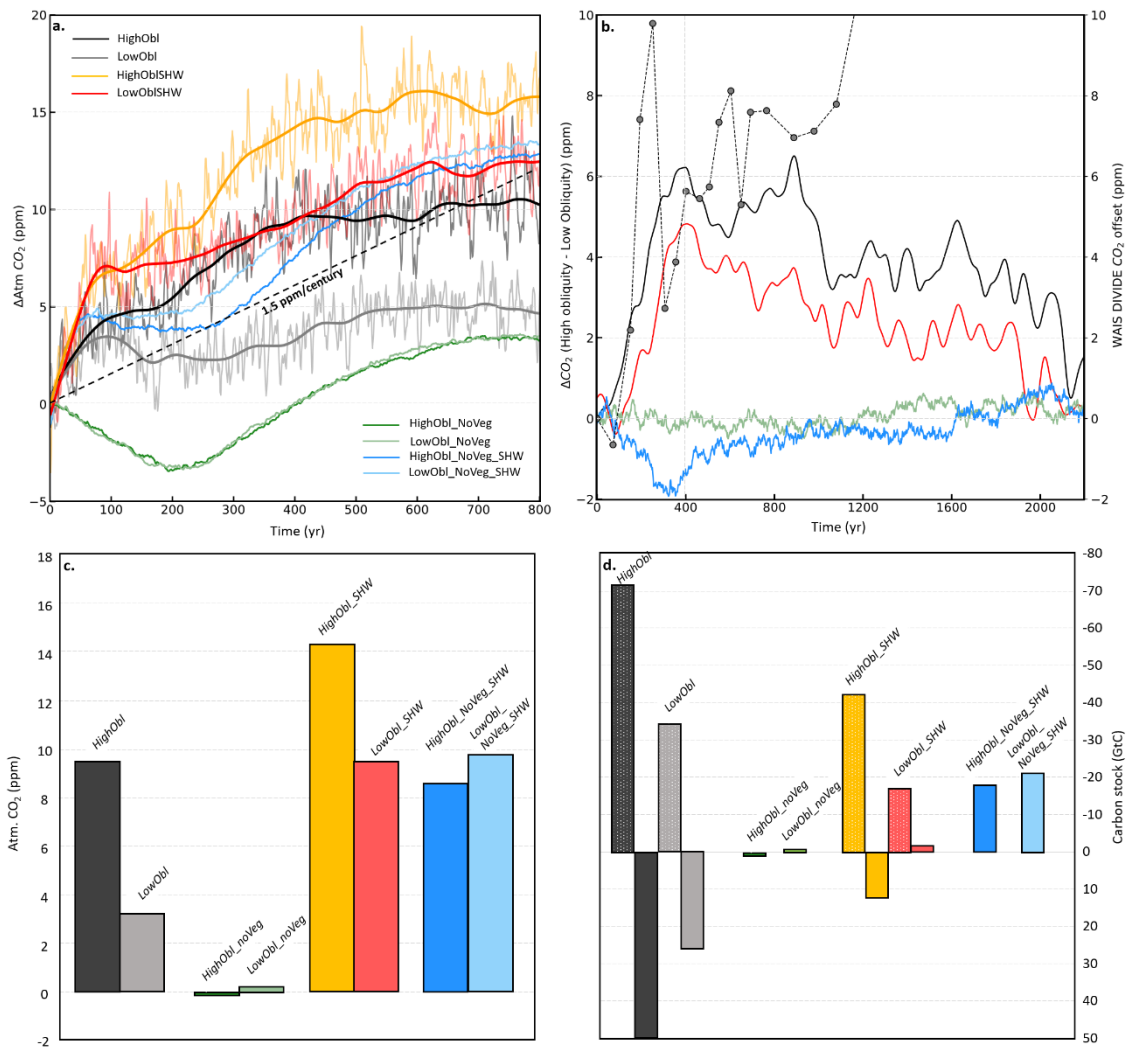
283

284 **Fig. 1: Improvement of the temporal resolution of the ice-core atmospheric CO₂ record since the composite**
 285 **CO₂ record from ref. ⁴² over the last 500 ka. a. Top: High-resolution records are represented in blue ¹, red (this**
 286 **study), brown ¹², green ⁸, dark green ⁴³, grey ⁴⁴, and light-green dots ⁴⁵, plotted on their own published age scales.**
 287 **They are superimposed on the composite CO₂ record ⁴² (black line). Bottom: Temporal resolutions of all records**
 288 **computed as the running mean of 20 data points (colour codes similar to top panel). Data are not corrected for**
 289 **potential offsets due to the use of different experimental setups. Vertical red bands indicate periods where the ice-**
 290 **core CO₂ record is associated with a temporal resolution better than 500 years. b. Top: Zoom on our new EDC**
 291 **CO₂ record between 260-190 ka (red dots, black line) and CH₄ record from this study (light green) and previous**
 292 **studies ^{46,47} (dark green) plotted on the AICC2023 timescale ²². Vertical black dashed lines indicate the newly**
 293 **identified CDJs (see methods, supplementary materials). Middle: CO₂ rates of change from the detrended CO₂**
 294 **record for the smoothing spline (1 kyr cutoff period) ¹. Bottom: Residual CO₂ amplitude of the detrended CO₂**
 295 **record during the events occurring at a rate higher than 1.5ppm/century. Vertical back dashed lines indicate the**
 296 **timing of the identified CDJs. A centennial-scale CO₂ release is identified when the rate is higher than**
 297 **1.5ppm/century and the amplitude is higher than 5 ppm (dashed horizontal grey lines) ¹. MIS: Marine Isotope**
 298 **Stage.**



299

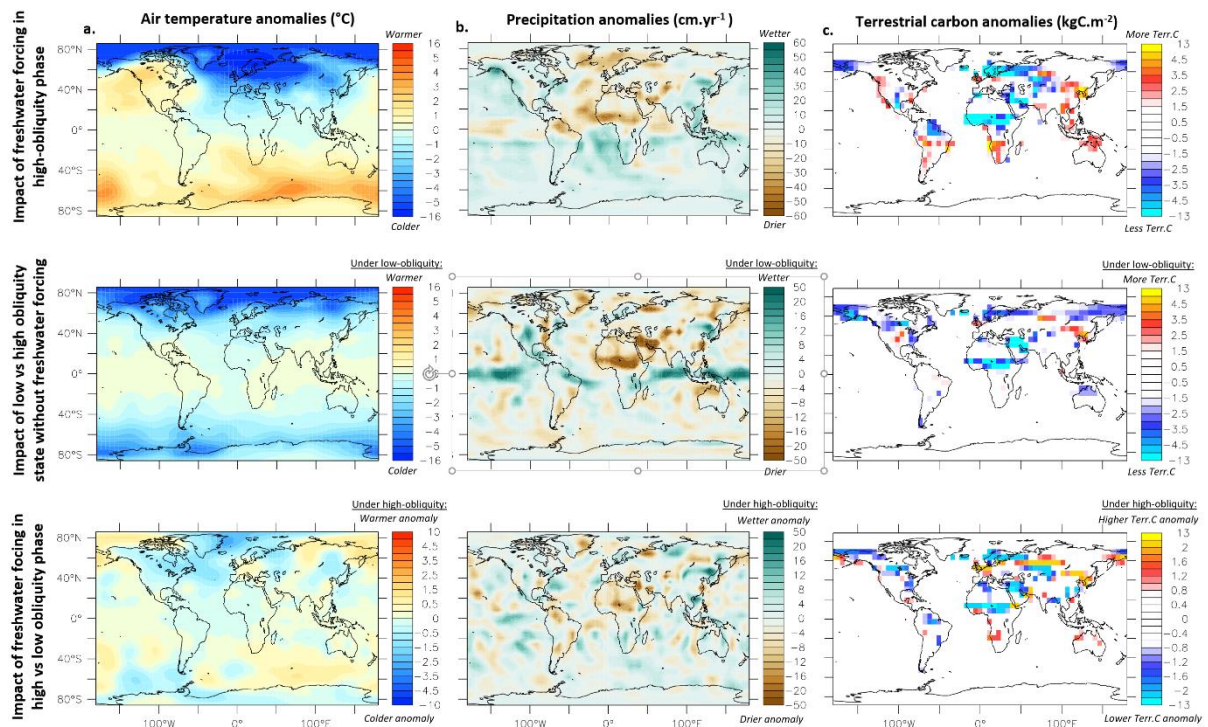
300 **Fig. 2: Climatic and obliquity states for centennial-scale releases of atmospheric CO₂ during the three**
 301 **periods associated with high-resolution ice-core CO₂ records.** a. EDC Deuterium record (δD)⁴⁸ on the
 302 AICC2023 ice age scale²² (blue line). b. Atmospheric CO₂ high-resolution records on the AICC2023 gas age scale
 303²² for the time interval 500-67 ka, on the WD2014^{49,50} time scale for the 67-12 ka interval, and on several original
 304 timescales for the 12-0 ka interval (this study; refs.^{1,8,12,42-45}; red line). c. Obliquity²⁴ (black). Horizontal dashed
 305 lines indicate the average value for each considered proxy record over the last 500 ka. Yellow, orange and white
 306 dots indicate the value of the record during the occurrence of CDJ-, CDJ+ and undetermined CDJ, respectively
 307^{1,8,17}. The CDJ- identified during HS 5 (~49 ka) and simulated with LOVECLIM is identified with black stars on
 308 the three represented climate variables.



309

310 **Fig. 3 Simulated carbon cycle response to an AMOC shutdown.** **a.** Evolution of atmospheric CO₂ for the eight
 311 simulations as a function of time. The dashed grey line corresponds to a 1.5 ppm/century CO₂ increase, which is
 312 also the threshold used to identify CDJ events in the ice-core CO₂ record. Bold lines are smoothing spline filters.
 313 **b.** Δ CO₂ between *HighObl* – *LowObl* (black line), *HighObl_SHW* - *LowObl_SHW* (red line), *HighObl_NoVeg* –
 314 *LowObl_NoVeg* (green line) and *HighObl_NoVeg_SHW* – *LowObl_NoVeg_SHW* (blue line). A positive value
 315 means that the CO₂ anomaly due to the perturbation is higher under a high-obliquity phase than under a low-
 316 obliquity phase. Grey dots with dashed line correspond to the atmospheric CO₂ record from the WAIS ice core
 317 during HS 5, the HS that is simulated in the present study. **c.** Paired coloured bars correspond to the atmospheric
 318 CO₂ offset values 400 years after the freshwater perturbation for simulations using the obliquity value at 49 ka
 319 (left, 24.3°) and a prescribed low-obliquity value (right, 22.1°). Words in *italic* refer to simulation names. **d.** Same
 320 simulation results as in panel c but with carbon stock in GtC. Negative carbon anomaly represents a carbon release
 321 from that reservoir into the atmosphere. Plain coloured bars represent the oceanic carbon stock and coloured bars
 322 with white dots represent the terrestrial carbon stock. Colors refer to the same simulation as in c. The year 400
 323 snapshot represents the period with the largest atmospheric CO₂ difference between the high and low obliquity
 324 simulations and corresponds to a time period where most of the CO₂ response to the freshwater forcing has occurred
 325 (see Supplementary Materials and Fig. S10).

326



327

328 **Fig. 4. Simulated impacts of the freshwater forcing and the obliquity state on the climatic conditions and**
 329 **terrestrial carbon stock.** a. Air temperature anomalies resulting from (top) a freshwater forcing under a high
 330 obliquity phase vs. no freshwater forcing under a high obliquity phase (*HighObl – HighOblCTR*), (middle) a low
 331 obliquity phase without a freshwater forcing vs. a high obliquity phase without a freshwater forcing (*LowOblCTR*
 332 *– HighOblCTR*) and (bottom) the impact of the freshwater forcing in a high vs. low obliquity phase (*HighObl*
 333 *- HighOblCTR*) – (*LowObl - LowOblCTR*) on air temperatures. b. Same as (a) for precipitation anomalies. c. Same
 334 as (a) for the terrestrial carbon anomalies.

335

336

337 References

- 338 1. Nehrbass-Ahles, C. *et al.* Abrupt CO₂ release to the atmosphere under glacial and early
 339 interglacial climate conditions. *Science* **369**, 1000–1005 (2020).
- 340 2. Capron, E. *et al.* The anatomy of past abrupt warmings recorded in Greenland ice. *Nat Commun*
 341 **12**, 2106 (2021).
- 342 3. North Greenland Ice Core Project members. High-resolution record of Northern Hemisphere
 343 climate extending into the last interglacial period. *Nature* **431**, 147–151 (2004).
- 344 4. Voelker, A. H. L. Global distribution of centennial-scale records for Marine Isotope Stage (MIS)
 345 3: a database. *Quaternary Science Reviews* **21**, 1185–1212 (2002).

- 346 5. Kindler, P. *et al.* Temperature reconstruction from 10 to 120 kyr b2k from the NGRIP ice core.
347 *Clim. Past* **10**, 887–902 (2014).
- 348 6. Ruddiman, W. F. Late Quaternary deposition of ice-rafted sand in the subpolar North Atlantic (lat
349 40° to 65°N). *Geol Soc America Bull* **88**, 1813 (1977).
- 350 7. Rhodes, R. H. *et al.* Enhanced tropical methane production in response to iceberg discharge in the
351 North Atlantic. *Science* **348**, 1016–1019 (2015).
- 352 8. Bauska, T. K., Marcott, S. A. & Brook, E. J. Abrupt changes in the global carbon cycle during the
353 last glacial period. *Nat. Geosci.* **14**, 91–96 (2021).
- 354 9. Bauska, T. K. *et al.* Carbon isotopes characterize rapid changes in atmospheric carbon dioxide
355 during the last deglaciation. *Proc. Natl. Acad. Sci. U.S.A.* **113**, 3465–3470 (2016).
- 356 10. Rae, J. W. B. *et al.* CO₂ storage and release in the deep Southern Ocean on millennial to
357 centennial timescales. *Nature* **562**, 569–573 (2018).
- 358 11. Ronge, T. A. *et al.* Southern Ocean contribution to both steps in deglacial atmospheric CO₂ rise.
359 *Sci Rep* **11**, 22117 (2021).
- 360 12. Shin, J. *et al.* Millennial-scale atmospheric CO₂ variations during the
361 Marine Isotope Stage 6 period (190–135 ka). *Clim. Past* **16**, 2203–2219 (2020).
- 362 13. Petit, J. R. *et al.* Climate and atmospheric history of the past 420,000 years from the Vostok ice
363 core, Antarctica. **399**, 10 (1999).
- 364 14. Enting, I. G. On the use of smoothing splines to filter CO₂ data. *J. Geophys. Res.* **92**, 10977
365 (1987).
- 366 15. Past Interglacials Working Group of PAGES. Interglacials of the last 800,000 years. *Rev.*
367 *Geophys.* **54**, 162–219 (2016).
- 368 16. Bauska, T. K. *et al.* Controls on Millennial-Scale Atmospheric CO₂ Variability During the Last
369 Glacial Period. *Geophys. Res. Lett.* **45**, 7731–7740 (2018).
- 370 17. Marcott, S. A. *et al.* Centennial-scale changes in the global carbon cycle during the last
371 deglaciation. *Nature* **514**, 616–619 (2014).
- 372 18. Gray, W. R. *et al.* Deglacial upwelling, productivity and CO₂ outgassing in the North Pacific
373 Ocean. *Nature Geosci* **11**, 340–344 (2018).

- 374 19. Bazin, L. *et al.* An optimized multi-proxy, multi-site Antarctic ice and gas orbital chronology
375 (AICC2012): 120–800 ka. *Clim. Past* **9**, 1715–1731 (2013).
- 376 20. Veres, D. *et al.* The Antarctic ice core chronology (AICC2012): an optimized multi-parameter and
377 multi-site dating approach for the last 120 thousand years. *Clim. Past* **9**, 1733–1748 (2013).
- 378 21. Extier, T. *et al.* On the use of $\delta^{18}\text{O}_{\text{atm}}$ for ice core dating. *Quaternary Science Reviews* **185**, 244–
379 257 (2018).
- 380 22. Bouchet, M. *et al.* The Antarctic Ice Core Chronology 2023 (AICC2023) chronological
381 framework and associated timescale for the European Project for Ice Coring in Antarctica
382 (EPICA) Dome C ice core. *Clim. Past* **19**, 2257–2286 (2023).
- 383 23. Berger, A. & Loutre, M. F. Insolation values for the climate of the last 10 million years.
384 *Quaternary Science Reviews* **10**, 297–317 (1991).
- 385 24. Laskar, J. *et al.* A long-term numerical solution for the insolation quantities of the Earth. *A&A*
386 **428**, 261–285 (2004).
- 387 25. Vettoretti, G., Ditlevsen, P., Jochum, M. & Rasmussen, S. O. Atmospheric CO₂ control of
388 spontaneous millennial-scale ice age climate oscillations. *Nat. Geosci.* **15**, 300–306 (2022).
- 389 26. Goosse, H. *et al.* Description of the Earth system model of intermediate complexity LOVECLIM
390 version 1.2. *Geosci. Model Dev.* **3**, 603–633 (2010).
- 391 27. Barker, S. *et al.* Icebergs not the trigger for North Atlantic cold events. *Nature* **520**, 333–336
392 (2015).
- 393 28. Brown, N. & Galbraith, E. D. Hosed vs. unhosed: interruptions of the Atlantic Meridional
394 Overturning Circulation in a global coupled model, with and without freshwater forcing. *Clim.*
395 *Past* **12**, 1663–1679 (2016).
- 396 29. Menviel, L. *et al.* Southern Hemisphere westerlies as a driver of the early deglacial atmospheric
397 CO₂ rise. *Nat Commun* **9**, 2503 (2018).
- 398 30. Schmitt, J. *et al.* Carbon Isotope Constraints on the Deglacial CO₂ Rise from Ice Cores. *Science*
399 **336**, 711–714 (2012).

- 400 31. Jeltsch-Thömmes, A. & Joos, F. Modeling the evolution of pulse-like perturbations in
401 atmospheric carbon and carbon isotopes: the role of weathering–sedimentation imbalances. *Clim.*
402 *Past* **16**, 423–451 (2020).
- 403 32. Bogotá-A, R. G. *et al.* Rapid climate change from north Andean Lake Fúquene pollen records
404 driven by obliquity: implications for a basin-wide biostratigraphic zonation for the last 284 ka.
405 *Quaternary Science Reviews* **30**, 3321–3337 (2011).
- 406 33. Zech, W. *et al.* Obliquity forcing of Quaternary glaciation and environmental changes in NE
407 Siberia. *Quaternary International* **234**, 133–145 (2011).
- 408 34. Li, T. *et al.* Continued obliquity pacing of East Asian summer precipitation after the mid-
409 Pleistocene transition. *Earth and Planetary Science Letters* **457**, 181–190 (2017).
- 410 35. Ferreira, J. Q. *et al.* Changes in obliquity drive tree cover shifts in eastern tropical South America.
411 *Quaternary Science Reviews* **279**, 107402 (2022).
- 412 36. Bosmans, J. H. C., Hilgen, F. J., Tüenter, E. & Lourens, L. J. Obliquity forcing of low-latitude
413 climate. *Clim. Past* **11**, 1335–1346 (2015).
- 414 37. Joannin, S., Bassinot, F., Nebout, N. C., Peyron, O. & Beaudouin, C. Vegetation response to
415 obliquity and precession forcing during the Mid-Pleistocene Transition in Western Mediterranean
416 region (ODP site 976). *Quaternary Science Reviews* **30**, 280–297 (2011).
- 417 38. Claussen, M., Fohlmeister, J., Ganopolski, A. & Brovkin, V. Vegetation dynamics amplifies
418 precessional forcing. *Geophys. Res. Lett.* **33**, L09709 (2006).
- 419 39. Caesar, L., Rahmstorf, S., Robinson, A., Feulner, G. & Saba, V. Observed fingerprint of a
420 weakening Atlantic Ocean overturning circulation. *Nature* **556**, 191–196 (2018).
- 421 40. Lenton, T. M. *et al.* Climate tipping points — too risky to bet against. *Nature* **575**, 592–595
422 (2019).
- 423 41. He, F. & Clark, P. U. Freshwater forcing of the Atlantic Meridional Overturning Circulation
424 revisited. *Nat. Clim. Chang.* **12**, 449–454 (2022).
- 425 42. Bereiter, B. *et al.* Revision of the EPICA Dome C CO₂ record from 800 to 600 kyr before
426 present: Analytical bias in the EDC CO₂ record. *Geophys. Res. Lett.* **42**, 542–549 (2015).

- 427 43. Menking, J. A. Multiple carbon cycle mechanisms associated with the glaciation of Marine
428 Isotope Stage 4. *Nature Communications* (2022).
- 429 44. Shin, J. *et al.* Millennial variations in atmospheric CO₂ during the early Holocene (11.7–7.4 ka).
430 *Clim. Past* **18**, 2063–2075 (2022).
- 431 45. Bauska, T. K. *et al.* Links between atmospheric carbon dioxide, the land carbon reservoir and
432 climate over the past millennium. *Nature Geosci* **8**, 383–387 (2015).
- 433 46. Loulergue, L. *et al.* Orbital and millennial-scale features of atmospheric CH₄ over the past
434 800,000 years. *Nature* **453**, 383–386 (2008).
- 435 47. Spahni, R. *et al.* Atmospheric Methane and Nitrous Oxide of the Late Pleistocene from Antarctic
436 Ice Cores. *Science* **310**, 1317–1321 (2005).
- 437 48. Jouzel, J. *et al.* Orbital and Millennial Antarctic Climate Variability over the Past 800,000 Years.
438 *Science* **317**, 793–796 (2007).
- 439 49. Buizert, C. *et al.* The WAIS Divide deep ice core WD2014 chronology – Part 1: Methane
440 synchronization (68–31 ka BP) and the gas age–ice age difference. *Clim. Past* **11**, 153–173
441 (2015).
- 442 50. Sigl, M. *et al.* The WAIS Divide deep ice core WD2014 chronology – Part 2: Annual-layer
443 counting (0–31 ka BP). *Clim. Past* (2016).

444

445

446

447

448

449

450

451

452

453 **Online Methods:**

454 **Atmospheric CO₂ measurements on the EDC ice core**

455 Atmospheric CO₂ measurements on the EDC ice core have been performed at Institut des
456 Geosciences de l'Environnement (IGE) using the ball mill dry extraction system coupled with
457 a gas chromatograph^{12,13}. A total of 203 new depth levels have been measured between 2043.8
458 and 2360.6 m corresponding to the time period from 258.6 to 190.0 ka on the AICC2023 gas
459 timescale²² (Fig. 1). Each data point corresponds to air extracted from a single ice sample of
460 40 g and the resulting CO₂ amount fraction is the average of five successive injections of the
461 same air sample made at different pressure levels in the gas chromatograph. The pooled
462 standard deviation of the five injections is 0.9 ppm. Thirty injections of a standard gas (synthetic
463 air from Air Liquide) containing 229.5 ± 0.3 ppm of CO₂ in dry air, which was referenced to
464 two primary standards (241.24 ± 0.015 ppm from NOAA, JB03097, and 260.26 ± 0.2 ppm from
465 CSIRO, CSIRO1677), are used to calibrate the gas chromatograph. First, we correct our data
466 for the crushing process CO₂ contamination that is estimated to be on average of 2.6 ± 0.9 ppm
467 (1σ standard deviation), ranging from 1.0 to 5.4 ppm. This correction is necessary as some CO₂
468 is released from the CO₂ extraction chamber during the crushing process, which is
469 contaminating our extracted air from the ice sample. Blank tests are conducted by measuring
470 the CO₂ concentration of a standard gas of known amount fraction and crushing artificial gas-
471 free ice. The difference between the measured and expected CO₂ amount fraction is attributed
472 to the crushing process itself. The additional CO₂ amount fraction is then converted into CO₂
473 levels to normalize the correction to the volume of injected gas. Blank measurements were
474 performed for every ten measured samples for each of the four extraction cells. Following the
475 procedure of ref.¹², the new CO₂ data are then corrected for gravitational fractionation
476 occurring in the firn. For that we use a record of the isotopic composition of nitrogen in the
477 trapped air covering our studied time interval ($\delta^{15}\text{N}$ of N₂)⁵¹ (not shown here). The average
478 correction is -1.4 ± 0.3 ppm (1σ standard deviation), ranging from -0.9 to -2.1 ppm. The average
479 overall propagated uncertainty of the CO₂ amount fractions is 1.3 ppm. This uncertainty
480 includes the uncertainty related to the five injections (one standard deviation), the uncertainty
481 of the measurement system as determined by standard gas over blank ice measurements (one
482 standard deviation), and the uncertainty associated with and the correction for gravitational
483 settling based on $\delta^{15}\text{N}$ corrections.

484 Over the 260-190 ka time interval, the existing composite CO₂ record⁴² includes data measured
485 on the Vostok ice core, associated with a temporal resolution of ~ 0.85 ka¹³ (Fig. S1). The
486 comparison between our new EDC and the Vostok CO₂ records reveals an offset already

487 observed in ref. ¹² where these data had been measured using an earlier version of the Ball Mill
488 extraction system. Especially, the Vostok CO₂ concentrations are slightly higher by 5.5 ppm on
489 average. This offset can be explained by the fact that the Vostok CO₂ measurements were not
490 corrected for the gravitational fractionation and no blank correction was applied ¹³. When we
491 apply these two corrections on the Vostok CO₂ record, the observed offset is reduced to ~1.5
492 ppm (Fig. S1).

493 **High resolution CO₂ data compilation**

494 In addition to this study, four multi-centennial-scale resolved atmospheric CO₂ datasets have
495 been published since the atmospheric CO₂ composite record from ref. ⁴² was compiled (Fig. 1).
496 Data presented in Fig. 1 are plotted as published and no corrections have been applied.
497 However, this does not affect the results of our study as we focus our analysis on the relative
498 and not absolute variations of CO₂ amount fractions. If we add the duration of all periods with
499 a resolution better than 0.5 ka, we obtain a cumulative duration of 275 ka (vertical red areas,
500 Fig. 1) covering 429 to 329 ka ¹, 258 to 200 ka (this study), 188 to 153 ka ¹², and 84 to 0 ka ^{8,43–}
501 ^{45,52–54}. These periods associated with sub-millennial-scale CO₂ resolution allow to identify
502 centennial scale abrupt variability of atmospheric CO₂ (Fig. 2). In the case of ref. ¹², results of
503 the CDJ identification should be taken with caution as experimental-induced noise make it hard
504 to distinguish natural centennial-scale variability from measurement-induced noise (Fig. S11).
505 Especially, potential CDJ during this time interval could have been missed. The point-to-point
506 variability registered during some periods of the record (186-183 ka; 170-168 ka) confirms that
507 any interpretation of centennial-scale variability during this period needs to carefully take into
508 account this higher variability. We consider that apart from the 429-329 ka, 258-200 ka, 188 to
509 153 ka and the 84-0 ka periods (Fig. 2), potential CDJs occurrences are not identifiable due to
510 insufficient temporal resolution and larger uncertainty associated with the Vostok data. In
511 addition, ice older than 500 ka is affected by strong thinning and higher resolution CO₂
512 measurements should be performed in the future, in particular taking advantage of new semi-
513 continuous analytical techniques ⁵⁵.

514 **Atmospheric CH₄ measurements on the EDC ice core**

515 CDJ+ have been linked to atmospheric CH₄ releases of more than 50 ppb ¹ in the ice core record.
516 However, their identification requires multi-centennial scale resolution of the CH₄ record.
517 Three of the new CDJs identified in this study show a potential CH₄ variability but the
518 associated resolution (> 0.5 kyr) was not good enough to validate the occurrence of a

519 synchronous CH₄ increase. The existing CH₄ EDC record for Marine Isotopic Stage (MIS) 8a
520 – 6e is based on measurements performed on the IGE and the University of Bern experimental
521 setups⁴⁶. We perform 18 new measurements on the time interval of the CDJ+7a, CDJ 7b and
522 CDJ-8a.2, in order to detect a potential CH₄ rise associated with these events. These CH₄
523 measurements on the EDC ice core were performed at IGE using a melt-refreezing extraction
524 method coupled with a gas chromatograph. The method used for the analysis of these samples
525 is identical to that described in ref.⁴⁶. Each sample represents ~40 g of ice from which the air
526 is extracted with a melt-refreezing method. The air is then analysed with a gas chromatograph.
527 15 injections of a single standard gas (synthetic air from Air Liquide) containing 498.1 ± 2.7
528 ppb of CH₄ in dry air, which was referenced to one primary standard 393.9 ± 2.6 ppb from
529 CSIRO, CSIRO1657), are used to calibrate the gas chromatograph. The average CH₄ analytical
530 uncertainty is 5 ppb (1 sigma). We do not correct the concentration for gravitational enrichment
531 to avoid an offset with the previously published record from ref.⁴⁶. Corrections would be ~3
532 ppb on average, less than 1% of the CH₄ concentrations signal⁴⁶. A total of 18 new depth levels
533 has been measured focusing on the depth interval where centennial-scale atmospheric CO₂
534 releases have been identified. All samples are corrected for blank contributions using gas-free
535 ice. All CH₄ data are shown in Fig. S1.

536 **Identification of the centennial-scale CO₂ events**

537 In order to identify the presence of CDJs in our new CO₂ record between 260 and 190 ka, we
538 follow the method developed by ref.¹. We can summarize this methodology as follows: first,
539 we remove the orbital- and millennial-scale trend in the CO₂ record using smoothing splines¹⁴
540 with a cut-off frequency ranging from 6 to 14 ka to evaluate the best detrending method. The
541 definition of the cut-off frequency is derived from the equation (9) of ref.¹⁴. It corresponds to
542 the period at which 50% of the signal is attenuated by the spline-fitting process. The aim is to
543 find a good compromise between removing multi-millennial- to orbital-scale trends while
544 preserving the centennial scale variability (Fig. S2). Then, a second series of splines ranging
545 from 0.4 to 1.2 ka is applied on the detrended CO₂ record in order to obtain evenly-spaced
546 records aiming at smoothing out measurement uncertainty while still preserving the centennial
547 scale variability. Third, the rate of change of the final residual CO₂ record is computed (Figs.
548 S2,3). To identify a CDJ, we apply the thresholds of 1.5 ppm/century and 5 ppm as in ref.¹. For
549 the 188 to 153 ka¹² and 84 to 0 ka^{8,43–45,52–54} intervals, we use the exact same method of
550 identification (Figs. S11, S12, S13). For the 429 to 329 ka interval, we compile the CDJs already
551 identified using the same method¹.

552 Other detection methods of centennial-scale variability have previously been applied during the
553 last glacial period and the last deglaciation. The approach from ref. ¹⁷ is based on the analysis
554 of the raw curve of CO₂ concentrations without any corrections to remove the orbital- or the
555 millennial-scale trends. Such an approach is appropriate to identify the centennial-scale
556 atmospheric CO₂ changes of the last termination as the record is very highly resolved (<0.1 ka).
557 In addition, the centennial-scale variability is of such magnitude (~12 ppm) that it prevents any
558 error of identification. Recently, ref. ⁸ applied a new approach for the identification of the
559 centennial-scale atmospheric CO₂ variability, using the δD record measured on the ice. Based
560 on the assumption that this local surface temperature proxy does not include centennial-scale
561 climate variability during the studied intervals ¹⁷, they use the δD as a filter for identifying
562 centennial-scale CO₂ release. The first step is to estimate the phase relationship between CO₂
563 and δD in order to align the two records. Then, by subtracting a normalised δD curve to the
564 CO₂ record, they obtain a residual CO₂ signal. This method is well adapted to identify
565 centennial-scale CO₂ release during the last glacial period, where millennial-scale variability is
566 the dominant climatic pattern. Such an approach assumes that δD is a template for millennial-
567 scale CO₂ variability, which is not the case for all time periods, especially during deglaciations
568 ⁵⁶⁻⁵⁸ and the end of interglacials ⁵⁹. The coupling between δD and CO₂ during the 260-190 ka
569 interval, which is mainly composed of a deglaciation and an interglacial period, is thus not
570 trivial. In addition, with that method, all centennial-scale variability of carbon cycle is
571 investigated. Hence, we consider that the method of ref. ¹ based on the smoothing spline is most
572 adapted for the identification of the largest centennial-scale atmospheric CO₂ releases, i.e. the
573 CDJ events.

574 Note that applying the ref. ¹ methodology to the most recent period (70-0 ka) where the
575 methodology of ref. ⁸ was originally used to identify potential CDJs (Fig. S13), led to the same
576 results. Also, the coherency between the two methodologies used for the identification of
577 centennial-scale CO₂ release underlines that the main result of the study, i.e. the influence of
578 the obliquity on the occurrence of such events, is not dependent on the choice of the CDJ
579 detection method.

580 Centennial-scale variability in a recent atmospheric CO₂ record measured on the Taylor glacier
581 ice core has been observed during the Marine Isotope Stage 5-4 transition ⁴³. However, the short
582 time interval covered by the high-resolution CO₂ record (~13 ka) and the absence of water
583 isotope measurements in the same ice core prevent to apply directly the CDJ methodology
584 identification from ref. ¹ or from ref. ⁸. To circumvent this issue, we merged the record from

585 ref. ⁴³ and refs. ^{54,60} to produce a continuous record over the 90-45 ka interval (Fig. S14). We
586 then applied the method of ref. ¹ to this merged record. Note that while applied to the whole
587 interval, this test would only allow to identify CDJ on the 74-59 ka interval, where the
588 atmospheric CO₂ concentration resolution is below 500 years ⁴³ (Fig. 1, Fig. S12).

589 **Chi-square test**

590 We apply a statistical method to investigate the potential role of the Earth's obliquity in the
591 centennial-scale atmospheric CO₂ variability. The Chi-square method allows to test the null
592 hypothesis that a distribution of a parameter (centennial-scale variability occurrences) versus
593 another (obliquity value) is independent. This method assumes a normal distribution of the
594 probability results for the computation of the confidence level. Such approach was applied to
595 determine the impact of external forcing on the climate system in previous studies ⁶¹⁻⁶³. For
596 that, we separate the centennial-scale events in two categories depending on whether they occur
597 in the context of an obliquity value above or under the average obliquity of the 12 obliquity
598 cycles of last 500 ka (corresponding to the mean obliquity value of the 494.5-9.5 ka period, i.e.
599 23.33°).

600 For that, we compute:

$$601 \quad X = \frac{(\textit{observed} - \textit{expected})^2}{\textit{expected}}$$

602 With *observed* the number of centennial-scale events occurring below the average obliquity
603 value of the 12 obliquity cycles of the last 500 ka, here 4, and *expected* the theoretical value
604 expected under the null hypothesis. The theoretical value would be 11 (i.e. half of the total
605 number of detected CDJs) if the studied period would contain as many high obliquity intervals
606 than low obliquity periods. However, only 44.1 % of the studied period is below the average
607 obliquity value taken as reference (23.33°). The theoretical value is thus 9.7. We found:

$$608 \quad X = 3.4$$

609 This value is higher than $\alpha_{0.1}$, the risk at 10% to accept the null hypothesis even if it is wrong,
610 which is 2.7 for a degree of freedom of 1. In other words, the value 2.7 is the 90th percentile of
611 the chi-square distribution ⁶⁴.

612 We can thus reject the null hypothesis that the distribution of centennial-scale CO₂ events is
613 independent of the obliquity state with a confidence level of 90%. In order to test the sensitivity
614 of the chosen threshold (here the average obliquity value of the 12 obliquity cycles of the last

615 500 ka), we performed a chi-square test for the interval of obliquity values (22.7 -23.9°)
616 systematically reached during each obliquity cycle over the last 500 ka (Fig. S16). Our analysis
617 reinforces the observation of missing CDJ during low-obliquity periods.

618 We also apply the Chi-square test for the Earth's precession and eccentricity parameters using
619 the mean values of the last 500 ka (Table S2). The null hypothesis of an independence of
620 centennial-scale CO₂ events from precession and eccentricity context could not be rejected at a
621 confidence level of 90%.

622 **Experimental design of carbon cycle modelling**

623 To understand the processes that could lead to a different response of the carbon cycle during
624 an AMOC shutdown as a function of obliquity, numerical experiments are performed with the
625 Earth system model LOVECLIM²⁵ (Table S4). LOVECLIM includes a free surface primitive
626 equation ocean model with a horizontal resolution of 3°x3° and 20 unevenly spaced vertical
627 levels, a dynamic/thermodynamic sea-ice model, a quasi-geostrophic T21 atmospheric model,
628 a dynamic global vegetation model (DGVM) and a marine carbon cycle model. The DGVM
629 used, VECODE (Vegetation Continuous Description model), simulates the vegetation
630 structure, and associated terrestrial carbon reservoirs²⁶.

631 The initial 49 ka state was derived from a transient experiment that started at 140 ka. The
632 penultimate deglaciation (140-120 ka) followed the PMIP4 protocol⁶⁵, with the model being
633 forced by changes in orbital parameters⁶⁶, atmospheric greenhouse gases⁶⁷ and changes in
634 continental ice-sheets⁶⁵. That simulation was continued between 120 and 49 ka forced with
635 estimates of changes in continental ice-sheets from an offline simulation⁶⁸. The Bering strait
636 was gradually closed at 70 ka, and kept closed until the early Holocene.

637 From that initial state at 49 ka, the model was run for 4000 years with prognostic atmospheric
638 CO₂ concentration and under constant 49 ka boundary conditions (HighOblCTR). The last 1000
639 yrs of this experiment serve as control run for the 49 ka experiments (Fig. S17).

640 From the initial transient state, another experiment was run under 49 ka boundary conditions
641 but with an obliquity of 22.1°. This experiment was first run for 4000 years with a constant
642 atmospheric CO₂ concentration of 204 ppm, after which the CO₂ was prognostic for 2000 years
643 (LowOblCTR) (Fig. S17).

644 From these control runs (HighOblCTR and LowOblCTR), two meltwater experiments were
645 performed (HighObl and LowObl) by adding 0.3 Sv of meltwater into the North Atlantic (60-

646 10°W, 50-60°N) for 1000 years thus leading to an AMOC shutdown in ~300 years. The
647 meltwater flux was then stopped for 800 years, after which a negative meltwater flux was added
648 to the North Atlantic (-0.1 Sv) for 400 years so that the AMOC would recover.

649 Two experiments with similar forcing to HighObl and LowObl but with a 40% increase of the
650 westerly wind stress over the Southern Ocean between 65°S and 34°S from year 0 to 1800
651 (HighObl_SHW and LowObl_SHW) were also performed.

652 Finally, two experiments similar to HighObl and LowObl, and two experiments similar to
653 HighObl_SHW and LowObl_SHW were performed, in which the terrestrial carbon fluxes did
654 not impact atmospheric CO₂ (HighObl_NoVeg, LowObl_NoVeg, HighObl_NoVeg_SHW and
655 LowObl_NoVeg_SHW). Note that for these experiments, the model was first run for 2000 years
656 without any meltwater so that the atmospheric CO₂ concentration would equilibrate.

657

658 **Online Method References:**

- 659 1. Shin, J. *et al.* Millennial-scale atmospheric CO₂ variations during the
660 Marine Isotope Stage 6 period (190–135 ka). *Clim. Past* **16**, 2203–2219 (2020).
- 661 2. Petit, J. R. *et al.* Climate and atmospheric history of the past 420,000 years from the Vostok ice
662 core, Antarctica. **399**, 10 (1999).
- 663 3. Bouchet, M. *et al.* The Antarctic Ice Core Chronology 2023 (AICC2023) chronological
664 framework and associated timescale for the European Project for Ice Coring in Antarctica
665 (EPICA) Dome C ice core. *Clim. Past* **19**, 2257–2286 (2023).
- 666 4. Bréant, C. *et al.* Unveiling the anatomy of Termination 3 using water and air isotopes in the Dome
667 C ice core, East Antarctica. *Quaternary Science Reviews* **211**, 156–165 (2019).
- 668 5. Bereiter, B. *et al.* Revision of the EPICA Dome C CO₂ record from 800 to 600 kyr before
669 present: Analytical bias in the EDC CO₂ record. *Geophys. Res. Lett.* **42**, 542–549 (2015).
- 670 6. Nehrbass-Ahles, C. *et al.* Abrupt CO₂ release to the atmosphere under glacial and early
671 interglacial climate conditions. *Science* **369**, 1000–1005 (2020).
- 672 7. Bauska, T. K., Marcott, S. A. & Brook, E. J. Abrupt changes in the global carbon cycle during the
673 last glacial period. *Nat. Geosci.* **14**, 91–96 (2021).

- 674 8. Rubino, M. *et al.* Revised records of atmospheric trace gases CO₂,
675 CH₄, N₂O, and
676 $\delta^{13}\text{C-CO}_2$ over the last 2000
677 years from Law Dome, Antarctica. *Earth Syst. Sci. Data* **11**, 473–492 (2019).
- 678 9. Bauska, T. K. *et al.* Links between atmospheric carbon dioxide, the land carbon reservoir and
679 climate over the past millennium. *Nature Geosci* **8**, 383–387 (2015).
- 680 10. Shin, J. *et al.* Millennial variations in atmospheric CO₂ during the early Holocene (11.7–7.4 ka).
681 *Clim. Past* **18**, 2063–2075 (2022).
- 682 11. Ahn, J. & Brook, E. J. Siple Dome ice reveals two modes of millennial CO₂ change during the
683 last ice age. *Nat Commun* **5**, 3723 (2014).
- 684 12. Bereiter, B. *et al.* Mode change of millennial CO₂ variability during the last glacial cycle
685 associated with a bipolar marine carbon seesaw. *Proc. Natl. Acad. Sci. U.S.A.* **109**, 9755–9760
686 (2012).
- 687 13. Menking, J. A. Multiple carbon cycle mechanisms associated with the glaciation of Marine
688 Isotope Stage 4. *Nature Communications* (2022).
- 689 14. Mächler, L. *et al.* Laser-induced sublimation extraction for centimeter-resolution multi-species
690 greenhouse gas analysis on ice cores. *Atmos. Meas. Tech.* **16**, 355–372 (2023).
- 691 15. Loulergue, L. *et al.* Orbital and millennial-scale features of atmospheric CH₄ over the past
692 800,000 years. *Nature* **453**, 383–386 (2008).
- 693 16. Enting, I. G. On the use of smoothing splines to filter CO₂ data. *J. Geophys. Res.* **92**, 10977
694 (1987).
- 695 17. Marcott, S. A. *et al.* Centennial-scale changes in the global carbon cycle during the last
696 deglaciation. *Nature* **514**, 616–619 (2014).
- 697 18. Parrenin, F. *et al.* Synchronous Change of Atmospheric CO₂ and Antarctic Temperature During
698 the Last Deglacial Warming. *Science* **339**, 1060–1063 (2013).
- 699 19. Chowdhry Beeman, J. *et al.* Antarctic temperature and CO₂: near-
700 synchrony yet variable phasing during the last deglaciation. *Clim. Past* **15**, 913–926 (2019).

- 701 20. Landais, A. *et al.* Two-phase change in CO₂, Antarctic temperature and global climate during
702 Termination II. *Nature Geosci* **6**, 1062–1065 (2013).
- 703 21. Ai, X. E. *et al.* Southern Ocean upwelling, Earth’s obliquity, and glacial-interglacial atmospheric
704 CO₂ change. *Science* **370**, 1348–1352 (2020).
- 705 22. Lüthi, D. *et al.* CO₂ and O₂/N₂ variations in and just below the bubble–clathrate transformation
706 zone of Antarctic ice cores. *Earth and Planetary Science Letters* **297**, 226–233 (2010).
- 707 23. Liautaud, P. R., Hodell, D. A. & Huybers, P. Detection of significant climatic precession
708 variability in early Pleistocene glacial cycles. *Earth and Planetary Science Letters* **536**, 116–137
709 (2020).
- 710 24. Huybers, P. & Wunsch, C. Obliquity pacing of the late Pleistocene glacial terminations. *Nature*
711 **434**, 491–494 (2005).
- 712 25. Lohmann, J. & Svensson, A. Ice core evidence for major volcanic eruptions at the onset of
713 Dansgaard–Oeschger warming events. *Clim. Past* **18**, 2021–2043 (2022).
- 714 26. Efron, B. & Morris, C. Data Analysis Using Stein’s Estimator and its Generalizations. *Journal of*
715 *the American Statistical Association* **70**, 311–319 (1975).
- 716 27. Goosse, H. *et al.* Description of the Earth system model of intermediate complexity LOVECLIM
717 version 1.2. *Geosci. Model Dev.* **3**, 603–633 (2010).
- 718 28. Menviel, L. *et al.* The penultimate deglaciation: protocol for Paleoclimate Modelling
719 Intercomparison Project (PMIP) phase 4 transient numerical simulations between 140 and 127 ka,
720 version 1.0. *Geosci. Model Dev.* **12**, 3649–3685 (2019).
- 721 29. Berger, A. L. Long-Term Variations of Caloric Insolation Resulting from the Earth’s Orbital
722 Elements. *Quat. res.* **9**, 139–167 (1978).
- 723 30. Köhler, P., Nehrbass-Ahles, C., Schmitt, J., Stocker, T. F. & Fischer, H. A 156 kyr smoothed
724 history of the atmospheric greenhouse gases CO₂,
725 CH₄, and N₂O and their radiative forcing. *Earth*
726 *Syst. Sci. Data* **9**, 363–387 (2017).
- 727 31. Abe-Ouchi, A. *et al.* Insolation-driven 100,000-year glacial cycles and hysteresis of ice-sheet
728 volume. *Nature* **500**, 190–193 (2013).

APPENDIX 7.6

Co-authored study in preparation:

Paul, C., Piel, C., Sauze, J., Yang, J.-W., Bouchet, M., Jossoud, O., Dapoigny, A., Romanini, D., Prié, F., Devidal, S., Jacob, R., Milcu, A. and Landais, A., Air oxygen fractionation associated with respiration and photosynthesis processes in plants: impact on the study of the global Dole effect, in preparation.

I contributed to the study for the reviewing process and for developing the Section 2.2 focusing on the evolution of the Dole effect over the last deglaciation. A perspective to this study would be to employ a chronological framework that is coherent for glacial archives and marine sediments for calculating the Dole Effect on a coherent age scale.

Air oxygen fractionation associated with respiration and photosynthesis processes in plants: impact on the study of the global Dole effect

Clémence Paul¹, Clément Piel², Joana Sauze², Ji-Woong Yang¹, Marie Bouchet¹, Olivier Jossoud¹, Arnaud Dapoigny¹, Daniele Romanini⁴, Frédéric Prié¹, Sébastien Devidal², Roxanne Jacob¹, Alexandru Milcu^{2,3} and Amaëlle Landais¹

¹Laboratoire des Sciences du Climat et de l'Environnement, LSCE/IPSL, CEA-CNRS-UVSQ, Université Paris-Saclay, 91191 Gif-sur-Yvette, France

²Ecotron Européen de Montpellier (UAR 3248), Univ Montpellier, Centre National de la Recherche Scientifique (CNRS), Campus Baillarguet, Montferrier-sur-Lez, France

³Centre d'Ecologie Fonctionnelle et Evolutive, Univ Montpellier, CNRS, Univ Paul Valéry, EPHE, IRD, Montpellier, France

⁴Laboratoire Interdisciplinaire de Physique, Univ Grenoble Alpes, CNRS/UGA, Saint-Martin-d'Hères, France

Correspondence: Clémence Paul (clemence.paul@lsce.ipsl.fr)

1. Introduction

Oxygen is the most abundant element on Earth. Photosynthesis is the biological mechanism by which oxygen is produced by terrestrial and marine organisms, while it is consumed by another process, respiration. Oxygen concentration largely varied in the past because of geological oxidation events (Liu et al., 2019) or changes in ecosystems productivity (Vilovic et al., 2023). The study of dioxygen isotopic composition makes it possible to study all the fundamental biogeochemical cycles, in particular those of O₂, CO₂ and water. The analysis of air bubbles in ice cores provides a signal of past variations in the $\delta^{18}\text{O}$ of O₂ in atmospheric air (also known as $\delta^{18}\text{O}_{\text{atm}}$). The $\delta^{18}\text{O}_{\text{atm}}$ variations can be interpreted as variations in the hydrological cycle at low latitudes and/or as variations of the relative proportion of the oceanic vs terrestrial biosphere productivity (Bender et al., 1994; Luz et al., 1999; Malaizé et al., 1999; Severinghaus et al., 2009; Blunier et al., 2002; Landais et al., 2010; Luz and Barkan, 2011). Several studies have measured the enrichment of the atmospheric oxygen $\delta^{18}\text{O}$ ($\delta^{18}\text{O}_{\text{atm}}$) vs the $\delta^{18}\text{O}$ of water of the global ocean (the Vienna Standard Mean Ocean Water, VSMOW) to 23.5 - 24 ‰ (Kroopnick and Craig, 1972; Barkan and Luz, 2005; Pack et al., 2017; Wostbrock and Sharp, 2021). This difference between $\delta^{18}\text{O}_{\text{atm}}$ and $\delta^{18}\text{O}_{\text{sw}}$ (sw for sea water) varies with time and is named the Dole effect (DE). Subsequently, several studies have attempted to estimate this Dole effect in order to get as close as possible to this value of 24 ‰ (Bender et al., 1994; Hoffman et al., 2004; Luz and Barkan, 2011) and better understand the processes involved.

Interpretation of $\delta^{18}\text{O}_{\text{atm}}$ and Dole effect variations in the past is still an open question. Historically, Bender et al. (1994) found that $\delta^{18}\text{O}_{\text{atm}}$ oscillates with precession and this enabled ice cores to be dated using this proxy (Petit et al., 1999; Dreyfus et al., 2007). It is well established that $\delta^{18}\text{O}_{\text{atm}}$ is influenced by changes in the hydrological cycle at low

latitudes (Bender et al., 1994; Severinghaus et al., 2009; Landais et al., 2010; Seltzer et al., 2017). This is supported by the strong resemblance over the last 650 ka between variations in $\delta^{18}\text{O}_{\text{atm}}$ and in $\delta^{18}\text{O}_{\text{calcite}}$, studied in East Asian speleothems (Wang et al., 2008; Cheng et al., 2016) which are driven by changes in the low-latitude water cycle (monsoons).

In addition, Bender et al. (1994), Malaizé et al. (1999) and Hoffmann et al. (2004) suggested that variations of the Dole effect are mainly influenced by the relative proportion of terrestrial vs oceanic productivity. The reason for this interpretation is that the terrestrial Dole effect (i.e. the enrichment in $\delta^{18}\text{O}$ of O_2 in the atmosphere vs $\delta^{18}\text{O}_{\text{sw}}$ due to the fluxes issued from the terrestrial biosphere) was estimated to be several permil higher than the oceanic Dole effect (i.e. the enrichment in $\delta^{18}\text{O}$ of O_2 in the atmosphere vs $\delta^{18}\text{O}_{\text{sw}}$ due to the fluxes issued from the oceanic biosphere). These estimates of the oceanic and the terrestrial Dole effect relied on some rare determinations of the fractionation coefficients associated with biological processes, during both terrestrial and oceanic respiration and photosynthesis (Guy et al., 1993; Angert and Luz, 2001; Hendricks et al., 2004; Helman et al., 2005; Eisenstadt et al., 2010; Luz and Barkan, 2011). Using these fractionation coefficients, the first estimate of the global Dole effect by Bender et al. (1994) was too low by more than 3 ‰ than the measured value (24 ‰) which questioned the validity of these approaches. In particular, no discrimination was associated with oceanic and terrestrial photosynthesis (Guy et al., 1989; Vinogradov et al., 1959; Helman et al., 2005). When Eisenstadt et al. (2010) detected an oceanic photosynthetic discrimination approximately equal to 6 ‰, it was easier to reconcile the estimated and measured Dole effect. Moreover, it permitted to increase the calculated oceanic Dole effect estimates to the level of terrestrial values and led Luz and Barkan (2011) to propose that Dole effect is only a marker of variations in the hydrological cycle at low latitudes. However, a recent study

by Paul et al. (2023) noticed that a non-zero terrestrial photosynthetic discrimination of 3.7 ‰ still challenges the proper interpretation of the Dole effect.

The terrestrial photosynthetic discrimination evidenced by Paul et al. (2023) needs to be verified since the experiment was carried out on one plant only. Moreover, this experiment was not performed at the micro-organism scale as in previous studies (Helman et al., 2005; Eisenstadt et al., 2010) but at the scale of the ecosystem, hence involving the presence of soil. While this approach may be closer to the reality, other processes than photosynthesis occur during light period which can influence the determination of the fractionation coefficient associated with photosynthesis.

The first objective of our study is to better quantify the discriminations associated with terrestrial respiration and photosynthesis on closed chambers on a larger number of terrestrial plants. As a second objective, we want to revise the interpretation of the Dole effect using new estimated fractionation coefficients.

The manuscript is organized as follows. In a first section, we present the general evolution of ideas on the calculation and the interpretation of $\delta^{18}\text{O}_{\text{atm}}$ and the Dole effect. The second section is devoted to materials and methods and provides the details on the plants studied and on the controlled biological chambers. Modeled gross primary production outputs from Palaeoclimate Modelling Intercomparison Project (PMIP) were also used to help interpretation of the global Dole effect. The third section presents the results of biological fractionation coefficients for the different plants. Finally, the last section is dedicated to the implication of the new calculation of fractionation coefficients for the interpretation of the Dole effect.

2. State of art: general concept of calculation and interpretation of $\delta^{18}\text{O}_{\text{atm}}$

2.1. Calculations of $\delta^{18}\text{O}_{\text{atm}}$ and Dole effect

2.1.1. The definition of Dole effect

The $\delta^{18}\text{O}_{\text{atm}}$ is expressed with respect to present-day atmospheric air as a standard. In contrast, $\delta^{18}\text{O}_{\text{sw}}$ is expressed with respect to the international standard for water: Vienna Standard Mean Ocean Water (V-SMOW). There is a difference in the $\delta^{18}\text{O}$ of O_2 value for present-day atmosphere and in the $\delta^{18}\text{O}$ of H_2O for the V-SMOW standard. This difference is called the Dole effect (DE) and we can express:

$$\delta^{18}\text{O}_{\text{atm}} = \delta^{18}\text{O}_{\text{sw}} + DE \quad (1)$$

The Dole effect is due to the different processes involved in the coupled cycle of dioxygen and water. In particular, the main O_2 fluxes on Earth are due to biological processes with photosynthesis producing O_2 from H_2O contained in the biosphere and respiration consuming atmospheric O_2 , preferentially the lightest isotopic forms (^{16}O - ^{16}O vs ^{16}O - ^{18}O).

We can thus define the Dole effect as:

$$DE = \delta^{18}\text{O}_{\text{water,biosphere}} + {}^{18}\epsilon_{\text{respi}} + {}^{18}\epsilon_{\text{photo}} \quad (2)$$

Where $^{18}\epsilon_{respi}$ represents the discrimination associated with the respiration of organisms and $^{18}\epsilon_{photo}$ represents the discrimination associated with the photosynthesis of organisms. $\delta^{18}O_{water,biosphere}$ is the $\delta^{18}O$ of the water consumed by the biosphere during photosynthesis and is expressed with respect to V-SMOW.

In the ocean, the $\delta^{18}O_{water,biosphere}$ is equal to the $\delta^{18}O_{sw}$ and the oceanic Dole effect can directly be expressed as:

$$DE_{ocean} = ^{18}\epsilon_{respi,ocean} + ^{18}\epsilon_{photo,ocean} \quad (3)$$

Where $^{18}\epsilon_{respi,ocean}$ represents the discrimination associated with the respiration of marine organisms and $^{18}\epsilon_{photo,ocean}$ represents the discrimination associated with the photosynthesis of autotrophic marine organisms.

On Earth, leaf water is consumed by plants during photosynthesis. The $\delta^{18}O$ of leaf water can be related to the $\delta^{18}O$ of soil water which is then modified by evapotranspiration (Hoffmann et al., 2004; West et al., 2008) so that the terrestrial Dole effect can be defined as follows:

$$DE_{terr} = \delta^{18}O_{soil_water} + ^{18}\epsilon_{evapotranspi} + ^{18}\epsilon_{respi,terr} + ^{18}\epsilon_{photo,terr} \quad (4)$$

Where $^{18}\epsilon_{evapotranspi}$ represents the discrimination associated with evapotranspiration, $^{18}\epsilon_{respi,terr}$ represents the discrimination associated with the respiration of terrestrial organisms and $^{18}\epsilon_{photo,terr}$ represents the discrimination associated with the

photosynthesis of autotrophic terrestrial organisms. At first approximation, the $\delta^{18}\text{O}_{\text{soil_water}}$ can be estimated as the annual mean $\delta^{18}\text{O}$ of meteoric water or $\delta^{18}\text{O}_{mw}$.

From the definition of the oceanic and terrestrial Dole effects and making the steady state assumption, i.e. that the biological fluxes of dioxygen production (photosynthesis) and dioxygen consumption (mainly respiration) are equal, it is possible to express the global Dole effect as:

$$DE_{global} = \frac{GPP_{ocean} \times DE_{ocean} + GPP_{terr} \times DE_{terr}}{GPP_{totale}} \quad (5)$$

with GPP_{ocean} corresponding to the gross primary productivity of the ocean, GPP_{terr} corresponding to the gross primary productivity of the land, GPP_{total} corresponding to the gross primary productivity of the ocean and land (i.e. $GPP_{total} = GPP_{ocean} + GPP_{terr}$).

By simplifying the equation with the parameter $r = \frac{GPP_{ocean}}{GPP_{total}}$, we can write the definition of

DE_{global} as follows:

$$DE_{global} = r \times DE_{ocean} + (1 - r) \times DE_{terr} \quad (6)$$

2.1.2. The main drivers of Dole effect

In order to identify the main drivers of the Dole effect, it is necessary to have estimates of the different terms in the equations 3, 4 and 5.

The value of $\delta^{18}\text{O}_{\text{mw}}$ (as the main driver of $\delta^{18}\text{O}_{\text{soil_water}}$) varies temporally and spatially because of changes in the $\delta^{18}\text{O}_{\text{sw}}$ (especially over glacial – interglacial transitions) and of the distillation occurring between the evaporation source and the precipitation site. This distillation leads to decreased values of $\delta^{18}\text{O}$ in continental regions and toward high latitudes with the respect to evaporation regions (Aggarwal et al., 2010). At first approximation, the $\delta^{18}\text{O}$ soil water can be approximated by the annual average of the $\delta^{18}\text{O}$ of meteoric water (Anderson et al., 1998; Helliker and Richter 2008) equal on average to - 8 ‰ (Bender et al., 1994; Landais et al., 2006.) Then, $\delta^{18}\text{O}$ of leaf water is enriched with respect to $\delta^{18}\text{O}$ of soil water due to evapotranspiration, the main contribution being the evaporation of water in leaves. This enrichment shows large temporal and spatial variations due to the diversity of leaf types and anatomies as well as to fluctuations in temperature, humidity and surrounding water vapor $\delta^{18}\text{O}$ (e.g. Flanagan et al., 1991; Cernuzak et al., 2016). Despite the strong spatial variability, measurements of $\delta^{18}\text{O}$ of CO_2 led to an estimate of the global value of 7 ‰ for the difference between $\delta^{18}\text{O}_{\text{lw}}$ (lw = leaf water) and $\delta^{18}\text{O}_{\text{sw}}$ for present-day (Gillon and Yakir, 2001; West et al., 2008).

The value for $^{18}\epsilon_{\text{respi}}$ should be calculated considering the different biological processes consuming O_2 . Bender et al. (1994) listed three main processes which should be considered both in the terrestrial and oceanic biosphere: dark respiration, Mehler reaction and photorespiration. For the first estimate of $^{18}\epsilon_{\text{respi,terr}}$ (18.0 ‰), Bender et al. (1994) used the most recent values observed for dark respiration, Mehler reaction and photorespiration from biological experiments driven at the scale of the enzyme or the cell (Guy et al., 1992, 1993). For the first estimate of $^{18}\epsilon_{\text{respi,ocean}}$ (18.9 ‰), Bender et al. (1994) used measurements of $\delta^{18}\text{O}$ of O_2 and O_2 concentrations from oceanic samples or from biological experiments performed on several marine organisms (bacteria, microalgae, copepods, etc.). Over the years, these estimates were refined using studies performed at

the cell scale (Helman et al., 2005) or at a more global scale (e.g. soil samples, Angert et al., 2003; ocean samples, Hendricks et al., 2004).

As for the $^{18}\epsilon_{respi,ocean}$, the first studies detected no discrimination (Guy et al., 1989, studies on cyanobacteria (*Anacystis nidulans*) and diatoms (*Phaeodactylum tricornutum*); Vinogradov et al., 1959; Helman et al., 2005). However, more recently, Eisenstadt et al. (2010), study a diversity of marine organisms (phytoplankton) and found a non-zero photosynthetic discrimination for eukaryotic algae: 4.5 ‰ for *Phaeodactylum tricornutum* diatoms, 3 ‰ for *Nannocloropsis sp.* diatoms, 5.5 ‰ for Coccolithophores *Emiliana huxleyi* and 7 ‰ for *Chlamydomonas reinhardtii*. A non-zero value for the photosynthetic discrimination is difficult to explain either from the physiological point of view (Tcherkez and Farquhar, 2007) or by the diffusion during the production of O₂ and then the diffusion in the free air (O¹⁶ is diffusing more rapidly than O¹⁸ so that we should have measured an apparent negative discrimination during photosynthesis). Eisenstadt et al. (2010) also ruled out the existence of large O₂ consumption reaction fractionating O₂ and hence affecting the determination of the $^{18}\epsilon_{photo,terr}$ value because there was no O₂ in their experimental environment. Paul et al. (2023) performed controlled experiments with fescue for the terrestrial photosynthesis and found a first value of 3.7 ‰ for $^{18}\epsilon_{photo,terr}$.

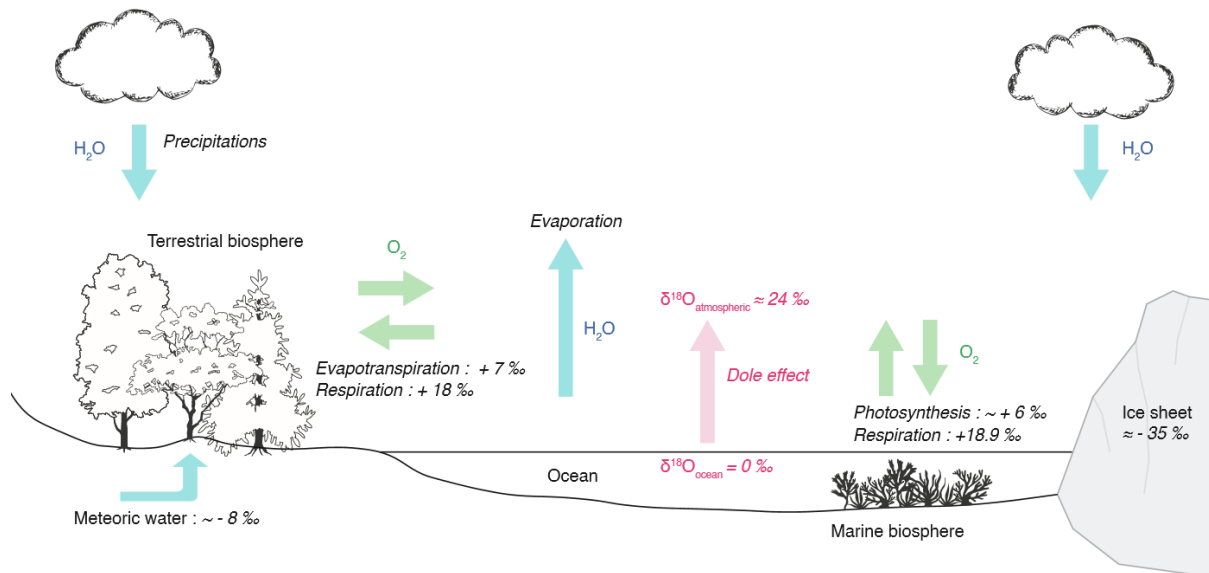


Figure 1. The water and oxygen cycle and fractionation factors involved in hydrological and biological processes. Blue arrows show hydrological fluxes, green arrows show biological fluxes and the red arrow shows the global Dole effect.

2.1.3. Different estimates of Dole effect

In their first estimates of the terrestrial and oceanic Dole effects, Bender et al. (1994) used the global estimates presented above and found a significantly lower value for the oceanic Dole effect compared to the continental Dole effect (Fig.2). Hoffmann et al. (2004) revisited this first calculation through a different integration of the isotopic effects: they used various models (an atmospheric general circulation model with water isotopes, a model of vegetation and an ocean model with a module for biological productivity) to calculate global $\delta^{18}\text{O}_{\text{mw}}$ and $^{18}\epsilon_{\text{respi}}$ as well as biological fluxes. They confirmed the results of Bender et al. (1994) that the oceanic Dole effect should be lower than the terrestrial one and even found a much larger difference between these two contributions. If the terrestrial and oceanic Dole effects are significantly different (Fig.2), it is then expected that the change in the relative proportion of the terrestrial and oceanic

productivities is one of the main drivers of the variations of the global Dole effect as measured in climatic archives.

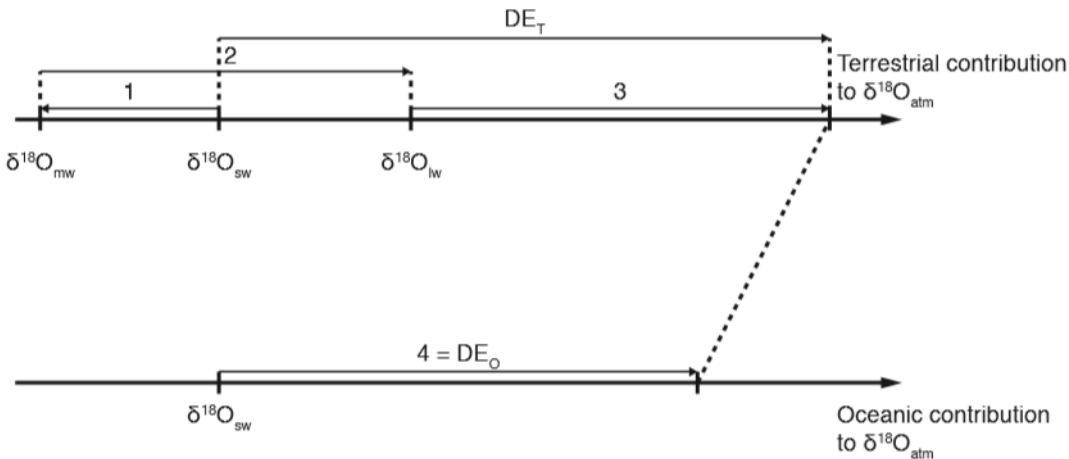


Figure 2. Diagram of the main contributions to $\delta^{18}\text{O}_{atm}$. (1) Fractionation of water associated with evaporation and precipitation. (2) Fractionation of water associated with evapotranspiration. (3) Fractionation of atmospheric oxygen associated with terrestrial respiration and mixing with oxygen issued from leaf photosynthesis. (4) Fractionation of atmospheric oxygen associated with oceanic respiration and mixing with oxygen issued from oceanic photosynthesis. (5) Fractionation associated with oceanic photosynthesis. DE_T = terrestrial Dole effect and DE_o = oceanic Dole effect (from Landais et al., 2007).

Using latest estimates of $^{18}\epsilon_{respi}$ and $^{18}\epsilon_{photo}$, Luz and Barkan (2011) found a different result: DE_{terr} and DE_{ocean} are equal to about 24 ‰ each (Fig.3). This difference is due to the fact that their estimate of $^{18}\epsilon_{respi,terr}$ is smaller than initially because of the diffusion in the soil and $^{18}\epsilon_{photo,ocean}$ is estimated to 6 ‰ instead of 0 ‰ in the first calculations. In this case (Fig.3), the relative proportion of terrestrial and oceanic productivities cannot explain the variations of the global Dole effect which are expected to be simply the result of variations in monsoon cycles leading to variations in the $\delta^{18}\text{O}_{mw}$ and $\delta^{18}\text{O}_{lw}$ (Luz and Barkan, 2011; Landais et al., 2010).

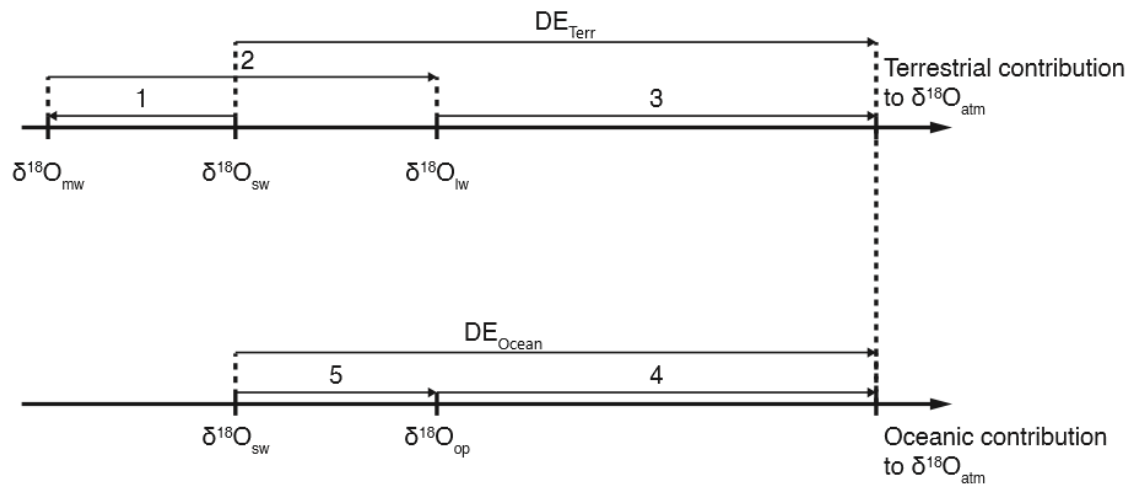


Figure 3. Diagram of the main contributions to $\delta^{18}\text{O}_{atm}$. (1) Fractionation of water associated with evaporation and precipitation. (2) Fractionation of water associated with evapotranspiration. (3) Fractionation of atmospheric oxygen associated with terrestrial respiration and mixing with oxygen issued from leaf photosynthesis. (4) Fractionation of atmospheric oxygen associated with oceanic respiration and mixing with oxygen issued from oceanic photosynthesis. (5) Fractionation associated with oceanic photosynthesis. DE_{Terra} = terrestrial Dole effect and DE_{Ocean} = oceanic Dole effect (modified from Landais et al., 2007).

Recently, further research was carried out by Paul et al. (2023) on the study of terrestrial biological fractionations in a closed chamber. The major result of this study is the discovery of a terrestrial photosynthetic discrimination equal to 3.7 ‰. If confirmed, this result questions the interpretations of variations in the global Dole effect, since according to equations 4 and 5, the terrestrial Dole effect would then be increased and be again higher than the oceanic one. Thus, according to equation 6, the ratio r between terrestrial and oceanic productivity would not only affect the variations of the hydrological cycle at low latitudes but also the variations of the global Dole effect (Fig.3).

In our study, we seek to confirm or infirm the results of Paul et al. (2023) by studying a broader range of plant species and to apply the results to an updated interpretation of the Dole effect over the last deglaciation.

2.1.4. Available values for Dole effect

In this section, we detail all the parameters used to calculate Dole effects in the literature. (Table 1).

Table 1. (a) Parameters used to calculate oceanic, terrestrial and the current global Dole effects in literature. *found in their own study, ¹Farquhar et al. (1980); ²Keeling and Shertz (1992); ³Kiddon et al. (1993) and others defined after; ⁴Farquhar et al. (1993); ⁵Guy et al. (1992), (1993); ⁶West et al. (2008); ⁷Landais et al. (2007); ⁸Luz and Barkan (2011). (b) Calculation of the Dole effects (oceanic, terrestrial and global) in their own study. + the calculation of oceanic, terrestrial and global Dole effects was not explicitly done in their own study; thus, we have calculated them here using Eq.3 and 4 and for the global DE with the equation given by Luz and Barkan (2011): $DE_{terr} * f_{terr} + DE_{oce} * f_{oce} - \epsilon_{stratosphere}$, with $f_{terr} = 0.63$ (the fraction of the land), $f_{oce} = 0.37$ (the fraction of the ocean) and $\epsilon_{stratosphere} = 0.3$ (the contribution due to exchange of O₂ between the troposphere and the atmosphere).

a)

	Bender et al. (1994)	Hoffmann et al. (2004)	Luz and Barkan (2011)	Paul et al. (2023)
GPP-O ₂ ocean (Pmol O ₂ /yr)	12 ¹	7.6*		
GPP-O ₂ land (Pmol O ₂ /yr)	20.4 ²	16.79*		
¹⁸ $\epsilon_{respi,ocean}$	18.9 ³	20 ³	19.7*	19.7 ⁸
¹⁸ $\epsilon_{photo,ocean}$	0 ⁵	0 ⁵	4 ⁵	4 ⁵
$\delta^{18}O_{lw}$	4.4 ⁴	5-6*	6.5 ⁶	6.5 ⁶
¹⁸ $\epsilon_{respi,terr}$	18 ⁵	20 ³	17.7 ⁷	17*
¹⁸ $\epsilon_{photo,terr}$	0 ⁵	0 ⁵	0 ⁵	3.7*

b)

	Bender et al. (1994)	Hoffmann et al. (2004)	Luz and Barkan (2011)	Paul et al. (2023)	Ciais et al. (2012)	
	Present				PI	LGM
DE_{ocean}	18.9	16.9	23.5	23.7	19.8	20
DE_{terr}	22.4	26.9	23.5	26.5	28.3	29.5
$DE_{global_calculated}$	20.8	23.5	23.2	25.1 ⁺	24.9 ⁺	25.7 ⁺

The calculation of oceanic respiration discrimination by Bender et al. (1994) and Hoffmann et al. (2004) depends on the average value given by Kiddon et al. (1993) of 20 ‰ for the euphotic zone and on the average value of 12 ‰ by Bender (1990) for the deep-water zone. We note different DE_{ocean} values for Bender et al. (1994) and Hoffmann et al. (2004) due to the fact that they did not take the same fractions of marine respiration attributed to O₂ uptake at oceanic depths below the euphotic zone (20 % for Hoffmann et al., 2004 and 5 % for Bender et al., 1994). The high terrestrial Dole effect of Hoffmann et al. (2004) and Ciais et al. (2012) is the result of a higher $\delta^{18}O_{lw} = 6$ ‰ (calculated in their study) instead of the 4.4 ‰ used by Bender et al. (1994) based on the work of Farquhar et al. (1993). The discovery by Eisenstadt et al. (2010) of oceanic photosynthetic discrimination thus increases the value of the oceanic Dole effect for Luz and Barkan (2011). For Paul et al. (2023), the largest value of the terrestrial Dole effect compared to Luz et Barkan (2011) is linked to the finding of a fractionation during terrestrial photosynthesis.

2.2. The evolution of the Dole effect over the last deglaciation

Figure 4 shows the evolution of the Dole effect calculated using different datasets and age models for the oceanic $\delta^{18}O$ from the Last Glacial Maximum (LGM) at 20 ka BP, to the

Pre-Industrial period (PI), at 0 ka BP. For the atmospheric $\delta^{18}\text{O}$ we used the high resolution (100 years on average) record from the WAIS Divide ice core (Seltzer et al., 2017). For the oceanic $\delta^{18}\text{O}$, the three following series were used: (i) the benthic $\delta^{18}\text{O}$ stack of Lisiecki and Raymo (2005) whose age model is tuned to the EPICA Dome C ice core timescales (Parrenin et al., 2007; Veres et al., 2013; Bouchet et al., 2023), (ii) the benthic $\delta^{18}\text{O}$ volume-weighted stack of Lisiecki and Stern (2016) on its original radiocarbon age scale and (iii) the ice-sheet contribution of the oceanic $\delta^{18}\text{O}$ modeled by Bintanja et al. (2005). We calculate the three resulting scenarios for the Dole effect fluctuations. Huang et al. (2020) argue that it may be more appropriate to use a stack for sea surface term $\delta^{18}\text{O}_{\text{surf}}$ rather than the mean oceanic water $\delta^{18}\text{O}$ to calculate the Dole effect. The reason for this choice is that when using the $\delta^{18}\text{O}_{\text{ocean}}$ in the calculation of the Dole effect, a 100 ka frequency, that is not present in the $\delta^{18}\text{O}_{\text{atm}}$ record, appears. Because $\delta^{18}\text{O}_{\text{surf}}$ is mainly driven by precession, as $\delta^{18}\text{O}_{\text{atm}}$, the calculation of Dole effect (DE) with these two terms does not display any 100 ka periodicity. Therefore, the alternative Dole effect (DE*) suggested by Huang et al. (2020) is also shown in Fig.4 (pink line).

Although all DE scenarios are approximately equal to zero at LGM and PI, they undergo significant fluctuations ($\pm 0.4 - 0.6 \text{ ‰}$) over the last deglaciation from 10 to 3 ka BP. The variations observed during the deglaciation, from 20 to 11 ka BP, are inconsistent and diverge from one scenario to another by up to 0.5 ‰, except the DE* evaluated by Huang et al. (2020) which remains close to zero. Hence, we believe that the important deviations affecting the other DE scenarios might result from the omission of the substantial influence of the hydrological cycle on the oceanic $\delta^{18}\text{O}$. By contrast, all DE and DE* scenarios well agree over the 10-3 ka BP time interval and indicate an excursion of 0.4 ‰ towards negative values. This deviation seems to be driven by the evolution of the ice core atmospheric $\delta^{18}\text{O}$ signal (panel c). The potential origins of this cavity-shaped feature detected in all DE scenarios at the mid-Holocene period (~ 6 ka BP) will be discussed in the following sections.

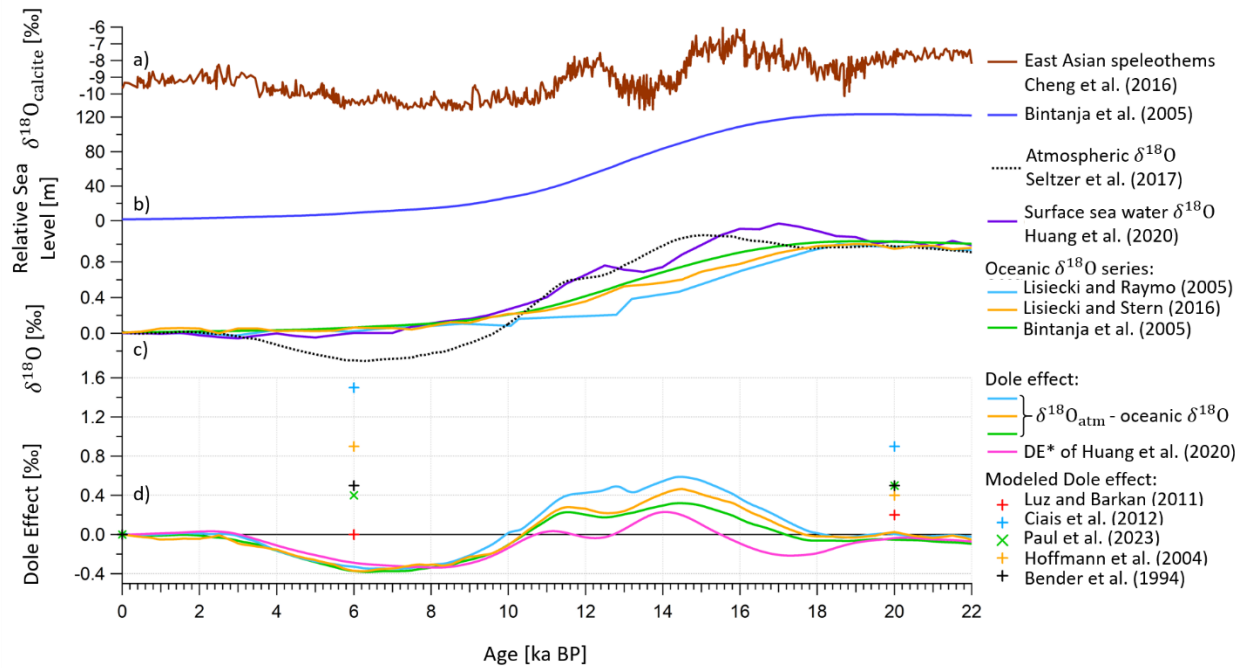


Figure 4. Different Dole effect scenarios calculated using marine and ice core $\delta^{18}\text{O}$ data between 25 and 0 ka BP. a) Uranium-Thorium-dated $\delta^{18}\text{O}_{\text{calcite}}$ from speleothems of Hulu and Sambaos caves (Cheng et al., 2016). b) Sea level relative to PI (Bintanja et al., 2005). c) $\delta^{18}\text{O}$ series: $\delta^{18}\text{O}_{\text{atm}}$ from WAIS Divide ice core on WD2014 age model (black dotted line) (Seltzer et al., 2017; Sigl et al. 2016) and surface sea water $\delta^{18}\text{O}$ global stack on its radiocarbon age model (purple line) (Huang et al., 2020). The five oceanic $\delta^{18}\text{O}$ series: (i) the benthic $\delta^{18}\text{O}$ from the LR04 global stack (Lisiecki and Raymo, 2005) synchronized to the ice core age scale (blue line, Antarctic Ice Core Chronology 2023) (Parrenin et al., 2007; Bouchet et al., 2023), (ii) the benthic $\delta^{18}\text{O}$ from the LS16 global stack on its radiocarbon age model (orange line) (Lisiecki and Stern, 2016) and (iii) the modeled ice-sheet contribution to oceanic $\delta^{18}\text{O}$ (green line) (Bintanja et al., 2005). The benthic $\delta^{18}\text{O}$ data have been scaled between 0 (PI) and 1 ‰ (LGM) values (Schrag et al., 1996). d) The five scenarios of Dole effect calculated as per $\delta^{18}\text{O}_{\text{atm}}$ - oceanic $\delta^{18}\text{O}$ for the five oceanic $\delta^{18}\text{O}$ series (same colors) and the DE* of Huang et al. (2020) (pink line). The crosses indicate the difference with respect to the pre-industrial period of the Dole effect at 6 ka and LGM as estimated by the different previous studies as summarized in Table 8 (here, we chose to display only the calculation of the Dole effect performed with the MIROC-ES2L model).

3. Material and Methods

3.1. Study of oxygen isotope fluxes in multiplexed closed chambers on a variety of C3 and C4 plants

3.1.1. Plant varieties

Different plants were chosen: *Musa acuminata*, *Nerium oleander*, *Cupressus sp.*, *Festuca arundinacea* and *Zea mays*. A first selection criterion was to have model plants (fescue and maize) no taller than 50 cm to fit into the biological chamber with the soil. In addition, we chose plants adapted to different climates (temperate and tropical) and plants with different anatomical characteristics. We also wanted to compare C3 and C4 plants, since C4 plants do not photorespire. The plants to be analyzed are presented in Table 2.

Table 2. Characteristics of the five plants studied in the biological experiments.

Scientific name of the plant	Common name of the plant	Climate	Characteristic	Photosynthesis strategy
<i>Festuca arundinacea</i>	Fescue	Temperate	Herbaceous plant	C3
<i>Nerium oleander</i>	Laurel	Temperate - warm	Broadleaved evergreen shrub	C3
<i>Musa acuminata</i>	Banana tree	Tropical	Broadleaved evergreen herbaceous plant	C3
<i>Cupressus sp.</i>	Cypress	Temperate-cold	Needleleaved evergreen tree	C3
<i>Zea mays</i>	Maize	Tropical	Broadleaved summergreen herbaceous plant	C4

3.1.2. Set-up of the study of the oxygen isotope fluxes on terrestrial plants in closed chambers

3.1.2.1. Set-up of the multiplexed chambers

The general set-up of the experiments is equivalent to that referred to in Paul et al. (in prep). For each plant study (fescue, laurel, banana, maize, cypress and soil only), we used three biological chambers simultaneously.

The set of three airtight transparent welded polycarbonate chambers (120 L volume) were adapted from the chamber described in Paul et al. (2023) and Milcu et al. (2013). The main controlled environmental parameters inside the closed chambers were temperature, light intensity, CO₂ concentration, relative humidity and differential pressure. Each chamber was used as a closed gas exchange system, and placed in a separate controlled environment growth chamber, in the Microcosms experimental platform of the Montpellier European Ecotron. A multiplexing system has been built to be able to handle the three chambers in parallel (Paul et al., in prep). With this set-up, we continuously measured the isotopic composition of O₂ using an online optical spectroscopy instrument based on the Optical Feedback Cavity Enhanced Absorption Spectroscopy (OF-CEAS) (Piel et al., in prep).

As in Paul et al. (in prep), we have also obtained IRMS measurements using a flanged air recovery system. In the studies of plants with soil, i.e. fescue 1, laurel, banana tree, maize 1 and cypress, we could not use the optical spectrometry analyzer system, as the instrument was under repair.

In the different studies performed with the optical spectrometer, we did two-point calibrations using two reference gases once every day. Because the measured difference in isotopic and elemental composition between the two reference gases was very stable over days, we used only one reference gas calibration (dry atmospheric air) during the

day. The measurement sequence was the following: - 6 min of measurement of atmospheric air - 6 min of measurement of air in chamber 1. This sequence was then applied to each of the three chambers and a full sequence lasted 36 min for the three chambers.

3.1.2.2. General strategy for experiments

We present here the general strategies of experiments carried out on maize, fescue, laurel, banana tree and cypress grown on a typical compost soil (*Terreau universel*, Botanic, France. Composition: black and blond peat, wood fiber, green compost and vermicompost, organic and organo-mineral fertilizers and micronutrient fertilizers) in three parallel closed chambers. These soil + plant experiments lasted between three and six days, alternating between dark and light periods (except for the cypress, only a dark period) as follows in Table 3. In addition to soil experiments, we chose to grow two plants in hydroponics: maize and fescue (called maize 2 and fescue 2 in Table 3). We studied fescue and maize under hydroponic conditions so as to dispense with the soil factor in discriminations calculations, to try to better understand the 3 ‰ discrimination found by Paul et al. (2023). Hydroponics makes it possible to study the biological fractions associated solely with the plant, and thus dispenses with the respiratory fractions of the soil. From a biological point of view, this discrimination raises the question of whether there is indeed a discrimination associated with photosynthesis, or whether it's just an effect of the soil respiration that counterbalances the effect of photosynthesis. All experiments are summarized in the Table 3.

Table 3. Experimental strategies for the five plants studied: experiment times for fescue and maize (1 for experiment 1 with soil and 2 for experiment 2 to compare hydroponic with soil experiment) and laurel, banana tree, cypress with soil and soil only. * = the lack of data for fescue in hydroponic is the result of a leakage problem encountered at the end of the experiment for the last day period.

Plant	Duration of all experiment (day)	Day 1 duration (hour)	Night 1 duration (hour)	Day 2 duration (hour)	Night 2 duration (hour)	Day 3 duration (hour)	Analysis strategy
Fescue 1 + soil	6	7	65	7	65	7	IRMS
Laurel + soil	4	7	19	11	21	11	IRMS
Banana tree + soil	6	7	66	7	65	8	IRMS
Maize 1 + soil	3	9	19	11	24	12	IRMS
Cypress + soil	5	X	98	X	X	X	IRMS
Soil	4	X	97	X	X	X	IRMS
Fescue 2 + soil	5	10	27	11	27	13	IRMS + OF-CEAS
Fescue 2 hydroponic	4	23	31	24	22	*	OF-CEAS
Maize 2 with soil	6	5	38	6	57	10	IRMS + OF-CEAS
Maize 2 hydroponic	5	10	54	9	57	7	IRMS + OF-CEAS

3.1.2.3. Hydroponic experiment strategy

The principle of hydroponic cultivation is described below:

For maize, 15 seeds per petri dish were placed on crushed clay beads (which have been previously washed with bleach to avoid contamination by bacteria/fungi/algae). The petri dishes were placed in the dark. After two days, the seeds had germinated and their roots were sufficiently developed for hydroponic cultivation. The seeds were transplanted into Eppendorfs tubes (1 cm in diameter) with the bottom cut off. The Eppendorfs were then inserted through a polystyrene plate ($L \times P \times H = 340 \times 240 \times 7$ mm) previously drilled with 12 holes divided into four rows of three holes along its length. This polystyrene plate rested on the surface of a 12 L plastic tray filled with 10 L of nutrient solution. The roots were in permanent contact with the nutrient solution, and the maize plants have grown above the polystyrene support to reach a height of around 30 cm after a cultivation period of one month. Germination and growth times were similar to those for growing maize plants in soil. The nutrient solution was changed twice a week.

For fescue, seeds were spread over the surface of plastic garden pots ($L \times D \times H = 70 \times 70 \times 80$ mm). The pots were filled with sand previously rinsed with diluted bleach. Pots were grouped by 12 and placed in plastic basins ($L \times D \times H = 290 \times 440 \times 70$ mm) containing nutrient solution. The pots were irrigated by capillary action through the sand, and the nutrient solution was renewed twice a week to prevent bacterial contamination and algae growth. The seeds germinated and the fescue plants grew on the sand for about one month. Once the fescue plants were sufficiently robust (strands of around 10 cm), the intertwined roots formed a clod of fescue that was easier to handle than a single strand. The clods were removed from their pots and the roots plunged into a tub of osmosis water before being rinsed to remove all the sand. The root balls were then transplanted into the hydroponics tank through a polystyrene plate ($L \times D \times H = 360 \times 260 \times 7$ mm).

This polystyrene plate, pierced with 12 square holes (15 × 15 mm), could accommodate 12 fescue clods. This plate rested on the surface of a 9 L plastic tray (W × D × H = 400 × 300 × 100 mm) containing nutrient solution. The nutrient solution was changed twice a week, and the growing time in the nutrient solution (roots in contact with it) lasted about two weeks to one month.

As the plants grew in the nutrient solution, an aquarium pump (Brand: Nicrew/model YDQB4105) was connected to a bubbler which was placed in the solution to oxygenate the aqueous medium.

The nutrient solution was produced using 11 powders (Sigma/Aldrich) and osmosed water. A first one-liter stock solution was produced by mixing powders 2 to 11 (Table 4) in 1 L of aqueous solution (osmosis water) in a volumetric flask. The concentrations of each chemical element are given in Table 4 for this first solution produced. The maizestock solution was four times more concentrated for all elements. Next, a dilution was made: 12.5 mL of Fescue stock solution was mixed in a 5 L Erlenmeyer flask filled with osmosis water, and 5 mL of maizestock solution in a 5 L Erlenmeyer flask. Concentration stock solution values are given in Table 4. Calcium nitrate powder no.1 (7.08 g for the maizestock solution and 1.77 g for the fescue stock solution) was mixed into the solution at this point, as otherwise this powder would not dissolved in the first stock solution. These working solutions were then placed in the trays where the plants were deposited. For fescue, 7.5 L of daughter solution in the 9 L tub, and for maize, 10 L of daughter solution in the 12 L tub.

Table 4. Composition of the 11 powders and concentrations stock solution for fescue and maize.

No. Powder	Chemical formula	Name	Concentration stock solution fescue (mM)	Concentration stock solution maize (mM)
1	Ca(NO ₃) ₂ , 4 H ₂ O	Calcium nitrate tetrahydrate	1.5	6
2	KNO ₃	Potassium nitrate	1.25	5
3	KH ₂ PO ₄	Potassium phosphate monobasic	0.5	2
4	MgSO ₄ , 7 H ₂ O	Magnesium sulfate heptahydrate	0.75	3
5	Na ₂ SiO ₃ , 5 H ₂ O	Sodium metasilicate pentahydrate	0.1	0.4
6	Na-Fe-EDTA	C ₁₀ H ₁₂ N ₂ NaFeO ₈	0.05	0.2
7	H ₃ BO ₃	Boric acid	0.05	0.2
8	MnSO ₄ , H ₂ O	Manganese sulfate monohydrate	0.012	0.048
9	ZnSO ₄ , 7 H ₂ O	Zinc sulfate heptahydrate	0.001	0.004
10	CuSO ₄ , 5H ₂ O	Copper sulfate pentahydrate	0.0007	0.0028
11	Na ₂ MoO ₄ , 2 H ₂ O	Sodium molybdate dihydrate	0.00024	0.00096

Hydroponics experiments lasted between four and six days, with alternating dark and light periods as follows in Table 3.

3.2. Quantification of fractionation factors associated with respiration and photosynthesis processes

In order to calculate the fractionation factors associated with dark respiration and photosynthesis of soil and plants, we use the following equations 6 and 8 (for details, refer to Paul et al., 2023).

The isotopic discrimination for dark respiration, $^{18}\epsilon_{dark_respi}$, is given by:

$$^{18}\epsilon_{dark_respi} = ^{18}\alpha_{dark_respi} - 1 = \frac{\ln\left(\frac{\delta^{18}O_t + 1}{\delta^{18}O_{t0} + 1}\right)}{\ln\left(\frac{n(O_2)_t}{n(O_2)_{t0}}\right)} \quad (6)$$

Where $^{18}\epsilon_{dark_respi}$ is the dark respiration fractionation factor, t_0 is the starting time of each dark period and t is the time of the experiment.

$\frac{n(O_2)_t}{n(O_2)_{t0}}$ is linked to $\delta\left(\frac{O_2}{N_2}\right)$ as:

$$\frac{n(O_2)_t}{n(O_2)_{t0}} = \frac{\frac{\delta\left(\frac{O_2}{N_2}\right)_t + 1}{1000}}{\frac{\delta\left(\frac{O_2}{N_2}\right)_{t0} + 1}{1000}} \quad (7)$$

Photosynthesis fractionation factor, $^{18}\epsilon_{photosynthesis}$, is calculated as:

$$^{18}\alpha_{photosynthesis} = \frac{n(O_2)_t / n(O_2)_{t0} \times a^{18}R + ^{18}R_t \times (F_{photosynthesis} - F_{total_respi} + ^{18}\alpha_{total_respi} \times F_{total_respi})}{^{18}R_{lw} \times F_{photosynthesis}} \quad (8)$$

Where, ^{18}R is the ratio of the concentration $^{18}R = \frac{n(^{18}O)}{n(^{16}O)}$ with n the number of moles of O_2 containing ^{18}O or ^{16}O , $a^{18}R = \frac{d^{18}R}{dt}$, during the light period, $F_{photosynthesis}$ and F_{total_respi} are, respectively, photosynthesis and consumption processes fluxes of oxygen and lw stands for leaf water.

$^{18}\alpha_{photosynthesis}$ depends on the values of $^{18}\alpha_{total_respi}$ and of F_{total_respi} , themselves depend on the values of $^{18}\alpha_{Mehler}$ (fractionation factor associated with Mehler reaction), F_{Mehler} (flux of oxygen related to Mehler reaction), $^{18}\alpha_{dark_respi}$, F_{dark_respi} , $^{18}\alpha_{photorespi}$ (fractionation factor associated with photorespiration) and $F_{photorespi}$ (photorespiration flux of oxygen).

We have:

$$^{18}\alpha_{total_respi} = ^{18}\alpha_{photorespi} \times f_{photorespi} + ^{18}\alpha_{Mehler} \times f_{Mehler} + ^{18}\alpha_{dark_respi} \times f_{dark_respi} \quad (9)$$

With,

$$f_{dark_respi} + f_{photorespi} + f_{Mehler} = 1 \quad (10)$$

And,

$$\frac{F_{dark_respi}}{F_{total_respi}} = f_{dark_respi} \quad (11)$$

f indicates the fraction of the total oxygen uptake flux corresponding to each process (dark respiration, photorespiration and Mehler reaction).

Because maize is a C4 plant, we consider that photorespiration and Mehler reaction were not involved in the O₂ consumption by the plant (Laisk and Edwards, 1997) which makes calculations of $^{18}\epsilon_{photosynthesis}$ easier.

For C3 plants, we need to consider photorespiration and Mehler reactions. In the absence of further constraints, we used here, as first approximation, the global values from Landais et al. (2007) for f_{dark_respi} (0.6), $f_{photorespi}$ (0.3) and f_{Mehler} (0.1). Values for $^{18}\epsilon_{photosynthesis}$ and $^{18}\epsilon_{Mehler}$ were based on the most recent estimates of Helman et al. (2005). The initial value for photorespiration isotopic discrimination is - 21.3 ‰ for $^{18}\epsilon_{photo_respi}$ as given by Helman et al. (2005). For the Mehler reaction we also chose the value proposed by Helman et al. (2005): $^{18}\epsilon_{Mehler} = - 10.8$ ‰. For more details, see Paul et al. (2023).

We also calculate the fractionation factors associated with only photosynthesis of plant during light period assuming zero respiratory flux because the flux of oxygen uptake is difficult to estimate during the day. We note this fractionation: the net photosynthesis fractionation. Then, we only focus on the light period during which the plant produces oxygen by photosynthesis.

$$dn(O_2) \times \alpha_{photo_{net}} \times {}^{18}R_{lw} + n(O_2)_t \times {}^{18}R_t = n(O_2)_{t+1} \times {}^{18}R_{t+1} \quad (12)$$

$$(\alpha_{photo_{net}} \times {}^{18}R_{lw} - {}^{18}R_t) \times dn(O_2) = n(O_2)_t \times d^{18}R_{t+1} \quad (13)$$

After integration,

$$\frac{n(O_2)_t}{n(O_2)_{t0}} = \frac{\alpha_{photo_{net}} \times {}^{18}R_{lw} - {}^{18}R_{t0}}{\alpha_{photo_{net}} \times {}^{18}R_{lw} - {}^{18}R_t} \quad (14)$$

$$\alpha_{photo_net} = \frac{{}^{18}R_{t0} - \frac{n(O_2)_t}{n(O_2)_{t0}} \times {}^{18}R_t}{{}^{18}R_{lw} \times \left(1 - \frac{n(O_2)_t}{n(O_2)_{t0}}\right)} \quad (15)$$

3.3. Presentation of PMIP model used and GPP-O₂ calculations on plants selected for experiments using model outputs

For estimate of Dole effect variations with time, we calculate the global GPP-O₂ in terrestrial- and ocean biosphere using the outputs of Paleoclimate Modelling Intercomparison Project (PMIP) simulations. We use the IPSL-CM5A (PMIP3), MIROC-ESM (PMIP3), and MIROC-ES2L (PMIP4) models since these provide both land and ocean biogeochemistry results for pre-industrial (PI), mid-Holocene (MH) 6ka, and Last Glacial Maximum (LGM) experiments and available for download on the Earth System Grid Federation (ESGF) database.

The global mean GPP-O₂ is calculated from PMIP data following the methodologies described by Blunier et al. (2002) with some modification. In terrestrial biosphere, the models calculate the gross carbon productivity (GPP-C) of each plant functional type (PFT). The modelled global GPP-C is partitioned between GPP-C by C3 plants and GPP-C by C4 plants. The Earth System Models usually have one or two PFT of C4 grass. We therefore partition GPP-C by C3 and GPP-C by C4 plants by assuming that all PFTs other than C4 grass are C3 plants. A portion of photosynthetic production of O₂ in the C3 plants is consumed via photorespiration. Here we assume no photorespiration in C4 plants. To estimate the GPP-C of C3 plants without consumption by photorespiration, the ratio of total (i.e., dark respiration and photorespiration) to dark respiration is multiplied by the

GPP-C of C3 plants. Following von Caemmerer and Farquhar (1981), this ratio is calculated as following:

$$\frac{\text{Dark respiration} + \text{Photorespiration}}{\text{Dark respiration}} = \frac{4.5}{4} \times \frac{C_i + (7/3) \times \Gamma_*}{C_i - \Gamma_*} \quad (16)$$

where C_i is the partial pressure of CO_2 inside the leaf and Γ_* is the CO_2 compensation point. To calculate C_i , we assume a constant ratio (0.65) of C_i following Blunier et al. (2002). The CO_2 compensation point is calculated according to the following equation by Prentice et al. (2017) to account for temperature changes:

$$\Gamma_* = 42.75 \times \exp \left[\frac{37830 \text{ J mol}^{-1}}{8.314 \text{ J mol}^{-1} \text{ K}^{-1}} \times \left(\frac{1}{298} - \frac{1}{T_K} \right) \right] \quad (17)$$

here T_K is temperature in Kelvin, and is taken from the simulated 2-meter air temperature by the models. The resulting ratio of dark respiration and photorespiration to dark respiration is ranging between 1.9 and 2.4 depending on the model used and the boundary conditions. The GPP-C is converted to GPP- O_2 by multiplying the photosynthetic quotient of 1.07 (Keeling, 1988). To take into account the Mehler reaction, the GPP- O_2 is then divided by 0.9 assuming a constant fraction (10 %) of Mehler reaction in the consumption of O_2 . as

The marine biogeochemistry components of the PMIP models do not calculate marine GPP-O₂. Instead, we calculate the marine GPP-O₂ from the simulated net primary productivity in terms of carbon (NPP-C) by multiplying by 2.7, the ratio of ¹⁸O-based GPP-O₂ (measured by incubation with ¹⁸O-labelled water) to ¹⁴C-based primary production rate (measured by incubation with ¹⁴C-labelled bicarbonate) found in the compilation of the JGOFS (Joint Global Ocean Flux Study) measurements (Marra, 2002).

4. Results

4.1. Study of oxygen isotopes fractionation factors in multiplexed closed chambers on a variety of C3 and C4 plants

4.1.1. Oxygen isotopes fractionation factors on a variety of C3 and C4 plants with soil by IRMS analysis

We present here the discrimination associated with dark respiration, photosynthesis and net photosynthesis of experiments carried out on fescue, banana tree, laurel and cypress with soil (Table 5).

Table 5. Average and standard deviation of the isotopic discriminations of fescue, banana tree, laurel and cypress over three chambers and the number of measurement (isotopic and elemental composition of oxygen) for each experiment. Isotopic compositions were analyzed by IRMS. X = no light period, thus no $^{18}\epsilon_{\text{photosynthesis}}$ value for cypress experiment. * Photosynthetic flux is low during the day and barely compensates for respiratory flux, so the net photosynthetic flux was considered to be almost zero and the associated isotopic discrimination could not be calculated.

	$^{18}\epsilon_{\text{dark_respi}}$	$^{18}\epsilon_{\text{photosynthesis}}$	$^{18}\epsilon_{\text{photo_net}}$	Number of data
Fescue	-16.9 ± 2.6	5.0 ± 2.4	4.0 ± 2.9	22
Banana tree	-19.2 ± 2.2	10.4 ± 5.6	8.0 ± 6.8	22
Laurel	-21.4 ± 5.8	13.3 ± 3.3	*	18
Cypress	-17.6 ± 0.6	X	X	9

The overall $^{18}\epsilon_{\text{dark_respi}}$ values range from around - 16 to - 21 ‰. It can be seen that the values of $^{18}\epsilon_{\text{dark_respi}}$ for banana and laurel are stronger than for fescue and cypress (the same observation can be done for $^{18}\epsilon_{\text{photosynthesis}}$). We note that $^{18}\epsilon_{\text{photo_net}}$ has lower values than $^{18}\epsilon_{\text{photosynthesis}}$ (lower by at least 1 ‰). We can see that for each plant, a positive discrimination exists for photosynthesis, which is between 5 and 13 ‰. Some high values are also the result of high uncertainties in our measurements.

4.1.2. Comparison of oxygen isotopes fractionation factors on hydroponics and with soil experiments for a C3 (fescue) and C4 (maize) plants by OF-CEAS and IRMS analysis

We present here the discrimination associated with dark respiration, photosynthesis and net photosynthesis of experiments carried out on fescue and maize with soil and without soil under hydroponic conditions (Table 6).

Table 6. Average and standard deviation of the isotopic discriminations of fescue and maize over three chambers and the number of measurement (isotopic and elemental composition of oxygen) for each hydroponic and with soil experiment. X = the lack of data for fescue in hydroponics is the result of a leakage problem (at the level of the sampling of the flask system) encountered at the end of the experiment for the last day period.

Plants	$^{18}\epsilon$	Average (‰) and standard deviation over 3 chambers		Number of data	
		IRMS	OF-CEAS	IRMS	OF-CEAS
Maize with soil	$^{18}\epsilon_{dark_respi}$	-17.8 ± 0.9	-16.1 ± 1.1	18	249
	$^{18}\epsilon_{photosynthesis}$	3.2 ± 2.6	9.6 ± 5.4	21	78
	$^{18}\epsilon_{photo_net}$	2.8 ± 2.7	9.9 ± 6.1		
Maize hydroponic	$^{18}\epsilon_{dark_respi}$	-16.7 ± 1.5	-18.9 ± 4.7	12	264
	$^{18}\epsilon_{photosynthesis}$	7.7 ± 3.3	6.1 ± 3.8	16	93
	$^{18}\epsilon_{photo_net}$	7.8 ± 3.4	6.0 ± 4.2		
Fescue with soil	$^{18}\epsilon_{dark_respi}$	-18.9 ± 0.6	-19.0 ± 1.9	10	180
	$^{18}\epsilon_{photosynthesis}$	4.3 ± 1.2	4.7 ± 2.8	10	108
	$^{18}\epsilon_{photo_net}$	1.9 ± 3.7	3.9 ± 3.0		
Fescue hydroponic	$^{18}\epsilon_{dark_respi}$	X	-22.1 ± 7.4	X	183
	$^{18}\epsilon_{photosynthesis}$	X	8.4 ± 3.1	X	164
	$^{18}\epsilon_{photo_net}$	X	9.4 ± 4.1		
Soil only	$^{18}\epsilon_{soil_respi}$	-15.4 ± 1.1	-17.8 ± 0.8	12	339

The overall $^{18}\epsilon_{dark_respi}$ values (Table 6) range from around - 16 to - 19 ‰ for plant + soil experiment. For hydroponic experiments we can notice that the isotopic discriminations associated with respiration is stronger when plants are without soil (except for the maize experiment with IRMS). We cannot here notice a difference on respiration discrimination between C3 and C4 plants (fescue and maize) on OF-CEAS or IRMS analyses. For $^{18}\epsilon_{photosynthesis}$, we note that $^{18}\epsilon_{photo_net}$ is lower than $^{18}\epsilon_{photosynthesis}$ by at least 1 ‰. We can see that for each plant, a positive discrimination exists for photosynthesis, which is between 5 and 13 ‰. Some high values may also result from high uncertainties in our

measurements (especially OF-CEAS). It should also be noted that measurement uncertainty is higher when measurements have been made using the OF-CEAS technique rather than the IRMS, but this does not prevent us from being able to interpret the data (Table 6).

4.2. Estimate of GPP-O₂ quantification of model outputs

We present here the GPP-O₂ of ocean and land calculated by three models: MIROC-ES2L, IPSL-CM5A-LR and MIROC-ESM for the preindustrial period (PI), 6 ka BP period and LGM period (Table 7).

Table 7. Output results from the MIROC-ES2L, IPSL-CM5A-LR and MIROC-ESM terrestrial and oceanic GPP-O₂ (Pmol O₂/yr) models during the pre-industrial period (PI), at 6 ka BP and during the LGM (last glacial maximum).

	Model	Domain	PI GPP-O ₂ (Pmol O ₂ /yr)	6 ka GPP-O ₂ (Pmol O ₂ /yr)	LGM GPP-O ₂ (Pmol O ₂ /yr)
PMIP4- CMIP6	MIROC-ES2L	Ocean	0.67	0.67	0.68
		Land	2.42	2.31	1.66
PMIP3- CMIP5	IPSL-CM5A- LR	Ocean	0.79	0.81	0.70
		Land	2.68	2.70	1.36
	MIROC-ESM	Ocean	0.66	0.69	0.66
		Land	3.30	3.50	2.35

We can see for all model outputs that the terrestrial GPP-O₂ is always at least three times greater than the oceanic GPP-O₂ for each time period. We also note that oceanic GPP-O₂ does not vary over time. However, terrestrial GPP-O₂ is twice as high at preindustrial

period and 6 ka BP than at LGM (2.4 and 1.7 Pmol O₂/yr respectively for MIROC-ES2L model).

5. Discussion

5.1. Interpretation of the respiratory and photosynthesis discriminations observed on the diversity of plants and experiments

5.1.1. Comparison between different types of plants

The results given in Table 5, for fescue, banana tree, laurel and cypress, all grown on soil, show terrestrial respiratory ¹⁸O/¹⁶O discrimination (greater than - 17 ‰) in agreement with the literature: - 17 ‰ in Paul et al. (2023) for fescue grown on soil and - 18 ‰ in Guy et al. (1993) on a diversity of terrestrial plants (- 17 to - 19 ‰ for COX respiration). The same conclusion can be drawn from the data for maize and fescue with soil in Table 6.

All plants studied here show terrestrial photosynthetic discrimination as in Paul et al. (2023). This is opposite to the classical use of a ¹⁸ε_{photosynthesis} of 0 ‰ for terrestrial plants (Guy et al. (1993), Helman et al. (2005).

However, we can note that for banana tree and laurel, the terrestrial respiratory discrimination is slightly higher than 17 ‰, i.e. more than 20 ‰. One hypothesis is that these organisms have thicker leaf tissue (sclerenchyma), in which diffusion is stronger, thus increasing the discrimination value. Particular attention should be paid to the fact that the uncertainty of these measurements is quite high.

C3 and C4 plants cannot be distinguished in terms of respiratory discrimination. Therefore, it is impossible to draw conclusions about the typical value of respiratory discrimination for either type of plant from the experiments conducted (Table 6).

5.1.2. Comparison between plants/soil and hydroponics experiments

Hydroponics experiments enable study of only plant respiration (i.e. without soil respiration). The isotopic discrimination associated with respiration is stronger for plants alone than when respiration is also taking place (for example maize with soil measured with OF-CEAS: -16.1 ‰ and hydroponic: -18.9 ‰, except for maize measured with IRMS). We can conclude from this observation that plant dark respiration fractionates more than soil respiration (Angert et al., 2001). This result is supported by our determination of $^{18}\epsilon_{respi_soil}$ which is lower (- 15.4 ‰) than the $^{18}\epsilon_{respi_plant}$ values with plants involved ($^{18}\epsilon_{respiration}$ between - 16 ‰ and - 19 ‰). Our results agree with previous studies who found a lower $^{18}\epsilon_{respi_soil}$ because of diffusion (Angert et al., 2001, - 15.4 ‰) than for $^{18}\epsilon_{respi_plant}$ (Paul et al., 2023, - 19.1 ‰ for fescue).

5.2. The existence of the terrestrial photosynthesis fractionation

Previous experiments performed on mesophyll cells (Guy et al., 1993) and on cyanobacteria in the absence of O₂ (Helman et al., 2005) in lab conditions concluded that photosynthesis was not fractionating. However, Eisenstadt et al. (2010) performed lab experiments similar to those of Helman et al. (2005) and found a positive discrimination for aquatic organisms. Paul et al. (2023) also identified a positive discrimination (+ 3.7 ‰) with terrarium experiments similar to the set-up used here. Because these estimates are

crucial for accurately interpreting and understanding the implications of the Dole effect, it is imperative to confirm or refute these outcomes.

When we calculated the value for $^{18}\epsilon_{\text{photosynthesis}}$ in Tables 5 and 6, we found a positive discrimination value for each species studied. Because the calculation of $^{18}\epsilon_{\text{photosynthesis}}$ depends on the oxygen uptake, we also calculated a net photosynthetic discrimination ($^{18}\epsilon_{\text{photo_net}}$) making the extreme hypothesis that no oxygen uptake occurs in parallel to the photosynthesis. Since oxygen uptake has the effect of increasing $\delta^{18}\text{O}$ of O_2 in the biological chamber while photosynthesis has the opposite effect on $\delta^{18}\text{O}$ of O_2 , $^{18}\epsilon_{\text{photo_net}}$ is the minimum possible value for $^{18}\epsilon_{\text{photosynthesis}}$ in these conditions. We could only estimate the $^{18}\epsilon_{\text{photo_net}}$ for two species (fescues and banana) and the lowest value is 4 ‰. A second source of uncertainty which could affect our result is the value of the discrimination associated with oxygen uptake. For the fescue experiment, i.e. the one with the smallest $^{18}\epsilon_{\text{photosynthesis}}$ a discrimination for terrestrial respiration of - 40 ‰ should be imposed so that the calculated $^{18}\epsilon_{\text{photosynthesis}}$ is equal to zero. This value is unrealistic with respect to the values for $^{18}\epsilon_{\text{respiration}}$ determined in the previous section or in any previous studies. The last source of uncertainty in our calculation is the value of the leaf water isotopic composition. During experiments, it was observed that the $\delta^{18}\text{O}$ of irrigation water increased (Paul et al., 2023), so a high value was measured. To achieve zero photosynthetic fractionation for fescue, the $\delta^{18}\text{O}_{\text{lw}}$ should be increased from 5 ‰ to 9 ‰. Our determination of $\delta^{18}\text{O}_{\text{lw}}$ is certainly overestimated since $\delta^{18}\text{O}_{\text{lw}}$ is measured at the end of the experiments (we have observed that $\delta^{18}\text{O}_{\text{lw}}$ was increasing by up to 2 ‰ during the course of an experiment). This observation however suggests that the estimated value of 5 ‰ for $\delta^{18}\text{O}_{\text{lw}}$ is a maximum value so that we cannot explain a wrong estimate of $^{18}\epsilon_{\text{photosynthesis}}$ by this possible overestimate of $\delta^{18}\text{O}_{\text{lw}}$.

We thus conclude that in terrarium experiments which is the closest analog for real conditions in this type of experiment, $^{18}\epsilon_{\text{photosynthesis}}$ is positive.

The photosystem II process of O_2 generation through water oxidation by the oxygen evolving complex cannot easily be associated with oxygen fractionation (Tcherkez and Farquhar, 2007). Involving preferential diffusion of the lightest isotopologues in the stomates (either preferential diffusion of H_2^{16}O vs H_2^{18}O in the leaf water before photosynthesis or preferential diffusion of $^{16}\text{O}^{16}\text{O}$ vs $^{16}\text{O}^{18}\text{O}$ of produced O_2 after photosynthesis) would also go into the wrong direction. These diffusion effects would indeed lead to a lower difference between $\delta^{18}\text{O}_{\text{lw}}$ and $\delta^{18}\text{O}$ of O_2 in the atmosphere of the biological chamber than the true difference and hence to an underestimated value of $^{18}\epsilon_{\text{photosynthesis}}$. The last possible hypothesis would be that an additional oxygen consuming process occurs during photosynthesis (Eisenstadt et al., 2010). This process should be associated to a strong negative discrimination to compensate for the calculated $^{18}\epsilon_{\text{photosynthesis}}$. Summarizing, we cannot yet explain why $^{18}\epsilon_{\text{photosynthesis}}$ is associated with a positive isotopic discrimination. However, coherent observations for several terrarium experiments and several plants suggest that this discrimination is true and should be considered when calculating a global budget for the Dole effect.

5.3. Implications of these fractionation factors for interpreting the global Dole effect

We use here the latest estimates of the different fractionation factors and global estimates of terrestrial and oceanic productivities during the last deglaciation to reevaluate the main drivers of the Dole effect. In particular, we aim to decipher the role of the low latitude

hydrological cycle (i.e. $\delta^{18}\text{O}$ of soil and leaf water) and the role of the ratio of terrestrial to oceanic productivity as the main drivers of the Dole effect variations in the past.

The new experiments carried out in this study confirm the existence of a positive discrimination associated with terrestrial photosynthesis as presented in the work of Paul et al. (2023). Also, the discrimination values observed during respiration agree with those suggested by Paul et al. (2023). Thus, using the new results given in Paul et al. (2023) (Fig.5), we can calculate a Dole effect of 25.1 ‰, as shown in Table 1.

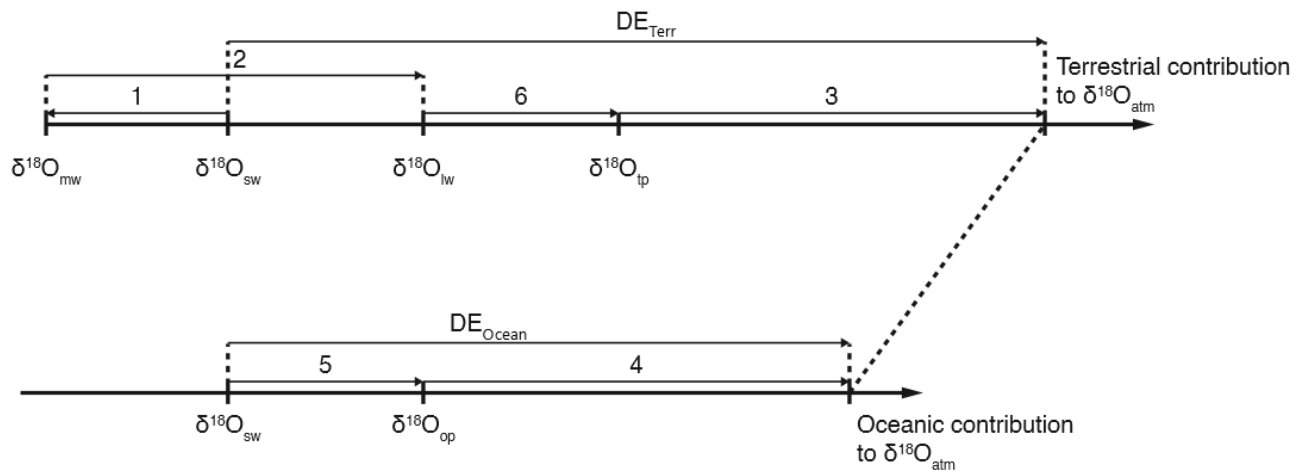


Figure 5. Diagram of the main contributions to $\delta^{18}\text{O}_{\text{atm}}$. (1) Fractionation of water associated with evaporation and precipitation. (2) Fractionation of water associated with evapotranspiration. (3) Fractionation of atmospheric oxygen associated with terrestrial respiration and mixing with oxygen issued from leaf photosynthesis. (4) Fractionation of atmospheric oxygen associated with oceanic respiration and mixing with oxygen issued from oceanic photosynthesis. (5) Fractionation associated with oceanic photosynthesis. (6) Fractionation associated with terrestrial photosynthesis. DE_{Terr} = terrestrial Dole effect and DE_{Oceanic} = oceanic Dole effect (modified from Landais et al., 2007).

For this calculation, we rely as much as possible on the latest available estimates for isotopic discrimination (Paul et al., 2023) including the finding that $^{18}\epsilon_{\text{photosynthesis}}$ is positive and estimated to 3.7 ‰. The value of $^{18}\epsilon_{\text{dark_respi}}$ has been slightly revised by

Paul et al. (2023) to 17 ‰ from that given by Luz and Barkan (2011) of 17.7 ‰. With these new estimates, we end up with a respectively terrestrial and oceanic Dole effect of 22.9 and 26.5 ‰ in the study of Paul et al. (2023) compared to 23.5 and 23.5 ‰ in the latest study of Luz and Barkan (2011). Oldest Dole effect estimates are displayed in Table 1.

Because we are interested in the change of the Dole effect over the last deglaciation, we also need to estimate Dole effect for the last glacial maximum as it was done by Ciais et al. (2012). In line with previous studies, we assume that the isotopic discrimination for the different biological processes does not vary with time. However, $\delta^{18}\text{O}_{\text{lw}}$ value varies during this period (Ciais et al., 2012) as well as $^{18}\epsilon_{\text{soil_respi}}$ and the ratio between C3 and C4 plants which affects the value for global $^{18}\epsilon_{\text{respiration}}$ due to its influence on photorespiration proportion (Landais et al., 2007). The change in the proportion of C3 and C4 plants is calculated by the models presented in Section 3.3. and results in a variation of less than 0.1 ‰ on the global $^{18}\epsilon_{\text{respiration}}$. The change in $^{18}\epsilon_{\text{soil_respi}}$ was calculated by Landais et al. (2007); it is 0.5 ‰ stronger during the LGM than today, resulting in a variation of less than 0.3 ‰ for the global $^{18}\epsilon_{\text{respiration}}$. Finally, $\delta^{18}\text{O}_{\text{lw}}$ is higher during the LGM by 1 ‰ compared to the pre-industrial period. Because the $\delta^{18}\text{O}_{\text{ocean}}$ value is also higher by 1 ‰ during the LGM, we estimate that the terrestrial DE is higher by 0.3 ‰ during the LGM compared to today. The oceanic Dole effect for LGM is assumed similar to the present one.

Table 8 display the results for the global DE with our most recent estimates.

Table 8. Global Dole effects based on GPP-O₂ variations of three model outputs (MIROC-ES2L, IPSL-CM5A-LR and MIROC-ESM) for three different periods (pre-industrial period (PI), 6 ka BP and LGM) (a) and adding the photosynthetic fractionation value of Paul et al. (2023) (b). These calculations were made using equation 6.

a)

		Bender et al. (1994)	Hoffmann et al. (2004)	Luz and Barkan (2011)	Ciais et al. (2012)	Paul et al. (2023)
Preindustrial	IPSL-CM5A-LR	21.3	24.3	23.2	26.4	25.5
	MIROC-ES2L	21.3	24.4	23.2	26.5	25.5
	MIROC-ESM	21.5	24.9	23.2	26.9	25.7
6 ka BP	IPSL-CM5A-LR	21.3	24.3	23.2	26.3	25.3
	MIROC-ES2L	21.3	24.4	23.2	26.4	25.5
	MIROC-ESM	21.5	24.9	23.2	26.9	25.7
LGM	IPSL-CM5A-LR	21.1	23.4	23.2	25.4	25.4
	MIROC-ES2L	21.3	23.9	23.2	25.8	25.6
	MIROC-ESM	21.6	24.6	23.2	26.4	25.8

b)

		Bender et al. (1994)	Hoffmann et al. (2004)	Luz and Barkan (2011)	Ciais et al. (2012)
Preindustrial	IPSL- CM5A-LR	24.2	27.2	26.1	25.3
	MIROC- ES2L	24.2	27.3	26.1	25.4
	MIROC- ESM	24.6	28.0	26.3	26.9
6 ka BP	IPSL- CM5A-LR	24.1	27.1	26.0	25.3
	MIROC- ES2L	24.2	27.2	26.1	25.4
	MIROC- ESM	24.6	28.1	26.3	26.9
LGM	IPSL- CM5A-LR	23.5	25.8	25.8	24.9
	MIROC- ES2L	23.7	26.3	25.8	25.1
	MIROC- ESM	24.2	27.3	26.1	25.3

In general, our determinations for the pre-industrial DE are slightly higher than the measured values. When looking at the LGM values, we find very similar values for the Dole effect compared to the values for the pre-industrial Dole effect. This result does not depend on the model used to calculate the GPP-O₂ and agrees with the measurements showing similar Dole effect for the pre-industrial period and for the LGM. For the 6 ka Dole effect, if we keep the same values for terrestrial and oceanic Dole effect than at the pre-industrial period, we do not predict any change in the calculated Dole effect while

there is huge change in the measured Dole effect. With very similar values for terrestrial and oceanic Dole effects, it is impossible to explain the change in the Dole effect by a change in the ratio of terrestrial vs oceanic gross primary productivity. We thus conclude that oceanic or terrestrial Dole effects vary with time and that the DE variations observed in ice cores cannot be explained by fluctuations in the relative proportions of oceanic and terrestrial gross primary productivity as suggested by Bender et al. (1994) and by Ciais et al. (2012). In their case, the oceanic and terrestrial Dole effects have very different values. We thus confirm previous studies suggesting that variations in the Dole effect are mainly resulting from low latitude changes in hydrological cycle leading to changes in $\delta^{18}\text{O}$ of the meteoric water transmitted to $\delta^{18}\text{O}$ of soil water, to $\delta^{18}\text{O}_{\text{lw}}$ and to $\delta^{18}\text{O}_{\text{atm}}$ through photosynthesis (Landais et al., 2007; Severinghaus et al., 2009; Seltzer et al., 2017; Huang et al., 2020). This would well explain the 6 ka minimum in DE which is also captured in the $\delta^{18}\text{O}_{\text{calcite}}$ of low latitude speleothem, also sensitive to variations in $\delta^{18}\text{O}$ of meteoric water (Hu et al., 2019).

6. Conclusion

In this article, we studied a variety of plants (fescue, laurel, banana, maize, cypress and soil only) using multiplexing system (Paul et al., in prep) in order to quantify more precisely the fractionations associated with biological processes such as respiration and terrestrial photosynthesis. Our study is already in agreement with the literature regarding estimate of terrestrial respiratory discrimination (plant + soil), and we confirm the existence of a positive terrestrial photosynthetic fractionation on different plants studied at the scale of a terrarium. This finding motivates a new study of the main drivers of the variations of the global Dole effect which we provided here focusing on the last deglaciation and using productivity inferred from three global Earth models. In our estimate of the Dole effect,

we used the latest fractionation factors evaluated by these models and found no significant change of the Dole effect over the last deglaciation. This is in agreement with the data when comparing to the measured change of Dole effect between the LGM and the pre-industrial period. However, the calculations do not show any change for the Dole effect at 6 ka while the data show a clear decrease by 0.5 ‰ at that period. We thus conclude that the Dole effect variations are in phase with those of the hydrological cycle at low latitudes but cannot be used as a tracer of the ratio between terrestrial and oceanic productivity.

Our study relies on strong assumptions, such as the influence of climatic parameters on the fractionation factors, which could be further investigated using the experimental set-up that we have used in this study.

References

Aggarwal, P. K., Alduchov, O. A., Froehlich, K. O., Araguas-Araguas, L. J., Sturchio, N. C., and Kurita, N.: Stable isotopes in global precipitation: A unified interpretation based on atmospheric moisture residence time, *Geophysical Research Letters*, 39, 2012GL051937, <https://doi.org/10.1029/2012GL051937>, 2012.

Anderson, W. T., Bernasconi, S. M., McKenzie, J. A., Saurer, M., and Schweingruber, F.: Model evaluation for reconstructing the oxygen isotopic composition in precipitation from tree ring cellulose over the last century, *Chemical Geology*, 182, 121–137, [https://doi.org/10.1016/S0009-2541\(01\)00285-6](https://doi.org/10.1016/S0009-2541(01)00285-6), 2002.

Angert, A. and Luz, B.: Fractionation of oxygen isotopes by root respiration: Implications for the isotopic composition of atmospheric O₂, *Geochimica et Cosmochimica Acta*, 65, 1695–1701, [https://doi.org/10.1016/S0016-7037\(01\)00567-1](https://doi.org/10.1016/S0016-7037(01)00567-1), 2001.

Angert, A., Luz, B., and Yakir, D.: Fractionation of oxygen isotopes by respiration and diffusion in soils and its implications for the isotopic composition of atmospheric O₂, *Global Biogeochemical Cycles*, 15, 871–880, <https://doi.org/10.1029/2000GB001371>, 2001.

Barkan, E. and Luz, B.: High precision measurements of ¹⁷O/ ¹⁶O and ¹⁸O/ ¹⁶O ratios in H₂O, *Rapid Comm Mass Spectrometry*, 19, 3737–3742, <https://doi.org/10.1002/rcm.2250>, 2005.

Bender, M., Sowers, T., Dickson, M.-L., Orchardo, J., Grootes, P., Mayewski, P. A., and Meese, D. A.: Climate correlations between Greenland and Antarctica during the past 100,000 years, *Nature*, 372, 663–666, <https://doi.org/10.1038/372663a0>, 1994.

Bender, M. L.: The δ ¹⁸O of dissolved O₂ in seawater: A unique tracer of circulation and respiration in the deep sea, *J. Geophys. Res.*, 95, 22243–22252, <https://doi.org/10.1029/JC095iC12p22243>, 1990.

Blunier, T., Barnett, B., Bender, M. L., and Hendricks, M. B.: Biological oxygen productivity during the last 60,000 years from triple oxygen isotope measurements, *Global Biogeochemical Cycles*, 16, <https://doi.org/10.1029/2001GB001460>, 2002.

Bouchet, M., Landais, A., Grisart, A., Parrenin, F., Prié, F., Jacob, R., Fourré, E., Capron, E., Raynaud, D., Lipenkov, V. Y., Loutre, M.-F., Extier, T., Svensson, A., Legrain, E., Martinerie, P., Leuenberger, M., Jiang, W., Ritterbusch, F., Lu, Z.-T., and Yang, G.-M.: The AICC2023 chronological framework and associated timescale for the EPICA Dome C ice core, *Ice Dynamics/Ice Cores/Milankovitch*, <https://doi.org/10.5194/egusphere-2023-1081>, 2023.

Cernusak, L. A., Barbour, M. M., Arndt, S. K., Cheesman, A. W., English, N. B., Feild, T. S., Helliker, B. R., Holloway-Phillips, M. M., Holtum, J. A. M., Kahmen, A., McInerney, F. A., Munksgaard, N. C., Simonin, K. A., Song, X., Stuart-Williams, H., West, J. B., and Farquhar,

G. D.: Stable isotopes in leaf water of terrestrial plants, *Plant Cell & Environment*, 39, 1087–1102, <https://doi.org/10.1111/pce.12703>, 2016.

Cheng, H., Edwards, R. L., Sinha, A., Spötl, C., Yi, L., Chen, S., Kelly, M., Kathayat, G., Wang, X., Li, X., Kong, X., Wang, Y., Ning, Y., and Zhang, H.: The Asian monsoon over the past 640,000 years and ice age terminations, *Nature*, 534, 640–646, <https://doi.org/10.1038/nature18591>, 2016.

Ciais, P., Tagliabue, A., Cuntz, M., Bopp, L., Scholze, M., Hoffmann, G., Lourantou, A., Harrison, S. P., Prentice, I. C., Kelley, D. I., Koven, C., and Piao, S. L.: Large inert carbon pool in the terrestrial biosphere during the Last Glacial Maximum, *Nature Geosci*, 5, 74–79, <https://doi.org/10.1038/ngeo1324>, 2012.

Dreyfus, G. B., Parrenin, F., Lemieux-Dudon, B., Durand, G., Masson-Delmotte, V., Jouzel, J., Barnola, J.-M., Panno, L., Spahni, R., Tisserand, A., Siegenthaler, U., and Leuenberger, M.: Anomalous flow below 2700 m in the EPICA Dome C ice core detected using $\delta^{18}\text{O}$ of atmospheric oxygen measurements, *Clim. Past*, 3, 341–353, <https://doi.org/10.5194/cp-3-341-2007>, 2007.

Eisenstadt, D., Barkan, E., Luz, B., and Kaplan, A.: Enrichment of oxygen heavy isotopes during photosynthesis in phytoplankton, *Photosynth Res*, 103, 97–103, <https://doi.org/10.1007/s11120-009-9518-z>, 2010.

Farquhar, G. D., Lloyd, J., Taylor, J. A., Flanagan, L. B., Syvertsen, J. P., Hubick, K. T., Wong, S. C., and Ehleringer, J. R.: Vegetation effects on the isotope composition of oxygen in atmospheric CO₂, *Nature*, 363, 439–443, <https://doi.org/10.1038/363439a0>, 1993.

Flanagan, L. B., Bain, J. F., and Ehleringer, J. R.: Stable oxygen and hydrogen isotope composition of leaf water in C₃ and C₄ plant species under field conditions, *Oecologia*, 88, 394–400, <https://doi.org/10.1007/BF00317584>, 1991.

Gillon, J. and Yakir, D.: Influence of Carbonic Anhydrase Activity in Terrestrial Vegetation on the $\delta^{18}\text{O}$ Content of Atmospheric CO_2 , *Science*, 291, 2584–2587, <https://doi.org/10.1126/science.1056374>, 2001.

Guy, R. D., Berry, J. A., Fogel, M. L., and Hoering, T. C.: Differential fractionation of oxygen isotopes by cyanide-resistant and cyanide-sensitive respiration in plants, *Planta*, 177, 483–491, <https://doi.org/10.1007/BF00392616>, 1989.

Guy, R. D., Berry, J. A., Fogel, M. L., Turpin, D. H., and Weger, H. G.: Fractionation of the stable isotopes of oxygen during respiration by plants: The basis of a new technique to estimate partitioning to the alternative path, *Plant Respiration, Molecular, Biochemical and Physiological Aspects*, SPB Academic Publishing, The Hague, the Netherlands, 443–453, 1992.

Guy, R. D., Fogel, M. L., and Berry, J. A.: Photosynthetic Fractionation of the Stable Isotopes of Oxygen and Carbon, *Plant Physiol.*, 101, 37–47, <https://doi.org/10.1104/pp.101.1.37>, 1993.

Helliker, B. R. and Richter, S. L.: Subtropical to boreal convergence of tree-leaf temperatures, *Nature*, 454, 511–514, <https://doi.org/10.1038/nature07031>, 2008.

Helman, Y., Barkan, E., Eisenstadt, D., Luz, B., and Kaplan, A.: Fractionation of the Three Stable Oxygen Isotopes by Oxygen-Producing and Oxygen-Consuming Reactions in Photosynthetic Organisms, *Plant Physiology*, 138, 2292–2298, <https://doi.org/10.1104/pp.105.063768>, 2005.

Hendricks, M. B., Bender, M. L., and Barnett, B. A.: Net and gross O_2 production in the southern ocean from measurements of biological O_2 saturation and its triple isotope composition, *Deep Sea Research Part I: Oceanographic Research Papers*, 51, 1541–1561, <https://doi.org/10.1016/j.dsr.2004.06.006>, 2004.

Hoffmann, G., Cuntz, M., Weber, C., Ciais, P., Friedlingstein, P., Heimann, M., Jouzel, J., Kaduk, J., Maier-Reimer, E., Seibt, U., and Six, K.: A model of the Earth's Dole effect, *Global Biogeochemical Cycles*, 18, 2003GB002059, <https://doi.org/10.1029/2003GB002059>, 2004.

Hu, Y. B., Xiao, W., Qian, Y. F., Liu, Q., Xie, C. Y., Zhang, X. F., Zhang, W. Q., Liu, S. D., and Lee, X. H.: [Effects of Water Vapor Source and Local Evaporation on the Stable Hydrogen and Oxygen Isotopic Compositions of Precipitation]., *Huanjing kexue*, 40, 573–581, <https://doi.org/10.13227/j.hjkx.201805227>, 2019.

Huang, E., Wang, P., Wang, Y., Yan, M., Tian, J., Li, S., and Ma, W.: Dole effect as a measurement of the low-latitude hydrological cycle over the past 800 ka, *Sci. Adv.*, 6, eaba4823, <https://doi.org/10.1126/sciadv.aba4823>, 2020.

Keeling, R. F.: Development of an interferometric oxygen analyzer for precise measurement of the atmospheric O₂ mole fraction, Harvard Univ., Cambridge, Mass., 1988.

Keeling, R. F. and Shertz, S. R.: Seasonal and interannual variations in atmospheric oxygen and implications for the global carbon cycle, *Nature*, 358, 723–727, <https://doi.org/10.1038/358723a0>, 1992.

Kiddon, J., Bender, M. L., Orchardo, J., Caron, D. A., Goldman, J. C., and Dennett, M.: Isotopic fractionation of oxygen by respiring marine organisms, *Global Biogeochemical Cycles*, 7, 679–694, <https://doi.org/10.1029/93GB01444>, 1993.

Kroopnick, P. and Craig, H.: Atmospheric Oxygen: Isotopic Composition and Solubility Fractionation, *Science*, 175, 54–55, <https://doi.org/10.1126/science.175.4017.54>, 1972.

Laisk, A. and Edwards, G. E.: Oxygen and electron flow in C₄ photosynthesis: Mehler reaction, photorespiration and CO₂ concentration in the bundle sheath, *Planta*, 205, 632–645, <https://doi.org/10.1007/s004250050366>, 1998.

Landais, A., Barkan, E., Yakir, D., and Luz, B.: The triple isotopic composition of oxygen in leaf water, *Geochimica et Cosmochimica Acta*, 70, 4105–4115, <https://doi.org/10.1016/j.gca.2006.06.1545>, 2006.

Landais, A., Lathiere, J., Barkan, E., and Luz, B.: Reconsidering the change in global biosphere productivity between the Last Glacial Maximum and present day from the triple oxygen isotopic composition of air trapped in ice cores, *Global Biogeochemical Cycles*, 21, 2006GB002739, <https://doi.org/10.1029/2006GB002739>, 2007.

Landais, A., Dreyfus, G., Capron, E., Masson-Delmotte, V., Sanchez-Goñi, M. F., Desprat, S., Hoffmann, G., Jouzel, J., Leuenberger, M., and Johnsen, S.: What drives the millennial and orbital variations of $\delta^{18}\text{O}_{\text{atm}}$?, *Quaternary Science Reviews*, 29, 235–246, <https://doi.org/10.1016/j.quascirev.2009.07.005>, 2010.

Lisiecki, L. E. and Raymo, M. E.: A Pliocene–Pleistocene stack of 57 globally distributed benthic $\delta^{18}\text{O}$ records, *Paleoceanography*, 20, 2004PA001071, <https://doi.org/10.1029/2004PA001071>, 2005.

Lisiecki, L. E. and Stern, J. V.: Regional and global benthic $\delta^{18}\text{O}$ stacks for the last glacial cycle: Last Glacial Cycle Benthic $\delta^{18}\text{O}$, *Paleoceanography*, 31, 1368–1394, <https://doi.org/10.1002/2016PA003002>, 2016.

Liu, H., Zartman, R. E., Ireland, T. R., and Sun, W.: Global atmospheric oxygen variations recorded by Th/U systematics of igneous rocks, *Proc. Natl. Acad. Sci. U.S.A.*, 116, 18854–18859, <https://doi.org/10.1073/pnas.1902833116>, 2019.

Luz, B. and Barkan, E.: The isotopic composition of atmospheric oxygen: ISOTOPIC COMPOSITION OF AIR OXYGEN, *Global Biogeochem. Cycles*, 25, n/a–n/a, <https://doi.org/10.1029/2010GB003883>, 2011.

Luz, B., Barkan, E., Bender, M. L., Thiemens, M. H., and Boering, K. A.: Triple-isotope composition of atmospheric oxygen as a tracer of biosphere productivity, *Nature*, 400, 547–550, <https://doi.org/10.1038/22987>, 1999.

Malaizé, B., Paillard, D., Jouzel, J., and Raynaud, D.: The Dole effect over the last two glacial-interglacial cycles, *J. Geophys. Res.*, 104, 14199–14208, <https://doi.org/10.1029/1999JD900116>, 1999.

Marra, J.: Approaches to the Measurement of Plankton Production, in: *Phytoplankton Productivity*, edited by: Williams, P. J. L. B., Thomas, D. N., and Reynolds, C. S., Wiley, 78–108, <https://doi.org/10.1002/9780470995204.ch4>, 2002.

Milcu, A., Allan, E., Roscher, C., Jenkins, T., Meyer, S. T., Flynn, D., Bessler, H., Buscot, F., Engels, C., Gubsch, M., König, S., Lipowsky, A., Loranger, J., Renker, C., Scherber, C., Schmid, B., Thébault, E., Wubet, T., Weisser, W. W., Scheu, S., and Eisenhauer, N.: Functionally and phylogenetically diverse plant communities key to soil biota, *Ecology*, 94, 1878–1885, <https://doi.org/10.1890/12-1936.1>, 2013.

Pack, A., Höweling, A., Hezel, D. C., Stefanak, M. T., Beck, A.-K., Peters, S. T. M., Sengupta, S., Herwartz, D., and Folco, L.: Tracing the oxygen isotope composition of the upper Earth's atmosphere using cosmic spherules, *Nat Commun*, 8, 15702, <https://doi.org/10.1038/ncomms15702>, 2017.

Parrenin, F., Barnola, J.-M., Beer, J., Blunier, T., Castellano, E., Chappellaz, J., Dreyfus, G., Fischer, H., Fujita, S., Jouzel, J., Kawamura, K., Lemieux-Dudon, B., Loulergue, L., Masson-Delmotte, V., Narcisi, B., Petit, J.-R., Raisbeck, G., Raynaud, D., Ruth, U., Schwander, J., Severi, M., Spahni, R., Steffensen, J. P., Svensson, A., Udisti, R., Waelbroeck, C., and Wolff, E.: The EDC3 chronology for the EPICA Dome C ice core, *Clim. Past*, 3, 485–497, <https://doi.org/10.5194/cp-3-485-2007>, 2007.

Petit, J. R., Jouzel, J., Raynaud, D., Barkov, N. I., Barnola, J.-M., Basile, I., Bender, M., Chappellaz, J., Davis, M., Delaygue, G., Delmotte, M., Kotlyakov, V. M., Legrand, M., Lipenkov, V. Y., Lorius, C., PÉpin, L., Ritz, C., Saltzman, E., and Stievenard, M.: Climate and atmospheric history of the past 420,000 years from the Vostok ice core, Antarctica, *Nature*, 399, 429–436, <https://doi.org/10.1038/20859>, 1999.

Prentice, I. C., Cleator, S. F., Huang, Y. H., Harrison, S. P., and Roulstone, I.: Reconstructing ice-age palaeoclimates: Quantifying low-CO₂ effects on plants, *Global and Planetary Change*, 149, 166–176, <https://doi.org/10.1016/j.gloplacha.2016.12.012>, 2017.

Schrag, D. P., Adkins, J. F., McIntyre, K., Alexander, J. L., Hodell, D. A., Charles, C. D., and McManus, J. F.: The oxygen isotopic composition of seawater during the Last Glacial Maximum, *Quaternary Science Reviews*, 21, 331–342, [https://doi.org/10.1016/S0277-3791\(01\)00110-X](https://doi.org/10.1016/S0277-3791(01)00110-X), 2002.

Seltzer, A. M., Severinghaus, J. P., Andraski, B. J., and Stonestrom, D. A.: Steady state fractionation of heavy noble gas isotopes in a deep unsaturated zone, *Water Resources Research*, 53, 2716–2732, <https://doi.org/10.1002/2016WR019655>, 2017.

Severinghaus, J. P., Beaudette, R., Headly, M. A., Taylor, K., and Brook, E. J.: Oxygen-18 of O₂ Records the Impact of Abrupt Climate Change on the Terrestrial Biosphere, *Science*, 324, 1431–1434, <https://doi.org/10.1126/science.1169473>, 2009.

Sigl, M., Fudge, T. J., Winstrup, M., Cole-Dai, J., Ferris, D., McConnell, J. R., Taylor, K. C., Welten, K. C., Woodruff, T. E., Adolphi, F., Bisiaux, M., Brook, E. J., Buizert, C., Caffee, M. W., Dunbar, N. W., Edwards, R., Geng, L., Iverson, N., Koffman, B., Layman, L., Maselli, O. J., McGwire, K., Muscheler, R., Nishiizumi, K., Pasteris, D. R., Rhodes, R. H., and Sowers, T. A.: The WAIS Divide deep ice core WD2014 chronology – Part 2: Annual-layer counting (0–31 ka BP), *Clim. Past*, 12, 769–786, <https://doi.org/10.5194/cp-12-769-2016>, 2016.

Tcherkez, G. and Farquhar, G. D.: On the $^{16}\text{O}/^{18}\text{O}$ isotope effect associated with photosynthetic O_2 production, *Functional Plant Biol.*, 34, 1049, <https://doi.org/10.1071/FP07168>, 2007.

Veres, D., Bazin, L., Landais, A., Toyé Mahamadou Kele, H., Lemieux-Dudon, B., Parrenin, F., Martinerie, P., Blayo, E., Blunier, T., Capron, E., Chappellaz, J., Rasmussen, S. O., Severi, M., Svensson, A., Vinther, B., and Wolff, E. W.: The Antarctic ice core chronology (AICC2012): an optimized multi-parameter and multi-site dating approach for the last 120 thousand years, *Clim. Past*, 9, 1733–1748, <https://doi.org/10.5194/cp-9-1733-2013>, 2013.

Vilović, I., Schulze-Makuch, D., and Heller, R.: Variations in climate habitability parameters and their effect on Earth's biosphere during the Phanerozoic Eon, *Sci Rep*, 13, 12663, <https://doi.org/10.1038/s41598-023-39716-z>, 2023.

Vinogradov, A. P., Kutuyurin, V. M., and Zadorozhnyi, I. K.: Isotope fractionation of atmospheric oxygen, *Geochem. Int.*, 3, 241–253, 1959.

Von Caemmerer, S. and Farquhar, G. D.: Some relationships between the biochemistry of photosynthesis and the gas exchange of leaves, *Planta*, 153, 376–387, <https://doi.org/10.1007/BF00384257>, 1981.

Wang, Y., Cheng, H., Edwards, R. L., Kong, X., Shao, X., Chen, S., Wu, J., Jiang, X., Wang, X., and An, Z.: Millennial- and orbital-scale changes in the East Asian monsoon over the past 224,000 years, *Nature*, 451, 1090–1093, <https://doi.org/10.1038/nature06692>, 2008.

West, J. B., Sobek, A., and Ehleringer, J. R.: A Simplified GIS Approach to Modeling Global Leaf Water Isoscapes, *PLoS ONE*, 3, e2447, <https://doi.org/10.1371/journal.pone.0002447>, 2008.

Wostbrock*, J. A. G. and Sharp, Z. D.: Triple Oxygen Isotopes in Silica–Water and Carbonate–Water Systems, *Reviews in Mineralogy and Geochemistry*, 86, 367–400, <https://doi.org/10.2138/rmg.2021.86.11>, 2021.

Author contributions

AL and CPi designed the project. CPi, JS, SD and CPa carried out experiments at ECOTRON of Montpellier and CPa, FP, RJ, AD and OJ at LSCE. CPa, CPi and AL analyzed the data from the optical spectrometer and CPa and AL analysed the data from IRMS. JW has output the data and calculated the GPP-O₂ of the models. CPa, CPi and AL prepared the manuscript with contributions from JW, MB and AM.

RÉSUMÉ EN FRANCAIS

Les données paléoclimatiques fournissent des estimations empiriques des changements climatiques pré-anthropiques à des échelles de temps variées. Elles ont documenté des réchauffements globaux de la Terre (+5 à 10°C) se déroulant sur des milliers d'années tous les ~100 000 ans au cours du dernier million d'années, les déglaciations. Ces transitions sont particulièrement intéressantes pour les projections climatiques, car elles permettent d'estimer le taux de fonte des calottes glaciaires. Les données paléoclimatiques témoignent aussi d'événements plus rapides (quelques décennies), les "points de bascule", qui indiquent que le système climatique peut être déstabilisé significativement.

Les forages polaires sont uniques car ils fournissent une mesure directe de la composition atmosphérique passée et permettent la reconstruction du climat local. Mon doctorat s'est concentré sur le forage EPICA Dome C (EDC) en Antarctique de l'Est, qui fournit le plus long enregistrement continu à ce jour. Il documente les changements climatiques qui se sont produits à l'échelle de quelques décennies à plusieurs milliers d'années au cours des derniers 800 000 ans.

Alors que les isotopes de l'eau mesurés dans les archives glaciaires sont classiquement utilisés pour déduire les variations passées de la température et de précipitation locales, nous montrons que le $\delta^{15}\text{N}$ de N_2 mesuré dans les bulles d'air piégées dans la glace peut être utilisé de façon complémentaire. En effet, le $\delta^{15}\text{N}$ de N_2 reflète la profondeur de piégeage des bulles dans la glace, elle-même déterminée par la température et le taux d'accumulation de neige à la surface. Un nouvel enregistrement de $\delta^{15}\text{N}$ de N_2 est présenté. Il permet d'identifier précisément le phasage entre le CO_2 atmosphérique et le climat de l'Antarctique au cours des huit dernières déglaciations.

Deuxièmement, j'ai développé une chronologie cohérente pour quatre forages situés en Antarctique et un forage au Groënland, couvrant les 800 000 dernières années. Cette chronologie a été construite à l'aide du modèle probabiliste Paleochrono-1.1 et est contrainte par de nouvelles mesures faites sur le forage EDC et par des données issues de modélisation glaciologique. L'incertitude de l'échelle d'âge d'EDC est réduite de 1700 à 900 ans en moyenne. La chronologie révisée est en meilleur accord avec des chronologies absolues obtenues de manière indépendante pour d'autres paléo-archives.

Enfin, une méthodologie est proposée pour construire des chronologies cohérentes, relatives et absolues pour les archives marines et glaciaires au cours des sept dernières déglaciations. Elle permet d'identifier de manière plus précise l'ordre dans lequel se produisent les changements relatifs de l'insolation, de concentration atmosphérique en gaz à effet de serre, du niveau de la mer et des températures régionales lors des déglaciations. Dans une étude préliminaire, nous avons identifié une avance de quelques milliers d'années du CO_2 sur le niveau marin lors des déglaciations. Des perspectives de recherche sont proposées pour atteindre une meilleure compréhension des relations de cause à effet entre le forçage externe et la réponse interne du climat.

Mon travail de thèse a combiné la modélisation glaciologique et statistique, l'analyse expérimentale de l'air piégé dans la carotte de glace EDC ainsi que l'analyse de données

paléoclimatiques issues d'archives polaires, de carottes sédimentaires marines et de spéléothèmes. Mes recherches contribuent à l'amélioration (i) des reconstructions climatiques à partir des forages polaires et (ii) des chronologies des forages polaires et marins. Ces avancées sont essentielles pour mieux comprendre la réponse du climat à un forçage externe lors des changements climatiques de grande amplitude, ce qui est essentiel pour prévoir les changements climatiques à venir.